Cyclic Properties of Sand: Dynamic Behaviour for Seismic Applications

THÈSE N^{O} 4546 (2009)

PRÉSENTÉE LE 11 DÉCEMBRE 2009

À LA FACULTÉ ENVIRONNEMENT NATUREL, ARCHITECTURAL ET CONSTRUIT

LABORATOIRE DE MÉCANIQUE DES SOLS

PROGRAMME DOCTORAL EN MÉCANIQUE

ÉCOLE POLYTECHNIQUE FÉDÉRALE DE LAUSANNE

POUR L'OBTENTION DU GRADE DE DOCTEUR ÈS SCIENCES

PAR

Emilie RASCOL

acceptée sur proposition du jury:

Prof. J.-F. Molinari, président du jury
Prof. L. Vulliet, directeur de thèse
Prof. H. Di Benedetto, rapporteur
Prof. D. Muir Wood, rapporteur
Prof. J. Zhao, rapporteur

ÉCOLE POLYTECHNIQUE
FÉDÉRALE DE LAUSANNE

Suisse
2009

à mes parents,

à mon frère

Résumé

La propagation des ondes sismiques dans les sols granulaires peut induire des déformations de grande amplitude en cas de tremblements de terre de forte magnitude. Tous les mouvements sismiques ont un contenu fréquentiel variable, des amplitudes irrégulières, et trois différentes composantes dans des directions orthogonales. Dans ce contexte, l'objectif principal de cette recherche est de traiter des effets non-linéaires observés dans les sols granulaires soumis à de tels chargements complexes. Les hypothèses et les simplifications utilisées habituellement pour représenter le chargement sismique sont évaluées en se concentrant sur deux aspects principaux: (i) la fréquence de la contrainte cyclique appliquée à l'échantillon et (ii) la superposition de deux contraintes indépendantes. Pour cela, le comportement non-linéaire de deux sables différents, le Sable du Leman et le Sable de Fonderie, est exploré grâce à des tests triaxiaux cycliques et sismiques. Ces tests sont effectués en condition de chargement unidirectionnel ou bidirectionnel, pour des déformations de moyennes et grandes amplitudes, avec des fréquences correspondant à celles induites par les tremblements de terre.

Une presse triaxiale dynamique a été développée pour effectuer ces essais, sur des échantillons de sable secs ou saturés non-drainés. Les contraintes latérales et axiales peuvent être appliquées indépendamment avec de grandes amplitudes et de nombreuses formes de signaux dynamiques. Un système innovant de capteurs sans contact a été développé pour mesurer, en continu, le rayon de l'échantillon. Cet équipement se compose de trois capteurs lasers, installés autour de la cellule triaxiale et qui détectent la position de la surface de l'échantillon grâce à la triangulation optique. Les données mesurées sont traitées grâce à un système complexe de calibration, pour fournir au final l'évolution des déformations radiales à mi-hauteur de l'échantillon. La structure qui supporte les capteurs permet leur positionnement précis, et est équipée d'un mécanisme manuel de balayage vertical du profil de l'échantillon.

Des premiers tests triaxiaux sont effectués avec des chargements cycliques classiques pour caractériser le comportement des deux sables dans des conditions pseudo-dynamiques. Ces tests secs et saturés permettent de décrire la diminution de la rigidité et le développement d'un état de rupture, qui peut se produire par liquéfaction lorsque le sable est saturé non-drainé.

Des tests cycliques secs et non-drainés effectués sur le Sable du Leman à différentes fréquences de 0.1 à 6.5 Hz montrent que le comportement de ce matériau granulaire dépend de la fréquence. La rigidité du sol, qui prend des valeurs différentes selon l'état de contrainte imposé, semble influencer les effets de la fréquence de chargement sur le comportement du sol: lorsque la rigidité est faible, la réponse de l'échantillon est significativement amplifiée dans les basses fréquences (les amplitudes de déformation sont plus grandes, la pression interstitielle augmente plus, etc...) par rapport aux plus hautes fréquences testées. La forte sensibilité de ce sable aux effets de la fréquence pourrait être liée à l'angularité des grains constituant le Sable du Leman.

D'autres tests cycliques saturés non-drainés démontrent que la superposition de deux chargements indépendants, l'un axial et l'autre latéral (tests bidirectionnels), induisent des effets de couplage dans le comportement non-linéaire du sol. Les effets bidirectionnels entrainent une amplification de la réponse du sable jusqu'au développement de la liquéfaction cyclique. Le déphasage entre les contraintes axiales et latérales est le paramètre clé influençant le couplage. De plus, des tests unidirectionnels et bidirectionnels sont effectués pour des amplitudes irrégulières représentant un chargement sismique. Ils montrent que les conditions bidirectionnelles irrégulières influencent légèrement la réponse non-drainée du sable, avec des effets d'amplification très similaires aux tests cycliques bidirectionnels.

Les résultats expérimentaux cycliques sont finalement modélisés avec un modèle linéaire équivalent et avec un modèle élastoplastique à multi-mécanismes (ECP Hujeux). Les effets non-linéaires observés en laboratoire sont bien représentés par le modèle élastoplastique, en particulier (i) l'augmentation de l'amplitude des déformations qui mène à la liquéfaction cyclique du sable dense, et (ii) le couplage de la déformation avec la pression interstitielle. Le modèle linéaire équivalent donne une approximation rudimentaire du comportement cyclique non-drainé, même pour des déformations de moyenne amplitude, et n'est pas adapté à l'évaluation de la diminution de la rigidité observée dans nos tests cycliques.

Pour conclure, l'évaluation du comportement des sols granulaires sous chargement sismique nécessite de prendre en compte les aspects non-linéaires du comportement du sable, en terme de génération de pressions interstitielles et d'amplitudes de déformation. En particulier, le contenu fréquentiel et les chargements bidirectionnels influencent la réponse du sable pour des déformations moyennes à grandes. Ces résultats expérimentaux pourraient être pris en compte pour améliorer l'analyse des mouvements de terrain de forte amplitude. Ils constituent une contribution importante à la promotion de modélisations non-linéaires plus précises des effets de site dans les sables naturels.

Mots clés: chargement bidirectionnel; fréquence; tremblement de terre; test triaxial dynamique; sable; comportement non-linéaire; liquéfaction cyclique; modèle élastoplastique; modèle linéaire équivalent.

Abstract

Seismic wave propagation in granular soils can induce large strain amplitudes in case of strong earthquakes. Seismic motions are irregular in frequency content and in amplitude, and have three different components in orthogonal directions. In this context, the main objective of this PhD research deals with nonlinear effects observed in granular soils under such complex loadings. The assumptions and simplifications usually considered for representing seismic loadings are evaluated, focusing on two main aspects: (i) cyclic stress frequency applied to the sample (ii) superposition of two independent stresses. For that purpose, the nonlinear behaviour of two different sands, Leman Sand and Fonderie Sand, is explored with cyclic and seismic triaxial tests. These tests are performed with unidirectional or bidirectional loadings, at medium to high strain amplitude, and in the earthquake frequency range.

A dynamic triaxial press was developed to perform such tests, with dry and undrained saturated sand samples. Axial and lateral stresses can be applied independently with large amplitudes for various loading shapes. An innovative non-contact measurement technique was developed to continuously monitor the sample radius; this testing equipment is based on three laser sensors, set up around the triaxial cell, which detect the position of the sample surface thanks to optical triangulation. The obtained data are processed through a complex calibration system to provide the radial strain evolution at mid-height of the sample. The mounting structure supporting the sensors allows precise positioning and is equipped for manual vertical scanning of the sample profile.

The first triaxial tests are performed with classical cyclic loadings, to characterize the behaviour of the two sands in pseudo-dynamic conditions. These dry and undrained saturated tests allow to describe the decrease of stiffness which leads to failure of the sand sample. Failure of undrained saturated sand occurs by liquefaction.

Dry and undrained cyclic tests performed on Leman Sand at various frequencies from 0.1 to 6.5 Hz show that the behaviour of this granular material is frequency-dependent at medium to large strains.

Sand stiffness, which depends on stress conditions, seems to influence the extent of frequency effects on soil behaviour: for tests with lower stiffness, the soil response to low frequency is significantly amplified (i.e. higher strain amplitude, more pore pressure increase, etc...) compared to the high frequency range. The overall rate-sensitivity may be enhanced by the angularity of the grains.

Other cyclic undrained saturated tests on Leman Sand demonstrate that the superposition of two different loadings, one axial and one lateral (bidirectional tests), induce coupling effects in the nonlinear soil response. Bidirectional effects result in an amplification of the sand response until the occurrence of cyclic liquefaction. The phase angle between axial and lateral stresses is the key parameter influencing the coupling. Moreover, the comparison between unidirectional and bidirectional irregular seismic loadings show that bidirectional conditions slightly influence undrained sand response, with conditions of amplification very similar to cyclic tests.

Experimental results are finally modelled with the linear equivalent method and with a multi-mechanism elastoplastic model (ECP Hujeux). Nonlinear effects observed in laboratory experiments, and particularly the increase of strain amplitude leading to cyclic liquefaction of dense sand, are well captured by the elastoplastic model. The linear equivalent method gives a very crude approximation, even at medium strain level, and is not suitable for accurate evaluation of stiffness degradation observed during our cyclic tests.

To conclude, assessing the behaviour of granular soils under earthquake loadings requires to take into account the nonlinear features of sand behaviour in terms of pore pressure generation and strain amplitude. In particular, frequency content and bidirectional loadings influence the sand response for medium to large strains. These experimental results could be considered for improving the analysis of strong ground motions. They constitute an important contribution for promoting more accurate nonlinear modelling of site effects in natural sands.

Key words: bidirectional loading; frequency; earthquake; dynamic triaxial test; sand; nonlinear behaviour; cyclic liquefaction; elastoplastic model; linear equivalent model.

Remerciements

Chaleureux merci tout d’abord à mon directeur de thèse, le Professeur Laurent Vulliet, pour m’avoir guidée dans ce travail de thèse. Je salue la justesse et la pertinence de ses conseils, et je tiens à le remercier pour la liberté qu’il m’a laissée pour mener à bien ce travail, et pour sa confiance répétée en mon jugement.

Mes remerciements vont ensuite aux membres de mon jury de thèse, les Professeurs Zhao, Di Benedetto et Muir Wood, pour avoir accepté de me faire l’honneur d’être les rapporteurs de ma thèse. Merci également au Professeur Molinari d’avoir accepté de présider le jury de thèse.

Le soutien du Professeur Lyesse Laloui, directeur du Laboratoire de Mécanique des Sols, m’a permis de réaliser mon doctorat dans d’excellentes conditions. Je tiens à le remercier pour son accueil et ses conseils précieux.

J’ai eu la chance de rencontrer des chercheurs talentueux, qui m’ont donné conseils, commentaires positifs et idées pour avancer: Dr. Jean-François Semblat, Prof. Arézou Modaressi, Dr. Stanislav Lenart, Dr. Luca Lenti et certainement quelques autres. Un merci spécial à Dr. Clotaire Michel, qui a été mon expert en sismologie.

Je remercie ensuite les personnes qui m’ont aidé à venir à bout des nombreux essais en laboratoire que j’ai dû effectuer. Merci de tout coeur à Gilbert Gruaz, Patrick Dubey et Laurent Gastaldo pour leurs conseils et leur disponibilité. Merci à Jean-Marc Terraz, super mécanicien, qui a donné forme à toutes les concepts que j’ai pu imaginer. Merci aussi aux apprentis, Jérôme, Qazim et Samuel. Je remercie également l’équipe de Temeco, qui m’a aidée à maîtriser la presse dynamique, Messieurs Conrad Keiser et Beat Renner. Concernant les lasers, je remercie Beat Rudolf et Peter Bischoff pour l’intérêt qu’ils ont porté à mon projet. Merci aussi à Irina Andria-Ntoanina et François Huot pour leurs conseils.

Merci à «mon stagiaire» Emad Jahangir, pour le courage dont il a fait preuve et les bons résultats expérimentaux qu’il a obtenus avec le Sable de Fonderie.

Pour le support technique, je n’oublie pas les informaticiens du laboratoire, Laurent et Thierry, et merci aussi à Nicolas et Stefano ainsi qu’à leurs apprentis. Merci aux secrétaires de choc, Karine Barone, Antonella Simone et Rosa-Ana Menendez, ainsi qu’à Anh Le. J’en profite aussi pour reconnaître la disponibilité de Jean-Paul Dudt et la convivialité de Gilbert Steinmann, et je n’oublie pas Messieurs Jean-François Mathier et Vincent Labiouse.

Merci à tous les doctorants et post-docs du LMS et LMR. Certains m’ont particulièrement aidé au niveau scientifique, en discutant ou simplement en m’écoutant quand j’en avais besoin. Je pense particulièrement à Simon, Mathieu, et Rafal. Un grand merci à mes collègues de bureau, qui se sont relayés pour donner une ambiance de travail toujours conviviale : Nina Mattsson, Yonggeng Ye, Marta Rizzi, Davide Ceresetti et Yanyan Duan. Merci aux collègues et amis, qui ont tous participé à l’ambiance chaleureuse de ces quelques trois ans et demi : Rafal Obrzud, Suzanne Fauriel, Mathieu Nuth, Bertrand François, Simon Salager, Azad Koliji, Irene Manzella, Federica Sandrone, Hervé Péron, Claire Silvani, Raphaël Rojas, Thibaud Meynet, Alessio Ferrari, sans oublier Andréa Battiato, Ma Hongsu, Claire Sauthier, Jacopo Abbruzzese et Tohid Kazerani. Je pense aussi aux moitiés, tellement importantes pour les bières à Sat’ et les barbecues : Jennifer, Anne-Christine, Jonathan, Solène, Stefano, Ewa, Azin, Véronique, Paul, Marco. Merci aussi à mes alpinistes préférés, Valérie et Yannick. Une mention spéciale pour John Eichenberger, qui a produit des efforts très appréciés de soutien moral durant les derniers mois de la thèse.

Merci à mes amis de France, ceux qui sont venus jusqu’à Lausanne et aussi ceux avec qui j’ai pu passer des week-ends et vacances françaises tellement sympathiques. Je pense particulièrement à Mohamed, à Cécile, aux nantais et aux «filles».

Pour finir, un gros merci collectif à ma famille, qui m’a encouragé et donné la possibilité d’en arriver là. Merci aussi pour votre compréhension, et pour le soutien que vous m’avez apporté.

Cette recherche a été financée principalement par le Fonds National Suisse de la Recherche Scientifique, bourse n°200021-108174.

Table of Contents

RÉSUMÉ i

ABSTRACT iii

REMERCIEMENTS v

LIST OF SYMBOLS xv

CHAPTER 1. INTRODUCTION 1

1.1 General framework 2
1.2 Objectives 3
1.3 Structure of the thesis 4

CHAPTER 2. DYNAMIC GRANULAR SOIL BEHAVIOUR 5

2.1 Introduction 6
2.2 The dynamic problem 6
2.2.1 Cyclic, dynamic and static load 6
2.2.2 Nature of dynamic loadings 8
2.3 Geotechnical earthquake engineering 9
2.3.1 Introduction to geotechnical earthquake engineering 9
2.3.2 Seismic hazard in Switzerland 10
2.3.3 Earthquake characterization 10
2.3.4 Seismic wave propagation 13
2.3.5 Site effects 15

2.4 Introduction to soil behaviour under cyclic loading 17
2.4.1 Effective stress 17
2.4.2 Notations of stress and strain 17
2.4.3 Monotonic loading in triaxial compression and triaxial extension 21
2.4.4 Critical state and steady state 22
2.4.5 Dilatancy and phase transformation in granular media 23
2.4.6 Qualitative soil response to cyclic loading 24
2.4.7 Effect of the number of cycles 26
2.4.8 Link between cyclic behaviour and dilatancy 26
2.4.9 Strain range dependency of cyclic soil behaviour 27
2.4.10 Volumetric cyclic threshold shear strain and stiffness degradation 28
2.4.11 Pore water pressure increase in undrained saturated conditions 28
2.4.12 Definition of failure 29
2.4.13 Liquefaction and cyclic softening 30
2.4.14 Conclusions 37
2.5 Dynamic material parameters 38
2.5.1 Secant shear modulus 38
2.5.2 Damping ratio 39
2.5.3 Strain dependency of dynamic parameters 44
2.5.4 Evaluation of the elastic shear modulus 46
2.5.5 Factors influencing the secant shear modulus and damping ratio 47
2.6 Constitutive modelling of granular soils for cyclic loading 50
2.6.1 Introduction 50
2.6.2 Linear elastic model 50
2.6.3 Linear viscoelastic model 51
2.6.4 Linear equivalent model 51
2.6.5 Elastoplastic models 53
2.6.6 Domain of application 57
2.7 Rate effects in granular materials 59
2.7.1 Phenomenons involved in time-dependent sand behaviour 59
2.7.2 Interpretation of rate effects 60
2.7.3 Influence of viscous behaviour on cyclic loading 61
2.7.4 Time-dependency in granular media from laboratory experiments 61
2.7.5 Constitutive modelling and numerical approach of rate effects in sand 65
2.7.6 Conclusions 66
2.8 Superposition of loadings 67
2.8.1 Introduction 67
2.8.2 Laboratory experiments 67

2.8.3 Multidirectional site effect analyses 69
2.8.4 Conclusions 70
2.9 Irregular loading of sand under seismic motion 70
2.9.1 Introduction 70
2.9.2 A few laboratory studies 70
2.9.3 Use of test data for design purposes 73
2.9.4 Summary 74
2.10 Conclusions 74

CHAPTER 3. CYCLIC TRIAXIAL EXPERIMENTS 77

3.1 Dynamic measurement techniques 78
3.1.1 Introduction 78
3.1.2 Laboratory testing 78
3.1.3 Conclusions 85
3.2 Experimental device for cyclic triaxial loading 85
3.2.1 Description of the cyclic triaxial press 85
3.2.2 Stress and strain states of the sample 92
3.2.3 Laser-based measurement of radial strains 95
3.3 Validation tests 115
3.4 Experimental procedures 116
3.4.1 Sand sample mounting 116
3.4.2 Saturation 119
3.4.3 State of the sample for cyclic shear 119
3.5 Soil characteristics 119
3.5.1 Leman Sand 119
3.5.2 Fonderie Sand 120
3.6 Conclusions 121

CHAPTER 4. CHARACTERIZATION OF NONLINEAR SAND BEHAVIOUR WITH MONOTONIC AND CYCLIC TRIAXIAL TESTS 123

4.1 Introduction 124
4.2 Monotonic tests on Leman Sand 125
4.2.1 Presentation 125
4.2.2 Description of typical test results in compression and extension 126
4.2.3 Summary of observed monotonic behaviour of dense Leman Sand 129
4.2.4 Phase transformation lines 129

4.2.5 Behaviour at large strain 131
4.2.6 Comments and conclusions on the monotonic results 131
4.3 Preliminary undrained cyclic triaxial tests 132
4.3.1 Introduction 132
4.3.2 Typical stress-controlled test results 133
4.3.3 Effect of loading conditions 136
4.3.4 Conclusions 139
4.4 Detailed description of cyclic undrained tests on Leman Sand for small to large strains 140
4.4.1 Introduction 140
4.4.2 Example of a cyclic test with failure by cyclic liquefaction 141
4.4.3 Excess pore pressure increase 143
4.4.4 Comparison of criterion for failure 143
4.4.5 Small strain secant shear modulus 147
4.4.6 Analysis of the Gsec - g curve 148
4.4.7 Evolution of the damping ratio with the number of cycles 149
4.4.8 Analysis of the D - g curve 151
4.4.9 Effect of the initial state 151
4.4.10 Discussion 152
4.4.11 Conclusions 153
4.5 Nonlinear Fonderie Sand behaviour in undrained saturated conditions 154
4.5.1 Introduction 154
4.5.2 Summary of monotonic behaviour 155
4.5.3 Overview of cyclic test results and failure with Fonderie Sand 155
4.5.4 Excess pore pressure ratio increase in cyclic tests with stress reversal 160
4.5.5 Dynamic parameters 161
4.5.6 Discussion 165
4.5.7 Summary 165
4.6 Evaluation of the laser measurement technique with an undrained test 166
4.6.1 Presentation 166
4.6.2 At medium to large strain 167
4.6.3 At small to medium strain 169
4.6.4 Conclusions 172
4.7 Dry cyclic triaxial tests on Leman Sand 173
4.7.1 Introduction 173
4.7.2 Presentation of a typical dry cyclic triaxial test 173
4.7.3 Effect of initial conditions on strain accommodation and failure 177
4.7.4 Volumetric behaviour 179

4.7.5 Secant shear modulus 181
4.7.6 Comparison with undrained test results 183
4.7.7 Damping ratio 183
4.7.8 Induced anisotropy 184
4.7.9 Conclusions 185
4.8 Shear strain localization in cyclic tests at large strain amplitude 186
4.8.1 Tests concerned 186
4.8.2 Direct observation of shear strain localization with laser sensors 187
4.8.3 Consequences on test results 188
4.8.4 Conclusions 189
4.9 Summary 190

CHAPTER 5. FREQUENCY EFFECTS IN LEMAN SAND 193

5.1 Introduction 194
5.2 Monotonic undrained conditions 194
5.2.1 Tests characteristics 194
5.2.2 Results 195
5.2.3 Discussion 197
5.2.4 Conclusions 197
5.3 Preliminary cyclic tests 198
5.3.1 Presentation of the tests 198
5.3.2 Cyclic test results 199
5.3.3 Conclusions 200
5.4 Frequency effect in undrained conditions at medium strain level 203
5.4.1 Presentation 203
5.4.2 Frequency effect on tests characteristics 204
5.4.3 Discussion 210
5.4.4 Conclusions 212
5.5 Frequency effect in cyclic dry conditions 212
5.5.1 Test presentation 212
5.5.2 Frequency effect on dry Leman Sand test results 213
5.5.3 Discussion 217
5.5.4 Conclusions 218
5.6 Discussions on rate effect in Leman sand 219
5.6.1 Experimental artefacts 219
5.6.2 Physical interpretation and general comments 220
5.7 Conclusions 222

CHAPTER 6. EFFECT OF MULTIDIRECTIONAL AND IRREGULAR STRONG LOADINGS 223

6.1 Introduction 224

6.2 Multidirectional effects on cyclic behaviour 225

6.2.1 Tests characteristics and examples 225
6.2.2 Introduction to test results 230
6.2.3 Stress-strain relation 230
6.2.4 Deviatoric strain amplitude 230
6.2.5 Number of cycles to failure 232
6.2.6 Effective stress paths 233
6.2.7 Excess pore pressure 234
6.2.8 Multidirectional effects on dynamic parameters 236
6.2.9 Analyses of multidirectional effects 239
6.2.10 Conclusions 242

6.3 Irregular seismic loading in multidirectional condition 243

6.3.1 Description of irregular loadings with a seismic signal 243
6.3.2 Description of stress paths 247
6.3.3 Deviatoric strains 248
6.3.4 Stress-strain relation 251
6.3.5 Pore pressure increase 251
6.3.6 Discussion on seismic bidirectional triaxial tests 253
6.3.7 Conclusions 257

6.4 Comments on bidirectional and irregular effects 258

6.4.1 Effect of complex loadings on nonlinear soil behaviour 258
6.4.2 Physical interpretation 259
6.4.3 Consequences for modelling and design purposes 260

6.5 Conclusions 260

CHAPTER 7. CONSTITUTIVE MODELLING OF CYCLIC SAND BEHAVIOUR 263

7.1 Introduction 264

7.2 Cyclic modelling of Leman Sand with a viscoelastic linear equivalent analysis 265

7.2.1 Introduction 265
7.2.2 Description of the procedure for linear equivalent simulations 265
7.2.3 Results 268
7.2.4 Effect of frequency and complex loading in the linear equivalent model 271

7.2.5 Discussion 272
7.2.6 Summary 272
7.3 Behaviour of Leman Sand with a multi-mechanism elastoplastic constitutive law 273
7.3.1 Introduction 273
7.3.2 Model calibration 273
7.3.3 Results 276
7.3.4 Discussion 286
7.3.5 Summary 287
7.4 Comparison and evaluation of the models 288
7.5 Conclusions 290

CHAPTER 8. CONCLUSIONS AND PERSPECTIVES 291

8.1 Achievements 292
8.1.1 Developments of laboratory equipment 292
8.1.2 Cyclic dense sand behaviour 293
8.1.3 Frequency-dependence of granular materials 294
8.1.4 Effect of cyclic bidirectional conditions on undrained sand behaviour 295
8.1.5 Seismic unidirectional and bidirectional loading 296
8.1.6 Modelling the cyclic behaviour of dense sand 296
8.2 Outlook 297

REFERENCES 299

Appendix 1. In situ testing for the evaluation of dynamic soil behaviour 1

Appendix 2. Determination of deviatoric and confining stresses from seismic acceleration recordings 7

Appendix 3. Additional results: modelling of an undrained cyclic test with the elastoplastic model 13

Appendix 4. Test data are provided in a CD-ROM

List of symbols

Roman Symbols

1D, 2D, 3D	multidimensional (Chapter 2).
1D	unidirectional.
2D	bidirectional.
a	function of the Hujeux model which appears in the calculation of the degree of plastification (Eq. 2.49).
a, a'	slope of the two bisectors which define the centre of the sample for the calculation of the radius with laser sensors (Eq. 3.7 and Eq. 3.8).
A	empirical parameter for the determination of G_{max} (Eq. 2.36).
a_{cyc}	parameter of the Hujeux model for the cyclic part of the hardening law of deviatoric mechanisms.
a_i	model parameter for the empirical evaluation of G_{max} (Eq. 4.2).
A_{loop}	area of the stress - strain loop in the ε_q - q plane.
A'_{loop}	area of the stress - strain loop in the ε_1 - q plane.
a_m	parameter of the Hujeux model for the monotonic part of the hardening law of deviatoric mechanisms.
b	parameter of the Hujeux model for the shape of the yield surface (Eq. 2.47).
b, b'	intercept point of the bisectors which define the centre of the sample for the calculation of the radius with laser sensors (Eq. 3.7 and Eq. 3.8).
B coefficient	Skempton's B coefficient, which indicates the degree of saturation of the soil sample (B = 1 involves full saturation).
B_1	in-phase bidirectional loading (straight line in the p - q plane).
B_2	out-of-phase bidirectional loading (oval shape in the p - q plane).
b_i	model parameter for the empirical evaluation of G_{max} (Eq. 4.2).

c	volumetric hardening parameter of the Hujeux model (Eq. 2.51).
c	viscous damping (section 2.6.2).
C	centre of the circle defined from the three points measured by laser sensors.
c_c	critical damping coefficient (section 2.6.2).
c_{cyc}	volumetric hardening parameter of the Hujeux model for cyclic loading.
c_m	volumetric hardening parameter of the Hujeux model for monotonic loading.
CM test	irregular unidirectional triaxial test with the maximum stress in compression.
c_p	velocity of P wave.
CPT	cone penetration test.
c_s	velocity of S wave.
CSR	cyclic stress ratio.
CSR^{EQ}	maximum cyclic stress ratio in irregular loading.
CTC	conventional triaxial compression.
C_w	compressibility of water.
d	parameter of the isotropic hardening law for the Hujeux model.
d	displacements (1*3) (Chapter 2).
D	damping ratio.
D	rigidity tensor (6*6 for the matrix formulation of Hooke's law).
d_{60}	diameter of the sieve which lets pass 60% of the soil mass.
DA	double amplitude.
d_{ext}	external measure of the vertical displacement in the dynamic press.
DI	degradation index.
d_{int}	internal measure of the vertical displacement in the dynamic press.
D_{min}	small strain damping ratio.
e	deviatoric strain tensor (3*3 matrix) (Chapter 2).
e or e_0	void ratio.
E	Young's modulus.
E^*	Anisotropic Young's modulus, equal to E_v.
E_h, E_v	Anisotropic Young's moduli in the horizontal and vertical direction.

EM test	irregular unidirectional triaxial test with the maximum stress in extension.
e_{max}, e_{min}	maximum and minimum void ratios.
ep	thickness of membrane and paint layer in the laser calibration function.
E_{sec}	secant Young's modulus.
f	frequency.
F	force exerted on the SDOF system in forced harmonic vibrations (section 2.6.2).
F_{ax}	axial force applied to the loading bar of the dynamic press.
F_c	compacity function (Eq. 2.36 and Eq. 2.37).
f_{ext}	body forces.
FFT	Fast Fourier transform.
f_{iso}	isotropic yield limit of the Hujeux model.
f_k	yield limit of the deviatoric mechanism k of the Hujeux model.
F_k	function included in the yield limit of the deviatoric mechanism k of the Hujeux model (Eq. 2.47).
g	gravity acceleration.
G	shear modulus.
G^*	complex modulus.
GDS	laboratory equipment company (http://www.gdsinstruments.com/).
G_{max}	small strain or maximum shear modulus.
G_{ref}	reference value of the shear modulus in the elastoplastic Hujeux model (definition in Eq. 2.43).
G_{sec}	secant shear modulus.
G_{sec}^N, G_{sec}^1	secant shear modulus at the N^{th} cycle and 1^{st} cycle.
I_{2D}	second unvariant of the strain tensor.
i_c	critical refraction angle in seismic refraction.
I_D	relative density.
J_{2D}	second unvariant of the stress tensor.
k	stiffness (section 2.6.2).
k	empirical soil parameter for the determination of G_{max} (Eq. 2.36).
k	Darcy permeability.

K_0	coefficient of earth at rest.
K_b	bulk modulus.
KC, LC	two bisectors which meet at the centre *C* of the sample (calculation of the radius with laser sensors).
K_{max}	small strain bulk modulus (Hujeux model).
K_{ref}	reference value of the bulk modulus in the elastoplastic Hujeux model (definition in Eq. 2.43).
L	coefficient of reduction between the maximum strain measured by laser sensors and the average strain over the height of the sample.
LVDT	Linear Variable Differential Transformer, displacement sensor.
m	soil parameter of the Hujeux model for the hysteretic domain.
m	mass (section 2.6.2).
M_{ax}	moment applied to the loading bar of the dynamic press.
M_c	slope of the steady state line in compression.
M_e	slope of the failure line in extension.
M_{inst}	slope of the instability line in the *p'* - *q* plane (Chapter 2).
M_{PT}	slope of the phase transformation line in the *p'* - *q* plane.
M_{PTc}	slope of the phase transformation line in compression.
M_{PTe}	slope of the phase transformation line in extension.
MR_1	measuring range of the laser sensor in the air (normal conditions).
MR_2	measuring range of the laser sensor through the cell glass window and water layer.
m_{ref}	laser measurement of the three points at the surface of the reference steel cylinder for the calibration function (1*3).
M_{SS}	slope of the stead state line in the *p'* - *q* plane.
Mw	moment magnitude of an earthquake.
n	porosity.
N	number of cycles.
N	scale reduction number in centrifuge tests (Chapter 3).
n_1, n_2, n_3	refractive index of air, glass and water (Chapter 3).
N_1, N_2, N_3	coordinates of the three points at the sample surface, calculated from the laser measurements at any time (1*2).
N_I	number of SPT blowcount (Chapter 3).

N_{crit}	critical cycle, during which flow liquefaction occurs (Chapter 2).
n_e	empirical adimentional parameter for the stress-dependency of elastic moduli.
N^f	number of cycles at failure for the criterion based on strain amplitude threshold.
N^{fd}	number of cycles at failure for the criterion based on *DI* threshold.
N^{fu}	number of cycles at failure for the criterion based on pore pressure threshold.
OCR	overconsolidation ratio.
p and *p'*	mean total and effective stress in triaxial conditions, also called spherical stress.
P wave	compressional wave.
p'_c	preconsolidation pressure in the Hujeux model.
p'_{c0}	initial preconsolidation pressure in the Hujeux model.
PGA	peak ground acceleration.
PIDR	proportional, integrative, derivative and las gain in the motion regulation system of the dynamic press (Chapter 3).
PI	plasticity index.
p'_k	mean effective stress of the deviatoric mechanism *k* in the Hujeux model.
p_{ref}	reference value of the spherical stress (1 MPa).
PT	phase transformation.
PU	polyurethane cylinder.
q	deviatoric stress in triaxial conditions.
Q	quality factor (Chapter 2).
q_{av}	mean / initial deviatoric stress.
q_k	deviatoric stress in the deviatoric mechanism *k* (Hujeux model).
r	radius of the wave front (Chapter 2).
r	radius of the reference steel cylinder (Chapter 3)
R	radius of the soil sample, measured at all time steps by the laser sensors.
R_0	initial radius of the soil sample, measured at the beginning of each loading by the laser sensors.
R_1	shape of the stress path corresponding to unidirectional loading of CTC and RTE type.
R_1, R_2, R_3	coordinates of the reference cylinder for laser calibration in Eq. 3.5 and Eq. 3.6.
R_2	shape of the stress path corresponding to hydrostatic compression (horizontal line

	in the p - q plane).
r_d	stress reduction factor to calculate seismic loadings (section 2.10).
REV	representative elementary volume.
r_{iso}	degree of plastification of the isotropic mechanism (Hujeux model).
r_{iso}^{ela}	radius of the elastic domain of the isotropic mechanism (Hujeux model).
r_k	degree of plastification of the deviatoric mechanism k (Hujeux model Eq. 2.48).
r_k^{ela}	radius of the elastic domain of the deviatoric mechanism k (Hujeux model).
r_k^{hys}	radius of the hysteretic domain of the deviatoric mechanism k (Hujeux model).
r_k^{mob}	radius of the mobilized domain of the deviatoric mechanism k (Hujeux model).
RTE	reduced triaxial extension.
S	surface of the cylindrical sample.
S wave	shear wave.
SASW	geophysical test, spectral analysis of surface waves.
SDOF	single degree of freedom.
SH wave	horizontal plane component of the shear wave.
SPT	standard penetration test.
SS	steady state.
std	standard deviation.
SV wave	vertical plane component of the shear wave.
t	deviatoric part of the stress tensor (Chapter 2) (3*3 matrix).
t	time.
u	pore water pressure.
u_0	amplitude of the displacement in the forced SDOF system (section 2.6.2).
u_r	pore (water) pressure ratio.
$u_{r,m}$	Maximum pore (water) pressure ratio during one cycle.
u_r^{comp}	pore pressure ratio resulting from the radial stress (defined in Eq. 6.2).
u_r^q	pore pressure ratio resulting from the axial stress (defined in Eq. 6.3).
$u, \dot{u}, \ddot{u}$	displacement, velocity, acceleration (Chapter 2, Eq. 2.1 and Eq. 2.29).
V	volume of the sample or domain.

V_1, V_2	velocity of wave propagation in seismic refraction method (Fig. 3.7).
W	work.
W_D	energy dissipated during one cycle (section 2.6.2).
W_S	maximum elastic stored energy (section 2.6.2).
x_1, x_2, x_3	coordinate on the x-axis of the points N_1, N_2 and N_3 (laser calibration).
x	equivalent laser measurement in the air (real distance).
X, Y	coordinates of the centre C of the sample (calculation of the radius with laser sensors).
xr	laser measurement through the cell glass window and the water layer.
y_1, y_2, y_3	coordinate on the y-axis of the points N_1, N_2 and N_3 (laser calibration).
z	depth.

Greek Symbols

α	dilatancy coefficient of the Hujeux model (associated flow rule when $\alpha = 1$).
α	angle of diffuse reflection of the laser beam in the air (Fig. 3.21a).
α, β, γ	incident and refracted angles in the air, glass and water (Fig. 3.21b).
α^*	Anisotropy coefficient.
α_k	function defining the degree of mobilization of the deviatoric mechanism k, depending on r_k (Hujeux model).
β	plastic compressibility of the soil (Hujeux model).
δ	angle if internal friction (Chapter 2).
δc_1	uncertainty on the scaling coefficient Γ for calibration of laser sensors.
δc_2	uncertainty on the effect of the confining pressure on the calibration of laser sensors
δc_3	uncertainty on the position of the reference cylinder for calibration of laser sensors.
$\delta \Delta R$	uncertainty on the variation of the sample radius during a cyclic test.
$\delta \varepsilon_{3,l}$	uncertainty on the local radial strain measured with laser sensors.
$\delta \varepsilon_{3,m}$	uncertainty on the radial strain averaged over the sample.

δi_1	uncertainty on the vertical misalignment due to scanning procedure of laser sensors.
δl_1	uncertainty on the thickness of the paint layer.
δl_2	uncertainty due to the transmission of the laser beam through interfaces.
δR	uncertainty on the sample radius measured by laser sensors.
$\delta\theta$	uncertainty on the angular horizontal and vertical misalignment of the position of the laser.
$\Delta\varepsilon$, Δe	general increment of the strain tensor and of the deviatoric part of the strain tensor (3*3 matrix) (Eq. 2.16).
$\Delta\varepsilon_1$, $\Delta\varepsilon_3$, $\Delta\varepsilon_q$, $\Delta\varepsilon_V$	general increment of the axial, radial, deviatoric and volumetric strain (Eq. 2.16 and Eq. 2.17).
$\Delta\varepsilon_1$, $\Delta\varepsilon_3$	axial and radial strain amplitude in sinusoidal loading (simple amplitude).
$\Delta\varepsilon_q$	deviatoric strain amplitude in sinusoidal loading (simple amplitude).
$\Delta\varepsilon_v$	volumetric strain amplitude in sinusoidal loading (simple amplitude).
$\Delta p'$, Δq, $\Delta\sigma_3'$	general increment of the spherical stress, deviatoric stress and effective confining pressure (Eq. 2.9).
Δq	deviatoric stress amplitude in sinusoidal loading (simple amplitude).
$\Delta p'$	spherical stress amplitude in sinusoidal loading (simple amplitude).
ΔR	variation of the sample radius during a cyclic test.
$\Delta\sigma_3$, $\Delta\sigma_3'$	total and effective confining pressure amplitude in sinusoidal loading (simple amplitude).
$\Delta\sigma_3^{EQ}$	maximum amplitude of confining pressure during seismic loading.
$\Delta\sigma_{ij}'$, Δt_{ij}	general increment of the stress tensor and of the deviatoric part of the stress tensor (3*3 matrix) (Eq. 2.9).
$\Delta\tau$	shear stress amplitude in sinusoidal loading (simple amplitude).
Δu	excess pore water pressure.
$\bar{\varepsilon}$	strain tensor (3*3 matrix).
ε_1	axial strain.
$\dot{\varepsilon}_1$	axial strain rate for monotonic (strain-controlled) loading at constant strain rate.
ε_3	radial strain.
$\varepsilon_{3,l}$	local radial strain calculated from the sample measure at mid-height.
$\varepsilon_{3,m}$	mean radial strain averaged over the total sample height.
ε_q	deviatoric strain.

$\dot{\varepsilon}_q$	mean deviatoric strain rate, defined Eq. 5.1.
$\dot{\varepsilon}_q^{max}$	maximum deviatoric strain rate over the cycle.
$\varepsilon_{q,k}^{p}$	plastic component of the deviatoric strain induced by the deviatoric mechanism *k*.
ε_v	volumetric strain.
ε_V^p	volumetric plastic strain (Hujeux model).
$\varepsilon_{v,iso}^{p}$	volumetric plastic strain induced by isotropic mechanism (Hujeux model).
$\dot{\varepsilon}_{v,k}^{p}$	rate of increase of the volumetric plastic strain induced by the deviatoric mechanism *k*.
ϕ'	effective friction angle mobilized at critical state.
ϕ_{PT}	friction angle mobilized at phase transformation.
ϕ_{SS}	friction angle mobilized at steady state.
γ	shear strain.
Γ	scaling coefficient obtained from the laser calibration procedure for transforming the measured value into the real distance.
γ_w	volumetric weight of water.
γ_{tv}	volumetric cyclic threshold shear strain.
η	loss factor (Chapter 2).
κ	Slope of the elastic isotropic compression line in the *e* - ln(*p'*) plane (Eq. 7.1).
λ	Lamé coefficient.
λ_c	Slope of the virgin isotropic compression line in the *e* - ln(*p'*) plane (Eq. 7.1).
λ^{iso}	plastic multiplier of the isotropic mechanism (Hujeux model).
$\dot{\lambda}_k^p$	plastic multiplier of the deviatoric mechanism *k* (Hujeux model).
λ_w	wave length .
μ	Lamé coefficient.
ν	Poisson's ratio.
ν^*	Anisotropic Poisson's ratio.
ρ	soil density.
$\bar{\sigma}$	stress tensor (3*3 matrix).
σ'	effective stress tensor (3*3 matrix).
$\sigma_1,\ \sigma_1'$	total and effective vertical (principal) stress in triaxial conditions.

$\sigma_3,\ \sigma_3'$	total and effective confining pressure (lateral principal stress in triaxial conditions).
$\sigma_3'^0$	initial effective confining pressure.
σ_3^0	mean confining pressure (bidirectional tests).
σ_n	normal stress.
σ_t, σ_t'	total and effective overburden pressure.
σ_V', σ_H'	effective vertical and horizontal stress for in situ conditions.
τ	shear stress.
ω	angular frequency.
ω_0	natural angular frequency (section 2.6.2).
$\bar{\omega}$	harmonic angular frequency in the forced *SDOF* system (section 2.6.2).
ψ	dilatancy angle (Hujeux model).
Ψ	specific damping capacity (Chapter 2).
ζ	phase angle.

Operators

:	inner product of tensor with double contraction.
d(.)	incremental value.
$\dot{x} = \frac{\mathrm{d}(x)}{\mathrm{d}t}$	temporal derivative of the variable *x*.
δ_{ij}	Kronecker delta type function, $\delta_{ij} = 1$ if $i = j$ and $\delta_{ij} = 0$ otherwise.

Nota Bene: Throughout this dissertation, the sign convention is the usual convention in soil mechanics, i.e. compression is positive.

CHAPTER 1

INTRODUCTION

1.1 General framework

Soil dynamics is a special branch of geotechnical engineering which has important consequences on mitigation of seismic risks. Actually, the developments of soil dynamics over the last decades were motivated by the occurrence of catastrophic seismic events. Ground motion itself may not be a major threat, but it is the main triggering phenomenon of most seismic hazards, like building collapse among the most dramatic cases. A well-known consequence of strong ground motion is liquefaction, which is the total loss of strength of the granular medium. Another major issue is the stability of slopes and of earth structures subjected to seismic loading.

Ground shaking results from the travelling of seismic waves through the earth's crust and through the upper rock and soil layers. Looking at a particular area, the intensity of surface motion highly depends on the magnitude of the earthquake associated to the mechanical properties of the ground material. Indeed, local amplification of the ground surface acceleration can occur as a result of disadvantageous soil properties. This phenomenon, called site effects, should be accurately taken into account to guarantee a safe design of foundations, structures and buildings. From that point of view, it is crucial to be able to evaluate soil behaviour in conditions of strong and transient loading characterising ground motions during large earthquakes.

The behaviour of granular materials subjected to dynamic loading remains not fully understood, and is currently the subject of interesting research worldwide. Advanced laboratory testing techniques are specifically developed to understand and characterise soil response to dynamic loading. Numerical tools as well are adapted to this particular problem, to solve complex multi-physics equation systems.

Site effects being a significant part of the estimation of earthquake hazard, specific tools are developed for modelling dynamic soil behaviour. Some of them are now used in engineering problems; they should be carefully evaluated and can be improved to take into account new knowledge issued from the research community.

The idea behind this research project is to produce high quality laboratory test results on dynamic soil behaviour, which are directly applicable to strong earthquake motion and in particular for modelling site effects. This means that the tests are performed in conditions close to in situ soil layers subjected to strong seismic waves, where stress amplitudes are large and irregular, the signal is complex in terms of frequency content, and the soil element is subjected to stress components in three orthogonal directions.

The study focuses on the dynamic behaviour of granular materials with regard to these complex features of seismic loading. For that purpose, a special triaxial press was installed and further developed in the Soil Mechanics Laboratory (LMS) at EPFL thanks to grants from the Swiss National Science

Foundation R'Equip programme and from the EPFL.

At first sight, the context of western Europe seismicity may look inappropriate for the study of strong ground motions. However, strong destructive earthquakes can occur in countries like Switzerland, as demonstrated by the most famous Basel event of 1356. As a consequence, seismic risks are taken into account, especially for the centre of the alpine region of Valais and around Basel. Indeed, seismic hazard is non negligible in these regions, and may concern densely populated areas, were the occurrence of an earthquake could threaten the lives and properties of tens of thousands inhabitants.

1.2 Objectives

The main objective of this PhD thesis is to assess, in the laboratory, the effect of complex loading features of strong earthquake motions on granular soil behaviour. More precisely, the assumptions and simplifications usually considered for seismic loading conditions are questioned, focusing on two main aspects: (i) cyclic loading frequency (ii) superposition of loading. The parameters influencing these complex loading features, in particular the importance of the pore fluid, are neither well known nor understood. The impact of loading conditions on nonlinear behaviour of granular materials and on the development of large strains within saturated and dry sand samples will be evaluated.

An intermediate issue is to characterise dynamic nonlinear sand behaviour with cyclic and seismic triaxial tests in the earthquake frequency range, at medium to high strain amplitude. This work involves practical developments of laboratory equipment, to provide experimental results of adequate quality. The limits of the device will be carefully analysed, and the reliability of test results will be demonstrated.

Finally, two very different constitutive models designed for geotechnical earthquake engineering will be evaluated with regard to the experimental results: the linear equivalent model and the multi-mechanisms elastoplastic model of Hujeux. The ability and limits of these numerical tools for dynamic modelling of sand behaviour at medium to large strains will be assessed.

1.3 Structure of the thesis

The content of the PhD thesis is organised in line with the objectives above-mentioned.

The context of the research is presented in **Chapter 2**. Geotechnical earthquake engineering issues related to the present work are recalled. The notions necessary to understand the general nonlinear behaviour of sand subjected to cyclic and seismic loading are then summarized. A particular attention is paid to the review of the state of the art on dynamic material parameters, modelling of sand under cyclic loading, rate and viscous effects, multidirectional effects and irregular loading effects.

The description of the testing methods and of the techniques developed to obtain high quality test results is the core of **Chapter 3**. In particular, the dynamic triaxial press and the new laser sensors are presented in detail and fully validated.

In **Chapter 4**, different tests performed under «classical» cyclic triaxial conditions are presented and analysed. The effects of boundary conditions on cyclic sand behaviour are outlined, by means of dry or saturated undrained tests performed under various initial stress states. The importance of soil fabric is addressed by comparing the cyclic response of two different soils, Leman Sand and Fonderie Sand, which have quite different grain size distribution and particle shapes. Validations of the experimental processes are also presented in this chapter, with an evaluation of the laser sensor measurement system for an undrained sand sample and with the analyses of shear strain localization occurring at large strain.

In **Chapter 5**, rate effects observed in cyclic dry and undrained saturated triaxial tests are described for Leman Sand. Loading frequency is shown to influence the behaviour of this granular material at medium strain amplitudes.

Chapter 6 focuses on the effects of bidirectional cyclic and seismic loading on Leman Sand behaviour for synchronised variations of axial and radial stresses in the dynamic triaxial press. Leman Sand is tested in undrained conditions corresponding to the development of failure by cyclic liquefaction.

In **Chapter 7**, the determination of material parameters of Leman Sand is presented for the two different models, the linear equivalent model and the multi-mechanism elastoplastic Hujeux model. Both of them can take into account cyclic loading of granular soils. Some of the triaxial test results presented in the previous chapters are modelled with these two constitutive laws. It is thus possible to evaluate the ability of both models to describe the cyclic behaviour of sand at medium to large strain.

Chapter 8 concludes this work and proposes perspectives for future research based on the numerical and laboratory results.

CHAPTER 2

DYNAMIC GRANULAR SOIL BEHAVIOUR

2.1 Introduction

Characterizing soil behaviour under seismic loading was one of the first issues that led part of the geotechnical community to focus on dynamic problems. Seismic waves can induce strong motions in the upper ground layers, even far from the epicentre. These motions may even be amplified within particular topographical and geological conditions: this phenomenon is called site effects. A wider range of applications for dynamic soil behaviour was then introduced: fatigue behaviour linked with human activities as traffic, vibratory excitations from various industries, effect of underground blasting. Measurement techniques for soil in motion were specially designed to obtain accurate dynamic soil models and safe design rules.

In this chapter, a synthetic broad introduction to soil dynamics is presented, before the more detailed overview of cyclic sand behaviour in laboratory tests. To be more precise, a brief clarification on the dynamic problem in soils (section 2.2) is followed by some considerations on geotechnical earthquake engineering (section 2.3), with a special focus on site effects which introduces the importance of nonlinear dynamic soil behaviour. The concepts needed for describing the actual mechanical behaviour of granular soils under cyclic loading, which are extensively used in the next chapters of the thesis, are described in section 2.4. A detailed overview on dynamic material parameters, namely secant shear modulus and damping ratio, follows in section 2.5. The constitutive models used in the thesis (Chapter 7) are described in section 2.6. The three next sections present particular features of loading characteristics: rate effects (section 2.7), the effects of multidirectional loading (section 2.8) and the effect of irregular loading (section 2.9) on cyclic soil behaviour. These subjects are treated in Chapter 5 and Chapter 6 of the dissertation. Finally, the conclusions close this chapter (section 2.10).

2.2 The dynamic problem

2.2.1 Cyclic, dynamic and static load

Strictly speaking, the concept of dynamic loading of soil refers to the propagation of stress waves within the continuous medium. The general dynamic equation of motion of a homogeneous solid is (e.g. Martin 2007):

$$f_{ext} + \mathrm{div}\,\bar{\sigma} = \rho\,\ddot{u} \tag{2.1}$$

where f_{ext} are body forces, $\bar{\sigma}$ is the stress tensor, ρ is the density and $\ddot{u}$ the acceleration. By combining this equation with the constitutive law, which relates the stress tensor to the strain tensor (and possibly

other field variables like strain rate), field equations can be derived. The definitions of stress and strain tensors for triaxial conditions can be found in section 2.4. Developments of the constitutive laws for sand loaded in cyclic conditions are described in section 2.6.

For fluids, the equation of motion has the same pattern, although very different conditions prevail (e.g. the notion of small deformations is not valid any more), velocities are used instead of accelerations, and the definition of the terms of this equation, in particular the stress tensor, are different for fluids and solids. Details of the modelling of pore fluid behaviour is out of the scope of this work, and will not be mentioned further.

Dynamic loading is opposed to static loading, which refers to slow monotonic variations of the soil state. Referring to Eq. 2.1, one could say that the loading is static (or pseudo-static) when the inertia term (right side of the equation) is negligible.

In laboratory experiments, the limit between static and dynamic is not a clear boundary. Instead, the change is continuous and scattered with intermediate states, such as quasi-static and pseudo-dynamic. In between, periodic cyclic loadings are a particular case. Fig. 2.1 compares the different types of loading.

The term «cyclic loading» refers to systems oscillating with constant amplitude and frequency. According to parameters such as loading frequency or wave length, the soil volume of interest may experience wave propagation inside its boundaries (true dynamic load), or a homogeneous stress with an amplitude which evolves with time (pseudo-static load). However, both situations can be used for the purpose of creating constitutive models which take into account dynamic soil behaviour. Actually, cyclic loading is commonly classified within dynamic loading, as its purpose is intrinsically linked with the dynamic problem.

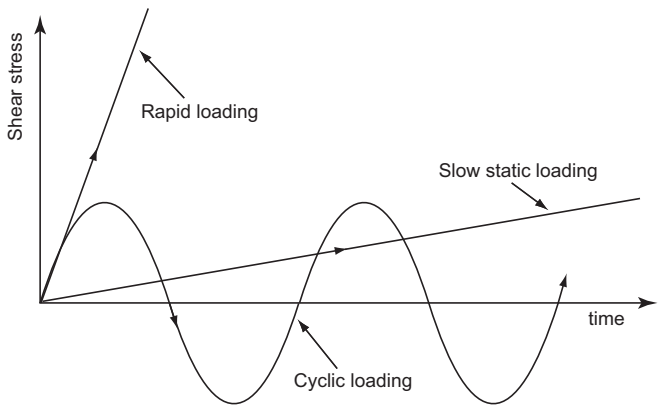

Fig. 2.1. Loading types.

2.2.2 Nature of dynamic loadings

2.2.2.1 Introduction

In the field of soil mechanics, dynamic loadings are the consequences of numerous kinds of excitations. The various possible sources induce different oscillations of the ground. Fig. 2.2 presents a qualitative classification of the dynamic sources. Each problem is classified by its number of cycles and by the time of loading.

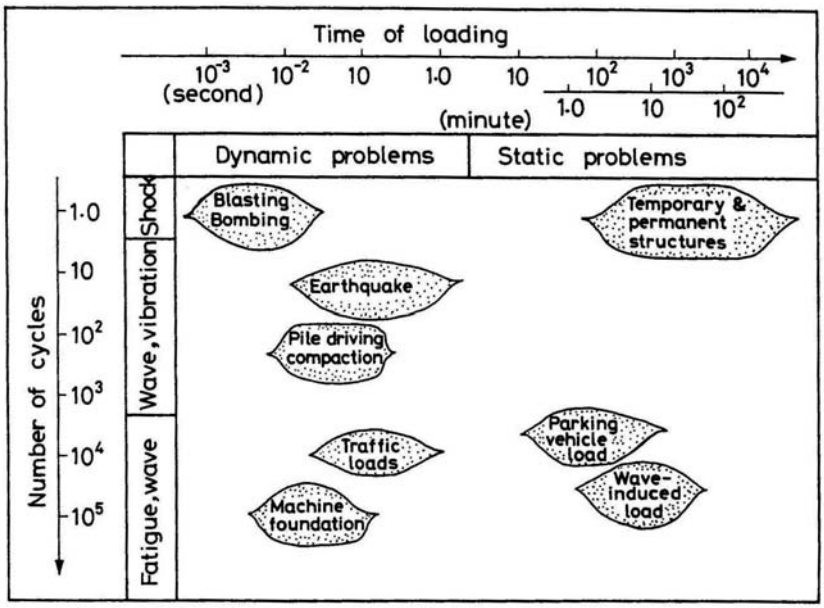

Fig. 2.2. Classification of dynamic problems (Ishihara 1996).

2.2.2.2 Seismic waves («Earthquake» in Fig. 2.2): transient loading

Earthquakes are due to plate tectonics, which is the phenomenon of interaction and motion of the parts which constitute the earth's crust. These interactions manifest themselves both at the boundaries of the plates and at their core. Upon motion of the different plates, large stresses accumulate in several points near the boundaries, where they eventually induce breaking along fault lines. The energy liberated by the sudden displacement is the origin of seismic waves, which diffuse inside the plates. In a given area, ground motion depends on many parameters, such as the magnitude of the earthquake, the distance with the epicentre, global and local physical characteristics of the ground.

Soil elements submitted to seismic wave propagation are considered to undergo cyclic stress conditions (Seed 1979). Stress time series have random pattern, but there is agreement on their cyclic nature (confirmed experimentally by our triaxial tests in Chapter 6). Seismic motion is generally characterized by 10 to 20 loads of irregular amplitudes. The frequency content of a seismic excitation is also irregular and varies mostly from 0.1 to 10 Hz. More details on geotechnical earthquake engineering issues are given in section 2.3.

2.2.2.3 Vibrations due to human activities («Pile driving compaction», «machine foundation» and «traffic loads» in Fig. 2.2)

They are essentially due to civil engineering (drilling, pile driving), circulation of heavy vehicles (trucks, train) and operation of industrial mechanical devices (vibrations due to cyclic machines, shock associated to fabrication process). These excitations are characterized by small amplitude motions with an enormous amount of cycles. Because of that, they can induce or increase settlement of soft soil layers.

2.2.2.4 Blasting and bombing (Fig. 2.2): shock waves

Shock waves are characterized by the liberation of an enormous amount of energy (at the scale of a very big seism) in a single loading cycle. The most powerful blasting excitation can arise because of underground or surface tests of atomic and thermonuclear bombs.

A more civil application to blasting is linked to mining, underground work and foundation engineering, where blasting is one of possible excavation technique. Blasting can also be purposely used to densify loose ground previous to building construction.

A new field of activity for geotechnics is the resistance to terrorism attacks.

2.3 Geotechnical earthquake engineering

2.3.1 Introduction to geotechnical earthquake engineering

Earthquake engineering is a young discipline which deals with the effect of earthquakes on people, structures and more generally the environment, and the means developed to reduce these effects. These broad objectives concern geologists, seismologists, structural and geotechnical engineers, risk analysts among the technical field, but also sociologists, insurers, economists and politicians.

The geotechnical aspect of earthquake engineering is a major component of this large battlefield, because ground shaking amplitude, duration and frequency content are key parameters influencing the costs of an earthquake in terms of human life and structures. The name *geotechnical earthquake engineering* covers site effects and microzonation, soil-structure interaction, strong ground motion, wave propagation, soil dynamics, slope stability, dams, embankments, earth structures and quay walls behaviour under transient loading. Among popular research subjects, there are in situ soil characterization, laboratory testing for soil behaviour characterization, physical models in centrifuge

testing, and modelling of soil stratum and structures in one, two or three dimensions.

Soil dynamics is described in details in other chapters. The following part focuses on a few chosen aspects of geotechnical earthquake engineering: the evaluation of seismic hazard and the characterization of earthquakes, a short description of seismic wave propagation, and the application of soil dynamics to site effects.

2.3.2 Seismic hazard in Switzerland

Seismic hazard in a particular region is evaluated through careful analysis of both history of seismic activity and geological evidences. Each country produces hazard maps and delimits regions according to different degrees of seismic hazard (e.g. Demircioglu et al. 2007 for Turkey). These maps are based on a classification according to peak ground acceleration (PGA, defined in section 2.3.3) induced by representative seismic events of the region.

The occurrence of a major earthquake in Switzerland is called a «moderate» hazard (hazard map in Fig. 2.3). However the consequences of such an event could be disastrous in terms of lives and costs. In Chapter 7, we compare the maximum peak ground accelerations predicted for Switzerland with the motions induced during our laboratory tests.

2.3.3 Earthquake characterization

An earthquake is in essence a mostly unpredictable phenomenon, for both its location and its timing. The characteristics of a seismic motion that are interesting for engineering purposes, i.e. for the design of structures, concern its magnitude, its frequency content, its amplitude and the duration of the motion. All of these four parameters vary significantly between seismic events. The laboratory tests presented in Chapters 4, 5 and 6 address the effects of motion amplitude, frequency content and superposition of stress waves on sand behaviour.

The magnitude of an earthquake is the quantitative measurement of its «*size*» (Kramer 1996). It is calculated from the measurement of the ground shaking. Many parameters were invented for describing the magnitude, for example the Richter local magnitude, the surface wave magnitude, the body wave magnitude and the moment magnitude based on the seismic moment. Each scale has its advantages, but the moment magnitude is usually preferred because it represents strong earthquakes more accurately. The prediction of the magnitude of a potential seism is related to the fault length. It is then estimated by fault mapping of every dangerous area of the globe. In Chapter 6, we use the moment magnitude to describe the seismic loading applied to our undrained triaxial sand samples (San Simeon earthquake 2003, moment magnitude 6.5).

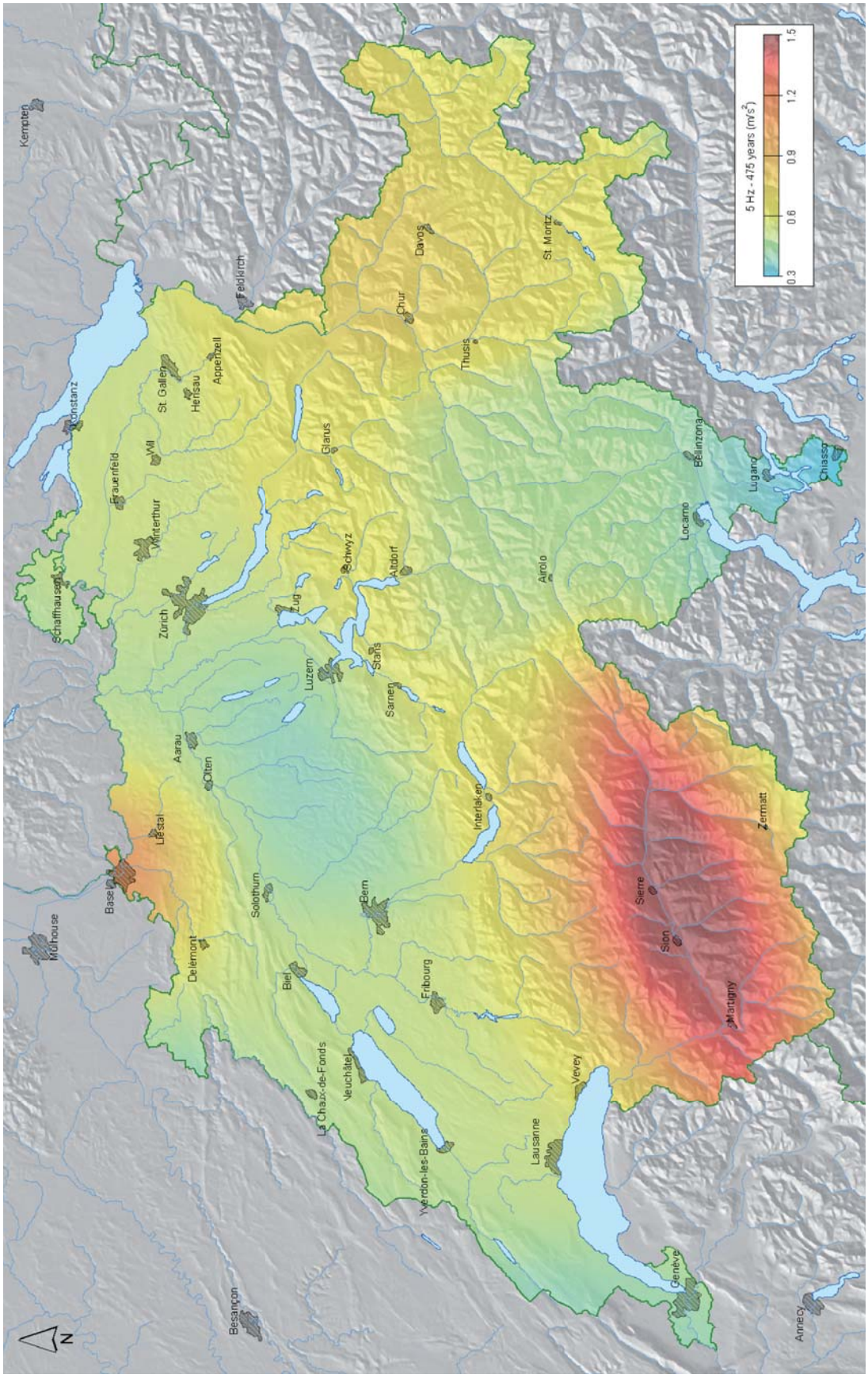

Fig. 2.3. Seismic hazard in Switzerland (Giardini et al. 2004).

Ground motions in a particular site can be recorded by various instruments, such as seismographs and accelerographs (an acceleration time history is shown in Appendix 2). The sensor usually records three orthogonal acceleration of the ground in translation. Laboratory tests with sinusoidal and seismic bidirectional conditions are presented in Chapter 6; they take into account two perpendicular motions. Acceleration time histories are too complex to be used as raw data, also ground motion parameters are extracted from these curves. The amplitude of each component is commonly measured by the peak ground acceleration (PGA), in the horizontal or vertical direction. The frequency content of the motion is also important, as it greatly influences the damage to structures. The Fourier amplitude spectrum of acceleration clearly depicts the distribution of the motion amplitude with respect to the frequency (e.g. Appendix 2).

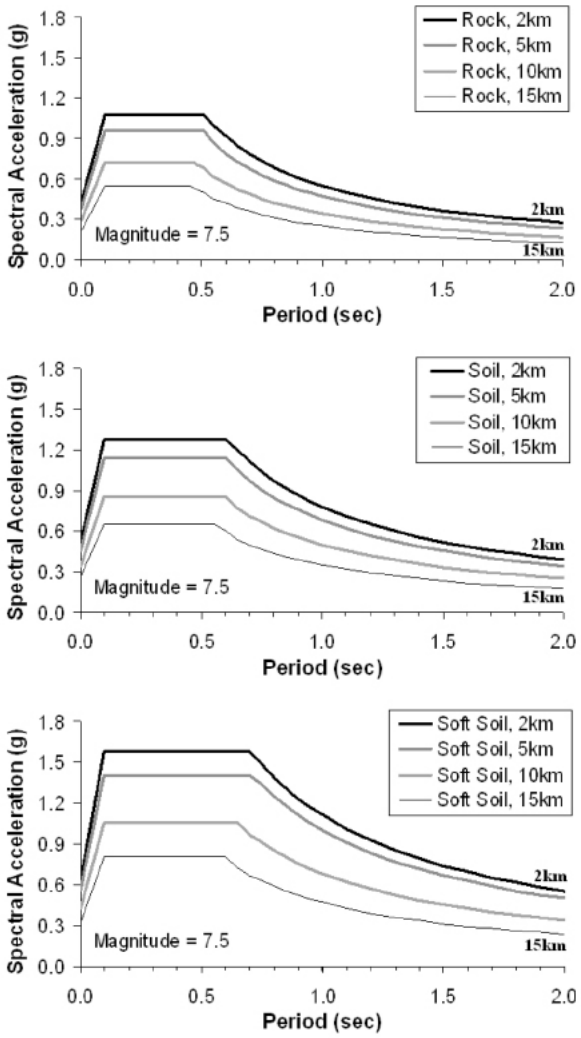

Fig. 2.4. Design response spectrum (Kalkan & Gülkan 2004).

When seismic hazard is considered for the design of a structure, the most potentially damaging earthquake frequency content for the structure should be used for its design. This parameter is unknown

a priori. That is why design response spectra (e.g. Fig. 2.4), forged with probabilistic analysis, are provided by statutory procedures. For example, Studer et al. (2004) review design spectra used in Switzerland and suggest a new soil classification for the response to strong motions. Fig. 2.4 shows the influence of the type of geomaterials on the amplification of the spectral acceleration. In the same conditions, soils involve higher accelerations than rock (cf. site effects in section 2.3.5).

2.3.4 Seismic wave propagation

2.3.4.1 Elastic volumetric waves

Seismic wave propagation inside an elastic continuum has been extensively described (e.g. Kramer 1996). Soil is assumed as a homogenous monophasic isotropic elastic medium. A more complex theory, poroelasticity, has been developed since Biot (1956) for wave propagation inside a biphasic porous material, where the pores are saturated with a fluid.

An elastic wave is a discontinuity surface separating two elastic volumes (Nowacki 1978). Ground shaking during an earthquake is due to the upward propagation of body waves from an underlying rock formation. Those body waves propagating inside a homogenous isotropic soil can be distinguished into two kinds (Fig. 2.5):

- Compressional (also called longitudinal and primary) waves (P waves) alternately induce compressional and dilational stresses in the soil body.
- Shear (or secondary or transverse) waves (S waves) induce a shearing deformation with motions perpendicular to the propagation direction. S waves can be divided into two components: SV (vertical plane motion) and SH (horizontal plane motion). In elastic medium, they do not induce volumetric changes, nor can be sustained by fluids. S waves propagate slower than P waves.

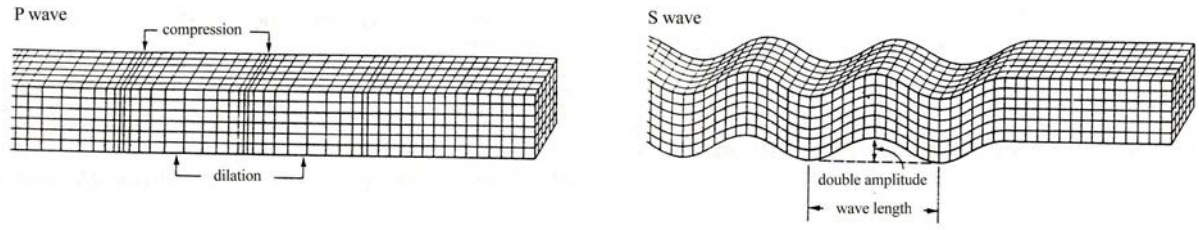

Fig. 2.5. Elastic body waves: P wave and S wave.

The celerity, or propagation velocity, of body waves plays an important role in soil dynamics. The velocity of P wave (c_p) and S wave (c_s) depends on elastic soil properties, i.e. any of two of the following constants: Lamé coefficients λ and μ, Young's modulus (E), shear modulus (G) and Poisson's ratio (ν):

$$c_p = \sqrt{\frac{\lambda + 2\mu}{\rho}} = \sqrt{\frac{E(1-\nu)}{\rho(1+\nu)(1-2\nu)}} \qquad c_s = \sqrt{\frac{\mu}{\rho}} = \sqrt{\frac{G}{\rho}} = \sqrt{\frac{E}{2\rho(1+\nu)}} \tag{2.2}$$

where ρ is the density. These equations are used to calculate P wave and S wave velocities of Leman Sand, which are needed for the linear equivalent method (cf. Chapter 7).

2.3.4.2 Attenuation of stress waves

The amplitude of stress waves decreases with the distance from the source. The total attenuation is the sum of geometric spreading, apparent attenuation and material losses (Wang & Santamarina 2007). Only damping arising from material losses are considered in this research, because we work at the scale of a soil element.

Geometrical attenuation

When getting further from the earthquake source, the energy per unit volume dissipates. As a consequence, their amplitude decreases. For example, in a homogenous medium, the geometric attenuation is simple for spherical or cylindrical wave propagation: for a wave front of radius *r*, the amplitude decreases in 1/*r*.

Apparent attenuation

This is the decay of the wave amplitude by partial transmission, mode conversion, diffraction and scattering at interfaces and anomalies.

Damping

Energy loss, ultimately by heat, arises in the continuum along the wave propagation. This energy loss is accompanied by a decrease of the wave amplitude. In soil mechanics, material losses are quantified with the damping ratio. An extended description of the damping ratio in sand is provided in section 2.5. The viscoelastic model, which allows to take into account material damping in the constitutive equation, is described in section 2.6.

2.3.4.3 Nonlinear wave propagation

The threshold for considering nonlinear effects was first an acceleration of 0.1*g*, then 0.4*g* (Delepine 2007). This last value is referred to in Chapter 7, when the linear equivalent model is compared to laboratory test results. Some constitutive models for nonlinear wave propagation exist (e.g. Gerolymos & Gazetas 2005, and the Hujeux model, section 2.6). They take into account the degradation of shear modulus and damping with shear strain (Drosos et al. 2007).

2.3.5 Site effects

Site effects are shortly described now, to evaluate the importance of soil dynamics in a geotechnical earthquake engineering application. This problem is particularly concerned by the choice of a soil model, which should take into account dynamic effects. The comparison, in Chapter 7, of two different models, both suitable for seismic wave propagation simulations, could have important impact on the evaluation of site effects.

2.3.5.1 Definition and description of site effects

There can be great differences in the degree of damages resulting from an earthquake depending on ground conditions. This phenomenon is called site effects. It is of major importance for the design of buildings in seismic areas. Three main effects are considered in this perspective (Okamoto 1973) for unidimentional amplification:

- The influence of soil type on the intensity, waveform and velocity of earthquake motion (e.g. Fig. 2.4)
- The influence of soil characteristics (density, damping) on soil - structure interaction
- The decrease in strength of soil when subjected to earthquake loading.

In simple cases, motion amplification in a particular site is characterized by the ratio of the peak ground acceleration (PGA) at the soil surface over the PGA at a reference rock surface. The ratio depends on soil type, peak acceleration value and soil layer thickness. It is usually higher than one for peak acceleration until 0.5*g*. However this threshold could be higher for thin layers of sandy material. Amplification spectra only roughly takes into account site amplification phenomenon (Semblat et al. 2005).

The topography of the area is also known to play an important role in site effects. Indeed, site amplification can be the consequence of seismic wave reflections and surface wave propagation in geometrically complex situations, like earth dams or valleys. More precisely, in an earth structure, seismic waves are trapped above the bedrock. These trapped waves can induce resonance of the ground motion when the wave frequency reaches the natural frequency of the structure. For complex topography, the amplification is thus frequency-dependent. Bard & Riepl (2000) report three physical phenomena for explaining topography effect: (i) the sensitivity to the incidence angle of shear waves, (ii) their multiple reflections and corresponding motion amplitude increase and (iii) interference patterns between direct and diffracted waves.

2.3.5.2 Multidimensional amplification

Amplification analysis is very sensitive to the numerical model; there is sometimes a non negligible

difference between unidimentional (1D) and multidimensional (2D and 3D) responses. The choice of the type of analysis then depends on the site configuration and on the importance of the accuracy of the investigation. Bard & Riepl (2000) computes the spectral response of simple cosine-shaped basin, which shows that resonance frequencies are higher for multidimensional basin. Moreover, the amplification ratio is higher for 3D computations. Delepine (2007) also models 1D, 2D and 3D ellipsoidal basins. He concludes that 2D models gives higher amplification ratios than the unidimentional simulation. They are even higher with 3D computation of sedimentary basin.

2.3.5.3 Estimation of site effects by microzonation

Introduction

Methods for estimating site effects can be classified in three types (Bard & Riepl 2000): experimental methods, numerical methods and empirical methods. For microzonation purpose, experimental methods are more widely used because their cost is lower, and they allow large scale estimations. Numerical methods are reserved to highly hazardous areas, or for case studies of previously damaged sites. Empirical correlations, based on surface geology and geotechnical properties, can be applied to sites of known ground composition. Some numerical methods are briefly compared below.

Numerical modelling

The choice of the constitutive law used for characterizing site effects depends on the earthquake intensity which can be expected in the studied area. For regions of low to medium seismic activity, linear equivalent models are commonly used. Viscoelastic models can also be appropriate for site effects modelling. The use of more complicated models for site effects estimation is uncommon, despite the fact that nonlinear behaviour is critical for large motions (e.g. Iai & Tobita 2006).

For 1D amplification analysis, the linear equivalent method, performed in the frequency domain, is widely used. Linear equivalent models can lead to an overestimation of the amplification as a result of «spurious resonance». Its main shortcoming is that it can not represent pore water pressure increase. But it can be more efficient, in terms of computer cost, than nonlinear analyses. For low strain level, it is usually considered as accurate enough.

Nonlinear models for microzonation can be implemented by a direct integration in the time domain. They are mostly based on simple models following the Masing's rule, like the Ramberg-Osgood model or the hyperbolic model. It is also possible to use advanced constitutive models, like in DYNAFLOW (Popescu et al. 2006). Nonlinear models, which can also reproduce pore water pressure generation, are particularly recommended for stronger strain levels. Their main shortcoming is the difficulty which arises at the determination of soil parameters.

Hartzell et al. (2004) compare site amplification for five soil types and increasing peak input motions from 0.1*g* to 0.9*g*. Different models are tested, the simplest being the linear equivalent method and the more complex being an advanced coupled model NOAHB. For very stiff soils, there is not much difference between the models, but nonlinear effects increase in soft and medium soils, for high deformation amplitude. The nonlinear approach is recommended in these cases.

For such inelastic soil behaviour, two site amplification characteristics should be accounted for. The fundamental frequency of the soil deposit decreases if the seismic frequency band is lower than the natural soil frequency. This decrease changes in turn the spectral amplification. On the other hand, the damping ratio increases, which reduces the peak ground acceleration, especially for high frequencies.

2.3.5.4 Extension towards soil dynamics issues

The development of nonlinear soil models based on effective stress principles is thus essential for increasing the accuracy of site effects analyses in case of strong ground motion. The ease of calibration of such models is a priority, and should not be an obstacle towards the use of advanced nonlinear soil models. Chapter 7 provides examples and additional insight into this subject.

2.4 Introduction to soil behaviour under cyclic loading

After the description of important features of monotonic soil behaviour, a few chosen aspects of cyclic soil behaviour are presented, thanks to the description of laboratory studies from the literature. Only the behaviour of granular material is addressed in the thesis.

2.4.1 Effective stress

The system studied is composed of a soil matrix, made of sand grains, and a one-phase fluid, saturating the pores. This fluid is either air or water. The stresses within the porous medium are ruled by the concept of Terzaghi of effective stress (Terzaghi 1943). The effective stress σ' is defined as the difference between the total stress σ and the pore fluid pressure u.

2.4.2 Notations of stress and strain

The definitions of stress and strains rely on the assumption of small strains, which is assumed valid for all experimental results. For limit cases, at large strain above failure, a special care is taken to monitor localization (cf. section 4.8).

2.4.2.1 Stress field for triaxial test

The effective stress tensor is written as follows, in the case of an axisymmetric triaxial test:

$$\bar{\sigma}' = \begin{bmatrix} \sigma'_1 & 0 & 0 \\ 0 & \sigma'_3 & 0 \\ 0 & 0 & \sigma'_3 \end{bmatrix} \tag{2.3}$$

where σ'_3 is the effective confining pressure. In the triaxial cell, the confining stress is isotropically applied and the axial stress σ'_1 can be calculated by:

$$\sigma'_1 = \sigma'_3 + \frac{F_{ax}}{S} \tag{2.4}$$

where F_{ax} is the force applied by the axial loading rod (Chapter 3) and S is the surface of the sample.

It is useful to introduce the classical decomposition of the stress tensor in a deviatoric (t_{ij}) and a spherical part (p'):

$$\sigma'_{ij} = t_{ij} + p'\delta_{ij} \tag{2.5}$$

The first invariant of the stress is $p' = 1/3\ \sigma'_{kk}$. The deviatoric part is then:

$$t = \frac{F_{ax}}{3S}\begin{bmatrix} 2 & 0 & 0 \\ 0 & -1 & 0 \\ 0 & 0 & -1 \end{bmatrix} \tag{2.6}$$

The second invariant of the deviatoric part of the stress, J_{2D}, is defined and calculated below:

$$J_{2D} = \frac{1}{2} t_{ij} t_{ij} = \frac{1}{3}\left(\frac{F_{ax}}{S}\right)^2 \tag{2.7}$$

another form of the second invariant is generally used in the case of the triaxial test:

$$q = \sqrt{3 J_{2D}} = \frac{F_{ax}}{S} = \sigma'_1 - \sigma'_3 \tag{2.8}$$

also called the deviatoric stress.

It is useful, for the determination of dynamic parameters in complex loadings, to define a general effective stress increment corresponding to a change in both the deviatoric stress (Δq) and the confining pressure ($\Delta\sigma'_3$). The following equation gives the effective stress increment, the deviatoric and the

spherical increments ($\Delta\sigma'_{ij} = \Delta t_{ij} + \Delta p' \delta_{ij}$):

$$\begin{bmatrix} \Delta q + \Delta\sigma'_3 & 0 & 0 \\ 0 & \Delta\sigma'_3 & 0 \\ 0 & 0 & \Delta\sigma'_3 \end{bmatrix} = \begin{bmatrix} 2/3\,\Delta q & 0 & 0 \\ 0 & -1/3\,\Delta q & 0 \\ 0 & 0 & -1/3\,\Delta q \end{bmatrix} + \left(\frac{1}{3}\Delta q + \Delta\sigma'_3\right)\begin{bmatrix} 1 & 0 & 0 \\ 0 & 1 & 0 \\ 0 & 0 & 1 \end{bmatrix} \tag{2.9}$$

Major and minor principal stresses are either the axial stress (on the top of the cylinder), either the lateral stress. By convention, the total stress applied onto the top cap is always called σ_1, and the lateral stress σ_3. Even in case of extension, when there is rotation of principle stresses of 90°, their name is not exchanged for the sake of clarity. Because of that, the deviatoric stress can be negative and, if so, is the opposite of the second stress invariant.

2.4.2.2 Strain field for triaxial test

The strain tensor inside the sample is also diagonal:

$$\bar{\varepsilon} = \begin{bmatrix} \varepsilon_1 & 0 & 0 \\ 0 & \varepsilon_3 & 0 \\ 0 & 0 & \varepsilon_3 \end{bmatrix} \tag{2.10}$$

As all the strain components are in the principal directions, they are written:

$$\varepsilon_i = d_{i,i} = \frac{\partial d_i}{\partial x_i} \tag{2.11}$$

with d_i the displacement in the ith direction. The measurement of the strain component is made between two points x_1 and x_2. The integration of d_i over the domain gives the relations:

$$\begin{aligned} &\int_{x_1}^{x_2} \varepsilon_i \,\mathrm{d}x_i = l\,\varepsilon_i = \int_{x_1}^{x_2} \frac{\partial d_i}{\partial x_i}\,\mathrm{d}x_i = d(x_2) - d(x_1) \\ &\forall x_k \in [x_1, x_2], \quad \varepsilon_i(x_k) = \frac{d(x_2) - d(x_1)}{l} \end{aligned} \tag{2.12}$$

In the same manner as the stress tensor, strain is separated into two parts:

$$\varepsilon_{ij} = e_{ij} + \frac{1}{3}\varepsilon_{kk}\,\delta_{ij} \tag{2.13}$$

The first invariant of ε_{ij} is $\varepsilon_V = \varepsilon_{kk} = \varepsilon_1 + 2\varepsilon_3$ and the deviatoric strain tensor e_{ij} is then:

$$e_{ij} = \frac{\varepsilon_1 - \varepsilon_3}{3}\begin{bmatrix} 2 & 0 & 0 \\ 0 & -1 & 0 \\ 0 & 0 & -1 \end{bmatrix} \tag{2.14}$$

The second invariant of strain, called here the deviatoric strain, can be defined in two forms:

$$I_{2D} = \frac{1}{2} e_{ij} e_{ij} = \frac{\left(\varepsilon_1 - \varepsilon_3\right)^2}{3} \quad \text{and} \quad \varepsilon_q = \sqrt{3 I_{2D}} = \varepsilon_1 - \varepsilon_3 \tag{2.15}$$

The definition of deviatoric strain selected for our work is this value ε_q, which is more convenient than the alternative definition taken as 2/3 (ε_1 - ε_3).

As for the stress increment, the general strain increment corresponding to any state change is defined by:

$$\Delta\varepsilon_{ij} = \Delta e_{ij} + \frac{1}{3}\Delta\varepsilon_V \, \delta_{ij} \tag{2.16}$$

$$\begin{bmatrix} \Delta\varepsilon_1 & 0 & 0 \\ 0 & \Delta\varepsilon_3 & 0 \\ 0 & 0 & \Delta\varepsilon_3 \end{bmatrix} = \frac{\Delta\varepsilon_q}{3}\begin{bmatrix} 2 & 0 & 0 \\ 0 & -1 & 0 \\ 0 & 0 & -1 \end{bmatrix} + \frac{\Delta\varepsilon_V}{3}\begin{bmatrix} 1 & 0 & 0 \\ 0 & 1 & 0 \\ 0 & 0 & 1 \end{bmatrix} \tag{2.17}$$

The work W of any general loading path in triaxial conditions can be calculated by:

$$\delta W = \sigma'_1 \, \delta\varepsilon_1 + 2\sigma'_3 \tag{2.18}$$

that can be rewritten as:

$$W = p'\varepsilon_v + \frac{2}{3} q \varepsilon_q \tag{2.19}$$

with p', ε_v, q and ε_q defined in Eq. 2.5, Eq. 2.13, Eq. 2.8 and Eq. 2.15. The work can be used to calculate the stored energy and dissipated energy in cyclic stress - strain loops (section 2.5.2).

With this precise definition of the stress and strain components, soil behaviour can be described in monotonic and cyclic conditions.

2.4.3 Monotonic loading in triaxial compression and triaxial extension

In situ state of stress in soils is not always as simple as level ground conditions. Within a simple embankment, the states of triaxial compression and triaxial extension are found, together with all intermediary states of rotation of the principal stresses (Fig. 2.6).

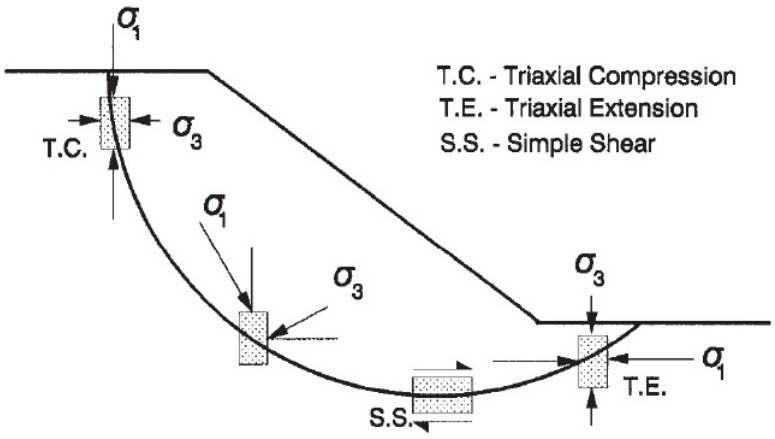

Fig. 2.6. Stresses below an embankment along the failure surface (Uthayakumar & Vaid 1998).

Undrained loading is highly dependent on the direction of loading (Vaid et al. 1990; Uthayakumar & Vaid 1998; Benahmed 2001; Sivathayalan & Vaid 2002; De Gennaro et al. 2004; Finge et al. 2006; Wichtmann et al. 2007b and others). Considering the triaxial cell, with a given initial confining pressure concealing an isotropically consolidated sample, compression is obtained by increasing the deviatoric stress ($q > 0$) and extension is obtained by decreasing the deviatoric stress ($q < 0$). In the compression phase, the major principal stress is vertical. The major and intermediate principal stresses are in the horizontal plane during triaxial extension.

The qualitative response to triaxial compression or extension is usually different (e.g. Fig. 2.7). Vaid et al. (1990) performed triaxial tests on sand, which show that triaxial extension and triaxial compression does not imply the same soil response: (i) pore pressures are larger in extension than in compression (ii) for a certain range of void ratio, the undrained response can be dilative in compression but contractive in extension (iii) liquefaction is triggered at lower strain and deviator stress level in extension. The decrease of undrained strength between compression and extension load is due to larger pore pressures induced in extension, which are explained by a greater horizontal compressibility. This study underlines the importance of the deposition method, standing for techniques of sample reconstitution close to the natural process of soil deposition.

In the nonlinear range, the rotation of principle axes can be viewed as an aggravating factor for the pore-pressure builds-up (Choi & Arduino 2004). However, such effects were observed in isotropic conditions only, and seem to disappear in K_0 conditions (Li 1997).

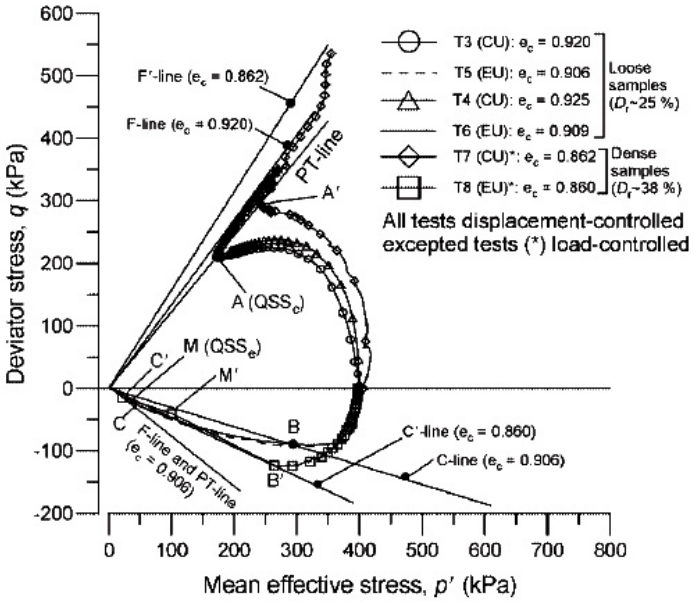

Fig. 2.7. Monotonic triaxial stress paths in extension and compression (De Gennaro et al. 2004).

2.4.4 Critical state and steady state

The concept of critical state (Schofield & Wroth 1968) is at the base of many constitutive models of current soil mechanics (Muir Wood 2004). Whether the initial state of the soil is loose or dense (Fig. 2.8), normally consolidated or overconsolidated, drained or undrained, monotonic and cyclic stress paths join the critical state line at sufficiently large strains. After that moment, the volumetric strain rate is equal to zero while large shear strain develop. This means that the void ratio is constant, as well as the excess pore pressure in the undrained case.

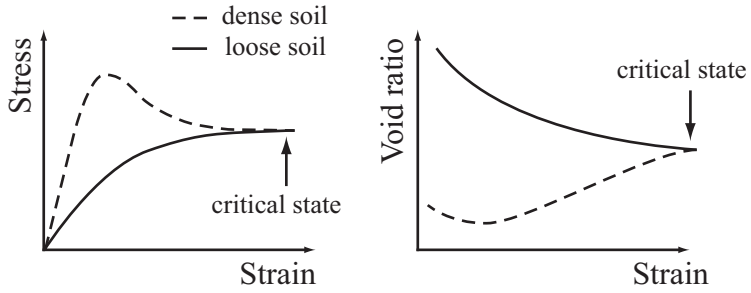

Fig. 2.8. Critical state for dense and loose soil.

A rival concept is the steady state (SS) concept (Poulos 1981). It can be used instead of critical state for undrained monotonic and cyclic loading of sand (Vaid et al. 1990; Chu 1995; Benahmed 2001). During steady state, the initial structure of the porous medium is destroyed and the memory of previous loading is lost. A flow structure develops, which only depends on shear rate (necessarily constant), and normal effective stress.

The uniqueness of the steady state at a given void ratio is not clear; Benahmed (2001) reports contradictory evidences. Some test results support the idea of a unique SS (Poulos 1981; Verdugo & Ishihara 1996), and others show that the strain rate, the deformation mode, the loading path (compression or extension), the deposition mode might influence the steady state line (Vaid et al. 1990; Riemer & Seed 1997).

Following the trend in the field of undrained cyclic loading of sand, we choose to refer to the steady state concept.

2.4.5 Dilatancy and phase transformation in granular media

Soil response to shear loading includes a tendency to change its volume. Volume change is a result of the rearrangement of grains by slip-down (repacking into denser state) and roll-over (repacking into looser state) motions. Jaeger & Nagel (1992) explains that *«dilatancy arises from the need of a densely packed material to spread in order to make room for passing grains»*. Either it is free to do so, and the soil matrix exhibits contractive or dilative behaviour, or, when volume changes are prevented, this tendency is conveyed through pore water pressure evolution (increase or decrease).

The dilative or contractive nature of the volumetric behaviour of sand is linked to the initial state of the porous medium, in terms of void ratio and stress state. For medium and dense sand monotonically sheared, a contractive phase starts before the dilative motion. The characteristic state (Habib & Luong 1985), or phase transformation state (Ishihara et al. 1975) is the moment which marks the limit between contractive and dilative behaviour. These two competing ideas are considered equivalent (Chu 1995). The concept of phase transformation line (PT line), shown in the stress plane in Fig. 2.9, is popular for characterizing undrained sand behaviour. For loose sand, the phase transformation line usually coincides with the steady state line.

The uniqueness of PT line for a sand is not clear, some reference mention that it is an intrinsic value (Luong 1980; Uthayakumar & Vaid 1998) but others say that its slope M_{PT} depends on the stress path (Benahmed 2001; De Gennaro et al. 2004).

On the side of a unique PT angle, Vaid et al. (1990) and Ibsen (1994) show that PT lines are the same in compression and extension, and for all loading history, even for anisotropic samples.

The proofs against an intrinsic PT line were obtained with Hostun sand, for which two different values M_{PT} were found in compression and in extension (Benahmed 2001; De Gennaro et al. 2004). Moreover the mobilized friction angle at phase transformation, which is rather independent from the void ratio, slightly increases with the confining pressure (Benahmed 2001).

The quasi steady state is another specific feature of the behaviour of granular media (Vaid et al. 1990). At the moment of phase transformation, loose sand may experience *«flow with limited deformation»* during laboratory tests exploring liquefaction (Ishihara 1996). Uthayakumar & Vaid (1998) report that the quasi steady state and phase transformation state coincide. A temporary decrease of the deviatoric stress, accompanied by large strain, may occur before the actual steady state is reached at large strain. It is an unresolved question whether the strength at quasi steady state, which is lower than the residual strength, should be taken as the real residual strength value (Zhang & Garga 1997). De Gennaro et al. (2004) observed a quasi steady state line, corresponding to the phase transformation line, for medium dense sands.

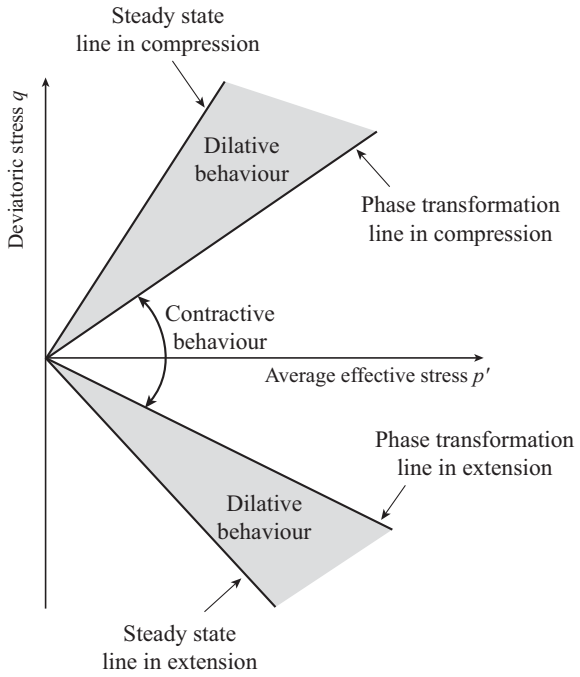

Fig. 2.9. Phase transformation line and steady state line in the stress plane.

2.4.6 Qualitative soil response to cyclic loading

Soils behave with a hysteretic component, which means that some energy is dissipated during cyclic loading. The representation of such behaviour in the stress-strain plane resembles a loop, which is either closed or open depending on loading conditions (Fig. 2.10). It is often referred to as a hysteretic loop.

Under cyclic loading, and with stress-controlled cyclic motions of constant amplitude, different mechanical behaviour can be observed depending on initial conditions and loading amplitude:

- «Adaptation»: cyclic stress-strain loops stabilize on a straight line, giving a perfectly linear elastic response without energy dissipation. It is now acknowledged that such behaviour does not exist,

because a small amount of energy dissipation always appears during cyclic loading (more details in section 2.5.2 on damping ratio).

- «Accommodation»: stress-strain cycles, which evolve at the beginning of the loading, eventually stabilize, and become closed loops with no more plastic strain accumulation. The dissipative behaviour of the material is maintained. It can take thousands of cycles to reach a true accommodated state.

- «ratchet»: strains increase continuously and become very large. Soil failure is eventually reached if loading continues. In case of undrained shear of saturated sand, the deposit reaches failure either by sudden loss of stiffness (flow liquefaction) or by a more regular strain increase (cyclic liquefaction).

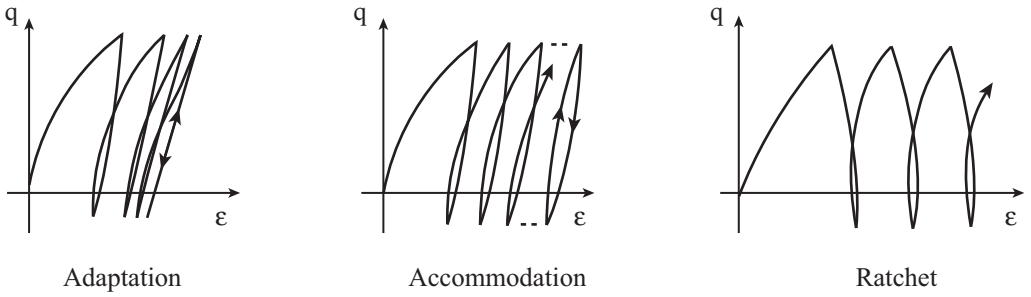

Fig. 2.10. Cyclic behaviour of sand under stress-controlled motions of constant amplitude.

From the point of view of soil stiffness, two types of evolution are possible upon cyclic loading (Fig. 2.11):

- Cyclic hardening: stiffness of the soil increases, with higher secant moduli (defined in section 2.5).

- Cyclic softening: stiffness decreases, and the inclination of the cycles decreases.

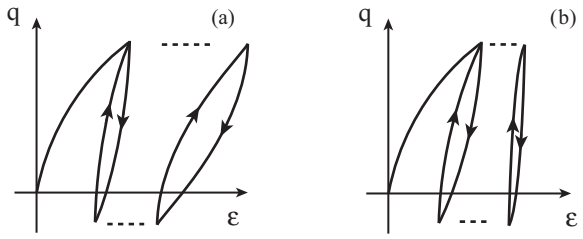

Fig. 2.11. Cyclic softening (a) and cyclic hardening (b) of sand.

The evolution of the secant modulus, either increase or decrease, does not necessarily correspond to true hardening or softening of the soil, respectively. The definition of hardening, with respect to the evolution of the yield surface, can be expressed by: *«Any stress path that produces plastic deformation inside the failure surface results in hardening»* (Lade & Prabucki 1995). More precisely, the stress path can push out the yield surface, i.e. hardening occurs, while the secant modulus decreases, because of

the coupling of the volumetric and deviatoric shear. Moreover, *«true softening occurs past the peak failure surface»*. Anyway, for the description of cyclic test results, the expressions «cyclic softening» and «cyclic hardening» will be used as a simple way to evoke decrease and increase of soil stiffness, respectively.

2.4.7 Effect of the number of cycles

The accumulation of cyclic loads corresponds to a particular soil behaviour, very different from monotonic behaviour. The effect of the number of cycles depends on the inversion of the sign of strain or stress rate (Ishihara 1996); it is also referred to as stress/strain reversal effect. The increasing number of cycles may induce stiffness degradation, or cyclic softening of the soil and as well as energy dissipation, ultimately by heat. The two major consequences of the effect of the number of cycles, even at very low frequencies, are (i) the generation of resilient deformations under stress controlled cycles, and (ii) excess pore water pressure increase in undrained conditions (Pecker 1984; O'Reilly & Brown 1991).

When a very large amount of cycles occur, it may induce cyclic effects that can be referred to as fatigue. For example, Wichtmann et al. (2005) studied the effect of thousands to millions of low amplitude cycles on strain accumulation in sand. Li & Yang (1998) studied the effect of vibration loading history on shear modulus and damping ratio of dry sand.

2.4.8 Link between cyclic behaviour and dilatancy

Under monotonic loading, medium and densely packed granular soils first contract, and then rapidly develop dilative behaviour (e.g. Kramer 1996). For cyclic loading, medium and dense sand behaviour is more complex. In case of undrained conditions, an increase of excess pore water pressure first occurs (which would be contractive behaviour in drained conditions), at a rate which depends on the shear strain amplitude (Dobry et al. 1982). In the stress plane, the increase of excess pore pressure corresponds to a displacement of the loops towards lower effective average stress *p'*. At one point, the effective stress path eventually crosses the phase transformation line and punctual decrease of the excess pore pressure (which would be dilative behaviour in drained conditions) occur (point number 1 in Fig. 2.12). During one cycle, contractive and dilative parts alternate at each intersection with the phase transformation line. High strain amplitudes are rapidly reached, while the rate of increase of the pore pressure is high, leading to «ratchet» behaviour. On the contrary, if the phase transformation line is not reached, the rate of increase of the pore pressure can decrease to zero: this is the accommodation phenomenon.

Luong (1980) performed drained cyclic stress-controlled loading of sands. He concludes that:

i) If the average deviatoric stress is below the PT line, cyclic soil behaviour is contractive. Conversely, soil behaviour is dilative for average deviatoric stress above the PT line.

ii) Accommodation appears when the maximal stress is lower than PT line, and ratchet appears in the other case.

iii) Contraction decreases close to the PT line, and dilation increases when stress exceeds phase transformation on the side of high deviatoric stress.

iv) Contraction is higher during extension parts.

v) Dilation is stronger when soil is denser.

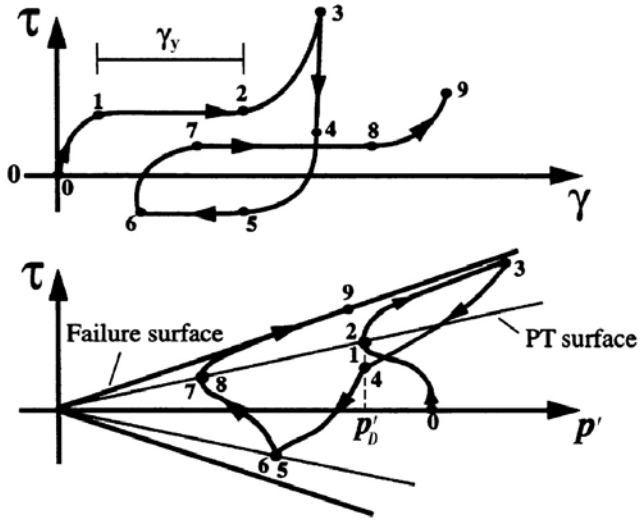

Fig. 2.12. Undrained cyclic behaviour of medium and dense sand (Elgamal et al. 2002).

2.4.9 Strain range dependency of cyclic soil behaviour

The level of strain, while soil faces a dynamic load, influences the mechanical response of the medium. Soil characteristics, means of measurements and modelling are strongly linked with the range of strain amplitude. Deformations concerning soil dynamics vary from very small strains (10^{-6}) to very large strains (10^{-1}), which is above material failure.

In static soil mechanics, very small strains are usually not studied. Indeed their impact on foundations and structures is negligible. However, as soon as a dynamic load is applied to the soil, inertial forces can become significantly great whenever deformation motion is rapid enough, which means their influence can not be neglected even at strains as small as 10^{-6}. This aspect of dynamic problems has been studied for the last 15 years thanks to improvements and modifications of standard triaxial, torsional, simple shear and resonant column devices (Vucetic 2004).

While strain increases above the linear threshold (10^{-5} to 10^{-4}), soil specimens tend to present nonlinear viscoelastic behaviour with decreasing shear modulus (Ishihara 1996) and energy dissipation occurring during cyclic loading. The number of cycles is not known to influence soil behaviour, which mostly depends on the shear strain amplitude. This range of strain will be called small strain from now on.

At larger strains, the volumetric cyclic threshold shear strain, further detailed in section 2.4.10, is usually exceeded. This is the medium strain range, from 10^{-4} to 10^{-2}. Numerous changes progressively appear in soil behaviour, in particular pore water pressure increase, stiffness degradation of saturated soils and hardening of dry and unsaturated soils. Large irrecoverable plastic strains occur, they induce cracks and differential settlement in soil. The number of cycles has an impact on soil properties and the stress - strain relation.

Large strains, above 10^{-2}, induce failure like slope instability or liquefaction (cf. section 2.4.13).

2.4.10 Volumetric cyclic threshold shear strain and stiffness degradation

There is a shear strain amplitude, called the volumetric cyclic threshold shear strain γ_{tv}, above which significant permanent volume changes or permanent development of excess pore water pressure occur in the soil (Vucetic 1994). This threshold is higher than the linear cyclic threshold of approximately 1.5 log-scale. It increases, for any soil, with (i) OCR (ii) initial average stress (iii) plasticity index (iv) degree of saturation (v) smaller diameter of the grains. In sand, it is independent from relative density, initial effective confining pressure and fabric. The threshold shear strain is around 10^{-4} for most sands and silty sands, independently from relative densities (Dobry et al. 1982; Erten & Maher 1995). We also evaluate this parameter for Leman Sand in Chapter 4.

For cyclic strains below the volumetric cyclic threshold shear strain, there is no permanent microstructural change, residual excess pore water pressure does not develop in undrained conditions and there is no permanent volume change in drained conditions. This corresponds to the stabilized hysteretic behaviour.

Above the threshold, there is irreversible alteration of the microstructure, permanent pore water pressure develop or permanent volume change accumulate, and the soil stiffness changes irreversibly: cyclic softening occurs in undrained condition. «Stiffness degradation» is another expression used for that phenomenon.

2.4.11 Pore water pressure increase in undrained saturated conditions

The pore water pressure tends to increase during cyclic loading for strain amplitudes above γ_{tv}. Excess

pore water pressure increase is controlled by the shear strain amplitude (Fig. 2.13). Other parameters like void ratio, confining pressure, number of cycles, silt content, also affect excess pore water pressure increase (Erten & Maher 1995).

The excess pore water pressure is usually expressed as the pore water pressure ratio u_r, defined by:

$$u_r = \frac{\Delta u}{\sigma_3'^0} \tag{2.20}$$

The excess pore water pressure Δu is normalized by the initial effective confining pressure $\sigma_3'^0$. This normalization is defined for triaxial tests. The definition naturally results from the fact that cyclic tests with stress reversal induce u_r to reach 100% when there is complete loss of strength.

Tests with no stress reversal can also experience great amount of strains, but the pore pressure ratio does not necessarily reach 100%. Moreover, in silty sand and sandy silt, u_r seems to be able to reach only 90 to 95%, while great strain amplitudes are observed (Ishihara 1996).

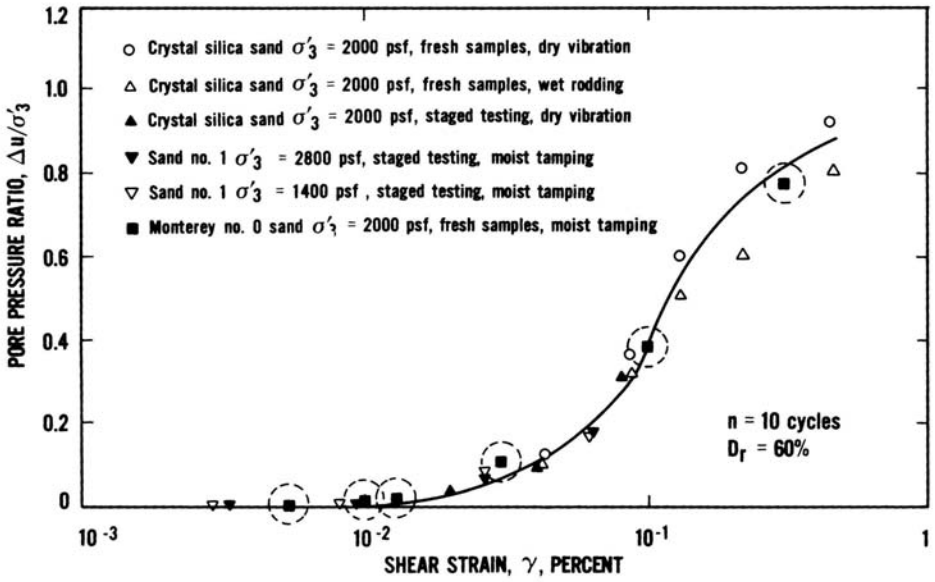

Fig. 2.13. Increase of u_r with axial strain amplitude (Dobry et al. 1982).

2.4.12 Definition of failure

While shear strength of soil is defined at the point of failure, the actual failure definition can be chosen in many different ways. In the field, failure involves deformations above a serviceability limit. As a consequence, a definition based on a threshold strain level seemed appropriate for laboratory tests. Ishihara (1996) proposes a threshold strain amplitude of 5% DA (double amplitude, i.e. distance between minimum and maximum values; opposed to single amplitude which is the half of DA). Alternatively, a threshold pore pressure ratio of 100% was used to define the point of failure (Seed

1979). Due to limitations of the pore pressure ratio exposed in section 2.4.11, the failure criterion based on a threshold strain is preferred for consistency between all kinds of soils and stress paths. A comparison of failure criteria is developed in section 4.4.4.

2.4.13 Liquefaction and cyclic softening

2.4.13.1 Introduction

Liquefaction, which is induced by strong soil vibration, is a secondary effect of earthquakes which can cause major damage if it happens in inhabited areas. It has long been acknowledged that all soil types are not susceptible to liquefy. All kinds of soil submitted to strong cyclic motions can experience large deformations, but flow behaviour characterizing liquefaction seems to happen only in granular media. Many granular soils are prone to liquefaction, from silty sand (Erten & Maher 1995; Amini & Qi 2000; Sitharam et al. 2004; Tsukamoto et al. 2004) to gravels (Kokusho et al. 2004; Choi & Arduino 2004). Usually, the development of such instability happens in saturated granular soils loaded in undrained conditions.

The initial state and the volumetric behaviour of sands greatly influences the response of a deposit to cyclic loading. There is a progressive evolution of the cyclic soil response from very stable behaviour of dense dilative materials to very unstable behaviour of loose contractive sands. Concepts like phase transformation lines, flow liquefaction line, critical state line are very important characteristics for the estimation of soil motions upon cyclic loading.

Over the years, different phenomena emerged from the initial concept of liquefaction. Flow liquefaction, cyclic softening, cyclic liquefaction, and cyclic mobility are different ways of considering soil failure, depending on the initial soil conditions. Robertson (1994) described the liquefaction-related terminology.

2.4.13.2 Flow liquefaction

Definition

Flow liquefaction is a possible consequence of either static or dynamic loadings (Kramer 1996). It typically appears in very loose soils submitted to high confining pressure which can produce high increase of the excess pore pressure (contractive tendency in undrained conditions). These conditions are not commonly found in situ, also flow liquefaction seldom spontaneously occurs.

Flow liquefaction is characterized by a sudden and complete loss of strength which follows a rapid increase of the pore water pressure. The pore pressure converges towards the initial effective stress, which is reached at a critical cycle, called N_{crit}. When the effective stress is equal to zero, any

additional load induces very large strains, followed by secondary effects like localization in shear bands, slope failure, sinking of building into the soil, lurching of structures, damage of underground structures, etc...

Flow liquefaction can appear only when the total shear stress (static and dynamic) exceeds the residual strength. In natural environment, large static shear stress can be induced by the presence of a slope, a retaining wall or a basement pile (Kramer 1996). If a small perturbation arises, failure can occur. On the contrary, if the static shear stress is low, a large dynamic excitation is needed to initiate flow liquefaction.

Flow liquefaction under cyclic conditions can be obtained in laboratory experiments by various devices, among which the most famous ones are the triaxial test (example in Fig. 2.14), the simple shear test and the torsion shear test (Finn et al. 1971; Nagase & Ishihara 1988; Boulanger & Seed 1995; Endo & Komanobe 1995; Vaid & Sivathalayan 1996; Hyodo et al. 1998; Benahmed 2001; De Gennaro et al. 2004; Kokusho et al. 2004; Toyota et al. 2004; Hyde et al. 2006; Lopez-Querol & Blazquez 2007; Georgiannou et al. 2008; Georgiannou & Tsomokos 2008).

Conditions of occurrence of flow liquefaction

The conditions of initiation of flow liquefaction (Vaid et al. 1989) require that (i) the soil is contractive during drained monotonic loading (ii) the maximum shear (static value + cyclic amplitude) must be above the residual strength (i.e. the stress at steady state) (iii) the number of cycles must be large enough, so that the stress path reaches the instability line.

The instability line, defined in the stress space, marks the boundary between stable and unstable states during undrained shearing. It is also called flow liquefaction surface (Kramer 1996), or CSR line (Vaid et al. 1989), in reference to the cyclic stress ratio (defined in Eq. 2.21). The locus of instability in the p' - q plane is a straight line which crosses the origin of the stress plane and depends on the void ratio. Its slope M_{inst} decreases when the void ratio increases, i.e. looser materials are more unstable. The slope of the instability line linearly increases with the relative density (Benahmed 2001). For large relative density, the instability line reaches the phase transformation line, excess pore pressure decreases and flow liquefaction is prevented. For a given soil, the evaluation of the instability line is mainly obtained by the cyclic stress approach or the cyclic strain approach. Advanced models based on effective stress provide a more rigorous approach to liquefaction problems, although the number of soil parameters and their complexity prevent their extensive use outside of research laboratories.

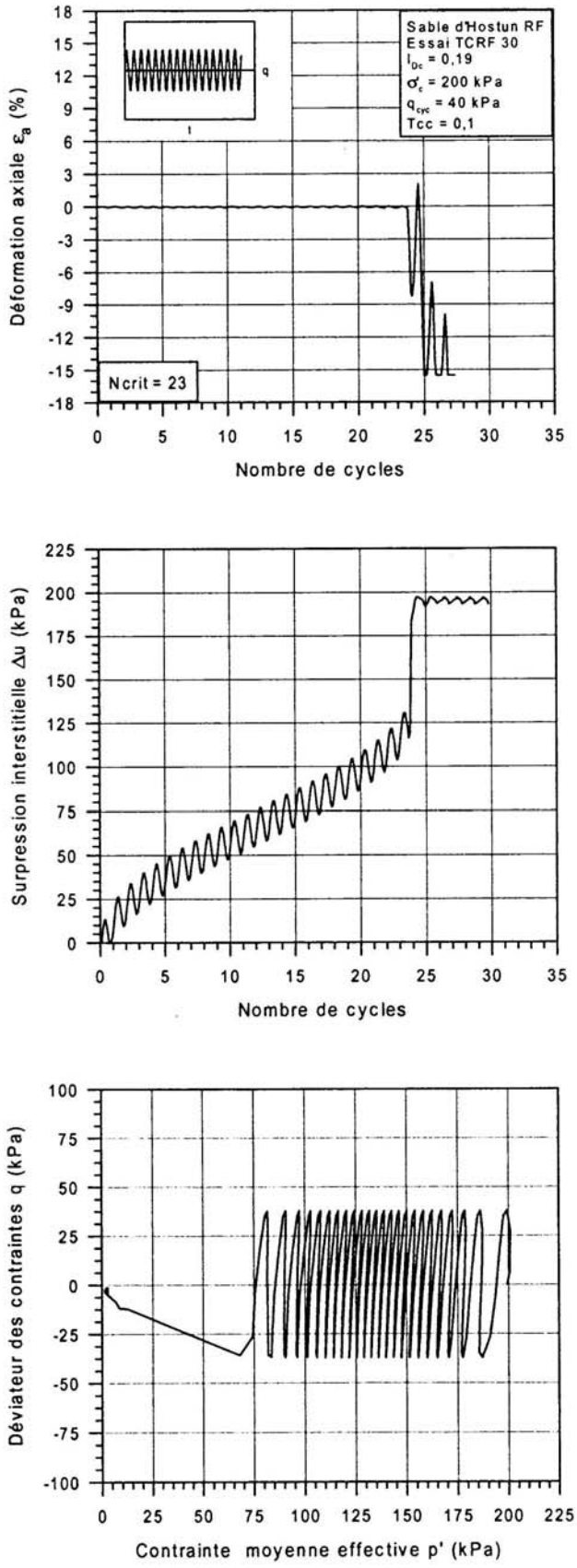

Fig. 2.14. Liquefaction of Hostun Sand by triaxial tests with stress reversal (Benahmed 2001).

2.4.13.3 Cyclic softening, cyclic liquefaction and cyclic mobility

Contrary to liquefaction, cyclic mobility and cyclic liquefaction arise in all soil types susceptible to dilate in a state of medium to dense fabric. Failure is not the result of a flow mechanism, but a gradual accumulation of strains. *Cyclic softening* is the progressive pore pressure increase due to dynamic loading. Excess pore pressure induces a decrease of effective stress, causing progressive increase of strain amplitude. Above the failure threshold strain amplitude, the terms *cyclic liquefaction* and *cyclic mobility* are used instead. Cyclic liquefaction refers to failure caused by loading paths including shear stress reversal (alternation of the sign of *q*). On the contrary, cyclic mobility refers to one-way loading only in compression or in extension. As conditions of zero effective stress do not develop, deformation is usually smaller. An example of cyclic liquefaction obtained by a triaxial test, for an undisturbed coarse sand sample, is given in Fig. 2.15.

At cyclic liquefaction, the pore pressure ratio reaches 100% momentarily, once or twice per cycle, when the deviatoric stress is equal to zero. Most of irreversible axial strains develop at zero effective confining pressure. The alternation of increase and decrease of pore pressure during each cycle corresponds to stress paths of «wings» shape (e.g. Fig. 2.15d).

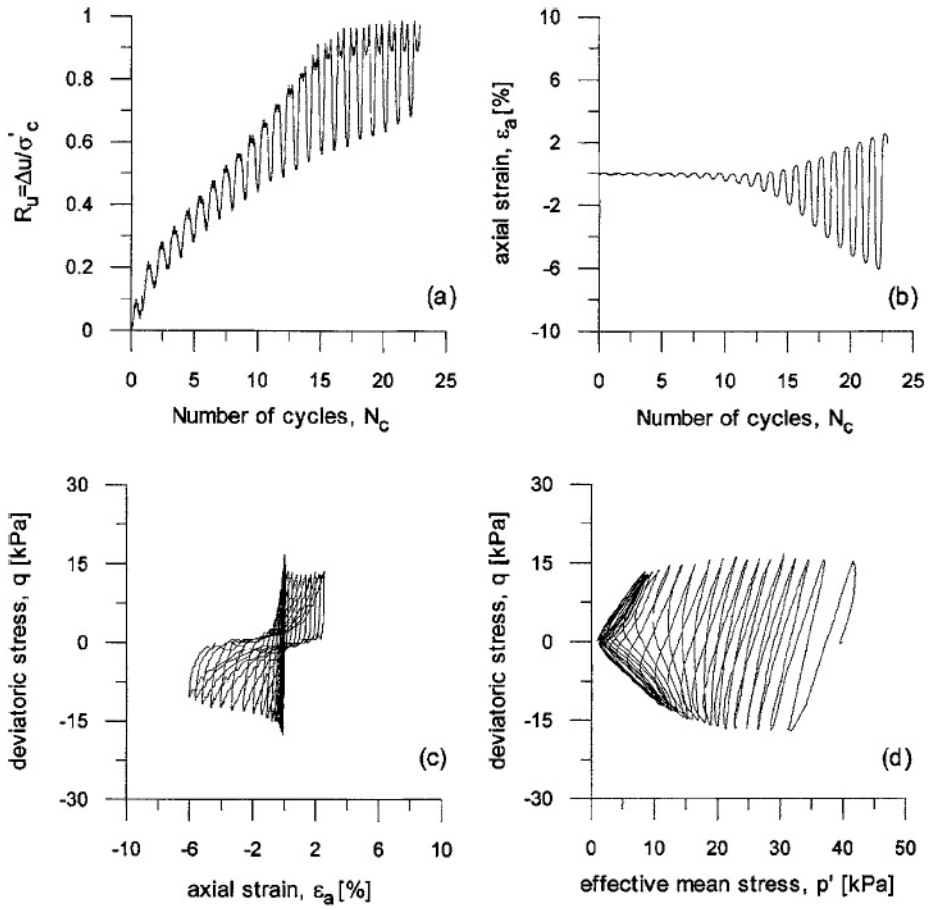

Fig. 2.15. Cyclic liquefaction of undisturbed coarse sand (Ghionna & Porcino 2006).

Cyclic liquefaction has been observed in many experimental study, for silts, sands and gravels, for reconstituted or intact samples (Luong 1980; Mohkam 1983; Ishihara & Nagase 1988; Vaid et al. 1989; Endo & Komanobe 1995; Hyodo et al. 1998; Benahmed 2001; Choi & Arduino 2004; Toyota et al. 2004; Bray & Sancio 2006; Ghionna & Porcino 2006; Sanin & Wijewickreme 2006; Hyde et al. 2006; Porcino et al. 2008).

2.4.13.4 The cyclic stress approach

For a given soil layer, the assessment of liquefaction susceptibility by the cyclic stress approach follows three steps:

- Characterization of earthquake loading: an irregular earthquake motion of known moment magnitude is turned into an equivalent cyclic loading of regular amplitudes with a certain number of cycles.
- Characterization of liquefaction resistance of soil: the cyclic stress ratio CSR at a given number of cycles and a given void ratio is obtained by laboratory tests or correlations with in situ tests.
- Evaluation of the factor of safety, which is the ratio of the CSR required to cause liquefaction on the CSR equivalent to earthquake-induced shear stress.

The cyclic stress ratio CSR is a simple concept widely used to evaluate the strength of soil upon cyclic load, for both flow liquefaction and cyclic liquefaction failure type. This parameter is obtained for stress-controlled laboratory tests. CSR is defined as the ratio of the maximum cyclic shear stress to the initial average effective normal stress. For the triaxial test, it is calculated by:

$$\mathrm{CSR} = \frac{q^{max}}{2\sigma_3'^0} \tag{2.21}$$

For a given void ratio and a given soil, the CSR is supposedly uniquely related to the *number of cycles at failure* (Finn et al. 1971), where the criterion for failure is usually based on a strain amplitude of 5% DA. An example of CSR curves determined for silty sand is shown in (Fig. 2.16). CSR mainly depends on relative density, also it is used as a criterion for instability upon liquefaction.

The CSR obtained by triaxial tests is multiplied by a correction factor for matching the values of CSR in simple shear tests or in the field (Kramer 1996). The loading pattern also is important; Benahmed (2001) showed that CSR is higher for tests without stress reversal ($q > 0$ only) than for tests with stress reversal. CSR is finally very sensitive to sample preparation, prestraining, OCR and aging effects (Dobry et al. 1982). The comparison between angular sand (Hostun sand) and round sand (Fontainebleau sand) shows that cyclic strength is higher for angular materials (Benahmed 2001).

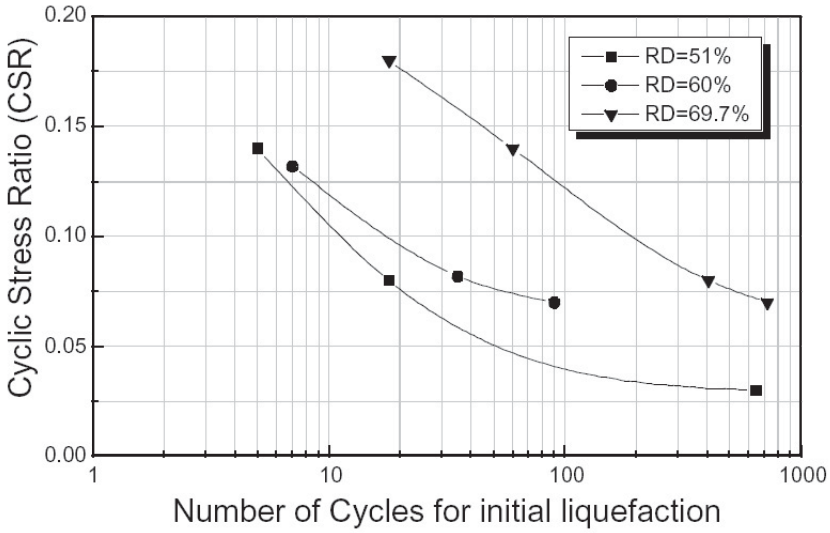

Fig. 2.16. Decrease of the cyclic stress ratio when the number of cycles to reach failure increases, at three relative densities (Sitharam et al. 2004).

2.4.13.5 Influence of the initial state and loading pattern on failure

Relative density

The major parameter influencing undrained cyclic behaviour of sands is the relative density (I_D) of the soil deposit:

$$I_D = \frac{e_{max} - e_0}{e_{max} - e_{min}} \tag{2.22}$$

where e_{max}, e_{min} and e_0 are the maximum, minimum and current void ratios. Maximum and minimum void ratios are intrinsic soil constants. The value of relative density controls whether cyclic liquefaction or flow liquefaction happens, and it also influences the cyclic strength. When the void ratio increases, the liquefaction potential increases too.

Initial effective stress

For two samples at the same relative density, the effect of initial effective confining pressure is also important. There is contradiction on the qualitative effect of initial confining pressure among laboratory tests results. Benahmed (2001) shows that cyclic strength increases with $\sigma_3'^0$. For two Hostun Sand samples at I_D = 0, the number of cycles to reach liquefaction is more than doubled when $\sigma_3'^0$ increases from 200 to 400 kPa, although the CSR remains the same. On the contrary, Hyodo et al. (2002) performed cyclic tests on dense sand (I_D = 80%) and obtained a decrease of cyclic strength with high $\sigma_3'^0$ (Fig. 2.17).

For dense rockfill (coarse granular) materials, cyclic and monotonic strength increases when the mean effective stress increases (Yasuda et al. 1997).

The effect of anisotropic consolidation on cyclic strength has also been studied. For Seed (1979) and Ishihara (1996), the liquefaction resistance increases with the consolidation stress ratio K_0. On the contrary, Benahmed (2001) shows that increasing K_0 can lead to liquefaction, when an isotropic consolidation had induced accommodation. For Ghionna & Porcino (2006), an increase of K_0 from 0.59 to 1 results in a decrease of cyclic strength for samples prepared with water sedimentation method, but it induces a small increase of CSR for the air pluviation method. We estimate the effect of $\sigma_3'^0$ for dry and undrained saturated cyclic loading of Leman Sand in Chapter 4.

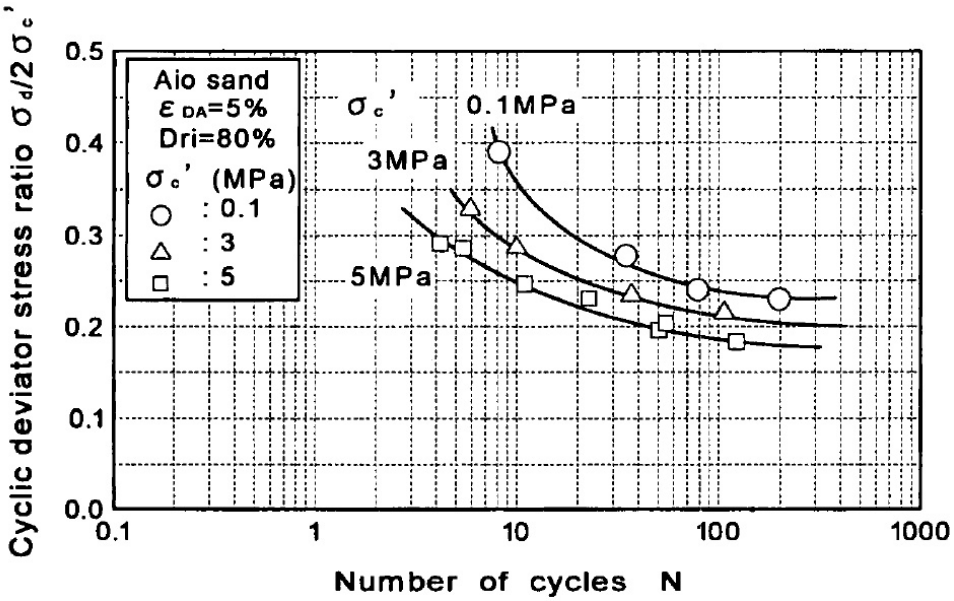

Fig. 2.17. Effect of initial confining pressure (Hyodo et al. 2002).

Stress reversal and one-way loadings

The soil response to triaxial tests is not the same whether the stress path includes stress reversal (alternation of the sign of q) or whether it is a one-way loading (only compression or extension cyclic loading). One-way loading in compression is more stable than a loading with stress reversal, whether they are isotropic or anisotropic (Ghionna & Porcino 2006; De Gennaro et al. 2004). These tests show that failure by cyclic mobility can arise during one-way loading in compression. Flow liquefaction can arise as well during one-way cyclic loading in compression (Benahmed 2001).

De Gennaro et al. (2004) show that one-way loading in extension induce more instability than the same test in compression, with an apparition of flow liquefaction instead of cyclic mobility. Moreover, the same test performed with symmetric stress reversal shows an even faster failure by cyclic liquefaction. When there is isotropic stress reversal, flow liquefaction always happens in the side of extension (Benahmed 2001; De Gennaro et al. 2004).

2.4.14 Conclusions

The principles and phenomena necessary to understand and analyse cyclic sand behaviour are described in this section, with an emphasis on conditions prevailing in triaxial tests. Indeed, these concepts are all used further during the interpretation of our test results, presented in Chapters 4, 5 and 6. The key concepts are summarized with a short mention of the context in which they are used for our triaxial tests:

- The distinction between triaxial extension and triaxial compression is of major importance to understand all monotonic and cyclic test results including stress reversal.
- The definition of steady state and phase transformation introduces the SS and PT lines (in the p' - q plane), which are obtained for the two sands tested during this project. These concepts are also used in the elastoplastic model described in section 2.6 and implemented in Chapter 7.
- The importance of strain amplitude for identifying the soil response is mentioned several times in this section, and is repeatedly observed in our tests. The classification of cyclic motions into small, medium and large strain amplitude is often used further for the description of soil behaviour (Chapters 4 to 7).
- Dilatancy phenomenon and the increase of pore pressure ratio are important to understand failure by cyclic liquefaction, which is often mentioned in all experimental and numerical results on dense sand.
- Stiffness degradation and failure mechanisms under cyclic loading are presented, with mentions of triggering factors. The definition of failure, based on a threshold deviatoric strain amplitude, is analysed in Chapter 4 for cyclic liquefaction of Leman Sand. Both stiffness degradation and failure are analysed for many experimental conditions, and they are also important for the evaluation of the two models presented in Chapter 7.

After this qualitative description of sand behaviour under cyclic loading, the dynamic material parameters are introduced below to allow a quantitative estimation of the soil response.

2.5 Dynamic material parameters

The secant shear modulus and the damping ratio are two material parameters used for characterizing cyclic soil behaviour. They are defined in this section, and detailed results of laboratory studies on dynamic parameters of granular materials are presented.

2.5.1 Secant shear modulus

2.5.1.1 General definition

Stiffness is the most basic parameter to evaluate soil behaviour. In the case of cyclic loading, the overall inclination of the stress-strain loop is more useful information than the instantaneous modulus. The average shear modulus over one cycle is best described by the secant shear modulus G_{sec}, which is proportional to the slope of the line reaching the points of higher and lower shear strain over one cycle (Fig. 2.18). The concept of secant shear modulus is well established in soil dynamics, thanks to models like the linear equivalent method, widely used in practice.

As it will be further discussed below, the secant shear modulus evolves primarily with the strain amplitude, with an influence of other parameters like relative density, number of cycles, stress state.

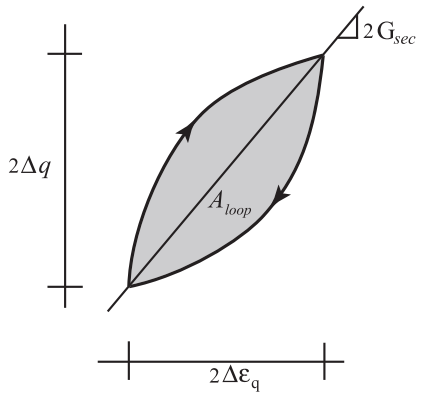

Fig. 2.18. Geometry of a cyclic loop, defined with invariants of stress and strain.

2.5.1.2 Definition of the shear modulus for multidirectional loading paths with the dynamic triaxial press

To obtain the shear modulus, the deviatoric parts of the linear model (presented later in Eq. 2.44) are equated. For the case of general effective stress (Eq. 2.9) and strain (Eq. 2.17) increments, the shear modulus G is calculated by:

$$G = \frac{\Delta q}{2\Delta \varepsilon_q} \tag{2.23}$$

For fully saturated undrained tests, no volume change occurs, i.e. $\varepsilon_v = \varepsilon_1 + 2\ \varepsilon_3 = 0$; as a consequence,

ε_3 = -1/2 ε_1 and ε_q = 3/2 ε_1. Thus the shear modulus can be calculated by:

$$G = \frac{\Delta q}{3\Delta\varepsilon_1} \tag{2.24}$$

Considering a cyclic loading, the secant shear modulus G_{sec} is usually used (cf. below).

2.5.1.3 Other elastic parameters

Young's modulus and Poisson's ratio

The linear elastic equation with E and ν can be written, for the triaxial case and for an effective stress increment $\Delta\sigma'_{ij}$ (defined in Eq. 2.9), as

$$\begin{bmatrix} \Delta\varepsilon_1 & 0 & 0 \\ 0 & \Delta\varepsilon_3 & 0 \\ 0 & 0 & \Delta\varepsilon_3 \end{bmatrix} = \frac{\Delta q}{E}\begin{bmatrix} 1 & 0 & 0 \\ 0 & -\nu & 0 \\ 0 & 0 & -\nu \end{bmatrix} + \frac{(1-2\nu)\Delta\sigma'_3}{E}\begin{bmatrix} 1 & 0 & 0 \\ 0 & 1 & 0 \\ 0 & 0 & 1 \end{bmatrix} \tag{2.25}$$

The constants E and ν can be determined in this general stress increment since this reduces to two equations with two unknowns, which are easy to solve numerically.

In the simplified case of constant confining pressure ($\Delta\sigma_3$ = 0), E and ν are simply found by:

$$E = \frac{\Delta\varepsilon_1}{\Delta q} \quad and \quad \nu = -\frac{\Delta\varepsilon_3}{\Delta\varepsilon_1} \tag{2.26}$$

Bulk modulus

For drained tests with volume change, the bulk modulus can be calculated by identifying the spherical parts of the linear model (Eq. 2.44), in the case of a general stress increment:

$$K_b = \frac{\Delta p'}{\Delta\varepsilon_V} \tag{2.27}$$

2.5.2 Damping ratio

2.5.2.1 Introduction

Stress waves in a soil substratum induce cyclic shearing and compressional loadings with decay of the amplitude away from the source, which is partly due to material losses (cf. section 2.3.4). The energy transformation in the material is observed through its hysteretic behaviour. Loops of varying amplitude and direction appear in the stress-strain plane, which is a major difference between considering cyclic loading of soils from monotonic loadings. In the laboratory also, during harmonic or triangular loading, stress-strain curves form series of loops. The damping ratio quantifies those material losses. More than

just a model parameter, its physical meaning is crucial for understanding cyclic soil behaviour.

The most common way, among geotechnical engineers, to apprehend the energy loss of a soil submitted to cyclic loading is the damping ratio (D or ξ). There are other parameters which could also be used, and which are related in some way to the damping ratio (Kramer 1996; Wolf 1994):

- the Quality factor $Q = 1/(2D)$ is used by seismologists
- the loss factor $\eta = 2D$ is used in vibration analysis
- the specific damping capacity $\Psi = 2\pi D$
- the coefficient of friction $\tan\delta = 2D$, where δ is an angle of internal friction of the soil

In seismic analysis, the damping ratio can include both the material damping and the radiation, which is the geometrical decrease of stress waves with the increasing distance from the source. Semblat & Luong (1998) provide experimental evidences on the separation of the attenuation of spherical waves, propagating in a finite medium in centrifuge tests, into a material and a geometrical attenuation. The radiation damping is not taken into account in the following chapters.

2.5.2.2 Physical interpretation of damping

It is commonly admitted that the hysteretic behaviour of soils is caused by energy dissipation. The mechanisms causing material damping include friction, plastic yielding and ultimately heat generation (Kramer 1996). The damping ratio of a soil, for a given stress-strain loop, is associated with the dissipated energy divided by the maximum stored (i.e. elastic) energy per cycle.

Material damping is generally considered to include two types of mechanisms (Bolton & Wilson 1990; Wang & Santamarina 2007). The first is a frequency-dependent *viscous loss*, caused by the pore fluid and internal energy coupling. The second is a frequency-independent *hysteretic loss* due to the displacements in the soil matrix, namely friction occurring at contact points. In essence, dry granular material is generally assumed to be hysteretic and to absorb energy as a function of cyclic strain. Above the linear threshold, energy dissipation of cyclically loaded dry grains is preponderantly of frictional nature (Wang & Santamarina 2007).

For dry cohesionless soils, the deformation of the system is essentially due to rearrangement of the soil matrix, and not to the deformation of the grains (Verruijt & Cordova 2001). The sliding or slipping of grains involves friction at interparticle contact, which is associated with hysteretic damping ratio. It is also important that the rearrangement of the grains occurs during both loading and unloading parts of the cycle. The sliding can be irreversible, or reversible if the grains come back to their original place after unloading.

Wang & Santamarina (2007) offer a different mechanism for explaining small strain damping ratio of dry sand, measured by resonant column tests. Under the threshold linear strain, this value, D_{min}, is independent from the strain, from the confining pressure, from the number of cycles, and it is higher than zero (but lower than 1%). They show that Mindlin's contact model does not apply at such very small strain, also friction is said to not be responsible for the energy loss below the linear threshold. The suggested mechanism responsible for material loss at small strain is the *thermoelastic relaxation*. The air moisture, causing adsorbed water layers around the grains, can also affect the damping ratio.

This decomposition of damping as the sum of two processes is not widely accepted, and in the following analyses this distinction is considered with great care. The concept of Rayleigh damping (Semblat 1997; Ju & Ni 2007), which is associated with numerical studies, is not taken into account, as it was not seen appropriate to the present study.

2.5.2.3 SDOF models and experimental determination

Discrete systems are used to simplify the representation and modelling of dynamic problems (Kramer 1996). The assemblage of springs and dashpots linked to rigid masses forms discrete elements, or single degree of freedom systems (*SDOF*), which is a convenient way to model mechanical material behaviour. The mechanism for representing energy dissipation in many discrete systems is the viscous damping controlled by the dashpot. The Kelvin model associates the spring and dashpot in parallel, while they are mounted in series for the Maxwell model.

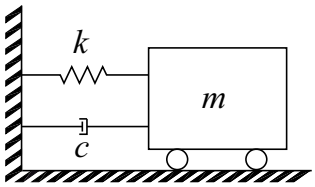

Fig. 2.19. Single degree of freedom Kelvin model with a mass *m*, a spring of stiffness *k* and a dashpot of viscous damping *c*.

Damped system in free vibrations

The field equation ruling the free vibrations of a *SDOF* system, as shown in (Fig. 2.19), is:

$$m\ddot{u} + c\dot{u} + ku = 0 \tag{2.28}$$

where u is the displacement. With the stiffness $k = m\omega_0^2$, where ω_0 is the natural circular frequency, and the critical damping coefficient $c_c = 2\sqrt{km}$, the equation is reduced to:

$$\ddot{u} + 2\frac{c}{c_c}\omega_0\dot{u} + \omega_0^2 u = 0 \tag{2.29}$$

The damping ratio is defined as the ratio $D = c/c_c$. The solution of the differential equation depends on the damping ratio value:

- if $D > 1$, the system is called overdamped. It monotonically reaches an equilibrium value.
- if $D = 1$, there is a unique oscillation before reaching the equilibrium value. This is the critically damped case.
- if $D < 1$, oscillations occur with a decreasing amplitude. This is an underdamped system. The smaller the damping ratio, the faster oscillation amplitudes decrease.

The underdamped case is the one that concerns earthquake engineering and vibratory analysis of structures.

The experimental evaluation of damping ratio can be performed in a free vibratory system. The resonant column test can be used in that way: after reaching the resonant frequency, the drive system is cut off. The decay of free vibrations is observed to determine the damping ratio (Ishihara 1996).

Damped system in forced harmonic vibrations

In such a *SDOF* system, the combination of the spring and the dashpot exerts a net force $F = ku(t) + c\dot{u}(t)$ on the mass. Considering a harmonic forced vibration $u(t) = u_0 \sin(\bar{\omega}t)$, the hysteresis force - displacement loops of the system are inclined ellipses, as depicted in Fig. 2.20.

The damping ratio of that system can be experimentally obtained from the force - displacement loop. The calculation of the energy dissipated during one cycle (W_D) gives:

$$W_D = \int_{t_0}^{t_0 + 2\pi/\bar{\omega}} F \frac{du}{dt} dt = \pi c \bar{\omega} u_0^2 \tag{2.30}$$

Resulting in $c = W_D / \left(\pi \bar{\omega} u_0^2 \right)$. Another parameter used for calculating the damping ratio is the maximum elastic stored energy (W_S), which is obtained at the point of maximum displacement. The calculation of W_S gives:

$$W_S = \frac{1}{2} k u_0^2 \tag{2.31}$$

thus $k = 2W_S / u_0^2$. The damping ratio definition for free vibrations can be expressed as $D = c\omega_0 / 2k$. Replacing *c* and *k* by the relations obtained above, and assuming $\bar{\omega} = \omega_0$, leads to the famous relation:

$$D = \frac{W_D}{4\pi W_S} \tag{2.32}$$

The damping ratio is obtained experimentally, from the geometry of stress-strain loops, thanks to this relationship (Eq. 2.32).

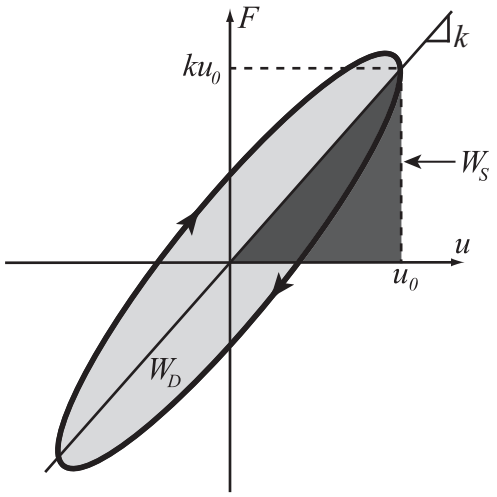

Fig. 2.20. Hysteretic loop for harmonic displacements of a damped *SDOF* system.

2.5.2.4 Damping ratio definition for unidirectional and multidirectional loadings with the dynamic triaxial press

The actual experimental value in condition of conventional triaxial tests (CTC) is obtained from the representation in the ε_1 - q plane (Fig. 2.21).

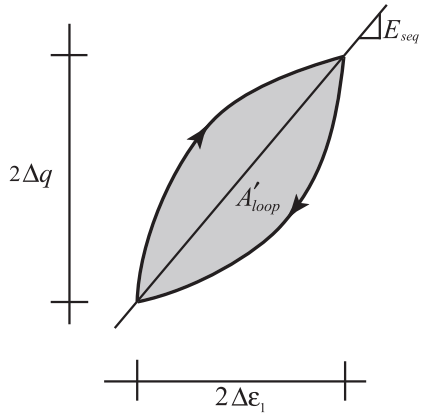

Fig. 2.21. Definition of the geometry of a stress - strain loop for CTC triaxial tests.

Expressing W_S in terms of Young's modulus and strain amplitude gives the following relation for cyclic triaxial tests with a constant confining pressure (e.g. Ishihara 1996):

$$D = \frac{A'_{loop}}{2\pi\, E_{sec} \cdot \Delta\varepsilon_1^2} \tag{2.33}$$

where A'_{loop} is the loop area shown in Fig. 2.21.

For multidirectional loadings (defined in Chapter 3 for triaxial conditions) and generalized stress increments, the damping ratio should be calculated with invariants of stress and strain. The actual

experimental value for triaxial tests is obtained from the loops represented in the ε_q - q plane (Fig. 2.18), by expressing the stored energy as a function of the characteristics of each stress - strain loop:

$$D = \frac{A_{loop}}{4\pi \dfrac{\Delta q \cdot \Delta \varepsilon_q}{2}} = \frac{A_{loop}}{4\pi \dfrac{2\,G_{sec} \cdot \Delta \varepsilon_q \cdot \Delta \varepsilon_q}{2}} \tag{2.34}$$

then

$$D = \frac{A_{loop}}{4\pi\ G_{sec}\ \Delta \varepsilon_q^2} \tag{2.35}$$

Eq. 2.35 is used for calculating the damping ratio from cyclic triaxial tests in Chapters 4 to 6.

In special cases, e.g. in the situation of undrained loading (when ε_q = 1.5 ε_1) and if the total confining pressure is constant ($\Delta\sigma_3$ = 0), this relation (Eq. 2.35) can be reduced to the definition found in the literature (Eq. 2.33) thanks to the following developments:

$$D = \frac{A_{loop}}{4\pi \dfrac{\Delta q \cdot \Delta \varepsilon_q}{2}} = \frac{A_{loop}}{2\pi\ \Delta q \cdot \Delta \varepsilon_q} = \frac{A_{loop}}{2\pi \left(E_{sec} \cdot \Delta \varepsilon_1\right) \cdot \left(\dfrac{3}{2} \Delta \varepsilon_1\right)} = \frac{A_{loop}}{3\pi\ E_{sec} \cdot \Delta \varepsilon_1^2} \tag{2.36}$$

The relation between the loop areas in the ε_1 - q and ε_q - q planes is (still in the special conditions given above):

$$A_{loop} = \int_{t_0}^{t_0+\frac{2\pi}{\omega}} q\ \frac{\mathrm{d}\,\varepsilon_q}{\mathrm{d}\,t}\,\mathrm{d}\,t = \int_{t_0}^{t_0+\frac{2\pi}{\omega}} q\ \frac{\mathrm{d}\left(\dfrac{3}{2}\varepsilon_1\right)}{\mathrm{d}\,t}\,\mathrm{d}\,t = \frac{3}{2} \int_{t_0}^{t_0+\frac{2\pi}{\omega}} q\ \frac{\mathrm{d}\,\varepsilon_1}{\mathrm{d}\,t}\,\mathrm{d}\,t = \frac{3}{2}\,A'_{loop} \tag{2.37}$$

Finally the usual damping ratio definition can be recognized:

$$D = \frac{3}{2} \frac{A'_{loop}}{3\pi\ E_{sec} \cdot \Delta \varepsilon_1^2} = \frac{A'_{loop}}{2\pi\ E_{sec} \cdot \Delta \varepsilon_1^2} \tag{2.38}$$

2.5.3 Strain dependency of dynamic parameters

Experimental observations have shown, in many different laboratory or in situ conditions, that the secant shear modulus and damping ratio are strongly influenced by the shear strain amplitude (e.g. Hardin & Drnevich 1972a; Kokusho 1980; Dobry et al. 1982; Seed et al. 1986; Ray & Woods 1988;

Vucetic & Dobry 1991; Vucetic 1994; Elgamal et al. 1996; Li & Yang 1998; Wang & Kuwano 1999; Puzrin & Shiran 2000; Hoque & Tatsuoka 2004; Sitharam et al. 2004; Hardin & Kalinski 2005; Bui et al. 2007; Georgiannou et al. 2008; Yamada et al. 2008; Cox et al. 2009; Karg & Haegeman 2009).

For very low strain level, sands exhibit a hysteretic behaviour, with cyclic stress-strain loops of small damping ratio D_{min} and high secant shear modulus G_{max}. When strain amplitude exceeds 10^{-5}, the damping ratio increases and the shear modulus decreases from G_{max}. The linear threshold shear strain γ_{tv} is the limit above which dynamic parameters change with the shear strain amplitude. Stiffness reduction curves represent the decrease of G_{sec} and increase of D with the shear strain (e.g. Fig. 2.22).

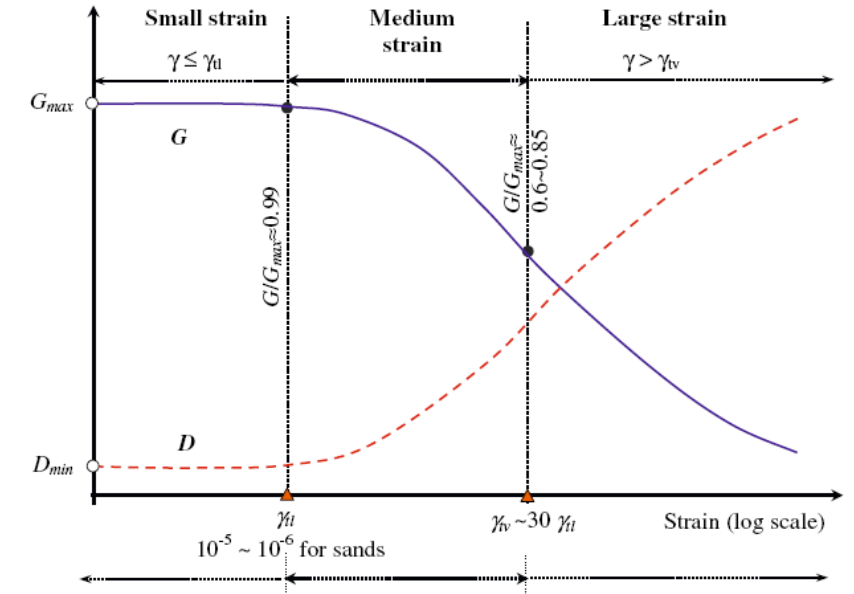

Small strain	Medium strain	Large strain
Strain-independent G_{max} & D_{min}	Minor fabric changes	Change in contact distribution
Deformation: at contacts	Small volume change	Destruction of initial fabric
Preserves molecular bonds	Strain-dependent G and D	Volume changes in drained loading
Very small energy loss	$G(\gamma) < G_{max}$	Pore fluid pressure changes if $\varepsilon_{vol}=0$
Poisson's ratio (S<100%): ν~0.1	$D(\gamma) > D_{min}$	High frictional energy loss
Quasi linear, elastic	Nonlinear, elastoplastic	Nonlinear

Fig. 2.22. Stiffness reduction curves (Wang & Santamarina 2007).

Wang & Santamarina (2007) recall that the damping ratio does not reach zero, even at really small strain. Under the linear threshold, it is equal to a constant value D_{min}, which is independent from the number of cycles, the frequency, the confining pressure and the strain amplitude in dry conditions. The frictional energy loss is proved to not appear in the case of really small strains, and the mechanism responsible for a non-zero damping ratio at small strain is the thermoelastic relaxation.

2.5.4 Evaluation of the elastic shear modulus

The elastic shear modulus, or maximum shear modulus, or initial shear modulus G_{max} can be calculated from the shear wave velocity (c_s), measured by in situ geophysical tests (cf. Appendix 1):

$$G_{max} = \rho c_s^2 \tag{2.39}$$

Laboratory studies, like bender element tests, resonant column tests and cyclic triaxial tests at small strain also allow to measure G_{max} on reconstituted or intact samples. Huot (1999) shows that G_{max} has the same value, whether it is obtained with ultra-sonic technique (acoustic transmission) or by pseudo-dynamic tests. There is now general agreement that soil elastic properties evaluated at very small strains by pseudo-static tests are consistent with the ones evaluated by dynamic tests, when same conditions prevail (Tatsuoka 2006).

If experimental or in situ data are not available, empirical equations derived from laboratory studies are numerous. Elastic shear modulus is usually given under the form (e.g. Kokusho 1980; Ishihara 1996):

$$G_{max} = AF_c(e)\,\mathrm{OCR}^k \left(\frac{p'}{p_{ref}} \right)^{n_e} \tag{2.40}$$

where A is a parameter depending on soil, F_c is the compacity function depending on void ratio e, p_{ref} is a reference value of pressure, n_e is an adimentional parameter, and the soil parameter k depends on OCR. The linear shear modulus mainly depends on void ratio and confining pressure. The function $F_c(e)$ can be evaluated by (Hardin & Drnevich 1972b):

$$F_c(e) = \frac{1}{0.3 + 0.7e^2} \tag{2.41}$$

The n_e coefficient is often defined by n_e = 0.5, although it can be determined by laboratory tests, depending of the soil type. Moreover, OCR widely influences elastic modulus value through the plasticity index PI. The most important factors influencing G_{max} and D_{min} are summarized in Tab. 2.1.

Tab. 2.1. Factors influencing small strain damping and secant shear modulus (Wang & Santamarina 2007)

"Increasing" Factors	The maximum shear modulus G_{max}		The minimum damping ratio D_{min}	
	Sands	Clays	Sands	Clays
Strain	Quasi constant (decisive decrease as $\gamma > \gamma_{tl}$)		Quasi constant (decisive increase as $\gamma > \gamma_{tl}$)	
Confining pressure, σ'	Increases with σ'		None/slight decrease with σ'	
Degree of saturation, S	Decreases with S[a]		Non monotonic variation with saturation	
Preloading	Isotropic: Slight-none, K_o: function of OCR	Increases with OCR	Slight or no effect	Decreases with OCR
Aging time, t	Increases with t		Decreases with t	
Cementation, c	High increase with c	Increase with c[b]	Inconclusive	May decrease with c

Note: [a] Caution: depends on drying-wetting history
[b] Cemented, high void ratio natural clays may exhibit higher stiffness after remolding and reconsolidation (same stress level but lower void ratio)

2.5.5 Factors influencing the secant shear modulus and damping ratio

Hardin & Drnevich (1972a) provide a list of the parameters influencing G_{sec} and D thanks to an extensive experimental campaign with hollow cylinder torsional tests and resonant column test. Shear strain amplitudes are from 0.2×10^{-4} to 10×10^{-4} for the shear test, and the resonant column measurements the G_{max} value at strain around 10^{-5}. Clean sands and cohesive soils are used. This study is the original reference for the parameters affecting the secant shear modulus and the damping ratio of soils at small to medium strain range. The summary of the relative influence of various parameters is found in Tab. 2.2.

Tab. 2.2. Parameters affecting G_{sec} and D (Hardin & Drnevich 1972a)

Parameter	IMPORTANCE TO[a]			
	Modulus		Damping	
(1)	Clean sands (2)	Cohesive soils (3)	Clean sands (4)	Cohesive soils (5)
Strain Amplitude	V	V	V	V
Effective Mean Principal Stress	V	V	V	V
Void Ratio	V	V	V	V
Number of Cycles of Loading	R[b]	R	V	V
Degree of Saturation	R	V	L	U
Overconsolidation Ratio	R	L	R	L
Effective Strength Envelope	L	L	L	L
Octahedral Shear Stress	L	L	L	L
Frequency of Loading (above 0.1 Hz)	R	R	R	L
Other Time Effects (Thixotropy)	R	L	R	L
Grain Characteristics, Size, Shape, Gradation, Mineralogy	R	R	R	R
Soil Structure	R	R	R	R
Volume Change Due to Shear Strain (for strains less than 0.5 %)	U	R	U	R

[a] V means Very Important, L means Less Important, and R means Relatively Unimportant except as it may affect another parameter; U means relative importance is not clearly known at this time.
[b] Except for saturated clean sand where the number of cycles of loading is a Less Important Parameter.

2.5.5.1 Confining pressure

Hardin & Drnevich (1972a) already mentioned that the effective mean principal stress influences the degradation curves of sand. The value G_{max} explicitly depends on *p'* for empirical equations and for some elastoplastic models (Hujeux 1985; Ling & Liu 2003), as well. *D* and G_{sec} / G_{max} are also affected directly by the confining pressure: the damping ratio is smaller with high confining pressure, and the shear modulus ratio is higher (Kokusho 1980; Ishihara 1996; Kramer 1996; Cascante & Santamarina 1996; Assimaki et al. 2000; Elgamal et al. 2005; Altun & Goktepe 2006).

Augustesen et al. (2004) show that strain response to load application depends on the confining pressure. At small confining pressure, the sand response is almost instantaneous; deformations are due to grains rearrangement from the sliding and rolling. At high confining pressure, deformations are due to crushing and deformation of the grains, and they continue for a certain time period with a decreasing rate.

2.5.5.2 Void ratio

As previously mentioned, the void ratio controls whether the sand dilates or contracts, and in which extent. Besides the failure mode by flow or cyclic liquefaction, the shape of the stress-strain loop, thus the damping ratio, is influenced by the void ratio. Contrary to the response of loose sand, the degradation curve of damping ratio of dense sand can exhibit a peak (Elgamal et al. 2005). Damping ratio first increases with shear strain, but then it decreases for strains higher than 0.2%. The stress-strain loop present a typical «S shape», or «banana shape». It is explained that soil dilation is responsible for the decrease of energy dissipation after the peak value. Besides that peak phenomenon, *D* decreases when the void ratio increases for soft clays (Kramer 1996), but slightly increases in sands (Kokusho 1980).

The secant shear modulus as well depends on the relative density. The effect of the void ratio on G_{max} is explicitly taken into account in all empirical formulations. For most experimental results, the effect of the void ratio on the degradation curve of G_{sec} is removed by the normalization with G_{max} (e.g. Karg & Haegeman 2009), although Kokusho (1980) writes that G_{sec} / G_{max} of sand slightly decreases when the void ratio increases and Kramer (1996) reports that G_{sec} / G_{max} of soft clays increases with the void ratio.

2.5.5.3 Number of cycles

The number of cycles is the main parameter with regards to the loading history in cyclic loading. The evolution of the dynamic parameters of sand in dry or undrained conditions has been investigated by laboratory experiments.

Undrained conditions

Kramer (1996) summarizes the effect of the number of cycles on dynamic parameters for sands, under undrained stress-controlled conditions: (i) G_{sec} / G_{max} decreases after N for large enough strains (above the volumetric cyclic threshold shear strain) and (ii) the effect of N on D is not significant at moderate strain and number of cycles.

Stiffness degradation during cyclic loading is then viewed as a consequence of the variation (increase or decrease) of excess pore pressure, and strongly depends on the soil type. The degradation index DI is defined, to obtain a quantitative description of the phenomenon. For the Nth cycle, it can be expressed by:

$$DI = \frac{G_{sec}^{N}}{G_{sec}^{1}} \tag{2.42}$$

where G_{sec}^{N} is the shear modulus determined at the Nth cycle and G_{sec}^{1} is the initial shear modulus (during the first cycle).

Dry conditions

Contrary to the undrained case, the secant shear modulus of dry sand increases with the number of cycles, i.e. stiffness increases, while the damping ratio markedly decreases (Ray & Woods 1988; Li & Yang 1998). This observations holds only at strain amplitude above the volumetric cyclic threshold shear strain (Li & Yang 1998).

2.5.5.4 Other effects

Other soil or test parameters influence the dynamic parameters, such as soil anisotropy (Chaudhary et al. 2002; AnhDan et al. 2006), fine content of clayey sand (Wang & Kuwano 1999), plasticity index of fine-grained soils (Okur & Ansal 2007), irregular loading (Ray & Woods 1988), particle shape (Bui et al. 2007; Khan et al. 2008), degree of saturation (Wang & Santamarina 2007).

2.6 Constitutive modelling of granular soils for cyclic loading

2.6.1 Introduction

Many constitutive models may be selected for an overview of existing tools for dynamic modelling of soils. However, it is not the aim here to list all of them; it is intended instead to describe only those explicitly mentioned further within the exploitation of laboratory results (see Chapter 7). In particular, all the hysteretic models based on Masing's rule (hyperbolic model, Ramberg-Osgood model, Iwan model, Cundall-Pyke model, logarithmic function (Puzrin & Shiran 2000)), of intermediary complexity between the equivalent linear model and the multi-mechanisms elastoplastic model, are not mentioned anymore.

A concise description of four different models of increasing complexity is presented below:

- The linear model
- The linear viscoelastic model
- The linear equivalent model
- The multi-mechanisms elastoplastic model of Hujeux.

2.6.2 Linear elastic model

When strain is small enough ($\gamma < 10^{-5}$), soil is assumed to behave linearly. The deformations of granular soils are elastic and recoverable. The relationship between stress tensor and strain tensor is given by:

$$\overline{\sigma'} = \mathbf{D} : \overline{\varepsilon} \quad \text{or} \quad \sigma'_{ij} = D_{ijkl}\, \varepsilon_{kl} \tag{2.43}$$

where **D** is the rigidity tensor, which is of the fourth order in the general case. For the linear isotropic model, only two parameters are necessary to describe the system. The symmetry allows simplification to the relationship:

$$\sigma'_{ij} = t_{ij} + p' \delta_{ij} = 2 G e_{ij} + K_b\, \varepsilon_V\, \delta_{ij} \tag{2.44}$$

where G is the shear modulus and K is the bulk modulus. Other equivalent relations are used with different parameters: the Lamé coefficients μ and λ, the Young's modulus E and the Poisson's ratio ν are also used in soil mechanics.

The main subject of interest for this simple model is the influence of initial conditions, such as void ratio, confining pressure or overconsolidation state of the medium.

However, experimental evidences tend to show that even at very small strain, energy dissipation through damping exists as well during cyclic loading (Huot 1999; Wang & Santamarina 2007). Damping is neglected in linear elasticity, which is a major disadvantage. A viscoelastic model can be used instead, which uses a complex modulus with a viscosity parameter included.

2.6.3 Linear viscoelastic model

The linear viscoelastic model is a way of introducing a damping component, which induces stress - strain curves with hysteresis shapes. In unidimensional condition, the material is seen as a spring - dashpot system, in which model parameters are the spring constant (G) and the dashpot constant (η). The Kelvin-Voigt model, with spring and dashpot mounted in parallel, gives the constitutive relation (for the 1D problem):

$$\tau = G\gamma + \eta \frac{\mathrm{d}(\gamma)}{\mathrm{d}t} \tag{2.45}$$

Where τ the shear stress and γ the shear strain. A complex modulus G^* is defined, written as a function of the angular frequency (ω):

$$G^* = G + i\omega\eta \tag{2.46}$$

The viscoelastic model has a simple expression in the frequency domain:

$$\tau = G^*\gamma \tag{2.47}$$

2.6.4 Linear equivalent model

Nonlinear soil behaviour can be simply taken into account by considering the evolution of the dynamic parameters (G_{sec}, D) with shear strain within a modified viscoelastic model (e.g the programme SHAKE91 (Idriss & Sun 1992)). In the linear equivalent model, the complex modulus (G^*) is also a function of the shear strain γ, i.e. $G^* = \tilde{G}^*(\omega, \gamma)$, thanks to numerical iterations. The complex modulus (Eq. 2.46) depends on the secant shear modulus ($G = G_{sec}$) and the damping ratio ($\eta = 2D$), which are the model parameters defined for each soil as a function of γ. Actually, the input parameter of the linear equivalent model is not directly G_{sec}, but the normalized function G_{sec} / G_{max} vs. γ.

The curves of the decrease of G_{sec} / G_{max} and increase of D with γ are usually obtained from laboratory tests or from the literature. For example, Fig. 2.23 and Fig. 2.24 present the evolution of both parameters as a function of shear strain for different initial pressures. We provide such curves for Leman Sand and Fonderie Sand in various conditions (Chapters 4 to 6).

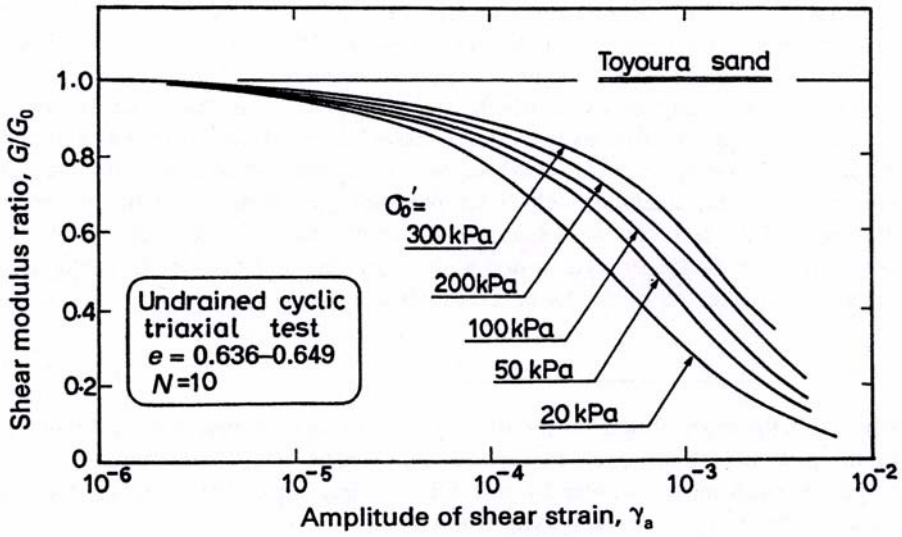

Fig. 2.23. Secant shear modulus ratio vs. shear strain (Ishihara 1996).

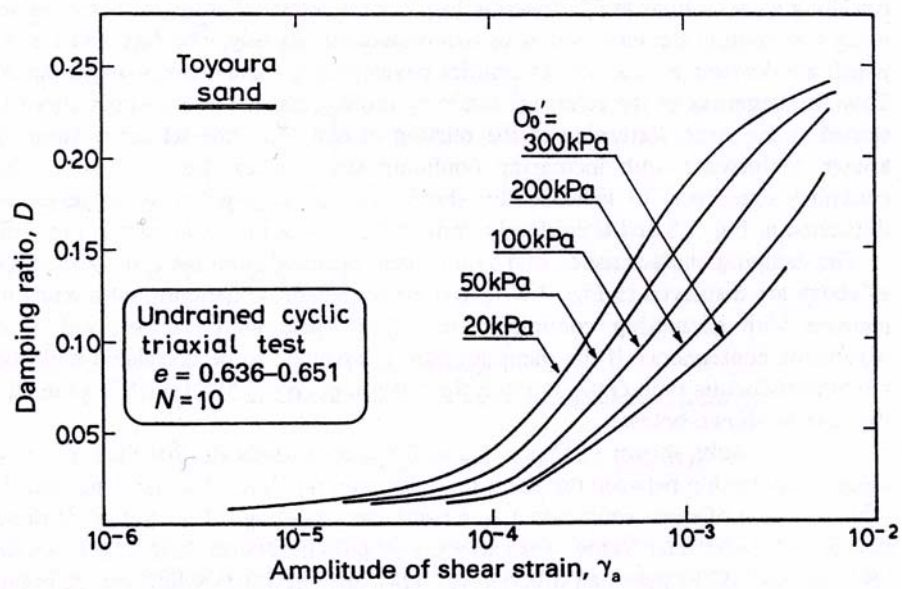

Fig. 2.24. Damping ratio vs. shear strain (Ishihara 1996).

The linear equivalent model is widely used in earthquake engineering, when taking into account the strain dependence of secant shear modulus and damping ratio. It is solved in the frequency domain, thus very convenient for soil response analyses, response spectra, and even site effect analyses at larger scale. Actually, microzonation studies can be performed with such a tool, in 1D or 2D (Cid et al. 2001; Lacave et al. 2008).

The main shortcoming of the linear equivalent model is that it disregards all irrecoverable strains; it is also usually implemented without hydro-mechanical coupling and ignores pore pressure increase. It is thus normally limited to strains below 10^{-3}, which approximately corresponds to the domain of

stabilized hysteretic behaviour (Hujeux 1985). Another drawback is the removal of most of the high-frequency content of the response, because of an overdamping of high frequencies (Hartzell et al. 2004). We implement the linear equivalent model in Chapter 7, and evaluate these problems with regard to our test results.

An example of a modified equivalent linear model by Yoshida et al. (2002) shows that this model is perfectible, and can still be promising. This new model is claimed *«to be applicable at more than 1% shear strain»*. Assimaki & Kausel (2002) also propose a new algorithm for the linear equivalent method, which improves the modelling of nonlinear site amplification, compared to the initial model.

2.6.5 Elastoplastic models

2.6.5.1 Introduction

Advanced constitutive models suitable for cyclic loading were also adapted from existing theories of plasticity, elastoplasticity, viscoplasticity, hypoplasticity. Those complete effective stress models describe soil behaviour on a range of stress paths. Their development is based on incremental relations between strain and effective stress. Such models predict transient and permanent deformations within the soil mass, and are then much more interesting than the linear equivalent model for modelling catastrophic displacements or collapse of soil structures (e.g. Muir Wood 1998).

Among advanced elastoplastic models, the multi-surface theory (Mroz et al. 1981) can reproduce cyclic behaviour with either two surfaces or an infinite number of nesting surfaces. An example of a multiple surface plasticity model with the «*u - p*» formulation is presented by Elgamal et al. (2002) for granular soils. Another family of models is the bounding surface theory. For example Khalili et al. (2005) applied it to cyclic loading of sand.

The advanced model used in this thesis (Chapter 7) is based on multi-mechanisms elastoplasticity. Hujeux (1985) describes its application to cyclic loading of sand. Laloui (1992), Mellal (1997), Lopez-Caballero (2003), Cekerevac (2003) thoroughly developed the Hujeux model for all kinds of environmental loading, such as thermal loading, unsaturated soil behaviour and dynamic loading from earthquake. The thermo-hydro-mechanical coupling is included in the last advances of the model ACMEG in various PhD thesis presented at EPFL (François 2008; Koliji 2008; Péron 2008; Nuth 2009).

2.6.5.2 Description of the Hujeux model for cyclic loading

Using the concept of multi-mechanisms plasticity (Hujeux, 1985), the total irreversible deviatoric strain increment ε_q^p is induced by coupled dissipative processes: an isotropic and three deviatoric plastic

mechanisms (Fig. 2.25), respectively identified by the subscripts *iso* and *k*. Each of them produces a plastic strain increment, $\varepsilon_{q,iso}^{p}$ and $\varepsilon_{q,k}^{p}$, respectively. The coupling parameter of all four mechanisms is the volumetric plastic strain (ε_{V}^{p}), which is the sum of the volumetric plastic strain of the each mechanism. The preconsolidation pressure is a term in common for the deviatoric and the isotropic yield surface.

The main parts of the constitutive model summarized below are: (i) nonlinear elasticity, (ii) domains of behaviour, (iii) preconsolidation pressure, (iv) deviatoric mechanisms and deviatoric yield surface, (v) isotropic mechanism and isotropic yield surface.

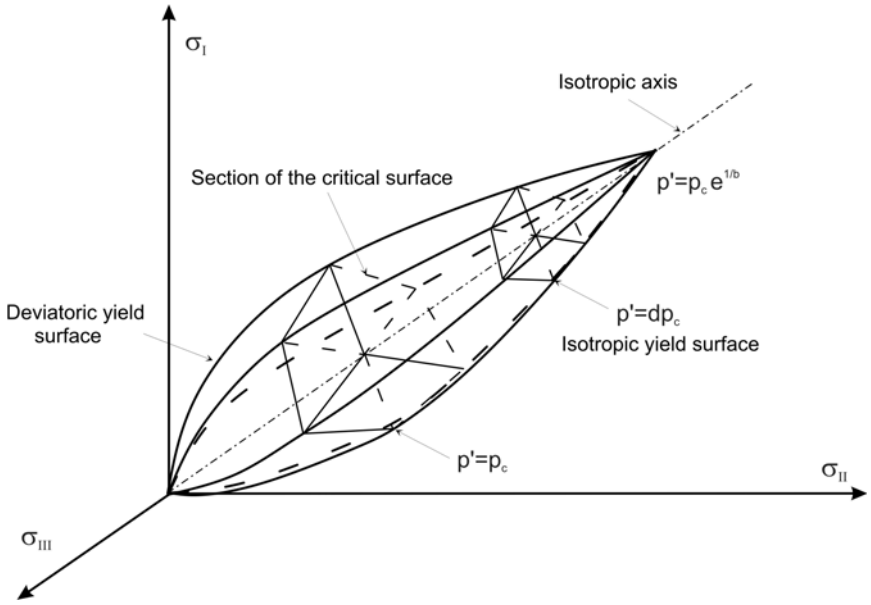

Fig. 2.25. Yield limits for the 4-mechanisms Hujeux model (Cekerevac 2003).

Nonlinear elasticity

The bulk and shear moduli at small strain depend on the mean effective stress *p'*:

$$K_{max} = K_{ref}\left(\frac{p'}{p'_{ref}}\right)^{n_e} \text{ and } G_{max} = G_{ref}\left(\frac{p'}{p'_{ref}}\right)^{n_e} \tag{2.48}$$

where K_{ref} and G_{ref} are elastic bulk and shear moduli at reference pressure p'_{ref} (default value 1 MPa), and n_e is an elastic parameter of the material.

Domains of behaviour

There are four domains of behaviour, defined for each deviatoric mechanism k: (i) the elastic domain at very small strains (ii) the hysteretic domain at small strains (iii) the intermediary domain at medium strains and (iv) the mobilized domain at large strains. The degree of plastification of each mechanism is

the parameter r_k, which is defined later within the description of the deviatoric yield surface. The domains are limited by three radiuses, so that:

- If $0 < r_k < r_k^{ela}$, the domain is elastic.
- If $r_k^{ela} < r_k < r_k^{hys}$, the hysteretic domain is defined by the relation $\alpha_k(r_k) = 0$.
- If $r_k^{hys} < r_k < r_k^{mob}$, the intermediary domain, which includes stiffness degradation, is defined by $\alpha_k(r_k) = \left(\frac{r_k - r_k^{hys}}{r_k^{mob} - r_k^{hys}} \right)^m$.
- If $r_k^{mob} < r_k < 1$, the mobilized domain is defined by $\alpha_k(r_k) = 1$.

Preconsolidation pressure

A unique preconsolidation pressure p_c' is defined for the four mechanisms. This parameter accounts for strain hardening in density.

$$p_c' = p_{c0}' \exp\left(\beta \varepsilon_V^p\right) \tag{2.49}$$

where β is the plastic compressibility of soil, and p_{c0}' is the initial preconsolidation pressure.

Deviatoric mechanisms and deviatoric yield surface

The decomposition of the deviatoric plastic response into three mechanisms is made in a fixed frame of reference (*i*, *j*, *k*). As an example, the yield limit associated with the *k*-axis is defined by the function:

$$f_k = q_k + \sin(\phi') p_k' F_k r_k \tag{2.50}$$

where ϕ' is the friction angle mobilized at critical state. The function F_k is obtained by:

$$F_k = 1 - b \ln\left(\frac{p_k'}{p_c'} \right) \tag{2.51}$$

where *b* is a soil parameter which influences the shape of the yield surface. If *b* = 0, the yield limit is the Mohr-Coulomb failure line, and if *b* = 1, the yield surface is the Cam-Clay type. For sands, it is commonly admitted that $0.1 \le b \le 0.2$.

For each deviatoric mechanism *k*, the degree of plastification r_k depends on the plastic component of the deviatoric strain $\varepsilon_{q,k}^p$:

$$r_k = r_k^{ela} + \frac{\varepsilon_{q,k}^p}{a + \varepsilon_{q,k}^p} \tag{2.52}$$

with the parameter *a* defined by:

$$a = a_{cyc} + \left(a_m - a_{cyc}\right)\alpha_k\left(r_k\right) \tag{2.53}$$

where a_m and a_{cyc} are soil parameters of the hardening law of the deviatoric mechanisms, for monotonic and cyclic parts respectively.

The flow rule of each deviatoric mechanism *k* assumes the form (Lopez-Caballero 2003):

$$\dot{\varepsilon}^p_{v,k} = \dot{\lambda}^p_k \left(-\alpha\, \alpha_k\left(r_k\right)\left(\sin\left(\psi\right) + \frac{q_k}{p'_k} \right) \right) \tag{2.54}$$

where α and ψ are the dilatancy coefficient and dilatancy angle, respectively. The dilatancy coefficient allows to define a non-associated flow rule, if $\alpha \neq 1$. $\dot{\lambda}^p_k$ is the plastic multiplier of each deviatoric mechanism, determined thanks to Prager's consistency equation.

Isotropic mechanism and isotropic yield surface

The isotropic yield surface, restricting the elastic domain in the effective stress space, is a vertical straight line in the *p'* - *q* plane and takes the following expressions:

$$f_{iso} = p' + d\, p'_c\, r_{iso} \tag{2.55}$$

Where *d* is a soil parameter. r_{iso} corresponds to the degree of plastification (mobilised hardening) of the isotropic yield limits. This enables a progressive evolution of the isotropic yield limit during loading and a partial comeback of this limit during unloading. The evolution of r_{iso} during loading is linked to the volumetric plastic strain induced by the isotropic mechanism. The hardening law for the isotropic mechanism is calculated by:

$$r_{iso} = r^{ela}_{iso} + \frac{\varepsilon^p_{v,iso}}{c + \varepsilon^p_{v,iso}} \tag{2.56}$$

where *c* is the volumetric hardening parameter and r^{ela}_{iso} the radius of the elastic domain of the isotropic mechanism. The parameter *c* takes the value c_m or c_{cyc}, depending on the loading scheme. $\varepsilon^p_{v,iso}$ is the plastic component of the volumetric strain of the isotropic mechanism.

The flow rule of the isotropic mechanism is associated and assumes the following form:

$$\dot{\varepsilon}^p_{v,iso} = \lambda^{iso}\, \frac{p'}{d\, p'_c} \tag{2.57}$$

The plastic multiplier λ^{iso} is determined using a consistency equation.

Summary of material parameters in the Hujeux model

Tab. 2.3 presents a summary of the 19 material parameters included in the Hujeux model for cyclic loading, with an indication of values found in the literature (e.g. Lopez-Caballero 2003).

2.6.6 Domain of application

As several models can account for cyclic soil behaviour, the choice of one model to solve geotechnical problems is linked with the particular application: although linear viscoelasticity reasonably fits very small cyclic strains, one can use perfect plasticity to account for strong motions near failure. A few models, including the Hujeux model, were specially adapted to take into account cyclic mobility or liquefaction (Ishihara et al. 1975; Pastor et al. 1990; Li et al. 1999; Elgamal et al. 2002; Elgamal et al. 2003; Ling & Liu 2003; Lopez-Caballero 2003; Gerolymos & Gazetas 2005; Lopez-Querol & Blazquez 2006; Popescu et al. 2006; Jeremic et al. 2008).

Tab. 2.3. Material parameters of the Hujeux elastoplastic model

Parameters	Unit	Name or description	Approximate range for sands
Elastic parameters			
K_{ref}	MPa	Elastic bulk modulus at reference pressure	100 to 1000
G_{ref}	MPa	Shear modulus at reference pressure	50 to 500
n_e	.	Elastic material coefficient	0 to 1 (usually 0.5)
Dilatancy rule			
φ	°	Dilatancy angle	20 to ϕ
α	.	Dilatancy coefficient	1 to 2 (1 for associated flow rule)
Deviatoric yield surface and hardening parameters			
ϕ	°	Friction angle mobilized at critical state	25 to 45
β	.	Plastic compressibility	10 to 100
b	.	Material parameter for the shape of the yield surface	0.1 to 0.2
a_m	.	Monotonic material parameter for the hardening law of deviatoric mechanisms	1×10^{-3} to 1×10^{-2}
a_{cyc}	.	Cyclic material parameter for the hardening law of deviatoric mechanisms	1×10^{-3} to 1×10^{-1}
Deviatoric domains			
r^{ela}	.	Radius of the elastic domain	1×10^{-6} to 1×10^{-2}
r^{hys}	.	Radius of the hysteretic domain	1×10^{-5} to 5×10^{-1}
r^{mob}	.	Radius of the mobilized domain	0.5 to 1
m	.	Plastification exponent of the mobilized domain	1 to 3 (usually 2)
Isotropic yield surface and hardening parameters			
d	.	coefficient of isotropic hardening	2 to 4 (usually 2)
c_m	.	volumetric hardening parameter for monotonic loading	1×10^{-3} to 5×10^{-2}
c_{cyc}	.	volumetric hardening parameter for cyclic loading	5×10^{-5} to 5×10^{-2}
r_{iso}^{ela}	.	radius of the elastic domain of the isotropic mechanism	usually 1×10^{-4}
Initial state			
p_{c0}	MPa	initial preconsolidation pressure	0.01 to 20

2.7 Rate effects in granular materials

Different aspects of rate effects in granular materials, which are further used to analyse our triaxial test results presented in Chapter 5 of this dissertation, are studied in this section.

2.7.1 Phenomenons involved in time-dependent sand behaviour

In soils, time-dependency can be due to different mechanisms, and implies several concepts depending on the loading characteristics. Three categories of time-dependent behaviours are reported here: viscous effects, dynamic effects and effects of coupling with the pore fluid. This separation is quite arbitrary, because there are some links between them. Moreover, the effect of ageing is totally disregarded here.

2.7.1.1 Viscosity in granular materials

The pseudo-static time-dependency, named viscous effect, is related to changes within the soil skeleton, as creep, relaxation, strain rate or frequency effect. Leroueil & Marques (1996) and Augustesen et al. (2004) give a large overview of the viscous time-dependency. An analogy is built between liquid or gas and soils: soils behave like extremely viscous fluids (Vulliet & Hutter 1988). This means that the material, subjected to a shear stress, offers a resistance to flow. The more viscous the material, the larger the resistance to flow. As they creep and relax less, i.e. they flow less, sands are considered more viscous than clays.

2.7.1.2 Dynamic time effect

Like all structures, soil mass is also prone to dynamic amplification which arises around a resonance frequency due to inertial effects within the porous medium. The frequency of wave propagation thus influences the response of dynamically loaded soil deposit (e.g. Iverson & LaHusen 1989; Popescu et al. 2006).

2.7.1.3 Coupling with the pore fluid

The influence of the pore fluid on the behaviour of the porous medium is not negligible in dynamic analysis of two-phase media. According to poroelasticity theory (Biot 1956), three kind of coupling appear in the wave propagation equations between the soil matrix and the fluid saturating the pores: inertial, mechanical and viscous (Gajo 1995; Gajo 1996). The viscous coupling has an effect on soil behaviour, in particular the interpretation of dynamic tests depends on the value of the coefficient $n^2 \gamma_w / k$, with n the porosity and k the Darcy permeability (Gajo 1995). If there is a large amount of high frequency content and high soil permeability, the intrinsic two-phase nature of the porous material may exhibit clear signs of viscous coupling.

In the pseudo-static range, the coupling between the granular matrix and the pore fluid is mainly mechanical, as contraction and dilation of the solid matrix influence the pore fluid pressure. However, the viscous behaviour of the two-phase medium is partly generated by the fluid flow within the pores even in pseudo-static tests (Gallage et al. 2005).

Another important fact is that the pore pressure dissipation can take time within the soil volume. This effect is viewed as an artefact of laboratory tests, and is not representative of true rate-dependent material behaviour (e.g. Muir Wood 2004). The main parameter which controls that time-dependent dissipation is the permeability coefficient. A short analysis, presented in Chapter 3, evaluates the time delay of pore pressure dissipation in our test conditions.

2.7.2 Interpretation of rate effects

One of the component of time effect is the loading rate (or strain rate), which represents the influence of speed of load application (respectively strain application) on soil behaviour. For our tests (Chapter 5), the expressions **frequency effect** and **rate effect** are equally used, as they both refer to **loading rate effect** in cyclic stress-controlled conditions; the difference with **strain rate effect** is commented below and in Chapter 5.

Rate effects in granular materials were observed during both monotonic (e.g. Yamamuro & Lade 1993; Augustesen et al. 2004; AnhDan et al. 2006) or cyclic loadings (e.g. Lin et al. 1996; Hoque & Tatsuoka 2004; Sassa et al. 2005; Meng 2007; Salvati & AnhDan 2008).

The usual interpretation of the viscous rate effect is explained by Matesic & Vucetic (2003):

«If the rate of loading or straining is smaller, more time is allowed for the soil to creep and relax, allowing the development of larger deformations at a given load increment and smaller shear stresses at a given deformation increment. The final result is a stress-strain curve that plots lower.»

This point of view can be completed. The rate-dependency is claimed to be due to interparticle viscous action added to flow of pore water in drained conditions (Gallage et al. 2005). The effect of particle crushing at high pressure is also an interesting assumption proposed by Yamamuro & Lade (1993). They state that at high strain rate, there is less time for particle crushing and rearranging, also the soil dilative behaviour is influenced. Dynamic amplification, which arises around a resonance frequency due to inertial effects, can also be included in rate effect phenomenons (Ghosh & Madabhushi 2003).

There is a difference between loading rate effects and strain rate effects. It is sometimes pointed up that loading rate exists only as a consequence of the change of time length of the strain application. For example, Sassa et al. (2005) explain that rate effects observed in torque-controlled laboratory tests are

due to the evolution of the shear strain amplitude with the frequency. They also show that displacement-controlled tests are independent from the frequency. This difference is explained by an energy-approach analysis.

2.7.3 Influence of viscous behaviour on cyclic loading

The viscous behaviour of granular material can influence its response to cyclic loading (Tatsuoka 2006):

«The pure effect of cyclic loading [...] can be accurately evaluated only when taking into account the viscous effect».

Part of our cyclic tests can be viewed as a confirmation of that statement, as non negligible viscous effects are isolated during cyclic loadings of granular materials (Chapter 5).

A discrimination between **inviscid cyclic loading effects** and **viscous effects** is proposed by Tatsuoka (2006). A laboratory study shows that in certain conditions (e.g. small cyclic amplitude), for dry sand under cyclic loading, the viscous property of sand is responsible for most of the residual strain while inviscid cyclic loading effect is small. At larger strain amplitude and with a high number of cycles, inviscid cyclic loading effect is more important. Moreover, the inviscid cyclic loading effect continues for a longer duration than the viscous effect.

2.7.4 Time-dependency in granular media from laboratory experiments

Laboratory studies reported below mainly deal with creep, relaxation, step change of rate, monotonic or cyclic loading of granular soils. In particular, the rate effect on strength of cohesive materials, which is very well documented (e.g. Richardson & Whitman 1963), is not further mentioned.

2.7.4.1 Creep, relaxation and step change in strain rate and monotonic loading

Augustesen et al. (2004) summarise viscous monotonic time-dependent behaviour in sands and clays. Strain rate effect on strength of cohesionless soil is addressed: it is mainly a temporary effect (over- and undershooting) which appears during a step change of strain rate, but it does not affect the stress-strain behaviour for monotonic loading with a constant strain rate. Creep and relaxation appear in sands as well as in clays, with a smaller intensity.

Results from laboratory experiments on creep, relaxation and change of strain rate in dry sand were obtained with various kind of tests (Tatsuoka 2006; Di Benedetto 2006; Pham Van Bang et al. 2007; Duttine et al. 2008). It appears that sand behaviour is sensitive to a change in strain rate, rather than the absolute value of strain rate. Saturated drained creep tests and step change of strain rate also exhibit

viscous behaviour (Matsushita et al. 1999; Kuwano & Jardine 2002; Enomoto et al. 2006; Ibraim et al. 2009).

Gallage et al. (2005) show that liquefied sands of various fine content under low confining pressure exhibit viscous behaviour and is sensitive to rate effect. Viscous behaviour is influenced by relative density, effective confining pressure, OCR, fines content, previous strain history and pore fluid. There is more creep deformation with water-saturated pores than for pores filled with air or vacuum. The authors assume that the viscous behaviour results mainly from the vortex flow of pore fluid among sand grains upon shear, and that grain-to-grain contact may also be responsible for additional viscosity.

The particle shape has an effect on dense dry sand creep behaviour (Enomoto et al. 2006; Tatsuoka 2006): the rounder the particle shape, the less creep appears. More generally, particle shape has a systematic effect on the viscosity type and the relative importance between the viscous effect and the inviscid cyclic loading effect.

Drained and undrained monotonic tests on sand is usually seen as not very sensitive to strain rate (e.g. Matsushita et al. 1999). However, Yamamuro & Lade (1993) present monotonic loading of dense sand under high confining pressure, for which the dilative behaviour, and thus the strength, is influenced by the strain rate. The friction angle at the peak deviatoric stress decreases when strain rate increases. The effect of strain rate appears to be more pronounced for undrained loading. The instability line, for the triggering of liquefaction, remains the same at all strain rates.

Concerning dynamic flow of matter, Iverson & LaHusen (1989) explore pore pressure gradients inside rapidly shearing granular materials. Artificial landslides are triggered, in order to measure the pore pressure inside the moving mass at different height. The fluctuations of pore pressure, when the shearing speed is high enough (critical speed, which is unknown, is linked with the properties of the matrix and viscosity of the fluid), locally induce contraction and dilation of the porous medium. Because of those local fluctuations, the effective stress is possibly significantly reduced, leading to large deformations in the sheared area.

2.7.4.2 Frequency effect in dry cyclic conditions

Several experimental studies focused on frequency effects in dry sand. Bolton & Wilson (1989, 1990) Hardin & Drnevich (1972a) and Karg & Haegeman (2009) concluded that dry sand behaviour was frequency-independent, and of purely hysteretic nature. However many other test results tend to show that there is an effect of the frequency on dry sand behaviour. The damping ratio at least is found frequency-dependent in different kind of tests, for small to medium strains (Lin et al. 1996; Hoque & Tatsuoka 2004; Zambelli et al. 2006; Khan et al. 2008). The test results are reported here with more

details.

Secant shear modulus

With full cylinder torsional tests at small strains on dense dry Ottawa Sand, Lin et al. (1996) found that the shear modulus is not very much rate sensitive, as it is constant until 50 Hz and then very slowly decreases.

For Matesic & Vucetic (2003), the secant shear modulus of Toyoura and Nevada Sands at small to medium strain increases with the average strain rate. The $\log(\dot{\gamma}) - G_{sec}$ relation is approximately linear for constant strain rate tests. However, the G_{sec} / G_{max} curve at small to medium strain is almost independent from the strain rate.

Zambelli et al. (2006) explore dry Toyoura Sand behaviour with a torsional shear device, at small to high strains, and from 0.01 to 2 Hz. At small strains, the secant shear modulus increases with the frequency while it is constant at higher strain level.

Damping ratio

With full cylinder torsional tests at small strains on dense dry Ottawa Sand, Lin et al. (1996) found that damping ratio is very rate sensitive between 0.1 and 100 Hz, with a peak around 50 Hz and much smaller values at frequencies around 1 Hz or 100 Hz. It can also be noticed that the peak of the damping ratio arises before the resonance frequency, i.e. the maximum strain amplitude. A more detailed analysis is performed for earthquake frequency range, where inertial effects are neglected. The damping ratio vs. frequency is a linear relation. It is the sum of a hysteretic part and a rate-dependent viscous part, which both depend on shear strain amplitude, confining pressure and relative density.

Moreover, Hoque & Tatsuoka (2004) performed small strain triaxial tests on dry Hostun Sand at frequencies from 0.005 to 2 Hz, and also concluded on the frequency-dependence of damping. The waveform, sinusoidal or triangular, does not influence the dynamic parameters.

For Zambelli et al. (2006) with dry Toyoura Sand, the damping ratio evolves non-linearly at small strain and small frequency and it increases linearly at higher frequency for both small and large strain level.

Khan et al. (2008) adds that dynamic parameters of dry sand at small strains just below the volumetric cyclic threshold shear strain are slightly frequency-dependent for frequencies of 40 Hz to 70 Hz, but it is considered as negligible in the paper.

Accumulated strain

Salvati & AnhDan (2008) performed triaxial tests on two dense dry sands of different particle shape. With two frequency levels 0.1 Hz and 1.5 Hz, the total accumulated strain is lower at high frequency in certain conditions. The influence of frequency is more marked at low confining pressure, and for high

ratio Δq / σ_3. It is the change in strain rate which is significant, rather than the change of loading frequency.

2.7.4.3 Frequency and strain rate effects in saturated cyclic conditions

Concerning frequency and strain rate effects, the results of several laboratory studies in drained and undrained saturated conditions are summarized below. There are some contradictions between these results. Those defending rate-independent behaviour of saturated sand, for pores filled with water, are first mentioned, followed by others which describe rate-dependent behaviour of granular soils.

Some laboratory studies suggest that loading frequency has no influence on cyclic saturated drained and undrained sand behaviour. For example, stiffness is found to be frequency-independent during drained cyclic test at $\gamma < 0.1\%$ (Karg & Haegeman 2009). An undrained strain-controlled study mentioned that frequency has no effect on pore water pressure builds up, liquefaction potential and shear modulus (Govindaraju & Sitharam 2007).

Quasi-static and dynamic torsional tests on sand were performed by Bolton & Wilson (1990) to provide insight into viscous damping. With oil filling the voids, this viscous part of the damping is not negligible, while damping ratio clearly increases with the frequency. But the frequency effect on D is found very small when pores are filled with water at frequency below 100 Hz.

On the contrary, other studies on various sands show that cyclic frequency effects occur in drained and undrained granular materials. They are summarized below.

As for dry tests, damping ratio is shown to increase with frequency around earthquake frequency range in undrained conditions (Govindaraju & Sitharam 2007).

Vucetic & Tabata (2003) performed laboratory tests on unremolded natural sands at different low frequencies and small to medium strain. The frequency-dependence is evaluated through the slope of secant shear modulus vs. shear strain rate. Rate effects are higher for clay than sand, but they are not totally negligible in sands. In this study, rate effects tend to decrease when the strain amplitude increases.

Sassa et al. (2005) present test results on liquefaction of saturated Osaka sand. While shear-torque-controlled tests are frequency-dependent, shear-displacement-controlled tests are frequency-independent (although the frequency range is lower for the latter). At the highest frequency for shear-torque-controlled tests, energy dissipation becomes lower, as well as total strain accumulation. Excess pore pressure generation is frequency-dependent in shear-torque-controlled tests.

Meng (2007) studied unidimensional variations of shear wave velocity (c_s) and quality factor (Q) for

natural soils, including a clayey sand, with a frequency range from 0.01 to 30 Hz at very small strains. This experimental study was performed with a non-resonance method, and a model issued with the definition of two functions $c_s(f)$ and $Q(f)$.

2.7.4.4 Summary and conclusions

In sand, viscous behaviour is observed during creep, relaxation and step change of strain rate. Some experimental works exist on frequency effects, but that phenomenon is far from being understood. Indeed, a few contradictions can be found concerning dry and saturated drained sand behaviour.

There seems to be an agreement on the fact that damping ratio increases with frequency around 0.01 to 20 Hz. Strain accumulation may decrease when frequency increases in both dry and drained conditions. The results are more contradictory concerning the secant shear modulus: some studies defend its rate-independency in sand, others show that it increases slightly with frequency around 0.01 to 20 Hz. The secant Young's modulus and the shear wave velocity may also increase with the frequency.

Most studies are based on quasi-static procedures or at very small strains and the nonlinear dynamic effects were not really considered. It seems that there is no laboratory test available in literature that has both frequencies up to 10 Hz and medium to large strain amplitudes ($> 10^{-3}$), especially during undrained cyclic tests.

2.7.5 Constitutive modelling and numerical approach of rate effects in sand

Elasto-viscoplastic, viscoelastic-viscoplastic and viscoplastic models were primarily developed for modelling time-dependent monotonic behaviour of fine soils, but some of them are adapted to model viscous effects in granular materials, even under cyclic strains. Boukpeti et al. (2004) propose an elasto-viscoplastic model which takes into account undrained monotonic loading of sand with creep and large strain rate. A cyclic viscoelastic-viscoplastic model for clay is proposed by Oka et al. (2004), and applied to a site amplification analysis for a multi-layered soil deposit. Pham Van Bang et al. (2007) model creep, relaxation and step change in strain rate at small to medium strain. Modelling creep and relaxation of dry sand, with specific effects such as non-isotach or TESRA behaviour, is possible thanks to the 3 component model (e.g. Di Benedetto & Tatsuoka 1997; Di Benedetto et al. 2002; Tatsuoka et al. 2002; Di Benedetto 2006).

In Ghosh & Madabhushi (2003), the authors have numerically investigated the behaviour of loose silica sand under large amplitude dynamic strains with different frequencies. The finite element software SWANDYNE implements differential equations of the solid and fluid phases fully coupled with the mass balance equation. The constitutive model is based on generalized plasticity, which allows here to take into account cyclic loadings.

The results show a significant dependency of pore water pressure to the frequency of the input motion. A peak of the pore pressure ratio is found for 1 Hz excitation, with a greater rate of generation of the excess pore pressure. This resonance frequency is characterized by a strong nonlinear response of the soil deposit, with high shear strains, liquefaction and stiffness degradation. While quasi-linear behaviour is obtained at higher and lower frequencies, with stiffer behaviour and less increase in the pore pressure. The rate-dependency is assumed to be linked with the closeness of the input loading frequency to the natural frequency of the soil deposit.

Other numerical studies related to seismic wave propagation raise interest about the importance of the frequency effect in soil deposits:

- Carvajal et al. (2002) perform inverse analysis of a site near Mexico City. The analysis compares results with frequency-dependent and frequency-independent dynamic properties. With frequency-dependent dynamic parameters, the acceleration time history are improved compared to the measured response of several seismic events. The displacements however are not improved.
- Meng (2007) performs a unidirectional seismic simulation using either frequency-dependent or frequency-independent dynamic soil properties. The two conditions give different results, thus proving the importance of taking into account rate-dependency within site amplification studies.
- Popescu (2002) performs finite element simulation of earth structures under earthquake loading. The frequency content of the seismic motion influences the dynamic response of the structures, in terms of pore water pressure generation, horizontal displacements and overall stability.

2.7.6 Conclusions

There are some contradictions on the effects of frequency experimentally observed in granular materials. They may not be very large, but time-dependent effects arise in sands. Several physical interpretations of time-dependent behaviour of sand are available, including viscous and dynamic effects, coupling with the pore fluid or particle breakage. The part attributed to the coupling with pore water is not very clear, but even dry sand exhibits rate-dependent behaviour. Although experimental results are not in total agreement with each other, dynamic parameters, and particularly the damping ratio, seem to increase with the frequency around earthquake frequency range. There is a lack of available test data on frequency effects in sands, in the earthquake frequency range and for medium to large strain amplitude, especially in undrained conditions. We present such results in Chapter 5. Moreover, time-dependent behaviour of soils has a non-negligible influence on the modelling of site effects.

2.8 Superposition of loadings

2.8.1 Introduction

For linear elastic soil behaviour, seismic wave propagation is the sum of several kinds of wave which are superimposed. In earth structures in particular, the amplification, reflection and refraction of the stress waves give very different wave pattern from the simple assumption of a unidimentional vertical propagation of a shear wave. Moreover, Ishihara (1996), while explaining the effect of stress waves on the soil behaviour, states that the compressional stress is transmitted through water in the pores, and that it does not affect the effective stress.

The principle of superposition does not apply in the range of nonlinear soil behaviour, i.e. for large acceleration above 0.4*g* (Bernardie et al. 2006). The superposition of confining and deviatoric stresses into a complex loading is thus another feature of loading characteristics which might influence the response of the soil.

On the other hand, in the poroelasticity theory, the propagation of earthquake-induced elastic stress waves in a saturated granular medium is based on two compressional waves and one rotational wave (Biot 1956). The displacements of the fluid and the granular phases are coupled within the dynamic equations. Disregarding the dynamic coupling effect between the water and the soil matrix might be of great importance.

These remarks explain our interest on the effect of superposition of stress loadings on soil behaviour. Laboratory experiments reporting the superposition of cyclic loading components and the effects on granular soil behaviour are described below. First, the superposition of two shear loads is briefly summarised. However, our tests concern the superposition of a confining and a shear loading, for which very few test data are available.

Finally, we would like to emphasize the difference between multidimensional soil analyses and multidirectional soil analyses. The multidimensional study, namely 2D or 3D effect, takes into account the geometry of the investigated area. For example site effects in a complex valley can be investigated with 2D or 3D models (e.g. Delepine 2007). In the multidirectional study, the loading has two or three orthogonal loading component, which accounts for the complexity of in situ wave propagation. A multidirectional study can be performed on a 1D soil column (e.g. Bernardie et al. 2006).

2.8.2 Laboratory experiments

2.8.2.1 Superposition of two shear stresses

The superposition of two shear stresses in orthogonal directions had been performed with bidirectional

simple shear tests (described in Chapter 3), or torsional shear tests with an axial vertical load. A few laboratory studies aimed at demonstrating the non negligible effect of cyclic bidirectional loading stress paths instead of the usual assumption of a single loading (Boulanger & Seed 1995; Seed et al. 2001). Multidirectional shaking table tests are also used since Pyke (1973).

Ishihara & Yamazaki (1980) studied saturated sand failure with a bidirectional simple shear apparatus. The pore water pressure ratio does not reach 1 during rotational shear tests, although high strains develop within the sample. Moreover, a release of the applied cyclic stress caused the pore pressure to immediately reach the initial confining pressure. The authors concluded that the number of cycles to reach failure decreases with bidirectional loading, i.e. cyclic strength decreases. The time lag and amplitude ratio between the two perpendicular shear stresses influence the value of cyclic stress ratio at failure.

Ishihara & Nagase (1988) performed bidirectional irregular loading tests on sand with a bidirectional simple shear device. They applied horizontal acceleration time histories of real japanese earthquakes to sand with a reduced time scale. It was observed that multidirectional loading effect, which slightly decreases soil strength, is almost independent from the relative density of sand. A design curve is produced, with one load irregularity factor and one multidirectional load factor. The multidirectional factor ranges from 0.82 for dense sand to 0.86 for loose sand, which means that cyclic strength is slightly reduced in bidirectional load conditions.

Kammerer et al. (2003; 2004) describe the behaviour of sand under bidirectional loading conditions, using an advanced bidirectional simple shear apparatus (Seed et al. 2001). The results emphasize several observations on liquefaction triggering. The bidirectional loading limits the maximum value of the excess pore pressure ratio to a threshold value lower than the custom value of 1 obtained in the unidirectional configuration. Though, large strains develop and the threshold value, which is for example 0.7 for Monterey 0/30 sand (Kammerer et al. 2004), is reached faster than in unidirectional conditions.

A different testing device is used in Aggour & Zhang (2006). The experimental study is based on a combination of longitudinal and torsional loadings in a resonant column. It appears that the rate of decrease of the shear modulus ratio and the rate of increase of the damping ratio is influenced by the combination of the two loadings. A threshold strain ratio between longitudinal and torsional strains is defined, above which the stiffness degradation of the sample has a higher rate than unidirectional loading.

The bidirectional application of load prevents the apparition of $u_r = 1$, and in the same time decreases the cyclic strength (failure definition with the threshold shear strain amplitude) of saturated sand in

bidirectional simple shear. In the same way, the bidirectional loading increases the rate of stiffness degradation in the case of the superposition of a torsional and deviatoric load.

2.8.2.2 Superposition of confining and deviatoric stresses in triaxial devices

Choi & Arduino (2004) performed true triaxial testing of gravelly soils, with monotonic, cyclic and rotational stress paths on narrow-graded Pea gravels. For several monotonic loadings in various directions, the peak stress ratio varies depending on the stress path direction. Circular (polarized) cyclic tests induce an increase of the pore water pressure.

Another interesting study addresses the evolution of sand behaviour with a high number of cycles in a bidirectional triaxial device developed in Bochum (Wichtmann & Triantafyllidis 2004; Wichtmann et al. 2005; Wichtmann et al. 2007a; Wichtmann et al. 2007b). Strain accumulation under drained cyclic loading depends on the shape and polarization of bidirectional stress-strain loops. The volumetric and deviatoric components of stress have a complex effect: the actual polarization and loop shape does not directly influence strain accumulation vs. the number of cycles, but a change of the polarization increases residual strains.

2.8.2.3 Remarks

It seems that the superposition of a cyclic confining stress to the deviatoric stress in the triaxial apparatus was not studied in undrained situations, in the range of medium to high strains. That is why there is no direct element of comparison with our cyclic bidirectional tests presented in Chapter 6. The results available (Wichtmann et al. 2007a) on drained situations at smaller strains tend to show that the shape of the input stress loop (cf. examples in Chapter 6) does not significantly influence strain accumulation.

2.8.3 Multidirectional site effect analyses

Li (1990) proposes a bounding surface hypoplasticity model which takes into account the rotation of shear stresses and multidirectional loading. The model is used with a fully coupled dynamic formulation to simulate a 1D column with multidirectional load (Li et al. 1998), i.e. with the superposition of three loadings in orthogonal directions. Compared to a real seismic event, there is reasonable agreement between the measured site effects and the simulation.

Bernardie et al. (2006) also model a 1D column with multidirectional loads, i.e. by taking into account the three components of motion NS, EW and UP. They propagate within an elastoplastic soil model implemented in a coupled dynamic formulation. In conclusions, the necessity to take into account the multidirectional load is emphasized, in order to «*obtain more realistic predictions*».

2.8.4 Conclusions

Laboratory studies have shown that the superposition of two shear loads on the boundary conditions affects soil behaviour. The most frequently used device for the superposition of loadings is the bidirectional simple shear apparatus, tested with sandy soils (Ishihara & Yamazaki 1980, Ishihara & Nagase 1988, Boulanger & Seed 1995, Kammerer et al. 2003, Ueng et al. 2006). Some experimental studies with a triaxial apparatus (Wichtmann et al. 2007a), a true triaxial apparatus (Choi & Arduino 2004) and a resonant column (Aggour & Zhang 2006) have also been performed. Multidirectional effects are mainly taken into account with a correction factor included in unidirectional procedures. While some numerical studies show that coupled soil behaviour of the pore fluid with the solid matrix influence the response of the soil deposit in case of multidirectional load, the transient behaviour of saturated sand under earthquake loading with a triaxial device under cyclic bidirectional loading have no available test data. We provide such results in Chapter 6.

2.9 Irregular loading of sand under seismic motion

2.9.1 Introduction

Laboratory testing of sand under seismic motion is technologically possible thanks to automated motion regulators and pseudo-dynamic or dynamic devices. Irregular loadings of sand were performed in triaxial, simple shear, torsional and centrifuge tests, as described in section 2.9.2. The consequences of observed behaviour for design procedures are briefly mentioned in section 2.9.3. These test results are compared to our irregular bidirectional tests performed in undrained conditions (cf. Chapter 6).

2.9.2 A few laboratory studies

The usual procedure for converting horizontal accelerations at the soil surface into stresses in the shallow regions of soil deposits was proposed by Seed & Idriss (1971): as the soil layers move together as a rigid body in the horizontal direction, the shear stress at a given depth is evaluated by the surface acceleration times the soil mass above that depth (Ishihara & Yasuda 1975). The equivalence between horizontal acceleration at a given time and the in situ stress at a certain depth z can be extrapolated, for simple shear devices, by:

$$\frac{\tau}{\sigma_t'} = \frac{a}{g} r_d \frac{\sigma_t}{\sigma_t'} \tag{2.58}$$

where τ is the shear strain in the horizontal plane, a is the horizontal acceleration, σ_t and σ'_t are total and effective overburden pressures at the depth considered and r_d is a stress reduction factor, with $r_d = 1 - 0.015z$. In triaxial conditions, an equivalence factor is added (Ishihara 1996). Such procedure is taken into account in most of the tests presented below. The concept is then evaluated for various loading conditions, and the equivalence factor could be refined.

An attempt to simulate real earthquakes in the laboratory was already found in Ishihara & Yasuda (1972). The acceleration time history of the Niigata earthquake (1964) was converted into stress-controlled triaxial loadings of undrained sand samples. These were used to analyse the liquefaction triggering of loose Niigata Sand (Fig. 2.26). The sand response to triaxial loading is not the same whether the direction of maximum acceleration is transposed to a maximum stress in compression (CM test) or in extension (EM test). In particular, the increase of pore pressure is very sudden in EM tests at unloading from the maximum stress; in CM tests, pore pressure increase is more regular, it happens in a few seconds, mostly during extension peaks following the maximum peak in compression. Moreover, pore pressure increases more in EM tests than in CM tests. A reduction factor is calculated between irregular loading and constant amplitude sinusoidal loading. Such tests of irregular loading excitation were also performed with a torsional device (Ishihara & Yasuda 1975).

Triaxial tests were also used by Kim et al. (2005) to compare various loading types, including several earthquake-types motions. Seismic loadings are classified into blazing (excess pore pressure increase is induced only by the higher peak) and terraced (high amplitude peaks follow the higher one, thus pore pressure build-up continues after the main first increase) types. The comparison with sinusoidal loading shows that the cumulated energy necessary to trigger liquefaction is higher with constant amplitude than random amplitude dynamic stress.

The sand response to earthquake loading includes a decrease of the volume of the medium, i.e. ground settlement. This phenomenon is delayed in saturated undrained conditions, and arises when pore pressure dissipation and drainage of the soil layer can occur. Sawada et al. (2004) performed irregular triaxial loadings of unsaturated sand specimens of various degree of saturation. First, residual shear strains are practically equal to the maximum shear strain, irrespective of hydraulic conditions. Moreover, settlements induced by the irregular load depend on the degree of saturation, except at very large strain. Zhang et al. (1997) and Shahnazari & Towhata (2002) also studied the dilatancy of granular media with torsional tests, including the volumetric response to irregular loadings.

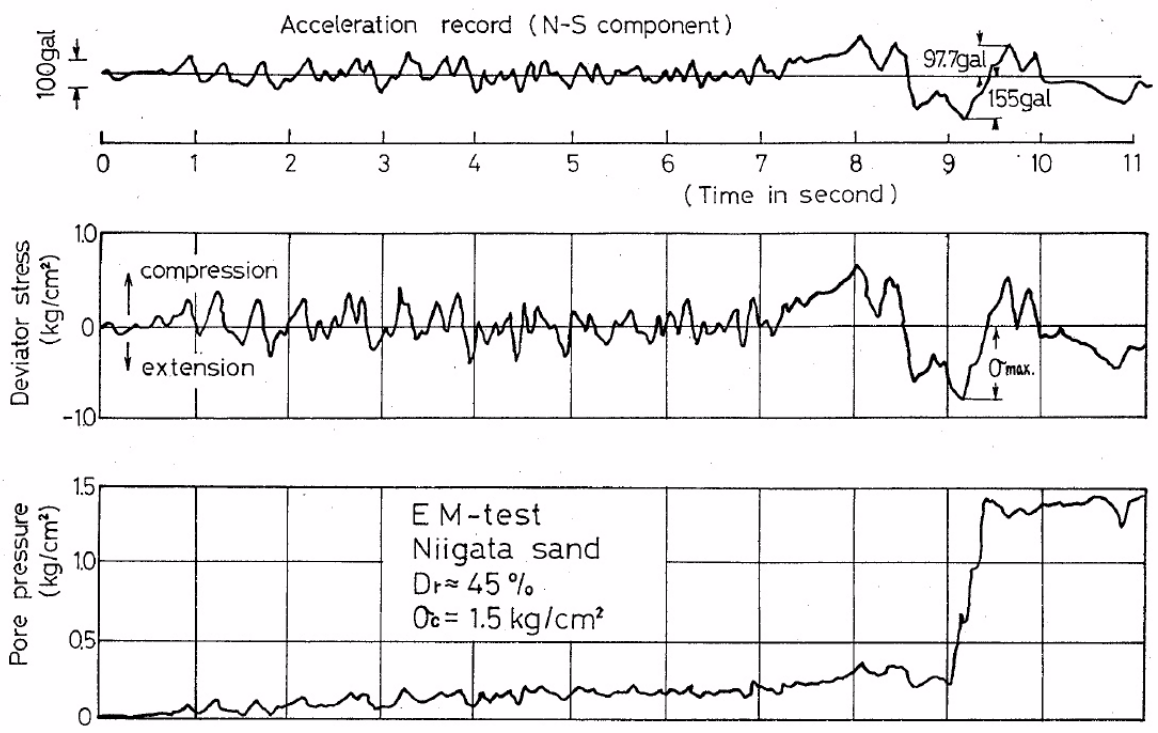

Fig. 2.26. EM triaxial test with liquefaction triggering of loose sand (Ishihara & Yasuda 1972).

A simple shear device was also used to assess the response of saturated sand to irregular loading (Nagase & Ishihara 1987; Nagase & Ishihara 1988). The strains induced by irregular loadings are compared for different void ratios and maximum stress amplitudes. The characterization of irregular tests involves the maximum cyclic stress ratio, CSR^{EQ}. The load irregularity strength factor, defined by Nagase & Ishihara (1987), is the ratio between the CSR for 20 cycles of sinusoidal loading and CSR^{EQ} for irregular loading. Depending on the sand relative density, the soil strength under irregular loading is either larger or equivalent to the strength evaluated with sinusoidal cyclic loading. Comparing unidirectional and bidirectional simple shear conditions, the effect of irregular loading on liquefaction-induced settlement is also assessed by Nagase & Ishihara (1988). The reconsolidation volumetric strain only depends on the maximum shear strain amplitude and relative density, and is independent from the loading type (unidirectional or bidirectional).

It is possible to calculate the dynamic parameters from irregular motion recordings performed in situ or in laboratory tests (Brennan et al. 2004; Elgamal et al. 2005). Such procedures are used to evaluate strain-dependent shear modulus and damping ratio, necessary in equivalent linear analyses. The dynamic parameters obtained in irregular loading conditions exhibit reasonable match with the curves obtained in cyclic loading, but there is more discrepancy in dynamic parameters calculated from seismic motions (Wang & Kuwano 1999; Elgamal et al. 2005).

Elgamal et al. (2005) evaluates the behaviour of undrained dense sand under seismic loading in

centrifuge tests. The tests show that «*practically undrained conditions*» prevail during seismic motion. Moreover, there is a strong influence of shear-induced dilation in the sand response. The shape of the stress-strain relation changes with the loading amplitude, because significant nonlinear behaviour appears (Fig. 2.27). The dynamic parameters are calculated from these stress - strain relations, and significant stiffness degradation occurs. However, strong dilation prevented complete reduction of the secant shear modulus ratio, while «S shape» curves appear in the stress - strain relation.

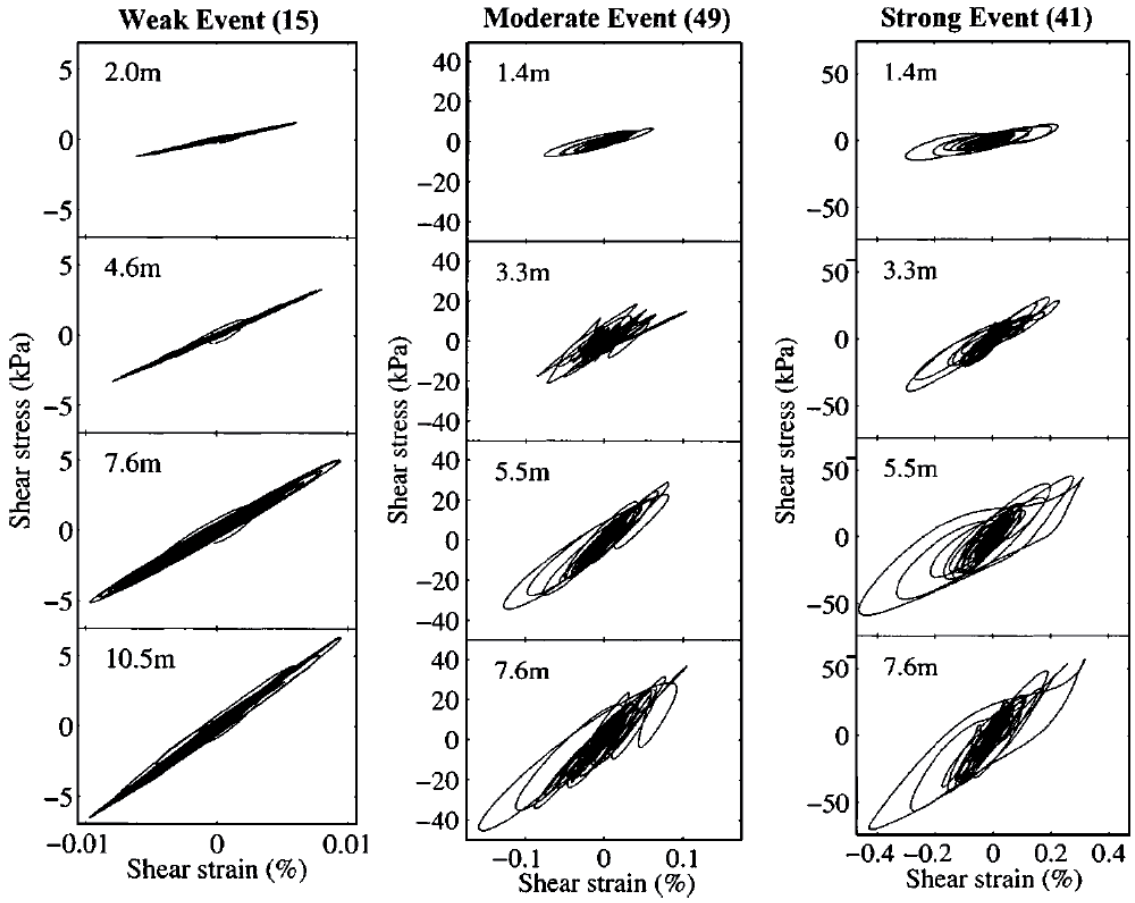

Fig. 2.27. Stress - strain relation during seismic loading (Elgamal et al. 2005).

2.9.3 Use of test data for design purposes

The usual procedure evaluating liquefaction potential of soils in level ground conditions was proposed by Seed (1979). Thanks to Eq. 2.58, irregular accelerations, provided by accelerograms recorded at the top of the soil layer, are converted into equivalent uniform cyclic stresses. Then, adequate cyclic tests can be performed to evaluate the strength of the given material in the conditions prevailing in situ.

Another complementary procedure is used to evaluate sand behaviour in irregular loading: sand strength under irregular tests is compared to cyclic strength from sinusoidal tests, by the means of the coefficient of irregularity (Ishihara & Yasuda 1972; Tatsuoka et al. 1980; Nagase & Ishihara 1987;

Ishihara 1996). This multiplicative factor is similar to the coefficient used for multidirectional loading, and both are actually combined to evaluate soil strength in japanese earthquake-resistant design.

Cyclic or irregular laboratory studies are used in soil modelling which can account for irregular seismic motions. The models have to be able to reproduce irreversible strains and excess pore pressure increase. For example, the requirements for modelling irregular seismic loading are summarized by Ishihara et al. (1975), and a deformation model for undrained sand results from these «postulates». Muravskii (2001) and Osinov (2003) incorporate constitutive laws based on Masing's rules into finite element codes, and they provide examples of nonlinear soil behaviour under irregular loading. Comparing laboratory tests and simulations with a Ramberg-Osgood model, Ray & Woods (1988) show that dry sand behaviour can be well reproduced by computing irregular loadings.

2.9.4 Summary

The effect of irregularity of loading, inherent to seismic motions, is addressed in laboratory studies on granular materials. Their nonlinear behaviour is observed in different tests equivalent to seismic motions. In undrained conditions especially, failure by cyclic liquefaction and flow liquefaction usually occurs after the peak of maximum stress. Shear strains and pore pressure ratio develop as a result of stiffness degradation which follows that peak. The equivalence between soil response to cyclic loading (with a sinusoidal shape) and irregular stresses (derived from earthquake acceleration recordings) is quantitatively evaluated thanks to multiplying coefficients. In particular, irregular and cyclic CSR provide an equivalence factor for the strength. Following a very different approach, several constitutive models suitable for cyclic liquefaction of sand are proved capable of modelling seismic motions. The irregular tests presented here do not take into account bidirectional effects in triaxial conditions, which are explored in Chapter 6.

2.10 Conclusions

The cyclic behaviour of sands was described with a focus on applications to earthquake geotechnical engineering. In particular site effects can be concerned by nonlinear soil behaviour in 1D, 2D or 3D site amplification. The importance of an accurate effective stress modelling, which takes into account plastic strain accumulation and pore water pressure increase, is acknowledged.

The particularities of cyclic soil behaviour were described, with many important factors: (i) importance of the variation of excess pore pressure (increase or decrease, assimilated to contractive and dilative

behaviour of the soil matrix prevented by the impossibility for volume change), (ii) effect of the number of cycles, with the difference between dry and undrained conditions, (iii) loading in compression and extension, and alternation of principle directions, (iv) strong strain dependency of nonlinear behaviour, with the definition of two important threshold shear strains: the linear threshold and the volumetric cyclic threshold, (v) pore pressure accumulation during undrained cyclic loading, (vi) failure by either flow liquefaction or cyclic mobility and (vii) the influence of initial conditions, in particular void ratio and isotropic or anisotropic consolidation. These subjects are addressed, particularly in Chapter 4, for the interpretation of our cyclic triaxial test results performed on two different sands in various conditions.

The dynamic parameters G_{sec} and D were defined, and their possible physical interpretation is presented. We calculated the secant shear modulus and damping ratio in triaxial conditions with stress and strain invariants, to use a unified definition in all loading conditions. The strain dependency, notions of maximum secant shear modulus and factors influencing G_{sec} and D (in particular confining pressure, void ratio and number of cycles) were described. These two parameters are evaluated, for various test conditions on Leman and Fonderie Sand, in Chapters 4 to 6. They are also used in Chapter 7 for the linear equivalent model.

A few constitutive models suitable for modelling granular soils under cyclic loading were presented in section 2.6. The viscoelastic equivalent linear method, which is widely used with the programme SHAKE91, takes into account soil non-linearity but does not allow strain accumulation or pore pressure increase. On the contrary, the elastoplastic multi-mechanism Hujeux model can account for them. The test results presented in Chapters 4 to 6 are used to evaluate and compare these two models in Chapter 7.

Rate effect in granular materials mainly results from viscosity, dynamic effects, coupling between the soil matrix and the pore fluid. Viscous behaviour is different in sands than in clays. In creep tests on sand, the transient effect of the change of strain rate is more important than the strain rate level. Viscous behaviour also influences cyclic behaviour. The loading frequency has an effect in dry and in saturated conditions. For both cases, experimental studies prove that the damping ratio increases with the frequency in the earthquake frequency range. In that same frequency range, the results are less clear for the secant shear modulus, but it seems that G_{sec} slightly increases with the frequency. Undrained frequency-dependence at medium strain range has not been experimentally evaluated. However, numerical approaches of this problem show that the frequency-dependence can be important, in particular it influences the results on site effect analysis. In Chapter 5, we provide new test results for cyclic loading conditions which correspond to this problem; they allow to isolate rate-dependent cyclic behaviour of granular soils.

The impact of loading characteristics on nonlinear soil behaviour is also addressed through the superposition of two loadings. Laboratory test results show that the superposition of two shear tests reduce cyclic strength, though the pore pressure ratio is apparently limited to values below 1 during bidirectional shear. The superposition of a confining and a deviatoric stress was not studied for transient undrained loading in earthquake applications. This is the subject of Chapter 6. It is possible to apply such boundary conditions for a fully coupled dynamic framework which uses constitutive models designed for cyclic soil behaviour (cf. Chapter 7).

It is finally shown, under various experimental conditions, that seismic motions also induce nonlinear behaviour and stiffness degradation of undrained saturated sand. In most laboratory tests, an effort is made to evaluate the equivalence between irregular and cyclic motions, so that regular cyclic tests, performed in repeatable conditions, are sufficient to evaluate sand response to seismic loading. Complementary experimental results are described in Chapter 6, with bidirectional irregular triaxial tests on Leman Sand.

The bibliographical study summarized above embraces all the concepts necessary to understand the relevance of our laboratory experiments. The nonlinear behaviour of sand under cyclic loading is strongly strain-dependent, but the influence of other characteristics of the applied load are non negligible. We chose to focus on the frequency effect and the effect of multidirectional loadings with the superposition of a cyclic compression with a cyclic deviatoric stress. None of these two loading characteristics had been studied in conditions of strong earthquake loading, i.e. in undrained conditions with medium to large strains and a frequency range between 0.1 and 10 Hz.

CHAPTER 3

CYCLIC TRIAXIAL EXPERIMENTS

3.1 Dynamic measurement techniques

3.1.1 Introduction

Testing methods applied to geotechnical earthquake engineering and soil dynamics had long existed, although the addition of automation and programming to experimental devices allowed major improvements in the last decade. Many kinds of dynamic laboratory apparatus were developed to assess dynamic soil behaviour. They are characterized by their strain range, frequency range, allowed stress paths and possible rotation of stress (Fig. 3.1). Then practical means which allow rapid characterization of soil for engineering purposes are needed. In situ measurement and correlations with mechanical characteristics of the soil layers proved to be useful (cf. Appendix 1). It is not the goal here to provide a detailed list of all existing testing methods. The intent is rather to outline the main advances and to situate our testing programme among other published works.

The review of laboratory equipment for dynamic soil testing can be found here, with the description of the dynamic triaxial press used for our tests.

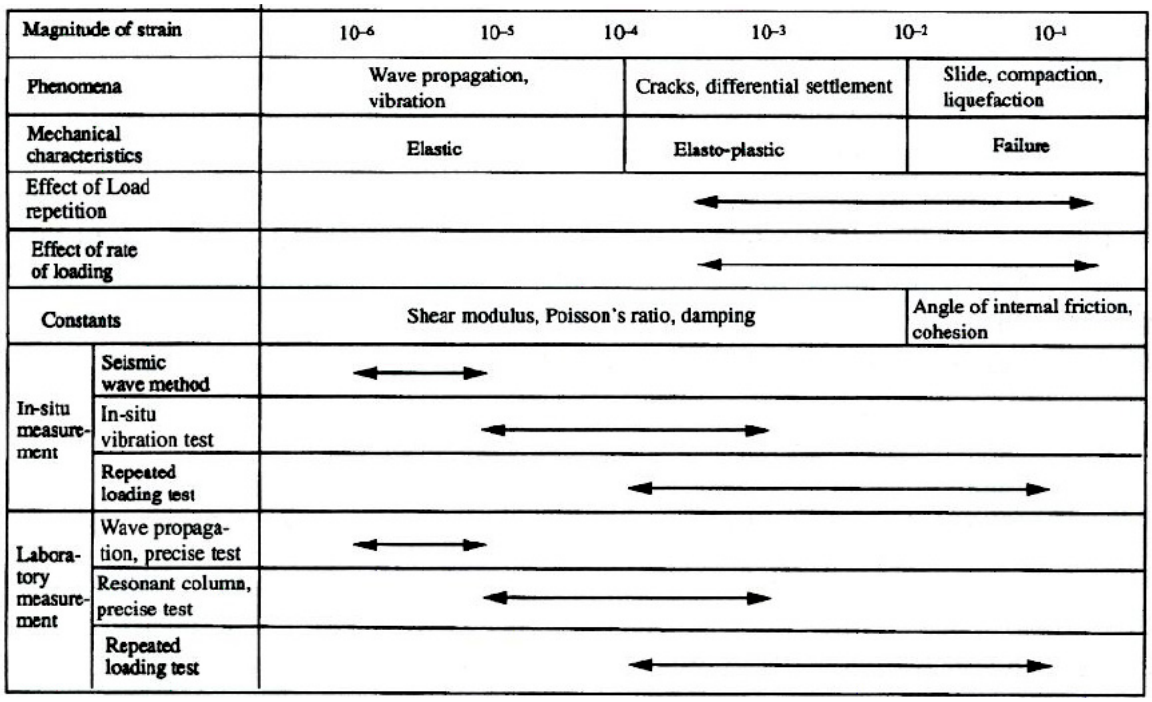

Fig. 3.1. Variation of soil properties and experimental methods (Ishihara 1996).

3.1.2 Laboratory testing

3.1.2.1 Idealization of real field wave propagation

It is a requirement for laboratory tests to reproduce, within the soil sample, stress and strain states of soil compatible with the field reality. Considering the stress waves in level ground conditions, the most

used assumption is based on a shear wave which propagates vertically in the soil. In this case, the state of stress of a soil element can be idealized as in Fig. 3.2. Purely compressional stress variations are disregarded because they are assumed to be transmitted through water in the pores.

The propagation of seismic waves is actually more complex than that. All the components, including the deviatoric and the spherical parts, vary irregularly with time, as well as the direction of principal stresses.

Laboratory testing are treated either like pseudo-dynamic or true dynamic problems. Three parameters allow to distinguish the approaches (Fig. 3.3): frequency range, strain amplitude and ratio of the wave length compared to the characteristic length of the problem (Semblat 1994).

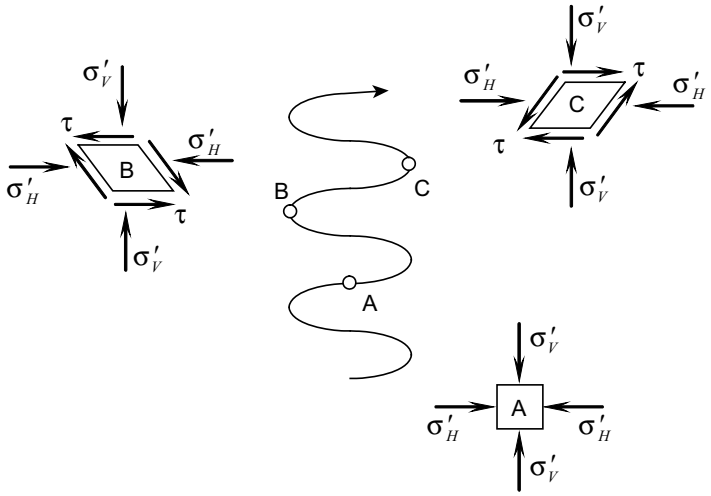

Fig. 3.2. In situ idealized stress components of soil elements under seismic loading.

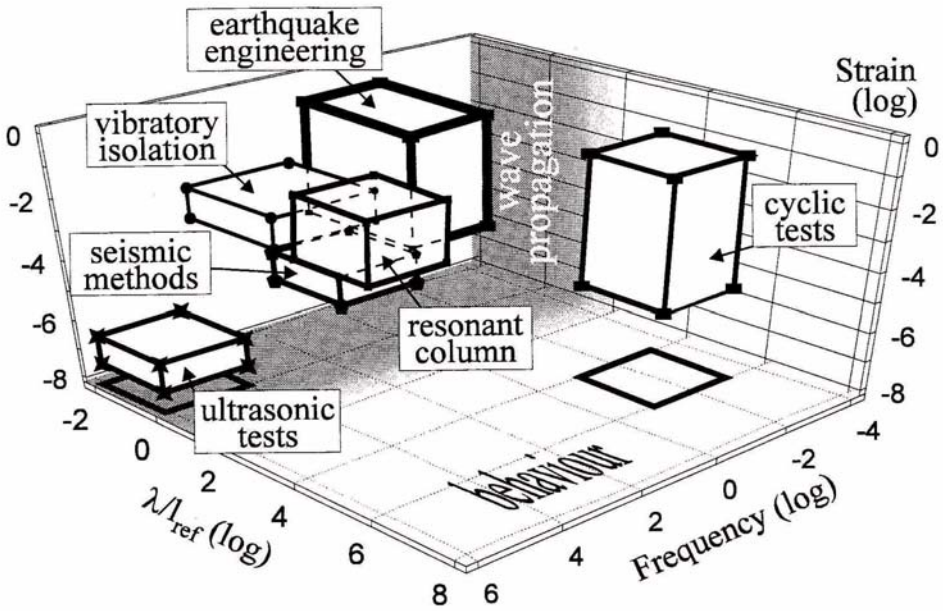

Fig. 3.3. Classification of dynamic tests on soils (Semblat et al. 1999).

3.1.2.2 Cyclic tests (pseudo-dynamic)

Features

Cyclic tests which are considered as pseudo-dynamic are a very convenient tool for characterizing soil behaviour. Indeed it is assumed that no wave propagates inside the sample, because the ratio of wave length to sample height is high enough. The problem is not dynamic, and inertial effects can be neglected. Thus the interpretation of test results is based on the same background as pseudo-static tests.

Cyclic triaxial test

This kind of test is widely used for the characterization of cyclic behaviour of fine-grained and cohesionless soil. In a typical triaxial testing device (Fig. 3.4), the cylindrical sample, which is under a constant hydrostatic pressure, is cyclically sheared by the application of a vertical load. Pore water pressure or the volumetric variation of water inside the sample must be recorded, as well as vertical displacement and force. Feedback control is mandatory for any cyclic test.

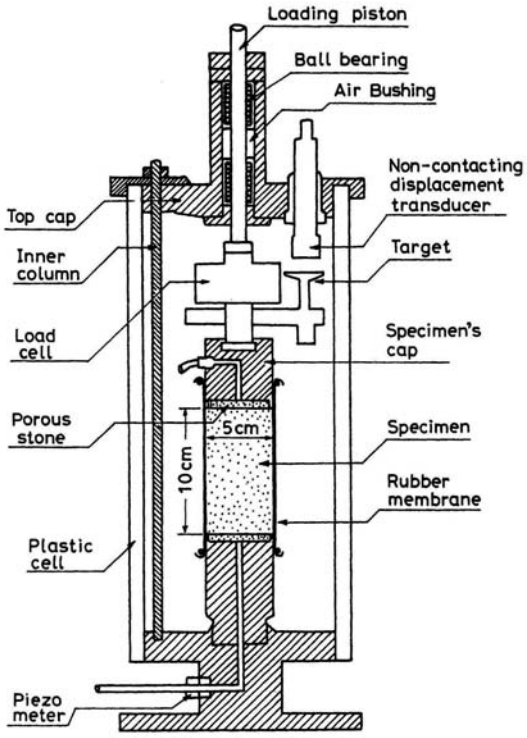

Fig. 3.4. A cyclic triaxial testing device (Ishihara 1996).

Triaxial tests allow uniform stress and strain states inside the sample, at least for small and medium deformations. When ends restraint are kept to a minimum, and before the apparition of localized failure, accurate measurement of stress and strain can be obtained.

Improved triaxial tests include precision sensors for very small strain level, to evaluate cyclic linear soil behaviour. Most of these techniques involve sensors installed inside the triaxial cell (Seed et al. 2001).

Local LVDTs mounted at the surface of the sample (Huot & Vulliet 1998) and load cell placed inside the triaxial cell are mandatory for measuring cyclic strains below 10^{-4}.

One recognized limitation of cyclic triaxial tests (Kramer 1996; Seed et al. 2001) is that the shear plane is not horizontal. This induces a slightly biased equivalence for the seismic application compared to the state of in situ soil layers. Another limit of the triaxial testing system is that the principal stress directions do not vary continuously, but instantaneously rotate of 90° twice per cycle.

Simple shear test

Simple shear test is a technique widely used for studying liquefaction. There are two types of simple shear apparatus: (i) NGI type, in which the sample side is surrounded by a wire-reinforced membrane (ii) SGI type, in which the sample side is made of stacked rings. The principle of simple shear is straightforward: a shear stress is applied in the horizontal direction. The sample is thus strained in the same way as a level ground soil element subjected to a vertical S wave. Constant overburden stress is applied by a vertical load.

Compared to triaxial tests, the main advantage of simple shear tests is that the shear plane is horizontal. Laboratory tests are then closer to in situ conditions. Its major shortcomings are: (i) shear stresses are not uniform in the sample, i.e. stress concentrations are found in the corners (ii) stress state on two of the four lateral boundaries can not be controlled, (iii) shear stress direction is limited to one direction, except for bidirectional simple shear apparatus (Fig. 3.5). Thanks to two independent loading rams, two perpendicular shearing are simultaneously imposed to the sample. Such device was developed to evaluate the influence of 2D shearing on liquefaction triggering and cyclic strength.

Torsional shear tests

Two types of torsional tests exist. The sample is either a full cylinder, as for triaxial tests, or a hollow cylinder (example in Fig. 3.6). As the torque induces non uniform stress field in horizontal planes inside the sample, hollow cylinders are usually preferred, despite the difficulty of sample mounting. Indeed, their particular shape allows to assume stress uniformity inside the thin soil layer.

Torsion is applied through a top cap, which may be provided with picks. They should allow tight connection and adherence with the soil, even for granular matrix. Two lateral pressures, inside and outside the sample, and the axial force are independently monitored.

(a)

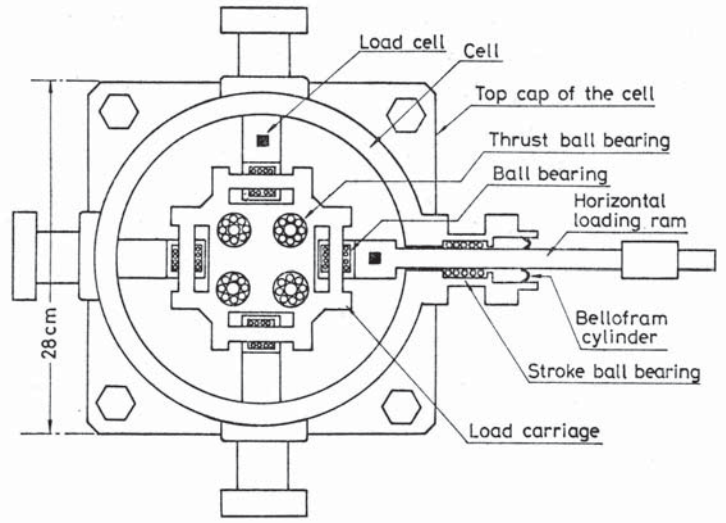

(b)

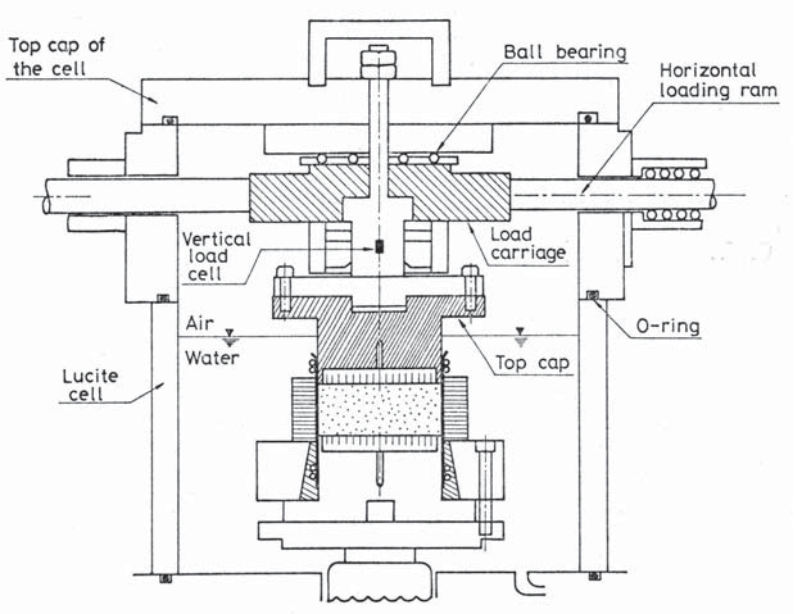

Fig. 3.5. Bidirectional simple shear apparatus (a) top view (b) side elevation (modified from Ishihara & Yamazaki 1980).

The numerous advantages of torsional shear tests perfectly fit with the study of soil behaviour under earthquake loading: (i) the shear plane is in the horizontal direction (ii) the rotation of principal stress is continuous and controlled (iii) high strain level are reachable, and thus residual strengths can be studied (iv) complex stress paths can be performed (Towhata & Ishihara 1985) (v) the initial coefficient of earth pressure at rest can be reproduced.

The two main shortcomings of torsional shear tests are (i) the non uniformity of the stress field, particularly for full cylinders, and (ii) the difficulty of sample mounting for hollow cylinder tests. That is why this kind of equipment is not widely available.

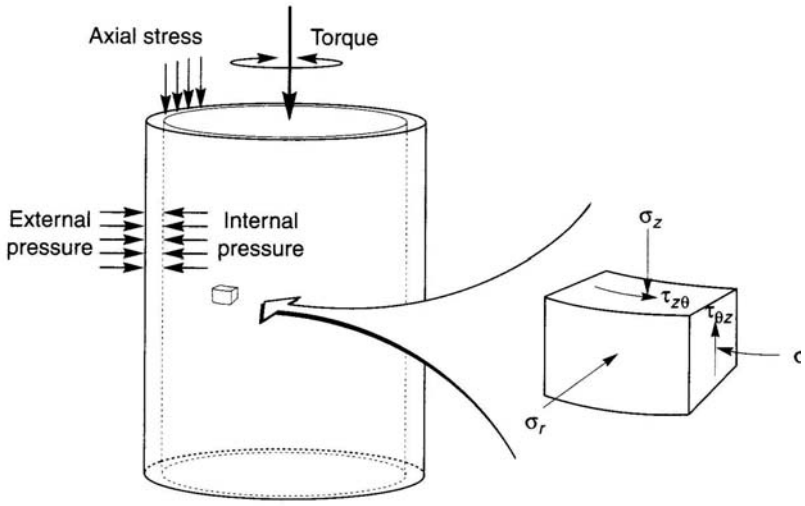

Fig. 3.6. Triaxial torsional test (Kramer 1996).

3.1.2.3 Wave propagation at low strain level

Resonant column test

The resonant column test allows to study true dynamic soil behaviour at small strain (Ishihara 1996; Kramer 1996; Pecker 1984). Small strain Young's modulus and shear modulus of the soil are calculated at the resonance frequency of the first vibration mode. The damping ratio is obtained from the decay of amplitudes during free vibrations, also at the resonance frequency. Full samples or hollow cylinders are used, either in torsional or vertical loading. The torsional load, applied by coils, can be harmonic waves or random irregular loading depending on the equipment.

Acoustic transmission

Piezoelectric elements induce P waves inside the sample, while bender elements induce S waves (Huot 1999). The measurement of the elastic wave velocity gives information on the linear behaviour of the soil tested. It is possible to induce both compression and shearing waves in the same time (Huot 1999; Muir Wood 2007; Sadek et al. 2007).

3.1.2.4 Very high strain rate

Alternative techniques had been developed for testing very high strain rates. A single shock is applied to the soil sample and strains are recorded through advanced measurement techniques. For example Hopkinson bars (Semblat 1994; Semblat et al. 1999) or dropping weight systems (Abrantes & Yamamuro 2002) were used to obtain strain rates up to 1000 s^{-1}. Hopkinson bars are designed to load materials at high speed and for a brief shock by the mean of cylindrical metallic bars. The shock wave propagates through the sample, and the deformation of surrounding bars is measured so that forces and displacements are calculated at every time step. Though this device is mostly used for metals, rocks or

concrete, it can also be used for soil thanks to the addition of an oedometric cell.

3.1.2.5 Physical models

An overview of large-scale testing facilities, like instrumented test sites, mobile laboratories, shaking tables and geotechnical centrifuges was issued by Elgamal et al. (2007). The results of such tests give valuable insight into soil behaviour under seismic loading; some of the following experimental studies will thus be compared with our results obtained with a dynamic triaxial equipment.

Shaking tables

Shaking tables were developed to overcome boundary and inhomogeneity issues associated with simple shear tests. Indeed, using very large tables and measuring mechanical properties far from the boundaries allows to neglect strain inhomogeneity. The motion of the table can be controlled in either one (Mohajeri & Towhata 2003) or two (Endo & Komanobe 1995; Ueng et al. 2006) directions. These tests do not allow to reproduce high overburden stress associated with deep ground conditions.

Centrifuge tests

Centrifuge tests allow to simulate the behaviour of a real structure of large dimensions from a model with a scaled size. Earthquake simulation is allowed thanks to small shaking tables embarked in the centrifuge basket (Chazelas et al. 2008). Centrifuge tests on sand can be used to evaluate soil response to cyclic loading (Brennan et al. 2004; Elgamal et al. 2005). The analysis of wave propagation in soils can be performed, thanks to explosive earthquake simulations. Semblat & Luong (1998) also proposed a drop-ball arrangement which creates a wave field of short excitation duration. This testing technique provides great insight into wave propagation in porous media. At mid-depth of the container, the induced P wave is shown to be spherical, with an attenuation separated into a geometrical and a material component.

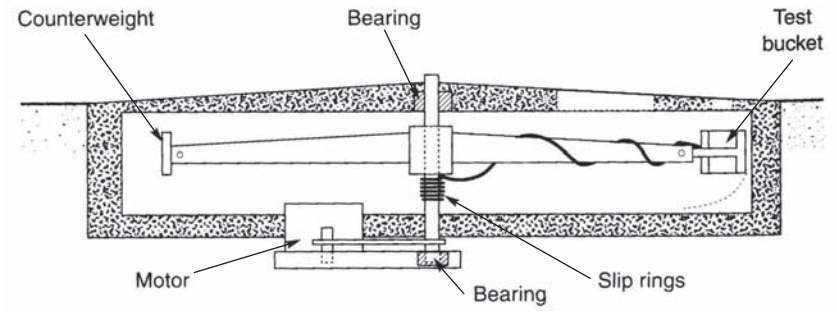

Fig. 3.7. Centrifuge test (Kramer 1996).

Centrifuge tests are performed under an artificial gravity of N**g* where N is the scale reduction number. Artificial gravity implies an equivalence between the behaviour of the model and the response of the real structure in natural gravity conditions. Scaling laws clarify the relation between all the parameters

of the test and the real scale problem. For example the frequency is multiplied by N, and the force is divided by N^2 (Madabhushi 2004; Muir Wood 2004).

3.1.3 Conclusions

The laboratory equipments presented above were developed to assess dynamic soil behaviour under various conditions of strain level, boundary conditions and rate and type of loading. Some of these tests are truly dynamic, with wave propagation phenomena within the sample. Others, called pseudo-dynamic tests, allow to induce cyclic loadings within the sample, and thus provide data for characterizing soil behaviour in these particular conditions (cf. description of the Hujeux model section 2.7.4).

The dynamic triaxial press used in this research study may be seen as a classical device; however, the following description demonstrates its enhanced capabilities for producing good quality data and innovative results.

3.2 Experimental device for cyclic triaxial loading

3.2.1 Description of the cyclic triaxial press

3.2.1.1 General overview

An advanced cyclic triaxial press has been used in this study. A detailed presentation is given here. The press was funded by the Swiss National Science Foundation and EPFL, within the framework of the R'Equip programme. At the beginning of this research project, I performed the first implementations of this complex system, which required various adjustments, calibrations, validation tests and the detailed definition of the experimental protocol.

The triaxial press INSTRON 8874 is a biaxial servohydraulic dynamic testing system. We have designed a special triaxial cell to suit the apparatus. The device controls three different cyclic motions: axial loading, confining pressure and rotation along the vertical axis. The physical limits of the three motions are summarized in Tab. 3.1. A picture of the dynamic press is provided in Fig. 3.8, and a general scheme of the press is drawn in Fig. 3.9.

Fig. 3.8. Dynamic triaxial press.

Tab. 3.1. Limits of the Instron dynamic press

Vertical force / displacement	+/- 10 kN and +/- 50 mm
Axial momentum / rotation	100 Nm and 270°
Confining pressure	3000 kPa
Frequency range	0.01 to 10 Hz
Signal type	Sinus, triangle, square, random, earthquake signals

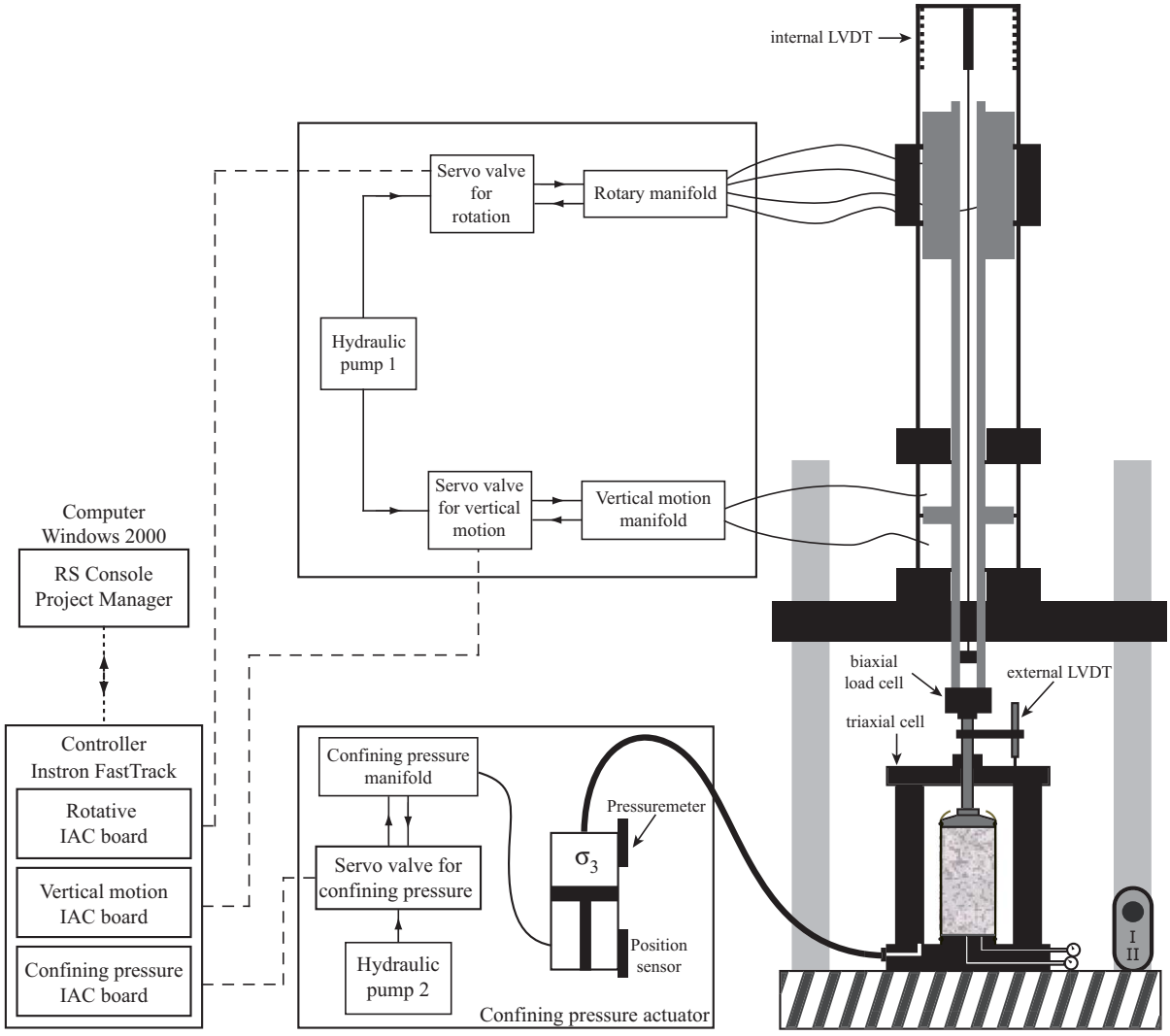

Fig. 3.9. Scheme of the dynamic press.

For the interpretation of test results, it is necessary to determine whether the press performs pseudo-dynamic or true dynamic loadings. In usual loading configurations, the minimum wave length (λ_w) is estimated by:

$$\lambda_w = \frac{c_s}{f} \simeq \frac{100}{10} = 10\ m \tag{3.1}$$

where f is the loading frequency and c_s the velocity of S wave propagation. The value c_s = 100 m/s is a low approximation for typical sand.

For samples of height 160 mm, which is the customary size, the ratio of the wave length to the sample height is around 60. This is why we consider that propagation phenomena are negligible within the sample (Semblat 1994).

3.2.1.2 Description of the different components

The controller

The system is monitored by a unique feedback control system, which is called Fast Track (Fig. 3.9). It generates orders which induce motions of the axes, and performs data acquisition. For each motion type, a driving parameter is defined as the command signal, which value is imposed on the system by the mean of the servo valves. Possible driving parameters are:

- displacement or force for the axial loading
- rotation or torque for the rotative loading
- piston rod position or confining pressure for the lateral loading

Three regulators are included in the controller: rotative, vertical motion and confining pressure Actuator Interface Card (IAC) boards (Fig. 3.9). They form, together with their respective actuator, closed loop systems (closed loop scheme in Fig. 3.10) in which a transfer function aims at minimizing the error between the command and the feedback value obtained by each sensor. Four values are triggered within each regulator: proportional gain (P), derivative gain (D), integral gain (I), las gain (R).

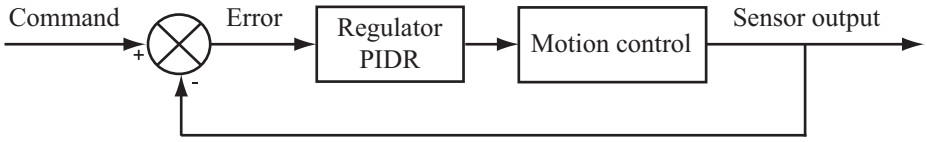

Fig. 3.10. Closed loop regulation system.

Motion regulation

Motions are controlled by three independent servo valves which provide the target amount of pressure to piston chambers. The vertical axis is a double-ended piston, which is moved by a regulated servo valve of 10 litre/min maximum flow. An identical servo valve controls the axial rotation. The structure of the vertical axis is a fixed rotative actuator in which the central piece can translate (see Fig. 3.11). The confining pressure is applied thanks to a third controlled servo valve of 3.5 litre/min maximum flow.

The hydraulic pumps

Dynamic axial and torsional motions are fuelled by a hydraulic pump which provides a 207 bar oil operating pressure to the system. The cooling medium is water. A three phase electric motor drives the hydraulic pump. The confining pressure is fuelled by an independent hydraulic pump.

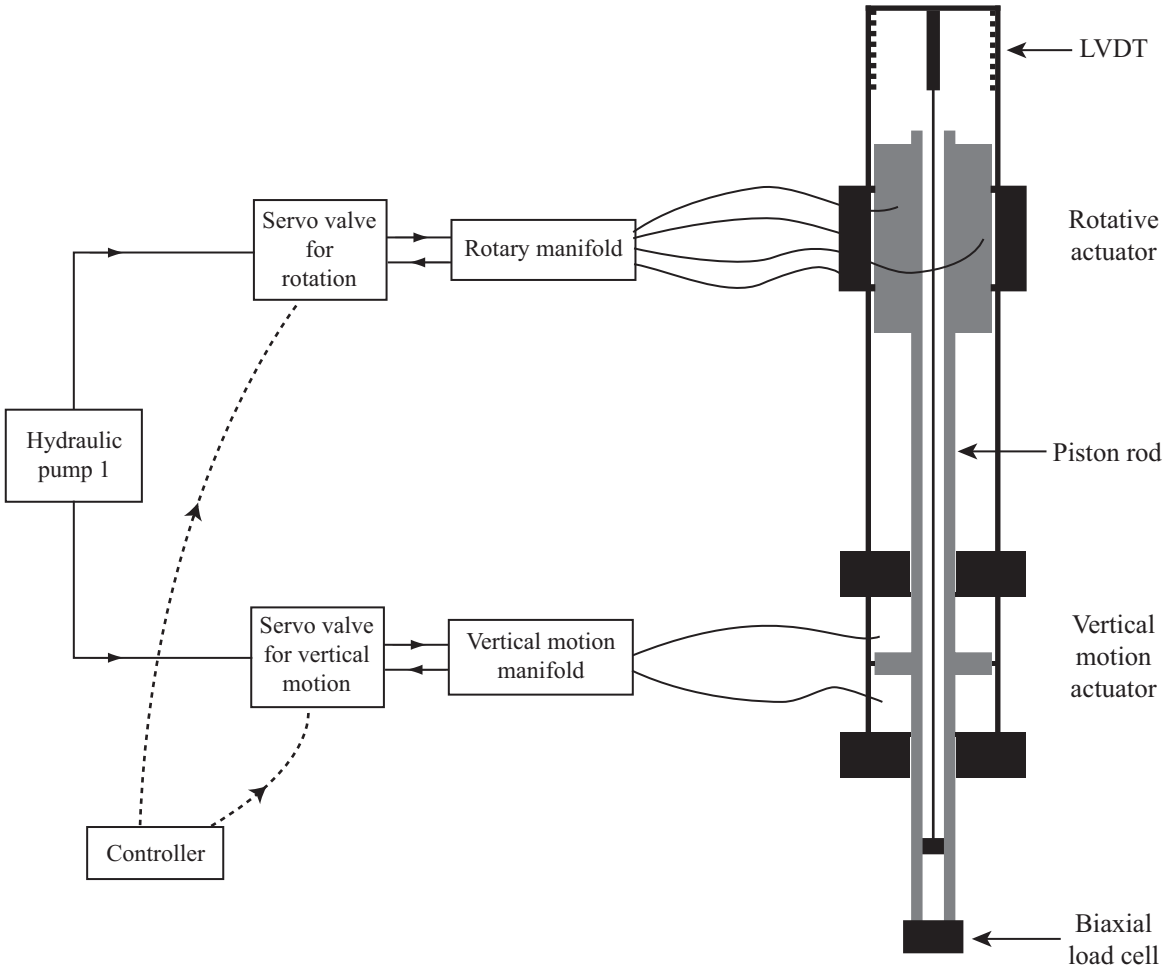

Fig. 3.11. Biaxial actuator scheme (axial and rotative motion).

The sensors

Each sensor of the test bed is linked to the Fast Track controller. At most four sensors can be linked with each actuator, also a maximum of twelve sensor outputs can be recorded. Data acquisition is performed with internal and external sensors:

- Vertical linear displacement (d_{int}) is recorded by a coaxial displacement transducer LVDT (linear variable differential transformer), which is fixed inside the piston rod (see Fig. 3.11).
- An external LVDT, shown in Fig. 3.9, is added to check the vertical linear displacement (d_{ext}). It is placed on the top of the triaxial cell. During the preliminary tests, a second external LVDT was installed to record the motions of the top of the cell from an external stem fixed to the press frame. The difference allowed a precise recording of the top cap motion. This measurement showed that d_{ext} value is not accurate when the confining pressure varies, and it is used only as a confirmation in specific conditions.

- The system is supplied with a biaxial load cell (Fig. 3.11) placed outside the triaxial cell (Fig. 3.12), at the bottom of the piston rod (Fig. 3.11). It is dynamically compensated to cope with inertial forces arising from the piston motion. The load cell records the axial force (F_{ax}) of the vertical translation and the momentum of the rotation (M_{ax}). Various studies (e.g. O'Reilly 1991) showed that it would be more accurate to place the load cell inside the triaxial cell. Indeed this position avoids to record friction between the loading stem and the triaxial cell. However, in our case, some preliminary tests of the device showed that friction is approximately of constant magnitude. Friction load doesn't depend on the speed of loading or the confining pressure, its approximate amplitude is 0.04 kN corresponding to 8 kPa for the 80 mm diameter sample. This value is taken into account for data processing.
- The confining pressure (σ_3) is monitored by a pressure meter installed on the actuator (Fig. 3.9).
- The pore water pressure (u) is dynamically measured by a pressure meter (Fig. 3.12) linked to the porous ceramic disc forming the lower end of the sample. A linear elastic finite element model of the sample revealed that the travelling time of pore pressure between top and bottom of the sample was only 1 to 10 ms. This delay, which of course depends on the values of Young's modulus and coefficient of permeability, is small compared to the shortest loading period of our tests, which is 150 ms. This comparison validates the measurement of the pore water pressure at the bottom of the cell for our frequency range.
- The volume change of the sample during drained consolidation can be recorded by a volume sensor (Fig. 3.12), called a GDS cell, which also controls the pressure inside the sample. This device is not connected to the controller.

Triaxial cell

The triaxial cell is a standard device used in soil and rock mechanics. An usual cell with perspex walls, as plotted in (Fig. 3.12), was used a the beginning of the project. A new aluminium triaxial cell was designed later, offering more rigidity and with three flat glass windows to allow non-contact measurement of the radius (description in section 3.2.3).

The cell allows to combine radial and axial loading. The confining fluid, kept under controlled pressure, imposes a homogeneous hydrostatic compression to the cylindrical sample. The axial load increases or decreases the vertical stress, which induces shearing of the sample in an oblique plane. The description of the stress states imposed in this research can be found in section 3.2.2.

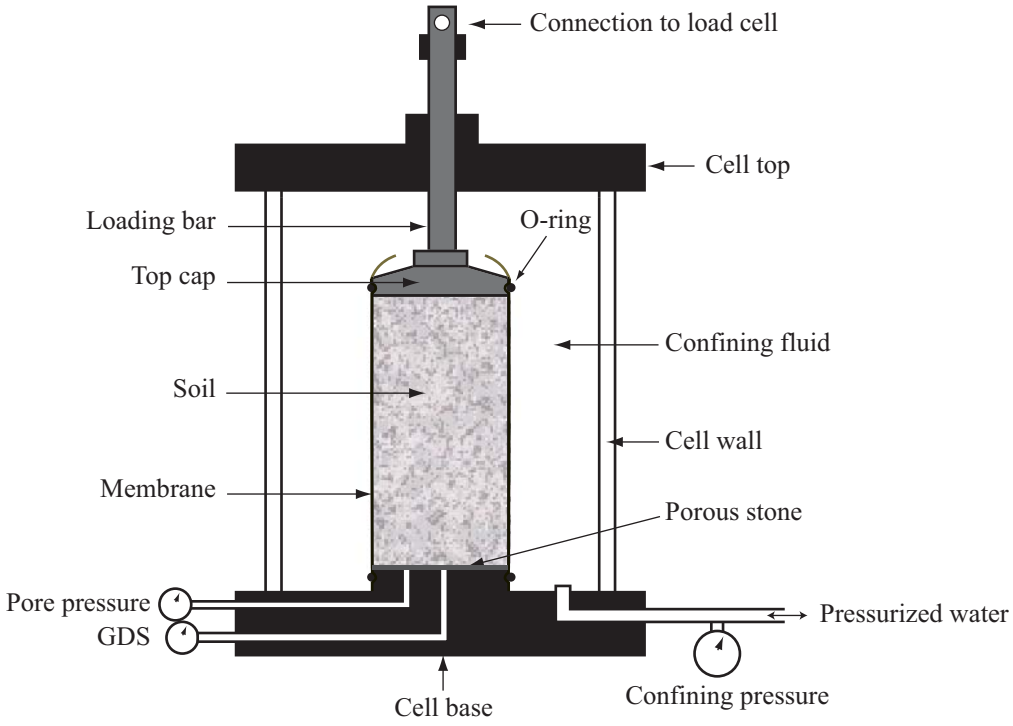

Fig. 3.12. Standard triaxial cell scheme.

Vertical loading connection

The transfer of the vertical load to the sample is performed with a specifically designed rod (Fig. 3.13). Both ends are threaded so that it can be perfectly linked and aligned with the top cap at its bottom and with the load cell at its top. This arrangement facilitates vertical alignment, prevents tilting, and allows both monotonic and cyclic motions with compression and extension phases (Baldi et al. 1988). A careful attention is paid to obtain a flat top surface of the sample, thus the contact between sand and top cap would be as perfect as possible. Previous studies (e.g. Abrantes & Yamamuro 2002) show that, for dynamic tests on sand, a paper filter is the best interface between the top cap and the sample. The filter avoids some of the lateral friction but does not introduce damping to the material behaviour. The use of grease as lubricant, which is recommended for other applications, is prohibited for cyclic tests because it prevents accurate determination of the damping ratio (defined in section 2.5).

Fig. 3.13. Vertical loading rod.

3.2.2 Stress and strain states of the sample

3.2.2.1 Homogeneity of the granular material

Despite its granular state, sand can be considered as a continuous medium thanks to the concept of the representative elementary volume *REV.* Soil is an assemblage of grains and fluids, usually air and water, which fills the pores. Considering both air and water together, namely unsaturated state, is a specific issue that will not be considered here. The mixture is only made of the grain skeleton and one fluid. The physical quantities which describe the soil state, like porosity or density, are heterogeneous at the microscopic scale. Their value varies from one point of the medium to the other. *REV* is the threshold volume above which the state parameters become constant values (Koliji 2008). The length of *REV* is an intrinsic soil parameter. At that scale, the medium is considered homogeneous, and the equations of continuum mechanics apply. The threshold length is ten times the diameter of the larger grain, and any deposit used in an experiment should have a bigger size than *REV.*

Compared to the size of the grains, which are smaller than 4 mm, the sample diameter is high (80 mm). As a consequence, the material is statistically homogeneous inside the sample. The test arises in conditions of *REV,* which means that the observed soil behaviour can be generalized for constitutive modelling. More precisely, a laboratory test provides a unique relation between the macroscopic average values of effective stress and strain for the tested granular material.

3.2.2.2 Boundary conditions

In this study, various boundary conditions are applied to the sample and different stress paths are considered:

- monotonic loading, with a constant radial stress and an increasing axial stress (i.e. conventional triaxial compression test, or CTC).
- unidirectional cyclic loading, with a constant radial stress and an axial stress which non-monotonically varies with time (e.g. the sinusoidal mode).
- bidirectional loading, with both axial and radial stresses varying with time.

Further, two initial conditions of the sample will be considered: dry or fully saturated with water.

Finally, two drainage conditions will be applied: fully drained (zero relative pore-fluid pressure) or fully undrained. Details on volume change measurement are given below.

Stress- and strain-controlled tests

Monotonic tests have a mixed uniform boundary condition, with a displacement imposed on the top of the sample, and a pressure applied along its side.

Cyclic tests have stress-controlled uniform boundary conditions. Actually on the top of the sample, the force only is controlled while the axial stress is calculated knowing the cross-section area. A known pressure is applied along the side of the sample. In undrained conditions, only the total pressure can be controlled because the effective stress depends on pore water pressure variations.

Saturated undrained conditions

For undrained conditions, water saturating the pores is blocked inside the medium, with no possibility of flowing between the grains. Upon loading, excess pore pressure develops, either positive or negative depending on the dilative behaviour of the granular matrix.

In most cases, monotonic and cyclic saturated tests are performed in undrained conditions. That means that the system is closed. The total volume of the sample is constant, assuming that:

- membrane penetration is neglected
- sand grains are incompressible
- Water compressibility is neglected. The bulk modulus of water is traditionally evaluated at 2 GPa. If one water bubble is included inside the closed volume of a triaxial sample, it decreases of a ratio of at least 10 (Huot 1999).

Saturated samples are submitted to back pressure to avoid any presence of air bubble (details in

section 3.4.2).

When the total volume of the sample remains constant, the volumetric strain is equal to zero at all time.

Cyclic unidirectional and bidirectional loading

Two types of loading were performed in stress-controlled mode: (i) a sinusoidal deviatoric stress of constant amplitude (Δq) and frequency (f) (ii) an irregular motion with varying amplitude and frequency content, representative of seismic loading (described in Chapter 7 and Appendix 2). The cyclic motion is described below.

The total spherical stress (p) is necessarily a positive value, but the deviatoric stress (q) can be negative (triaxial extension) in the case of stress reversal loading paths. Such loadings are very important in earthquake engineering, because they much more easily lead to cyclic mobility or liquefaction and give a better representation of earthquake loading in the shear plane.

Cyclic tests performed with a constant confining pressure are called unidirectional tests, in opposition to bidirectional tests for which a cyclic confining pressure $\sigma_3(t)$ varies at the same frequency as the deviatoric loading. This second cyclic load and the deviatoric cycles are superimposed. Their sinusoidal input is given below, they can be in-phase or out-of-phase:

$$\begin{aligned} q(t) &= \Delta q \sin(2\pi f t) \\ \sigma_3(t) &= \Delta\sigma_3 \sin\left(2\pi f t + \zeta \frac{\pi}{180}\right) \end{aligned} \tag{3.2}$$

where t is the time, $\Delta\sigma_3$ is the single amplitude of the confining pressure and ζ is the phase angle, i.e. the time-lag between the two sinusoidal loads (expressed in [°]).

The amplitude of cyclic confining pressure $\Delta\sigma_3$ is either constant along the shearing of increasing amplitude, or equal to 1.25 times the deviatoric stress amplitude Δq.

Four types of cyclic loading are defined for this research project (their respective schemes are presented in Fig. 3.14 in the σ_1 - σ_3 and p - q planes):

- the reference unidirectional loading R1 with varying q
- a second unidirectional loading R2 refers to a test without shearing; only the confining pressure varies cyclically.
- an in-phase bidirectional loading B1
- an out-of-phase bidirectional loading B2.

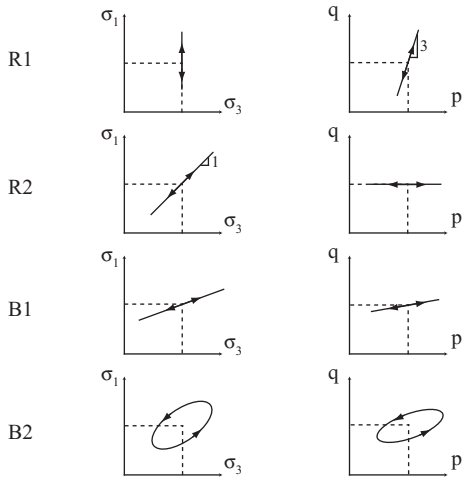

Fig. 3.14. Unidirectional and bidirectional loading paths.

3.2.3 Laser-based measurement of radial strains

3.2.3.1 Principles

Measuring the evolution of the radius of a cylindrical sample and its radial strain (ε_3) inside a triaxial cell can be a complex issue. This is especially the case when conventional technique consisting of measuring the outflow of interstitial water volume fails, as in the case of unsaturated or dry samples. Special attention has been paid for this matter in this study.

Depending on the loading amplitude and frequency, and also on the type of soil, the requirements are numerous for the design of a sensor used for such radial measurements: (i) it should not disturb the sample (ii) it should be applicable to the larger possible strain and frequency range (iii) it should not be influenced by the conditions of pressure, temperature, fluids in the cell as well as in the sample (iv) it should fit into the allowed space (v) it should preferably measure the variations of ε_3 along the height of the sample (vi) data acquisition must be fully automatic.

Several techniques are available. Local measurement with contact includes horizontally mounted LVDTs, local deformation collars or Hall effect transducers. They are fixed on the surface of the membrane, forming rings, and they record the evolution of the diameter. The problem is that they are both too heavy and too big for the case of medium to high strain measurement. Indeed their weight might disturb the sample. In general, non-contact techniques are preferred for the measurement of diameters of loose soils and for a wide range of strains. Possible candidates are contactless sensors or even image processing techniques. A major difficulty arises when dynamic loading is considered, where system response time is the key.

A contactless technique based on lasers, proposed for quasi-static conditions by Romero (1999), or

Messerklinger & Springman (2007), was developed for this thesis project (Fig. 3.15). The evolution of the diameter is measured by three lasers, installed in the same horizontal plane, which detect the horizontal displacement of the sample surface at three points thanks to optical triangulation (Fig. 3.16). The continuous measurement of the motion of these three points allows to obtain the evolution of the radius, and thus the radial strain, for all loading types at medium to high strains. It provides good accuracy and high time resolution, if great care is taken for the installation and calibration of the sensor. The continuous measurement gives the cyclic evolution of the radius at a chosen sample height. A manual scanning along the height of the sample allows to draw the sample shape, before and after cyclic loading.

Fig. 3.15. Close-up focusing on a laser sensor mounted in front of the aluminium triaxial cell.

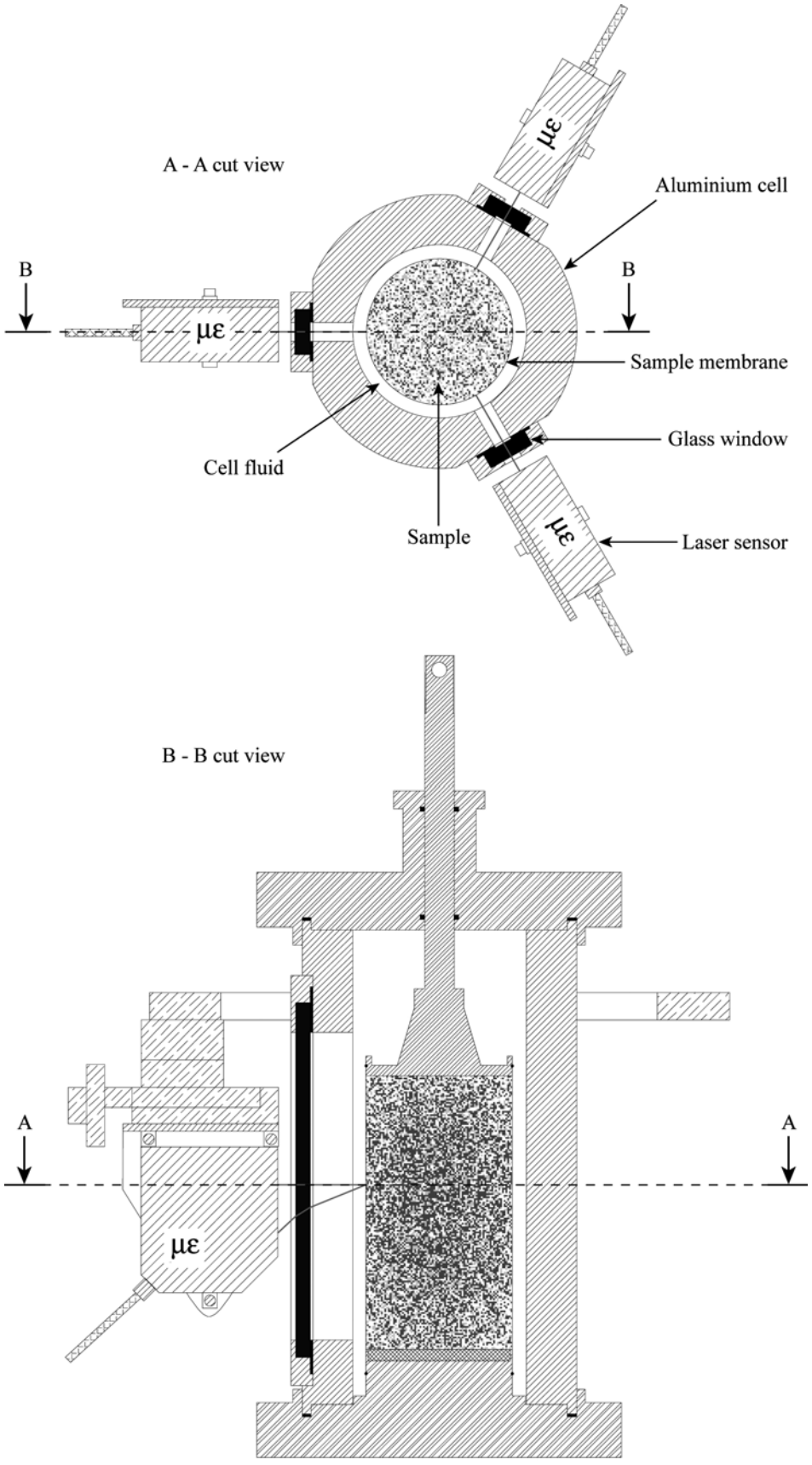

Fig. 3.16. Mounting of the laser sensors and aluminium triaxial cell.

3.2.3.2 Technical characteristics of the laser system

The characteristics of the laser sensors are summarized below:

- Manufacturer: MICRO-EPSILON MESSTECHNIK, Ortenburg, Germany (www.micro-epsilon.com)
- Type: optoNCDT ILD1700-10
- The measuring range in the air is 10 mm, but it is increased of 10 to 40% by the glass window and the water layer (lens effect, explained below in the theoretical section on optics).
- The sensor is placed at around 40 to 50 mm of the target. This distance is imposed by the manufacturer, and is also influenced by the cell and water layer.
- The laser is mounted vertically, so that the reception area of the laser beam is placed below the emission area of the beam.
- The sample surface is constituted of a latex membrane which is painted with a thin layer of white plastic paint.
- The acquisition frequency is from 312.5 Hz to 2.5 kHz, enough for earthquake-type loading.
- The data acquisition is an analogical system of 0 - 10 V. A converter included in the controller of the dynamic press provides digital data.

The calibration of the sensors is crucial, as there is a shift between the values measured in the air and those obtained in the cell, caused by the deviation of the laser beam at the two interfaces. The confining pressure evolution slightly influences the position of the side of the cell, also the calibration takes into account this value. The description of the calibration process is given in section 3.2.3.4.

Triaxial cell

A new rigid cell (in Fig. 3.17 and Fig. 3.16) was designed for this study. It is made of Certal aluminium. The advantage of this material is its light weight and slightly higher stiffness than classical aluminium; it is also easier to machine. Its thickness prevents most of the deformations under confining pressure variation. Flat glass windows are chosen to allow a good transmission of the laser beam. The calibration takes into account the very small motions of the cell induced by the variation of confining pressure, and the deviation of the beam due to the change of medium (air/glass/water interface).

The measurement is taken through the flat glass window which has a thickness of 8 mm and a water layer of around 30 mm. The triaxial cell was designed to sustain a confining pressure of 2 MPa. It is planned to use it for confining pressures lower than 1 MPa. However, the occurrence of a break of the glass window is considered, but we estimate that such event would not present a hazard to people nearby because the pressurized fluid is water. Any glass window failure would thus provoke a leak, and

not an explosion.

A 3D linear elastic model of both aluminium cell and windows was tested with a finite element software (the deformed mesh of the aluminium cell is shown in Fig. 3.18). The deformations of the cell were first considered, under maximum confining pressure of 2 MPa. The maximum horizontal displacement of the cell is 3.1 μm in this case (this value is obtained at the edge of window, close to middle height). This value is very small compared to sample radial displacement and the effect of cell deformation was estimated negligible.

Glass structural strength was then verified. In our FEM calculations, the Young's modulus of clear glass is estimated at 65 to 75 GPa, with a Poisson's ratio of 0.3. The 3D linear model gave a maximum compressive stress of 2.3 MPa in the central inner part, and a maximum tensile stress of 0.99 MPa in the inner part, where displacements are prevented at the boundaries. The tensile and compressive strength of glass being estimated at 35 and 50 MPa, the minimum factor of safety is thus 21 and the design proved to be valid. Forecasted displacements of the glass are below 0.2 μm, again negligible.

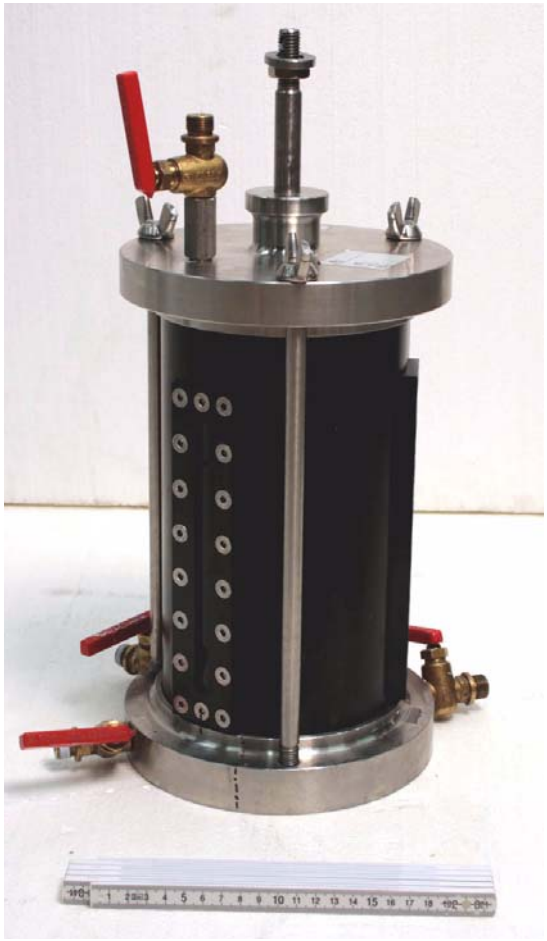

Fig. 3.17. Triaxial cell mounted with the aluminium walls and glass windows.

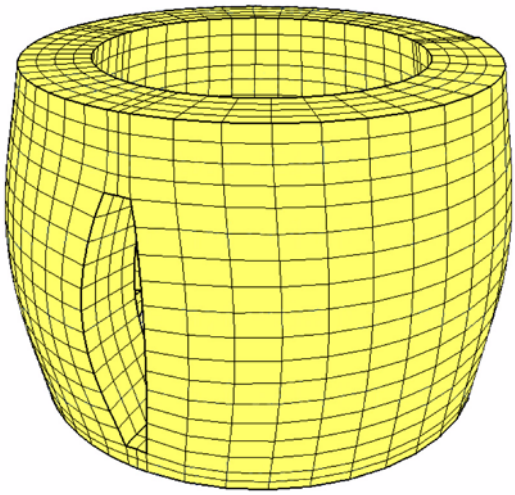

Fig. 3.18. Deformed mesh of the aluminium cell modelled in 3D.

Mounting frame for precise positioning

A frame (Fig. 3.19), independent from the press to avoid vibrations, was designed to allow precise and reproducible positioning of the laser sensors against the cell windows. It is fixed to the brick wall in four points, and rests on two feet. The part which holds the laser sensors translates vertically along a threaded rod, driven by a manually operated handling wheel. Each laser can individually rotate and translate in the horizontal plane. The translation is operated by a single-axis fast travel stage, and the rotation by a rotary stage, which can be locked into position without effect on the mechanism (both bought from GMP, Renens, Switzerland).

This frame is equipped for manual vertical scanning, which permits the determination of the shape of the sample. Special attention was dedicated to exactly obtain horizontal alignment of both the laser structure and the base supporting the triaxial cell. Consequently, the geometrical shift of the vertical scanning is kept to a minimum value, not discernible by our sensors.

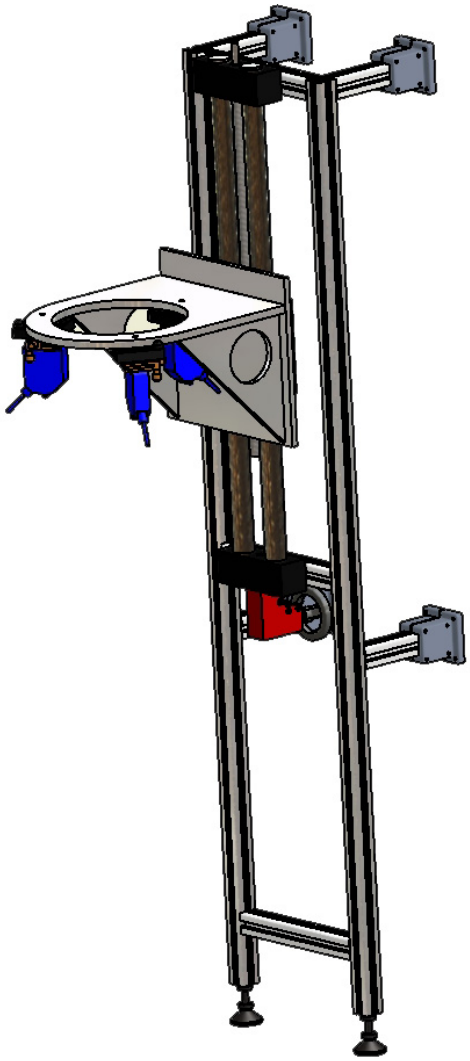

Fig. 3.19. Mounting frame for precise positioning of the three laser sensors

3.2.3.3 Theoretical points

In the following section, the principles of laser measurement by triangulation are explained for the specific conditions imposed by the presence of the triaxial cell, i.e. through three different media (air, glass and water). This study allowed to define the requirements for the precise radius measurement and the principles of the calibration. Then, the method of calculation of the radius from the three punctual laser measurements is described.

Laser principle and optics

In usual conditions, i.e. in the air (Fig. 3.20a), the laser beam exits the box through the emission point. It converges inside the measuring range (MR_1), in which the moving target is placed. Diffuse reflection (Fig. 3.21) happens, with an angle (α) such as $\alpha_{min} < \alpha < \alpha_{max}$, where $\alpha_{min} = 32.4°$ is at the end of the measuring range and $\alpha_{max} = 38.1°$ at its beginning (Instruction Manual optoNCDT1700, Micro-

Epsilon). The reflected beam first converges into a lens, and then touches the reception area at a different height, depending on the position of the target.

As the laser beam passes through three different media (Fig. 3.20b), the optical path is changed compared to the path in the air. At each interface, the Snell's law (Hecht 1998) applies between the angle of incidence and the angle of refraction:

$$n_1 \sin(\alpha) = n_2 \sin(\beta) = n_3 \sin(\gamma) \tag{3.3}$$

This law links the refractive index n_1, n_2 and n_3 to the incident and refracted angles α, β and γ, in the air, glass and water, respectively. Depending on the position of the target, the value of those three angles varies from their minimum value at the end of the measuring range to its maximum value at the beginning of the measuring range. The angle of diffuse reflection, which is γ in water, is assumed to have the same value as α in the air with only one medium. Then the values of each angle can be calculated, thanks to the geometrical properties of the laser beam.

The measuring range is increased by the presence of the interfaces, i.e. $MR_2 > MR_1$. At the same time, the distance between the emission point and the beginning of the measuring range is reduced. The angle at which the beam hits the reception lens is higher, that could be a source of instability for the measurement. The value of the measuring range, as well as the scaling effect of the interfaces, is sensitive to the refractive index. The index of the specific glass used is unknown; n_2 is assumed to be 1.523 as an average value for ordinary glass. A sensitivity analysis shows that an increase of 5% of n_2 decreases the measuring range of only 0.2%. The refractive index for water depends on the temperature and the pressure, however n_3 can be assumed constant at 1.333 as the variations of these two parameters are small. The refractive index of air, which is well known, has the value 1.000293.

The relative position of the glass layer influencing the measuring range, it is necessary to install the laser sensor at the same distance to the cell for accurate calibration. An increase of 1 mm of distance through the air increases the measuring range of 2%. It is also important to ensure that the laser beam hits the target at right angle.

The relation between the refraction angle and the measuring range is well represented by a quadratic fit in both cases, with air alone or with multiple interfaces. The relation between the theoretical measurement in the air (x) and the same distance for a point placed inside the cell (xr), inside the measuring range, is fitted with a linear curve of slope 1.140. This ratio corresponds to the scaling factor Γ obtained by calibration (section 3.2.3.4). The theoretical value calculated here is lower of 14% than the value obtained during manual calibration. The difference is certainly due to the diffuse reflection angle of the laser beam on the target, which is quite surely not the same in the air and in the water. Due

to the lack of information on the mechanism of the laser sensors, and particularly the geometry of the incident beam, it is impossible to properly calculate this angle.

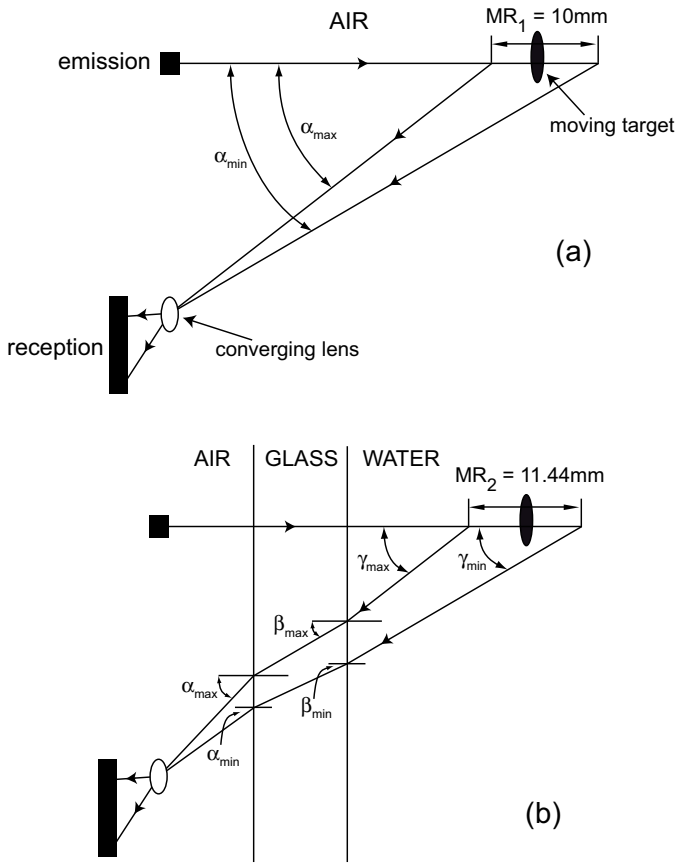

Fig. 3.20. Optical paths in the air (a) and with the triaxial cell (b).

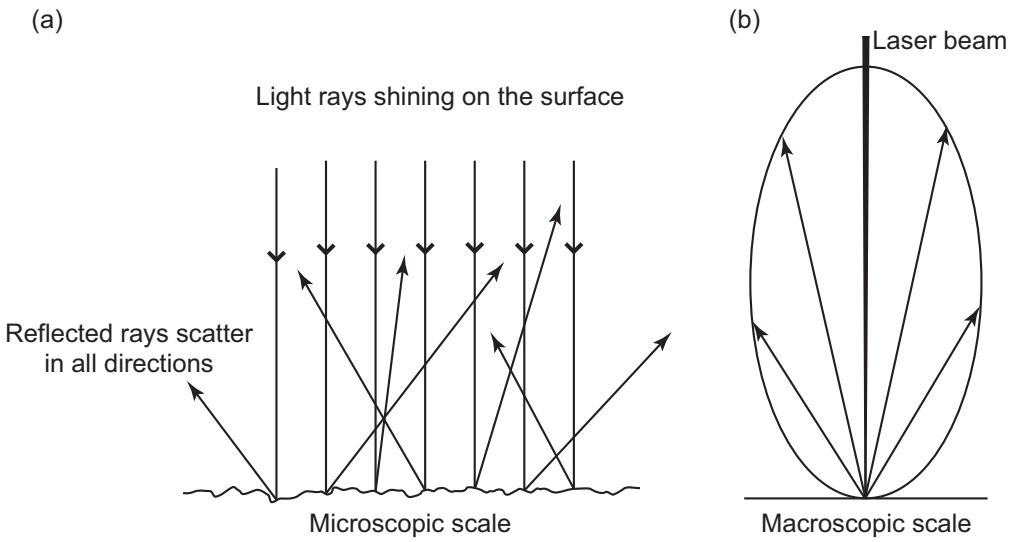

Fig. 3.21. Diffuse reflection principle.

To conclude, the accurate measurement of the displacement of the target points inside the triaxial cell requires to (i) place the three lasers at exactly the same distance to the glass (ii) verify that the laser beams hits the glass at right angle (iii) determine experimentally the scaling factor Γ for calibration (iv) ensure the same conditions of temperature during each test.

Calculation of the radius

Thanks to the three continuous measurements of the laser sensors, and assuming a perfect circular cross-section, the radius and the centre point of the cross section can be calculated at a given height (Fig. 3.22). A reference fixed point is designated for each laser sensor, thanks to a steel cylinder of known diameter used for calibration. Then the value of the radius of the sample can be calculated at each time step, by comparison with that reference. Fig. 3.22 summarizes the position of the laser sensors, the sample, the reference steel cylinder and the points used for the calculation. The triaxial cell is omitted in this figure for the sake of simplicity.

The horizontal plane is arbitrarily oriented with the x-direction aligned with the laser n°1. The orientation of the three laser beams in this plane is given by the angles [π -π/3 π/3] for laser sensors number 1, 2 and 3, respectively. It is assumed that the three laser beams converge at exactly the centre of the cell, which is aligned with the vertical axis of symmetry of the system. It was necessary to build a precise positioning system for the laser equipment because of this assumption.

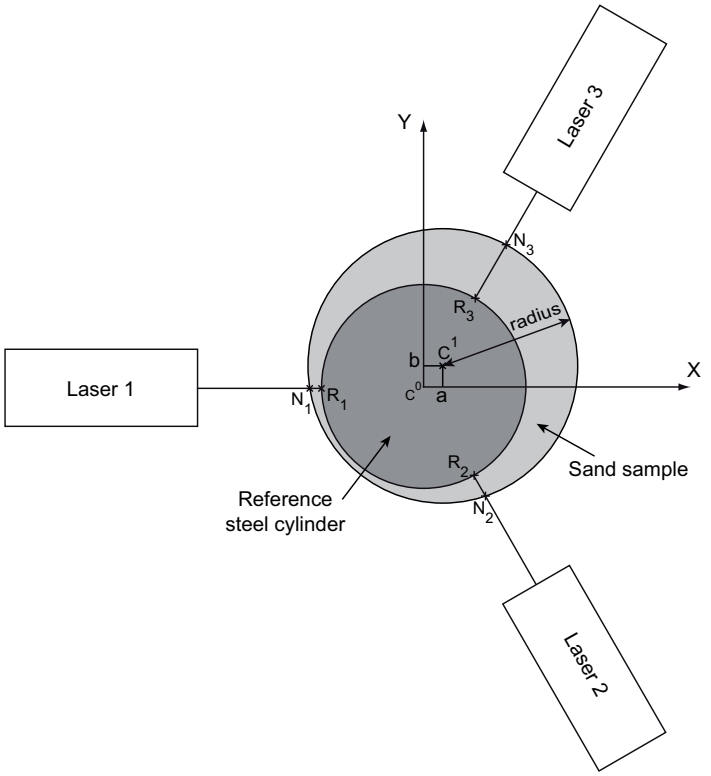

Fig. 3.22. Parameters for calculation of the sample radius.

The reference cylinder being centred, the coordinates of the points R_1, R_2 and R_3 are:

$$R_1 = \begin{bmatrix} -r \\ 0 \end{bmatrix} \quad R_2 = \begin{bmatrix} \frac{r}{2} \\ -\frac{r\sqrt{3}}{2} \end{bmatrix} \quad R_3 = \begin{bmatrix} \frac{r}{2} \\ \frac{r\sqrt{3}}{2} \end{bmatrix} \tag{3.4}$$

The radius of the reference steel cylinder is $r = 39.79$ mm at its middle height, including a thin homogeneous layer of white sprayed paint. The position of the reference points is associated with the respective measured values of the three laser sensors. Including the calibration at zero confining pressure, those measured values are called m_{ref}; they depend on the distance between the lasers and cell, also they are associated with a given calibration.

The points are taken on the external surface of the sample, also the thickness of the membrane and the paint layer are included in each initial laser measurement. The membrane thickness is directly measured with a slide callipers before each test. The paint layer thickness was evaluated at approximately 0.2+/-0.05 mm from several measurements taken after dismounting of the cell and sample, by carefully peeling off the paint from the membrane. The addition of these two constant shifts is called *ep*.

The absolute coordinates, in the cross section plane, of the points N_1, N_2 and N_3 situated on the inner surface of the sample, i.e. below the membrane, can be calculated now. The values measured by the laser sensors are n_1, n_2 and n_3. At each time step t, the points coordinates are:

$$\begin{aligned} N_1(t) &= \begin{bmatrix} x_1 \\ y_1 \end{bmatrix} = \left(R_1 - m_{ref}(1) + n_1(t) - ep\right)\begin{bmatrix} -1 \\ 0 \end{bmatrix} \\ N_2(t) &= \begin{bmatrix} x_2 \\ y_2 \end{bmatrix} = \left(R_2 - m_{ref}(2) + n_2(t) - ep\right)\begin{bmatrix} \frac{1}{2} \\ -\frac{\sqrt{3}}{2} \end{bmatrix} \\ N_3(t) &= \begin{bmatrix} x_3 \\ y_3 \end{bmatrix} = \left(R_3 - m_{ref}(3) + n_3(t) - ep\right)\begin{bmatrix} \frac{1}{2} \\ \frac{\sqrt{3}}{2} \end{bmatrix} \end{aligned} \tag{3.5}$$

The centre of the circle $C(t)$ which passes through the three points $N_1(t)$, $N_2(t)$ and $N_3(t)$ is the intersection of the two perpendicular bisectors, KC and LC, of the lines N_1N_2 and N_2N_3, respectively (Fig. 3.23). It is necessary to calculate the equations of the two perpendicular bisectors in order to obtain the coordinates of C, $X(t)$ and $Y(t)$.

$$
\begin{aligned}
y^{KC} &= ax + b & y^{LC} &= a'x + b' \\
a &= -\frac{(x_2 - x_1)}{(y_2 - y_1)} & a' &= -\frac{(x_3 - x_2)}{(y_3 - y_2)} \\
b &= \frac{x_2^2 - x_1^2 + y_2^2 - y_1^2}{2(y_2 - y_1)} & b' &= \frac{x_3^2 - x_2^2 + y_3^2 - y_2^2}{2(y_3 - y_2)}
\end{aligned}
\tag{3.6}
$$

Then the coordinates of their intersection are calculated by:

$$
\begin{aligned}
X(t) &= \frac{(b - b')}{(a' - a)} \\
Y(t) &= a\,X(t) + b
\end{aligned}
\tag{3.7}
$$

The radius is simply deduced from the distance between the centre and one of the points, for example here with N_2:

$$
radius = \sqrt{(x_2 - X)^2 + (y_2 - Y)^2}
\tag{3.8}
$$

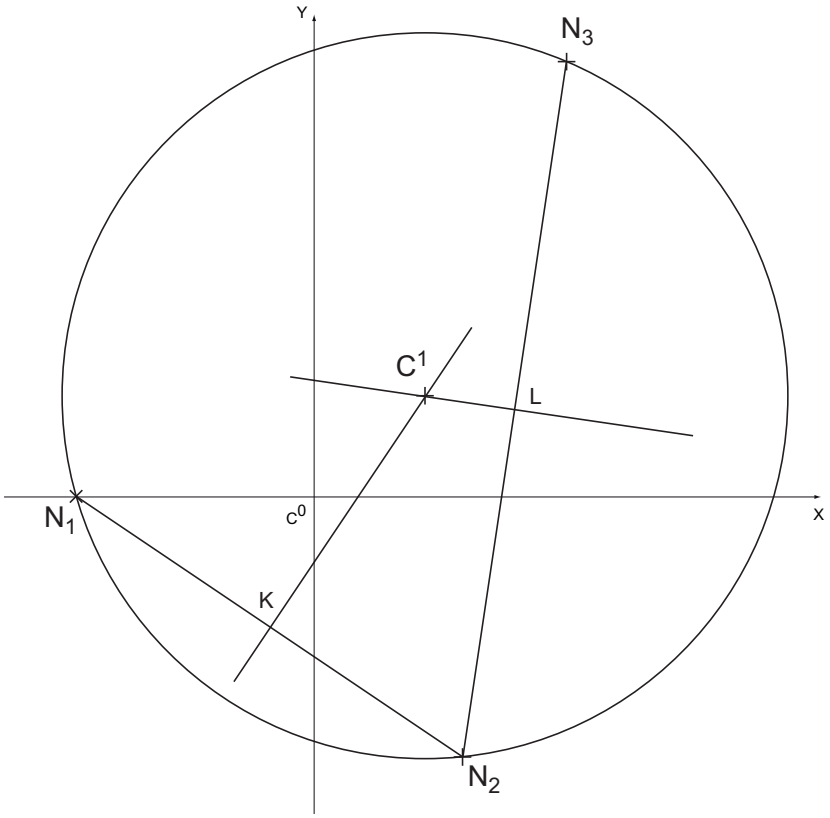

Fig. 3.23. Geometrical determination of the centre of the sample cross-section.

3.2.3.4 Detailed use of the laser sensors

Electrical connection

The power supply is a DC battery. The output data is recorded through analogical connection to the Instron data acquisition tower by a D-sub connector.

Parameters setting

The setting of the output parameters of the laser sensor is performed with the two buttons placed on the laser box. An internal filter averages the data, so that noise can be reduced. A recursive average is chosen. The sampling frequency can be 2.5 kHz at maximum, but decreasing that value increases the exposure time, which helps for signals of lower power. The minimum value 312.5 Hz was finally chosen.

Description of the precise positioning

The angular position of the three laser sensors at 120° from each other is fixed. However, each of them can rotate around that fixed position thanks to a manual rotary stage, which allows alignment in front of the glass window. A translation stage allows to adjust the distance from the cell, so that the measuring range covers the expected radial displacement of the sample. Two templates of different thickness were selected, also it is possible to chose between two reference positions. A calibration was performed for each of them. The larger one is preferred when an increase of the diameter is expected, and the thinner one corresponds to a decrease of the diameter in the case of triaxial extension tests.

The position of the cell is fixed thanks to a groove extruded from the upper surface of the base of the dynamic press. The cell is placed so that the glass windows are perpendicular to the laser beam. Before fixing the rotation of the cell by linking the vertical loading rod with the dynamic press, it is always checked that laser beams hit their respective glass window at the middle of the aperture, in order to avoid any misalignment with the vertical central axis. Once aligned, the position of both the triaxial cell and the laser sensors is tightly secured. The laser beam should hit the target at right angle. A difference of 5° induces a small error on the measured value, lower than 12 μm according to the user's manual of the laser sensors.

Calibration procedure

The laser sensor is first automatically calibrated thanks to the controller of the dynamic press. It transfers the measured voltage range into a length, with a scale of 1 mm corresponding to 1 V. Then a precise calibration is performed. The manual calibration is first done in the air, by targeting a moving element. Possible external drifts are tested; the laser beams are not highly sensitive to light and vibrations from the press. They are more sensitive to the target surface quality. This calibration shows that the automated calibration is valid, with a precision higher than 99.99%.

Then the calibration takes into account the new triaxial cell filled with demineralized deaired water at atmospheric pressure. As theoretical analyses showed that the relative positioning of the laser and glass windows influences the measurement, the calibration is performed once for each template. A calibration tool was developed for measuring real displacements inside the triaxial cell (Fig. 3.24). This specially designed cap is put on the cell instead of its usual upper part, while the cell is partly filled with deaired water. The weight of the aluminium cell cylinder is sufficient to avoid leakage at the base. The target is moved with a knob, while its real displacement is read on the micro-dial gauge placed on the top of the new tool. Each position associates a laser measurement with a real displacement. The linear regression of this relation is calculated separately for each laser (e.g. Fig. 3.25). The scaling coefficient Γ is obtained by averaging three slope values for back and forth travel.

The confining pressure is then taken into account for a maximum of 1 MPa. The deformations of the triaxial cell has a small impact on the measurement of the radius. To evaluate this aspect and include pressure effect inside laser sensor calibration procedure, other calibration tests were performed: the confining pressure increases and decreases while the laser beams point at a fixed target. Recorded displacements are thus representative of the effect of confining pressure only. It was chosen to use painted steel sample as a target to avoid any sample deformation caused by the confining pressure increase. Even if the cell is quite rigid, some displacements occur thus changing the measured value (cf. below). The theoretical aspects explaining why cell displacements induce measurement errors were described in section 3.2.3.3.

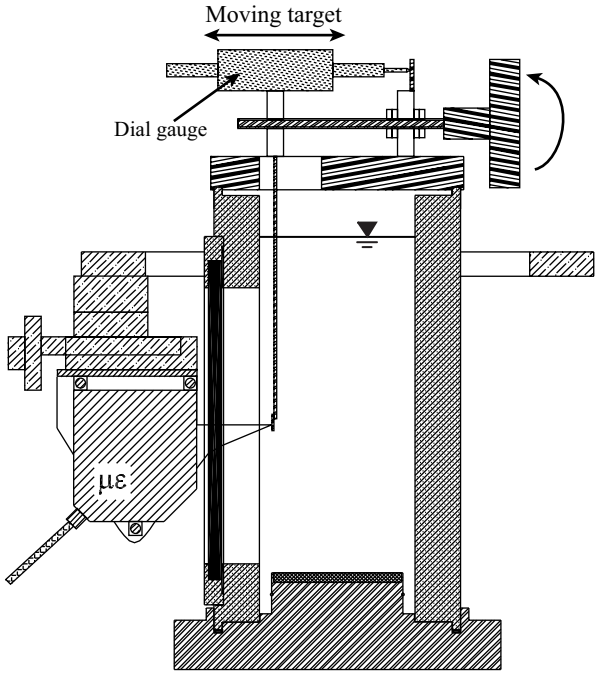

Fig. 3.24. Calibration tool for the scaling coefficient of the triaxial cell and water layer.

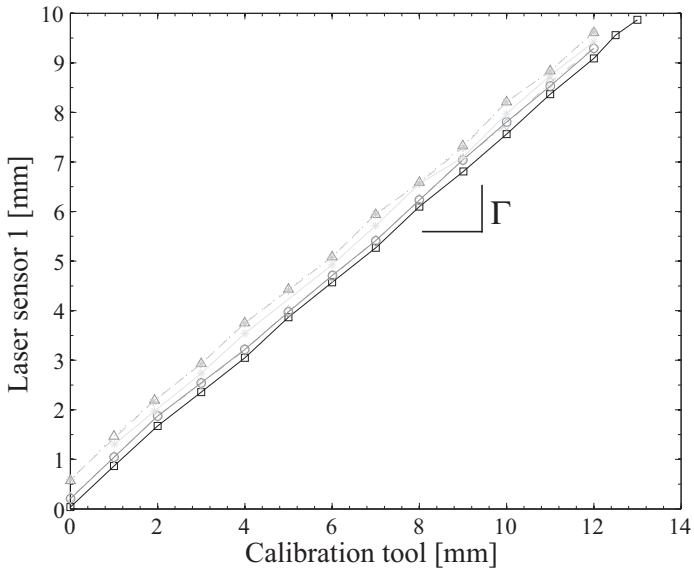

Fig. 3.25. Measurement of the scaling coefficient Γ for the laser sensor 1.

The effect of σ_3 on the observed steel sample radius is shown in Fig. 3.26. The radius falsely increases with the confining pressure, of around 0.005 mm/bar, or 50 μm for 1 MPa. This value is much higher than the displacements expected from the numerical simulations of the aluminium cell of 3.1 μm for 2 MPa (presented in section 3.2.3.2). The large difference might be due to a compression of rubber joints (placed between the glass and the aluminium profile), although they were especially selected for their high stiffness and initially compressed to the desired thickness. Very small motions might also result from fixation misalignment between the different parts of the system (screws, main cell body, cap holding the glass) and flatness defaults. Another surprise is that these variations are hardly reproducible. Some kind of relaxation of the cell appears, also the fifth increase of the confining pressure gives higher radii than the first loading. An hysteresis also appears, with higher values at increase than at decrease of σ_3.

In order to limit measurement errors, the effect of the confining pressure is applied directly to the calculated radius, instead of the measured displacements of the three points. Slow increase and decrease of the confining pressure are used for calculating average lines from 10 measures taken on the two ways. A polynomial fit is performed for the two lines, one for monotonic increase calibration and the other for the decrease of the confining pressure. The shift is compensated in the calibration procedure. However, the error on the radius during monotonic increase of the confining pressure can be quite large. A special calibration for cyclic variation of the confining pressure gives better precision inside a narrower band, resulting in a decrease of the error on the radius. These three different situations, monotonic increase, monotonic decrease and cyclic variation, are associated with three polynomials which depend on σ_3 and are included in the automatic radius calculation.

By combining the calculation of the radius and the calibration procedure, the radius $R(t)$ of the sample at the height of the laser mounting can be known at all time steps. The local radial strain can thus be calculated, with the equation:

$$\varepsilon_3 = 1 - \frac{R}{R_0} \tag{3.9}$$

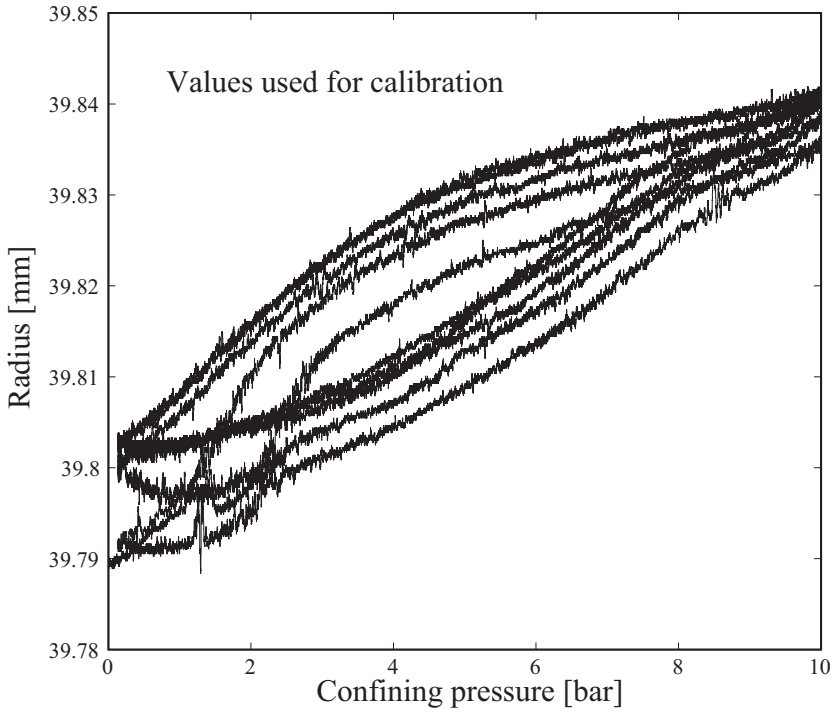

Fig. 3.26. Calibration of the effect of confining pressure on the observed radius of the steel sample.

Vertical scan for average radial strains and volume

The mounting frame of the three laser sensors is independent from the dynamic press, and the system can translate vertically in order to obtain the evolution of the diameter along the height of the sample. A dial gauge of 100 mm measures the covered distance, thus enabling to obtain a profile of the sample radius. That profile is incomplete, as the laser can not reach the bottom of the sample. However 2/3 of the profile is obtained, thus making it possible to extrapolate its shape.

The verification of the scanning procedure is first performed with the steel cylinder, which is painted with a homogeneous thin layer of white sprayed paint. From manual measurement, we know that the radius of the painted cylinder slightly increases from 39.785 mm at the top to 39.8 mm at the bottom. This evolution is distinguishable on Fig. 3.27; the trend is good, and the expected values are within a band of +/-0.015 mm around the measured radius.

For the polyurethane sample (PU), six manual scans are performed (Fig. 3.27). The initial radius of this sample, including the paint layer, is around 40.1 mm. The two first ones, performed in identical conditions of no pressure and no axial load, show that the reproducibility is good and the value of the radius is close to the expected value. The peaks are attributed to irregularities in the paint layer. It is interesting to compare them with the 5th scan, performed in identical conditions but without the triaxial cell. In that case, the radius is underestimated, mainly because the calibration is not as properly performed without the triaxial cell. Indeed it is not possible to identically and precisely position the sensors without the cell, which is the reference point for the lasers. However, it is clear that the evolution of the radius is similar in both situations, with or without the triaxial cell. When the axial load of 1.6 MPa is applied (scans 3, 4 and 6), the radius increases of approximately the same amount in the air and in the triaxial cell. The shape of the loaded sample is the same as the initial sample. Finally the increase of the confining pressure of 800 kPa at the 4th scan shows no influence, as expected (the rubber has a Poisson's ratio of 0.5, its volume can not change).

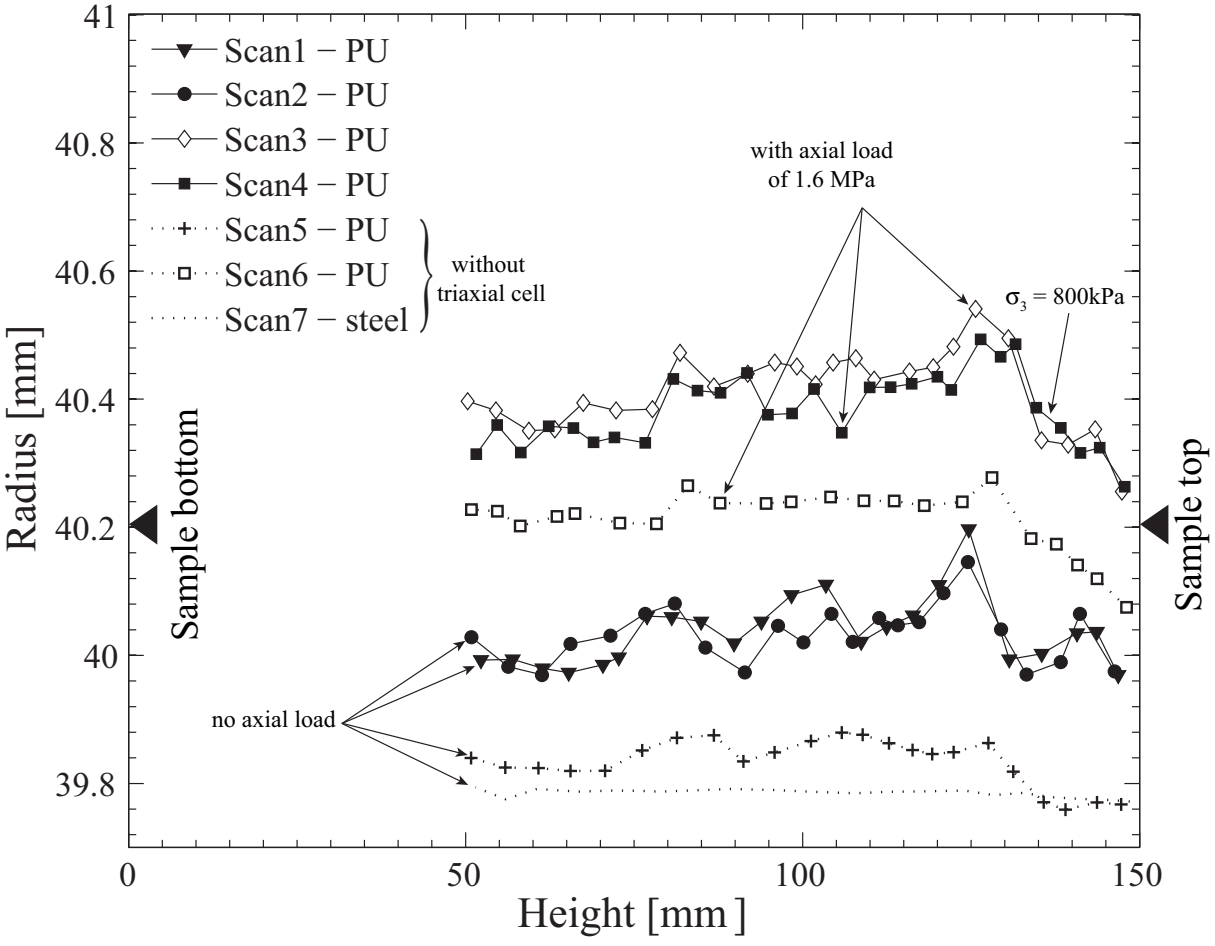

Fig. 3.27. Evolution of the radius along vertical profiles of the samples.

These observations validate the calibration of the sensors, with regard to the cell and the pressure effect. They also validate the method used for scanning the samples, including the good alignment of the cell and the scale structure holding the lasers.

For cylindrical sand samples sheared in compression in the triaxial apparatus, the usual assumption is to take a parabolic vertical profile. In that case, the deformations are such that the average radial strain is equal to 2/3 of the maximum strain at the peak. One sample profile of Leman Sand is presented in Fig. 3.28 for the case of a compression loading. The profile, for a failure in extension, is quite different as failure arises as a shear band rather than barrelling (cf. example in Chapter 4). These profiles allow to calculate a coefficient of reduction L between the local radial strain at one given height, $\varepsilon_{3,l}$ and the mean strain $\varepsilon_{3,m}$ along the sample. In order to measure the radial strain with maximum accuracy during continuous measurement, the laser sensors are placed at mid-height, where radial strains are expected to be the highest.

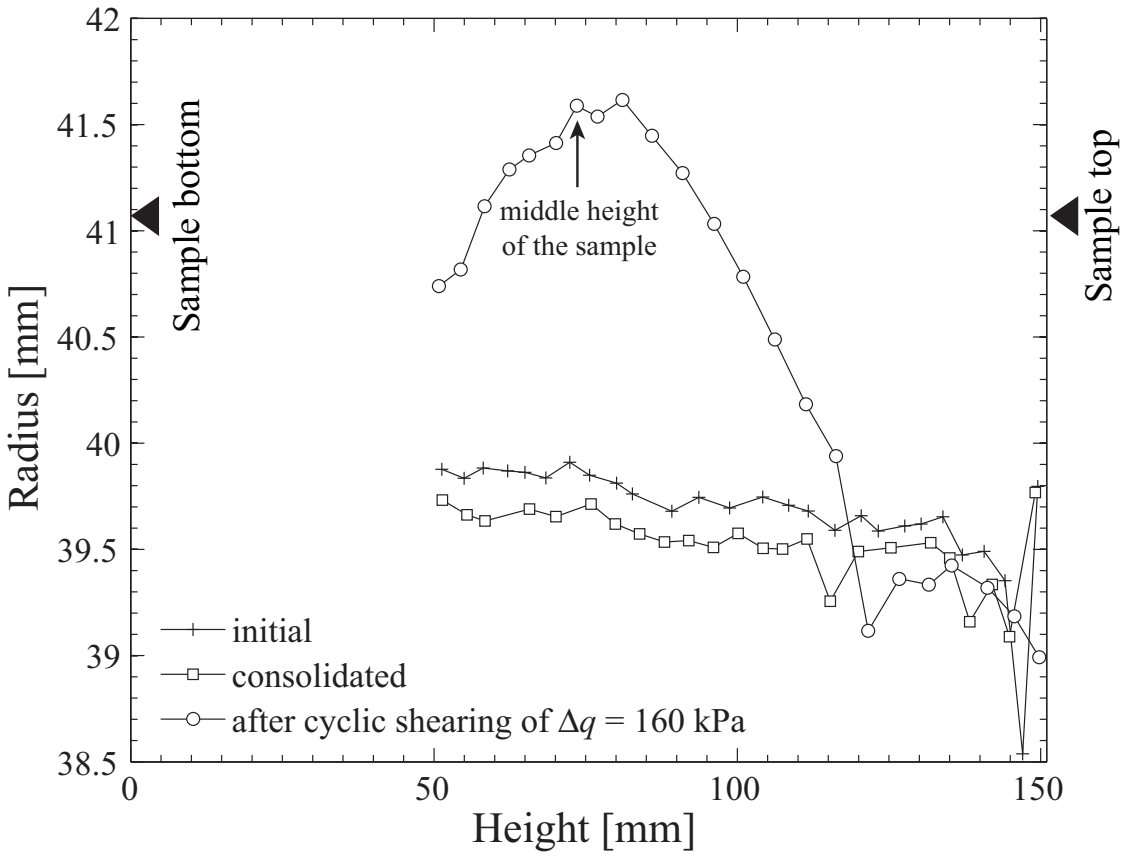

Fig. 3.28. Evolution with height of the radius of an undrained Leman Sand sample in compression (σ_3 = 200kPa).

To account for the variability of responses of the cylindrical samples, which depends on the loading type and initial sample shape, a single parameter L is not sufficient. It is thus decided that vertical scans of the samples would be performed for each test. The coefficient L is calculated independently for each

sample. An initial scan allows to evaluate the initial average radius and shape, and the scan performed after shearing gives the deformed shape. The coefficient *L* is calculated with the deformed shape.

To summarize, the scanning process increases the efficiency of the laser device, by taking into account the real shape of the sample. It is clear by that method that the assumption of a parabolic profile is not enough, especially for tests in extension.

3.2.3.5 Estimation of uncertainties

The uncertainties of the non-contact measurement technique with laser sensors are evaluated now. The uncertainties linked with the physical measurements are:

- The intrinsic laser sensor measurement error is neglected, it is around 0.5 μm.
- Thickness of the paint layer (δl_1 = 0.01 mm estimated from comparison of the thickness after the test)
- Thickness of the membrane, from initial thickness, membrane compressibility and membrane penetration. Membrane penetration is the most important of these three factors in undrained tests, because it evolves with the effective confining pressure. In dry tests however, the effective confining pressure remains constant and the error on the radius is thus constant during cyclic tests, after consolidation. The uncertainty on total membrane thickness can be neglected for the calculation of radial strain uncertainty because cyclic radial strains are not affected by the static errors on the radius. For the sample radius uncertainty, membrane penetration is usually broadly estimated by the half of D_{50} of the soil. But the paint layer clearly decreases membrane penetration also this value does not really reflect this uncertainty. It is finally assumed that the error on membrane thickness is negligible compared to the error on the thickness of the paint layer.
- Error at transmission of the laser beam through interfaces, from small heterogeneities of the glass and particles within the water (δl_2 = 0.005 mm, i.e. ten times the resolution of the laser used in the air)
- Angular horizontal and vertical misalignment of the position of the laser ($\delta\theta < 1°$ => negligible)
- Temperature variations: this can be neglected since the laboratory is temperature-controlled.

Uncertainties arising from the calibration procedure are:

- Stability of the automatic calibration (negligible)
- Precision on the scaling coefficient Γ, including the distance between the laser and the cell (δc_1 = 0.002 mm/mm from the comparison of the three values for each laser)

- Effect of confining pressure, with the repeatability of cell wall displacement and the accommodation due to creep of the cell (δc_2 = 0.015 mm/bar from Fig. 3.26)
- Precision of the reference position with the steel cylinder, for the calculation of the diameter (estimated broadly at δc_3 = 0.01 mm)
- Assumption of a perfect circular cross-section for the calculation of the diameter (unknown)

The coefficient of integration *L* for obtaining the average axial strain over sample height (introduced in the description of the scanning procedure) is calculated by comparing two scans of the sample, the initial and the sheared sample. The evaluation of uncertainties for that coefficient concerns an additional component:

- Misalignment of the structure holding the scan and the triaxial cell and fits in the vertical displacement system (δi_1 = 0.015 mm from the evaluation with the steel cylinder)

The total uncertainty on the position of each point N1, N2 and N3, is calculated at 0.06 mm before taking into account the confining pressure. The uncertainty on the radius is thus also at worst within this range of value. Adding the effect of confining pressure, the total uncertainty on the radius is then 0.08 mm, or a relative uncertainty of 0.2%. Taking also into account the vertical motion for scanning, total uncertainty on the radius includes δi_1, as well as the previously mentioned errors. This new uncertainty on the radius with the vertical translation of the equipment is δR = 0.1 mm, which corresponds to a relative error of 0.25%.

The static error on the radius at a given height, at any given time, is estimated from all uncertainty factors. Most of them remain constant during the whole test: δl_1, δc_1, δc_3 do not vary after the setting up of the triaxial cell. The error due to confining pressure δc_2 is also constant after the application of the isotropic consolidation, except for bidirectional loading. That is why the uncertainty calculated above does not apply for the variation of the radius ΔR measured during each phase of the test. Only the direct measurement error δl_3 is taken into account for the uncertainty of ΔR, which gives $\delta \Delta R$ = 0.005 mm. The uncertainty of the local radial strain measured with the laser technique is then $\delta \varepsilon_{3,l} = |\delta \Delta R / R_0| = 0.005 / 40 = 1 \times 10^{-4}$.

The uncertainty of the integration factor *L* is estimated at 5%, also the error on the average radial strain over the sample is, at medium strain range:

$$\delta \varepsilon_{3,m} = \delta \varepsilon_{3,l} * L + \varepsilon_{3,l} * \delta L = 1 \times 10^{-4} * 1 + 5 \times 10^{-3} * 0.05 = 4 \times 10^{-4} \quad (3.10)$$

This value is at the bottom of the range concerned by medium strains, also this might be an issue for the smallest motion amplitudes. The validity of laser sensor measurements is verified along a real triaxial

test on Leman Sand, described in section 4.6.

3.2.3.6 Summary

Laser-based measurement technique is a very sensitive equipment, but it allows to measure radial strains without contact in the range of medium to large strains. The technique is adapted for cyclic triaxial testing of granular materials in cyclic loading, for which large strains develop.

The development of this technique includes:

- an analysis of the optical path through three media (air, glass and water) to detect the factors influencing the measurement
- the design of a new aluminium cell with flat glass windows
- the design of a structure which allows precise positioning in front of the windows, at a given distance of the axis of the dynamic press. The system translates vertically to allow vertical scanning of the sample
- the design of a calibration procedure which takes into account the confining pressure, including the creation of a target which translates horizontally inside the cell
- an automated calculation procedure of the radius from the three laser measurements
- an evaluation of vertical scanning, and the creation of an integration factor to calculate an average radial strain from the continuous measurement of the local radial strain at mid-height of the sample.

A validation example on undrained Leman Sand is presented in Chapter 4, before the presentation of tests on dry sand.

3.3 Validation tests

A polyurethane cylinder was tested in the triaxial cell to check any drawback in the press and the measuring system. The vertical linear load and the confining pressure load were tested for constant, monotonic and cyclic commands, independently and with a slave - master relation on various stress paths. It was observed that stress-controlled and strain-controlled motions are equivalently precise within their range of use. The command error was found to be of the order of 0.5% for displacement motions of vertical cyclic amplitudes ranging from 0.05 mm / 40 kPa to 5 mm / 500 kPa, and at frequencies from 0.1 Hz to 10 Hz. This value is low for such wide range thanks to the possibility to trigger internal parameters of the control loop.

Fatigue tests were also performed, in order to verify the sensitivity of the device to tests of long duration. During a three hours long test, the displacement amplitude was satisfactorily observed to remain constant (0.1% variation) after 20000 cycles.

The servo-valve monitoring the cell pressure was also checked to be very precise: the total confining pressure can be maintained constant thanks to the internal regulation. Very small oscillations appear anyway, in the order of 0.3% of the actual pressure, at the beginning of the tests, and they can increase to 3.5% when large strains are induced, i.e. during cyclic mobility.

Because of friction between the loading rod and the top of the triaxial cell, we estimate that loadings with deviatoric stress amplitude below $\Delta q = 15$ kPa should not be considered. This is the criterion applied to withdraw non-valid test results.

The top and base of the sample are not smooth enough (only a paper filter boundary) to avoid end-restraint and the formation of barrel shapes during loading at rather large amplitudes. Indeed, the friction of the granular matrix against the filter is a boundary condition which prevents full homogeneity of the sample. Near these rough boundaries, less deformations are produced and the soil behaviour is more contractive than in other parts of the sample. The deformed shape of sand sample (Fig. 3.28) shows that barrelling may not be negligible. This inhomogeneity which may become predominant near failure (i.e. at large strain amplitude) is mentioned further in section 4.5.

3.4 Experimental procedures

3.4.1 Sand sample mounting

The production of sandy samples with good reproducibility of the sample size required to design a new mould (Fig. 3.29). This device is put on the base of the cell, around the membrane, and applies a vacuum between the membrane and the inner surface of the mould. The dimensions of the mould are exactly matched with the cell base, on which a membrane of thickness 0.3 mm and one O-ring are put. As a consequence, the membrane is plated against the walls and the inner volume is exactly the same for each sample. To allow convenient mounting and dismantling, the mould is made of two symmetric parts. They hold tightly together thanks to two collars.

For samples saturated with water, the mould is gradually filled with a known volume of water, and then small spoons of sand are poured. Between each spoon, the soil is lightly patted to avoid cavities inside

the soil fabric. During pouring, the level of water is kept above the soil level to avoid trapped water bubbles. Once the mould is filled to the desired height, the paper filter and the top cap are put in place, the membrane is unrolled and two O-rings are carefully placed. A negative pore water pressure of -5 kPa is imposed (commented below), so that the sample would not collapse before the confining pressure is applied, to allow dismantling of the mould. In case of dry samples, the exact same procedure is applied without water.

Compared to air entry value of sand (around 1 kPa, e.g. Fredlund & Xing 1994), the suction applied to the sample could involve a small desaturation. Indeed, small air bubbles trapped between the sample and the membrane could enter the porous medium. During this phase, no deformation was observed during the numerous tests performed, the water volume which exits the sample is small and we consider that the hydric hysteresis is negligible. The suction is removed after the application of a small confining pressure once the triaxial cell has been mounted inside the dynamic press. The saturation process, described below, ensures that all air bubbles are dissolved within the liquid phase before the major part of drained consolidation starts.

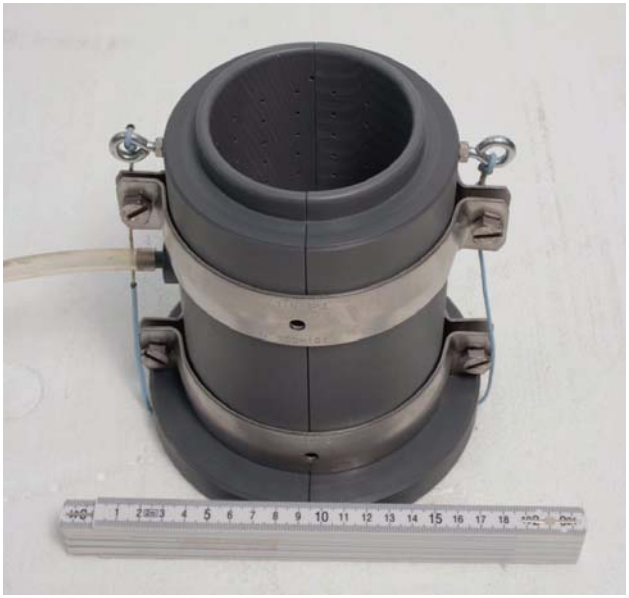

Fig. 3.29. Vacuum mould.

The upper part of the triaxial cell must be carefully put in place to avoid any disturbance of the sample. The friction of the vertical loading rod against the O-rings of the cell top generates unbearable shear of the sample. A special frame has been built to avoid the disturbance (Fig. 3.30); it holds the loading rod while the top of the cell is placed. This efficient process allows both a good vertical alignment of the rod and a minimal disturbance of the sample. The pore pressure of saturated sand samples typically increases of less than 1 kPa.

The accurate size of the sample is measured by complementary means. First the inner volume of the mould is known, given the membrane thickness; then outer measurements are performed with callipers. Moreover the exact weight of soil and the exact volume of water put inside the sample are known. The initial void ratio is thus calculated. This information is only indicative, as the void ratio actually taken into account for the characterization of cyclic loading is the final one, after consolidation and initial shear.

For dry sand samples, the same overall sample mounting procedure applies. The negative pore pressure of -5kPa is also used to help dismantling the mould, while the GDS cell is filled with air. In the following, the saturation process does not apply to dry samples, but the consolidation phase is similar. The final void ratio before cyclic loading is deduced from radius measurements with laser sensors.

Fig. 3.30. Mounting structure.

3.4.2 Saturation

Full saturation is required to perform constant-volume undrained tests. The back pressure technique is used in this study to ensure a saturated state. The Skempton's *B* coefficient was always higher than 0.95 in our tests. This value was reached for back pressure values of 300 or 400 kPa. For the purpose of allowing free decrease of the pore water pressure during monotonic tests, the back pressure is increased to 700 kPa. Even with this high value of back pressure, the *B* coefficient does not increase to 1, with an upper limit of 0.97. This result is consistent with observations (Head 1984) showing that stiff and very stiff materials, especially dense sand, do not allow *B* values of 1 at 100% saturation.

3.4.3 State of the sample for cyclic shear

Two means are available for measuring the final state of the sample before shearing, which is characterized by its void ratio. When the evolution of the sample radius is unknown (tests run without laser sensor system), the volume of water and sand only is used. It is assumed that no air bubbles remains thanks to the back pressure technique. As the height of the sample is always known, its radius is deduced from the sample volume. On the contrary, when the sample radius is available, the sample volume is calculated from the average radius and the height. Knowing the initial sand volume, the volume of voids and the void ratio are deduced.

3.5 Soil characteristics

Two types of soils were used in this study: a naturally deposited sand («Leman Sand») and a relatively uniform quartz sand («Fonderie sand»).

3.5.1 Leman Sand

Leman Sand is a grey sand dredged from the bottom of Lake Geneva (Switzerland) (Fig. 3.31). Its grain size distribution is given in Fig. 3.32. With an average uniformity coefficient of 3.1, this sand is classified as poorly-graded (Swiss standard SNV 670 008a). The slight natural variability of grain size distribution can be observed by comparing the ten depicted distributions. Since a good portion of the sand (8% by weight) consists of relatively large particles (from 2 to 4 mm in diameter), a sample diameter of 80 mm was used for all tests.

Leman Sand’s mineralogy consists of quartz (42%), Calcite (18%), Plagioclase (15%), K-Feldspar (11%), Micas (9%) and Chlorite (5%). The average specific weight is 2712.5 kg/m^3. The minimum

void ratio is 0.39, and the maximum void ratio is 0.64. When the confining pressure of 50 to 300 kPa is applied, the void ratio is around 0.46 for most tests, which corresponds to a relative density of 72%.

The permeability, averaged from eight tests, is $k = 5.9 \times 10^{-4}$ m/s.

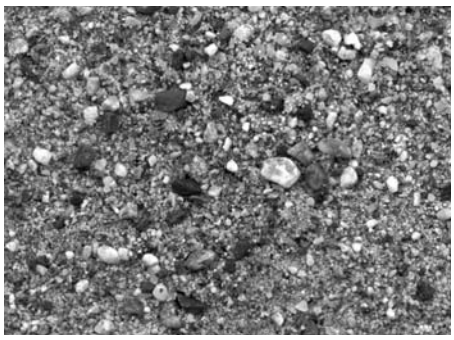

Fig. 3.31. Leman Sand.

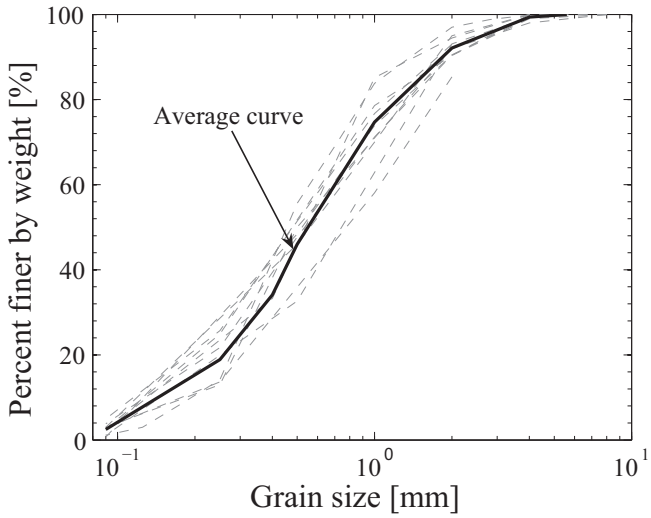

Fig. 3.32. Grain size distribution of Leman Sand.

3.5.2 Fonderie Sand

Fonderie Sand is a white sand made of quartz, with small amount of feldspar (Huot 1999). Its minimum void ratio is 0.53, and the maximum void ratio is 0.91 (Mayoraz 2002). The grain size distribution is narrow, as it was washed and sieved. The maximum size of the grains is 0.7 mm, with $d_{60} = 0.3$ mm. The grains are not susceptible to breakage. The specific weight is 2618 kg/m^3. The average permeability is 1.62×10^{-4} m/s.

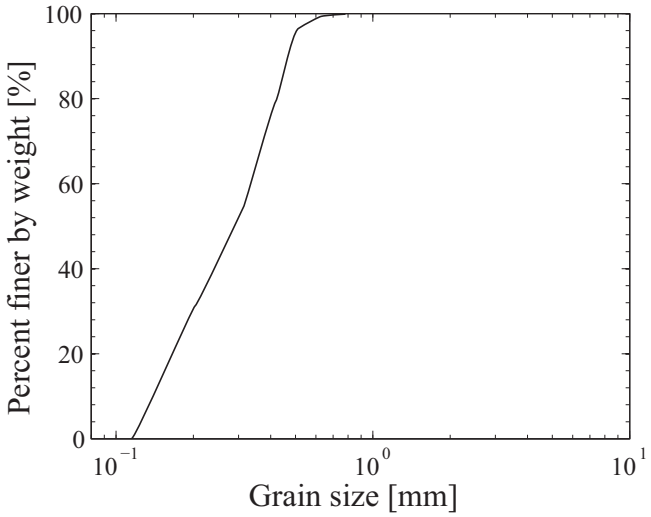

Fig. 3.33. Grain size distribution of Fonderie Sand.

3.6 Conclusions

Characterizing dynamic soil behaviour requires advanced laboratory equipments and complex procedures. The dynamic triaxial press used for the experimental tests developed for this PhD thesis allows to perform complex cyclic and seismic loadings, in conditions suitable for studying saturated and dry sand behaviour in the nonlinear regime (i.e. medium to large strains).

The laser sensors are capable of continuously measure local radial strains, at middle height of the sample, in various conditions of confining pressure and axial load, thanks to a very careful and complicated calibration procedure. The mounting frame also allows to perform vertical sample scanning. We showed that the usual value of 2/3, used to deduce mean radial strains of cylindrical samples deformed as barrels, is not suitable in the general case. That is why dry tests described in the following chapters were systematically scanned, and customized averaging parameters were used to calculate mean radial strains. The two other important issues, which must be considered during each drained test, are: (i) the laser sensors and the aluminium triaxial cell must be accurately positioned (ii) correct calibration parameters, which correspond to the actual distance between the glass and the laser sensors, must be used.

Other equipments were developed to ensure a good repeatability of the dynamic tests, mainly the sample mounting systems and the aluminium triaxial cell. Together with all described equipments, they

allowed to perform reliable triaxial tests in drained and undrained conditions. Moreover, it should be noticed that the use of all these devices is very complicated, requires full attention and precise gestures, and complete training of the user is necessary to understand the processes and implement the dynamic triaxial press.

CHAPTER 4

CHARACTERIZATION OF NONLINEAR SAND BEHAVIOUR WITH MONOTONIC AND CYCLIC TRIAXIAL TESTS

4.1 Introduction

Undrained saturated and dry monotonic and cyclic tests were performed with Leman and Fonderie Sand. In undrained tests, the dilative and contractive behaviour of the porous material appears as the evolution (increase or decrease) of the pore water pressure. The saturated undrained boundary condition leads to the assumption of a zero volumetric strain increment, thus relating the radial strain to the measured axial strain. In dry tests, the sample volume changes, and radial strains must be continuously measured by the laser system.

Cyclic loadings are stress-controlled with a constant cyclic deviatoric stress amplitude (Δq) applied to the sample. The total mean stress (p) is necessarily a positive value, but the deviatoric value (q) can be negative (triaxial extension) in the case of stress reversal loading paths.

Although non-conventional loading paths were studied using the dynamic press (see Chapter 6), only cyclic Conventional Triaxial Compression (CTC) and alternate cyclic Conventional Triaxial Compression and Reduced Triaxial Extension (CTC-RTE) test results are presented in this chapter. The Tab. 4.1 summarizes the characteristics of the monotonic tests, and Tab. 4.3, Tab. 4.4, Tab. 4.7 and Tab. 4.10 those of the cyclic tests.

After monotonic undrained tests on Leman Sand (section 4.2), preliminary cyclic tests (section 4.3) and undrained saturated cyclic tests (section 4.4) on Leman Sand are described. Then these results are compared with undrained tests on Fonderie Sand (section 4.5). Before presenting in details dry test results on Leman Sand (section 4.7), the validity of radial strain measurement with the lasers device is analysed with an undrained test (section 4.6): the soil response is computed with either laser-based measurement of ε_3 or with the assumption of no volumetric strain, and both results are compared. An analysis of the formation of the shear band at large strain amplitude (section 4.8) is finally presented, to evaluate the validity range of the test results.

For the sake of brevity, every test performed with the dynamic triaxial press is not described in detail within the thesis. Instead, examples illustrating their common features are presented, as well as figures which summarize several test results. Beyond the stress-strain relation and the stress path, the nonlinear cyclic behaviour of Leman and Fonderie Sand is summarized by (i) the development of excess pore pressure or volumetric strain, (ii) the secant shear modulus, (iii) the damping ratio. The material parameters of the two constitutive models (description in Chapter 2) are determined, from the tests presented here, in Chapter 7.

4.2 Monotonic tests on Leman Sand

4.2.1 Presentation

Quasi-static tests are first provided for Leman Sand. Such tests were also performed with the dynamic triaxial press, operated at low strain rate. By evaluating the soil response in standard loading conditions, a reference is provided for characterizing and modeling Leman Sand behaviour (e.g. Chapter 7). The term «monotonic» is used here as an opposition to the cyclic tests, although some of these tests include an unloading part and are not strictly monotonous.

The nine monotonic undrained strain-controlled tests were performed in triaxial compression or extension (Tab. 4.1). The void ratio is approximately the same for all tests, varying between 0.45 and 0.47, except for M1 and M2 tests (where higher void ratios were linked with problem in the measuring technique). These void ratios correspond to relative densities of 68% to 76%. The back pressure was first set to 300 kPa in the first tests, but this value was found to be not large enough to compensate the pore water pressure decrease due to dilative behaviour of the granular matrix. For this reason, the back pressure was then set to 700 kPa for tests M3, M4 and M7 to M9. The tests presented here were performed at «low speed», i.e. 0.01 to 0.03%/s.

Tab. 4.1. Monotonic tests on Leman Sand

N°	Test description	Date	Void ratio	$\sigma_3'^0$ [kPa]	Back pressure [kPa]	Strain rate [%/s]
M 1	Monotonic undrained compression	19/11/07	0.54	50	300	0.03
M 2	Monotonic undrained compression	22/11/07	0.52	150	300	0.03
M 3	Monotonic undrained compression	18/04/08	0.45	100	700	0.01
M 4	Monotonic undrained compression	07/05/08	0.46	100	700	0.03
M 5	Monotonic undrained extension	09/04/08	0.46	200	300	0.01
M 6	Monotonic undrained extension	10/04/08	0.47	100	400	0.01
M 7	Monotonic undrained extension	16/04/08	0.46	150	700	0.01
M 8	Monotonic undrained extension	09/05/08	0.47	150	700	0.03
M 9	Monotonic undrained extension	11/06/08	0.46	250	700	0.03

The initial confining pressure ($\sigma_3'^0$) varies between 50 kPa and 250 kPa. The loading history also plays a role in the soil response. When there is no failure, i.e. particularly in compression, unloading is performed in the opposite direction of deviatoric stress. The unloaded shearing, following either an extension or a compression virgin loading, is recorded and used for the calculation of the phase

transformation line and the large strain behaviour analysis. A schematic view of the response in compression and the definition of the phase transformation and steady state lines are depicted in Fig. 4.1.

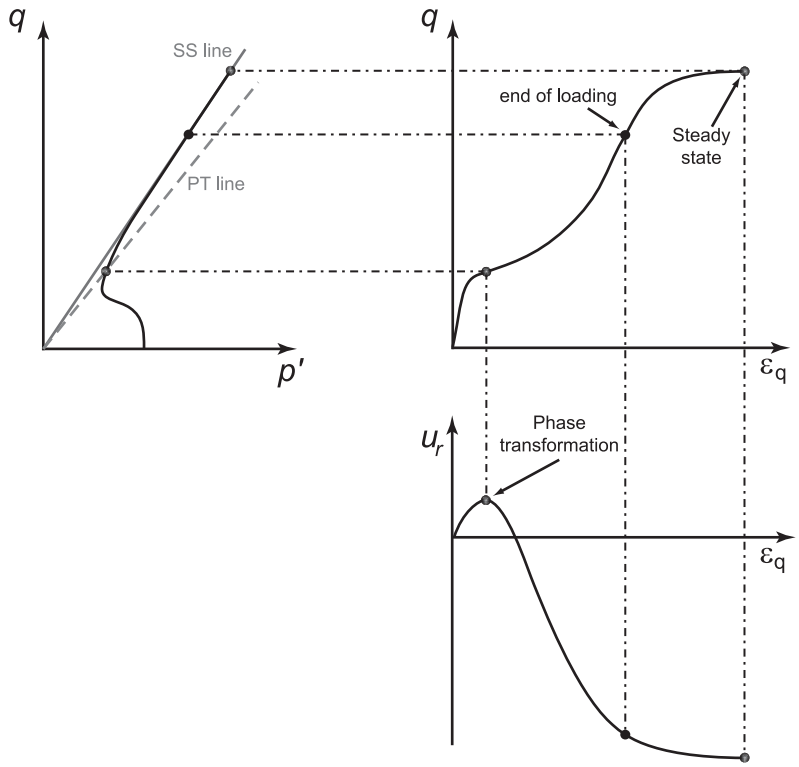

Fig. 4.1. Schematic view of the monotonic undrained dense sand behaviour in compression.

4.2.2 Description of typical test results in compression and extension

Two examples are presented now, one monotonic test in compression (M4) and another one in extension (M8).

In M4, triaxial compression is followed by an unloading which ends by a sudden failure in extension. Upon shearing by increase of the axial strain, the deviatoric stress (Fig. 4.2a) increases continuously until 1807 kPa, which is reached at ε_1 = 10.5%. There is no sign that steady state is obtained, because the plateau of deviatoric stress is not reached. The unloading is first an almost vertical linear relation in the compressive area (q > 0), and then a small quasi steady state peak appears at -67 kPa. After a plateau, the deviatoric stress decreases again, and reaches a minimum at -588 kPa for ε_1 = -1.6%, where a rapid increase arises. From visual observation, it is clear that a shear band forms at the moment of the peak of q. The shear band then disappears upon continuous shearing, while stiffness drops to be very small.

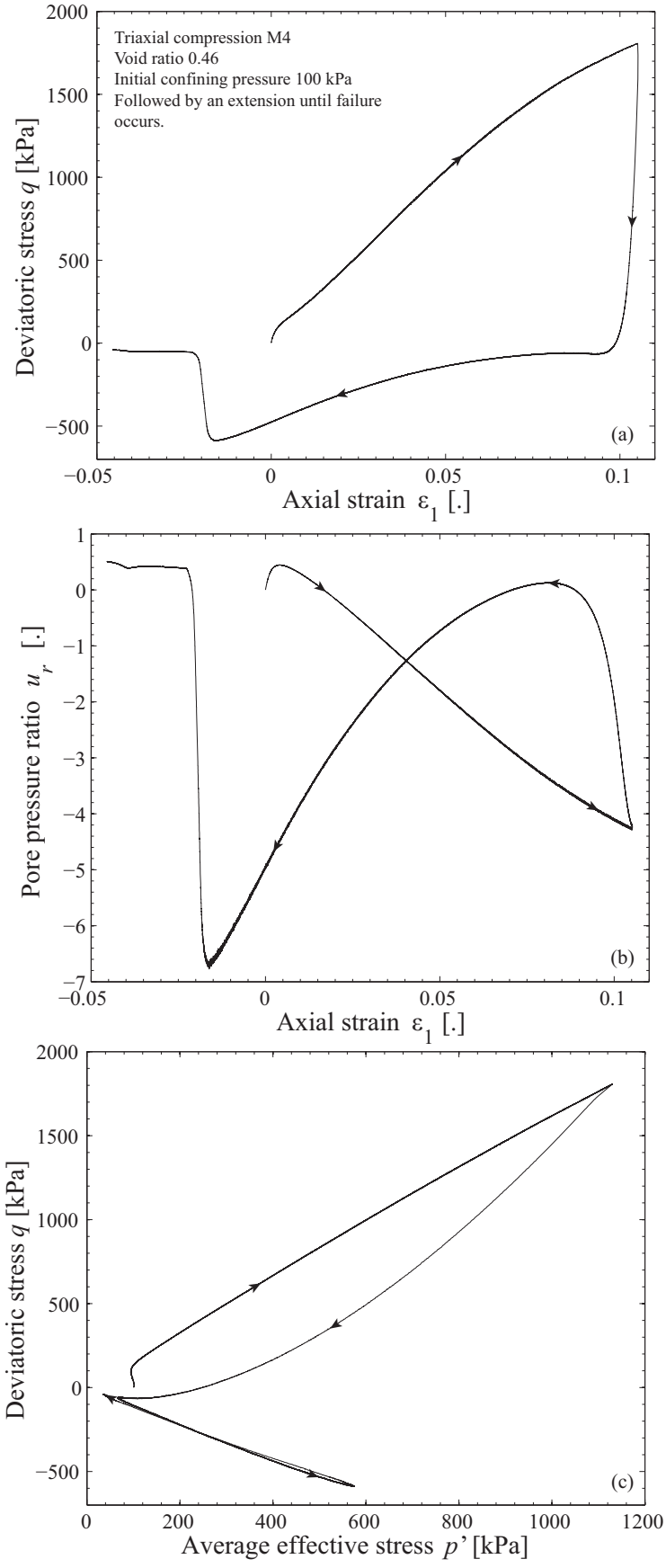

Fig. 4.2. Monotonic triaxial compression test, M4, on Leman Sand.

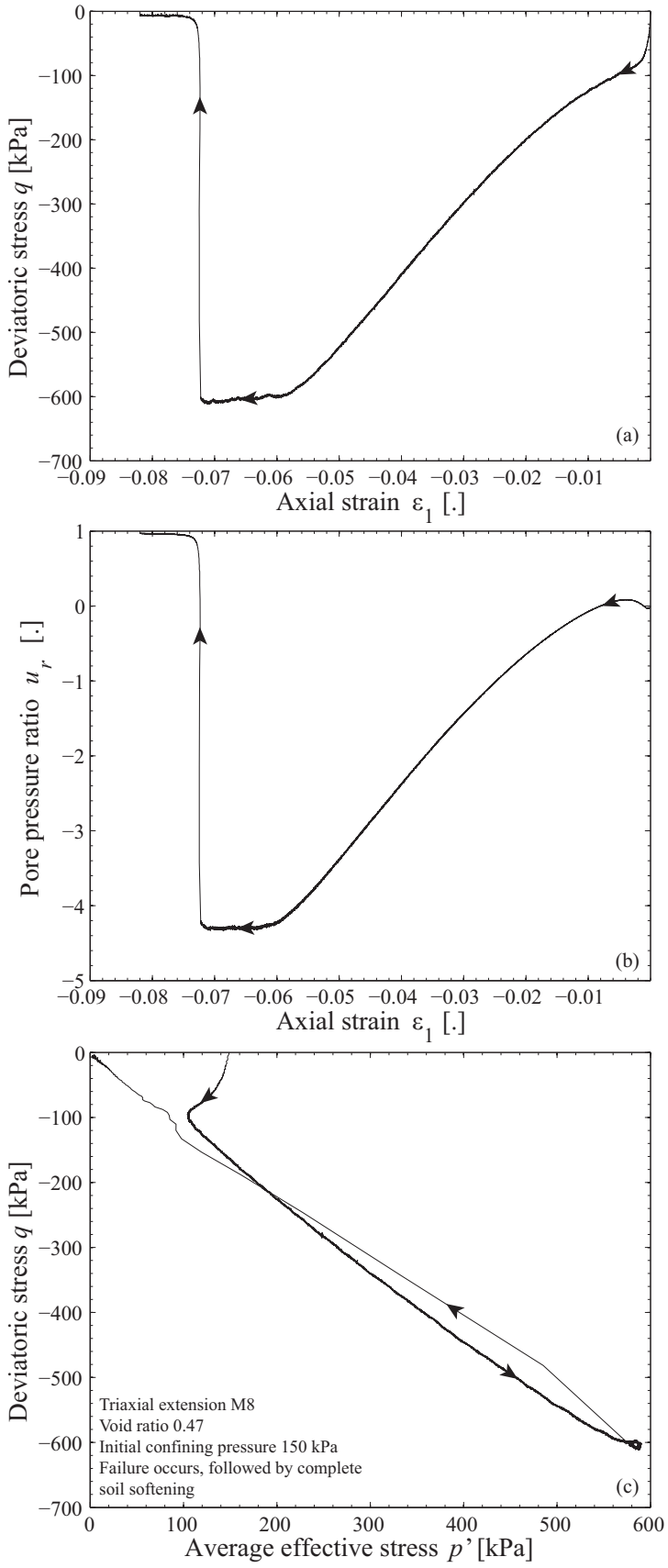

Fig. 4.3. Monotonic triaxial extension test, M8, on Leman Sand.

The pore pressure ratio (Fig. 4.2b) first increases, reaches a peak at u_r = 0.44 for ε_1 = 0.4%. Then the phase transformation line is reached and the pore pressure decrease is continuous until unloading, which arises for a local minimum u_r = -4.3. At unloading, the pore pressure ratio first increases, before decreasing again. The peak of pore pressure at unloading corresponds to the quasi-steady-state plateau in the stress-strain plane. The pore pressure ratio then decreases until a minimum of -6.7, at which failure occurs, and then suddenly increases.

The corresponding stress path (Fig. 4.2c) is typical of undrained triaxial compression loading of dense sand. At unloading, there is a strong increase of pore pressure before it decreases again. At failure, the stress path drops towards the origin of the stress plane.

For the undrained virgin loading in extension M8, the stress-strain relation (Fig. 4.3a), pore pressure ratio (Fig. 4.3b) and stress path (Fig. 4.3c) are very similar to the undrained loading in compression of M4, except that failure occurs in the same manner as the unloading from M4. After failure, the pore pressure ratio directly increases until u_r = 1 and the deviatoric stress is only -7 kPa.

4.2.3 Summary of observed monotonic behaviour of dense Leman Sand

The typical behaviour of undrained Leman Sand under monotonic loading shows that both extension and compression loading are first contractive, then strongly dilative. Moreover, when the specimen is not brought to failure during virgin loading, quasi-steady-state appears at unloading, both in compression and extension.

The comparison of the tests at different confining pressure shows that sand stiffness increases with the confining pressure, both in compression and extension (Fig. 4.4). At small and medium strain, stiffness is always smaller in extension than in compression, all other test parameters being otherwise equal. Finally, the main difference between monotonic extension and compression is the mode of failure with the formation of a shear band in extension.

4.2.4 Phase transformation lines

The effective stress paths of the virgin tests and the unloading tests, at all shearing speed values (including undrained monotonic tests at higher speed presented in Chapter 5), give a phase transformation line in compression and another one in extension (Fig. 4.5). The reference for the phase transformation points is the pore pressure peak. In the stress plane, the points are well aligned, and aligned with the origin, with R^2 coefficients of 0.98 and 1 in extension and compression respectively. The slopes of the phase transformation lines are different in compression and extension, with, respectively, M_{PTc} = 1.35 and M_{PTe} = 0.88. The equivalent mobilized friction angles are 33° and 31°.

The loading history has no influence on the phase transformation line, because the virgin loading points are on the same line as the unloading points.

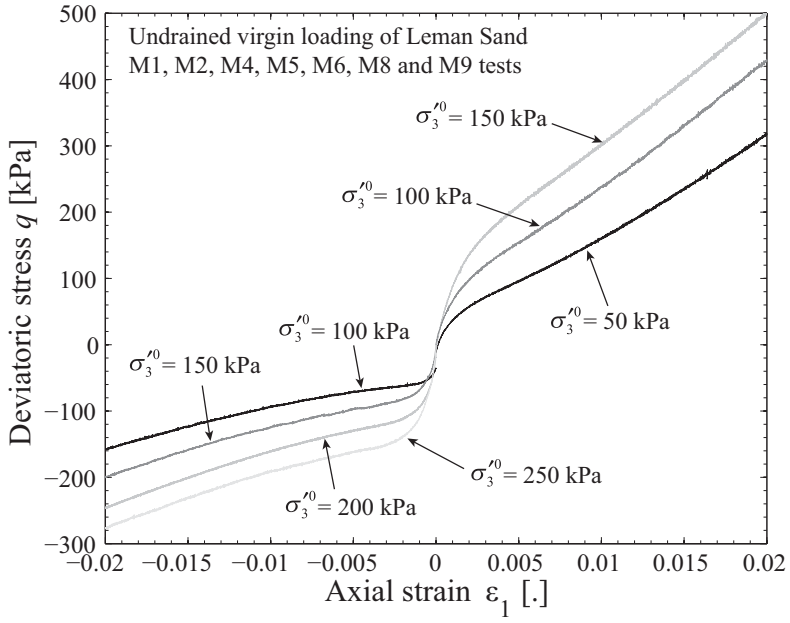

Fig. 4.4. Comparison of virgin loading stress - strain curves below 2% axial strain.

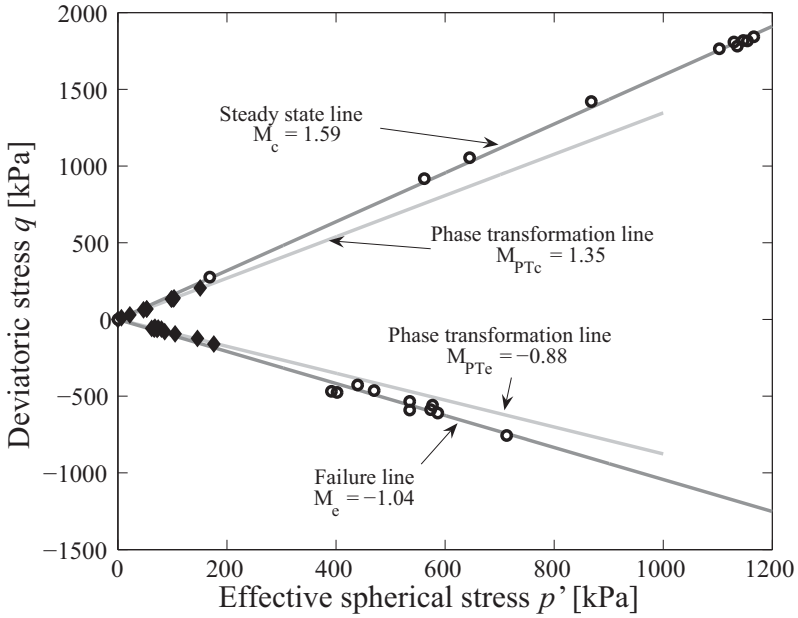

Fig. 4.5. Characteristic lines obtained in monotonic compression and extension for Leman Sand (tests M1 to M9 with also unloading points when they are available). Black diamond-shaped points represent PT points, and the circles are failure points in extension and SS points in compression.

4.2.5 Behaviour at large strain

The behaviour at large strain can be characterized by the peak of the stress-strain relation, or by the residual strength, which is also the stress at steady state or critical state. The steady state is not reached during the tests, because (i) in compression, the stiffness of the sample is so strong that the loading capacity is surpassed and (ii) in extension, shear bands appear thus creating heterogeneity in the sample. In compression, it is assumed that the stress-path envelop is on the steady state line, thanks to the behaviour depicted in Fig. 4.1. In extension, only the failure line can be obtained, which is not an intrinsic soil property.

In extension, the failure mechanism is clearly identified. The deviator stress peak occurs just before the pore pressure peak, and a shear band appears. When the axial strain is sufficiently large, the deviatoric stress tends to almost zero and the pore pressure ratio becomes equal to 1 after the peak. This complete softening is similar to liquefaction, although the stress path is not contractive. The shear band is no longer visible. In the p'- q plane, the loci of the extension peaks form a line passing through the origin, with a slope $M_e = 1.04$, a mobilized friction angle of 39° and a R^2 value of 0.98.

In compression, the maximum stress permitted by the equipment was reached at strains around 10%. The expected steady state plateau is not reached yet in the ε_1 - q plane. However in the p' - q plane, all the lines follow exactly the same stress path at large strain, which is assumed to be the steady state line of slope M_c (cf. Fig. 4.1). The points ending each compressional loading form a straight line passing through the origin, with a slope $M_c = 1.59$, a mobilized friction angle of 39° and R^2 value of 1.

These two slopes, in compression and extension, characterizing large strains in the p' - q plane, are independent from loading history and initial confining pressure; they are limited to void ratio values of 0.45 to 0.47. The mobilized friction angles are the same in compression and extension, at SS and failure respectively.

4.2.6 Comments and conclusions on the monotonic results

While the tested material is a natural sand, and the content of the samples can slightly vary, the phase transformation line and the stress path at large strains, obtained by linear regression, fit all the tests, regardless of test loading history or initial confining pressure. The mobilized friction angle at steady state is 39° in compression. The failure line in extension also corresponds to a peak friction angle of 39°.

The phase transformation lines in compression and extension are 33.3° and 31° respectively. Vaid et al. (1990) and Ibsen (1994) mention that PT lines and SS lines are the same in compression and extension, and for all loading history, even for anisotropic samples. However, De Gennaro et al. (2004) find two

different values, with Hostun sand, in compression (30°) and in extension (23°). The soil anisotropy caused by the deposition method is claimed to be responsible for the difference between compression and extension loadings. Also because of anisotropy, Hostun sand is stiffer in the vertical direction than in the horizontal direction. For the Leman Sand as well, the stiffness is higher in compression than in extension.

The characteristic PT and SS angles determined for Leman Sand are summarized in Tab. 4.2. They are used in Chapter 7, as material parameters for the Hujeux elastoplastic model.

Tab. 4.2. PT and SS characteristics of Leman Sand

	M_{PT} [.]	M_{SS} [.]	ϕ_{PT} [°]	ϕ_{SS} [°]
Compression	1.35	1.59	33.3	39
Extension	0.88	*(1.04)**	31	*(39)**

* The value given for the steady state in extension is rather a failure angle than a steady state angle.

4.3 Preliminary undrained cyclic triaxial tests

4.3.1 Introduction

The effect of confining pressure, strain or stress amplitude and average deviatoric stress are compared using four tests in stress-controlled mode and one test in strain-controlled conditions. The void ratio is in the same range as all other tests with Leman Sand (between 0.45 and 0.48). The frequency of all tests is 0.8 Hz.

These tests allowed to get an overview on the stress-strain response and pore pressure increase of saturated undrained Leman Sand. It should however be noticed that, because of an imperfect sample mounting procedure, full saturation is not reached, with a *B* coefficient varying between 0.6 and 0.9. The results can be biased by the different saturation index, they are thus only indicative of cyclic sand behaviour.

Tab. 4.3. Preliminary cyclic tests on Leman Sand

N°	Test description	Date	Void ratio	$\sigma_3'^0$ [kPa]	q_{av} [kPa]	Amplitude	B coefficient
PC 1	Cyclic undrained stress-controlled CTC and CTC-RTE	30/05/07	0.48	209	185	100 kPa 200 kPa 300 kPa	0.63
PC 2	Cyclic undrained stress-controlled CTC	31/05/07	0.47	207	390	100 kPa 200 kPa 300 kPa	0.75
PC 3	Cyclic undrained stress-controlled CTC and CTC-RTE	23/05/07	0.48	407	175	100 kPa 200 kPa 300 kPa	0.84
PC 4	Cyclic undrained stress-controlled CTC	24/05/07	0.47	406	380	100 kPa 200 kPa 300 kPa	0.86
PC 5	Cyclic undrained strain-controlled CTC and CTC-RTE	02/05/07	0.45	207	0	0.01% 0.1% 1%	0.77

4.3.2 Typical stress-controlled test results

Each test is performed at three amplitudes only, even if failure does not occur. Actually cyclic liquefaction arises only during PC1 and PC5, at the last amplitude level. The other tests exhibit a stable behaviour with accommodation process.

The test PC3 is described in details now (Fig. 4.6). Undrained sinusoidal cycles on Leman Sand are performed with constant deviatoric stress amplitudes (Fig. 4.6a). The cyclic deviatoric stress amplitude starts at Δq = 100 kPa for 25 cycles. Then the pore-water pressure is released, and 25 more cycles are performed at 200 kPa stress amplitude. This process is repeated in a third step, with a final amplitude of 300 kPa. The cyclic stress ratio (CSR, defined in Eq. 2.20) of each step is indicated in Fig. 4.6a for test PC3.

The mechanical response of the sample is primarily a cyclic deviatoric strain in phase with the stress loading (Fig. 4.6b). The deviatoric strain amplitude clearly increases when Δq increases at each step. Moreover, the strain cycles are not symmetric towards the axis ε_q = 0 and they regularly shift towards larger strains. In the same way, the pore pressure ratio amplitude regularly increases with the number of cycles (Fig. 4.6c).

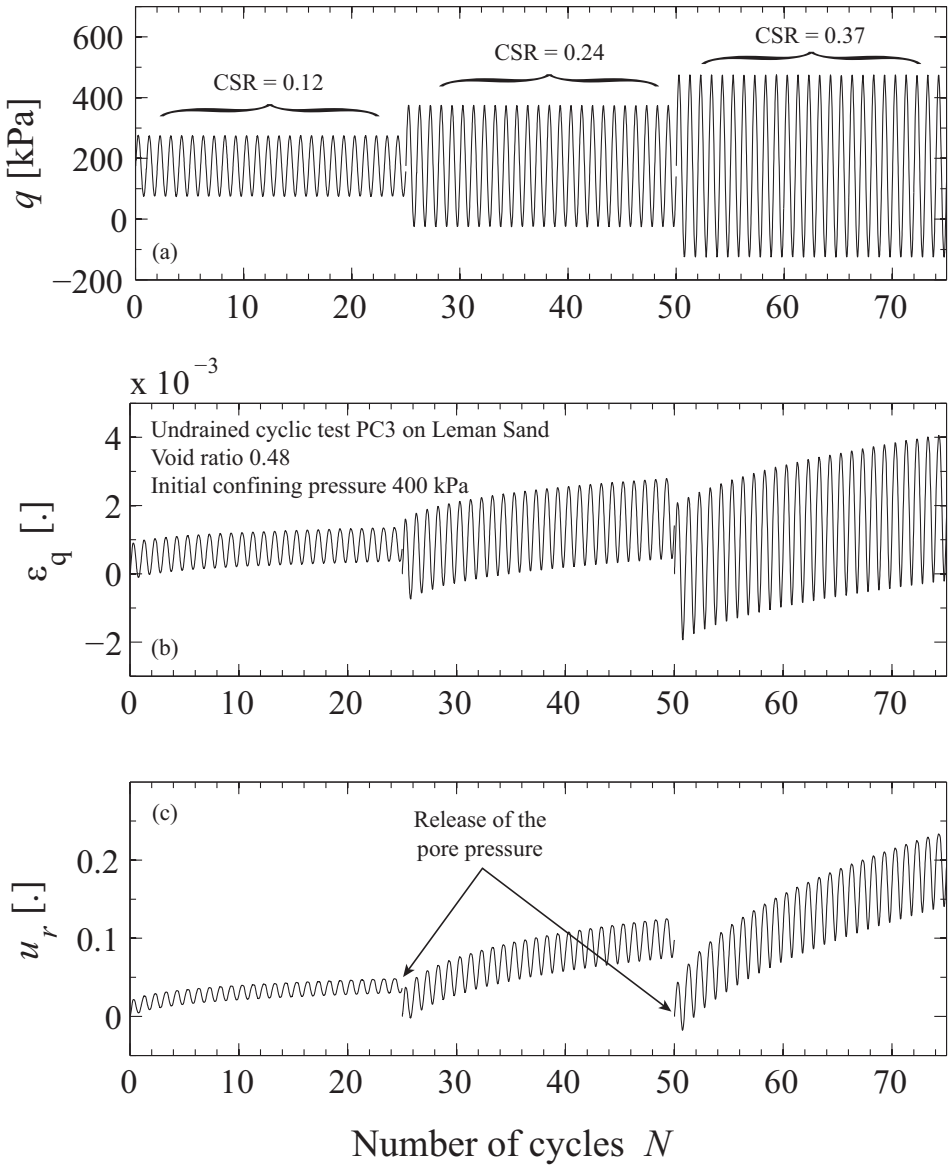

Fig. 4.6. Undrained cyclic loading, PC3 test on Leman Sand.

Cyclic soil behaviour is presented with hysteretic stress-strain loops in the ε_q - q plane. As an example, the loops of the third step are shown in Fig. 4.7. Plastic strain accumulates as the loops move towards positive strains. The shape of the loops remains the same, even after 25 cycles.

In the p' - q plane (Fig. 4.8), the stress path starts with a clear slope, close to the value 3, which is usually more representative of drained stress paths than undrained stress paths (which should start with vertical lines). This is an indication that the saturation of the sample might not be sufficient. Indeed, the fluid phase composed of air and water could be sufficiently compressible to allow partially drained behaviour. The stress path moves towards lower average stress p' while the pore pressure gradually increases. In the ε_q - u_r plane (Fig. 4.9), the accumulation of pore pressure ratio is clearly visible.

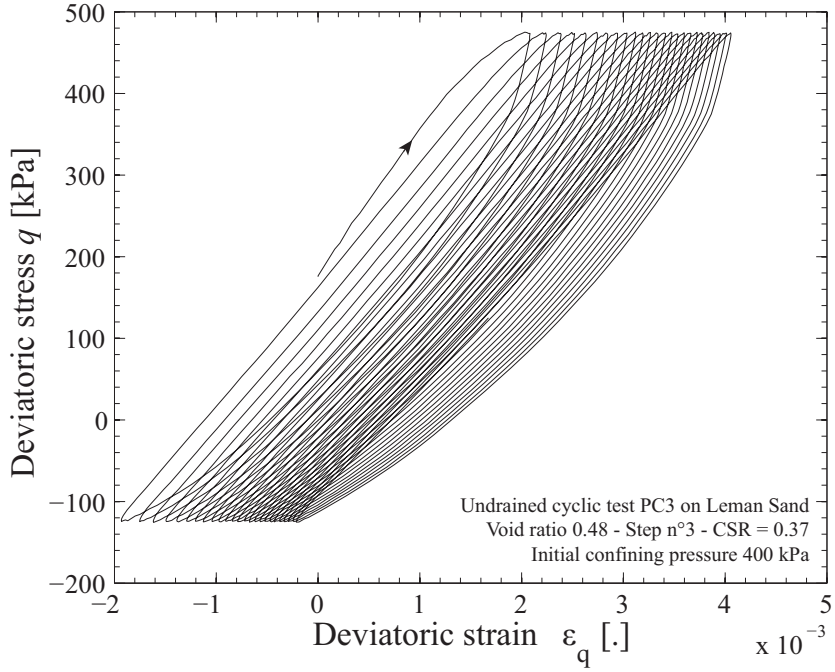

Fig. 4.7. Cyclic stress-strain relation, test PC3, step n°3.

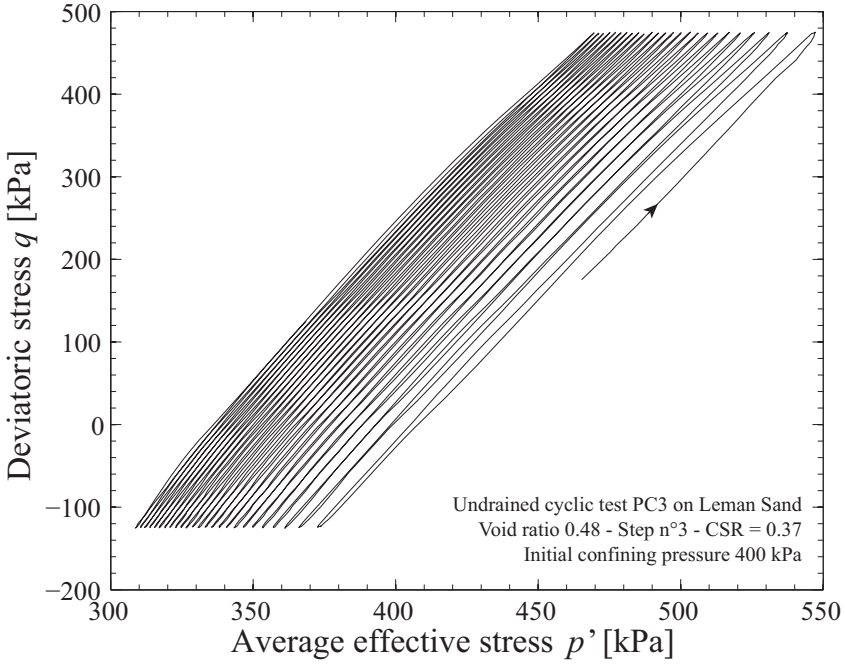

Fig. 4.8. Cyclic stress-path, test PC3, step n°3.

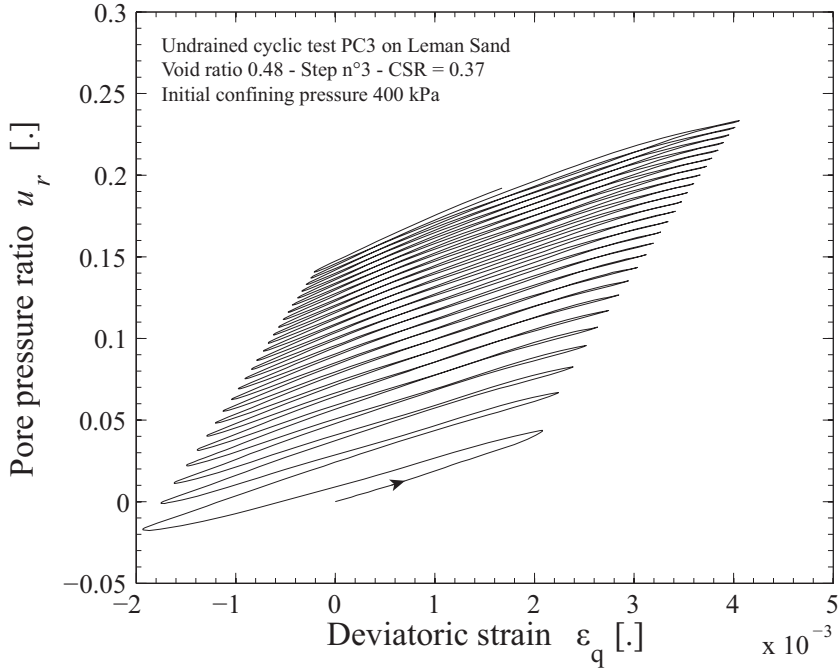

Fig. 4.9. Cyclic relation between the pore pressure and the deviatoric strain, test PC3, step n°3.

4.3.3 Effect of loading conditions

The comparison of the four stress-controlled tests and the strain-controlled test at different confining pressures and average deviatoric stresses is developed below. The test characteristics and parameters are depicted as a function of the number of cycles.

4.3.3.1 On the deviatoric strain amplitude

During most steps of the different tests, the deviatoric strain amplitude ($\Delta\varepsilon_q$) remains constant on a plateau (Fig. 4.10), at different level depending on the average deviatoric stress (q_{av}) or the initial confining pressure ($\sigma_3'^0$). A noticeable exception is the third step of PC1 which undergoes a gradual increase of $\Delta\varepsilon_q$. This increase of $\Delta\varepsilon_q$, which corresponds to strain softening (defined in section 2.4), is also called stiffness degradation, because it is associated with a decrease of the secant shear modulus. For the other stress-controlled tests with a constant strain amplitude, the absence of evolution of $\Delta\varepsilon_q$ means that the strain amplitude is below the threshold volumetric cyclic shear strain (defined in section 2.4).

Comparing two tests in different conditions but at the same stress amplitude Δq, the deviatoric strain amplitude $\Delta\varepsilon_q$ is lower for higher values of either q_{av} or $\sigma_3'^0$. An exception to that remark is for q_{av} = 400 kPa, where there is almost no difference between PC2 and PC4 though the confining pressure is doubled, i.e. the CSR is divided by two. The comparison of PC2 and PC4 behaviour is explained below in section 4.3.3.2.

Finally, the strain-controlled test PC5 logically exhibits constant deviatoric strain amplitudes.

4.3.3.2 On the pore pressure ratio

The pore pressure cyclically evolves in phase with the sine loading. The evolution of the pore pressure, i.e. its rate of increase, can be best viewed by selecting only the maximum value reached during each cycle, as shown in Fig. 4.11.

The pore pressure build-up is regular for all tests, with different rates depending on test conditions and stress amplitude. As shown in the literature review (Dobry et al. 1982), excess pore pressure increase is mainly controlled by the deviatoric strain amplitude. The effect of q_{av} and $\sigma_3'^0$ on the pore pressure increase is best viewed with the third step for cycles number 51 to 76 (Fig. 4.11). The increase of q_{av} clearly limits pore pressure build-up. However, the effect of $\sigma_3'^0$, in tests PC2 and PC4, does not follow the expected trend: as the confining pressure is higher in test PC4, its pore pressure increase should be lower than PC2. On the contrary, u_r is clearly higher in PC4. This unexpected effect may be due to the difference of saturation of the two tests: as PC2 has a lower *B* coefficient, it is less saturated and the pore fluid is more compressible, giving lower pore pressure increase. This also explains why the deviatoric strain amplitudes of PC2 and PC4 seem independent of the CSR.

For the strain-controlled test PC5, the rate of pore pressure increase is higher than PC1 at the second step, though it is clear in Fig. 4.10 that their deviatoric strain amplitude is approximately the same. Again, the lower saturation of PC1 compared to PC5 can explain the difference of pore pressure build-up.

4.3.3.3 On the secant shear modulus

The secant shear modulus G_{sec} calculated for each cycle is given in Fig. 4.12. G_{sec} clearly decreases when the stress amplitude increases, i.e. at cycles n° 26 and 51. In the same way as $\Delta\varepsilon_q$, the secant shear modulus remains constant for most steps. Limited stiffness hardening can happen at the beginning of tests PC3 or PC5, as well as strain softening for the last step of PC1, PC3 and PC5. The values of G_{sec} range from 2 MPa to 130 MPa. For stress-controlled conditions, they decrease when (i) the deviatoric stress amplitude increases (ii) the confining pressure decreases and (iii) the average deviatoric stress decreases.

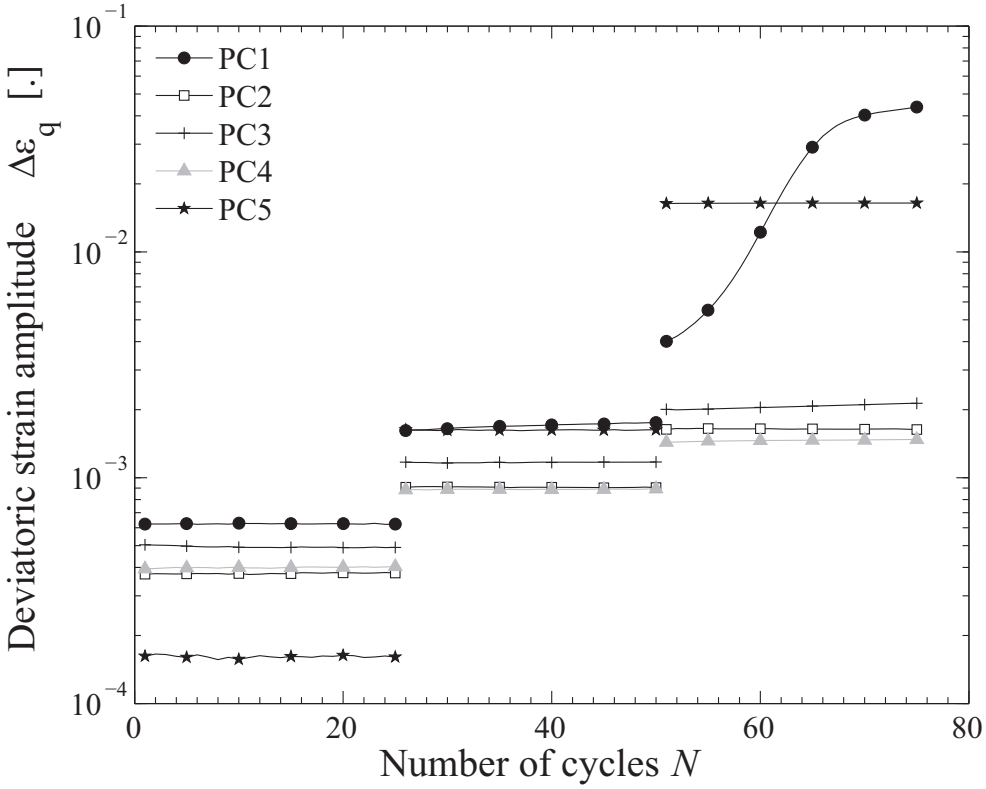

Fig. 4.10. Deviatoric strain amplitude vs. number of cycles for tests PC1 to PC5.

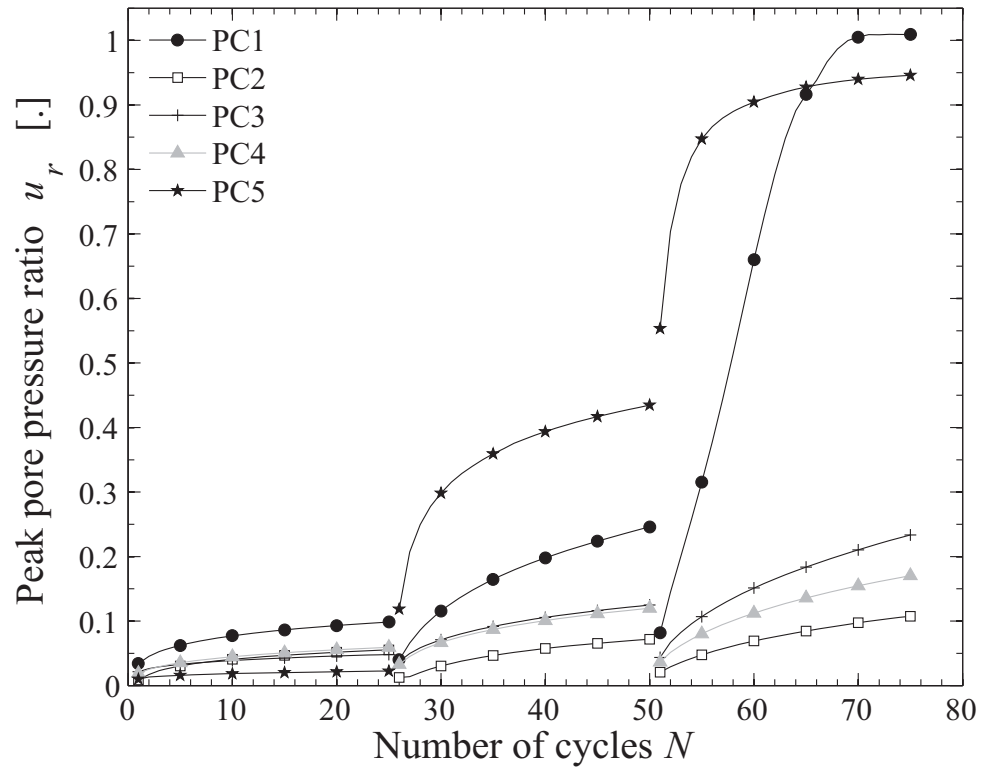

Fig. 4.11. Peak pore pressure ratio vs. number of cycles for tests PC1 to PC5.

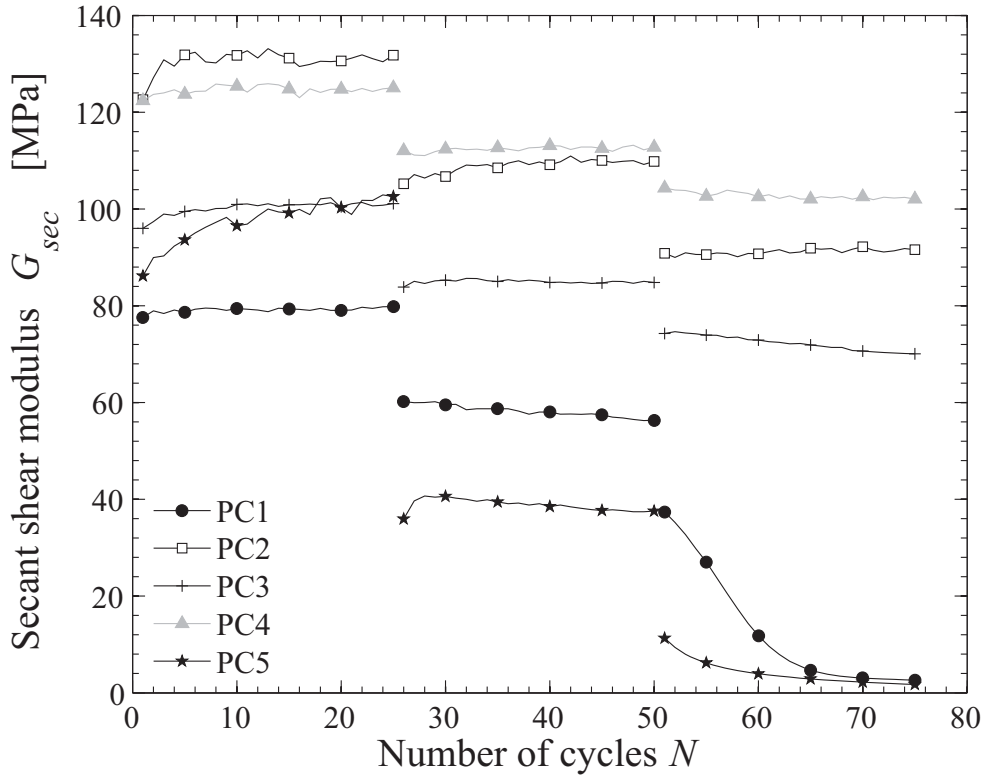

Fig. 4.12. Secant shear modulus vs. number of cycles for tests PC1 to PC5.

4.3.4 Conclusions

The preliminary cyclic experiments presented here demonstrate the possibilities of the device to produce good quality results in both stress-controlled and strain-controlled mode. It also demonstrates that full saturation must be reached to get meaningful conclusions on the evolution of the pore pressure ratio. Because of unsaturation, these results are not completely reliable and the stiffness degradation curves G - γ and D - γ are not proposed for the preliminary tests. Another lesson is that the number of steps can be increased, in order to reach failure for each test. The boundary conditions have considerable impact on the results, in particular high average deviatoric stress increases the stiffness as much as the initial confining pressure. The non-linearity is limited for these preliminary tests, it is thus later decided to decrease the average deviatoric stress and the range of confining pressure for the following undrained cyclic tests.

4.4 Detailed description of cyclic undrained tests on Leman Sand for small to large strains

4.4.1 Introduction

Cyclic CTC-RTE tests were performed under undrained conditions, in stress-controlled mode. The aim of these tests is to characterize the nonlinear behaviour of Leman Sand, with an emphasize on loading conditions such as confining pressure or average deviatoric stress. The nonlinear behaviour is shown to mainly depend on strain amplitude. Cyclic liquefaction develops at high strains, and the threshold definition of failure is analysed. Moreover, the analyses of the evolution of dynamic parameters provides insight into stiffness degradation.

Tab. 4.4 summarizes the characteristics of the cyclic stress-controlled tests with stress reversal. The deviatoric stress amplitude increases by step every 25 cycles (tests CYC1 to CYC4). Except for CYC4, the cyclic deviatoric stress amplitude starts at 40 kPa for 25 cycles. Then the pore-water pressure is released, and 25 more cycles are performed at 70 kPa stress amplitude. This process is repeated, with an increase of 30 kPa of the deviatoric stress at each step, until clear signs of failure, which are defined later, are spotted.

Tab. 4.4. Summary of cyclic CTC-RTE tests on Leman Sand*

N°	Test description	Date	Void ratio	$\sigma_3'^0$ [kPa]	q_{av} [kPa]	Δq [kPa]
CYC1	Cyclic undrained stress-controlled CTC-RTE	13/02/08	0.45-0.47	200	0	40, 70, 100, 130, 160.
CYC2	Cyclic undrained stress-controlled CTC-RTE	14/02/08	0.45-0.47	100	0	40, 70, 100.
CYC3	Cyclic undrained stress-controlled CTC-RTE	15/02/08	0.45-0.47	100	100	40, 70, 100, 130, 160, 190.
CYC4	Cyclic undrained stress-controlled CTC-RTE	03/04/09	0.49	100	0	10, 12, 14, 16, 18, 20, 22, 24, 26, 28, 30.

(*) *B* coefficient is higher than 0.95 for all tests. The loading frequency is f = 1 Hz. Sampling frequency of CYC4 is 312 Hz, and 100 Hz for the three other tests.

The test CYC4 is designed differently, in the sense that it is performed in the small to medium strain regime. The amplitude Δq is increased by small steps of 2 kPa around 15 to 30 kPa. As the accuracy of the displacement and force sensors are not optimum in this range of loading, the values of damping ratio of CYC4 are not taken into account for results analyses. Indeed, there is a log scale difference between accurate measurements of G_{sec} and accurate measurements of D. While it is considered that G_{sec} values are valid from around $\Delta\varepsilon_q = 5 \times 10^{-5}$, it is only from $\Delta\varepsilon_q = 5 \times 10^{-4}$ that damping is

satisfactorily measured.

As the pore water pressure is released before the beginning of each step (every 25 cycles), each step is considered to be a virgin loading that is comparable to the other ones. It is acknowledged that the response of the soil will not correspond to a true virgin loading, and that the soil memory cannot be erased by drainage. However, (i) the increase of 30 kPa in the stress amplitude is sufficient to induce major irreversible behaviour, and (ii) the comparison of the tests CYC1 to CYC3, which follow the same loading history, is still relevant. For the sake of clarity of the figures and explanations, the number of cycles is not reset to zero at the beginning of each step. However, a clear discontinuity appears in the figures every 25 cycles, pointing the shift to a stronger loading.

4.4.2 Example of a cyclic test with failure by cyclic liquefaction

Typical cyclic test results are first presented using the test CYC2. The stress-strain relation (Fig. 4.13), stress path (Fig. 4.14) and evolution of the pore water pressure (Fig. 4.15) are displayed. The phase transformation line (PT line) and steady state line (SS line), which had been obtained for the Leman Sand with monotonic tests under the same experimental conditions, are plotted on the stress path for comparison.

The first step is similar to preliminary tests with accommodation (section 4.3). For the second and third steps, the shape of the stress-strain relation is representative of cyclic liquefaction in stress-controlled triaxial tests (e.g. Benahmed 2001), it is elongated in the middle with pointed ends. The elongated part corresponds to points of very low effective stress, when p' is close to zero because of the increase of the pore pressure. At that moment, deviatoric strains can dramatically increase. Then the sample regains some stiffness when the pore pressure increases, which results in pointed ends. For the second and the third step, the deviatoric strain amplitude is not symmetric towards $\varepsilon_q = 0$, but shifted towards the extension side.

The shape of the stress path as well corresponds to the familiar representation of cyclic liquefaction, except that the «wings» are clearly not symmetric towards the axis $q = 0$. Indeed, the loop is larger and longer on the extension side ($q < 0$) than the compression side ($q > 0$). For the extension side in particular, it is clear that the loop is centred on the monotonic phase transformation line. Moreover, the stress paths leave the consolidation line almost vertically, which is consistent with the fact that saturation of the samples is much better than for the preliminary tests.

The increase of the pore pressure ratio is regular, with stronger amplitudes when Δq increases. Pore pressure spikes appear at the 30^{th} cycle, which means that the phase transformation line is first crossed during this cycle. The threshold $u_r = 1$ is first reached during the 44^{th} cycle. During the third step, it is noticeable that the pore pressure ratio amplitude is high, with a minimum value $u_r = -0.26$.

To conclude, this mode of failure of the saturated undrained sand sample results in strong deformations, with a total strain below -15% in extension. However, the final values are not taken into account, as it is noticed that shear bands occur for this range of deviatoric strains (section 4.8).

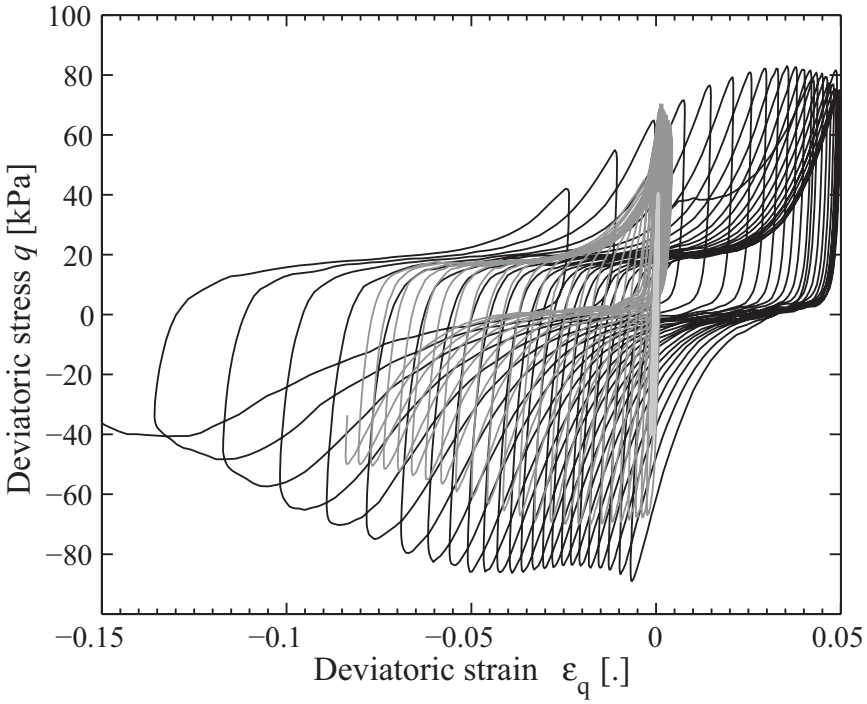

Fig. 4.13. Leman Sand stress - strain relation of a typical cyclic test with stress reversal (CYC2).

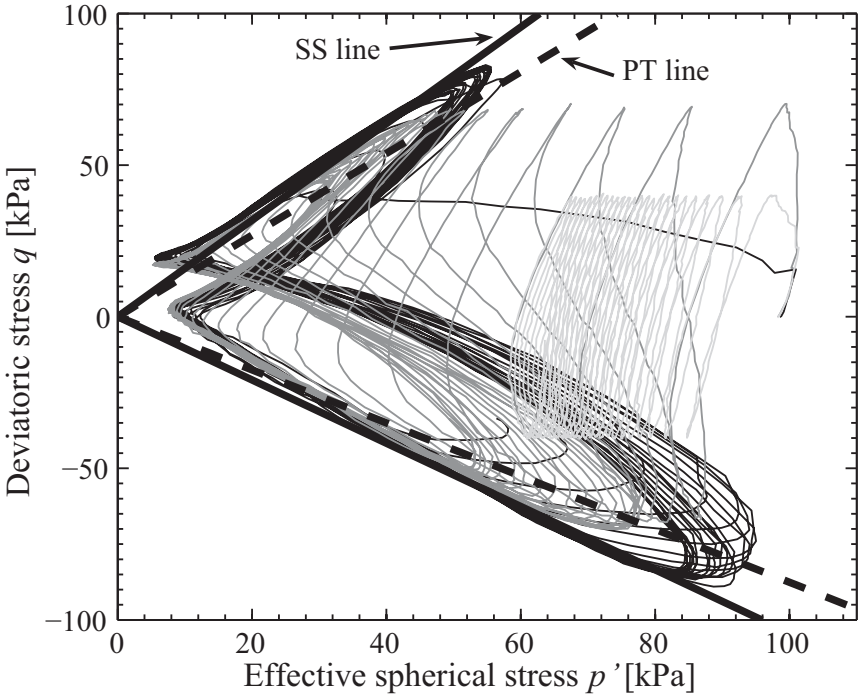

Fig. 4.14. Leman Sand stress path of a cyclic test with stress reversal (CYC2).

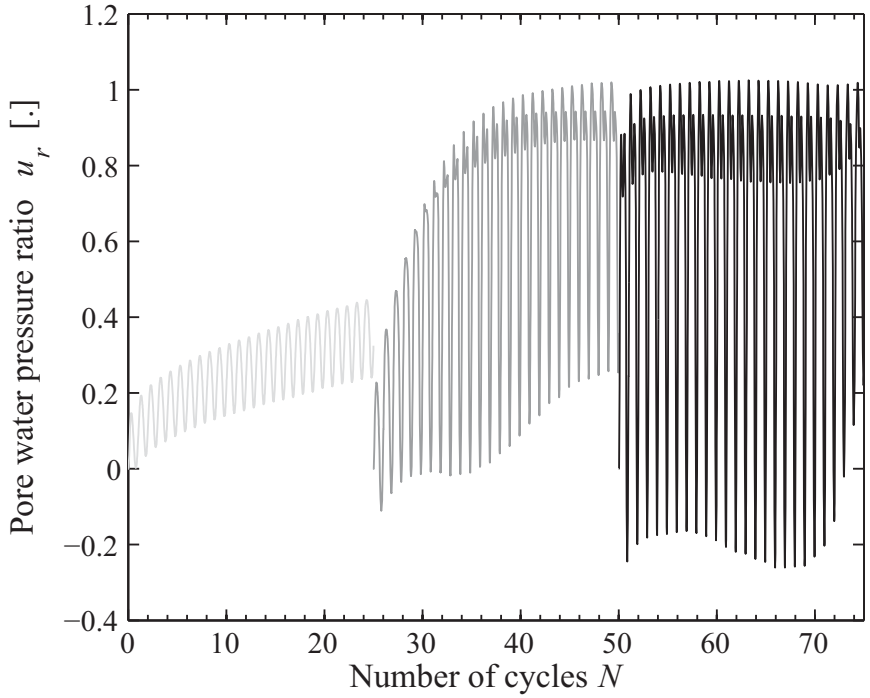

Fig. 4.15. Leman Sand progressive increase of the pore water pressure ratio (CYC2 test).

4.4.3 Excess pore pressure increase

The increase of the pore pressure as a function of the deviatoric strain amplitude is displayed in Fig. 4.16 for the four tests. The pore pressure increase starts from the threshold $\Delta\varepsilon_q = 10^{-4}$ for CYC4. This is thus the approximate value of the volumetric cyclic threshold shear strain under these loading conditions.

Above that threshold, the cluster of curves seems to be bounded within a narrow area. The lower boundary of this area corresponds to the first cycles of each loading step $N = 1$, while the upper boundary is made of the last points of each step $N = 25$. Otherwise, it seems that conditions of initial stress do not influence the pore pressure increase. It is rather the level of deviatoric strain amplitude which controls the rate of pore pressure ratio increase, as expected from the literature review (in particular Dobry et al. 1982).

4.4.4 Comparison of criterion for failure

Three tests, CYC1, CYC2 and CYC3, were chosen to illustrate the softening that occurs in granular soils during cyclic loading with stress reversal. The term softening refers to a decrease in stiffness, accompanied by an increase in the deviatoric strain amplitude. This process, which is known to occur above a given threshold shear strain (Vucetic 1994), is the basis for the development of cyclic liquefaction in granular soils. The mechanical behaviour observed during our cyclic tests is

characterized by the progressiveness of the failure. «Failure» is, consequently, not an obvious concept. The criterion chosen that defines failure is expressed in terms of a deviatoric strain amplitude threshold of 2.5%, which corresponds to the 5% failure limit by Ishihara (1996) (cf. Chapter 2). At such an amplitude, the secant shear modulus is much lower than its initial value, and the pore water pressure ratio has increased to a level close to unity. This corresponds to stress paths with a «wing» shape and stress-strain relations with «banana» shapes described in section 4.4.2.

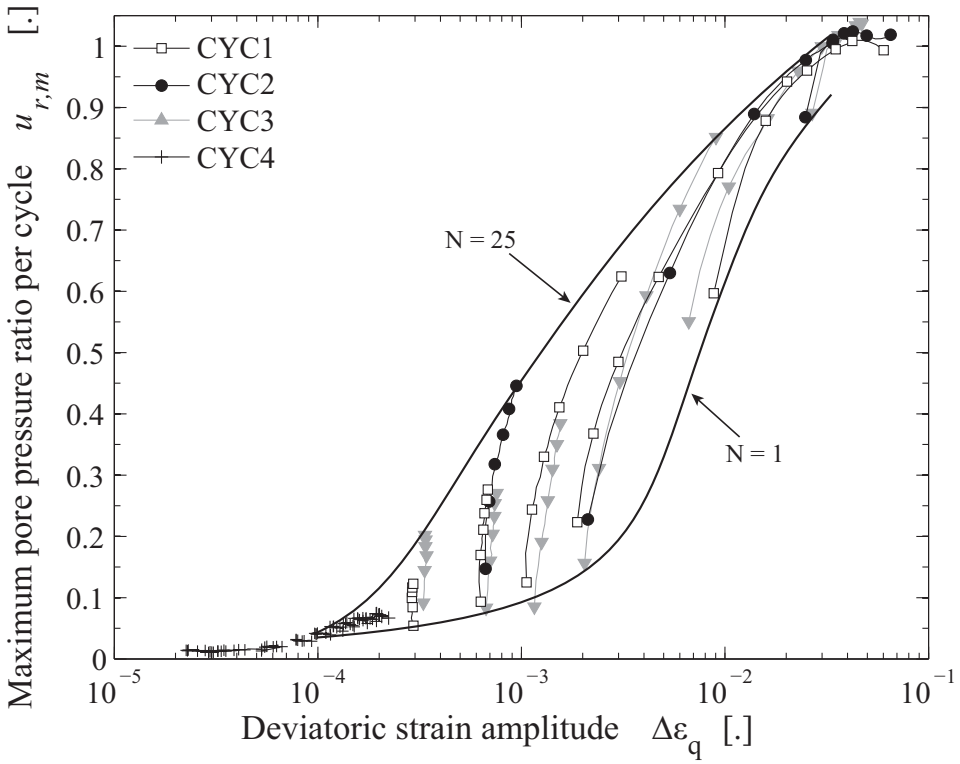

Fig. 4.16. Leman Sand pore pressure increase vs. deviatoric strain amplitude

Failure appears as a result of several occurrences. Strain amplitude, pore-pressure ratio and softening are, of course, interrelated. The above-mentioned strain amplitude based criterion is not the only possible approach. The first alternative relies on a threshold pore-pressure ratio of u_r = 1 (e.g. Seed 1979, see Chapter 2). The second is related to softening, which is characterized by the decrease of the secant shear modulus with the number of cycles. This evolution is quantified by the degradation index *DI*, the ratio between the secant shear modulus at the N^{th} cycle and the secant shear modulus at the first cycle.

The different failure criteria are compared in Tab. 4.5. The evolution of the deviatoric strain amplitude $\Delta\varepsilon_q$ with the number of cycles is displayed in Fig. 4.17. The number of cycles at which threshold deviatoric strain amplitude is exceeded, N^f, are summarized in Tab. 4.5 together with the values defined by the two alternative criteria.

The pattern of the pore-pressure ratio increase is given in Fig. 4.18. The number of cycles at $u_r = 1$, N^{fu}, is slightly higher than N^f. Its values are nonetheless meaningful, because they fit very well ($R^2 = 0.99$) with N^f. The criterion based on a threshold pore-pressure ratio is a good alternative to the one chosen here, at least for this natural sand and similar stress paths including stress reversal.

Soil softening is very clear from the 26th cycle for tests CYC1 and CYC3, and from the 1st cycle for CYC2 (Fig. 4.19). The values of *DI* at N^f are perfectly aligned at the failure limit; its equation is given in Fig. 4.19. The softening process, which is well represented by the degradation index, is a clear sign of the development of large strains in soils. In this case, the threshold value is *DI* = 0.05, corresponding approximately to $\Delta\varepsilon_q = 2.5\%$.

Tab. 4.5. Comparison of failure criterion

N°	N^f	$u_{r,m}$ at N^f	N^{fu}	*DI* at N^f	N^{fd}
CYC1	110	0.96	117	0.048	110
CYC2	41	0.99	44	0.036	39
CYC3	117	0.98	121	0.049	117

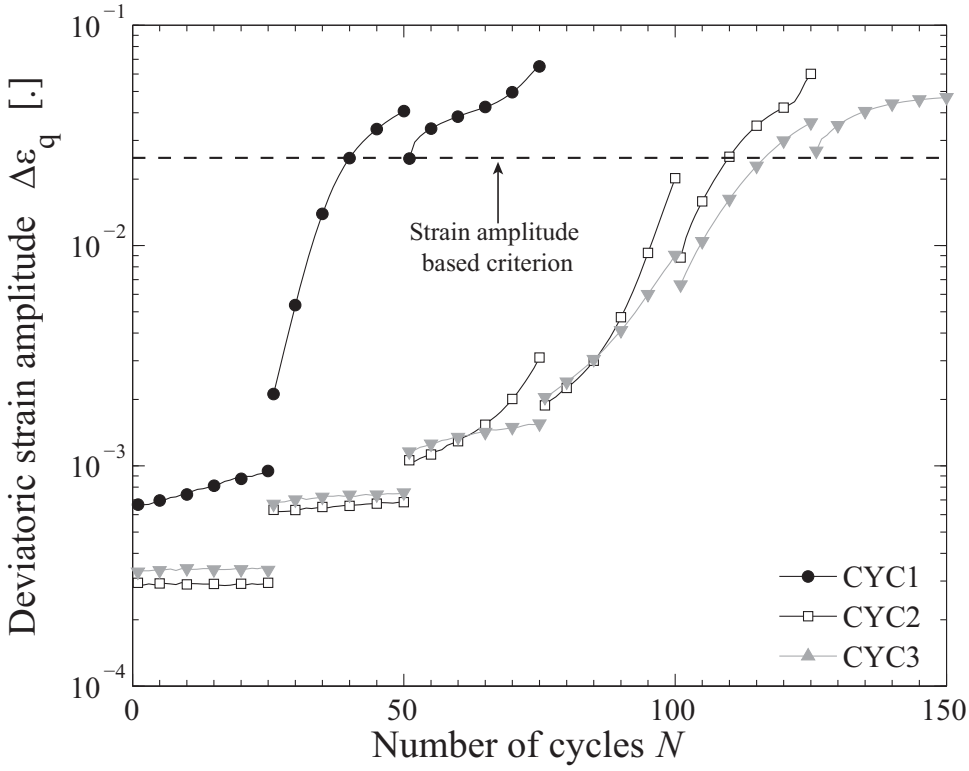

Fig. 4.17. Leman Sand increase of the deviatoric strain for CYC1, CYC2 and CYC3 and failure criterion based on a threshold strain amplitude.

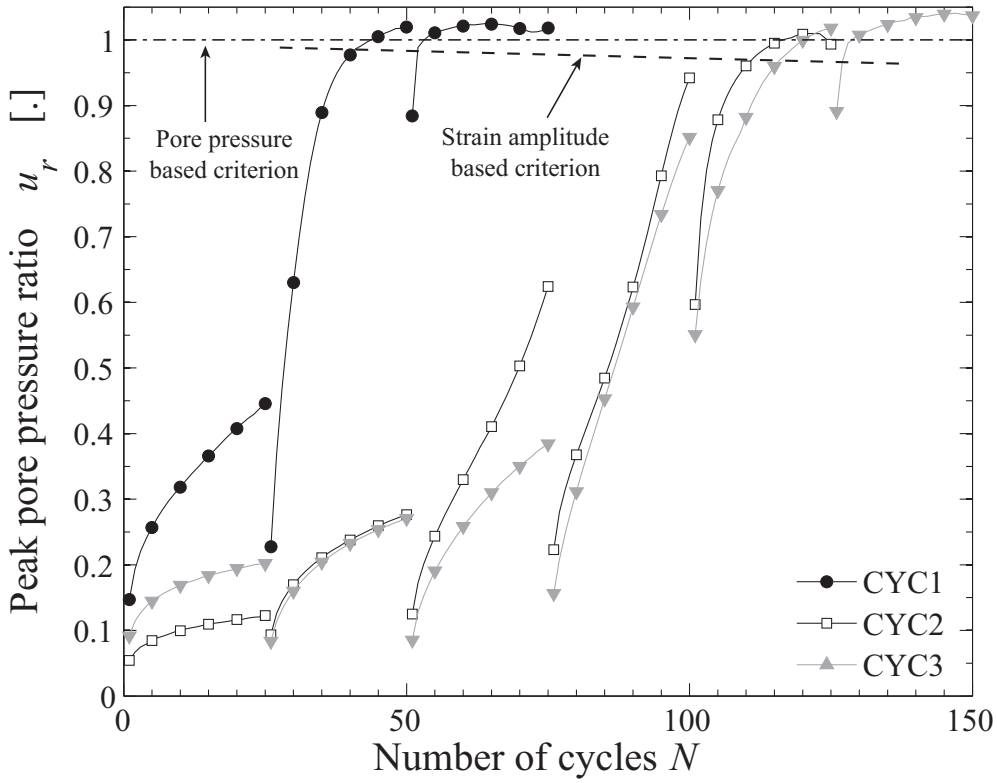

Fig. 4.18. Leman Sand increase of pore-pressure ratio for CYC1, CYC2 and CYC3 and failure criterions based on thresholds pore pressure ratio and strain amplitude.

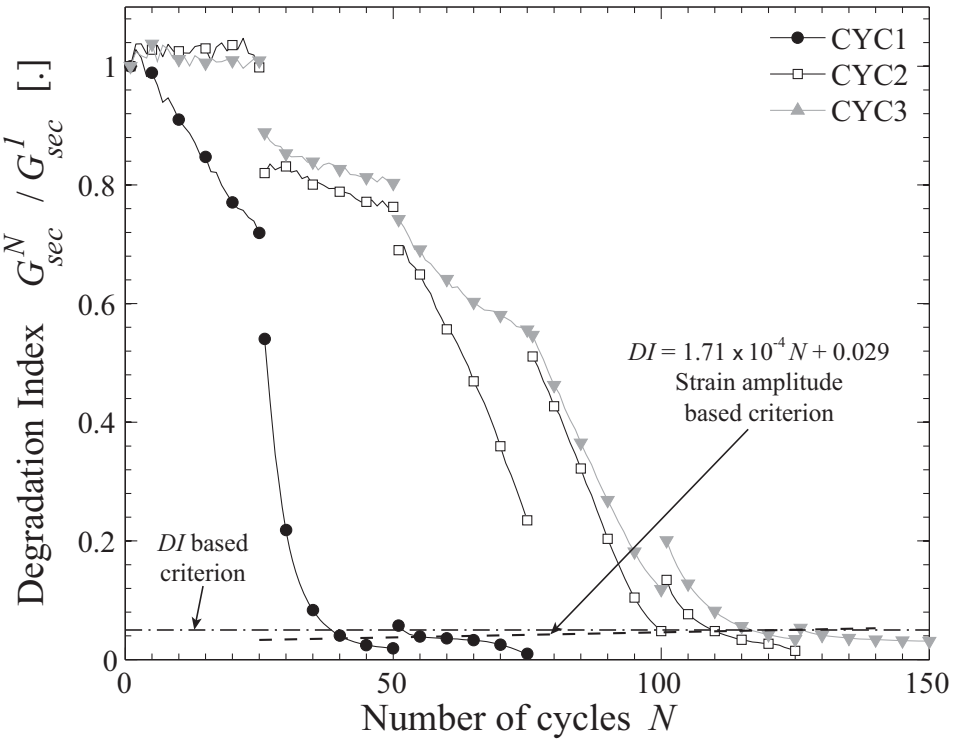

Fig. 4.19. Leman Sand stiffness degradation of CYC1, CYC2 and CYC3 and failure criterions based on thresholds *DI* and strain amplitude.

4.4.5 Small strain secant shear modulus

The knowledge of small strain behaviour, particularly the small strain secant shear modulus, is necessary for interpreting stiffness degradation and nonlinear sand behaviour. The difficulty which arises is that the triaxial press can accurately measure cyclic loadings for deviatoric stress amplitudes above Δq = 15 kPa (cf. Chapter 3). Below that value, friction may become predominant and the value of G_{max} might be overestimated.

The test CYC4 is performed at the limit of the device in the small strain regime, for an initial confining pressure of 100 kPa. The secant shear modulus is depicted in Fig. 4.20 as a function of $\Delta\varepsilon_q$. To help estimate G_{max}, the empirical equations provided for sand by Ishihara (1996) are also used (cf. values in Fig. 4.20). At $\sigma_3'^0$ = 100 kPa, G_{max} = 150 MPa is compatible with both the experimental values CYC2 and CYC4, and corresponds to the range of values obtained from empirical equations for sand. We thus select this value as a good approximation of the elastic secant shear modulus for $\sigma_3'^0$ = 100 kPa and for medium dense Leman Sand.

For estimating G_{max} at other confining pressures and for the same void ratio, the formula of the nonlinear elastic component of the Hujeux model is used (Eq. 2.48). For that, we need to calculate the model parameters G_{ref} and n_e.

A group of monotonic tests performed on Leman sand with a conventional triaxial cell provided values of the initial tangent Young's modulus at various void ratio and confining pressures. From those values, it was confirmed that the coefficient n_e = 0.5 is suitable, as for most sands (Lopez-Caballero 2003). The Poisson's ratio of Leman Sand is also calculated from those tests, we obtain ν = 0.3.

Using Eq. 2.48, it is then possible to estimate G_{ref} from the value G_{max} = 150 MPa at $\sigma_3'^0$ = 100 kPa obtained above. We obtain G_{ref} = 474 MPa. The estimation G_{max} at different initial mean effective stresses but for the same void ratio can now be performed using Eq. 4.1:

$$G_{max} = 474 \left(\frac{p'}{p'_{ref}} \right)^{0.5} \quad [MPa] \tag{4.1}$$

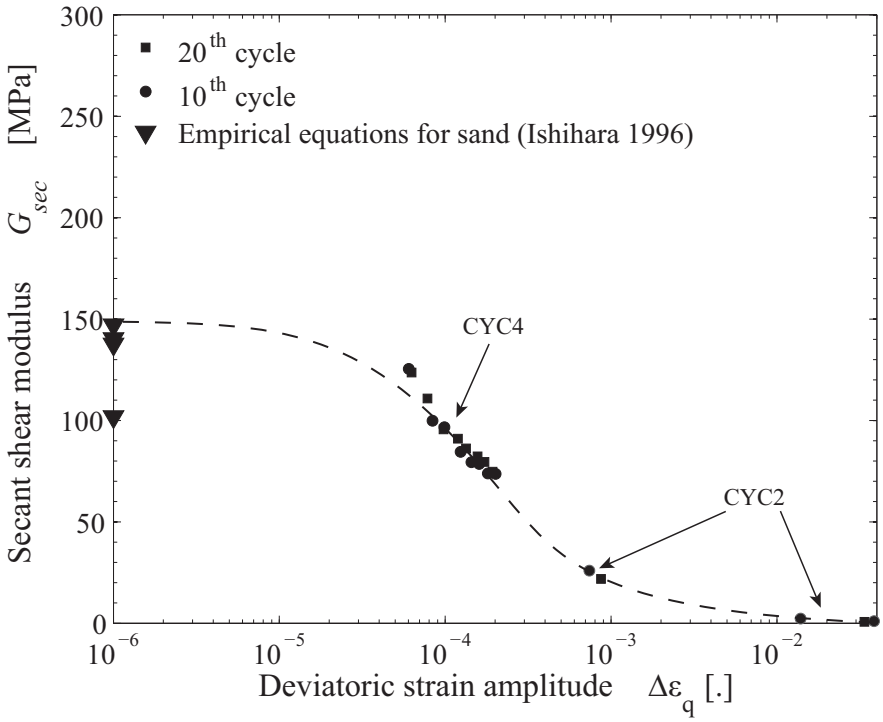

Fig. 4.20. Evaluation of G_{max} of Leman Sand.

4.4.6 Analysis of the G_{sec} - γ curve

The strain dependency of the dynamic parameters is a well-known indicator of the nonlinear behaviour of soils. The secant shear modulus tends to decrease with strain amplitude from its initial value, G_{max}, evaluated in section 4.4.5. The decrease of the normalized value G_{sec} / G_{max} with deviatoric strain amplitude is shown in Fig. 4.21. Secant shear moduli are slightly lower than the reference values for sands given by Seed et al. (1986). Note that these reference values are taken for the 5th cycle only, while in our tests, all points are displayed at each step.

When the initial effective confining pressure decreases from 200 kPa (CYC1) to 100 kPa (CYC2), the corresponding degradation curve is shifted down with lower G_{sec} / G_{max} values. For the same confining pressure of 100 kPa (CYC2 and CYC3), the G_{sec} / G_{max} ratio increases with average deviatoric strain, as indicated in Fig. 4.21 (q_{av} = 0 kPa for CYC2, and 100 kPa for CYC3). At large deviatoric strains, i.e., above the failure threshold $\Delta\varepsilon_q$ = 2.5%, the three curves converge to a very narrow band of G_{sec} / G_{max} ranging from 0 to 0.02. However, the sequence remains the same: CYC3 yields the highest G_{sec} / G_{max}, CYC1 is in the middle and CYC2 gives the lowest values.

For CYC4, the value of G_{sec} / G_{max} at the volumetric cyclic threshold shear strain 1 x 10^{-4} is about 0.65; this value is comparable with the degradation of the modulus for sands cited by Vucetic (1994), which could be an indication that our estimated G_{max} is accurate.

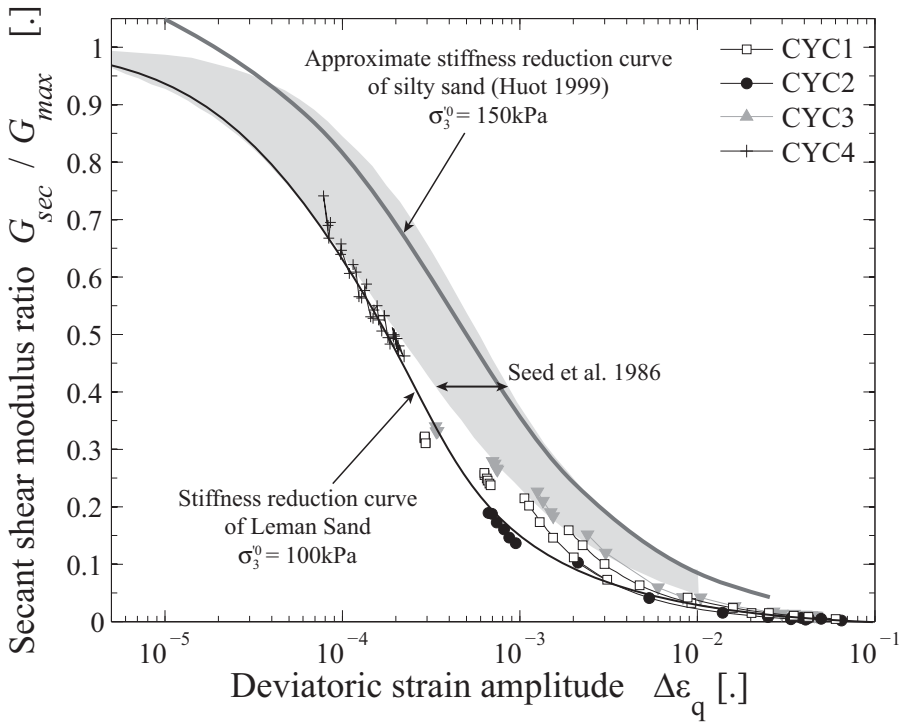

Fig. 4.21. Leman Sand degradation curves of the secant shear modulus ratio.

4.4.7 Evolution of the damping ratio with the number of cycles

The evolution of the damping ratio with the number of cycles *N* is different in the three tests CYC1, CYC2 and CYC3 (Fig. 4.22), in part due to the strain dependency. Damping ratio values can be very large at the first cycle of each step, as shown by the open shape of the first loop. Setting apart this first value, a short description of the evolution of *D* is given below:

- During the first and second steps of the CYC1 test, *D* is constant at 9%, and 11%, respectively. A steep increase arises during the third step when the strain amplitude also increases. The peak appears during the fourth step, with *D* = 20%. After a local minimum at 16%, *D* increases again at the end of the fifth step.

- The pattern of the CYC2 test is similar, except that (i) *D* is higher, from 14% to 26%, and (ii) *D* increases from the first step, instead of being constant.

- For CYC3, *D* decreases during the first and second steps, is constant during the third, a small peak at *D* = 18% appears during the fourth, and then *D* decreases again. *D* is lower in test CYC2 than in test CYC1.

This evolution is linked with changes in the loop shape. The shapes of the encountered loops during all three tests are displayed in Fig. 4.22. They are numbered 1 to 7. These numbers are also indicated in the *N* - *D* curves, where the loop shape change is located (circled number). Shapes 1 and 2, which appear at

low strains, concern the first steps at small to medium strain range. Shapes 3 to 5 appear at higher strains for the tests with symmetric stress reversal, and 6 and 7 concern the CYC3 test with an asymmetric stress reversal. *D* is high at the beginning of each step because the loops are open, i.e., the cycles do not close. After one or two cycles, the loops are almost closed.

Shape 1, which is extremely narrow, is the one encountered at the smallest strains; in this case, the damping is lower than 11%, and *D* is either constant or decreases. Shape 2 is wider, corresponding to higher values of *D* (from 12 to 20%). This corresponds to phases of increasing damping ratio. The peak of *D* is reached when Shape 3 appears. The loop is no longer convex, corresponding to the beginning of the so called «banana shape». The middle of the loop progressively flattens, which leads to Shape 4. At that moment, the strain is above 1%, and continuously increasing. The damping ratio has decreased from its maximum, since the stored elastic energy gets stronger while the area of the loop remains quite narrow. Above a few percent in strain, the loop shape eventually becomes wider, as shown in Shape 5, which is why *D* increases again. For asymmetric stress reversal, the loop shapes are the same as those at small strains, and they evolve differently at the peak and above. Indeed, the loops are asymmetric because of the asymmetry of the deviatoric stress loading towards the line $q = 0$ in the ε_q - q plane.

This emphasizes the non trivial role of loading at medium to large strain on dynamic parameter values.

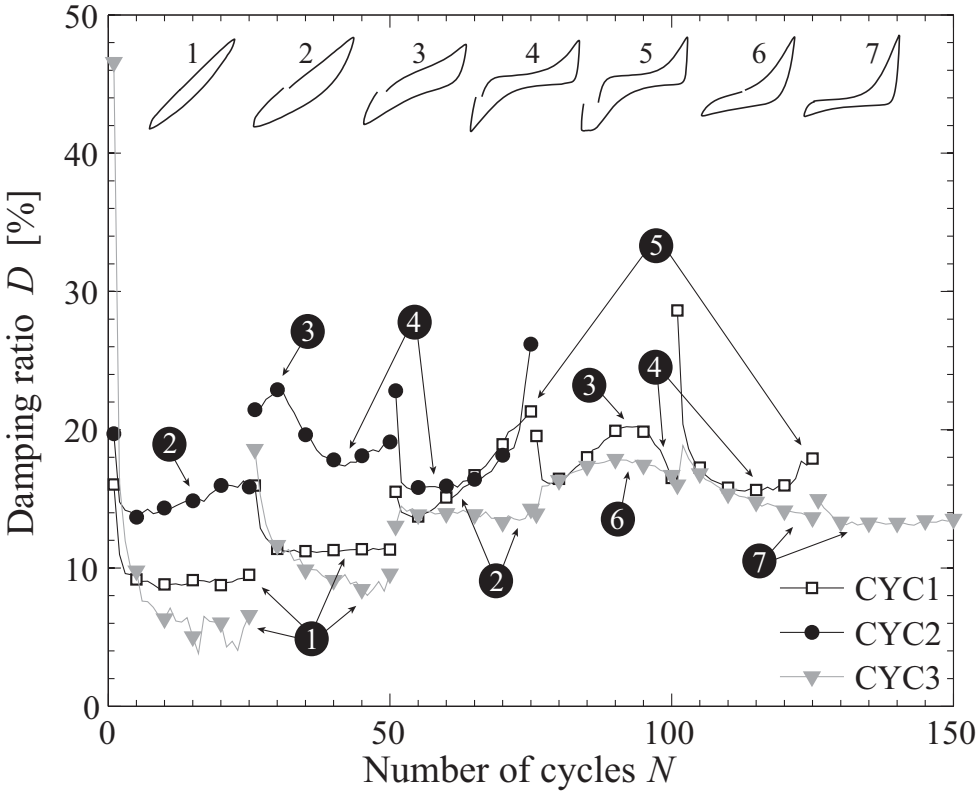

Fig. 4.22. Leman Sand evolution of the damping ratio with *N* and relation with loop shapes.

4.4.8 Analysis of the *D* - γ curve

The damping ratio also depends on the deviatoric strain amplitude (Fig. 4.23). *D* first increases with deviatoric strain amplitude, reaches a peak at $\Delta\varepsilon_q$ = 3 x 10^{-3} - 1 x 10^{-2}, and then decreases. The peak is thought to be a consequence of the dilative tendency of the granular matrix, which appears here because of the dense state of the material. Such a peak had been reported for the same range of $\Delta\varepsilon_q$ at the triggering of cyclic liquefaction (Wang & Kuwano 1999; Elgamal et al. 2005).

Because of this dilative tendency, the damping ratio is lower than the reference values from Seed et al. (1986) at high strain amplitudes. It should also be mentioned that *D* increases again for $\Delta\varepsilon_q$ higher than 3 x 10^{-2} for CYC1 and CYC2. To our knowledge, such an increase has never been reported; it can be explained by the formation of shear bands (see discussion in section 4.8). At those strains, the damping ratio values are still very different between the three tests; they do not converge to a narrower band.

On both sides of the peaks, it can be observed that the damping ratio increases when the confining pressure or the average deviatoric stress decreases.

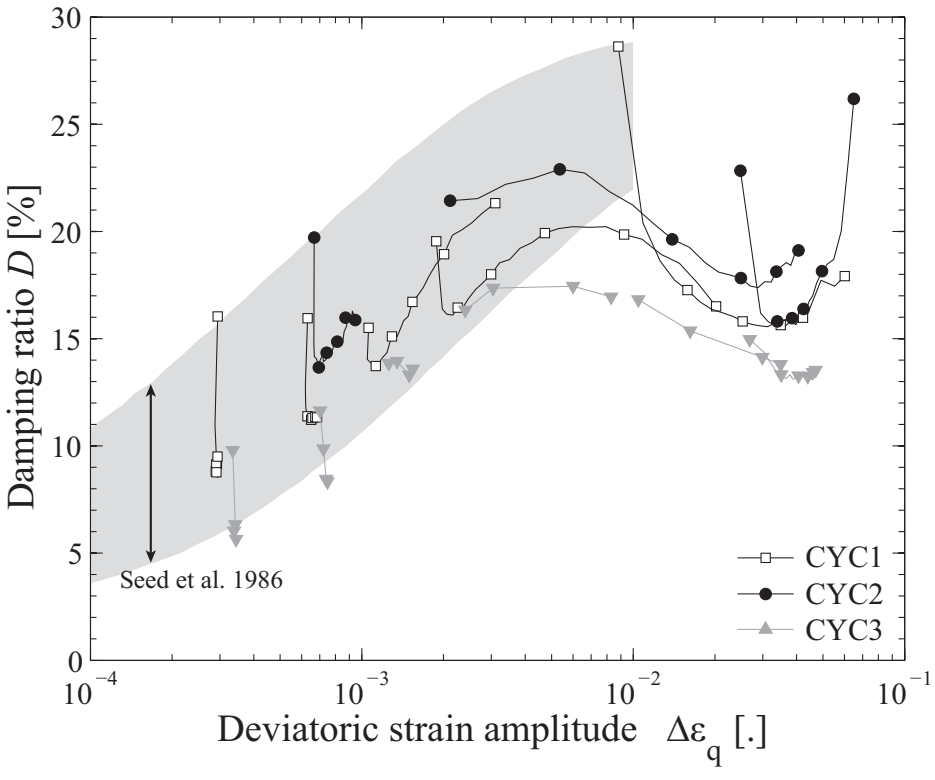

Fig. 4.23. Leman Sand degradation curves of the damping ratio.

4.4.9 Effect of the initial state

The evolution of the dynamic parameters is clearly strain-dependent and affected by the initial effective confining pressure and the static deviatoric stress. As was already mentioned by

Hardin & Drnevich (1972a), the effective mean principal stress influences the degradation curves of the sand. The observed effect of the confining pressure corresponds to the results obtained by Kokusho (1980) with Toyoura sand: G_{sec} / G_{max} increases and D decreases, i.e., they are shifted to the right on the degradation curves, when $\sigma_3'^0$ increases. The effect of the initial shear stress on cyclic sand behaviour is mentioned by Ishihara (1996); the cyclic strength is known to increase with the static shear stress for dense sand (while it decreases for loose sands). This observation is confirmed in our cyclic tests. Compared to symmetric loading with $q_{av} = 0$, the number of cycles to reach 2.5% axial strain is almost threefold when the static deviatoric stress is equal to 100 kPa. Moreover the secant shear modulus ratio is higher: at $N = 10$, G_{sec} / G_{max} more than doubles between the CYC2 and CYC3 tests, from 0.18 to 0.41. The damping ratio is clearly lower with, for example, a peak value circa 23% for CYC2 and only 17% for CYC3. The whole $\Delta\varepsilon_q$ - D curve is shifted down with a positive static deviatoric stress.

4.4.10 Discussion

This detailed analysis of four cyclic saturated undrained tests with stress reversal provides insight into stiffness degradation and the development of failure modes in Leman Sand. The increase of pore pressure above the volumetric cyclic threshold shear strain appears for the four tests at medium to large strain. Apparently, the curve u_r vs. $\Delta\varepsilon_q$ depends on the number of cycles only, and not on the confining pressure or average deviatoric stress, as observed by Dobry et al. (1982).

Among the salient features, the asymmetry of the mechanical response between extension and compression is noticeable, as well as for monotonic loading. Indeed, the asymmetry of stiffness and PT lines in monotonic loading are reflected in the response to cyclic loading as well. This asymmetry influences the stress-strain relation and the stress path.

Low void ratios are easily reached at the tested confining pressure. As a consequence, negative excess pore pressure develops, which stabilizes the sand. The mechanism that leads to the development of large strains and cyclic liquefaction actually starts when the stress path crosses a phase transformation line. Above the phase transformation line, excess pore pressure first decreases. Then, a strong increase of the pore-pressure ratio towards unity, accompanied by a gradual increase of the deviatoric strain, appears during the unloading parts of the cycle. At reloading, the sand strength increases again because of the decrease of excess pore pressure. As a consequence, the «*banana shape*», or «*S shape*» loop appears. The apparition of a peak of D in the $\Delta\varepsilon_q$ - D curve is explained by the evolution of the shape of the stress-strain loop.

The phase-transformation line is considered to be the same in monotonic and cyclic loading (De

Gennaro et al. 2004; Georgiannou et al. 2008; Shibuya et al. 2003). In addition, for the Leman Sand, the two wings in extension and compression seem centred on the monotonic phase transformation line in the p' - q plane (Fig. 4.14). Benahmed (2001) showed that the onset of instability usually appears on the extension side for two-way symmetrical loadings with stress reversal. It is also the case in the CYC1 test (at N = 91) and in the CYC2 test (at N = 29). Indeed, the slope of the phase transformation line is lower in extension. Larger strains in extension than in compression develop as well. The loops are not symmetric in the ε_q - q plane with regard to the vertical axis, and the negative deviatoric strains in extension are larger than the positive strains when the S-shape develops.

The effect of the number of cycles on G_{sec} and D has been studied for drained loading with a large number of cycles (Li & Yang 1998; Wichtmann et al. 2005) and for undrained tests with stiffness degradation (Vucetic 1994). Our experimental data show that, even at small and medium strains, D can significantly evolve with the number of cycles N. The analysis of the shape of the cycles shows that this evolution is recognizable from the loop shape, independent of the secant shear modulus.

Thanks to the estimation of the elastic shear modulus, the stiffness reduction curves G_{sec} / G_{max} can be plotted and compared to other results on sand (Fig. 4.21). Shear modulus ratio obtained for Leman Sand are slightly lower than the area of reference defined by Seed et al. (1986). However, the value of stiffness degradation of CYC4 at the volumetric cyclic threshold shear strain is in good agreement with Vucetic (1994) and Huot (1999), which confirms the values obtained for G_{max}.

As explained previously, the evolution of damping ratio vs. $\Delta\varepsilon_q$ has an unexpected shape. The increase of D with $\Delta\varepsilon_q$ is within the range of the reference from Seed et al. (1986), but a first peak appears because of dilatant mechanism at strain amplitude around 5×10^{-3}. The final increase of D at large strains ($\Delta\varepsilon_q > 3 \times 10^{-2}$), after this first peak, is seen as a consequence of the shear band which is visible at the end of CYC1 and CYC2 tests. With such localization, the measured stress and strain are doubtful. It is still interesting to see that the apparition of the shear band leads to a change in the shape of the stress-strain loop (Shape 5), which is a type of distorted S shape.

4.4.11 Conclusions

A laboratory study was performed on saturated Leman Sand samples in undrained conditions with an advanced triaxial apparatus, focusing on the cyclic behaviour at medium to large strains with an emphasis on (i) excess pore pressure increase (ii) sample failure definition (iii) the evolution of dynamic parameters (iv) the effect of initial and boundary conditions. The observations can be summarized as follows:

- Excess pore pressure increases from the threshold $\Delta\varepsilon_q = 10^{-4}$ and depends mainly on the strain amplitude. The number of loading cycles N also influences the pore pressure increase, in the sense that several curves $\Delta\varepsilon_q$ - u_r are obtained for the different values of N.

- Cyclic stiffness degradation arises by cyclic liquefaction. The material softens, and its degradation index reaches very low values. The failure criterion can be based on a threshold deviatoric strain $\Delta\varepsilon_q = 2.5\%$. It matches the level of the degradation index well, which can thus be used as an alternative criterion for failure. Another candidate can be the pore water pressure ratio.

- Stiffness degradation curves of the dynamic parameters as a function of the deviatoric strain amplitude are calculated for saturated Leman Sand. The small strain secant shear modulus is evaluated by cross-checking empirical equations for sands and cyclic test results at small to medium strain. The $\Delta\varepsilon_q$ - G_{sec} / G_{max} curves are thus obtained in the medium to large strain domain.

- Furthermore, the damping ratio strongly evolves between the 1st and the 25th cycle. This evolution is explained by the loop shape, which depends on the stress path. A peak of the damping ratio in the degradation curve arises at strains of 0.3 to 1%.

4.5 Nonlinear Fonderie Sand behaviour in undrained saturated conditions

4.5.1 Introduction

Monotonic and cyclic saturated undrained triaxial tests were also performed with Fonderie Sand (see soil characteristics in section 3.5.2). As it is a relatively uniform sand, it is possible to use pluviation technique to obtain samples at several relative densities. This sand is thus used to study the nonlinear soil behaviour at various relative densities, from medium to dense sand. The comparison with Leman Sand nonlinear behaviour also gives interesting perspectives in terms of effect of the soil fabric.

The monotonic tests are briefly summarized, before nonlinear stiffness degradation at medium to large cyclic strain is described. Failure appears thanks to pore pressure increase coupled with the plastic strain accumulation. The dynamic parameters are provided. Stiffness degradation curves are compared to reference values for sand and to the results obtained with Leman Sand.

4.5.2 Summary of monotonic behaviour

Seven monotonic tests in compression - extension or extension - compression were selected (Jahangir 2008), with void ratio from 0.56 to 0.59 at different confining pressure, to calculate the monotonic characteristics of Fonderie Sand (Tab. 4.6). The monotonic test results are very similar to Leman Sand. The slopes of phase transformation lines and steady state lines are measured in the way described in section 4.2.4.

Tab. 4.6. PT and SS characteristics of Fonderie Sand

	M_{PT} [.]	M_{SS} [.]	ϕ_{PT} [°]	ϕ_{SS} [°]
Compression	1.4	1.5	35	37
Extension	0.84	*(1.03)**	29	*(38)**

* The value given for the steady state in extension is rather a failure angle than a steady state angle.

There is more discrepancy in the test results with Fonderie Sand, maybe because of the larger variations of relative densities, from 84% to 93%. For that reason, there is more uncertainty on the monotonic characteristics of Fonderie Sand compared to Leman Sand.

As Leman Sand, the monotonic behaviour of Fonderie Sand exhibits non symmetric behaviour, in the sense that the PT and SS lines have higher slopes in compression than those in extension. As for Leman Sand, the mobilized friction angle at large strain (SS or failure) is almost equal in compression and extension. There is more difference in the phase transformation angles.

As no signs of particle segregation could be seen in the samples, the anisotropy is thought to be mainly stress-induced.

4.5.3 Overview of cyclic test results and failure with Fonderie Sand

4.5.3.1 Presentation of cyclic tests

The cyclic undrained tests were performed at different relative densities from 58% to 97%, for the same initial confining pressure 200 kPa (Tab. 4.7). The procedure is similar to saturated undrained cyclic tests on Leman Sand, with an increase by step of the deviatoric stress amplitude from 40 kPa, every 20 kPa, until failure. The increase of Δq after each step is chosen at 20 kPa, instead of 30 kPa for Leman Sand, in order to avoid a too fast reaching of instability and failure.

Tab. 4.7. Summary of undrained saturated cyclic CTC-RTE tests on Fonderie Sand*

N°	Test description	Date	Void ratio [.]	I_D [%]	N^f	*B* coefficient
FSC1	Cyclic undrained stress-controlled CTC-RTE	03/07/08	0.54	97	-	0.96
FSC2	Cyclic undrained stress-controlled CTC-RTE	02/07/08	0.58	86	93	1.0
FSC3	Cyclic undrained stress-controlled CTC-RTE	31/07/08	0.6	81	41	0.955
FSC4	Cyclic undrained stress-controlled CTC-RTE	08/07/08	0.62	77	91	0.96
FSC5	Cyclic undrained stress-controlled CTC-RTE	21/08/08	0.64	72	93	0.95
FSC6	Cyclic undrained stress-controlled CTC-RTE	23/08/08	0.69	58	73	0.95

(*) The loading frequency is f = 1 Hz. Sampling frequency is 100 Hz. All tests have symmetric stress reversal, i.e. q_{av} = 0 kPa, and the initial confining pressure is 200 kPa.

4.5.3.2 Failure

As was described in Chapter 2, for undrained cyclic loading of sand, failure arises by flow liquefaction or cyclic liquefaction depending on the void ratio and confining pressure. For FSC2 to FSC6, failure is more sudden than what was described for Leman Sand. The failure threshold $\Delta\varepsilon_q$ = 2.5% is surpassed during the fourth step for most tests. The relation between the number of cycles at failure and the void ratio does not appear as clearly as expected. For example, failure arises at the same cycle in FSC2 and FSC5, thought their relative density (I_D) is 86% and 72%, respectively.

Comparing the two tests FSC1 and FSC6, however, underlines the difference of behaviour with respect to relative density. In the dense state, for a relative density I_D = 97%, failure is not reached at the end of the test after 15 steps. As accommodation develops, the test is stopped at this point. In the looser state at I_D = 58%, the number of cycles at failure is N^f = 73 cycles. Failure arises suddenly, with very large strains developing within a few cycles. The comparison of FSC2 and FSC6 (Fig. 4.24) during their last respective step shows that the rate of increase of ε_1 around failure is clearly higher for FSC6 at higher void ratio.

Another interesting point is the shape of the excess pore pressure ratio around the threshold u_r = 1 (Fig. 4.25). Contrary to Leman Sand, the dilative behaviour of Fonderie Sand is very limited, i.e. the spikes of u_r disappear after a few cycles. This phenomenon never appeared for Leman Sand, while it is present in all tests which developed failure in Fonderie Sand. The relation between excess pore pressure increase and strain amplitude is further detailed in section 4.5.4.

We consider the rate of increase of the deviatoric strain close to failure as the best criterion to determine whether failure arises by cyclic liquefaction or flow liquefaction. As an analogy to the response of Hostun Sand in terms of both deviatoric strain and pore pressure, as they are described above (cf. Benahmed 2001), failure resembles more flow liquefaction in the test FSC6, while for FSC2, the response is assimilated to cyclic liquefaction. To verify this affirmation, and to determine the failure mechanism for tests of intermediate relative densities, Fig. 4.26 provides the strain amplitudes at failure of all tests concerned for Fonderie Sand. Apart from FSC2 for which the rate of increase of the deviatoric strain amplitude is slightly smaller, all tests exhibit a rapid failure as shown for the test FSC6.

4.5.3.3 Comparison with Leman Sand

Compared to Leman Sand in test CYC1, which is in the same initial condition as test FSC5 in terms of relative density and initial confining pressure, stiffness degradation of Fonderie Sand is sudden (Fig. 4.26). Strain amplitude is higher for Leman Sand of approximately one log-scale at the beginning of the tests, and regularly increases. On the contrary, the strain amplitude of Fonderie Sand is low and stable at the beginning of the tests, but it increases suddenly and reaches the level of the failure threshold within a few cycles.

As the behaviours of Leman Sand and Fonderie Sand seem quite different, the comparison of stress-strain relation and stress paths of CYC1 and FSC5 (similar relative density) at failure is given in Fig. 4.27 and Fig. 4.28. The cyclic stress ratio (CSR) at failure is smaller for Fonderie Sand; it thus seems that cyclic strength of Fonderie Sand is lower than cyclic strength of Leman Sand, thought this notion can not be ascertain by only these two tests.

The stress-strain relation presents a banana shape for both sands (Fig. 4.27). The shape of the stress-strain relation of Fonderie Sand decays because the stress amplitude decreases. This is due to the fact that the sand stiffness decreases so suddenly that the regulation system cannot impose the prescribed force. The increase of deviatoric strain arises predominantly in the side of extension for both sands. As seen before, the rate of increase of the deviatoric strain is faster in Fonderie Sand than in Leman Sand.

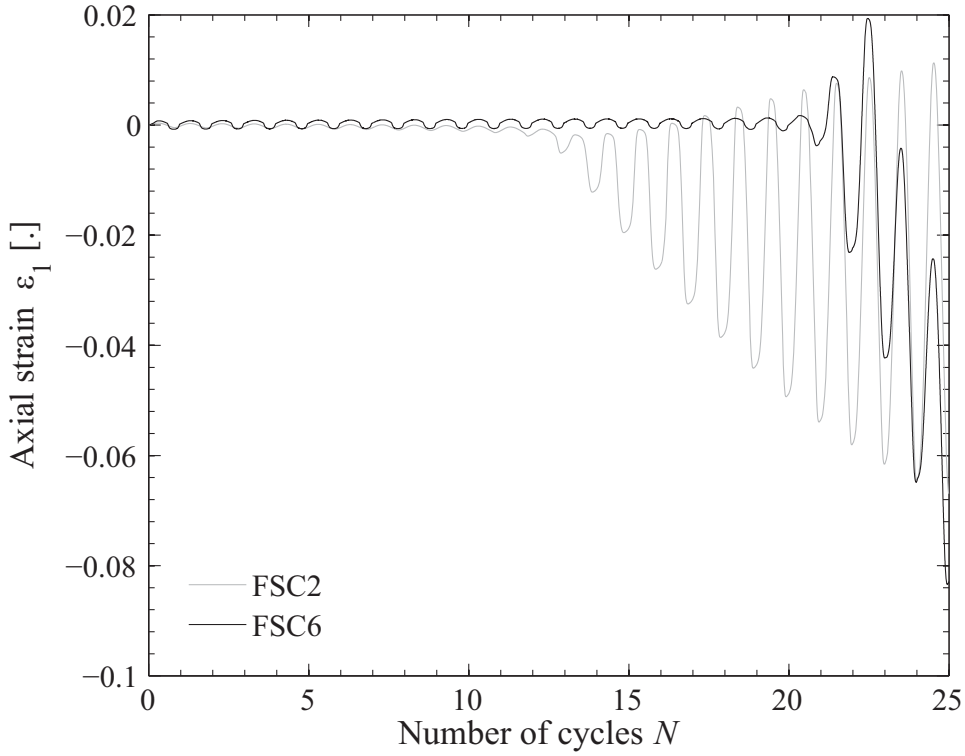

Fig. 4.24. Fonderie Sand strain accumulation close to failure for FSC2 and FSC6.

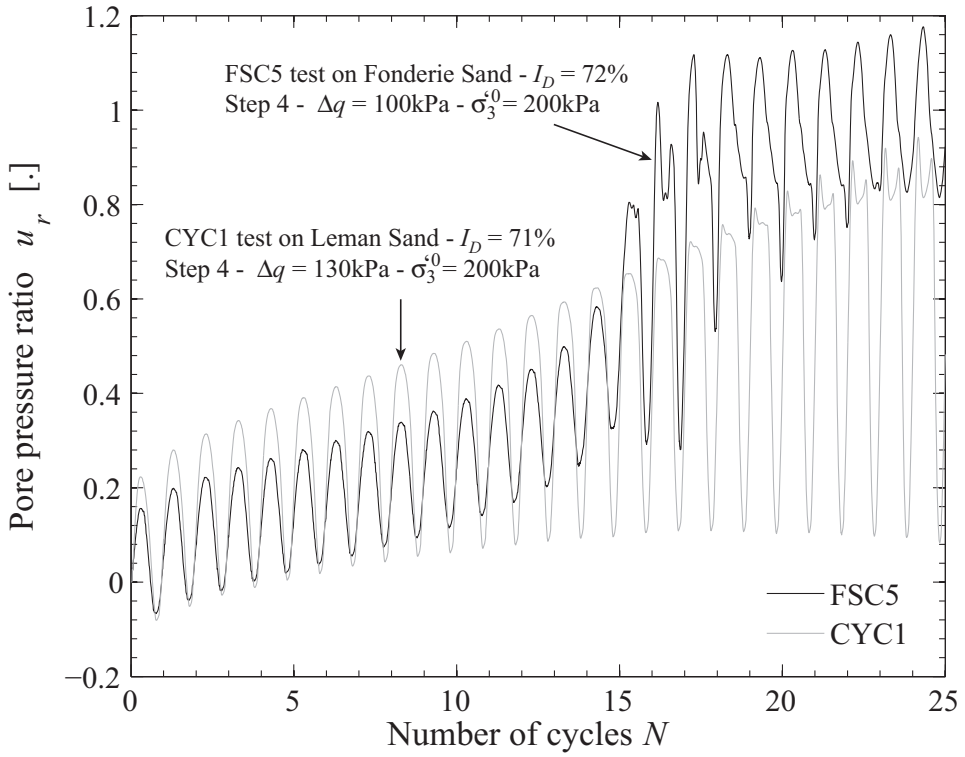

Fig. 4.25. Comparison of pore pressure ratio increase close to failure for Fonderie Sand and Leman Sand.

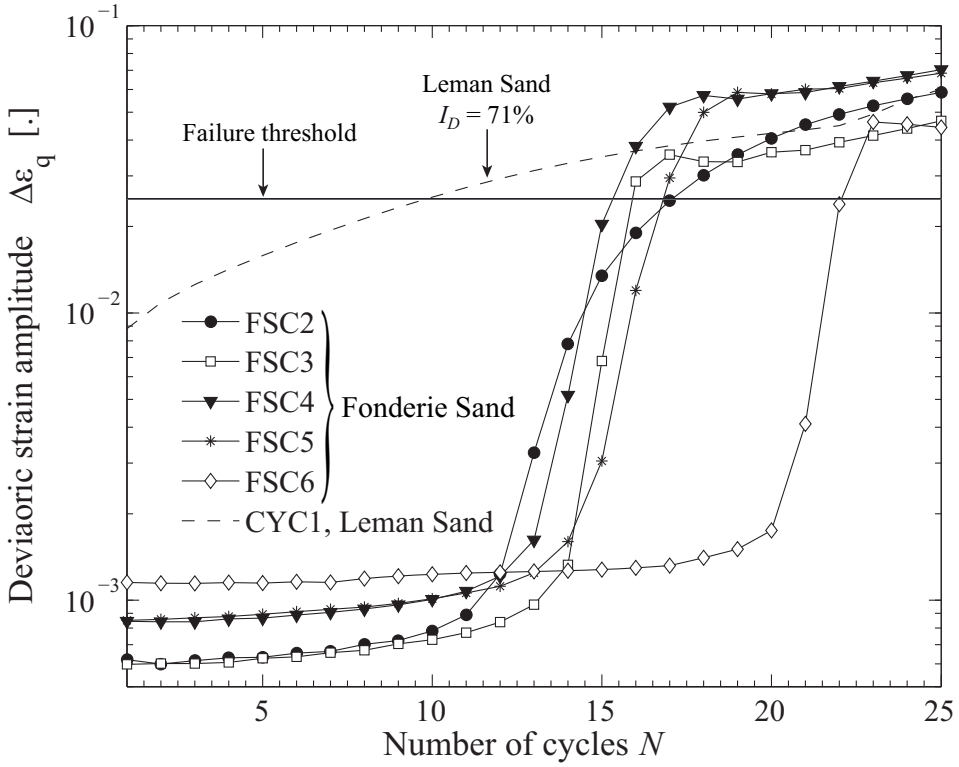

Fig. 4.26. Deviatoric strain amplitude at the step of failure for tests FSC2 to FSC6 for Fonderie Sand and test CYC1 for Leman Sand.

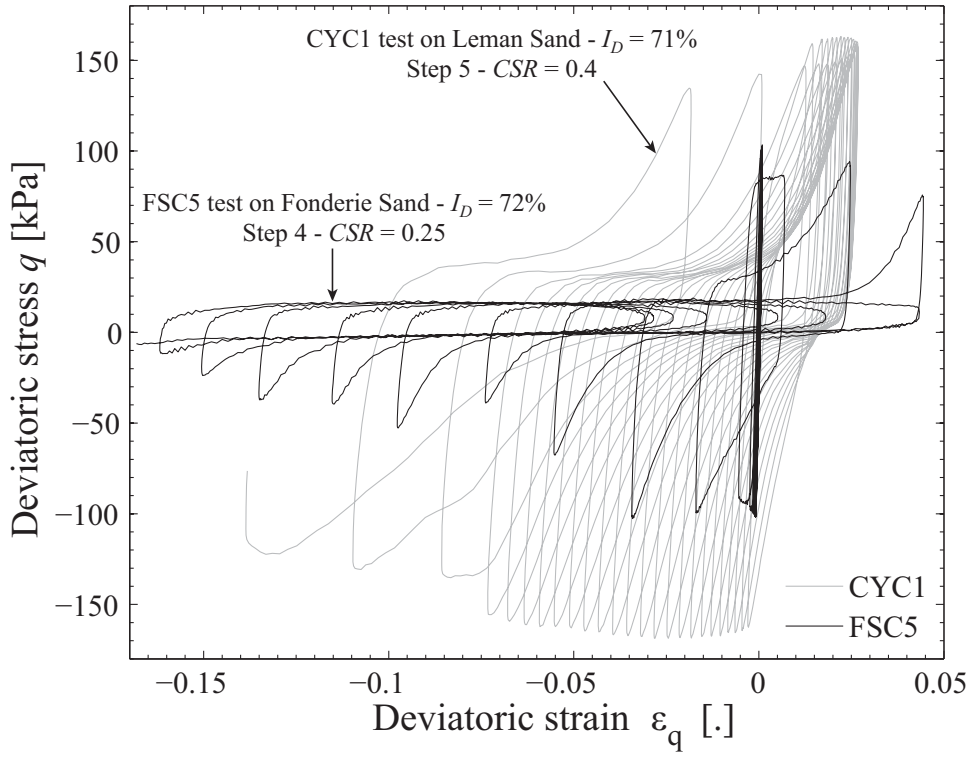

Fig. 4.27. Comparison of stress-strain relation of Fonderie Sand and Leman Sand at failure.

The stress paths (Fig. 4.28) reflect and enlighten the different behaviours of both sands. For Leman Sand, the typical shape of double wings, characteristic of the alternation of the increase and decrease of excess pore pressure, appears from the beginning of the tests. This explains why such high strains develop from the first cycle of this step. For Fonderie Sand, there is first an accumulation of pore pressure which induces regular shift of the stress path to the left. During that part of the test, strain accumulation is limited and the deviatoric strain amplitude is below 10^{-3}. When the stress path of FSC5 crosses the phase transformation line on the extension side, a few wings form but the decay of the deviatoric stress amplitude is rapid. This phase corresponds to the rapid increase of strain amplitude. As will be explained later, the pore pressure ratio exceeds the threshold u_r = 1 for this test, which is reflected here by the fact that the average stress *p'* takes negative values. This apparently absurd result is ignored for the moment.

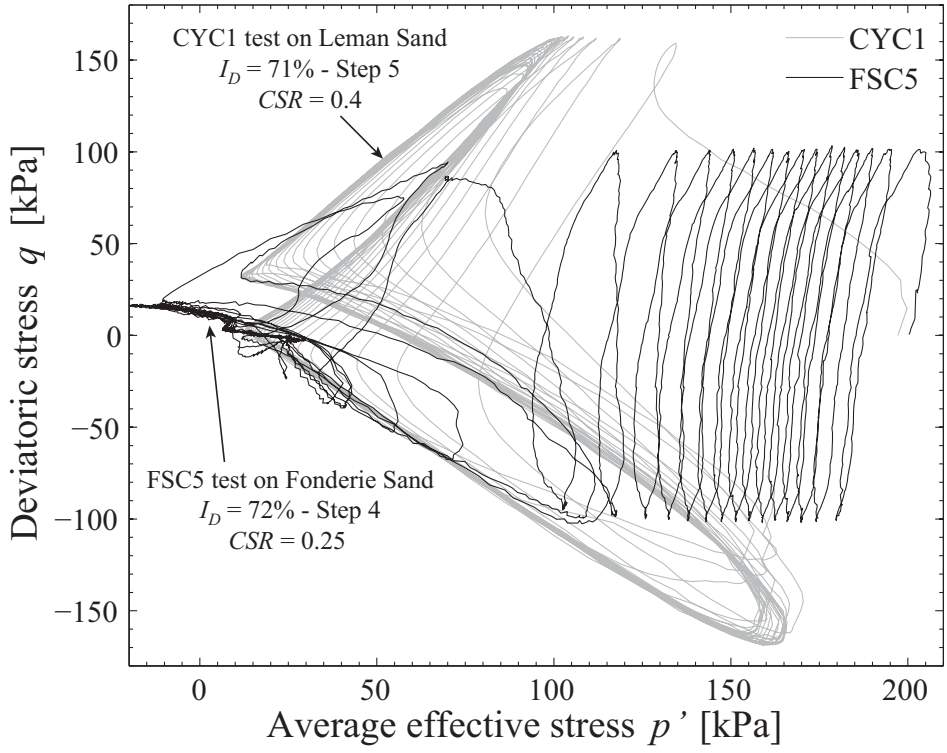

Fig. 4.28. Comparison of stress paths of Fonderie Sand and Leman Sand at failure.

4.5.4 Excess pore pressure ratio increase in cyclic tests with stress reversal

The increase of the pore pressure ratio as a function of the deviatoric strain amplitude has the same pattern for Fonderie Sand (Fig. 4.29) than for Leman Sand (Fig. 4.16).

It is again possible to delineate a narrow zone surrounding the relation $\Delta\varepsilon_q$ - u_r, with a lower limit made of the points representing the first cycles and the upper boundary made of points from the 25th cycle.

The void ratio does not seem to influence the relative positions of the curves representing each test within this area. The agreement is good between the cluster of curves and the area obtained for Leman Sand, depicted in gray in the figure. The upper boundaries in particular are very close to each other. It is clear however that higher excess pore pressure develops in Fonderie Sand, for the same level of deviatoric strain amplitude.

Except for test FSC1, which is very dense, the pore pressure ratio reaches values above 1 at the last step during failure triggering. A possible explanation for that behaviour is the formation of a shear band at the end of the failure phase. This assumption is analysed in section 4.8. Another possibility to consider is the fact that end-restraint at the base of the sample, where the pore pressure is measured, may involve non-negligible inhomogeneity of the sample (cf. section 3.3). Because of that, local increase of the pore pressure above the expected physical limits can occur due to contractive behaviour of the saturated sand.

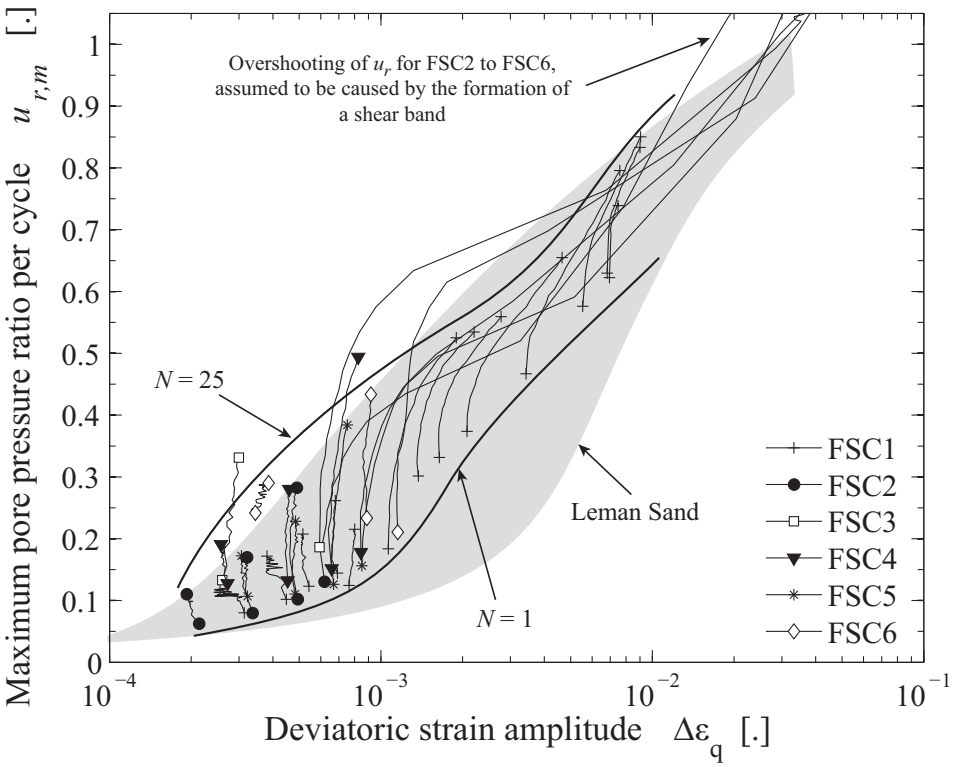

Fig. 4.29. Pore pressure increase vs. deviatoric strain amplitude of Fonderie Sand (in grey, the results of Leman Sand).

4.5.5 Dynamic parameters

To provide stiffness reduction curves, the elastic secant shear modulus G_{max} must be evaluated for Fonderie Sand. Some values of G_{max} are available from Huot (1999), but they correspond to initial

conditions different from those of our tests in terms of void ratio and initial confining pressure, also they are not directly usable. That is why we can only evaluate G_{max} thanks to empirical correlations. A first one, provided by Kokusho (1980) for Toyoura Sand, is chosen because it gives the best fit with available experimental values (relation n°1 in Tab. 4.8). The published selected empirical relation gives a good agreement, particularly for confining pressures between 100 kPa and 300 kPa. The maximum error between the experimental and the empirical values is 9% in that range of confining pressure.

As we have available good quality experimental points (Huot 1999), a new empirical model is also proposed specifically for Fonderie Sand. The model equation is the same as the reference from Kokusho (1980):

$$G_{max}^{model} = a_i \frac{\left(b_i - e_0\right)^2}{1+e_0} \left(\sigma'_3\right)^{0.5} \tag{4.2}$$

Two parameters, a_i and b_i, are optimized in order to obtain a best fit of the experimental points. The optimization technique is a classical minimization approach (described for example in Obrzud 2009).

Several possible couples, (a_i, b_i), are obtained from the optimization technique. Though there is great difference between candidates for both parameters, the values of G_{max} resulting from all possible parameters are very close to each other. Two reasons can explain the presence of several local minimum of the optimization function: (i) there are only a few experimental points (ii) the prescribed empirical relation is highly nonlinear. The set of parameters chosen (cf. Tab. 4.8), does not give the absolute minimum error, but the resulting G_{max} are extremely close (difference around 0.5%) to the minimum function. This couple (a_i, b_i) is preferred because both parameters are closer to the usual values proposed in the literature. G_{max} of Fonderie Sand, obtained with the newly designed empirical relation (relation n°2), are summarized in Tab. 4.8 for comparison with the experimental points.

Tab. 4.8. Evaluation of G_{max} of Fonderie Sand from experimental data and empirical relations

σ'^0_3 [kPa]	e_0 [.]	Experimental G_{max} [MPa] (*)	G_{max} from empirical relation n°1 [MPa] (♣)	G_{max} from empirical relation n° 2 [MPa] (#)
50	0.69	86	77	88
100	0.63	121	122	135
300	0.68	210	192	218
400	0.68	269	222	252

(*) Huot 1999, (♣) Kokusho 1980, a_i = 8400, b_i = 2.17 (#) a_i = 3157, b_i = 3.27 (Rascol and Obrzud)

Using the empirical relation from Kokusho (1980), estimate G_{max} range from approximately 150 to 200 MPa in our tests, depending on the void ratio and for σ'^{0}_{3} = 200 kPa. Using the new empirical relation instead, G_{max} is slightly higher, from 175 to 215 MPa. These values are then used instead for the following stiffness reduction curves, presented in Fig. 4.30.

The stiffness reduction curve of Fonderie Sand exhibits good agreement with the range of values provided by Seed et al. (1986) for sands, although some of the curves are placed just below that reference area (Fig. 4.30). The general trend is that G_{sec} / G_{max} curves of the samples with the highest void ratio are slightly lower than dense samples. This result corresponds to the description of Toyoura Sand behaviour from Kokusho (1980). There are exceptions though; the FSC3 test in particular, which has the lowest number of cycles at failure, is clearly below the other G_{sec} / G_{max} curves at large strain. It is possible that the void ratio is not accurate for that particular test. Otherwise, a problem may have occurred during the mounting of the sample, making it softer than usual samples.

In general, stiffness decreases more abruptly than for Leman Sand, as was shown during the analysis of failure. During the last step, the secant shear modulus ratio drastically decreases. For example in FSC2 test, G_{sec} / G_{max} decreases from 0.41 to 0.001 in 25 cycles during the fourth step.

The damping ratio (Fig. 4.31) is also placed within the range given by the reference values from Seed et al. (1986), which applies only to values below 1% deviatoric strain. Exactly like the damping ratio of Leman Sand, a peak arises in the range $\Delta\varepsilon_q = 3 \times 10^{-3}$ to 1×10^{-2}, and a marked decrease of D follows that peak because of dilative mechanism and the S shape of the stress - strain relation. The peak is even more distinct than for Leman Sand, because the maximum values of D are higher, with nearly 30%, and the following fall reaches values around 10%. The effect of void ratio on the damping ratio seems negligible in the range of relative density explored, although Kokusho (1980) reported that damping ratio of Toyoura Sand slightly increases with the void ratio.

The final increase of D, above $\Delta\varepsilon_q = 3 \times 10^{-2}$, which had also appeared with Leman Sand, and which is thought to be linked with the formation of a shear band, also appears in Fonderie Sand. However, it was shown in Fig. 4.27 that the shape of stress-strain loops is very deformed, also these very high values are not really comparable to other obtained results.

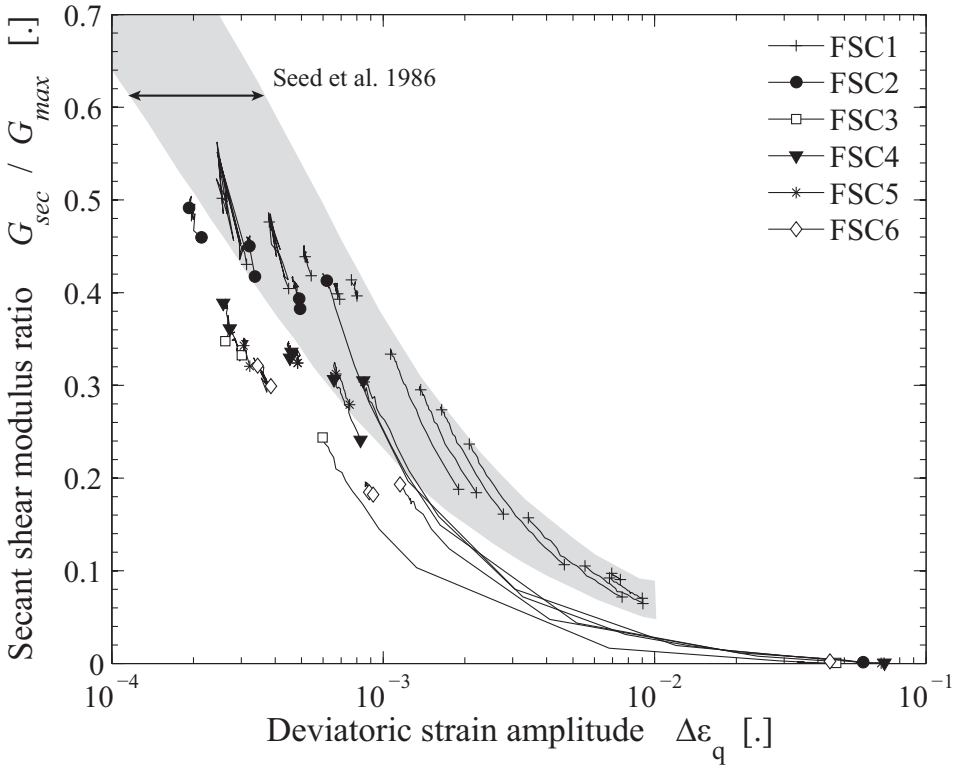

Fig. 4.30. Stiffness reduction curve of Fonderie Sand.

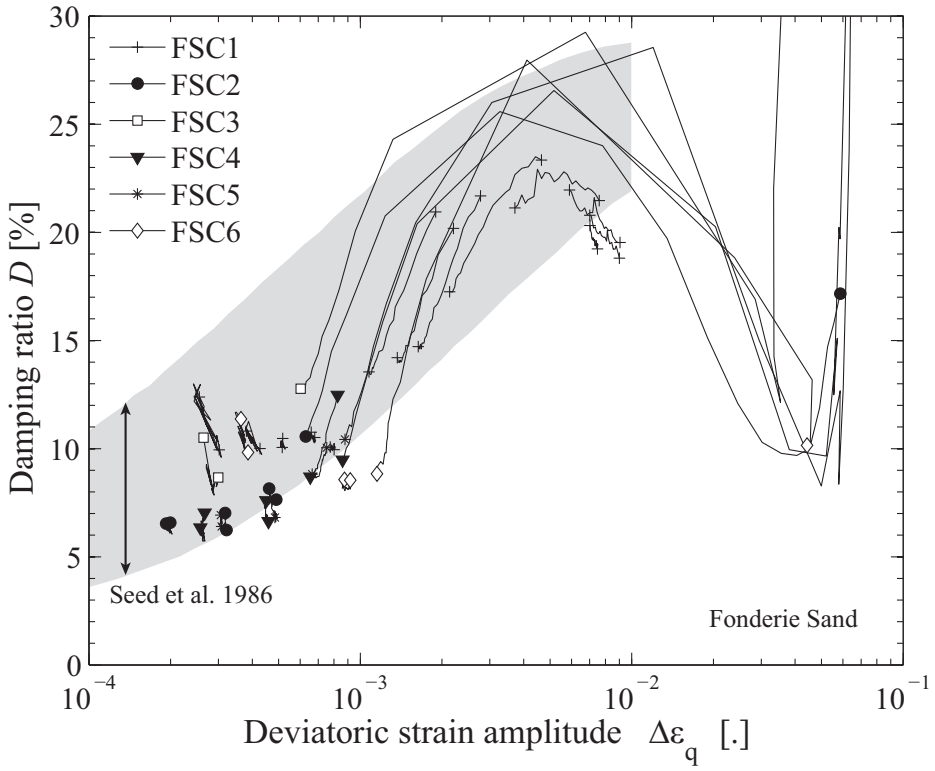

Fig. 4.31. Damping ratio of Fonderie Sand.

4.5.6 Discussion

In the first place, we did not obtain a simple quantitative relation between the relative density I_D of Fonderie Sand, in the medium to dense state, and the number of cycles to failure. It is however possible to distinguish three types of response: a dense behaviour with accommodation (FSC1), a dense behaviour with failure similar to cyclic liquefaction (FSC2) and a medium behaviour with sudden failure assimilated to flow liquefaction (FSC3 to FSC6). This classification of the failure mode as flow liquefaction relies on the comparison with test results of Benahmed (2001) with Hostun Sand. This interpretation may then depend on subjectivity.

The comparison with Leman Sand, for tests with the same initial confining pressure and relative density, provides perspective into the nonlinear behaviour of both sands. The mechanism of stiffness degradation is rather continuous and progressive in Leman Sand, while it is a sudden and rapid phenomenon in Fonderie Sand. The striking difference can be explained by a different liquefaction susceptibility. Kramer (1996) mentions that grain size distribution and the shape of the grains influence liquefaction susceptibility (see section 2.4.13): narrow graded sands are more susceptible to liquefaction than well graded sands, and rounded grains are more susceptible to liquefaction than angular grains. Fonderie Sand grains are rounder, and the particle size distribution is really narrow, compared to Leman Sand. Both aspects can thus explain the two different nonlinear behaviours. It also reflects the different values of phase transformation and steady state angles of the two sands.

On the other hand, the relations $\Delta\varepsilon_q$ - u_r, $\Delta\varepsilon_q$ - G_{sec} / G_{max}, and $\Delta\varepsilon_q$ - D are quite similar for Fonderie and Leman Sand. Particularly, the peak in the $\Delta\varepsilon_q$ - D curve, which was previously linked to the apparition of the dilative behaviour, occurs for both sands. As the banana shape of the stress-strain relation develop as well, it seems appropriate to obtain the same kind of stiffness degradation curves. There is anyway a small difference in the relation $\Delta\varepsilon_q$ - u_r between Fonderie and Leman Sand, which may be ascribed to the different particle size distribution and grain shape.

4.5.7 Summary

The steady state and phase transformation lines are drawn for Fonderie Sand from several monotonic tests performed in a dense state, at a relative density around 88% and for different confining pressures.

Cyclic tests on Fonderie Sand were performed in undrained conditions. Three different behaviours are obtained with regard to failure: the denser material exhibits accommodation, the following dense sample exhibits cyclic liquefaction while the rest of the medium-dense samples exhibit failure which resembles flow liquefaction. Near failure, the excess pore pressure ratio unexpectedly increases above 1. This phenomenon may be a symptom of soil inhomogeneity, either due to strain localization or

end-restraint mechanism (or certainly both). This is a limit of the dynamic triaxial press, which shows that test results above the failure threshold may not be considered as totally reliable, especially for Fonderie Sand tests.

The dynamic parameters and the relation between deviatoric strain and pore pressure increase are not found highly dependent on the relative density, in the range explored. The values of secant shear modulus and damping ratio are similar to Leman Sand characteristics.

The comparison with Leman Sand focused on stiffness degradation at medium to large strain, when the failure threshold is exceeded. The pore pressure increase, the stress-strain relation and the stress-path of tests CYC1 and FSC5, at the same relative density, give very different interpretation. While the increase of deviatoric strain upon loading is very progressive and stable for Leman Sand, it is sudden, rapid and induces instability of the motion control system for Fonderie Sand. For both sands, the phase transformation line in extension is touched first, and most of deviatoric strains arise on the side of negative strains.

The different behaviours of Leman and Fonderie Sand is ascribed to their respective particle shape and grain size distribution, which both induce higher liquefaction susceptibility of Fonderie Sand.

4.6 Evaluation of the laser measurement technique with an undrained test

4.6.1 Presentation

The laser measurement technique was developed to allow radial strain measurement of the sample, in order to perform dry cyclic dynamic triaxial tests. Thanks to a test performed in undrained saturated conditions, the use of the laser sensors for measuring radial strains is verified for a cyclic triaxial test under constant total confining pressure 200 kPa. The test sequence is similar to tests CYC1 to CYC3, with a failure threshold triggered at the sixth step. The loading frequency is 0.2 Hz, as this is the frequency chosen for dry tests.

The test results deduced from the usual assumption of saturated undrained conditions $\varepsilon_v = 0$ are compared with the results calculated from radial strains obtained from the laser sensors. Three possibilities are investigated for the signal processing of the continuous values of the sample radius: (i) raw radius data, (ii) smoothed radius data by local averaging and (iii) filtered radius data with a low-pass filter of cutoff frequency 8 Hz.

Both smoothing and low-pass filter are Matlab functions, calibrated for this particular cyclic loading. Smoothing is performed using locally weighted linear regression, i.e. each smoothed value is determined by neighbouring data points defined within the span; the method chosen is resistant to outliers (cf. Matlab user's manual).

4.6.2 At medium to large strain

For medium to large strains, i.e. above $\Delta\varepsilon_q = 10^{-3}$, the accuracy of laser measurement is very good. As an example, the fourth step of the undrained test is presented, with radial and volumetric strain (Fig. 4.32), deviatoric strain amplitude (Fig. 4.33), secant shear modulus (Fig. 4.34) and damping ratio (Fig. 4.35). We assume that the results are particularly accurate because the scan of the sample, which is used to calculate the integration factor for averaging radial strains over the sample height, is performed just after this step. That is why the obtained integration factor L is perfectly targeted for this step and the next one.

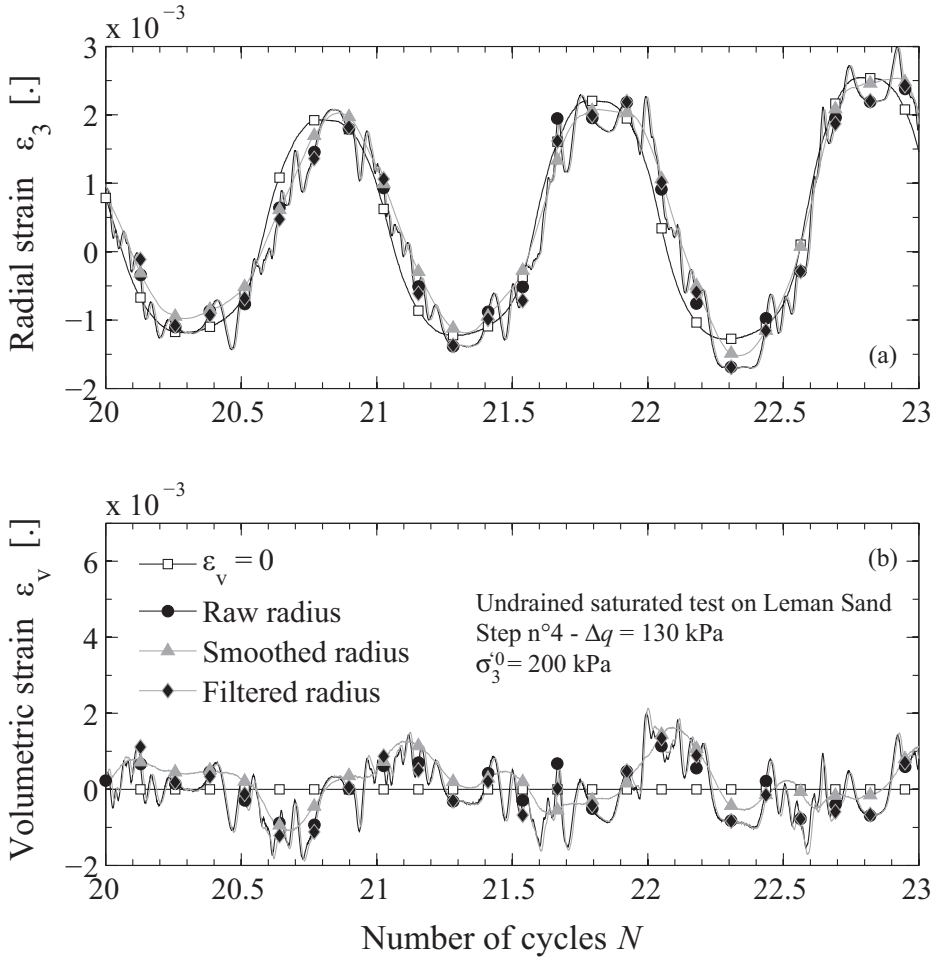

Fig. 4.32. Details of the radial and volumetric strains of Leman Sand for the evaluation of laser measurement (step 4).

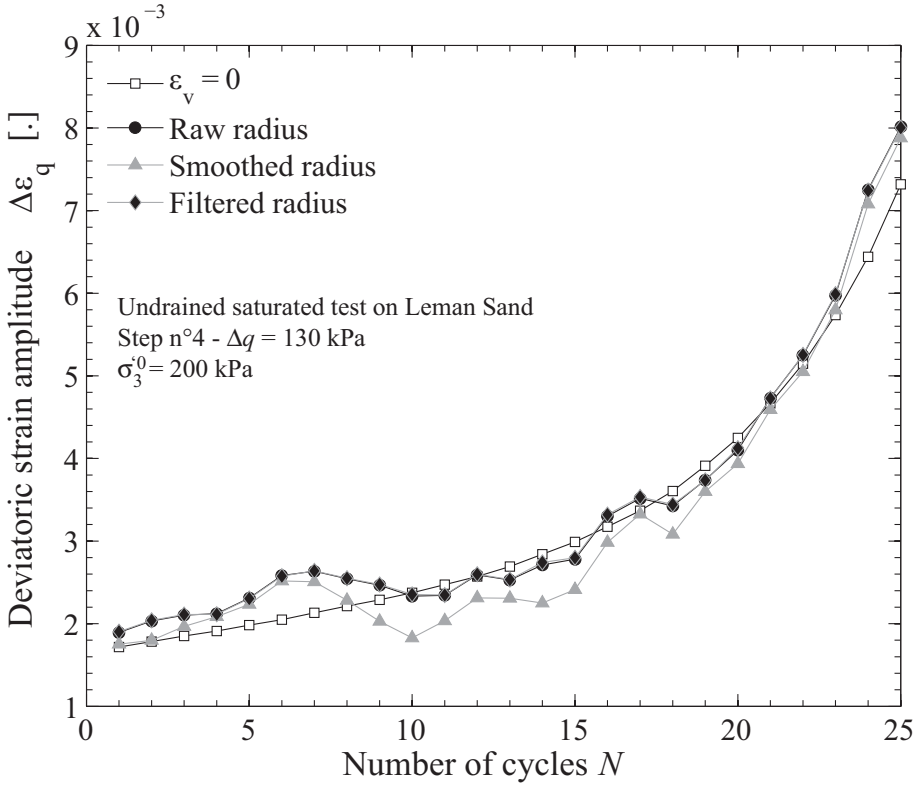

Fig. 4.33. Leman Sand deviatoric strain amplitude of step 4 for the evaluation of laser measurement.

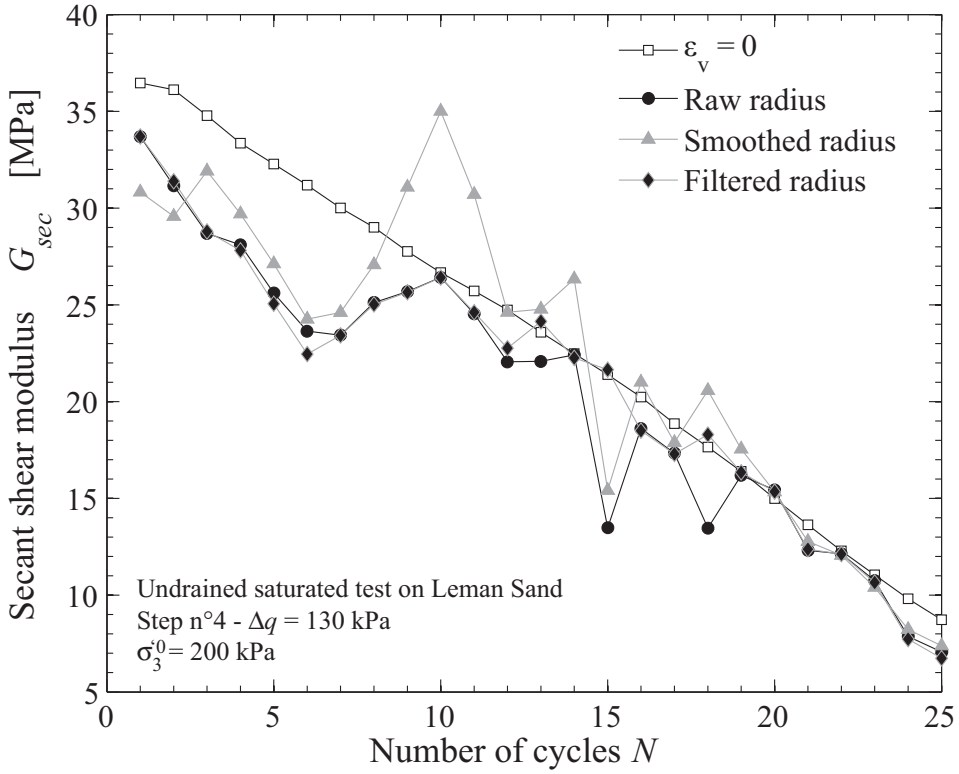

Fig. 4.34. Leman Sand secant shear modulus of step 4 for the evaluation of laser measurement.

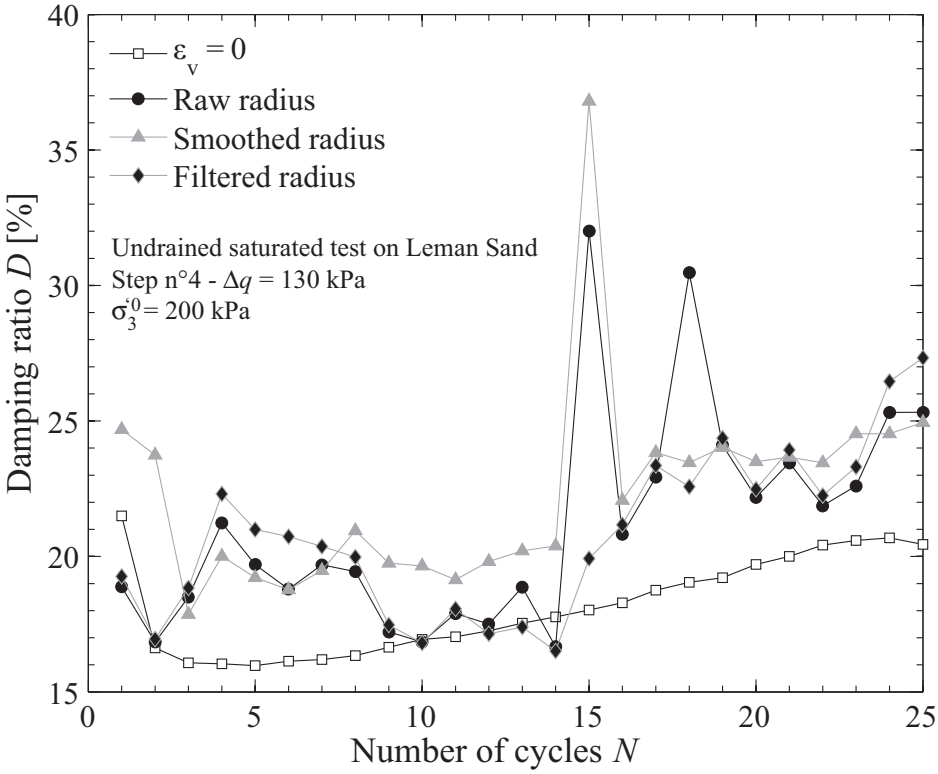

Fig. 4.35. Leman Sand damping ratio of step 4 for the evaluation of laser measurement.

The raw radius and the filtered radius yields almost the same result. The smoothed radius however gives slightly different values: as it systematically decreases the deviatoric strain amplitude, it increases the secant shear modulus. It also decreases the scatter of the damping ratio, but as a shortcoming it increases its average value. The damping ratio from laser sensors is systematically larger than the measurement obtained from the $\varepsilon_v = 0$ assumption, whatever signal processing tool is used.

4.6.3 At small to medium strain

For strain amplitude below $\Delta\varepsilon_q = 10^{-3}$, the test characteristics calculated from laser-based radial strains are still in a good range, but there is more scatter (Fig. 4.36, Fig. 4.37, Fig. 4.38 and Fig. 4.39). That is why it is proposed to take an average value over the 25 cycles for the secant shear modulus, the damping ratio and the deviatoric strain amplitude (Tab. 4.9). There is a loss of information from the averaging, because stiffness degradation exists between $\Delta\varepsilon_q = 10^{-4}$ to 10^{-3}; however, the degradation is small in this strain range, also the test characteristics do not evolve a lot. Moreover, their evolution is lost anyway in the uncertainty of the measurement technique. For the loading conditions of this particular test, the steps 1 and 2 only are concerned by the averaging.

As for higher strain amplitude, the smoothed radius gives better results for the deviatoric strain amplitude and the secant shear modulus, while it increases the error on the damping ratio.

Tab. 4.9. Comparison of average values for laser estimation

	Data type	Deviatoric strain amplitude [.]	Secant shear modulus [MPa]	Damping ratio [%]
Step 1 Δq = 40 kPa	$\varepsilon_v = 0$	2.27×10^{-4}	86	13.6
	Raw radius	2.53×10^{-4}	72	20.0
	Smoothed radius	2.35×10^{-4}	78	20.7
	Filtered radius	2.5×10^{-4}	74	20.6
Step2 Δq = 70 kPa	$\varepsilon_v = 0$	5.24×10^{-4}	65	12.4
	Raw radius	6.32×10^{-4}	48	18.9
	Smoothed radius	6.0×10^{-4}	51	19.4
	Filtered radius	6.28×10^{-4}	49	19.2

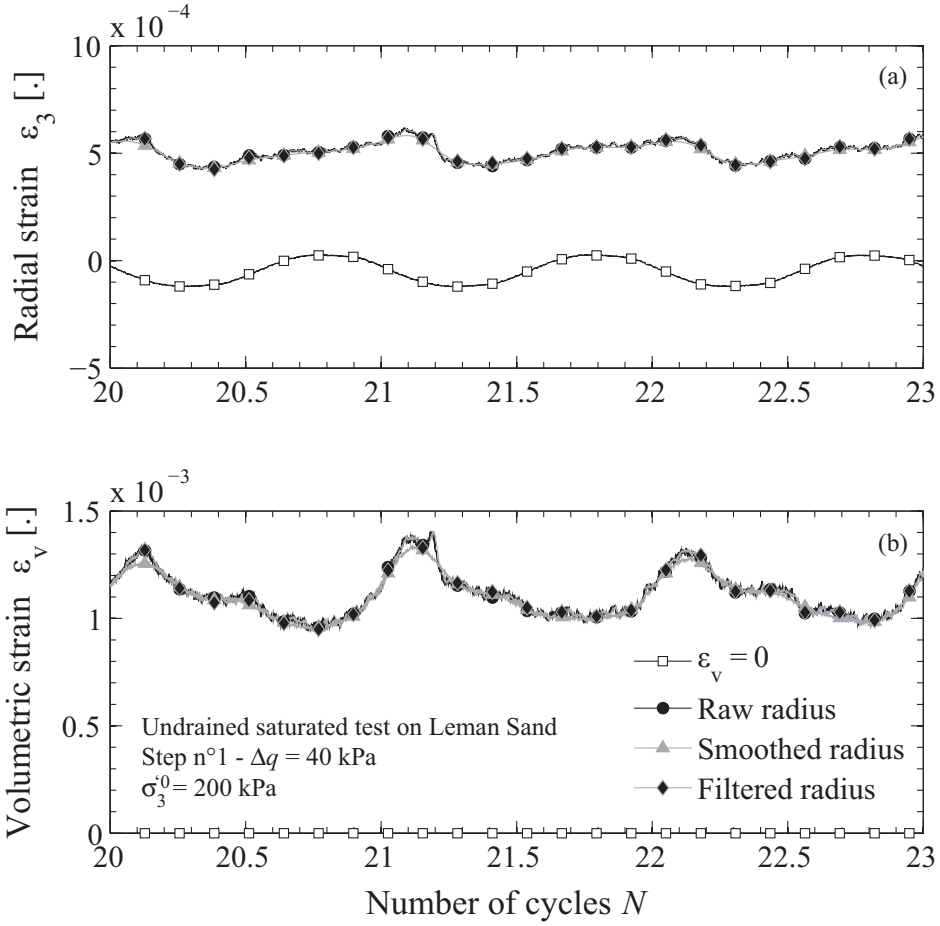

Fig. 4.36. Details of the radial and volumetric strains of Leman Sand for the evaluation of laser measurement (step 1).

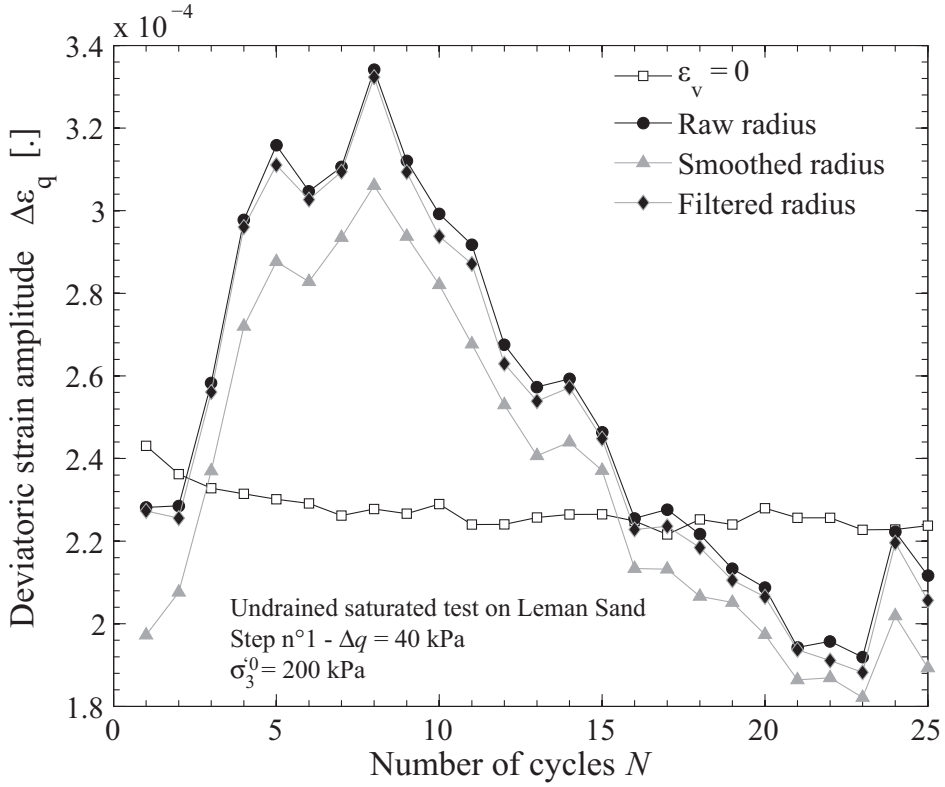

Fig. 4.37. Leman Sand deviatoric strain amplitude of step 1 for the evaluation of laser measurement.

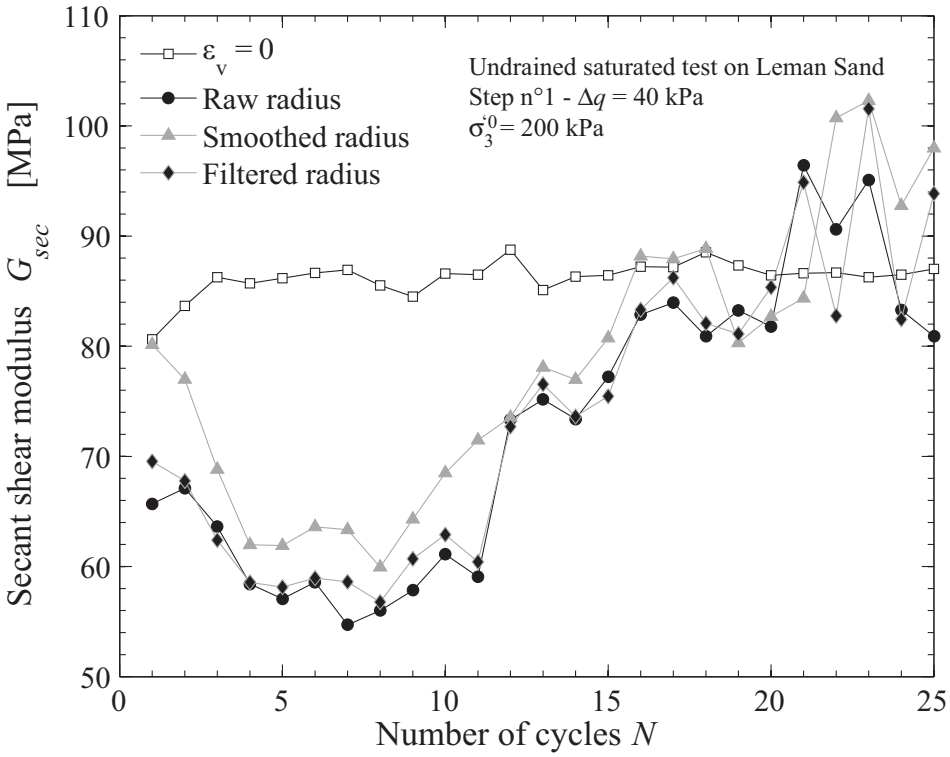

Fig. 4.38. Leman Sand secant shear modulus of step 1 for the evaluation of laser measurement.

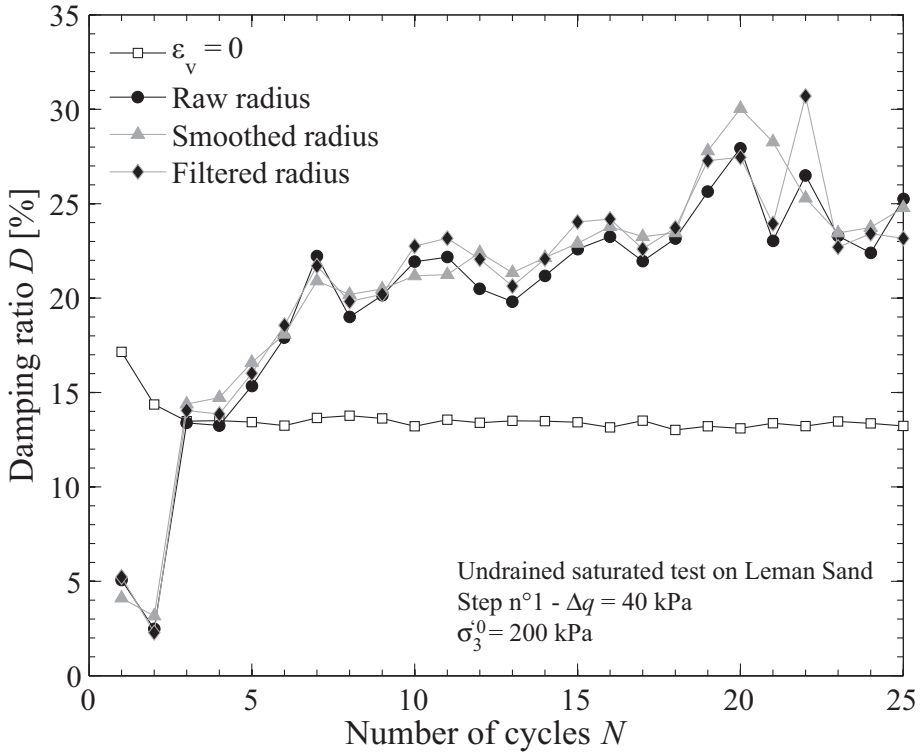

Fig. 4.39. Leman Sand damping ratio of step 1 for the evaluation of laser measurement.

4.6.4 Conclusions

The strain range clearly influences the accuracy of test results calculated with local radial strain. Above $\Delta\varepsilon_q = 10^{-3}$, the stiffness degradation of the sample is well captured by the laser sensors. Below that value, an averaging is suitable. Compared to the hypothesis of no volumetric strain, radial strains obtained with a smoothed radius give the best results for the deviatoric strain and the secant shear modulus. The damping ratio seems overestimated by the laser measurement of radial strain, compared to the usual calculation procedure. Moreover, it is reminded that the uncertainty on laser measurement is lower for dry sand compared to undrained sand, because membrane penetration effect is more important when the effective confining pressure changes (cf. Chapter 3). The evaluation of radial strain for dry tests is thus expected to be at least as good as the results presented in this section, and probably better.

4.7 Dry cyclic triaxial tests on Leman Sand

4.7.1 Introduction

To fully characterize Leman Sand behaviour under cyclic loading in the non-linear regime, complementary tests were performed on dry sand. Their characteristics are summarized in Tab. 4.10. At first, a typical test is presented in detail. Then all test results are analysed to get an overview of the nonlinear behaviour of dry Leman Sand. Upon cyclic loading at sufficiently large deviatoric stress amplitude, there is accumulation of plastic deviatoric and volumetric strains, which are analysed below. Qualitatively, dry behaviour, in terms of failure and dynamic parameters, is shown to depend on initial conditions in the same way as undrained test results.

Tab. 4.10. Summary of dry cyclic CTC-RTE tests on Leman Sand*

N°	Test description	Date	Void ratio	$\sigma_3'^0$ [kPa]	q_{av} [kPa]	Δq [kPa]
DRY1	Cyclic dry stress-controlled CTC-RTE	18/12/08	0.48-0.49	200	0	40, 70, 100, 130, 160.
DRY2	Cyclic dry stress-controlled CTC-RTE	25/02/09	0.52	100	0	40, 70, 100.
DRY3	Cyclic dry stress-controlled CTC-RTE	26/02/09	0.51-0.52	100	100	40, 70, 100, 130, 160, 190.
DRY4	Cyclic dry stress-controlled CTC-RTE	02/03/09	0.49-0.5	100	200	40, 70, 100, 130, 160, 190, 220, 250.
DRY5	Cyclic dry stress-controlled CTC-RTE	06/03/09	0.5-0.51	300	0	40, 70, 100, 130, 160, 190, 220.

(*) The loading frequency is f = 0.2 Hz. Sampling frequency is 312 Hz.

4.7.2 Presentation of a typical dry cyclic triaxial test

The test DRY1, which is the equivalent of the test CYC1 performed in undrained conditions, is presented now. This test is representative of the behaviour of Leman Sand in dry conditions. The variations of deviatoric stress (Fig. 4.40a), axial strain (Fig. 4.40b) and volumetric strain (Fig. 4.40c) are shown for the five steps selected. Upon increase of Δq during a sixth step, the sample experienced rapid failure with the formation of a shear band, that is why this step is not taken into account.

The test is performed in symmetric stress reversal conditions, with an increase by step of the cyclic stress ratio (CSR), every 25 cycles, from 0.1 to 0.41. The evolution of axial strain is different from undrained tests (e.g. Fig. 4.41). Upon increase of Δq, the cyclic amplitude increases strongly at the beginning of each step. Cyclic accommodation rapidly arises, the decrease of strain amplitude is

particularly remarkable during the fifth step. Interestingly, ε_1 is in the area of positive strains for the two first steps at small amplitudes, while it is completely on the negative side during the fifth step at large loading amplitude. For the third and fourth step, the axial strain is almost symmetric with respect to the axis $\varepsilon_1 = 0$, except for a progressive shift up towards positive values.

The volumetric strain ε_v follows a slightly different pattern, in the sense that there is volume contraction during the five steps. The cyclic amplitude of volumetric strain tends to increase when CSR increases at the beginning of each step. However, along each step, the amplitude of ε_v is almost constant, with a regular drift towards higher compression as there is accumulation of plastic volumetric strain (especially during the fifth step).

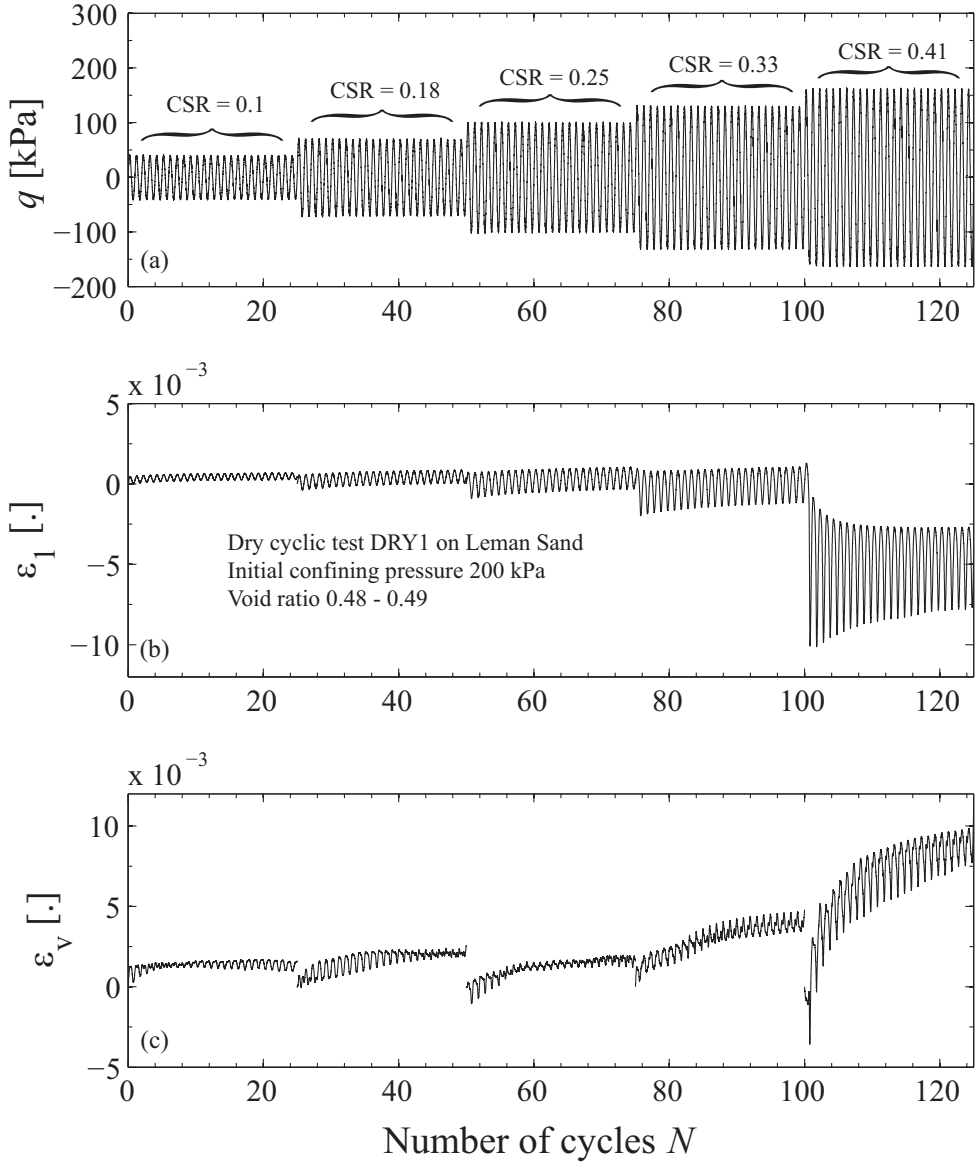

Fig. 4.40. Dry cyclic loading in DRY1, Leman Sand.

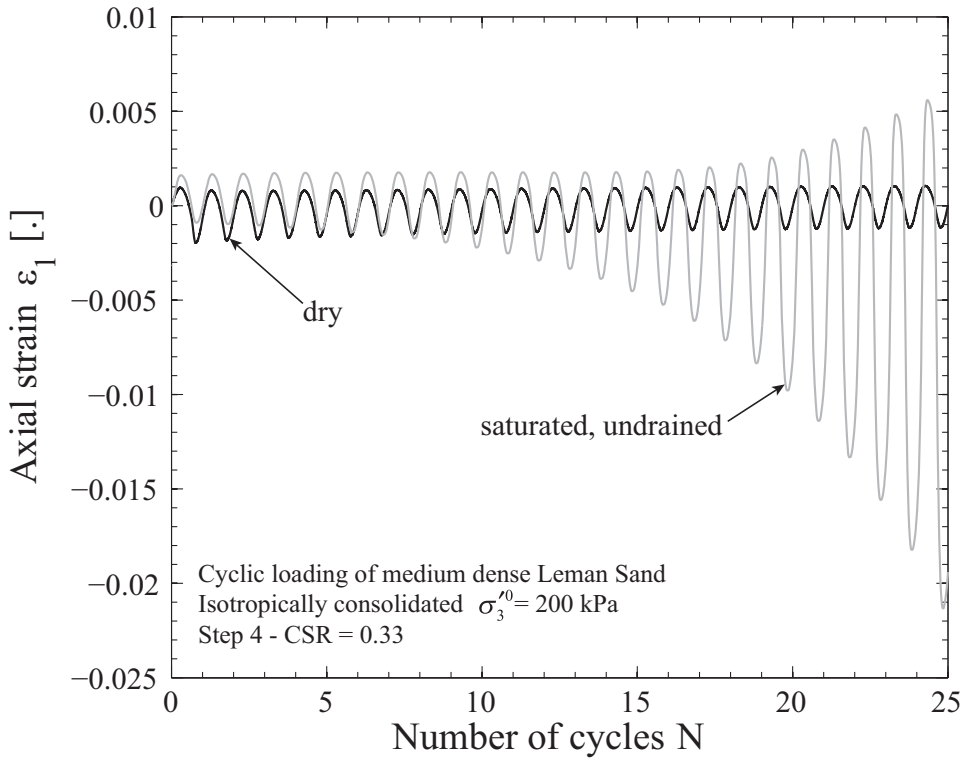

Fig. 4.41. Comparison of axial strains for dry (DRY1 test) and undrained saturated (CYC1 test) Leman Sand.

The stress-strain relation (Fig. 4.42), the volumetric strain evolution as a function of the axial strain (Fig. 4.43) and the stress path (Fig. 4.44) are given as an example for the fifth step only.

The shape of each stress-strain loop is similar to undrained cyclic loading, it is between shape 2 and shape 3 (defined in section 4.4.7), which also arise in the same strain range. There is clear accommodation of the dry sample, i.e. decrease of strain amplitude, instead of the gradual increase which arises in undrained loading. The large shift towards negative strains arises from the first cycle already. Cyclic accommodation follows, with loops which become superimposed after a few cycles. Accommodation is also clear in the ε_v - ε_1 plane. After a few large open loops, the rate of increase of the volumetric strain decreases, while the axial strain amplitude narrows. The stress path is representative of drained conditions, with an inclined straight line of slope 3.

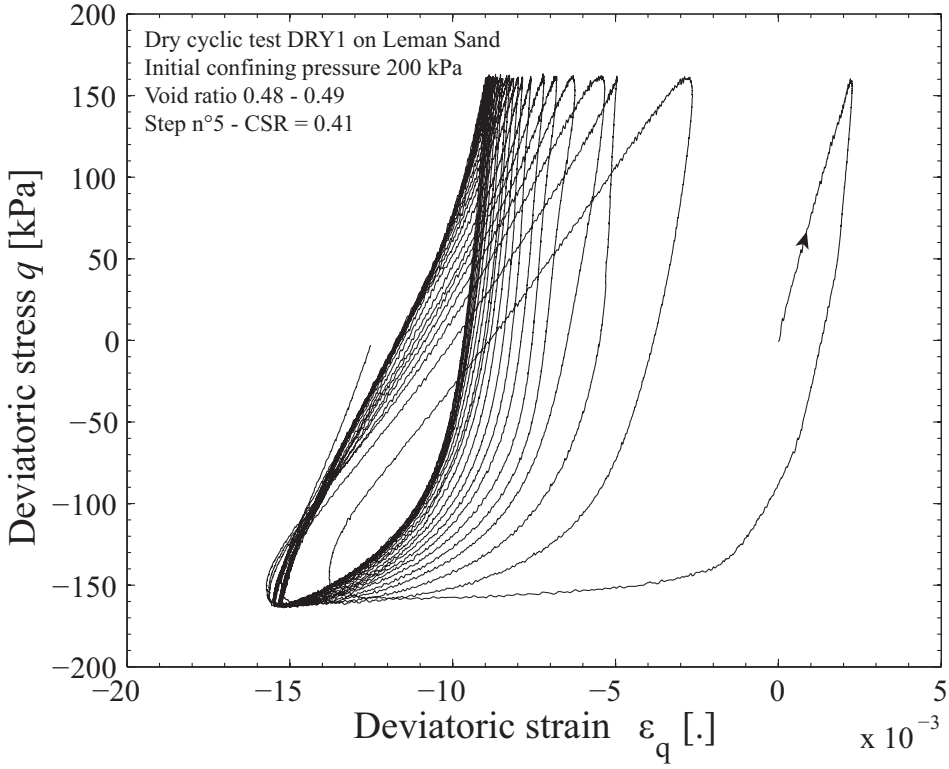

Fig. 4.42. Leman Sand stress - strain relation in dry sand at medium strain with stress reversal.

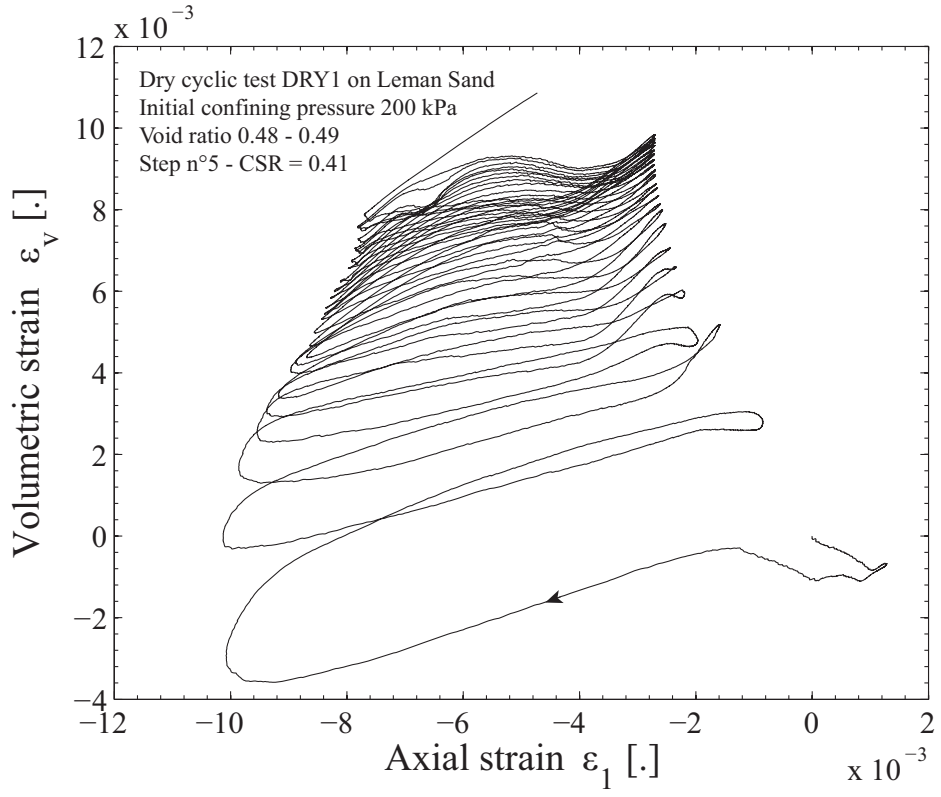

Fig. 4.43. Leman Sand volumetric strain vs. axial strain in dry cyclic condition at medium strain.

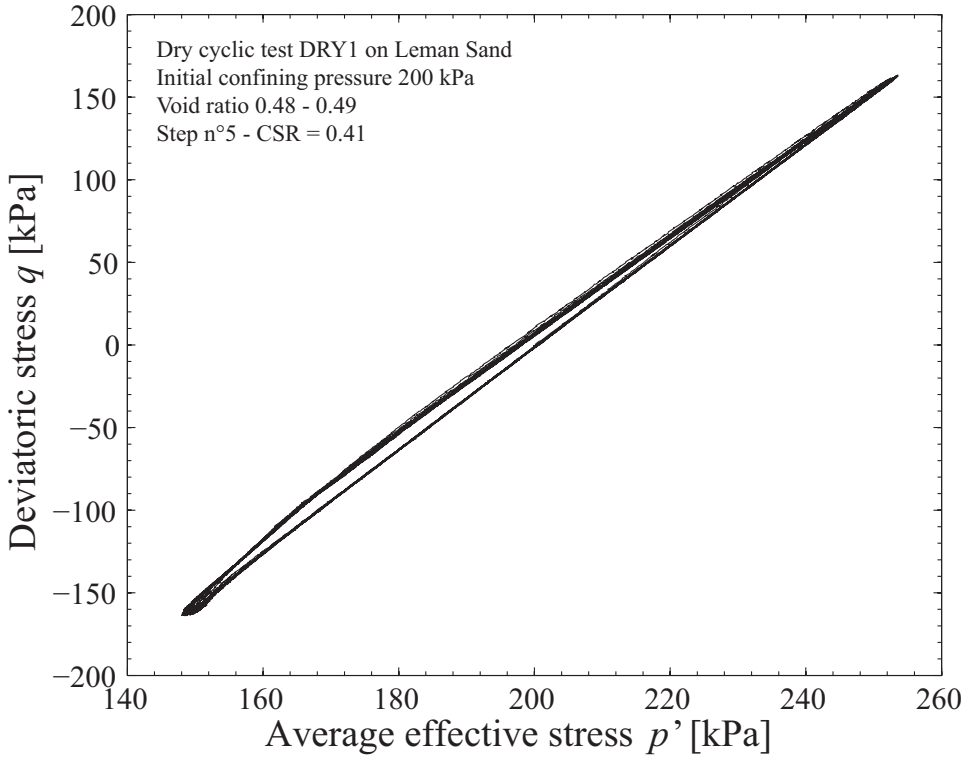

Fig. 4.44. Leman Sand stress path in dry cyclic conditions.

4.7.3 Effect of initial conditions on strain accommodation and failure

The five dry cyclic triaxial tests presented here were all performed with different initial boundary conditions. Their deviatoric strain amplitudes evolve between 2×10^{-4} and 2×10^{-2}, i.e. they correspond to medium to large strain level. For two steps, the second step of DRY3 and the third step of DRY5, the results, particularly the secant shear modulus, are absurd because of problems in the laser sensors. They are thus withdrawn from the following figures and analyses.

For $\Delta\varepsilon_q$ lower than 10^{-3}, the variations of $\Delta\varepsilon_q$ are neglected during each step, as was concluded from section 4.6, to increase the reliability of the results. In other words, the mean values on each step are given in Fig. 4.45, for the concerned steps, instead of the discrete points obtained. Thanks to that approximation, it is clear that there is a regular increase of $\Delta\varepsilon_q$ at each step, when the deviatoric stress amplitude is increased.

For $\Delta\varepsilon_q$ higher than 10^{-3}, all steps present a decrease of $\Delta\varepsilon_q$, i.e. strain accommodation develops even at medium and large strains. Compared to undrained cyclic tests, the failure threshold is not surpassed during these steps for that reason. Indeed, in undrained loading, the strain amplitude rapidly increases once excess pore pressure develops and the average effective stress decreases. On the contrary, in dry tests, the strain amplitude decreases after large first values, also the failure threshold is not surpassed.

However, failure appears very suddenly at the beginning of the step which follows the last one presented here. For most boundary conditions, a shear band appears and strain localization prevents accurate evaluation of the stress-strain relation (more details in section 4.8).

The rate of increase of the deviatoric strain amplitude depends on initial stress boundary conditions. The soil response can be divided into three groups:

- For DRY1 and DRY3, the rate of increase of $\Delta\varepsilon_q$ with each step is almost equivalent, except that an additional step is performed for DRY3
- This rate is higher for DRY2
- It is in the same order of magnitude for DRY4 and DRY5, but slightly higher for DRY4, and lower than the previous tests.

For the tests DRY1, DRY2 and DRY3, this ranking corresponds respectively to the response of the tests CYC1, CYC2 and CYC3, which are performed undrained with the same initial stress conditions. We remind that when the confining pressure increases or when the initial deviatoric stress increases, less deviatoric strain develops. The addition of the two other tests confirms that trend.

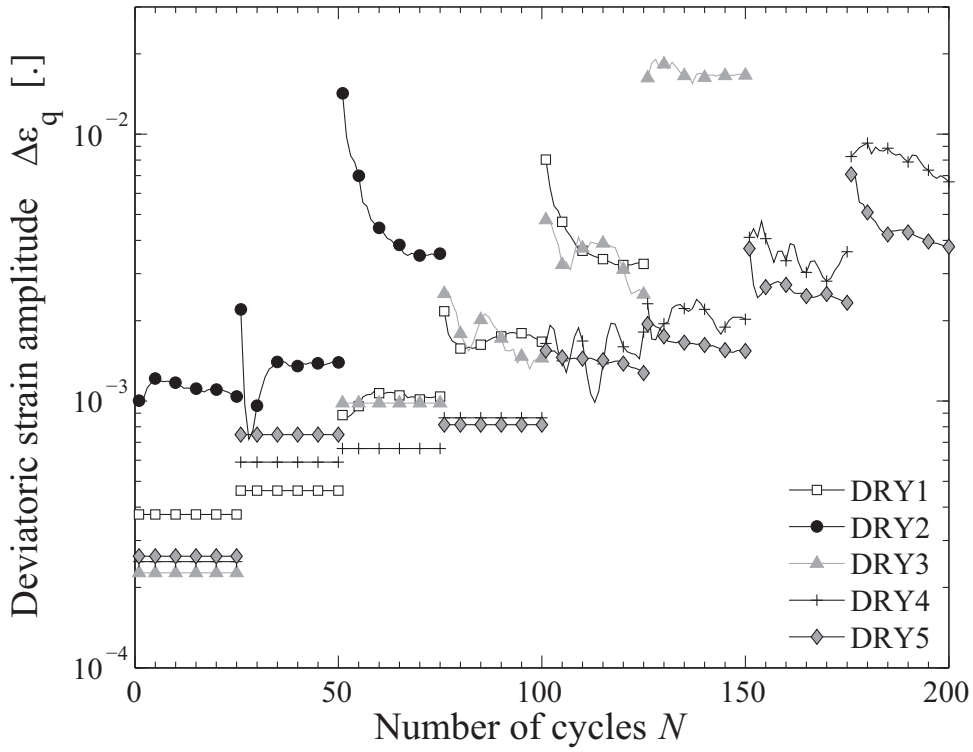

Fig. 4.45. Leman Sand deviatoric strain amplitude vs. number of cycles.

4.7.4 Volumetric behaviour

As an analogy to the deviatoric strain amplitude, a volumetric strain amplitude $\Delta\varepsilon_v$ is calculated for each cycle. It is the half value of the difference between the maximum and the minimum points of ε_v for each cycle. The averaging criterion is applied to $\Delta\varepsilon_v$: whenever $\Delta\varepsilon_q$ is averaged over a step, the mean value of $\Delta\varepsilon_v$ is taken as well. The values obtained range from 2×10^{-4} to 7×10^{-3}.

The evolution of $\Delta\varepsilon_v$ is presented first as a function of the number of cycles (Fig. 4.46). There is still a regular increase of $\Delta\varepsilon_v$ when Δq increases at each step, but with more discrepancy than $\Delta\varepsilon_q$. Strain accommodation is also visible for $\Delta\varepsilon_v$, particularly for the last steps of each test at large amplitude.

The comparison of tests with different initial boundary conditions, previously described for $\Delta\varepsilon_q$, are still valid, i.e. the rate of increase of $\Delta\varepsilon_v$ is stronger for DRY2, is intermediate for DRY1 and DRY3 and it is lower for DRY4 and DRY5. The effect of confining pressure on nonlinear sand behaviour is thus confirmed in dry conditions:

- the rate of $\Delta\varepsilon_v$ decreases clearly between DRY2, DRY1 and DRY5 with an increasing confining pressure of 100, 200 and 300 kPa, respectively.
- the rate of $\Delta\varepsilon_v$ also decreases clearly between DRY2, DRY3 and DRY4 with an increasing mean deviatoric stress q_{av} of 0, 100 and 200 kPa, respectively.
- the increase of the confining pressure or the mean deviatoric stress prevents volumetric deformations of dry Leman Sand in a similar way, for this range of initial conditions.

The increase of the volumetric strain amplitude as a function of the deviatoric strain amplitude is presented in Fig. 4.47. The envelope surrounding all curves is similar to the area delimited in undrained loading for the pore pressure ratio (Fig. 4.18). The analogy also relies on the fact that the initial conditions do not tend to influence the volumetric response, which may be only controlled by the deviatoric strain amplitude. The effect of the number of cycles is less marked than for undrained conditions, maybe because of higher discrepancy in the results.

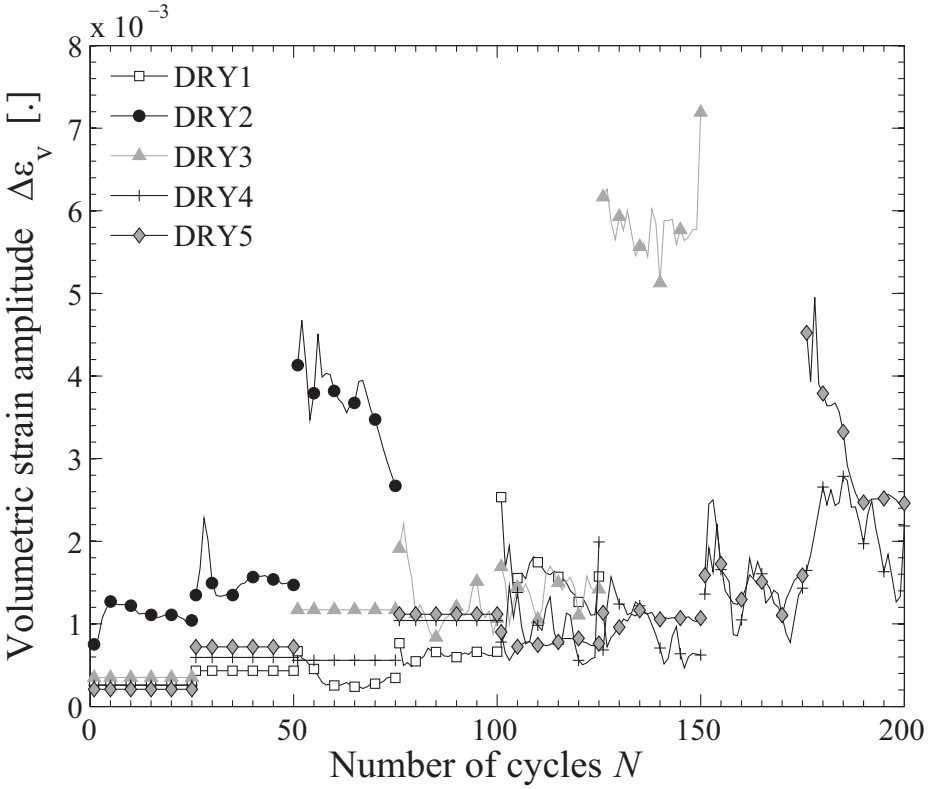

Fig. 4.46. Leman Sand volumetric strain amplitude vs. number of cycles.

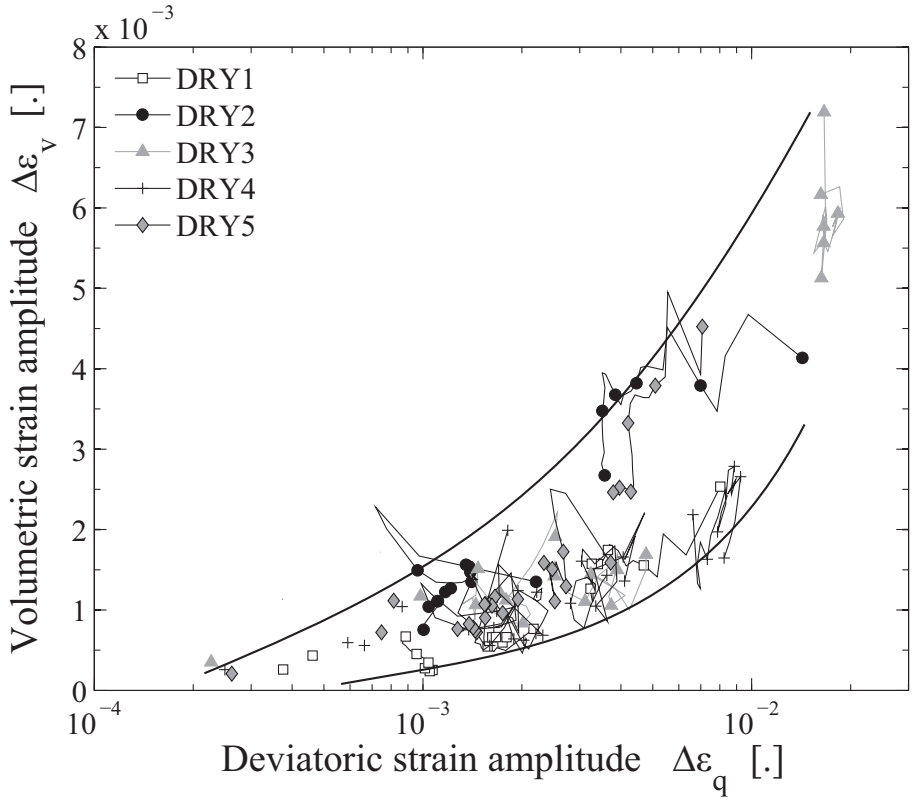

Fig. 4.47. Leman Sand relation between volumetric strain and deviatoric strain.

4.7.5 Secant shear modulus

The secant shear modulus is also averaged for $\Delta\varepsilon_q < 10^{-3}$. G_{sec} ranges from 3 MPa to almost 100 MPa, depending on the loading conditions (Fig. 4.49). Two competing phenomenon influence the evolution of G_{sec} with the number of cycles: (i) at the beginning of each step (every 25 cycles), Δq increases thus increasing $\Delta\varepsilon_q$ which decreases G_{sec} (ii) along each step, accommodation occurs as an increase of G_{sec}. The decrease of stiffness at different steps is progressive and even, and depends on initial boundary conditions: the higher q_{av} or $\sigma_3'^0$, the higher the secant shear modulus. On the other hand, accommodation phenomenon appears, even at large strains, as the secant shear modulus tends to increase during each step. This accommodation effect of the number of cycles on the secant shear modulus of dry sand is similar to the results reported in the literature review (Ray & Woods 1988; Li &Yang 1998).

The stiffness degradation curve is presented in Fig. 4.49. The same value of G_{max} as undrained tests is taken, assuming that the hydraulic condition does not have too much influence at such strains. The comparison with Seed et al. (1986) still holds, but dry G_{sec} / G_{max} are within a larger area than the reference values. For DRY4 at the highest q_{av} = 200 kPa, G_{sec} / G_{max} plots the highest at any deviatoric strain amplitude. Just below, there is DRY3, with q_{av} = 100 kPa. Then for the same value q_{av} = 0 kPa, the three other tests DRY1, DRY2 and DRY5 are ranked with respect to the initial confining pressure, with an increase of G_{sec} / G_{max} with $\sigma_3'^0$ at all deviatoric strain amplitudes.

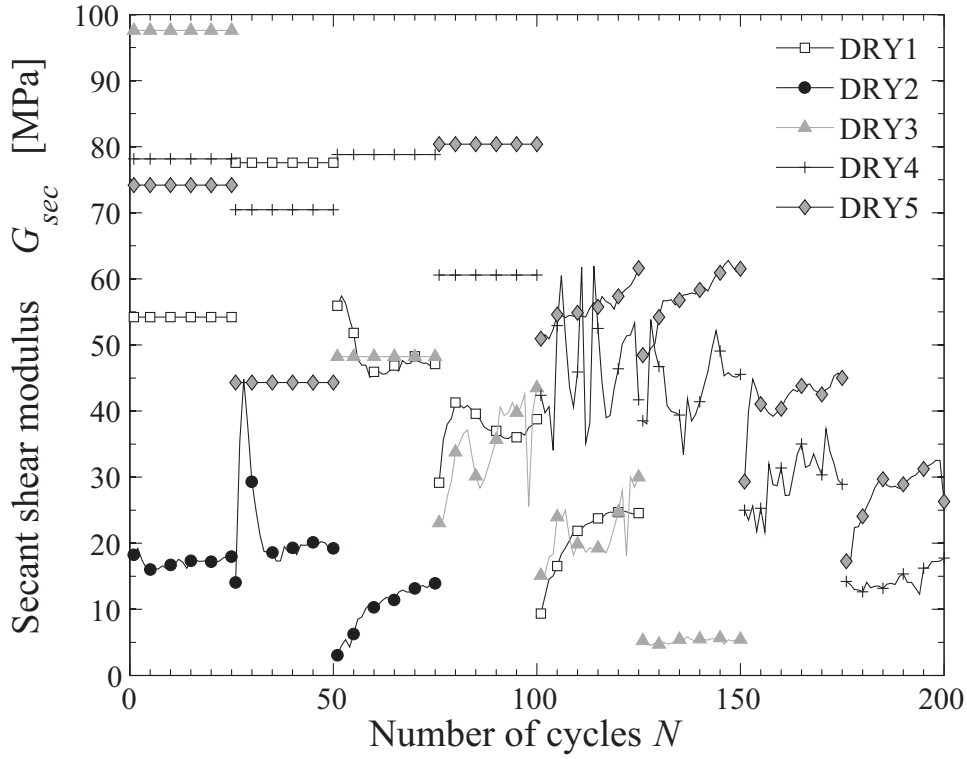

Fig. 4.48. Secant shear modulus of dry Leman Sand.

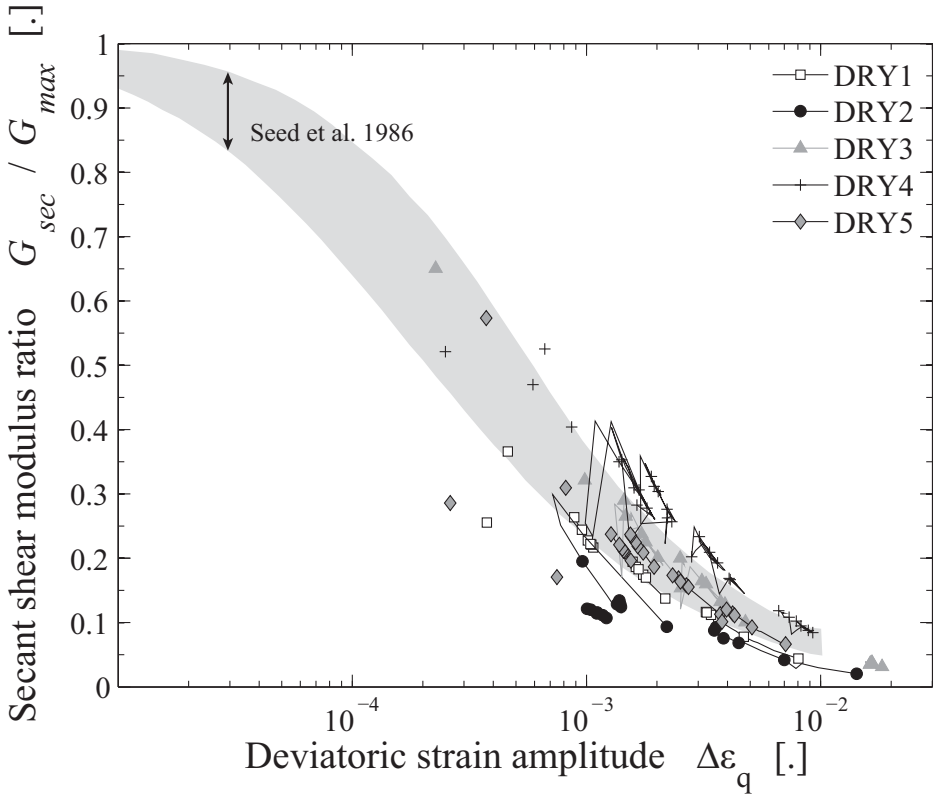

Fig. 4.49. Stiffness degradation curve of dry Leman Sand.

4.7.6 Comparison with undrained test results

Simplified curves of the secant shear modulus ratio are drawn in Fig. 4.50, in order to compare the nonlinear sand behaviour in dry and undrained conditions at medium to large strains.

It is first noticeable that the secant shear modulus ratio is higher for dry tests, though it was shown that the measurement of the secant shear modulus is slightly underestimated with the laser sensors (Tab. 4.9). There is almost coincidence between DRY2 and CYC2 in similar initial stress conditions. For the other pairs of tests DRY1 and CYC1 or DRY3 and CYC3, there is a noticeable difference below $\Delta\varepsilon_q = 5 \times 10^{-3}$, but then the paired curves clearly converge. At medium strains, the difference between dry and undrained stiffness degradation depends on boundary conditions: the distance increases with q_{av} (comparison of tests numbered 1 and 3), and increases with $\sigma_3'^0$ (comparison of tests numbered 1 and 2).

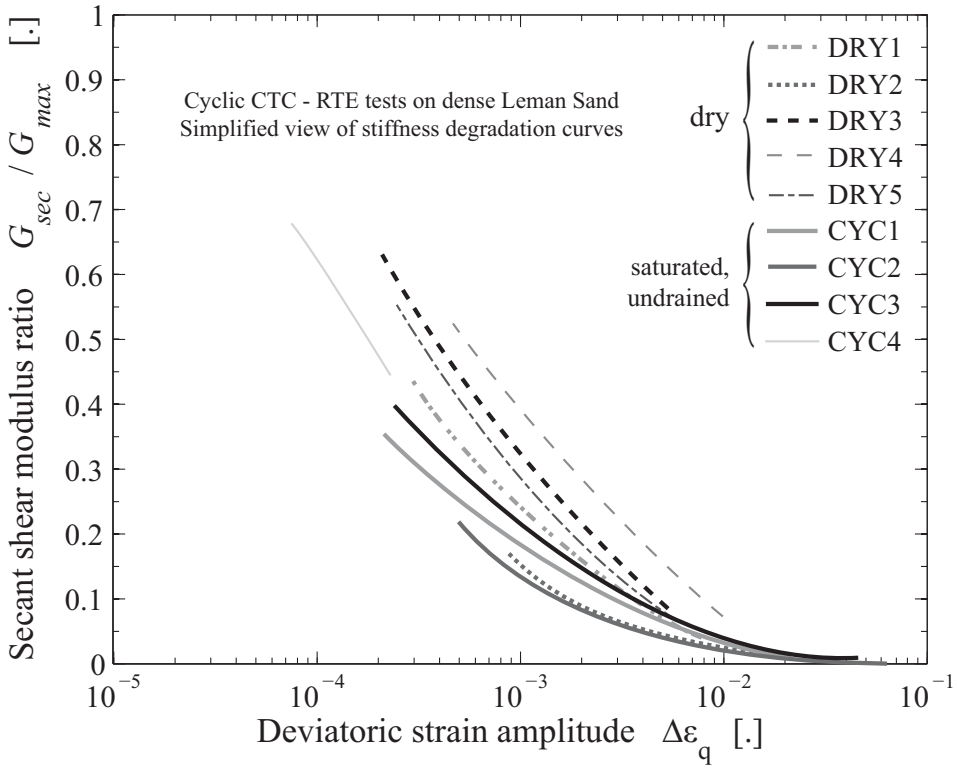

Fig. 4.50. Simplified stiffness degradation curves for dense dry and undrained Leman Sand.

4.7.7 Damping ratio

As for all other dry test parameters presented above, we use the averaging criterion for calculating damping ratio of dry cyclic tests. The values of damping shown in Fig. 4.51 correspond to the 5th and 20th cycles of each step; below $\Delta\varepsilon_q = 10^{-3}$, only the 20th value appear because damping is averaged over the step.

The damping ratio may be overestimated by the measurement of volumetric strain by the laser sensors (section 4.6). However, the points representative of most dry cyclic tests are within or below the limits provided by the reference curves of Seed et al. (1986).

Contrary to undrained sand behaviour of both Leman and Fonderie Sand, there seem to be no peak of the D - $\Delta\varepsilon_q$ curves in dry conditions. Moreover, damping ratio values are higher at the 5th cycle than the 20th cycle for most cases. These two facts are attributed to accommodation, previously described for dry sand behaviour; they are opposite to the damping ratio evolution of undrained sand.

Compared to Leman Sand damping ratio of undrained tests (in grey on Fig. 4.51 for the 20th cycle), dry damping ratios are in the same range at medium strain range, and they are higher from $\Delta\varepsilon_q = 5 \times 10^{-3}$.

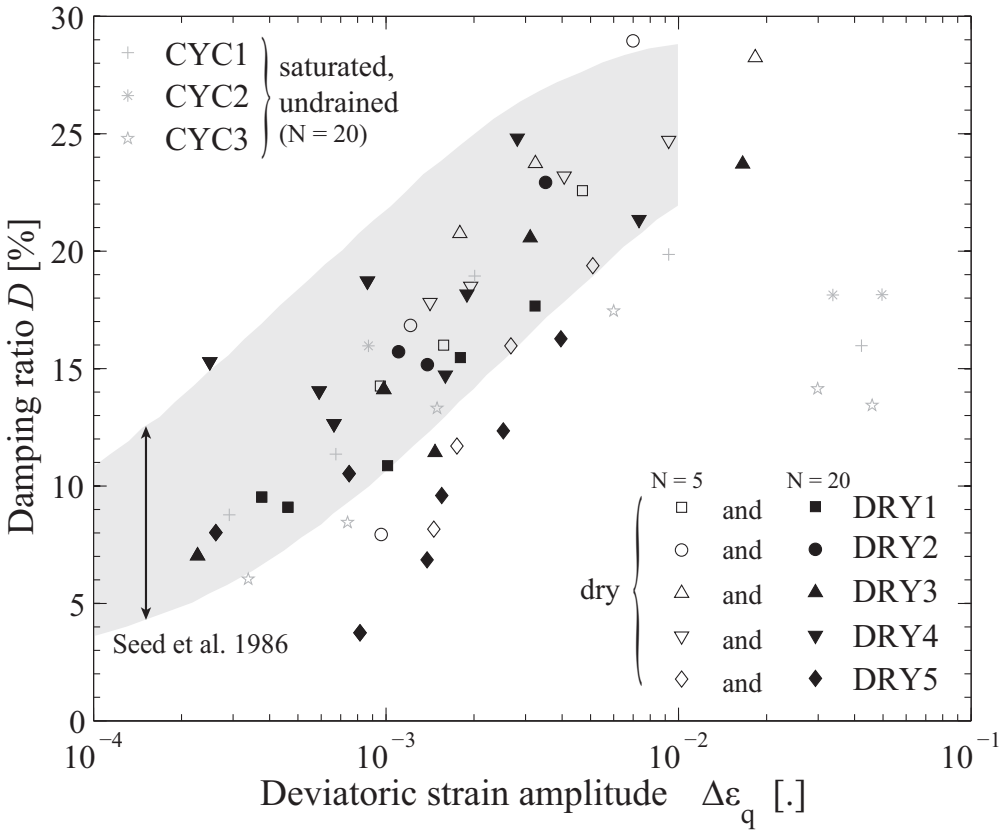

Fig. 4.51. Damping ratio vs. deviatoric strain amplitude for dry and undrained Leman Sand.

4.7.8 Induced anisotropy

The dynamic parameters calculated in the thesis all result from the assumption of an isotropic material. Although, the method of deposition may involve initial anisotropic arrangement of the granular matrix, and the cyclic loadings may cause stress-induced anisotropy. This could result in significant difference between the vertical and horizontal moduli. The dry test result DRY1 is used to verify that the isotropic assumption remains valid along the test.

Elastic transverse anisotropy can be characterized thanks to triaxial tests by three coefficients, E^* (which is equal to E_v, the vertical Young's modulus), ν^* and α^*, with the relation $E_h / E_v = (\alpha^*)^2$ (Muir Wood 1990). Moreover, the anisotropic secant shear modulus can be deduced from these three parameters. When $\alpha^* = 1$, the medium is isotropic. For example, an anisotropic clay can be characterized by the coefficient $\alpha^* = 0.2$. When $\alpha^* < 1$, the soil is stiffer vertically.

The reloading part of the 24th cycle of the last step of DRY1 is used to calculate these parameters. We find $\alpha^* = 0.99$, which means that anisotropy is very small. Moreover, there is only 1% difference between the Young's modulus calculated with the assumption of an isotropic material (61.2 MPa) and the Young's modulus calculated with the anisotropy assumption (E_v = 61.9 MPa). There is also 1% of difference for the shear modulus. The ratio E_h / E_v is equal to 0.97.

The same procedure used for the four previous steps yields a higher value of α^*, which tends to decrease from 1.03 to 1.01 between the first and the fourth step. This is an indication of a slight effect of stress-induced anisotropy during cyclic loading. These α^*-values are sufficiently close to 1 so that anisotropy can be considered as negligible.

4.7.9 Conclusions

Many comments arise from the analyses of the dry cyclic tests on Leman Sand, and by comparing the dry tests with undrained cyclic test results from section 4.4:

- Comparing the response between the different steps, $\Delta\varepsilon_q$ increases with Δq, which is the same answer as undrained tests. Inside each step, $\Delta\varepsilon_q$ decreases, which is the contrary of what happens in undrained conditions.
- Though the loading is symmetric with respect to the stress origin in tests DRY1, DRY2, DRY5, the volumetric and deviatoric strains are not symmetric with respect to their respective origin. The volumetric strain is positive, which corresponds to plastic contraction. For deviatoric strains, the answer is more complex: they are first positive at small CSR, but they gradually become negative when CSR increases.
- Accommodation behaviour is visible during steps of constant stress amplitude (i) in ε_q - q loops, (ii) in ε_1 - ε_v loops, and for $\Delta\varepsilon_q > 10^{-3}$, (iii) in $\Delta\varepsilon_q$, (iv) in $\Delta\varepsilon_v$, (v) in G_{sec} and (vi) in D.
- The effect of initial boundary conditions is the same as undrained loading. If q_{av} or $\sigma_3'^0$ increases, $\Delta\varepsilon_q$ and $\Delta\varepsilon_v$ are smaller, while G_{sec} and G_{sec} / G_{max} are higher.

- An area limiting the relation $\Delta\varepsilon_q$ - $\Delta\varepsilon_v$ is drawn for medium to large strains. By comparison with the relation between the pore pressure increase and the deviatoric strain in undrained test results, from the literature (Dobry et al. 1982) and with the Leman Sand (section 4.4.3), this area seems independent from the boundary conditions. The effect of the number of cycles is not discernible with our equipment, contrary to undrained tests.
- Stiffness reduction curves G_{sec} / G_{max} are similar to undrained conditions, and correspond to the results from Seed et al. (1986), except that the cluster of curves lies within a slightly larger area.
- A schematic view of both dry and undrained curves G_{sec} / G_{max} confirms the effect of q_{av} and $\sigma_3'^0$. More important, it allows to compare tests with the same boundary conditions except for the hydraulic condition. For tests with the same initial q_{av} and $\sigma_3'^0$, dry tests give higher G_{sec} / G_{max} at strain amplitude below 5×10^{-3}, but dry and undrained curves converge above that threshold. The distance between dry and undrained curves depends on initial boundary conditions.
- Damping ratios of dry Leman Sand are obtained for strain amplitudes between 2×10^{-4} and 2×10^{-2}. The numerous experimental points clearly show the increase of D with strain amplitudes. Accommodation can explain the difference with undrained saturated behaviour observed for Leman and Fonderie Sand. In dry sand, even at large strain, D decreases with the number of cycles, but without the formation of the peak of the D - $\Delta\varepsilon_q$ curves.
- Induced anisotropy is evaluated for the test DRY1 and considered as negligible with only 1% difference between the moduli calculated with the assumptions of isotropic or anisotropic elasticity.

4.8 Shear strain localization in cyclic tests at large strain amplitude

4.8.1 Tests concerned

The occurrence of a shear band at large strain amplitude is first estimated by direct visual observation. Most cyclic tests with symmetric stress reversal exhibit strain localization when the axial strain becomes very low on the extension side. Monotonic tests in extension also exhibit such failure mechanism. Localization usually occurs as a clear narrowing of the diameter on a limited part of the sample height (e.g. Fig. 4.52). When this failure is witnessed, the test is stopped and no other step is added. It is noticeable that strain localization was never observed during compressive tests with no

stress reversal or with small stress reversal.

With the new triaxial cell designed for laser sensors, the visual observation is limited to the moments between the steps, in order to not disturb the laser measurements. We try to replace the lack of direct observation by an indirect evaluation thanks to laser measurements at the surface of the sample. This is the case for tests on Fonderie Sand (with only one laser) and dry tests on Leman Sand (section 4.7). For two tests with symmetric stress reversal in particular, DRY2 and DRY5, the final increase of Δq produced rapid increase of axial strains; a sudden discontinuity was recorded after a few cycles in the raw measurements of two of the three lasers. This phenomenon is presented further in section 4.8.2.

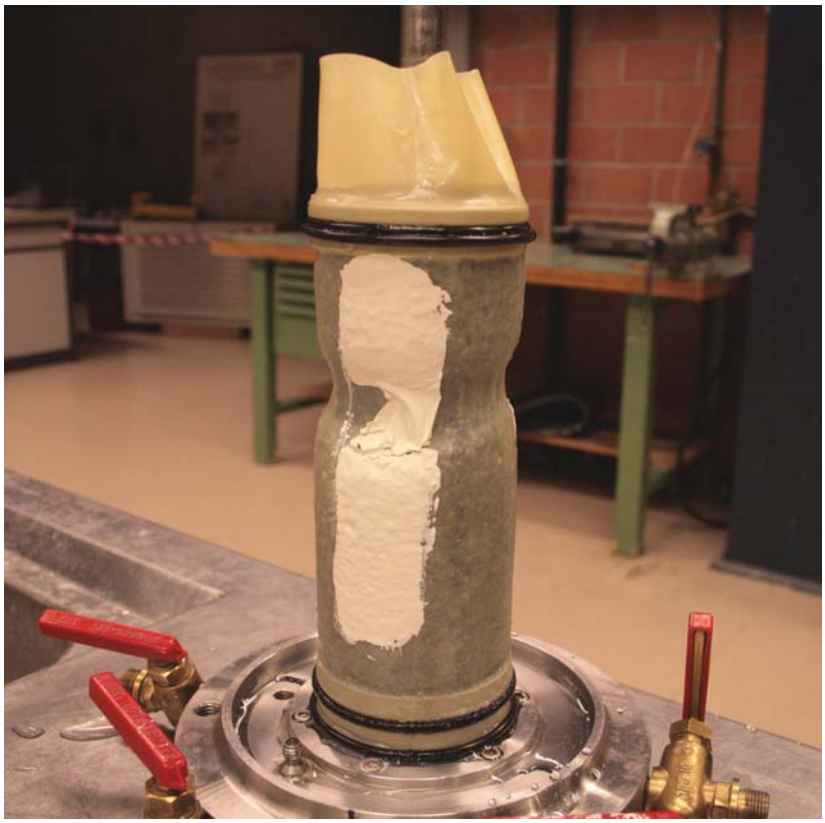

Fig. 4.52. Strain localization of a Leman Sand sample (paint layer in white for laser measurement).

For all tests concerned by strain localization, it is the very end of the last step which is questionable. When strain localization happens at the beginning of a step, this part is removed from test results. When there is a doubt whether a shear band appeared, it was mentioned in the description of test results.

4.8.2 Direct observation of shear strain localization with laser sensors

The test DRY2 is a good example of strain localization recorded by the laser measurement system. The failure point, which happens during step 4, is visible on two of the three laser measurements (Fig. 4.53). As was mentioned in section 4.7, the step of failure was not included in the analyses of test results (e.g.

strain amplitude, secant shear modulus, damping ratios, etc...) because failure arose at the second cycle already, as can be seen in Fig. 4.53.

The identification of the time of occurrence of localization (8.9 s) provides means to check that the formation of the shear band is not visible on axial strain, on the deviatoric strain, or even the radial strain.

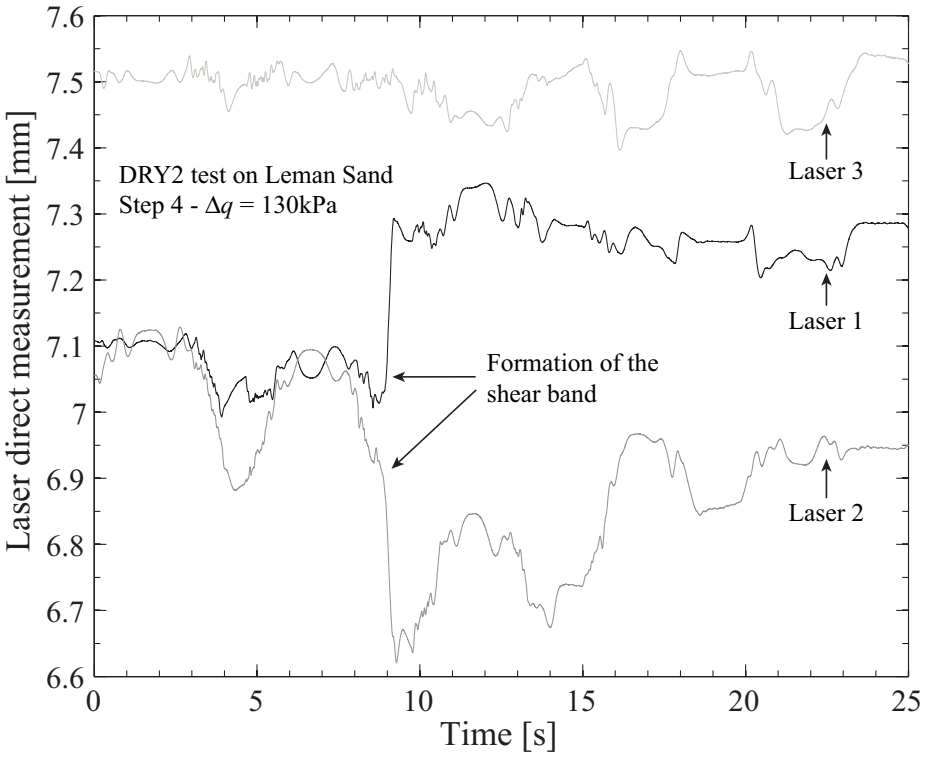

Fig. 4.53. Direct identification of the formation of a shear band with laser measurement.

4.8.3 Consequences on test results

The main visible effect of the formation of the shear band in extension is that the deviatoric strain increases drastically, above the failure threshold. When there is a very clear recording of the formation of a shear band in dry tests, it is possible to evaluate the limit strain at which the shear band appeared: it happens at ε_q = -4% and -5.3% for DRY2 and DRY5, respectively. The absolute value of the threshold strain at the apparition of the shear band might increase with the confining pressure.

At first sight, it seems fair to assume this range of values of ε_q is also a threshold for the formation of a shear band during undrained saturated tests. However, it was noticed that the increase of axial strain above the threshold $\Delta\varepsilon_q$ = 2.5% is much more sudden and faster in dry tests than in undrained tests of Leman Sand. If the failure mechanism is not really the same, the apparition and the extent of strain localization might be slightly different in undrained tests. The test data available does not provide any

recording, with the laser sensor, of the apparition of strain localization in undrained saturated tests of sands.

The final increase of the damping ratio at very large strain could be linked with the development of a shear band. For example, the final increase of the damping ratio arises for strains below ε_q = -5% in extension for test CYC2. As seen for dry tests, this value is sufficient to induce such localization, which may involve inhomogeneity in the stress and strain field.

The development of excess pore pressure ratio values above u_r = 1 seems an absurd result. However the pressure-meters were well calibrated, also these values were actually measured, at the bottom of the sample, after failure of Fonderie Sand. For example, the first large exceeding of u_r = 1 arises just after the deviatoric strain reaches a minimum at ε_q = -3.4% in extension for test FSC5. If strain localization appears at that moment, it may be associated with dilation bands (Muir Wood 2001), which would be conveyed as inhomogeneity in the pore pressure field. Moreover, preferential paths of pore fluid displacement may form within the sample. There are direct experimental evidences of local variations of the density within sand samples sheared at large strains (Muir Wood 2007). Even if critical state has not been reached, such inhomogeneity may also have appeared within cyclically sheared Leman Sand samples.

4.8.4 Conclusions

Shear strain localization, and the formation of inhomogeneity within the sample, is not suitable for a correct evaluation of sand behaviour. The occurrence of such phenomenon is only related to isotropically consolidated tests with symmetric stress reversal in the strain range and confining pressures tested for our experimental studies. The observation of direct recordings from the three lasers in dry tests shows that a clear discontinuity appeared on two of the three time histories, at the beginning of the large increase of deviatoric strains. This discontinuity occurs above the threshold deviatoric strain failure criterion, around ε_q = 4 to 5%. Strain localization may (i) depend on confining pressure, (ii) depend on the hydraulic conditions, and (iii) be responsible for large increase of the damping ratio and the excess pore pressure ratio.

4.9 Summary

Many monotonic and cyclic CTC-RTE tests on Leman Sand and Fonderie Sand were performed in the nonlinear regime. Phase transformation lines and steady state lines, in extension and compression, were obtained from the undrained monotonic tests. The different cyclic tests presented here provide deep insight into stiffness degradation of both sands, until failure. At large strain, the occurrence of cyclic liquefaction or flow liquefaction was observed, depending on the soil tested.

Preliminary cyclic tests demonstrated the importance of sample preparation, and in particular a special care was then devoted to get fully saturated samples. These tests also showed the importance of initial conditions and boundary conditions on the nonlinear soil response. These conclusions allowed to perform undrained saturated tests on Leman and Fonderie Sand with stiffness degradation and failure. Dry cyclic tests on Leman Sand were also performed and compared to the undrained response. The conclusions of the cyclic tests are now summarized.

- ***Effect of initial and boundary conditions***

The effect of boundary conditions, i.e. the average deviatoric stress and the initial confining pressure, is the same in undrained saturated and dry loading of Leman Sand: if q_{av} or $\sigma_3'^0$ increases, $\Delta\varepsilon_q$ and $\Delta\varepsilon_v$ (dry test) or u_r (undrained test) decrease, while G_{sec} and G_{sec} / G_{max} increase and the damping ratio of undrained Leman Sand decreases.

When the loading is symmetric with respect to the stress origin (isotropically consolidated sample) in tests CYC1, CYC2, DRY1, DRY2, DRY5 on Leman Sand and for all tests on Fonderie Sand, the deviatoric strains are not symmetric with respect to the origin. This different behaviour in compression and extension is significant in the stress - strain relations and the stress paths. It reflects well the difference of phase transformation angles in extension and compression for both sands.

- ***Volumetric behaviour of granular soils and pore pressure increase***

Excess pore pressure of undrained saturated Leman Sand increases from the threshold $\Delta\varepsilon_q = 10^{-4}$ and depends mainly on the strain amplitude. The number of loading cycles N also influences the pore pressure increase, in the sense that several curves $\Delta\varepsilon_q$ - u_r are obtained for the different values of N. They form a narrow band, which is also similar for undrained Fonderie Sand, although slightly higher pore pressures are obtained in the narrow-graded sand. A similar area surrounds the relation $\Delta\varepsilon_q$ - $\Delta\varepsilon_v$ for medium to large strains in dry tests on Leman Sand.

- ***Stiffness degradation***

Undrained saturated tests exhibit stiffness degradation during continuous cyclic stress-controlled

loading. When the stress amplitude is large enough (the threshold depends on initial and boundary conditions), the deviatoric strain amplitude increases, either regularly with Leman Sand, or more suddenly with Fonderie Sand. The pore pressure ratio, which is coupled to the deviatoric strain via the $\Delta\varepsilon_q$ - u_r curves, accordingly increases.

Stiffness degradation curves, i.e. the secant shear modulus and damping ratio as a function of the deviatoric strain amplitude, were obtained for saturated Leman and Fonderie Sand. Their small strain secant shear moduli were evaluated by cross-checking empirical equations for sands and cyclic test results at small to medium strain. The $\Delta\varepsilon_q$ - G_{sec} / G_{max} curves are thus obtained in the medium to large strain domain. The $\Delta\varepsilon_q$ - D curves of both sands exhibit a peak at deviatoric strains from 0.3 to 1%, which is linked with the occurrence of dilative behaviour and the banana shape of the stress-strain loops. Furthermore, we showed that the damping ratio of Leman Sand evolves with the number of cycles.

On the contrary, accommodation behaviour prevails in dry tests during steps of constant stress amplitude Δq. Stiffness degradation then occurs thanks to the increase of Δq every 25 cycles. The curves G_{sec} / G_{max} vs. $\Delta\varepsilon_q$ are similar in dry and undrained conditions, and correspond to the results from Seed et al. (1986), except that the cluster of curves lies within a slightly larger area for dry tests. Comparing tests with the same initial average deviatoric stress and confining pressure, dry conditions induce higher G_{sec} / G_{max} than undrained conditions at strain amplitude below 5×10^{-3}; dry and undrained curves converge above that threshold.

- ***Failure***

Sample failure of medium dense saturated undrained Leman Sand arises by cyclic liquefaction. The material softens, and its degradation index reaches very low values. The failure criterion can be based on a threshold deviatoric strain $\Delta\varepsilon_q$ = 2.5%. It matches the level of the degradation index well, which can thus be used as an alternative criterion for failure. Another candidate can be the pore water pressure ratio.

Three different behaviours are obtained with regard to failure in Fonderie Sand: the denser material exhibits accommodation, the slightly less dense sample exhibits cyclic liquefaction while the rest of the medium-dense samples exhibit failure which resembles flow liquefaction. At the same relative density, the increase of deviatoric strain upon loading is very progressive and stable for Leman Sand, while it is sudden, rapid and induces instability of the motion control system for Fonderie Sand. Fonderie Sand samples exhibit inhomogeneity above failure, especially concerning excess pore pressure which dramatically increases above 1 due to end-restraint and strain localization.

The different behaviours of Leman and Fonderie Sand is ascribed to their respective particle shape and grain size distribution, which both induce higher liquefaction susceptibility of Fonderie Sand. For both sands, the phase transformation line in extension is touched first, and most of deviatoric strains arise on the side of negative strains.

Failure of dry tests on Leman Sand is not shown because it arises brutally at the beginning of a new step, thanks to accommodation of dry samples. However, the behaviour of dry sand close to failure is analysed through the comments developed around the formation of a shear band at very large strain.

Shear strain localization, and the formation of inhomogeneity within the sample, violate the assumption of homogenous state of stress and strain in the sample. The occurrence of such phenomenon is only related to isotropically consolidated tests with symmetric stress reversal in the strain range and confining pressures tested for our experimental studies.

The observation of direct recordings from the three laser sensors in dry tests shows that a clear discontinuity appeared on two of the three time histories, at the beginning of the large increase of deviatoric strains. This discontinuity occurs above the threshold deviatoric strain failure criterion, around ε_q = 4 to 5%. Strain localization seems to (i) depend on confining pressure, (ii) depend on the hydraulic conditions, and (iii) be responsible for large increase of the damping ratio and the excess pore pressure ratio.

- ***Validation of the sample radius measurement by laser sensors***

The laser sensors used for measuring radial strains were calibrated and validated with various techniques presented in Chapter 3. The final validation of the laser sensors, presented in section 4.6, is based on the assumption of no volumetric strain during undrained loading of Leman Sand. Above $\Delta\varepsilon_q = 10^{-3}$, the stiffness degradation of the sample is well captured by the laser sensors. Below that value, an averaging is suitable.

Compared to the assumption of no volumetric strain, radial strains obtained with a smoothed radius give the best results for the deviatoric strain and the secant shear modulus. The damping ratio seems overestimated by the laser measurement of radial strain. As the uncertainty on laser measurement is lower for dry sand compared to undrained sand, the evaluation of radial strain for dry tests is expected to be at least as good as the results obtained for undrained saturated sand.

CHAPTER 5

FREQUENCY EFFECTS IN LEMAN SAND

5.1 Introduction

Rate effect in granular materials may result from viscosity, dynamic effects, coupling between the soil matrix and the pore fluid (section 2.7). In cyclic loading, sand was proved to exhibit frequency-dependence, with or without the pore water saturating the granular matrix. Most experimental studies reported in the literature showed that the damping ratio tends to increase with the frequency in the earthquake frequency range. For the same frequencies (f), the results are less clear for the secant shear modulus (G_{sec}), but it seems that G_{sec} slightly increases with f. Laboratory testing of undrained frequency-dependence of sand at medium strain range is poorly referenced. However, numerical approaches of this problem showed that the frequency-dependence can be important, in particular it influences the results on site effect analysis.

To our knowledge, laboratory testing of frequency effect on cyclic sand behaviour at medium and large strains and in the earthquake frequency range was never performed with a triaxial apparatus. The challenge is to combine strong loadings together with the precise measurement of small variations in the soil response.

We saw, in Chapter 4, that Leman Sand behaves in a very stable way at medium to large strains, compared to Fonderie Sand. This particular behaviour allowed us to perform tests in this strain range without inducing critical failure, and at different frequencies for the same sample. The effect of frequency (also called rate effect, cf. section 2.7) on the pore pressure ratio, deviatoric strain amplitude, dynamic parameters can thus be observed.

All tests presented in Chapter 5 were performed on medium dense Leman Sand. First, monotonic tests at four different strain rate show that it is not possible to discern any strain rate effect in the range of strain rates involved. Then cyclic undrained preliminary tests, of the same kind as preliminary tests of Chapter 4, are presented for four different frequencies. The main results in saturated undrained cyclic conditions are then presented in section 5.4, and an equivalent test in dry conditions is presented in section 5.5.

5.2 Monotonic undrained conditions

5.2.1 Tests characteristics

Four monotonic undrained strain-controlled triaxial tests were performed at different strain rate (Tab. 5.1). Compression, in CTC conditions, is followed by an unloading and triaxial extension RTE.

There is no sign of a shear band in the curves presented below, because the part at which failure occurs in extension is not considered (cf. section 4.8). The void ratio is from 0.46 to 0.47. The strain rate ($\dot{\varepsilon}_1$) ranges from 0.03 to 0.98 %/s; there is a multiplying factor of 33 between the slower and faster test.

Tab. 5.1. Monotonic tests on Leman Sand with varying strain rate (*)

N°	Test description	Date	Void ratio	Strain rate $\dot{\varepsilon}_1$ [%/s]
MSR 1	Monotonic undrained compression	07/05/2008	0.46	0.03
MSR 2	Monotonic undrained compression	20/05/2008	0.46	0.33
MSR 3	Monotonic undrained compression	13/05/2008	0.47	0.65
MSR 4	Monotonic undrained compression	12/06/2008	0.47	0.98

(*) The initial confining pressure is 100 kPa for all tests, with a back pressure of 700 kPa.

5.2.2 Results

The stress paths of the four tests are superimposed (Fig. 5.1). The phase transformation points in compression or in extension coincide well on two lines. There is no shift between the steady state lines in compression and extension.

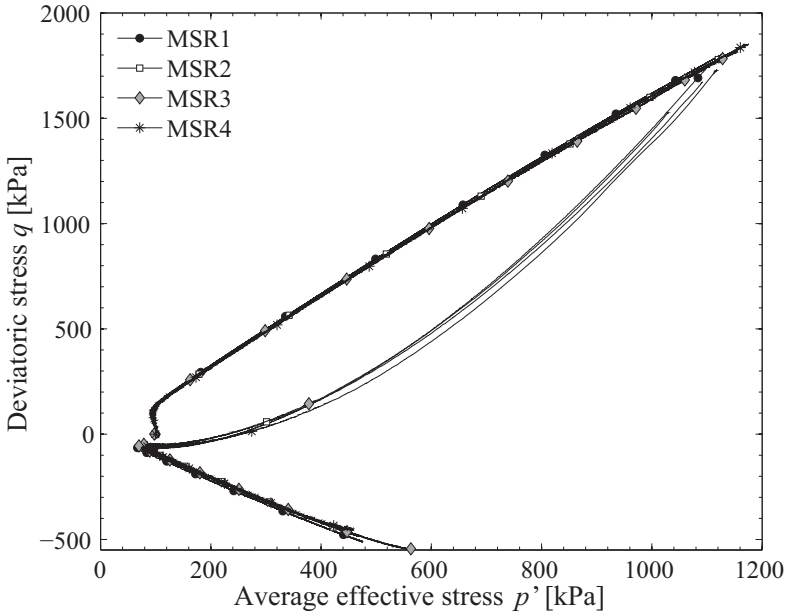

Fig. 5.1. Leman Sand effect of strain rate on the stress path (rate indicated in Tab. 5.1).

On the contrary, the stress-strain relations are not perfectly superimposed (Fig. 5.2a), but they are very similar; the difference between the four lines increases at high strain level, both in compression and extension. Considering the natural variability of test results, no sign of strain rate-dependency can be found. A comparison of the effect of the strain rate on the deviatoric stress at four axial strain levels is

found in Fig. 5.2b. It shows that the difference between the stress-strain curves is not correlated with the strain rate.

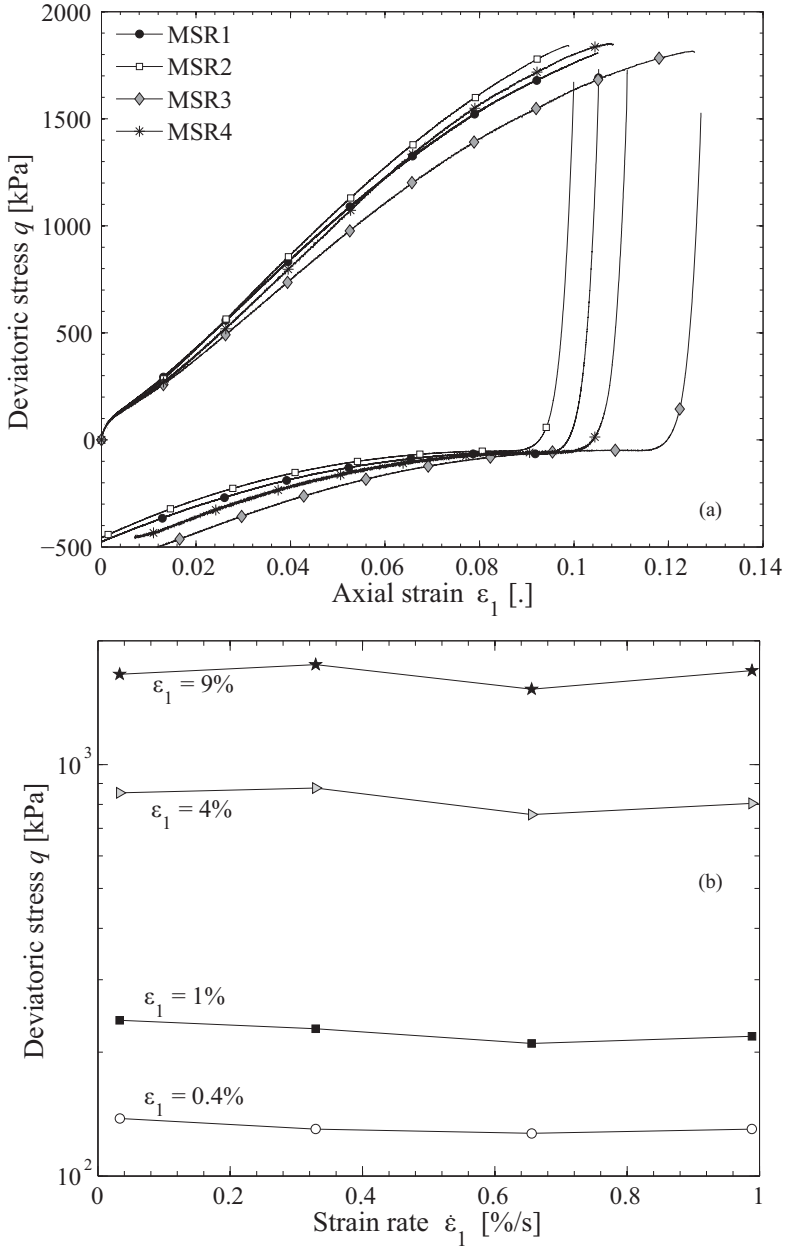

Fig. 5.2. Leman Sand effect of strain rate on the stress-strain behaviour.

In the same way, the pore water pressure ratio vs. axial strain is very similar in all four tests (Fig. 5.3) but not perfectly superimposed at large strain. The two peaks at phase transformation from contractive to dilative behaviour match well, especially in compression. The decrease of excess pore pressure is not perfectly superimposed, with a difference which increases at large strain. But the scattering is limited. Similarly to the stress-strain curve, those values are not correlated with the strain rate.

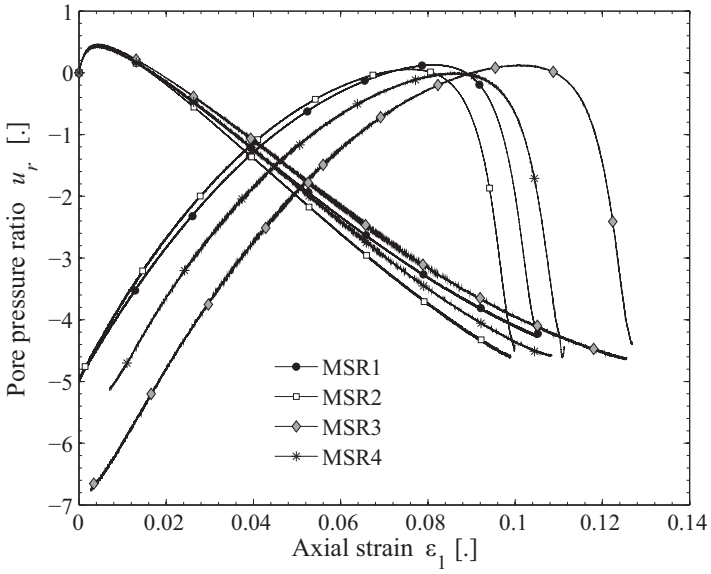

Fig. 5.3. Leman Sand effect of strain rate on the pore water pressure ratio.

5.2.3 Discussion

While the tested material is a natural sand, and the content of the samples can slightly vary, the phase transformation line and the stress path at large strains, obtained by linear regression, fit all the tests, regardless of test characteristics, strain rate, or initial confining pressure.

It is clear, from the previous descriptions, that the strain rate has no influence on the monotonic behaviour of the Leman Sand at the level of strain rates involved. The careful analysis of the results, for samples sheared at different strain rates, shows that the soil response is similar for strain rates from 0.03 to 0.98 %/s. This result confirms the usual findings on monotonic rate effect in sands, e.g. from Tatsuoka (2006) or Matsushita et al. (1999). However, the amplitude of the monotonic strain rates obtained by the equipment is limited; it could be possible to observe rate effects at higher strain rates. For example Matesic & Vucetic (2003) report a stronger strain rate effect on the compressive strength of clays for rates above 20 to 100 %/s.

While the mechanical behaviour is found to be exactly the same at small strains for all strain rates, the difference between the four responses at different strain rates increases at large strain. However, this is not correlated with any field variable but mostly scattered, maybe due to differences in grain size distributions between the sand samples.

5.2.4 Conclusions

There is no strain rate effect from the monotonic loading of Leman Sand for strain rates from 0.03 to 0.98 %/s. The slight variations of the stress-strain relation and the pore pressure ratio vs. axial strain are

thought to be linked with variations of the grain size distribution of individual samples.

These strain rates are much smaller than what can be observed in strong earthquakes. For example, the maximum velocity in the monotonic tests is close to 0.15 cm/s, while the recordings of Loma Prieta earthquake (1989) exhibit a peak velocity at the soil surface of about 40 cm/s (Kramer 1996). This limitation of the capability of the device disappears for cyclic loading, where frequencies in the range of earthquake frequency-content can be reached. The following laboratory results on the effect of frequency on cyclic soil behaviour are thus much closer to strong earthquake conditions.

5.3 Preliminary cyclic tests

5.3.1 Presentation of the tests

Four undrained stress-controlled cyclic tests on Leman Sand were performed at four different frequencies to evaluate a possible strain rate effect (Tab. 5.2). These tests are identical to the preliminary tests from section 4.3, and the same limitations prevail is terms of non-saturation. The variations in *B* values are significant, also test results may be scattered; they are thus only indicative of the soil response. As seen in section 4.3, the variations of pore pressure in particular are not fully reliable.

Tab. 5.2. Preliminary cyclic tests on Leman Sand with varying frequency (*)

N°	Test description	Date	Void ratio [.]	*B* coefficient [.]	f [Hz]	Δq [kPa]	$\dot{\varepsilon}_q$ (♣) [%/s]	$\dot{\varepsilon}_q^{max}$ [%/s]
LPF1	Cyclic undrained stress-controlled CTC	08/05/2007	0.47	0.85	0.2	100 200 300	0.05 0.13 2.4	0.07 0.19 14.7
LPF2	Cyclic undrained stress-controlled CTC	30/05/2007	0.48-0.49	0.63	0.8	100 200 300	0.2 0.55 12.9	0.3 0.9 45.8
LPF3	Cyclic undrained stress-controlled CTC	04/06/2007	0.47	0.79	1.6	100 200 300	0.27 0.82 6.3	0.53 1.6 20.4
LPF4	Cyclic undrained stress-controlled CTC	07/05/2007	0.47	0.85	6.4	100 200 300	1.3 3.7 12.1	2.1 6.2 22.6

(*) For all tests, the initial confining pressure is 200 kPa and the initial deviatoric stress also 200 kPa, with a back pressure of 200 kPa. LPF2 is the same test as PC1 in section 4.3. (♣) For the 20^{th} cycle (formula in Eq. 5.1).

The deviatoric stress amplitude increases by steps in three levels. Stiffness degradation occurs particularly at the third step, for Δq = 300 kPa.

For each step, the mean deviatoric strain rate ($\dot{\varepsilon}_q$) is calculated by:

$$\dot{\varepsilon}_q = 4\, f\, \Delta\varepsilon_q \tag{5.1}$$

This equation is obtained by integrating, over a quarter of a cycle, the deviatoric strain, assuming that the strain has the same sine shape as the loading stress. This value is not constant at each frequency, but evolves slightly when the deviatoric strain amplitude changes during stiffness degradation. The reference for the deviatoric strain amplitude is taken at the 20th cycle of each step.

The maximum deviatoric strain rate ($\dot{\varepsilon}_q^{max}$) is graphically measured at the 20th cycle by the slope of the tangent of the cyclic deviatoric strain. Its values are provided in Tab. 5.2 for the preliminary tests, in order to compare them with the mean strain rate. Fortunately, maximum strain rates are higher than the mean values. As these parameters are both representative of the strain rate developing in the sample, we chose to further refer to the mean value $\dot{\varepsilon}_q$ in the following developments of this chapter. Indeed, this value is much easier to compute than the manual estimation of $\dot{\varepsilon}_q^{max}$.

5.3.2 Cyclic test results

The deviatoric strains are different at low and high frequency for all cycles (Fig. 5.4). Two groups appear in the data; LPF1 and LPF2, loaded at 0.2 and 0.8 Hz respectively, have very close results, while the tests LPF3 and LPF4 at 1.6 and 6.4 Hz involve less strain amplitude. The results are slightly more scattered between these last two tests, referred to as «high frequency», because the interval of frequency is higher. The effect of frequency seems stronger at large motion amplitudes. The gap between low and high frequency test results is significant at the end of the test, as the deviatoric strain amplitude is multiplied by 8 between 0.2 Hz (LPF1) and 6.4 Hz (LPF4) at the last cycle. The failure threshold is surpassed for LPF1 and LPF2 at low frequency during the last step, but not for the two other tests.

The evolution of the secant shear modulus with the number of cycles in Fig. 5.5 emphasizes the frequency effect. The high-frequency tests are stiffer at all cycles. Comparing again the tests LPF1 and LPF4, the secant shear modulus is 30% and 480% higher, at high frequency, for the 20th and 70th cycles respectively.

The deviatoric stress amplitude is not perfectly the same in all tests, because the motion control is slightly sensitive to frequency for this series of tests: there is, at worst, -7.5% variation of Δq between

0.2 and 6.4 Hz at Δq = 300 kPa. Let us imagine that this slight variation influence the apparent rate-dependency. The deviatoric stress amplitude directly controls $\Delta\varepsilon_q$; it is thus conceivable that $\Delta\varepsilon_q$ is lower at high frequency because Δq is indeed slightly lower. However, the decrease of $\Delta\varepsilon_q$ at high frequency is about -87%, which is much more significant than the -7.5% variations of Δq. Moreover, the secant shear modulus G_{sec} is so much increased at high frequency that the nonlinear effect only can not account for such a difference.

Finally, the pore pressure ratio (Fig. 5.6) is quite similar for all tests during the two first steps, but there is a clear difference in the last part when stiffness degradation occurs. While the threshold value u_r = 1, indicating cyclic liquefaction, is reached at the end of LPF1 (f = 0.2 Hz), u_r = 0.62 only is reached during LPF4 (f = 6.4 Hz). It is also very clear, in Fig. 5.7 which compares these two tests near failure, that the amplitude of u_r is really different. Of course, the unsaturated condition reduces the impact of such results, but it should be noticed that LPF1 and LPF4 have the same B value, also their state is similar. Moreover, this result is in agreement with the evolution of the deviatoric strain amplitude.

5.3.3 Conclusions

The effect of loading frequency, from 0.2 Hz to 6.4 Hz, on cyclic undrained behaviour of dense sand at medium to large strain seems quite clear: at high loading frequency, strain amplitude decreases, stiffness increases while less pore pressure develops.

There is anyway some scatter in the data, as the different frequencies are tested for different samples and as saturation is incomplete. Moreover, because of the small decrease of the stress-controlled amplitude when frequency increases, the scope of the tests is limited, even if it was checked that this did not seem to affect much the results. Finally, the comparison of only four different frequencies might seem insufficient to broadly conclude on rate effect in sand. It is thus necessary to provide other test results, in saturated conditions, which could better reflect the effect of frequency on nonlinear behaviour of sand. The main results presented in section 5.4 fulfil these requirements.

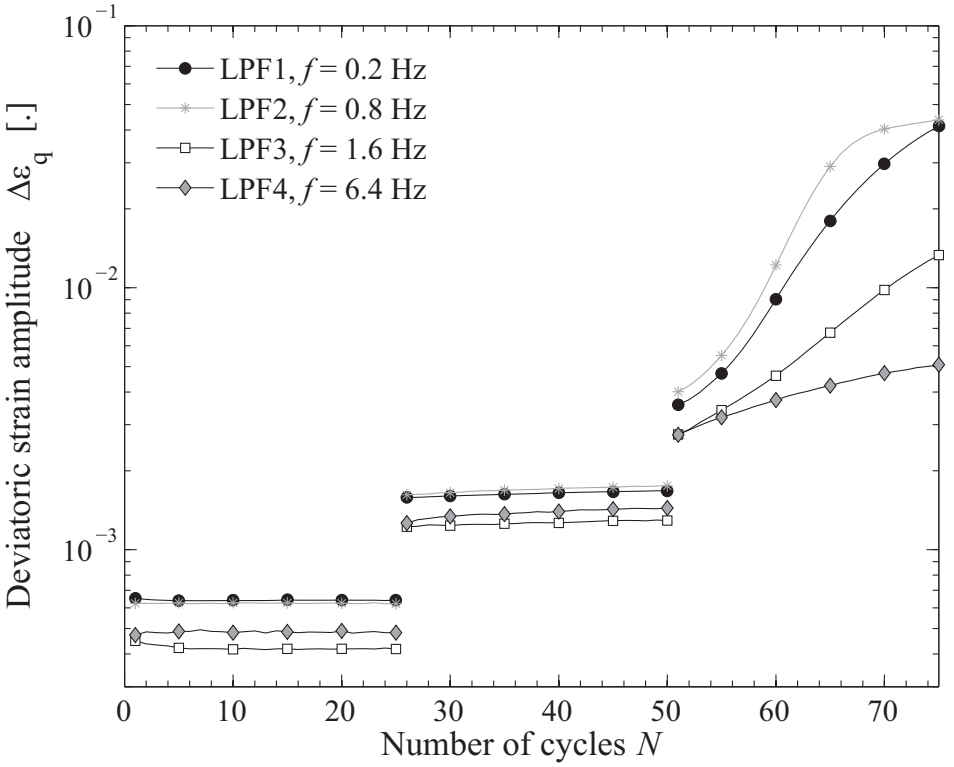

Fig. 5.4. Effect of frequency on the deviatoric strain amplitude.

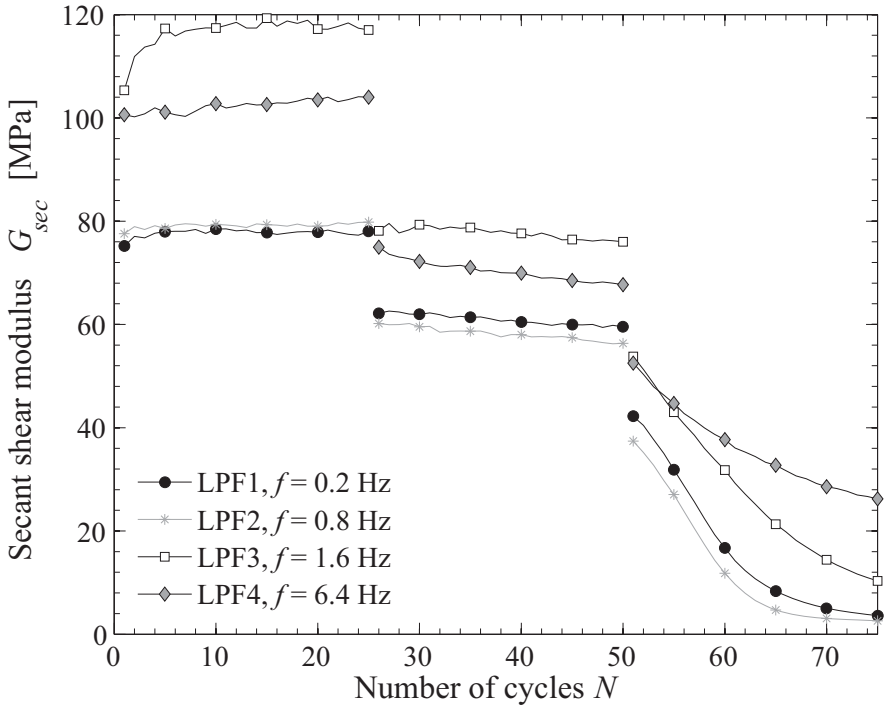

Fig. 5.5. Effect of frequency on the secant shear modulus.

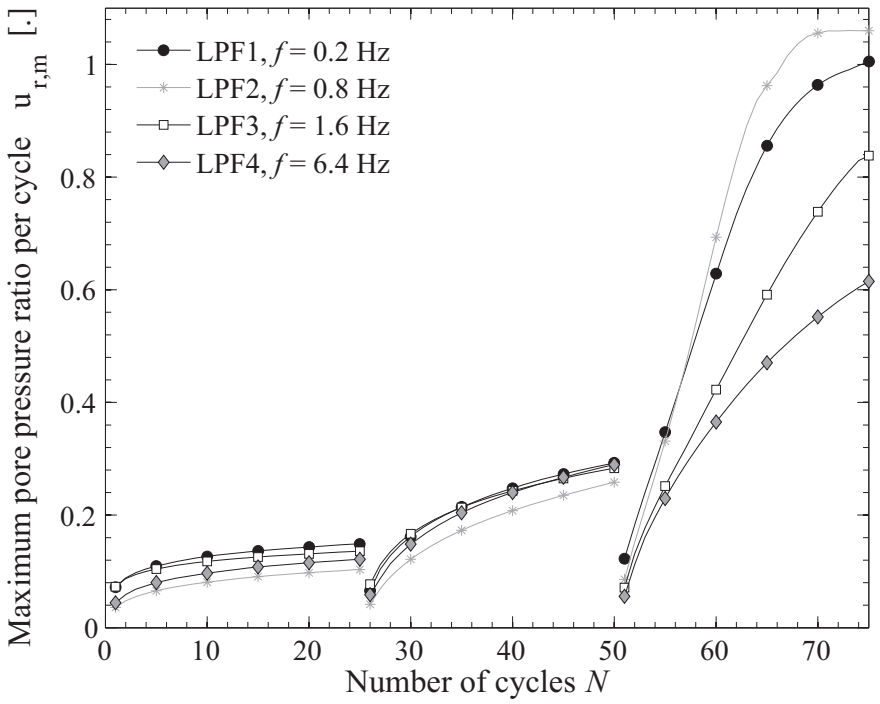

Fig. 5.6. Effect of frequency on the pore pressure ratio.

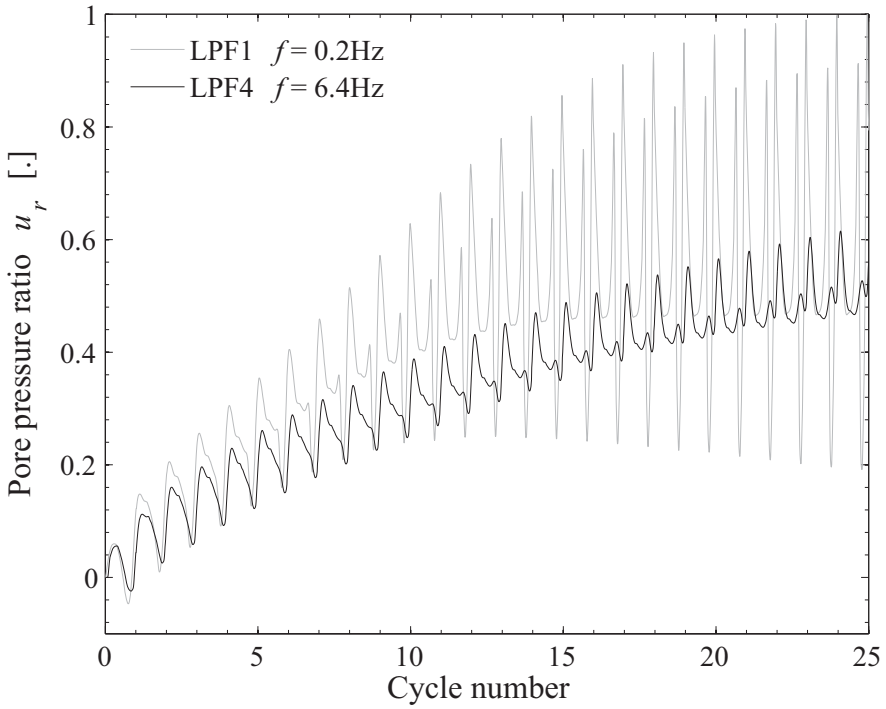

Fig. 5.7. Comparison of pore pressure ratio increase during stiffness degradation of the third step at low and high frequency.

5.4 Frequency effect in undrained conditions at medium strain level

5.4.1 Presentation

Special tests, designated by LF1 and LF2, were conducted to carefully evaluate the effect of frequency (*f*) at medium and high strain levels (Tab. 5.3). As will be further explained later, LF1a refers to the first part of LF1 (steps 1 to 9), while LF1b is the second part with a reduced stiffness (steps 10 to 15). They were performed under undrained stress-controlled conditions. The frequency range varies from 0.1 Hz to 6.5 Hz for LF1 and from 0.1 Hz to 5.1 Hz for LF2, with, respectively, fifteen and twenty steps arranged in random order. To avoid obtaining a too strong accommodation effect in the test results, it was decided to perform the two tests with preparatory cycles: 200 and 100 cycles were performed before the beginning of the actual tests at different frequencies, for LF1 and LF2, respectively. To decrease the scattering of the results, the sample is not drained between steps. Because of that, there are small variations in the CSR of the steps of a single test, as the initial confining pressure is not exactly the same for all frequencies. These variations are estimated thanks to the standard deviation of CSR and $\sigma_3'^0$, both given in Tab. 5.3.

Tab. 5.3. Cyclic undrained tests on Leman Sand with varying frequency (*)

N°	Test description	Date	Void ratio	Frequency [Hz]	CSR [.]	$\sigma_3'^0$ [kPa]	q_{av} [kPa]	$\dot{\varepsilon}_q$ (♣) [%/s]
LF1a	Cyclic undrained stress-controlled CTC	03/08/2007	0.51	4.1 - 0.9 - 3.3 4.9 - 0.5 - 6.1 4.5 - 2.5 - 1.7	4.38 std = 0.66	45 std = 8	196 std = 2	0.9 to 8.7
LF1b	Cyclic undrained stress-controlled CTC	03/08/2007	0.51	0.1 - 2.9 - 6.5 2.1 - 5.3 - 1.3	5.38 std = 0.66	35 std = 5	187 std = 4	0.5 to 10.2
LF2	Cyclic undrained stress-controlled CTC	03/12/2008	0.48	0.1 to 5.1 in 20 steps of random order	3.82 std = 0.25	61 std = 4	237 std = 6	0.1 to 6.1

(*) std = standard deviation. All tests have a back pressure of 304 kPa, yielding $B > 0.96$. (♣) For the 20th cycle.

During the LF1 test, a large increase in the pore-pressure ratio and deviatoric strain amplitude appears at the 10th step (which has the lowest frequency, 0.1 Hz). Failure, as it was defined earlier, is not reached, but partial softening of the sample arises. Consequently, the stiffness of the sample is reduced for all following steps. This clear stiffness decrease explains the separation between LF1a and LF1b that is necessary to allow the test results to be interpreted.

Four stress paths are given in Fig. 5.8 as illustrations of the numerous steps at different frequencies described in this section.

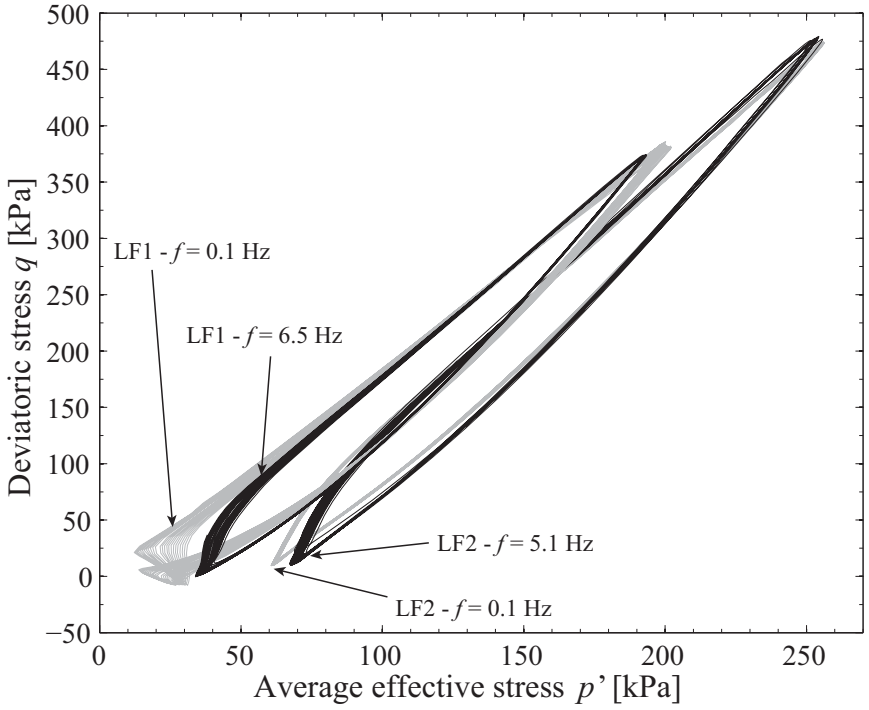

Fig. 5.8. Stress paths of saturated undrained Leman Sand in cyclic loading at different frequencies.

5.4.2 Frequency effect on tests characteristics

The goal of the LF1 and LF2 tests is to assess the effect of frequency on cyclic loading in a stress-controlled mode with natural sand behaviour. Six parameters are displayed (Fig. 5.9 to Fig. 5.15) as a function of the frequency, together with the most appropriate fitted curves (linear or power regression) and the R^2 coefficient. They are evaluated at each frequency and at the 20^{th} cycle for the parameters determined on one cycle only (namely $\Delta\varepsilon_q$, D and G_{sec}).

5.4.2.1 Deviatoric strain amplitude (Fig. 5.9)

The deviatoric strain amplitude developed during the LF2 test is independent of the frequency, with a constant value at 0.3%. It decreases when the frequency increases in LF1a, with values from 0.45% at low frequency to 0.3% at high frequency. For the softened part in LF1b, the rate of decrease of $\Delta\varepsilon_q$ is higher, with values from 1.2% at 0.1 Hz to 0.4% at 6.5 Hz. A power law is best suited for LF1b, while straight lines better fit the points of LF2 and LF1a.

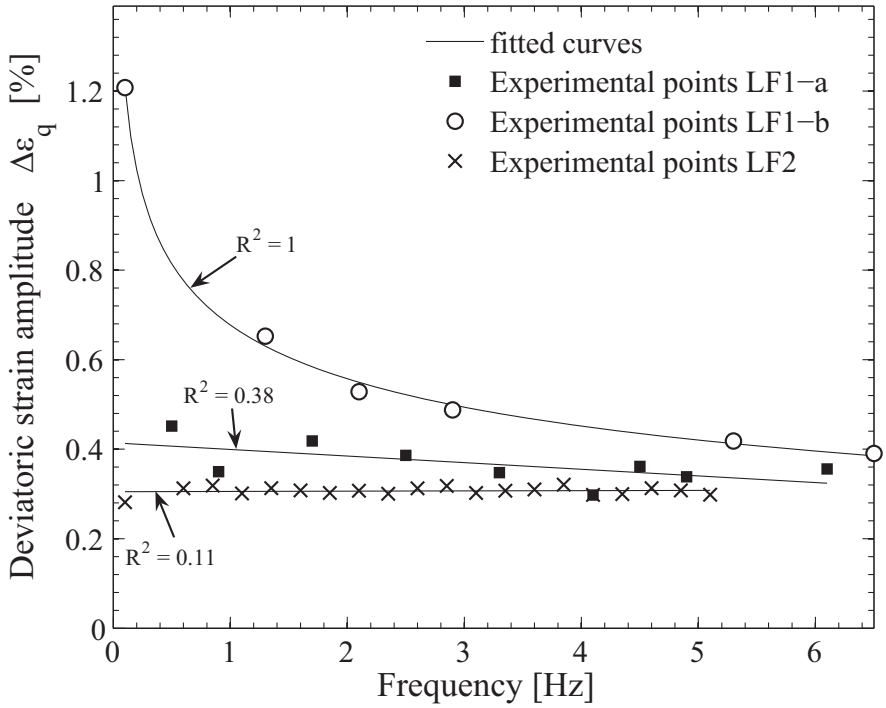

Fig. 5.9. Frequency effect on the deviatoric strain amplitude: experimental points and regression curves.

5.4.2.2 Excess pore water pressure ratio (Fig. 5.10 and Fig. 5.11)

The maximum pore water pressure ratio reached for a given frequency is plotted in Fig. 5.10. The three curves tend to decrease linearly when the frequency increases, but at different rates. In the LF2 test, the maximum pore water pressure ratio decreases from 0.22 to 0.09, while in the LF1a test it decreases from 0.46 to 0.13, and in the LF1b test from 0.9 to 0.2. Low frequencies involve higher pore-pressure ratio for the three cases.

Another parameter is introduced to observe the variation of u_r at each frequency: the rate of increase of u_r. This parameter is the slope of N vs. the maximum u_r measured for each cycle. The slope of the pore-pressure build up is calculated at each frequency for tests LF2 and LF1, and shown in Fig. 5.11. This value also decreases when the frequency increases for the LF1b curve, and it is almost flat for LF1a and LF2. There is no pore pressure build up for LF2, since the rate is close to zero. For LF1a, the rate of u_r is 0.007 per cycle. The rate at which pore pressure builds up is clearly frequency sensitive for LF1b, because the rate doubles between 6.5 Hz and 0.1 Hz. It could be argued that the sensor, placed at the bottom of the sample, records the pore pressure with increasing delay when frequency increases. However the frequency-independence of the rate of increase of the pore pressure during LF2 and LF1a validates the use of the pore-pressure sensor in that frequency range.

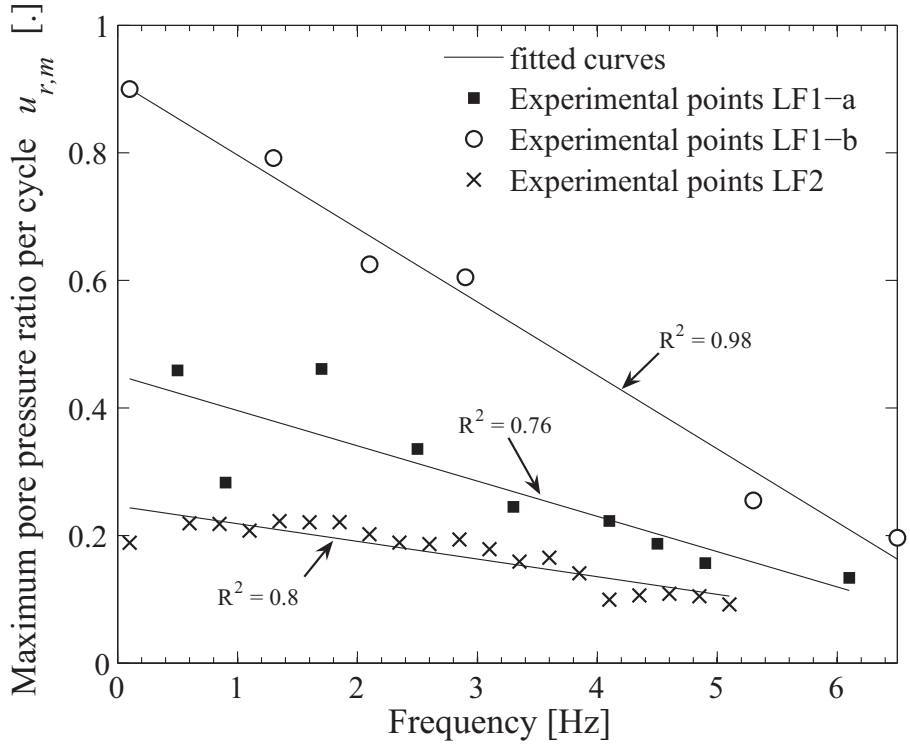

Fig. 5.10. Frequency effect on the maximum pore pressure ratio: experimental points and linear models.

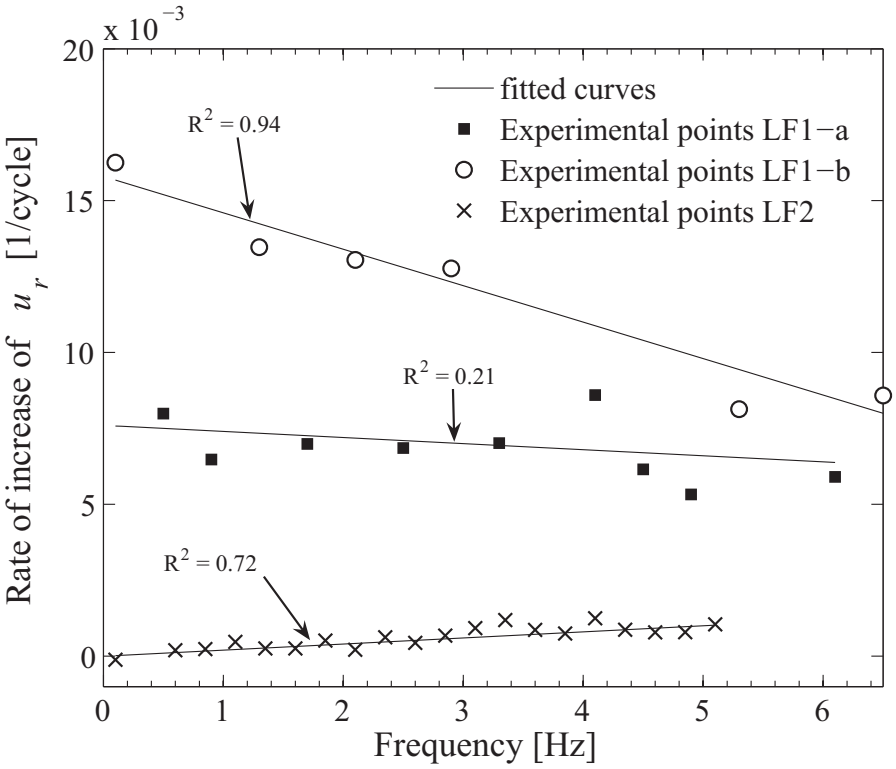

Fig. 5.11. Frequency effect on the rate of increase of the pore pressure: experimental points and linear models.

5.4.2.3 Damping ratio D (Fig. 5.12)

The LF1 test shows an increase of damping ratio with frequency (Fig. 5.12), with a different slope before or after softening. In fact, the softening does not play such a great role at high frequency; on the contrary, at low frequency, the damping ratio is lower for the LF1b test than for the LF1a. A power law better fits this series of data. The damping ratio of LF2 is more scattered, and no conclusion can be drawn concerning the frequency effect for this test.

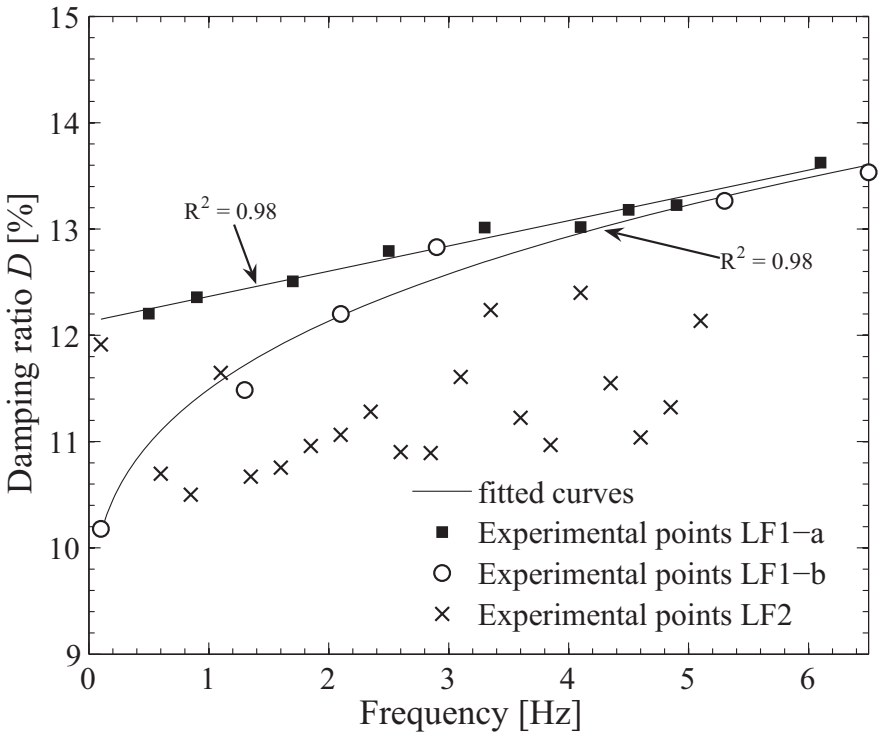

Fig. 5.12. Frequency effect on the damping ratio: experimental points and regression curves.

5.4.2.4 Secant shear modulus G_{sec} (Fig. 5.13)

As we don't have any data on the frequency effect on the elastic modulus G_{max} in Leman Sand, it seems inappropriate to study the ratio G_{sec} / G_{max}. Only total values of the secant shear modulus G_{sec} are thus studied now.

The frequency also influences the secant shear modulus, with large differences between tests (Fig. 5.13). There is a clear separation of the G_{sec} level between the three curves. LF2 is stiffer than LF1a, which is stiffer than LF1b. The secant shear modulus of LF2 is not frequency-dependent, with a mean value of 37 kPa and a standard deviation of 1 kPa. In LF1a, G_{sec} slightly increases with frequency, but the data scattering is relatively large. Finally in LF1b, G_{sec} clearly decreases at low frequency, with a mean rate of 2.1 MPa per frequency unit.

The difference of behaviour between LF1 and LF2 is explained in the discussion section 5.4.3.

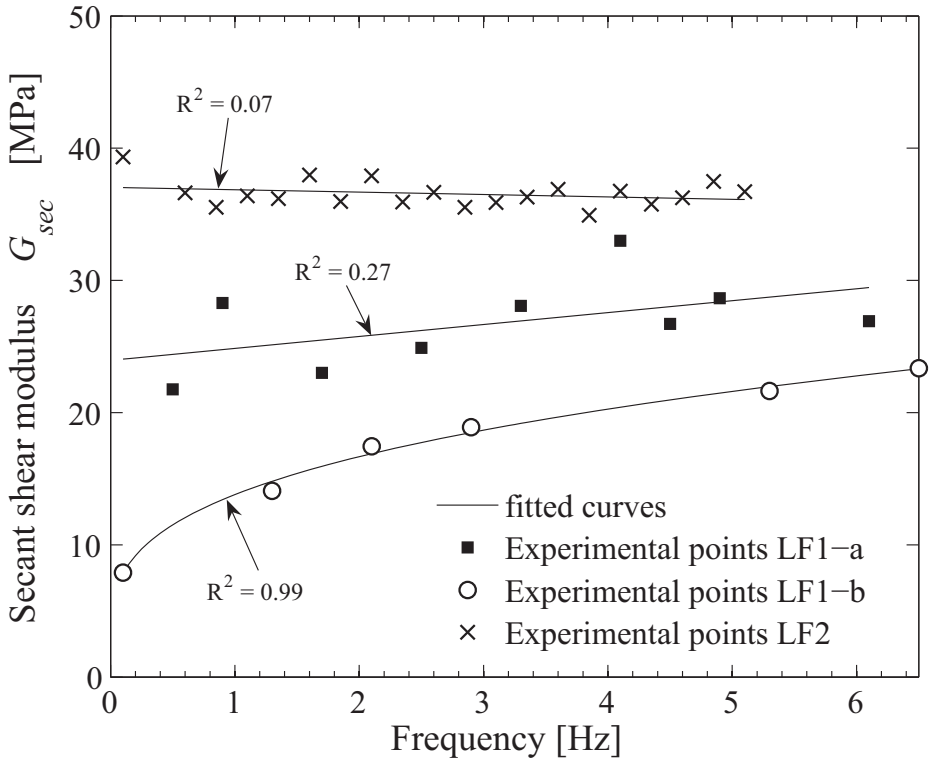

Fig. 5.13. Frequency effect on the secant shear modulus: experimental points and regression curves.

5.4.2.5 Degradation index DI (Fig. 5.14)

Observing the evolution of G_{sec} with the number of cycles, it seems that the degradation index *DI* is frequency-dependent in the LF1b test, but not for LF2 and LF1a. In order to quantify the frequency effect on *DI*, its slope is calculated, and named the rate of *DI*. The evolution of the rate of *DI* with frequency is presented in Fig. 5.14; its values are equal to -0.05% for LF2 and -0.7% for LF1a; both are almost independent from the frequency. This means that there is no softening for LF2, and a limited softening, of constant rate, for LF1a. For LF1b, the rate of *DI* has higher absolute value, and is clearly frequency-dependent. The lower the frequency, the higher the absolute value of the rate of *DI*, and its evolution follows a power law.

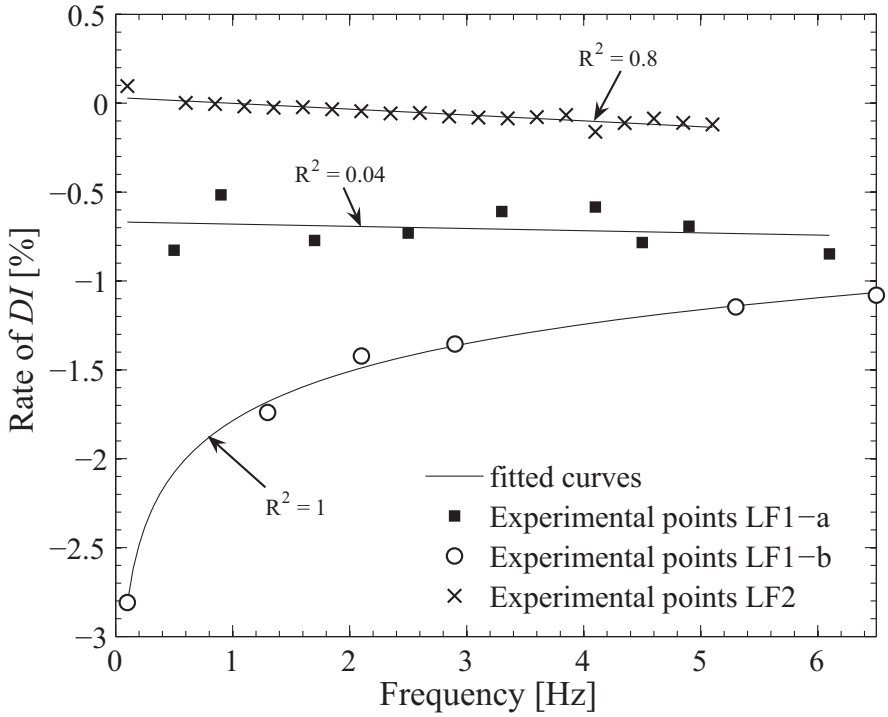

Fig. 5.14. Frequency effect on degradation index: experimental points and regression curves.

5.4.2.6 Summary of the frequency-dependence of Leman Sand

The six parameters describing the cyclic soil behaviour unanimously show frequency-dependence for the softened cycles of the LF1 test. When the frequency increases, the deviatoric strain, the pore pressure ratio and the rate of pore-pressure ratio decrease, while the damping ratio, the secant shear modulus and the rate of the degradation index increase. This means that amplification occurs for frequencies lower than 3 Hz. On the contrary, the parameters found in the LF2 test (where no softening was observed) are all frequency-independent, except for the pore water pressure, which slightly decreases when the frequency increases. A somewhat greater frequency-dependence is found for LF1a, particularly for the damping ratio. The difference in behaviour of the three tests with regard to frequency is analysed in the following discussion (section 5.4.3).

There is a strong correlation between the mean strain rate over one cycle, as calculated in Eq. 5.1, and the frequency. Fig. 5.15 pictures the dynamic parameters of LF1b as a function of $\dot{\varepsilon}_q$; the fits of the experimental points are as good as the frequency-dependent regression curves, which are best expressed as power laws. The other variables of the tests, which are sensitive to the frequency, are similarly strain rate-dependent for LF1a and LF1b. LF2 is still mostly independent of the strain rate.

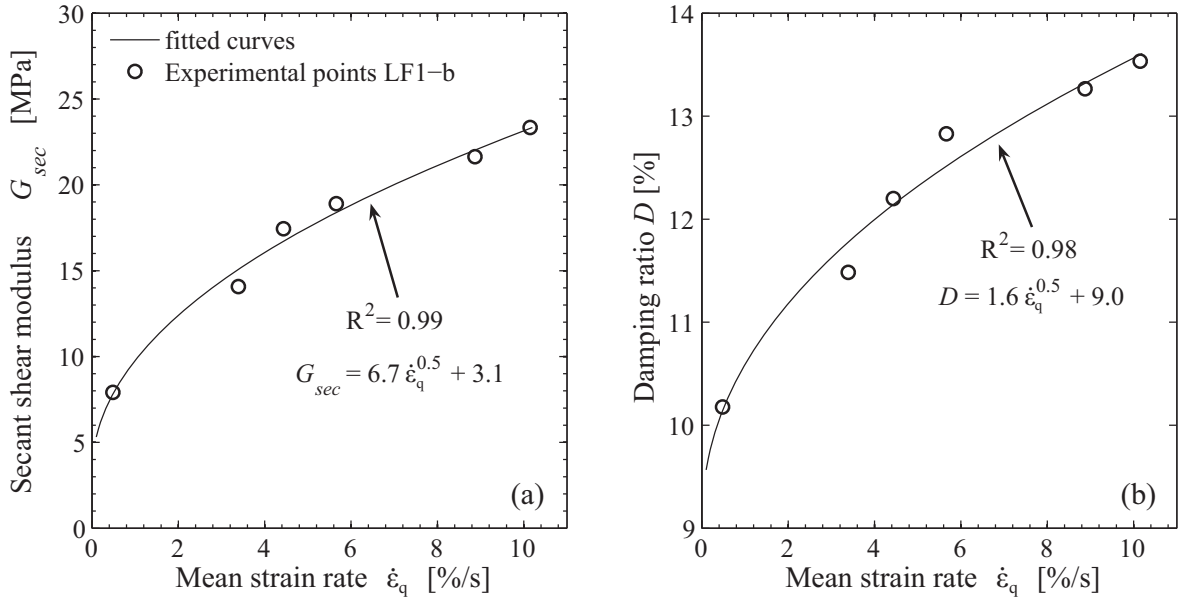

Fig. 5.15. Relation between the average strain rate and the dynamic parameters for LF1b (Leman Sand).

5.4.3 Discussion

Our cyclic tests performed at different frequencies show that a rate-dependency exists under certain conditions. The strain rate level is not the only cause for the apparition of the rate-dependency. Indeed, the LF1a and LF1b tests do not show the same sensitivity to the frequency, while they present the same range of strain rates. The main difference between these two tests is the stiffness, which is lower in LF1b because of a slightly lower initial effective confining pressure and higher deviatoric strains. Stress boundary conditions leading to lower stiffness also involve higher rate-dependent behaviour. The use of natural sand, with particles of different size and mineralogy, can also be responsible for the overall increased rate-dependency compared to other published laboratory tests, though the testing characteristics are also really different. These particular conditions lead to the observation of a marked rate-dependency for the excess pore-pressure generation, the dynamic parameters and the degradation index.

The different behaviour of LF1 and LF2 tests in similar conditions is explained by their stress path. They are both designed to allow accommodation, so that the same sample can be used at different frequencies while giving comparable data. Since the cyclic deviatoric stress amplitude is higher than the mean deviatoric stress for LF1, a small amount of extension is induced. This creates a more unstable response with higher axial strains and limited softening during the first part of the test. The softening is at its highest level during the 10^{th} step at 0.1 Hz; at this low frequency, larger strains develop, the shear modulus decreases and excess pore-pressure increases. This softening is the reason for the development of higher deviatoric strains in the following steps, which are sufficient to cause the amplification of the

frequency-dependent behaviour. While the quantitative parameters are in the same range before and after softening at the high frequency level, there is a clear difference at low frequencies. In the LF1b test between 6.5 Hz and 0.1 Hz, the deviatoric strain is multiplied by 3 and the pore-pressure ratio is multiplied by 4.5, while the secant shear modulus is divided by 3 and the rate of the degradation index by 2.5. Those parameters are not independent from each other; for example, the pore water pressure build up is controlled by the deviatoric strain, and it is expected that its variation with frequency is similar.

There is a regular progression in the level of rate-dependency for the three tests. While LF2 is mostly rate-independent, LF1a is slightly rate-dependent, and the behaviour of LF1b is strongly frequency-dependent. This evolution is correlated with the overall decrease of the stiffness along the three tests, and also follows the increase of CSR (Tab. 5.3). Thus, a link between the stress boundary conditions driving the sample stiffness and sensitivity to frequency is a possible explanation for the three different behaviours.

Gosh & Madabushi (2003) showed, in the case of finite element modeling of a saturated sandy deposit during real earthquake events at different frequencies, that the excess pore pressure is higher for lower frequencies. An amplification phenomenon is found at 1 Hz, which is called the «natural frequency» of the deposit. Not only the peak magnitude, but also the rate of increase of the excess pore pressure is found to be rate-dependent. This prediction is confirmed by the LF1b test for the peak value and for the rate of increase.

The practical consequences of the increase of $u_{r,m}$ with decreasing f might be crucial. It should thus be taken into account for the modeling of liquefaction phenomenon, and for scaled models that are performed at higher frequency. We also notice that it is rather positive to obtain an amplified low frequency behaviour, considering that pseudo-static tests are usually performed in the range of 0.1 to 1 Hz. This range of frequency thus yields the highest strain amplitudes, also such tests are conservative.

The increase of the damping ratio of dry sand with frequency, for typical earthquake frequency range, is observed by Lin et al. (1996) and Hoque & Tatsuoka (2004). The latter performed triaxial tests indicating a stronger increase in the damping ratio at high strains. The former group showed a linear relationship between D and the frequency using torsional tests on full cylindrical samples. The dynamic parameters of their linear model mainly depend on the shear strain amplitude and the effective confining pressure. All of these observations apply to our test results on Leman Sand in undrained conditions; however, none of the previous studies have addressed the rate effect at medium to high strains.

5.4.4 Conclusions

A clear frequency-dependence is found during cyclic loading under certain conditions, which are probably linked with stress boundary conditions leading to low stiffness of the Leman Sand sample. The deviatoric strain amplitude, the maximum excess pore water pressure ratio and the rate of increase of the pore-pressure ratio decrease when the frequency increases. The secant shear modulus, the damping ratio and the rate of the degradation index increase with frequency.

5.5 Frequency effect in cyclic dry conditions

5.5.1 Test presentation

One test, called LDF, was also performed at different frequencies on a sample of dry sand (Tab. 5.4). The boundary conditions and applied load are slightly different from the undrained cyclic tests at different frequencies, LF1 and LF2. The CSR is slightly lower than undrained saturated tests, because the effective confining pressure is higher; indeed, to avoid accommodation, preparatory cycles were performed for both kind of tests, but induced a decrease of the effective confining pressure only in undrained conditions. The void ratio is also higher in the dry test. It varies cyclically during loading, but the average value is very stable between all steps. There is no stress reversal and the point $q = 0$ is touched once per cycle.

Similarly to the undrained LF1 test, there is a clear separation (especially in G_{sec}) between steps performed before or after the step at which $f = 0.1$ Hz (step n°11 in LDF and step n°10 in LF1): for the interpretation of sand characteristics as a function of the loading frequency, the test is separated into two parts LDFa (steps 1 to 10) and LDFb (steps 11 to 22). Actually, the step n°11 is between the two trends, it could also be set apart from LDFb, as will be seen later.

In the same way as previous results analyses, the test characteristics selected for the following figures are all obtained at the 20^{th} cycle for each frequency.

Tab. 5.4. Cyclic dry test on Leman Sand with varying frequency (*)

N°	Test description	Date	Void ratio	Frequency [Hz]	CSR [.]	$\sigma_3'^0$ [kPa]	q_{av} [kPa]	$\dot{\varepsilon}_q$ (♣) [%/s]
LDFa	Dry cyclic stress-controlled CTC in 10 steps	05/03/2009	0.52 in average	0.5 - 0.9 - 1 1.7 - 2.5 - 3.3 4.1 - 4.5 - 4.9 6.1	1.7 std < 0.01	100 std < 1	170 std < 1	0.22 to 1.8
LDFb	Dry cyclic stress-controlled CTC in 12 steps	05/03/2009	0.52 in average	0.1 - 1 - 1.3 2.1 - 2.9 - 3.7 4.1 - 5.3 - 5.7 6.5	1.7 std < 0.01	100 std < 1	170 std < 1	0.04 to 1.85

(*) Four steps are performed twice at 1, 3.7, 4.1 and 5.7 Hz (♣) For the 20th cycle (formula in Eq. 5.1).

5.5.2 Frequency effect on dry Leman Sand test results

5.5.2.1 On the deviatoric strain amplitude (Fig. 5.16)

In both LDFa and LDFb, the deviatoric strain amplitude decreases when frequency increases. The multiplication factors of $\Delta\varepsilon_q$ between high and low frequency are 1.5 and 1.4, in LDFa and LDFb, respectively. For both tests, a power law fits very well (R^2 = 0.97 or 0.98) the f - $\Delta\varepsilon_q$ experimental points.

Concerning the qualitative aspect of these curves, the deviatoric strain amplitude is higher for the first part of the test LDFa, but the values of $\Delta\varepsilon_q$ in LDFa and LDFb converge above 4 Hz. Moreover, the strain range is much smaller than what was measured in undrained conditions in LF1 and LF2, mainly because the cyclic stress ratio is lower in the dry test.

5.5.2.2 On the volumetric strain amplitude (Fig. 5.17)

The volumetric strain amplitude $\Delta\varepsilon_v$ tend to increase with the frequency, with a higher rate for LDFa. The curves intersect just below 2 Hz. In LDFb, $\Delta\varepsilon_v$ is actually practically constant, except for step 11, at 0.1 Hz, which is slightly lower. On the contrary, $\Delta\varepsilon_v$ increases of a factor 2 between low and high frequency in LDFa. Again, there is very little discrepancy in both regression curves.

It is quite unexpected to find a volumetric strain amplitude which increases with the frequency. Indeed, the maximum pore water pressure per cycle decreases with the frequency in undrained tests (Fig. 5.10), also we would expect a dry volumetric behaviour which also decreases with the frequency.

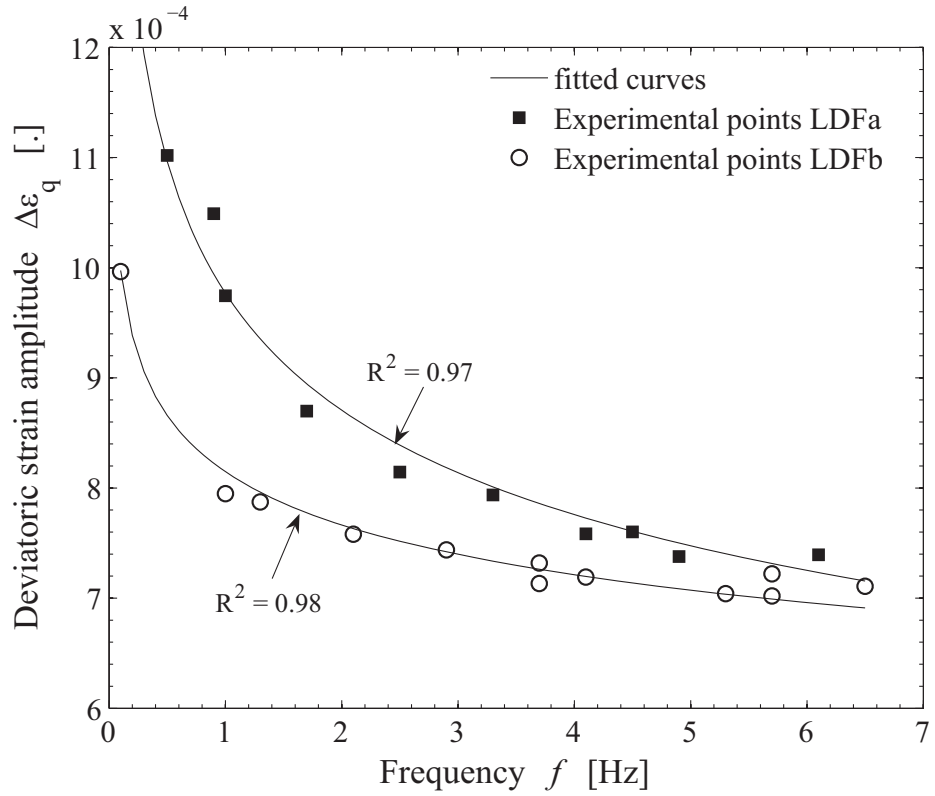

Fig. 5.16. Decrease of the deviatoric strain amplitude with the frequency.

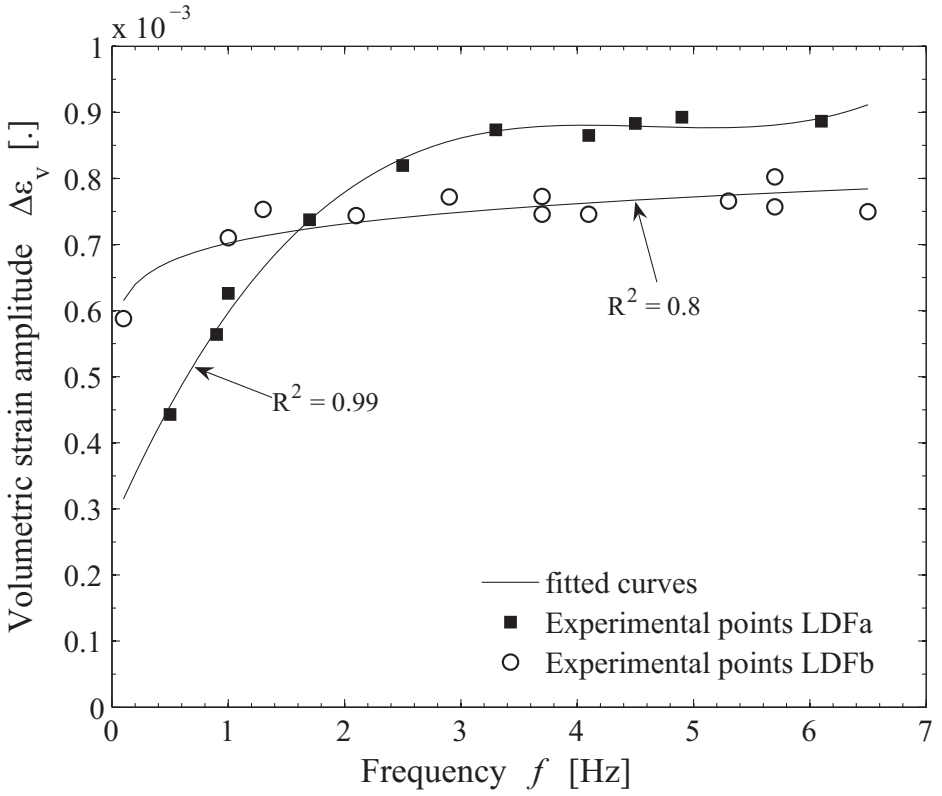

Fig. 5.17. Increase of the volumetric strain amplitude with the frequency.

5.5.2.3 On the secant shear modulus (Fig. 5.18)

Both parts of the dry cyclic test exhibit an increase of G_{sec} with the frequency (Fig. 5.18), as for undrained loading (Fig. 5.13). There is very small scatter in the data; the best fits are a straight line and a power law for LDFa and LDFb, respectively, with R^2 = 0.97 for both parts. LDFb is stiffer than LDFa, except at high frequency where the curves converge.

Contrary to undrained cyclic loading, the first part LDFa is softer than the second part LDFb, probably because of accommodation. We saw in chapter 4 that the response of dry sand can be very different from the undrained saturated response. Moreover, LDFa exhibits more rate-dependency: the ratio of the maximum (at 6.5 Hz) to the minimum (at 0.1 Hz) G_{sec}, from the regression curves, is 1.65 and 1.45 for LDFa and LDFb, respectively. This test is thus in agreement with the assumption that the intensity of rate-dependency increases at stress boundary conditions leading to lower stiffness (undrained test result in section 5.4.3).

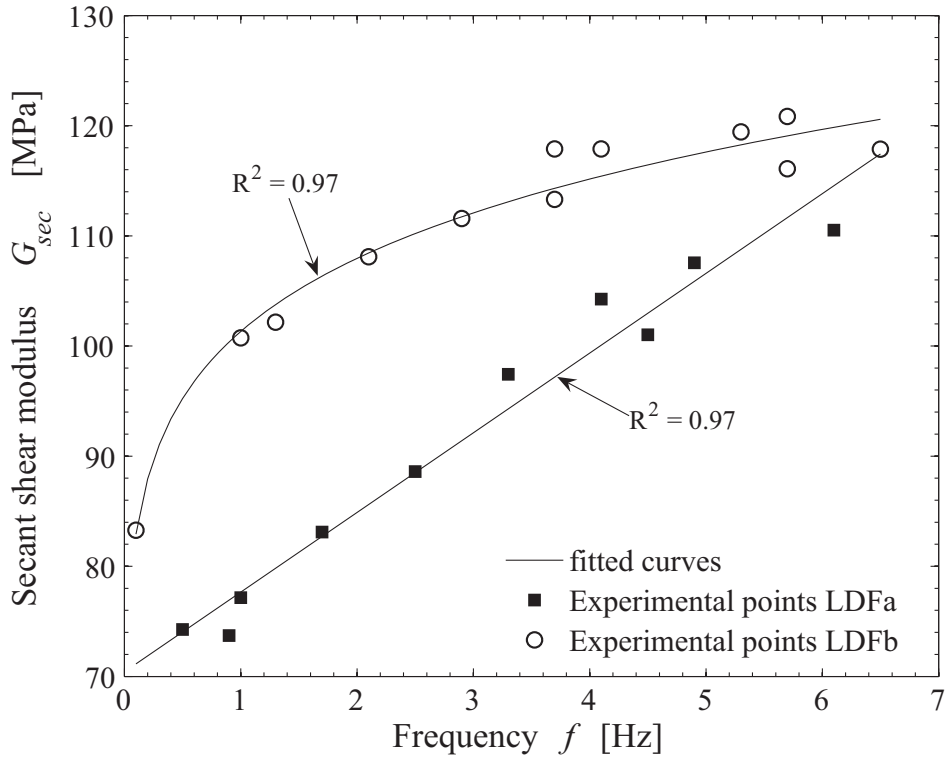

Fig. 5.18. Increase of the secant shear modulus with the frequency.

5.5.2.4 On the damping ratio (Fig. 5.19)

Damping ratios observed in LDFb test is independent from the frequency, with a mean value of 17% and a standard deviation of 1.3%. This value seems too high compared to the evolution of damping with the deviatoric strain amplitude in undrained conditions. Indeed, there is great limitations in the

measurement of the damping ratio in dry sand: the values of *D* are overestimated, because the uncertainties in the non-contact measurement of radial strains have a strong influence on the shape of the stress-strain relation (cf. section 4.6).

With this limitation, it seems however interesting to notice that there is a kind of peak in *D* around 2 Hz in LDFa. Damping is also too high in LDFa, compared to the range of deviatoric strains involved.

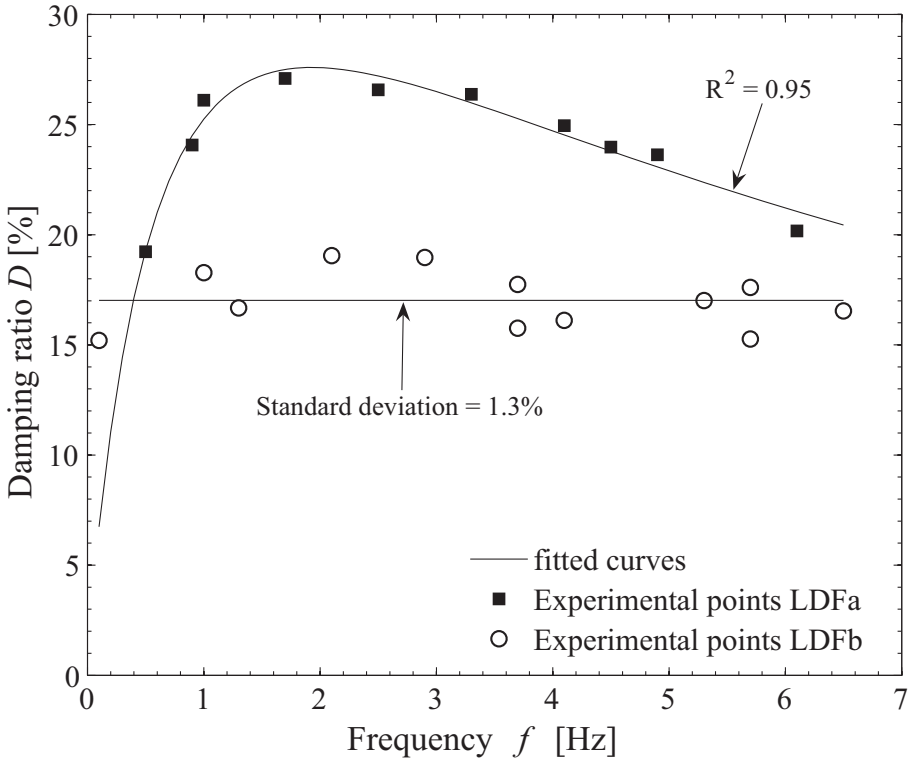

Fig. 5.19. Evolution of the damping ratio with the frequency.

5.5.2.5 Summary of rate effects in dry conditions in Leman Sand

Similarly to undrained saturated loading of Leman Sand, there is a clear frequency effect on dry sand behaviour. At low frequency, the deviatoric strain amplitude increases, the volumetric strain amplitude decreases and the secant shear modulus decreases. The ratio between the maximal and the minimal values of these parameters, at the extremal frequencies, is from 1.4 to 2 in case of rate-dependency.

The soil response is again separated into two parts corresponding to two levels of stiffness, which also have different sensitivity with regard to the frequency. In dry sand, there is an increase of stiffness after the step at low frequency f = 0.1 Hz. This opposite behaviour, compared to saturated undrained sand, is accompanied by a significant reduction of the frequency-dependence of the last part of the test, LDFb.

The mean strain rate is lower than what was obtained in undrained tests, because the strain amplitude is lower. There is however a clear effect of $\dot{\varepsilon}_q$ on the dynamic parameters, especially on G_{sec} (Fig. 5.20).

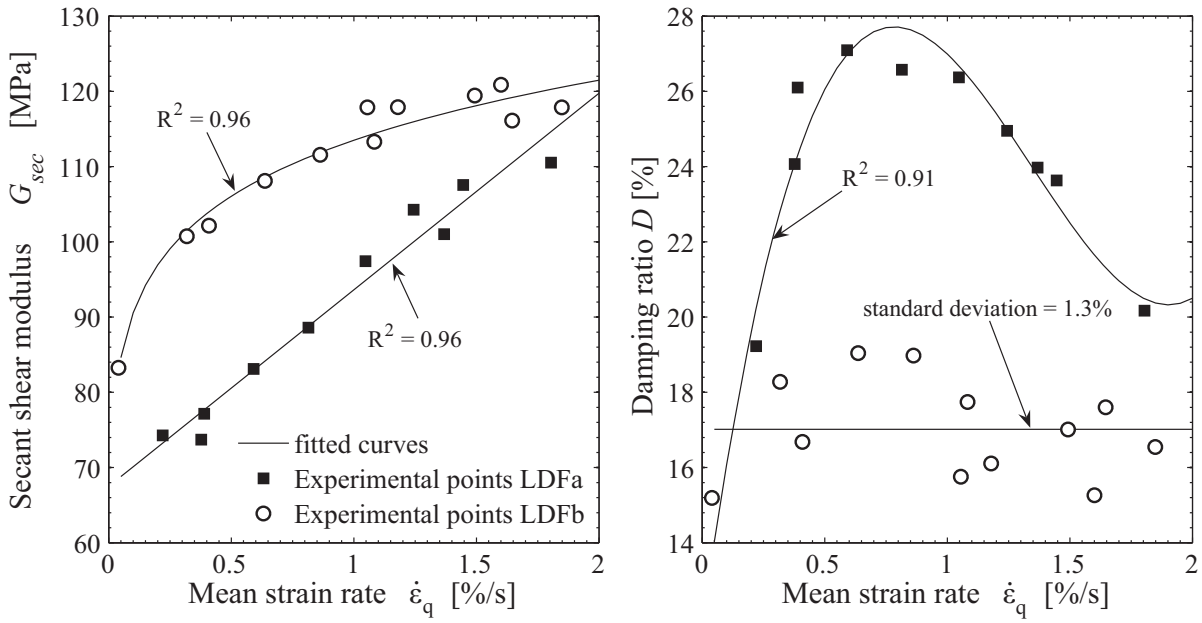

Fig. 5.20. Dynamic parameters vs. strain rate in dry medium dense Leman Sand.

5.5.3 Discussion

Based on the test described above, the overall cyclic behaviour of dry Leman Sand is frequency-dependent at a strain range of approximately $\Delta\varepsilon_q = 10^{-3}$. This result contradicts the observations of Bolton & Wilson (1989), but it is in accordance with other results around medium strain level (e.g. Zambelli et al. 2006; Salvati & AnhDan 2008).

The deviatoric strain amplitude and the secant shear modulus are linked through the definition of G_{sec}, which is inversely proportional to $\Delta\varepsilon_q$. Their respective frequency-dependence is thus interrelated; that is why finding, as in undrained conditions, that $\Delta\varepsilon_q$ decreases and G_{sec} increases when the frequency increases, is reasonable. For lower strain level, Lin et al. (1996) and Zambelli et al. (2006) had found that G_{sec} of dry sand is constant in that range of frequency, but Matesic & Vucetic (2003) had found a linear increase of G_{sec} vs. log($\dot{\varepsilon}$). For Salvati & AnhDan (2008), the total accumulated strain, which is not exactly the same concept as $\Delta\varepsilon_q$, also decreases when f increases.

The increase of the volumetric strain amplitude with frequency can not be compared to other test results. Though, it would be interesting to validate this unexpected sand behaviour, which appears very clearly in our dry tests.

A peak appears at 2 Hz in the D vs. f relation. This peak is not reported in other experimental studies on dry sand, such as Lin et al. (1996) or Zambelli et al. (2006), for which D increases linearly with f. In the undrained saturated tests on Leman Sand as well, D tends to increase with f. This result should to be considered with caution, as there is higher uncertainty in the measurement of the damping ratio in dry

triaxial tests.

As was shown previously in undrained saturated condition, dry Leman Sand is rate sensitive during cyclic loading. The conditions of CSR and strain range of our dry and undrained tests are not exactly similar, also it is not possible to deduce from this experimental study if dry and undrained saturated conditions yields the same amount of rate effect. Thus, the importance of water in rate effect cannot be evaluated with available experimental data. Nawir et al. (2003) showed that the effect of step changes of strain rate in sands was similar in dry and saturated drained conditions. We now add that, in cyclic loading, the change of frequency involves sizeable changes in both dry and saturated undrained sand behaviour at medium strain level.

The dry cyclic test LDF clearly separates into two frequency-dependent parts, which exhibit different levels of rate-dependency. The parallel between the undrained saturated response and the dry response of sand is striking: while the first part of the test is stiffer and less rate-dependent in the undrained test LF1a, the first part is less stiff and more frequency-dependent in LDFa. The difference of evolution of the overall stiffness may be expected, in the sense that dry sand exhibits accommodation while undrained sand involves stiffness degradation in the same conditions. The concordance of the sensitivity to frequency and the relative stiffness level in both hydraulic conditions is an interesting conclusion from the comparison of these cyclic tests. The stress boundary conditions leading to lower stiffness thus induce a suitable environment for enhanced cyclic rate effects in dry and undrained saturated sands.

Finally, for Salvati & AnhDan (2008), frequency-dependent behaviour of dry sand increases with low confining pressure and for high CSR. This comment enlightens the difference between our dry and undrained tests at different CSR. On one hand, higher frequency-dependence (i.e. more amplification at low frequency) is obtained in the saturated test LF1 with a higher CSR than the dry test LDF. On the other hand, the relation, found in our tests, between stiffness degradation and rate effect indirectly confirms the result of Salvati & AnhDan (2008). Indeed, considering that lower confining pressure reduces sand stiffness (cf. Chapter 4), the conditions of low stiffness and the effect of confining pressure both yield the same response in terms of frequency-dependence of sand behaviour. The test results presented here and the observations of Salvati & AnhDan (2008) are then compatible.

5.5.4 Conclusions

Dry Leman Sand is clearly frequency-dependent at medium strain level. At low frequency, the deviatoric strain amplitude increases, the volumetric strain amplitude decreases and the secant shear modulus decreases. The ratio between the maximal and the minimal values of these parameters, at the

extremal frequencies, is from 1.4 to 2 in case of rate-dependency (i.e. except for some parameters in LDFb). The second part of the test LDF, which is stiffer (but with the same CSR) than the first ten steps at ten frequencies (LDFa), seems also less frequency-dependent. Salvati & AnhDan (2008) had shown that the frequency-dependent response of dry sand depends on the confining pressure. As a complement, we show that stress boundary conditions leading to lower stiffness induce a suitable environment for enhanced cyclic rate effects in sands. This idea is supported by the comparison between dry and undrained saturated sand behaviour at different frequencies.

5.6 Discussions on rate effect in Leman sand

5.6.1 Experimental artefacts

Before concluding on the effect of frequency on Leman Sand behaviour, we must consider the hypothesis that the observed rate-dependent Leman Sand behaviour could be an artificial effect of the triaxial press or the measuring system. In other words, a small review of the different parts which could wrongly increase the frequency effect is listed now.

The possible test and measuring artefacts that we could foresee are: (i) the numeric filters used in the recording of sensor output (ii) the temporal resolution of the sensors (iii) the sensitivity of the motion control to the frequency (iv) local physical measurement errors of the pore pressure and the laser sensors. Their possible effect on the test results is analysed.

The numeric filters included in the Fast Track controlling system, which records sensor ouputs, are triggered with a cut-off frequency at the same level as the sampling frequency, which is itself adapted to the loading frequency. We checked that these values do not influence the output data. The test equipment was designed to allow frequencies up to 100 Hz, also the temporal resolution of sensors is not a problem either, as loading frequency remains below 10 Hz.

Motion regulation is performed via a closed loop system, which might be sensitive to loading frequency. However, the stress amplitude is very stable in dry tests, with a standard deviation of both the average and the amplitude values of q below 1%. Such stability is remarkable, and shows that motion regulation is not an issue with these loading features.

A linear elastic model of the test showed that the time necessary to equilibrate pore pressures within the sample is not a problem for loading frequency below the maximum used frequency $f = 6.5$ Hz (section 3.2.1). For the measurement of radial strains with the laser technique in dry tests, we can

wonder whether this measurement is sensitive to the frequency. However, the maximum sampling frequency with the lasers is 2.5 kHz; thus, the maximum admissible loading frequency should be one tens, i.e. 250 Hz. The range of loading frequency of our tests is then very much smaller than this maximum.

Finally, some test results were found frequency-independent in some conditions, or for some parts of the tests. For example, the deviatoric strain amplitude and the rate of increase of the pore pressure ratio is constant during the undrained test LF2. In the dry test LDFb, D and $\Delta\varepsilon_v$ are also almost constant values.

This small analysis enhanced our confidence in the test results on rate effect in Leman Sand presented in this chapter.

5.6.2 Physical interpretation and general comments

A clear definition of viscous time effects is given by Di Benedetto (2006):

«By definition time effects exist if a change in the stress-strain curve(s) is observed when changing the rate of loading».

Our cyclic tests on dry and undrained saturated Leman Sand demonstrate a clear time-dependent behaviour, as the cyclic loops depend on the stress frequency (e.g. the parameters $\Delta\varepsilon_q$, G_{sec}, D are shown to depend on frequency). Moreover, the stress frequency (or loading rate) and mean strain rate (which also depends on strain amplitude) have similar effects on material parameters (e.g. Fig. 5.12, Fig. 5.13 and Fig. 5.15).

It is not new that sand can exhibit time-dependent behaviour. The literature review provided examples and possible explanations of rate effects in granular media. In particular, recent experimental studies (e.g. Tatsuoka 2006; Duttine et al. 2008) demonstrated that granular materials are sensitive to changes in strain rate rather than the absolute strain rate values in monotonic conditions. We showed that the effect of frequency on the particular sand used, Leman Sand, which is an angular poorly-graded natural sand, can be non negligible in the range of strain amplitude and frequency content of a strong earthquake. Low frequency motions, i.e. between 0.1 and 1 Hz, are amplified by comparison with high frequency motions between 4 and 6.5 Hz. The strain amplitude, the volumetric behaviour (pore pressure in undrained condition and volumetric strain in dry condition), the dynamic parameters are all influenced by the loading frequency in certain conditions.

The test procedure and the stability of Leman Sand behaviour both allowed to obtain such distinct results. As the frequency-dependent behaviour of Leman Sand also appears in the preliminary tests, the

rate effect here is not caused only by a *change in strain rate*, as was shown for monotonic loads (Tatsuoka 2006; Duttine et al. 2008), but is necessarily linked with the value of frequency itself. However, the new procedure in which frequency changes by steps every 25 cycles, which allows to have exactly identical sample fabric, may also include this effect of change of strain rate during the first loading cycles of each step.

Duttine et al. (2008) demonstrated that the angularity of the grains influence the viscous behaviour of sand in case of direct shear monotonic tests; as Leman Sand is particularly angular, we assume that this enhanced viscous behaviour obtained in Leman Sand may be due to the angular grain shape.

The physical interpretation of such complex phenomenon is hazardous. In particular, the limited number of tests makes it difficult to get a perfect overview on the relative effects of density, confining pressure, CSR, etc.... A more detailed parametric study would be needed to assess, in particular, the role of the pore fluid in the frequency-dependence.

Anyway, as both dry and undrained tests exhibit frequency-dependent behaviour, the coupling of the grains and the pore fluid only is not responsible for that rate-dependent behaviour. This result is consistent with the description of rate-dependent dry sand behaviour presented by Pham Van Bang et al. (2007) in pseudo-static conditions (i.e. for creep, relaxation, and step change of strain rate). Our laboratory tests demonstrate that rate-dependent behaviour of dry sand can also be observed during cyclic loading at medium strain amplitude, and for larger strain rates.

Given the wave length of the loading (cf. section 3.2.1), even at the highest frequency, a true dynamic amplification due to wave propagation can be withdrawn from the possible meanings of the frequency-dependence observed in Leman Sand.

Inherent viscosity at the particle contact between the grains is a popular assumption for time-dependent sand behaviour. For example, Nawir et al. (2003) for triaxial compression tests of dry sand:

«The origin of such global viscous properties of sand [...] is time-dependent slipping at inter-particle contacts caused by viscous deformation inside particles at and near the inter-particle contacts [...]. It seems that, inside a sand specimen subjected to creep loading, such local viscous behaviour as described above is active only in limited zones at every moment and these zones are continuously moving while the overall viscous activities decay with time»

Such an explanation may be adapted and applied to the observed frequency-dependent cyclic behaviour of Leman Sand, in both dry and undrained conditions. However, such interpretation of our test results at the micro-scale level does not rely on tangible scientific proofs.

5.7 Conclusions

Four monotonic triaxial undrained compression tests performed at different strain rates, from 0.03 to 0.98 %/s, allowed to conclude that there is no monotonic strain rate effect in Leman Sand in this range of strain rate. The slight differences in the stress-strain and the pore pressure ratio vs. axial strain relations are thought to be linked with variations of the grain size distribution of individual samples.

In cyclic loading, the four preliminary tests at different frequencies, the two undrained saturated tests and the dry test, all performed on dense Leman Sand, allow to conclude on a cyclic effect of the frequency on sand behaviour. The overall rate-sensitivity of this granular material is thought to be enhanced by the angularity of the grains.

Though they were performed at a limited number of frequency and in imperfect conditions, the preliminary tests LPF1 to LPF4 show that, compared to low frequencies, high frequencies induce lower strain amplitude, higher stiffness and less excess pore pressure at medium to large strain.

The same consequences on stiffness degradation behaviour are inferred, in certain conditions, from the test LF1, where undrained saturated Leman Sand is cyclically sheared in various steps of different frequencies. A strong frequency-dependence is found in part of the results: in LF1b, the deviatoric strain amplitude decreases of a factor 3, the maximum pore pressure ratio decreases of a factor 4.5 and the secant shear modulus increases of a factor 3 when the frequency increases from 0.1 to 6.5 Hz. The rate of increase of the pore pressure ratio decreases with frequency, while the damping ratio and the rate of the degradation index increase. Though, the other test at lower CSR, LF2, is practically frequency-independent in approximately the same frequency range but with higher stiffness.

Dry Leman Sand is also frequency-dependent at medium strain level in certain conditions. As for undrained sand, the deviatoric strain amplitude increases and the secant shear modulus decreases at low frequency, while the volumetric strain amplitude decreases. The ratio between the maximal and the minimal values of these parameters, at the extremal frequencies, is from 1.4 to 2 in the rate-dependent part.

Both dry and undrained tests demonstrate an effect of stress boundary conditions on the sensitivity of sand behaviour to cyclic rate effect. The stiffer parts of the tests are less frequency-dependent, whatever other conditions, and especially independently of the cyclic stress ratio which remains constant in the dry test. As a complement to Salvati & AnhDan (2008), we show that stress boundary conditions leading to lower stiffness induce a suitable environment for enhanced cyclic rate effects in sands. This idea is supported by the comparison between dry and undrained saturated sand behaviour at different frequencies.

CHAPTER 6

EFFECT OF MULTIDIRECTIONAL AND IRREGULAR STRONG LOADINGS

6.1 Introduction

The propagation of seismic waves in subsurface soil layers induces complex stress fields. Seismic loadings are intrinsically irregular, in both amplitude and frequency content. They are known primarily by recordings of acceleration time-history at the soil surface, or possibly at a certain depth when seismographs were installed in boreholes. These measurements are performed in three perpendicular directions, as the soil motion is inherently multidirectional. The recent analysis of case histories of strong motions showed that, as well as the two horizontal motions, the vertical component can play an important role in the soil instability (e.g. Lin et al. 2009). It is then established that the three directions of motion are important, but there might as well be an interaction between them at the scale of a soil element (e.g. sample), without even looking at multidimensional site effects (section 2.3.5) and the influence of the geometrical characteristics of the substratum.

The laboratory tests presented in this chapter address the issue of bidirectional strong loadings, with either sinusoidal or irregular seismic motion. There are two main scopes: (i) evaluation of the assumption of the superposition of loadings in nonlinear soil motions and (ii) understanding the coupled nature of the response of the pore fluid and the granular matrix in the sand behaviour. The test results can not embrace totally these two broad fundamental questions, but they provide examples to enhance the comprehension of dynamic soil behaviour.

Previous laboratory studies showed that the superposition of two shear loads on the system boundaries affects soil behaviour (cf. Chapter 2). The multidirectional effect is mainly taken into account with a correction factor included in unidirectional procedures. Some numerical studies show that using a coupled dynamic formulation with an elastoplastic law is relevant for modelling multidirectional loadings of the soil deposit (e.g. Bernardie et al. 2006). However, the transient behaviour of saturated sand under earthquake loading with a triaxial device under cyclic bidirectional loading have no available test data.

«Complex loadings», in the frame of this thesis, are bidirectional cyclic and irregular stress-controlled loadings in triaxial conditions. They consist in the superposition of a deviatoric stress and a confining pressure of varying amplitudes, and possibly frequency content. All tests were performed using Leman Sand in undrained saturated conditions. In order to understand bidirectional effects in cyclic conditions, sinusoidal stresses at the same frequency and with constant amplitudes were first used. The application of cyclic test results to a seismic problem is then evaluated by conducting tests of varying amplitude and frequency. The bidirectional test procedures are first described for cyclic conditions, and test results are analysed (section 6.2). The description of irregular unidirectional and bidirectional loadings is presented in section 6.3. A discussion follows on the effects of complex loading on nonlinear soil

behaviour, with a tentative explanation for the observed phenomenon and some propositions to take the experimental results into account at the level of soil modelling (section 6.4).

6.2 Multidirectional effects on cyclic behaviour

6.2.1 Tests characteristics and examples

The tests LIP1 and OOP1 are unidirectional tests, while the other ones LIP2 to LIP4 and OOP2 to OOP6 are bidirectional tests with a variation of the total confining pressure, σ_3 (see Tab. 6.1 and Tab. 6.2). These complex loadings are first described. In cyclic bidirectional loading (2D), the two sinusoidal loads are defined by (cf. also section 3.2.2):

$$\begin{aligned} q(t) &= \Delta q \sin(2\pi f t) \\ \sigma_3(t) &= \Delta\sigma_3 \sin\left(2\pi f t + \zeta \frac{\pi}{180}\right) \end{aligned} \quad \text{in [kPa]} \qquad (6.1)$$

where t is the time, f the frequency, Δq and $\Delta\sigma_3$ are the amplitudes of the two signals and the phase angle ζ is in [°]. The in-phase bidirectional loadings are defined by ζ = 0°; out-of-phase loadings correspond to $\zeta \neq 0$. Unidirectional loadings are defined by $\Delta\sigma_3$ = 0.

6.2.1.1 In-phase bidirectional loading paths

Bidirectional loading paths are made of the superposition of a cyclic deviatoric stress with a cyclic confining pressure. In all cyclic tests, the frequency is the same in both directions. For in-phase tests, there is no time-lag between the two loadings (Tab. 6.1). The total stress path is a straight line of slope different than the value 3, which is obtained for unidirectional (1D) cyclic triaxial tests as those presented in Chapters 4 and 5. It is clear in Fig. 6.1 that, for the highest amplitude (CSR = 1.25), the stress path is not a perfect slope but a rather deformed shape. Indeed, the servo control system is less accurate close to failure, when large deformations occur in the sample.

The tests presented here were performed in three steps of 25 cycles each, with increasing deviatoric stress amplitude Δq between each step and constant confining pressure amplitude ($\Delta\sigma_3$). As a result, the inclination of the stress path changes, i.e. its slope increases at each step (Fig. 6.1). Compared to a 1D stress path, the slopes are lower in our in-phase tests. The pore water pressure is released between the steps, as for the cyclic tests presented in Chapter 4.

Most of the parts of each test are on the compressive side, except for a small extension at the 3rd step.

Tab. 6.1. Cyclic undrained in-phase bidirectional tests on Leman Sand (*)

N°	Test description	Date	Void ratio	CSR [.]	$\Delta\sigma_3$ [kPa]	B coefficient
LIP1	In phase unidirectional cyclic triaxial test	30/05/2007	0.48-0.49	0.75, 1, 1.25	0	0.63
LIP2	In phase bidirectional cyclic triaxial test	11/06/2007	0.5	0.75, 1, 1.25	48	0.89
LIP3	In phase bidirectional cyclic triaxial test	07/06/2007	0.47-0.48	0.75, 1, 1.25	94	0.85
LIP4	In phase bidirectional cyclic triaxial test	21/06/2007	0.49-0.5	0.75, 1, 1.25	138	0.84

(*) Loading frequency is f = 0.8 Hz, and sampling frequency is 80 Hz. The mean deviatoric stress is q_{av} = 200 kPa and the mean confining pressure is $\sigma_3'^0$ = 200 kPa.

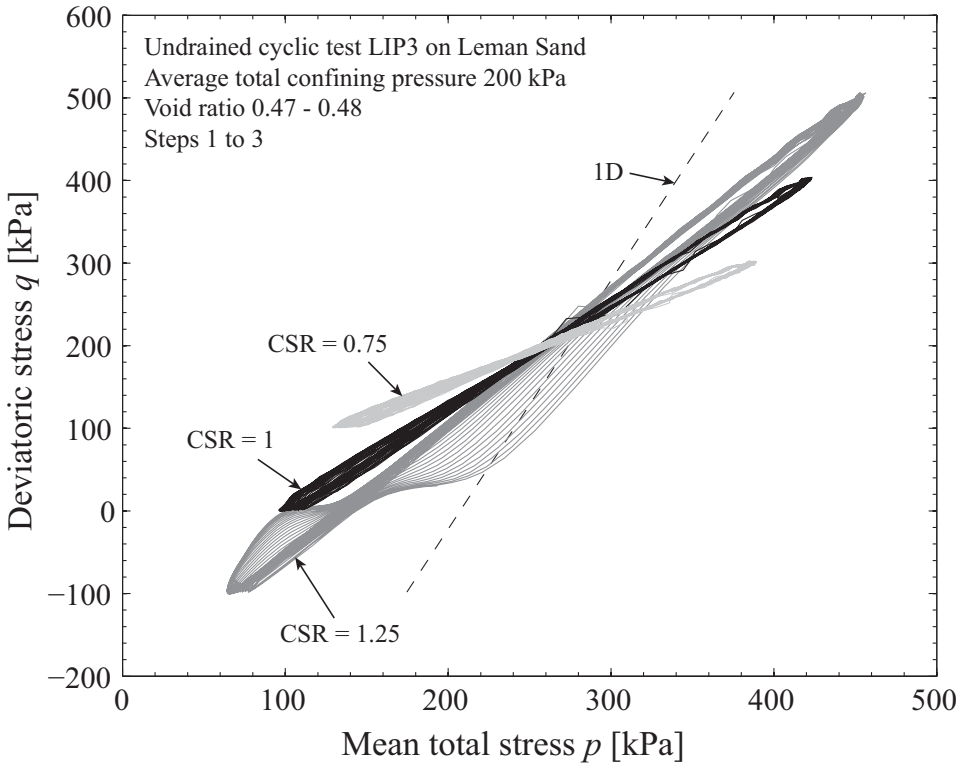

Fig. 6.1. Total stress paths of an in-phase bidirectional test.

6.2.1.2 Out-of-phase bidirectional loading paths

Out-of-phase bidirectional loading paths are performed with a time-lag between the sinusoidal deviatoric stress and confining pressure. The important parameters for the definition of loading are the confining pressure amplitude $\Delta\sigma_3$ and the phase angle between the two cyclic superimposed load. A positive phase angle means that the first peak of q arises before the peak of σ_3.

All tests start from isotropic compression at 200 kPa, with q = 0, and begin in the direction of compression with an increase of q (Fig. 6.2 and Fig. 6.3). The time-lag between σ_3 and q is triggered by the controller, which smoothly and rapidly make σ_3 joining the prescribed curve. The sign of the phase angle ζ sets the direction of rotation of the stress path, while its value influences their shapes (Fig. 6.2). The ratio $\Delta\sigma_3$ / Δq also modifies the shapes of the stress paths, as can be observed by comparing Fig. 6.2b and Fig. 6.2c.

Tab. 6.2. Cyclic undrained out-of-phase bidirectional tests on Leman Sand (*)

N°	Test description	Date	Void ratio	CSR [.]	$\Delta\sigma_3$ [kPa]	Phase angle ζ [°]
OOP1	Unidirectional cyclic triaxial test	13/02/2008	0.46-0.47	0.1 - 0.17 - 0.24 0.32 - 0.4	0	-
OOP2	Out-of-phase bidirectional cyclic triaxial test	28/03/2008	0.45-0.47	0.1- 0.18 - 0.25 0.32 - 0.4	49	103
OOP3	Out-of-phase bidirectional cyclic triaxial test	21/05/2008	0.45-0.46	0.1 - 0.17 0.25 - 0.33	48	-103
OOP4	Out-of-phase bidirectional cyclic triaxial test	28/05/2008	0.45-0.46	0.09 - 0.17 0.24 - 0.32	99	-57
OOP5	Out-of-phase bidirectional cyclic triaxial test	26/05/2008	0.46-0.47	0.1 - 0.17 0.25 - 0.33	49-160	-103
OOP6	Out-of-phase bidirectional cyclic triaxial test	08/04/2008	0.45-0.47	0.09 - 0.17 - 0.24 0.31 - 0.38	49-199	57

(*) Loading frequency is f = 0.2 Hz, and sampling frequency is 20 Hz. Tests have various back pressure, yielding B > 0.95. The mean deviatoric stress is q_{av} = 0 kPa and the mean confining pressure $\sigma_3'^0$ = 200 kPa.

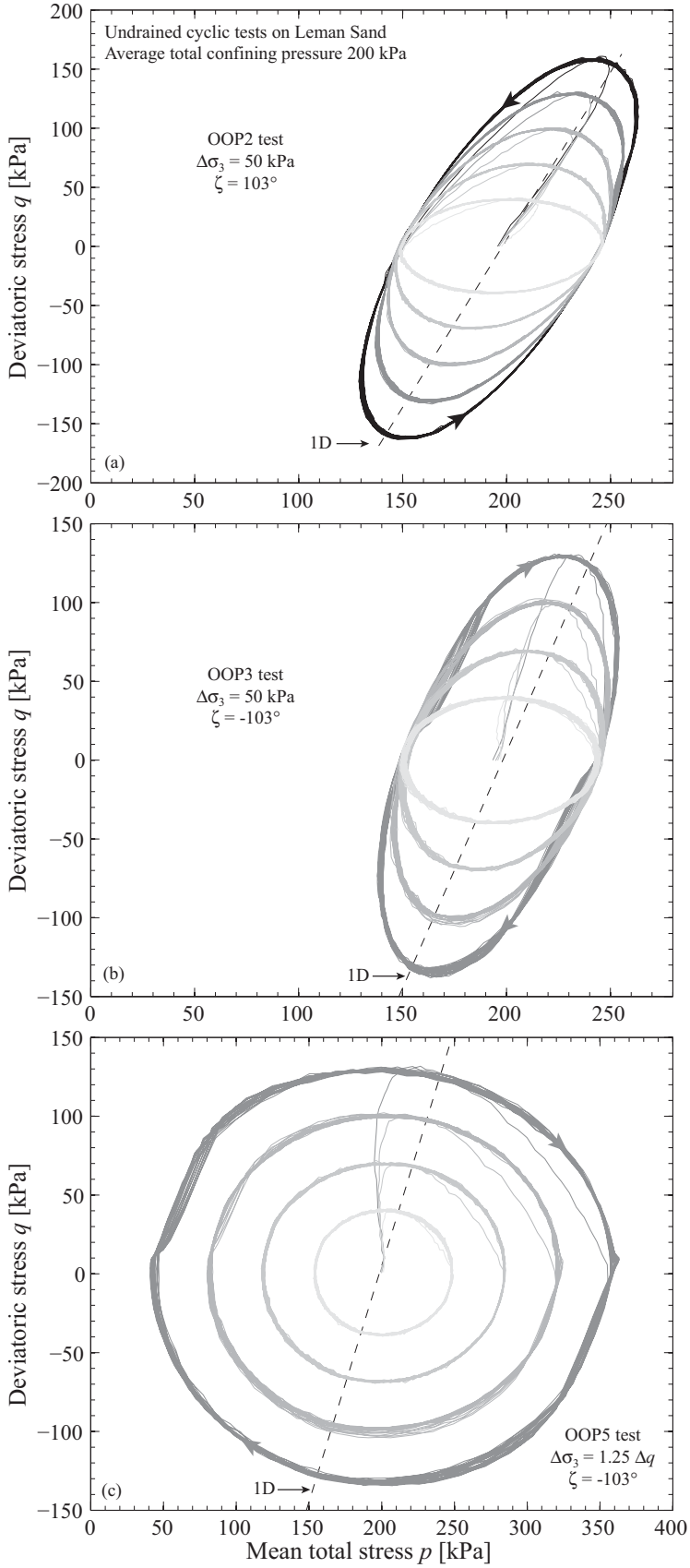

Fig. 6.2. Comparison of stress paths for cyclic out-of-phase bidirectional tests at different ζ and $\Delta\sigma_3$.

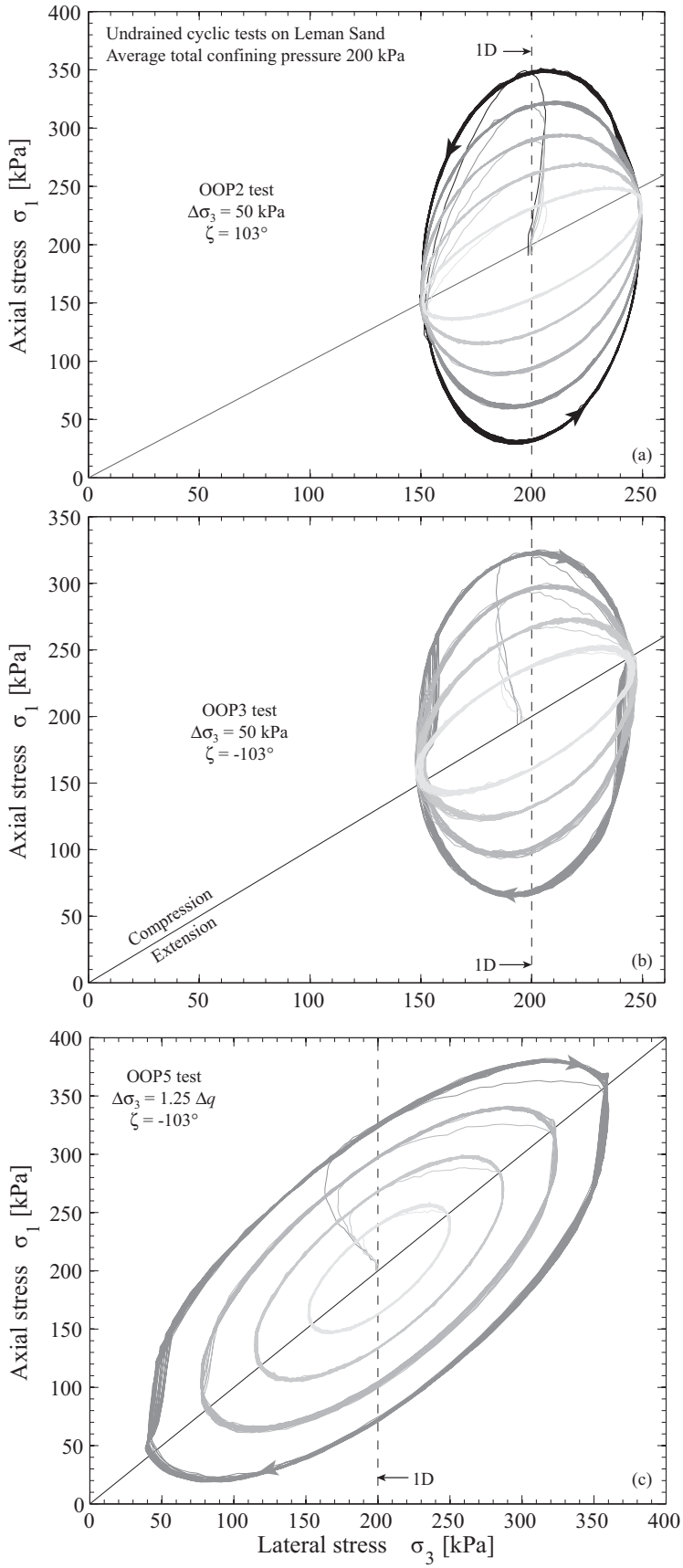

Fig. 6.3. Comparison of stress paths in the σ_1 vs. σ_3 plane for out-of-phase tests at different ζ and $\Delta\sigma_3$.

6.2.2 Introduction to test results

LIP1 to LIP4 tests were anisotropically consolidated, with a mean deviatoric stress of 200 kPa. Their behaviour is quite different from the isotropically consolidated bidirectional out-of-phase tests. However, deviatoric strain amplitudes are in the same range for all in-phase and out-of-phase tests, i.e. from 0.03% to 3%.

The effect of the superimposed compression is described below. These observations are based on values from the 10^{th} and 15^{th} cycle of each step, for anisotropic and isotropic tests respectively. As the cyclic behaviour of sand has a strong strain dependency, it was decided to show the results as functions of deviatoric strain amplitude.

6.2.3 Stress-strain relation

The stress-strain relation in unidirectional and bidirectional tests have similar patterns, whatever the characteristics of the bidirectional loading. To illustrate this observation, the four first steps of tests OOP1 and OOP5 are compared through their respective stress-strain relations (Fig. 6.4).

The following comments arise from the observation of these two tests:

- The shape of the stress-strain loops remains the same in unidirectional and bidirectional tests.
- For the four deviatoric stress amplitudes, there is more strain in extension in bidirectional tests.
- The development of cyclic liquefaction is faster in the bidirectional test.
- A fifth step is needed to reach failure in the unidirectional test.

6.2.4 Deviatoric strain amplitude

To compare the stress-strain relations in all multidimensional tests, the deviatoric stress amplitude vs. deviatoric strain amplitude is presented in Fig. 6.5. There is no large effect of the bidirectional in-phase loading (Fig. 6.5a), if we accept a small scattering due to soil variability. Out-of-phase bidirectional tests are slightly different from OOP1 (Fig. 6.5b).

Compared to the strain induced by unidirectional cyclic loading, the induced deviatoric strain of the bidirectional tests is first equivalent at 40 kPa, then lower at 70 and 100 kPa, then higher at 130 kPa and again lower at larger Δq. Three different overall shapes can be distinguished in Fig. 6.5b. The stress-

strain relation is (i) almost linear for OOP1, (ii) nonlinear with one inflexion point for OOP3, OOP4 and OOP5, and (iii) nonlinear with two inflexion points for the curves OOP2 and OOP6. The two different shapes encountered in bidirectional loadings are correlated with the sign of the phase angle (ζ). Curves with one inflexion point correspond to negative phase angles, and the curvy shape to positive phase angles.

The consequences of these different shapes are significant: at the fourth step (Δq = 130 kPa), there is a multiplying factor of 4 between $\Delta\varepsilon_q$ in unidirectional loading and in the out-of-phase tests with negative ζ. The value of the confining pressure amplitude $\Delta\sigma_3$ seems to have no influence on the stress-strain relation.

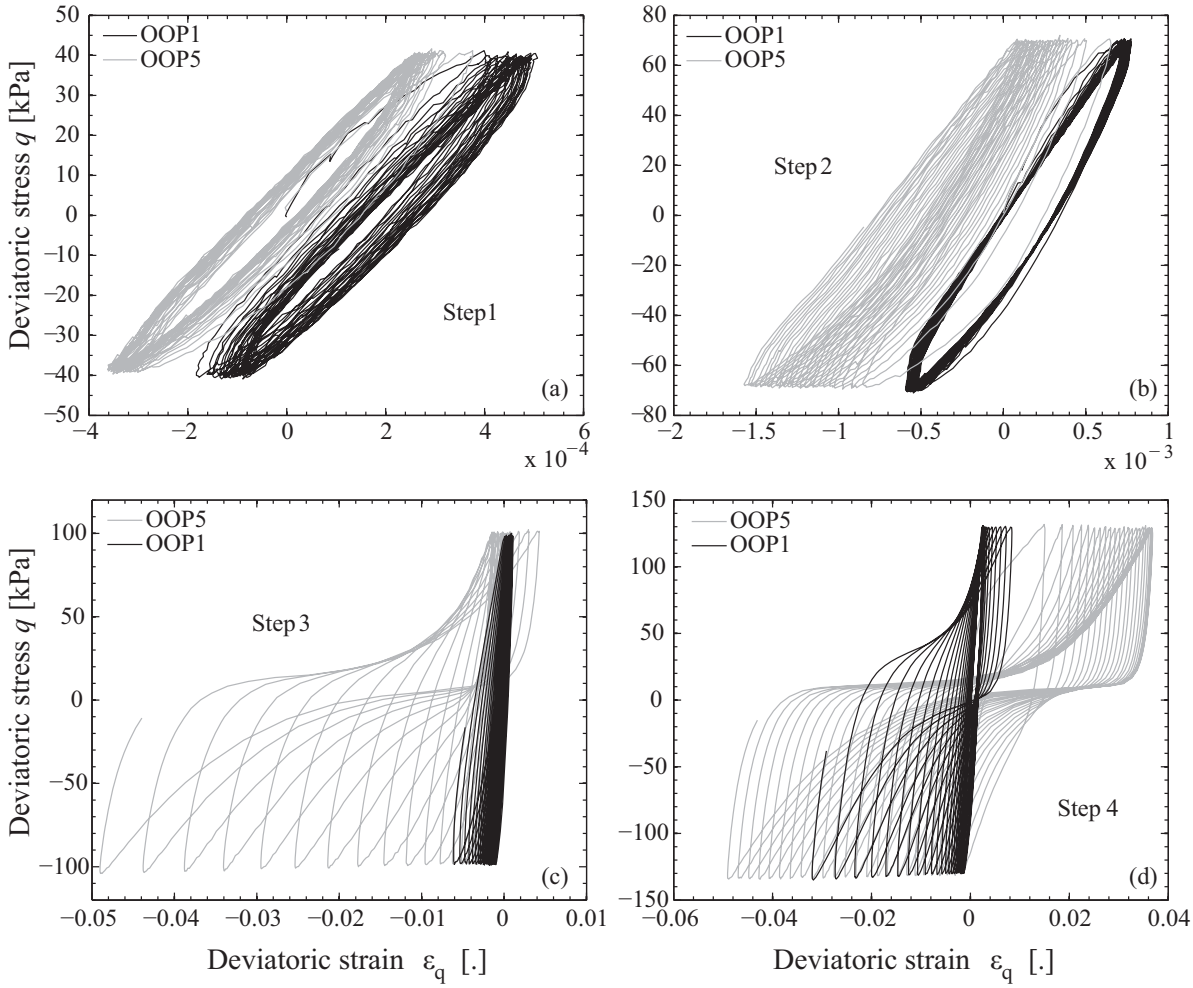

Fig. 6.4. Leman Sand stress-strain relations for 1D (OOP1) and 2D (OOP5) tests.

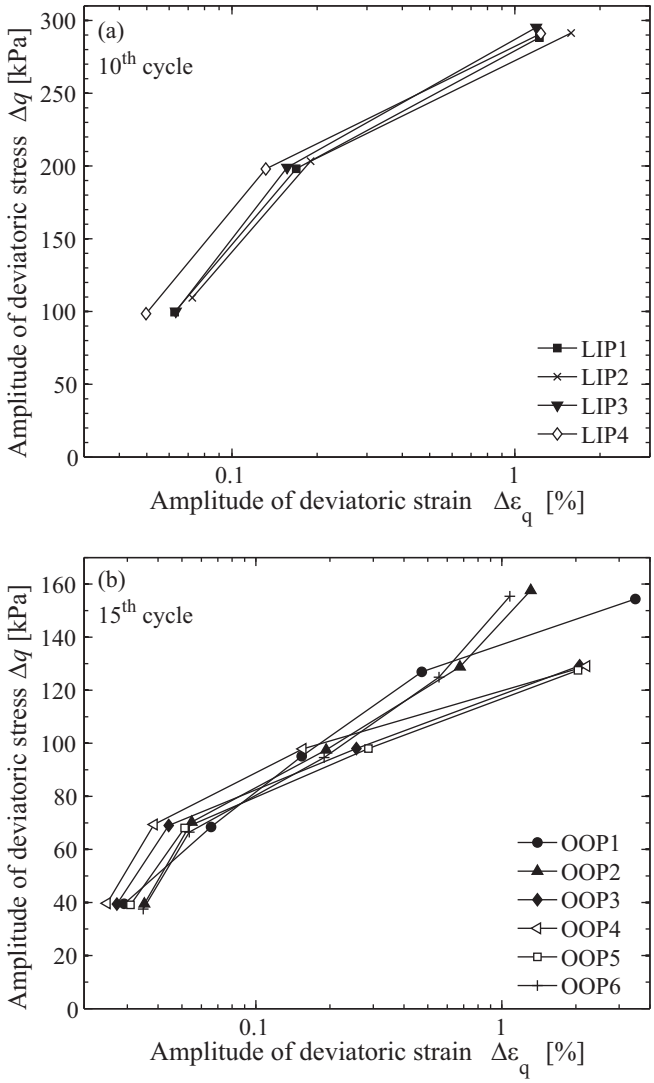

Fig. 6.5. Stress amplitude vs. strain amplitude (a) in-phase tests, (b) out-of-phase tests.

6.2.5 Number of cycles to failure

The number of cycles to reach failure is given for the out-of-phase tests in Tab. 6.3. Failure is not reached during in-phase tests. For negative phase angles, the number of cycles at failure is much lower than the reference test OOP1. On the contrary, failure is postponed for positive phase angles. In particular, the tests OOP2 and OOP3, which are exactly the same except for the direction of rotation, exhibit a major difference in the number of cycles to reach failure, with a 30% decrease of N^f caused by reversing ζ to negative.

Tab. 6.3. Number of cycles at failure for out-of-phase tests

Test	OOP1	OOP2	OOP3	OOP4	OOP5	OOP6
N^f	110	122	87	86	87	Reached $\Delta\varepsilon_q$ = 2.46% at N = 125
ζ	-	103	-103	-57	-103	57

6.2.6 Effective stress paths

As for the stress-strain relations provided in section 6.2.3, the effective stress paths of OOP1 (1D) and OOP5 (2D) are displayed in Fig. 6.6. They show that effective stress paths are also slightly sensitive to bidirectional effects.

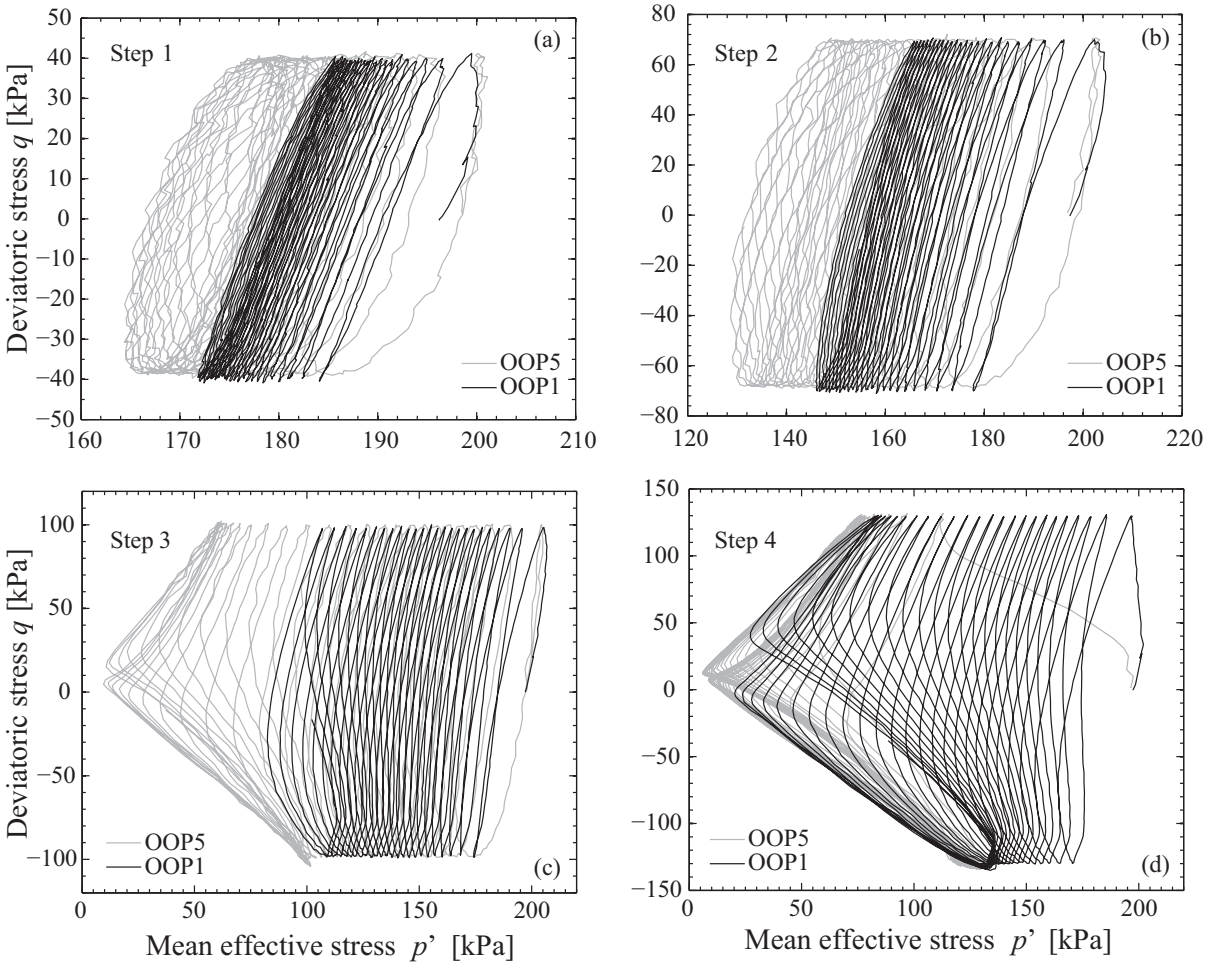

Fig. 6.6. Leman Sand effective stress paths of 1D and 2D tests.

It is again possible to see that stiffness degradation arises faster in bidirectional conditions, because the loops are always closer to the point p' = 0. The stress loops are rounder in bidirectional condition, because of the evolution of the cyclic confining pressure. However, the overall patterns of effective stress path are the same in unidirectional and bidirectional tests, with first a regular decrease of the

mean effective stress, and then the formation of wings around the phase transformation lines. At cyclic liquefaction in the fourth step (Fig. 6.6d), the bidirectional test exhibits very low effective stress.

6.2.7 Excess pore pressure

The maximum pore pressure ratio at each step is shown in Fig. 6.7, and the rate of increase of u_r along each step in Fig. 6.8. Overall, for tests with constant confining pressure amplitude, the maximum pore pressure lines are parallel to either LIP1 (Fig. 6.7a) or OOP1 (Fig. 6.7b). For the latter, the slope is steeper for OOP5 and OOP6 because the confining pressure amplitude increases at each step.

The increase of the maximum pore pressure ratio is close to a straight line for LIP1 to LIP4. On the contrary, for isotropic out-of-phase loadings, there is first an increase, and then a threshold for OOP2 to OOP6. For LIP1 and OOP1, the maximum value is 1 as expected for cyclic liquefaction. With the cyclic confining pressure, the threshold value is above 1, depending on the confining pressure amplitude and the phase angle. Moreover, the threshold pore pressure ratio is obtained at lower values of the strain amplitude for out-of-phase bidirectional tests.

The effect of bidirectional loading conditions on the pore pressure increase can be better quantified by introducing the rate of increase of the pore pressure ratio, rather than using $u_{r,m}$ itself. The rate of increase of the pore pressure ratio is calculated from the maximum point of u_r at each cycle of the test. As excess pore pressure build-up is gradual, linear regressions are chosen for calculation of the rate of increase. That value reflects the evolution of pore pressure along the 25 cycles.

For in-phase loadings (Fig. 6.8a), the rate of increase of u_r is similar for the four cases under 0.2% deviatoric strain. At larger strain, it seems to decrease as the confining pressure amplitude increases, i.e. in-phase bidirectional conditions induce lower pore pressure build-up when $\Delta\sigma_3$ is higher.

For out-of-phase loadings (Fig. 6.8b), the rate of increase is low at small strain, forms a peak at medium strain and decreases again at large strain, when the threshold u_r value is reached at cyclic liquefaction. Compared to the bidirectional tests, which form a narrow path, the OOP1 line is shifted to the bottom and to the right. The peak arises at the third step for OOP2 to OOP6 but only at the fourth step for OOP1.

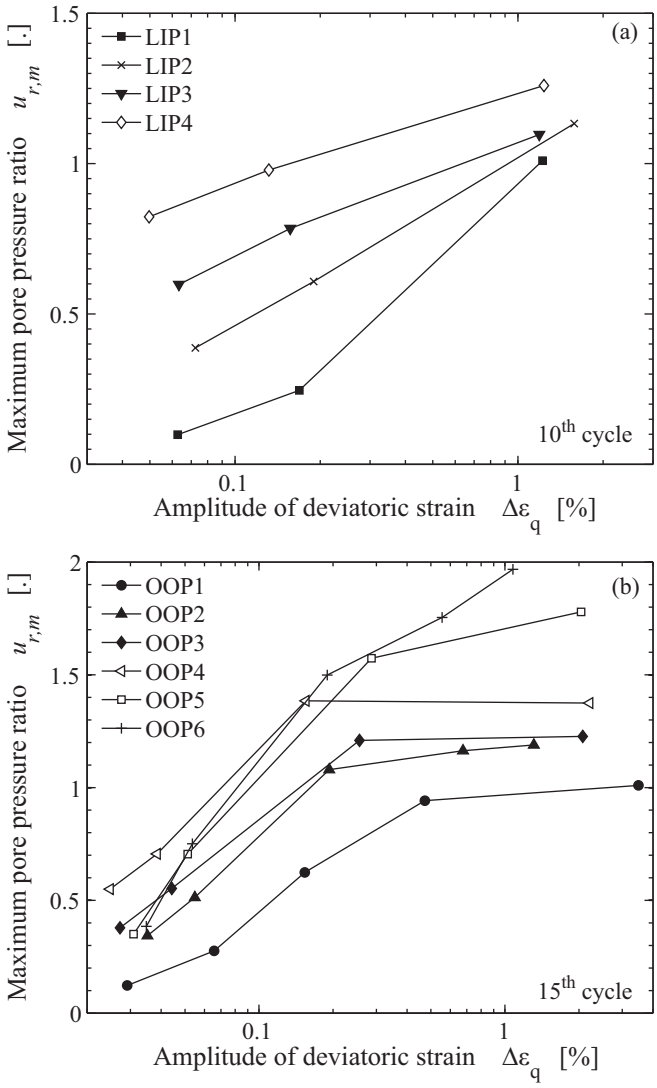

Fig. 6.7. Pore pressure ratio vs. deviatoric strain amplitude (a) in-phase tests, (b) out-of-phase tests.

This difference involves that the rate of pore pressure increase is stronger in bidirectional out-of-phase conditions before the occurrence of cyclic liquefaction, which thus arises faster in 2D tests than in the 1D test. Moreover, the maximum pore pressure build-up is reached at lower strain amplitudes in bidirectional conditions. This means that the coupling of strains and pore pressures may be influenced by bidirectional loading conditions.

Among the out-of-phase bidirectional tests, the higher values of the rate of increase of u_r are obtained for negative phase angles. The amplitude of the confining pressure is also important. For example, at the same phase angle ζ = -103°, the peak rate increases by 10% between OOP3 and OOP5, performed at 50 kPa and 125 kPa confining pressure amplitude, respectively.

These analyses show that bidirectional effects on the pore pressure build-up depend on the phase angle and the cyclic stress amplitudes, $\Delta\sigma_3$ and Δq.

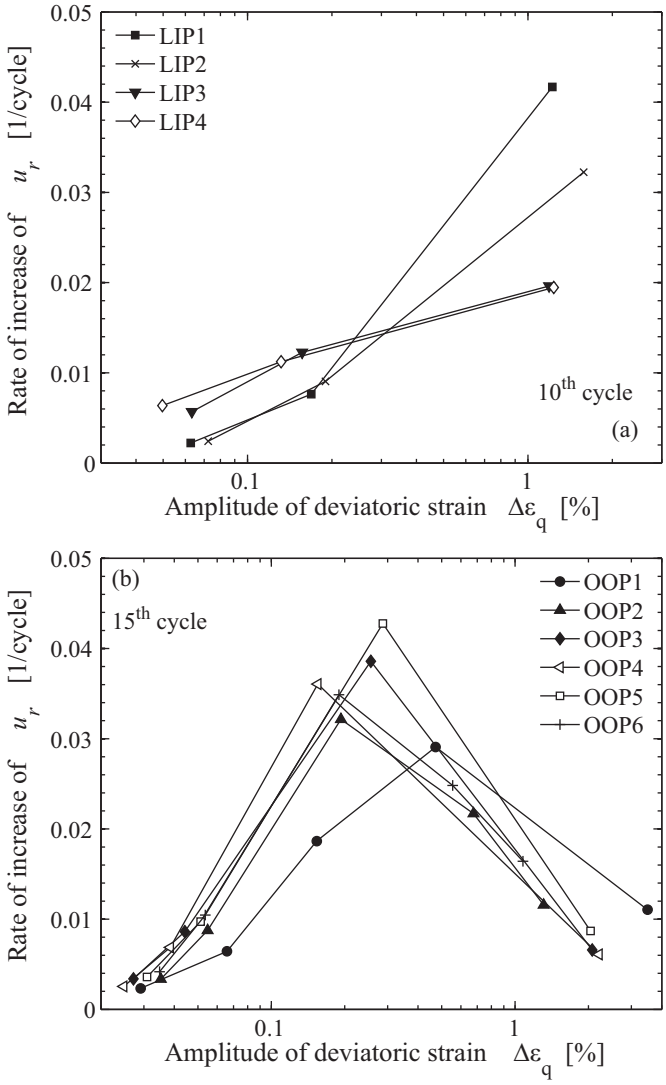

Fig. 6.8. Rate of pore pressure ratio increase vs. deviatoric strain amplitude (a) in-phase tests, (b) out-of-phase tests.

6.2.8 Multidirectional effects on dynamic parameters

The secant shear modulus tends to decrease with the deviatoric strain amplitude (Fig. 6.9), as experimental evidence usually shows. Enhancing the previous comments on the stress-strain relation, a major difference arises for out-of-phase bidirectional loadings: G_{sec} increases between the first and second step while the strain amplitude increases (Fig. 6.9b). As a consequence, a peak is formed in the degradation curve. The higher values of the peak correspond to negative phase angles. Moreover, at the same phase angle, lower confining pressure amplitude induces higher secant shear modulus. Above $\Delta\varepsilon_q = 0.1\%$, the six tests follow a unique line. For in-phase tests (Fig. 6.9a), there is hardly any difference between bidirectional and unidirectional loading.

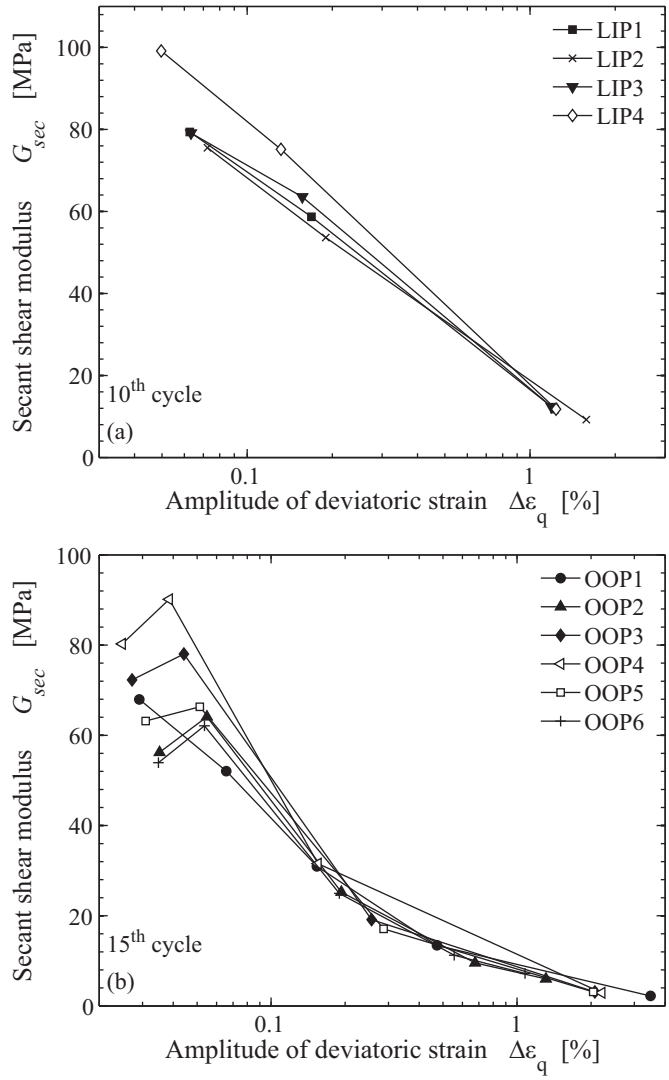

Fig. 6.9. Secant shear modulus vs. deviatoric strain amplitude (a) in-phase tests, (b) out-of-phase tests.

The damping ratio is displayed in Fig. 6.10. This parameter is very sensitive to friction between the axial load bar and the cell, because the shape of the curve is slightly changed at the moment of unloading. This friction appears at low strains on four cases here, and these values are thus disregarded.

For the other damping ratios, the different initial stress conditions between in-phase tests (Fig. 6.10a), which were anisotropically consolidated, and out-of-phase bidirectional tests (Fig. 6.10b), which were isotropically consolidated, are reflected on the overall shape of the $\Delta\varepsilon_q$ - D curves. Indeed, damping ratio monotonically increases with the strain amplitude in anisotropic conditions with no stress reversal (Fig. 6.10a), while it forms a peak around $\Delta\varepsilon_q$ = 0.15 to 0.5% in isotropic conditions performed with symmetric stress reversal (Fig. 6.10b). The occurrence of a peak in the $\Delta\varepsilon_q$ - D curve is due to the appearance of dilative behaviour when the stress path crosses the phase transformation line (cf. Chapter 4). This line marks the boundary, in the p' - q plane, between the dilative and the contractive

domains.

For in-phase tests, no trend appears in the evolution of damping ratio with regard to multidirectional conditions. However, the $\Delta\varepsilon_q$ - D relation is influenced by bidirectional out-of-phase conditions. The overall shape of this curve is slightly flatter in the 1D test OOP1. In this curve, the peak value of D arises at higher $\Delta\varepsilon_q$ than in 2D conditions. After the peak, the decrease of D is stronger for bidirectional loadings.

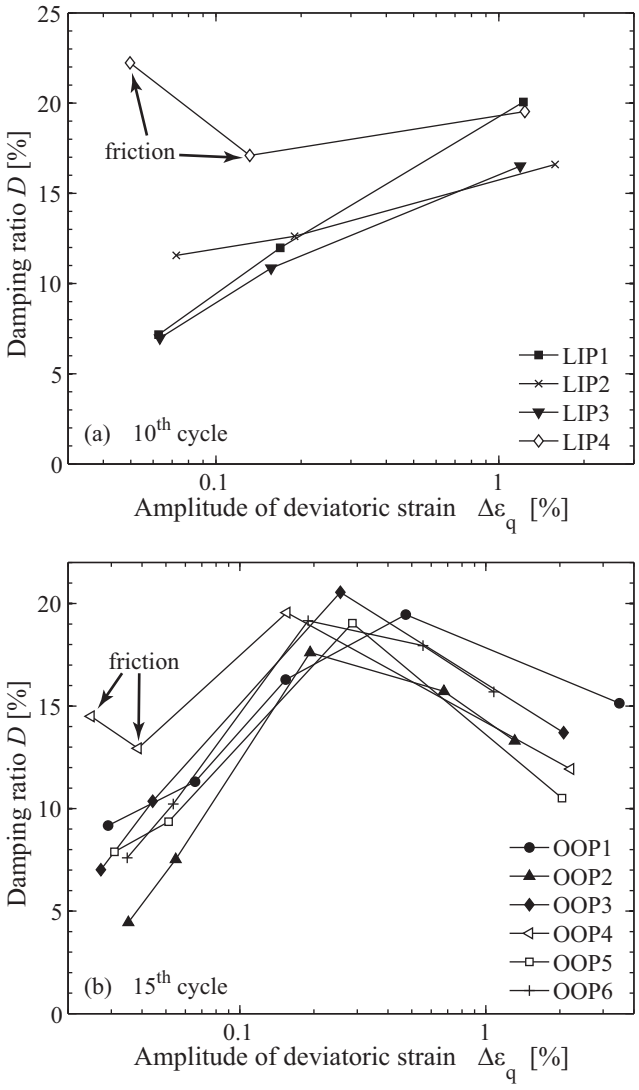

Fig. 6.10. Damping ratio vs. deviatoric strain amplitude (a) in-phase tests, (b) out-of-phase tests.

Moreover, the peak of damping ratio arises at the 4th step of the 1D test OOP1, and only at the 3rd step for OOP2 to OOP6 (2D tests). This is consistent with the evolution of pore pressure build-up (section 6.2.7), which show that the maximum rate of stiffness degradation arises sooner in out-of-phase bidirectional loadings.

6.2.9 Analyses of multidirectional effects

The comparison between unidirectional deviatoric cyclic tests and cyclic tests with superimposed confining and deviatoric stresses proves that superposition of the two loadings has an influence on undrained saturated sand behaviour.

6.2.9.1 Concerning pore pressures

First the theoretical evaluation of the effect of the cyclic confining stress alone is developed. In order to account for the change in applied total confining pressure, the pore pressure ratio is decomposed into two parts: $u_r = u_r^{comp} + u_r^q$.

We assume that the cyclic compression (sinusoidal variation of σ_3, with a mean value σ_3^0) of the saturated granular medium results in a cyclic pore pressure centred on its initial value, which is zero in our tests, with the same amplitude as the cyclic confining pressure. This gives a theoretical pore pressure variation resulting from the cyclic confining pressure $\Delta u = \sigma_3 - \sigma_3^0$.

On the other hand, the *B*-Skempton coefficient, which is calculated for each test, reaches approximately 0.96. Indeed, this dense sand has a high stiffness, thus *B* = 1 cannot be reached (Head 1984). To account for the compressibility of the pore fluid of each individual sample, which is usually neglected although it might not be exactly the same in all cases, the correction factor *B* is introduced within the theoretical pore pressure ratio resulting from the isotropic load, defined as:

$$u_r^{comp} = \frac{B\left(\sigma_3 - \sigma_3^0\right)}{\sigma_3^0} \tag{6.2}$$

In 1D tests, u_r^{comp} is always equal to zero. The pore pressure ratio u_r thus reflects only the hydro-mechanical coupling. For 2D tests, the part of the pore pressure ratio related to the cyclic confining pressure, u_r^{comp}, is added to the true pore pressure variations resulting from the soil tendency to dilate and contract, which we choose to call u_r^q. The notion of total pore pressure (u_r) is thus not equivalent in 1D and 2D tests, this is why u_r can reach values higher than 1 in bidirectional tests. The parameter u_r^q is thus introduced for 2D tests, to allow the comparison of excess pore pressure components resulting only from the deviatoric stress. The relation is explicitly:

$$u_r^q = u_r - u_r^{comp} \tag{6.3}$$

Thanks to this decomposition of the pore pressure ratio into two parts which takes into account the change of total applied stress path, the actual pore pressure increase due to cyclic loading, u_r^q, can thus be carefully analysed. Moreover, the pore fluid compressibility is also taken into account by including the *B*-Skempton coefficient into the component of isotropic loading. We thus ensure that u_r^q is

comparable between all tests. The following analyses then provide a solid verification for the results on pore pressure which were presented before (section 6.2.7).

The bidirectional effects on the pore pressure ratio components is shown for tests OOP1 (1D), OOP2 (2D) and OOP3 (2D) in Fig. 6.11. As expected, the shape of u_r for bidirectional loadings is different from the unidirectional loading. But using u_r^q instead, the shapes are very similar. At the triggering of cyclic liquefaction, a double peak appears in u_r when the stress path crosses the phase transformation line. The tips of the peak of u_r reach 1 at cyclic liquefaction during OOP1, and also for u_r^q during OOP2 and OOP3.

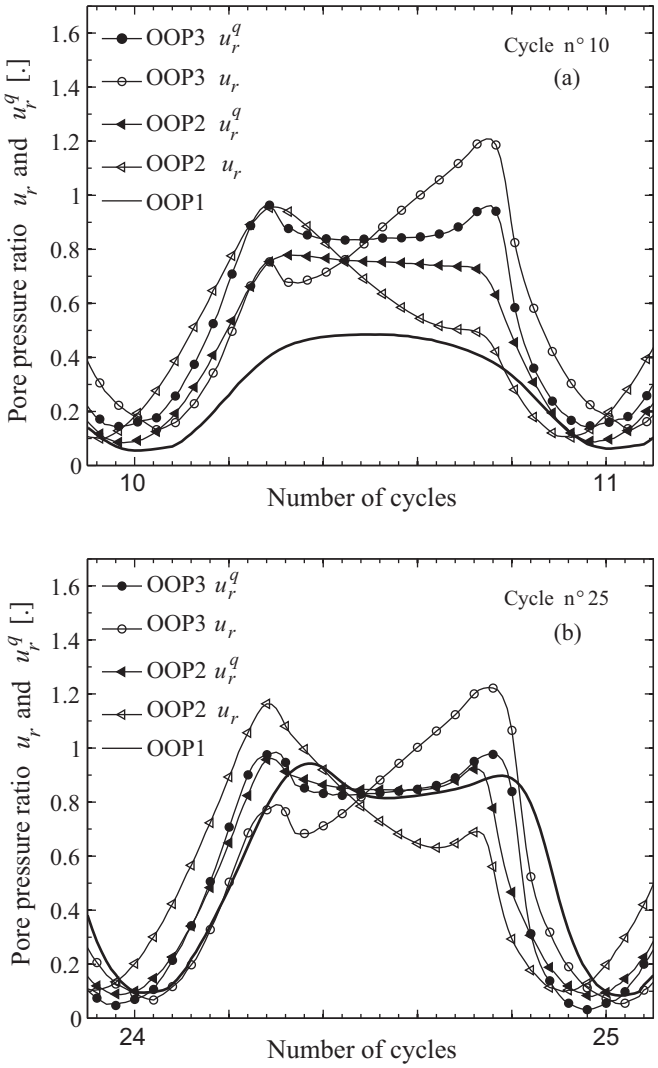

Fig. 6.11. Pore pressure ratio and effect of cyclic confining pressure during one cycle at cyclic liquefaction (step n°4) (a) cycle number 10 (b) cycle number 25.

We show, in Fig. 6.11a, that the increase of pore water pressure is not the same for the three tests. For OOP1, the maximum u_r reached during cycle number 10 is 0.48 and the double peak does not appear. For OOP2, the maximum value of u_r^q is 0.78 and the first peak starts appearing. Finally OOP3

maximum value is 0.95, with a clear double peak shape. This means that, at the same moment (cycle number 10), cyclic liquefaction is almost reached for one of the bidirectional test, while the unidirectional test still exhibits stiffness degradation and pore pressure build-up.

On the contrary, at the 25th cycle (Fig. 6.11b), cyclic liquefaction appears for all the curves. In that case, u_r^q and u_r are very similar for bidirectional and unidirectional loading respectively.

Depending on the phase angle and confining pressure amplitude, a peak of u_r may be either enhanced or decreased by the confining stress. It also confirms that the rate of increase of pore pressure is different between unidirectional and bidirectional conditions (cf. section 6.2.7). That difference in the development of excess pore water pressure can be linked to the analyses of deviatoric strains. Indeed, unidirectional deviatoric strains (OOP1) are much lower than the bidirectional values at the fourth step of out-of-phase loadings (cf. section 6.2.4).

To emphasize the effect of the phase angle on the pore pressure build up, the rate of increase of u_r is given as a function of the phase angle in Fig. 6.12 for out-of-phase loading at the third step. This is the maximum value of the rate of u_r for OOP2 to OOP6. It also shows that the amplitude of the confining pressure is important for bidirectional effects.

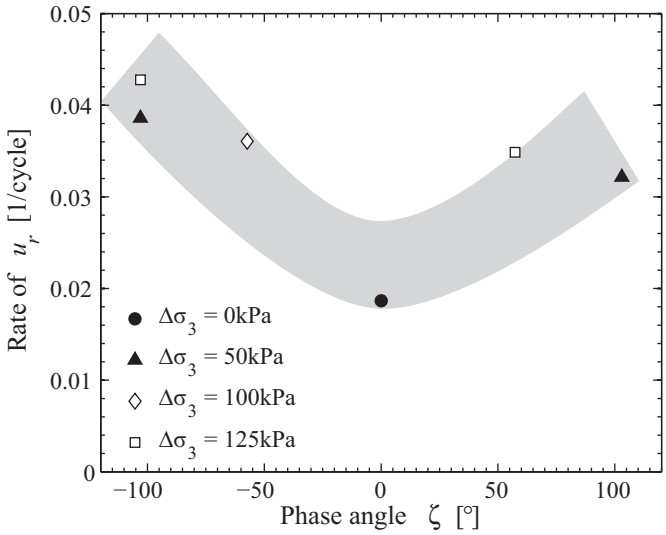

Fig. 6.12. Rate of u_r vs. phase angle for OOP1 to OOP6 at step n°3.

6.2.9.2 Concerning dynamic parameters

The stress - strain relation is also influenced by the complex loading. More precisely, it was observed that the phase angle plays a major role in soil response to complex loadings, and particularly on the increase of deviatoric strains. While in-phase tests hardly show any sensitivity to cyclic confining stress, out-of-phase loadings are much more sensitive to a change in the cyclic loading path.

This dependency arises at different strain levels. For the secant shear modulus, the main feature is a peak, close to 0.03%, in the secant shear modulus degradation curve, which is also reflected in the stress-strain relation. Out-of-phase bidirectional tests are stiffer at the second loading step. On the contrary, at the fourth loading step, and at a strain range from 0.5% to 2%, the unidirectional loading is stiffer than complex ones. At this strain level, however, the $\Delta\varepsilon_q$ - G_{sec} curve shape is not influenced.

The $\Delta\varepsilon_q$ - D relation, on the other hand, also depends on bidirectional effects. The main consequence of the superposition of loadings is the occurrence of the peak in the evolution of the damping ratio, which arises at smaller strains during out-of-phase bidirectional tests.

6.2.9.3 Interpretation of coupling effects

As shown in the total stress paths (Fig. 6.3), all tests, whether unidirectional or bidirectional, start with compression. The extension phase then arises, either on the left or on the right of the 1D line, depending on the sign of the phase angle. The increase of the rate of stiffness degradation with negative phase angles is thus due to the direction of rotation of the stress path.

As shown in Fig. 6.11a during the 10^{th} cycle (step n°4), when the rate of pore pressure increase is at its maximum, i.e. stiffness degradation also, u_r has a strong negative pore pressure second peak in OOP3. This is because the maximum value of σ_3 arises at the moment of that second peak. We then assume that the amplification of the soil response, during stiffness degradation and for negative phase angles, is related to the timing of dilative and contractive volumetric parts of the motion with regard to the evolution of the total confining pressure. If σ_3 is high during phase transformation at unloading, as shown for OOP3, the second spike of u_r is emphasized.

This can be related to the amplification of deviatoric strain amplitude, at that step, for negative phase angles (Fig. 6.5): $\Delta\varepsilon_q$ = 0.5%, 0.7% and 2.1% for OOP1 (1D), OOP2 ($\zeta > 0$) and OOP3 ($\zeta < 0$) respectively (15^{th} cycle). The three other bidirectional tests also confirm this amplification of deviatoric strains for negative phase angles. The coupling between the pore pressure and the deviatoric strain may then play an important role in the amplification of stiffness degradation in certain conditions of complex loading.

6.2.10 Conclusions

To conclude, the coupling effect due to superposition of a cyclic deviatoric and confining stress is complex, even if both are at the same frequency. The coupling mainly depends on the phase angle. The stress path and strain level are also important for the extent of the effect. The most important conclusion from the tests is that the triggering of cyclic liquefaction may happen earlier with the bidirectional loading in certain conditions. The development of pore water pressure, of deviatoric strain and the

degradation of the secant shear modulus are faster for OOP2 to OOP6. The peak in the damping ratio arises sooner. Failure triggering is slower for bidirectional tests with a positive phase angle, i.e. the development of large deviatoric strain amplitude is decreased in part of the bidirectional tests. On the contrary, failure arises much sooner for all bidirectional tests with a negative phase angle.

6.3 Irregular seismic loading in multidirectional condition

6.3.1 Description of irregular loadings with a seismic signal

Real earthquake acceleration recordings, obtained at the ground surface, are used to design the irregular signals given as input loading of varying amplitude and frequency content. As for the previous 2D experiments, two irregular loadings are superimposed on the principal directions σ_1 and σ_3. The seismic recording was obtained at 82 km of the earthquake epicentre, for an earthquake of moment magnitude of 6.5 (San Simeon earthquake, California, December 22nd 2003, acceleration recording data provided by COSMOS Virtual Data Center http://db.cosmos-eq.org/scripts/default.plx). These conditions do not correspond to in situ nonlinear behaviour. The seismic event was chosen anyway, because the rather large peak ground acceleration (PGA) of the vertical recording, once treated, gave interestingly large variations of the confining pressure.

Assuming initial stress isotropy, the imposed irregular functions $q(t)$ and $\sigma_3(t)$ (Fig. 6.13) are calculated from an elastic inverse analysis and a scaling of the original seismic recording, to obtain loadings in the nonlinear regime. The process used to obtain the functions $q(t)$ and $\sigma_3(t)$ is described in Appendix 2.

The aim of these tests is not to realistically reproduce the in situ response, but rather to evaluate the effect of bidirectional loading on sand response for an irregular signal representative of a seismic loading. The signal is representative of the bidirectional stress field at 10 m depth, in the middle of a thick Leman Sand layer. Arbitrarily, the maximum deviatoric stress, equivalent to the peak ground acceleration (PGA) at the surface, arises on the side of extension on the time-history of q.

The Fourier spectrum of both functions are also provided below (Fig. 6.14).

From the time-history of stresses at the desired depth (Fig. 6.13), three irregular tests were performed in different conditions (Tab. 6.4). Two parameters are introduced to characterize the irregular motion. CSR^{EQ} is the maximum amplitude of the cyclic stress ratio (defined in Eq. 2.20 for cyclic loading), while $\Delta\sigma_3^{EQ}$ is the maximum amplitude of confining pressure. They are both expressed as relative values compared to the initial stress.

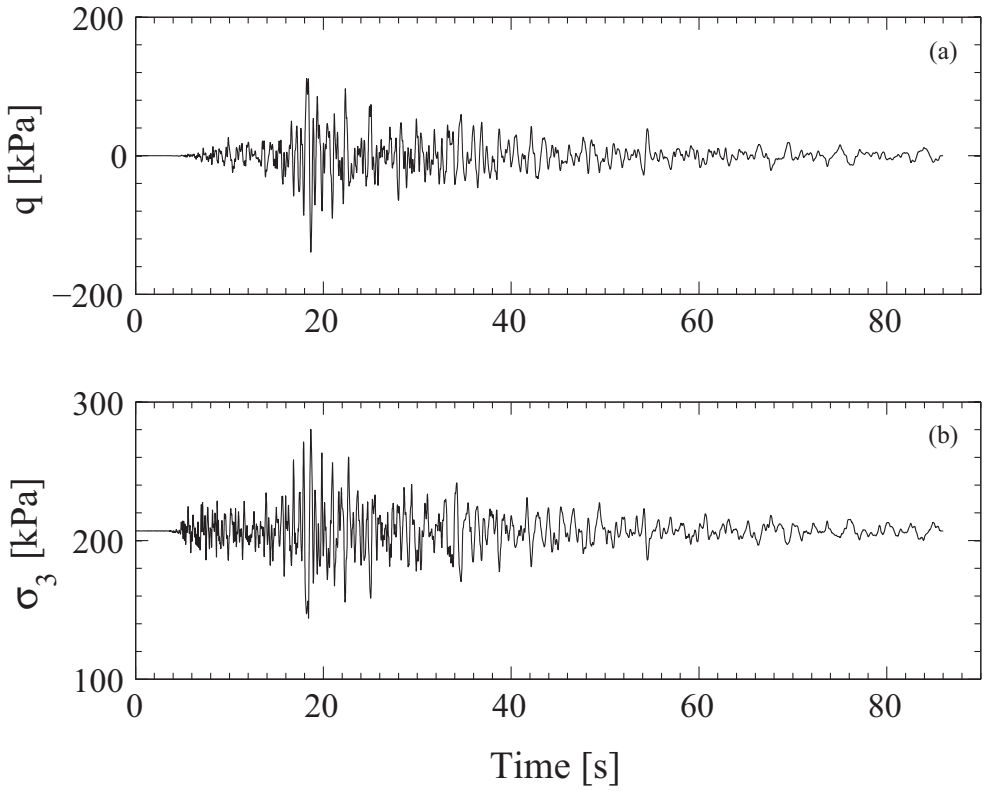

Fig. 6.13. Time-history of the deviatoric stress (a) and confining pressure (b) used for bidirectional irregular loading.

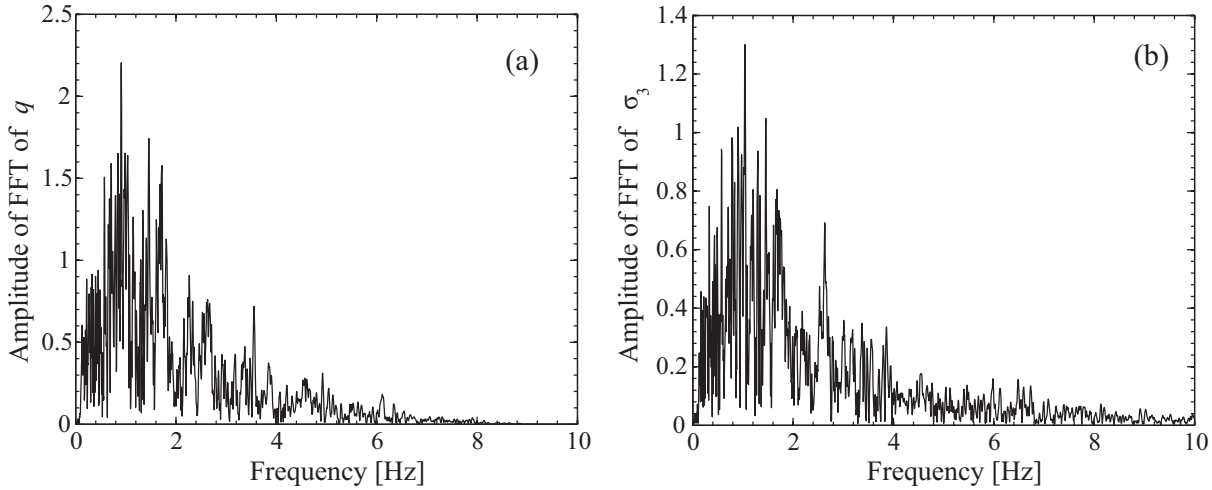

Fig. 6.14. Fourier spectrum of the irregular deviatoric stress (a) and confining pressure (b).

Tab. 6.4. Irregular undrained unidirectional and bidirectional tests on Leman Sand (*)

N°	Test description	Date	Void ratio	CSR^{EQ} [.]	$\Delta\sigma_3^{EQ}$ [kPa]
IUB1	Unidirectional irregular test with PGA in extension	18/02/2009	0.46-0.47	-0.3 -0.44 -0.68	0 0 0
IUB2	Bidirectional irregular test with PGA in extension	13/02/2009	0.47-0.48	-0.31 -0.43 -0.69	72 107 150
IUB3	Bidirectional irregular test with PGA in compression	11/02/2009	0.49	0.46	72

(*) Sampling frequency is 312 Hz. The initial deviatoric stress is q_{av} = 0 kPa and the initial confining pressure is $\sigma_3'^0$ = 207 kPa. The back pressure is 700 kPa for all tests.

The unidirectional test IUB1 only includes the irregular deviatoric stress, while the confining pressure remains constant ($\sigma_3(t)$ = 207 kPa). The bidirectional test IUB2 follows exactly the same variation of q as IUB1, with the maximum amplitude in extension, but the total confining pressure also evolves irregularly. For both tests, soil failure is not obtained during the first run of the time-history. A drainage is performed, and the load is re-run with an amplification factor of 1.5 for both amplitudes of deviatoric stress and confining pressure. This process is repeated again a third time, at which cyclic liquefaction appears.

The third irregular test IUB3 is slightly different. It is performed with the maximum deviatoric stress in compression and in bidirectional conditions. The time-history of σ_3 remains the same as IUB2, also q and σ_3 are sort of out-of-phase compared to the original signal. This method is analogous to the method proposed in Ishihara & Yasuda (1972), where the irregular stress-controlled tests either presented a maximum deviatoric stress in compression or extension. It was assumed that both represented equivalently the seismic load, and average characteristics were selected. In the case of bidirectional loading, the two superimposed loadings are defined in relation with each other, also reversing only one of them, as in IUB3, provides interesting insight into the effect of superposition of a volumetric and a deviatoric stress component.

The Mohr circles of total stresses of the three irregular tests are displayed below (Fig. 6.15, Fig. 6.16 and Fig. 6.17). They clearly spot the differences between the three similar loading, as the different assumptions lead to quite different Mohr circles. In unidirectional condition (Fig. 6.15), the confining pressure is constant, and is alternatively the major or the minor principal stress. The Mohr circles on the left have larger diameters, because the peak deviatoric stress is higher in extension. In bidirectional conditions, the Mohr circles are either clustered together in IUB2 (Fig. 6.16), or spread along the

normal stress in IUB3 (Fig. 6.17), because of the inversion of the sign of *q* in IUB3. It is interesting to see that the Mohr planes, which are closer to the representation of a seismic load, IUB2, yields a narrow cluster of Mohr circles.

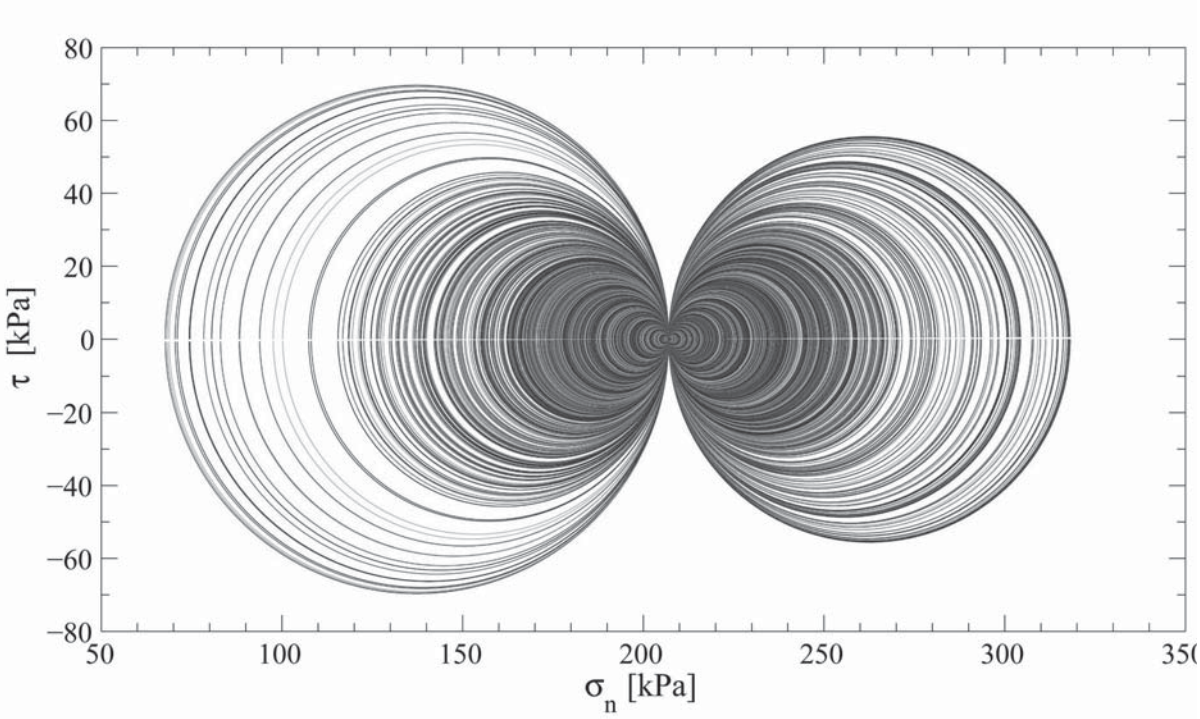

Fig. 6.15. Mohr planes extracted from IUB1 in unidirectional conditions.

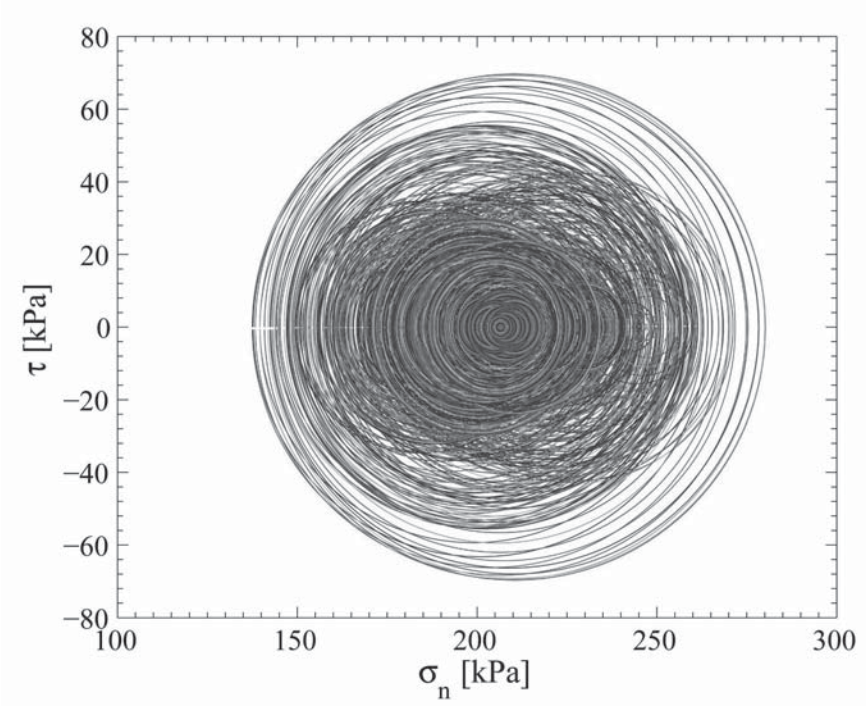

Fig. 6.16. Mohr planes extracted from IUB2 in bidirectional conditions.

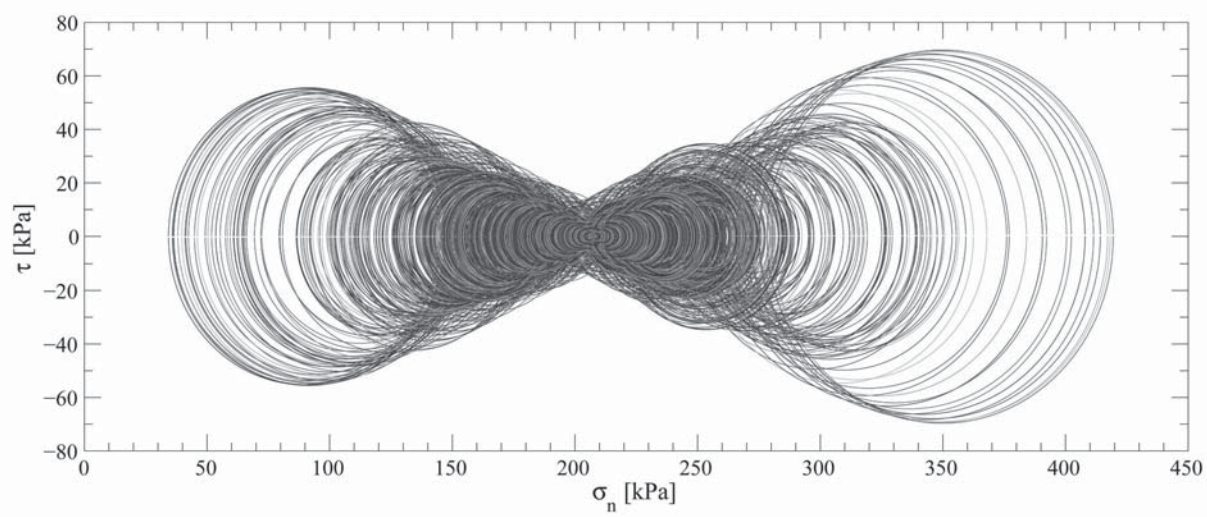

Fig. 6.17. Mohr planes extracted from IUB3 in bidirectional conditions with an inverse deviatoric stress.

Irregular tests with unidirectional and bidirectional seismic loading are then described and commented in the following sections. The three irregular tests are compared for each level of loading, i.e. for the three values of maximum cyclic stress ratio CSR^{EQ}. As the void ratio and the initial conditions are similar in the three tests, the different observed behaviours are only due to the choice of irregular parts of confining pressure and deviatoric stress.

6.3.2 Description of stress paths

For the three levels of CSR^{EQ}, the *p* - *q* relation is similar because the scaling coefficient of stress motions is applied to both the deviatoric stress and the confining pressure (Fig. 6.18a, b and c). The unidirectional test IUB1 clearly follows a straight line of slope 3, while the bidirectional test IUB2 has an ovoid shape close to out-of-phase bidirectional loadings. The test IUB3, added in Fig. 6.18b, is closer to in-phase bidirectional loading because of its elongated shape.

In the effective stress diagrams (Fig. 6.18d, e and f), the mean effective stress decreases as a consequence of the 1D and 2D loadings. The higher $|CSR^{EQ}|$, the more *p'* decreases, until complete softening at $p' = 0$, which causes temporary loss of strength. Although the bidirectional loading is fuzzier, the effective stress paths of IUB1 and IUB2 are very similar. They both take a pointed shape near the point $p' = 0$ (Fig. 6.18f). The effective stress path of IUB3 also has a similar shape, with the noticeable difference of reaching the point $p' = 0$ in only one step. This complete softening provides curves which are close to the sinusoidal effective stress paths with wing shapes. Their similarities are detailed in section 6.3.6

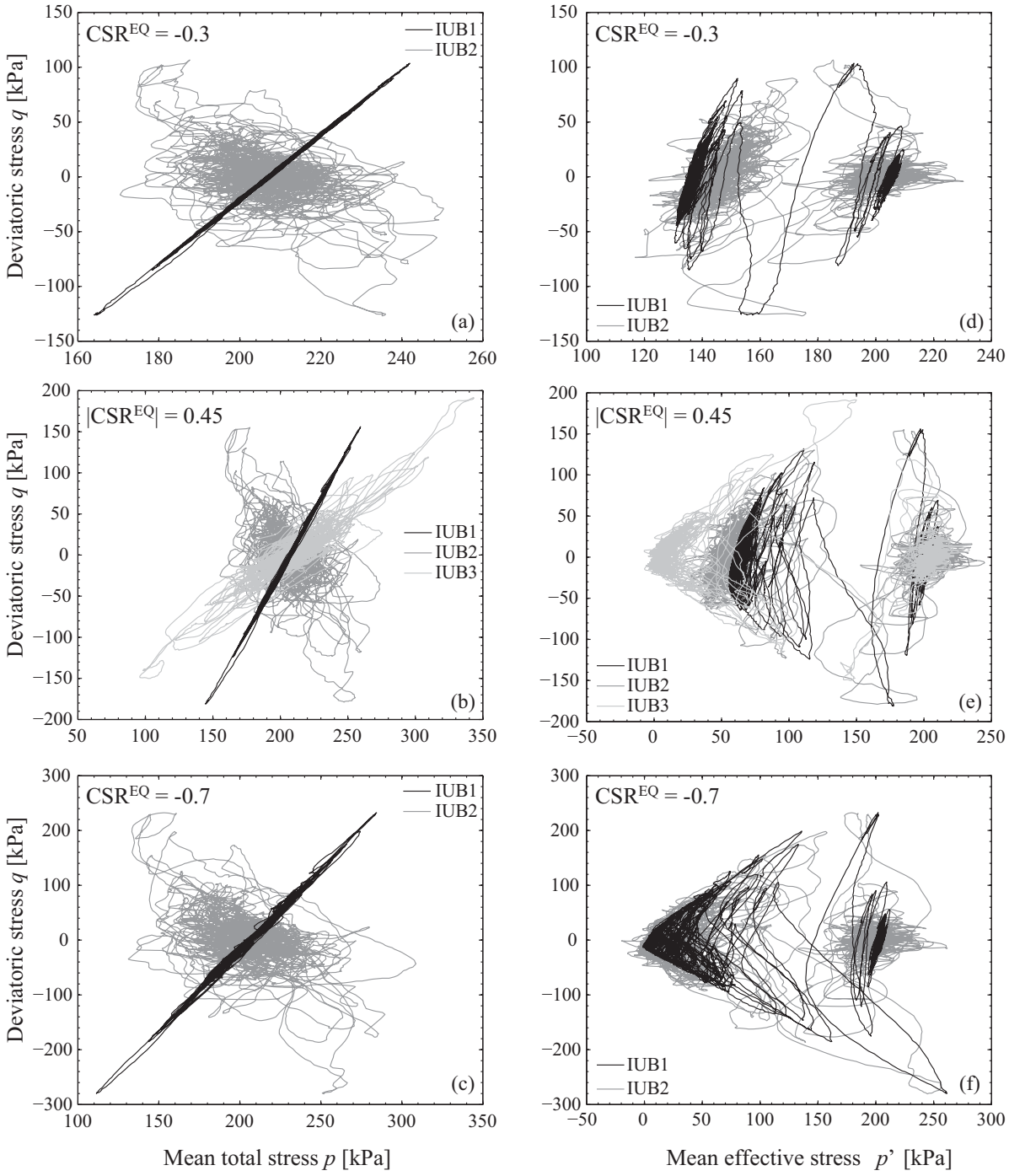

Fig. 6.18. Irregular multidirectional total (a, b, c) and effective (d, e, f) stress paths (Leman Sand).

6.3.3 Deviatoric strains

The time-history of deviatoric strains at the three loading amplitudes are given in Fig. 6.19. The irregular strain variations of IUB1 and IUB2 are evaluated thanks to the peak value, the residual value, the average and the standard deviation of ε_q (Tab. 6.5). At medium strains, i.e. for $|CSR^{EQ}| = 0.3$ and 0.45, motions are stronger in bidirectional than in unidirectional conditions. Indeed, the absolute mean

values, the standard deviations, the absolute peaks and the absolute residual strains are all higher for IUB2 in the two first steps. On the contrary, at CSR^{EQ} = -0.7, three of these four criteria imply a stronger soil response in unidirectional loading IUB1.

Tab. 6.5. Deviatoric strains in irregular loading of undrained Leman Sand (*)

N°	CSR^{EQ} [.]	Mean ε_q [.]	Standard deviation of ε_q [.]	Peak of ε_q [.]	Residual ε_q [.]
IUB1	-0.3	-2×10^{-4}	2×10^{-4}	-2×10^{-3}	-4×10^{-4}
IUB2	-0.31	1×10^{-3}	5×10^{-4}	3×10^{-3}	1×10^{-3}
IUB1	-0.44	-2×10^{-4}	8×10^{-4}	-5×10^{-3}	2×10^{-4}
IUB2	-0.43	-1×10^{-3}	9×10^{-4}	-7×10^{-3}	-1×10^{-3}
IUB1	-0.68	-2×10^{-3}	5×10^{-3}	-1.3×10^{-2}	-6×10^{-3}
IUB2	-0.69	-8×10^{-4}	5×10^{-3}	-1.2×10^{-2}	2×10^{-3}

The response predominantly consists of negative deviatoric strains for average, peak and residual strain values in most cases. This type of behaviour seems reasonable, because the maximum deviatoric stress amplitude is negative. There are some exceptions though, for both IUB1 and IUB2. For example, the deviatoric strain, in the first step of IUB2, is positive, with a significant residual value of 0.1%. In the third step as well, i.e. after complete softening with $p' = 0$, the residual strain of IUB2 is positive.

The peak of deviatoric strain is correlated with CSR^{EQ}, i.e. it increases accordingly to the maximum deviatoric stress amplitude, with the noticeable exception, mentioned before, of a positive peak in IUB2 during the first step only (i.e. at CSR^{EQ} = -0.3). The peak value of strain is obtained either at the maximum value of q, when there is no complete stiffness degradation, or after the peak q during the following large motion amplitudes at cyclic liquefaction. The relation between the peak deviatoric strain and the stress amplitude is further explored in the following discussion (section 6.3.6).

On the contrary, the residual strain is not so much in connection with the loading amplitude and seems more random, although it eventually increases at the last step after cyclic liquefaction.

In the bidirectional test IUB3, there is fast development of the deviatoric strain at large strain. The residual strain is positive as well, although the peak value is on the negative side.

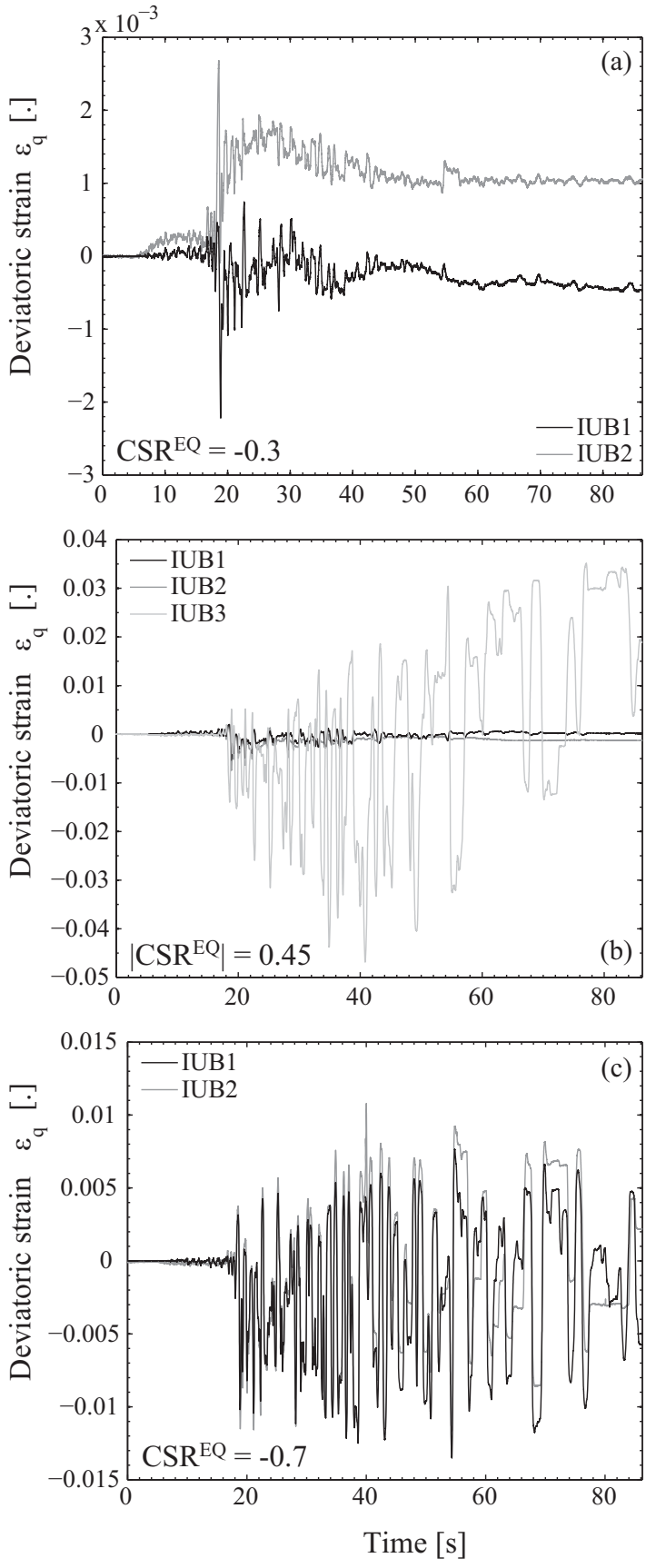

Fig. 6.19. Deviatoric strains induced during irregular loading of Leman Sand.

6.3.4 Stress-strain relation

As for sinusoidal loading, the stress-strain relation is made of loops (Fig. 6.20), which are more or less inclined depending on the strain level (nonlinear behaviour). Their shape is the same in unidirectional and bidirectional loadings. At cyclic liquefaction in particular, the banana shape tends to appear in the three tests. In conjunction with Tab. 6.5, the unidirectional deviatoric strains take lower values, in the extension side, than bidirectional strains, for the first and the third steps of CSR^{EQ}.

6.3.5 Pore pressure increase

The pore pressure ratio u_r increases as a result of the irregular loadings, accordingly to the three motion amplitudes (Fig. 6.21a, b and c). The part of the pore pressure resulting from the deviatoric load only, u_r^q (defined in section 6.2.9), increases with the same pattern (Fig. 6.21d, e and f). Contrary to bidirectional loading (IUB2 and IUB3), the two components u_r and u_r^q are identical in IUB1. As for sinusoidal loading, the pore pressure ratio can exceed the value $u_r = 1$ in bidirectional loading (mostly for large strains at cyclic liquefaction), while u_r^q is limited to the threshold 1.

Both components of pore pressure mostly increase just after the maximum amplitude at t = 18.8 s whether cyclic liquefaction is reached or not. After that step increase, their level increases slightly and then remains stable until the end of the event, although some spikes are clearly visible. The irregular peaks of u_r^q only face downward at cyclic liquefaction, because the threshold value 1 cannot be exceeded. The residual values of u_r^q, summarized on Fig. 6.21, clearly increase with $|CSR^{EQ}|$ for IUB1 and IUB2.

The close analysis of the time-history of u_r^q for IUB3 gives insight into its rapid failure. It appears that the step increase of u_r^q arises before the maximum peak in compression, at unloading from the previous peak in extension. This means that the phase transformation line was reached in this secondary main peak in extension. That can also be observed in the effective stress path (Fig. 6.18e). Following the step increase, the value of u_r^q remains high, with some downward spikes of excess pore pressure. This component reaches the threshold value 1 within a few seconds.

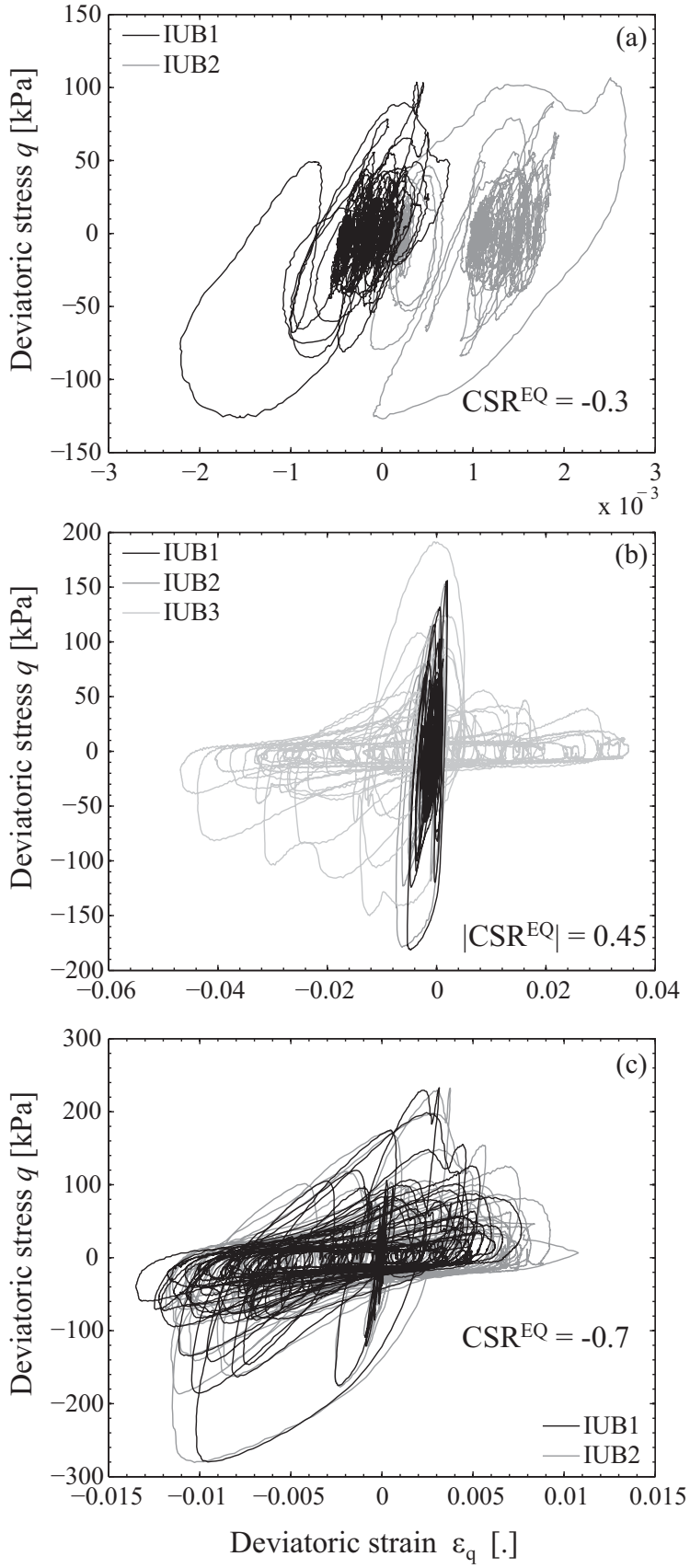

Fig. 6.20. Stress-strain relation of irregular undrained tests of Leman Sand.

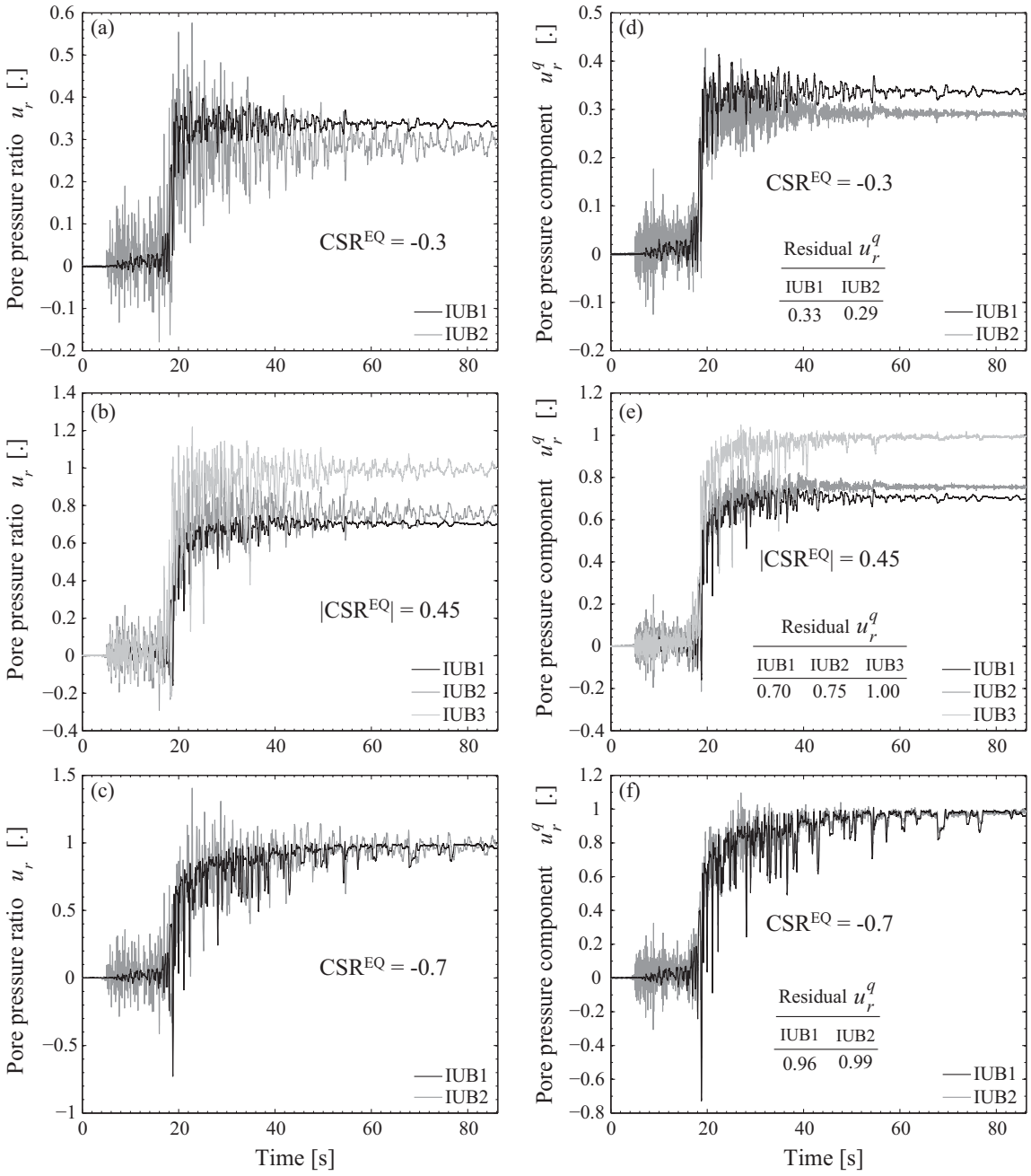

Fig. 6.21. Leman Sand pore pressure ratio u_r (a, b, c) and its component resulting from the deviatoric part of irregular loading, u_r^q (d, e, f).

6.3.6 Discussion on seismic bidirectional triaxial tests

Progressive stiffness degradation and cyclic liquefaction occurred as the result of the unidirectional and bidirectional irregular loadings representative of strong seismic motions. The irregular time-history of excess pore water pressure and deviatoric strains, the stress-strain relation and the effective stress paths have similar shapes between 1D and 2D loadings. There are small differences in the quantitative results of IUB1 and IUB2 tests, and a much larger difference with IUB3.

The characteristics of the irregular response are first commented and compared to the sand response to undrained cyclic loading, before taking into account the bidirectional effects.

6.3.6.1 Irregular effects

The shapes of effective stress path and stress-strain relation of seismic motions present similarities with cyclic loadings (Fig. 6.22). Especially at large loading amplitude, when cyclic liquefaction is triggered, the stress-strain loops exhibit «S shapes» (Fig. 6.22b). This means, as in cyclic loading, that sample stiffness punctually increases at large strain when dilatancy occurs. The «S shape» also appeared in a previous laboratory study on dense sand subjected to irregular motions in centrifuge tests (Elgamal et al. 2005).

Both peak and residual deviatoric strains are larger in extension for the majority of the steps, although there are some exceptions, as was explained in section 6.3.3. This asymmetric response with regard to the axis $\varepsilon_q = 0$ is similar to the undrained cyclic tests (Fig. 6.22b), except that even larger strains develop during sinusoidal loadings. The reason why some tests develop peak and residual strains in compression while the majority of the results are in extension is unknown. It may be linked with bidirectional effects, although, as was shown in Fig. 6.4, the bidirectional response in cyclic loading tends to be stronger on the side of extension.

Similarly to the laboratory results of Nagase & Ishihara (1987) for $\gamma < 3\%$, residual strains are smaller than peak strains, even after the triggering of cyclic liquefaction. For a different definition of residual strains, which includes reconsolidation strains occurring during drainage, Sawada et al. (2004) found that residual strains are practically equal to the maximum shear strain, irrespective of hydraulic conditions (saturated and unsaturated soils).

When the stress amplitude is multiplied by a factor 1.5 in the unidirectional irregular test IUB1, the peak deviatoric strain is multiplied by a factor 2 and then 2.3 at the second and third steps, respectively. This nonlinear amplification of the soil response is non negligible. In bidirectional loading as well, the sand response is nonlinear. This result shows that the irregular motions similar to earthquakes may produce nonlinear behaviour with non trivial relations between the peak stress and the peak strain. Such observations can be important in the analyses of seismic data such as microtremor studies.

The envelope of the cyclic and irregular unidirectional stress paths match perfectly (Fig. 6.22a). As for most earthquakes, the part of the irregular load with strong amplitude is followed by small amplitude variations of the deviatoric stress, which are symmetric with regard to the axis $q = 0$. As a result, the stress path, after cyclic liquefaction, is very close to the origin of the p' - q plane. This gives an overall pointed shape, different from the wing shapes of the stress paths in cyclic tests.

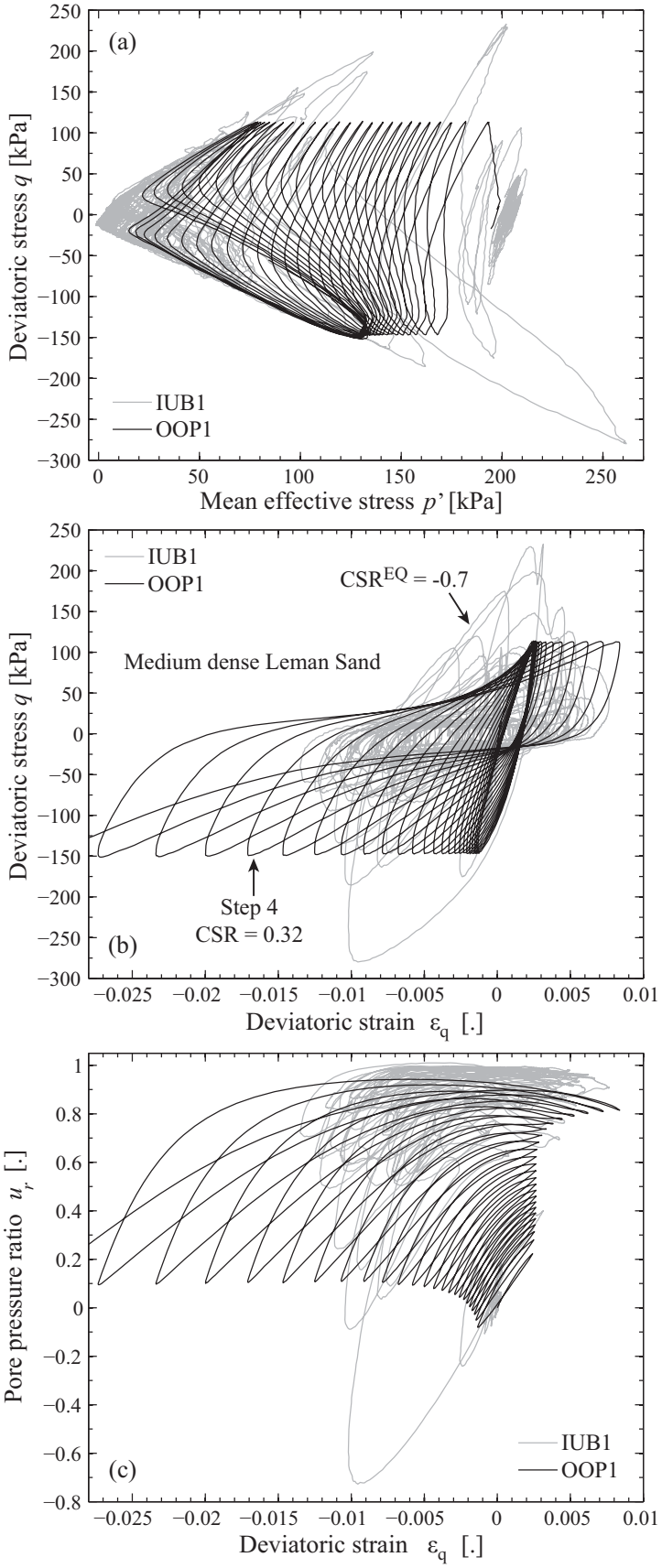

Fig. 6.22. Comparison of sinusoidal and irregular unidirectional loadings.

The excess pore pressure ratio increases in one step, following the peak deviatoric stress, whether cyclic liquefaction is triggered or not (Fig. 6.21). This is true at all steps, for all tests, including the test IUB3 with the maximum deviatoric stress in compression. This result is slightly different from the triaxial test results from Ishihara & Yasuda (1972). They showed that u_r also exhibits a fast increase in EM tests, but gradually reaches the threshold 1 in CM tests. After the triggering of cyclic liquefaction, the pore pressure presents negative spikes, particularly visible in Fig. 6.21f. These spikes all arise exactly at the same time as local peaks of q, mostly in extension. They are the consequences of the dilative tendency of the sand response to the higher peaks of the irregular loading.

The shape of the irregular pore pressure ratio vs. deviatoric strain is compared to the cyclic response in Fig. 6.22c for unidirectional conditions. It is interesting to see that, although the deviatoric strains have larger amplitudes, the pore pressure ratio is lower in cyclic tests. The overall shape of that relation is however very similar in irregular and cyclic conditions.

6.3.6.2 Influence of bidirectional effect in irregular loadings

The response of IUB3, the bidirectional test in compression, is clearly more unstable than the two other tests: pore pressure increases and especially deviatoric strains are much larger than the response of IUB1 and IUB2 at the same $|CSR^{EQ}|$. The time-history of deviatoric stress are opposite, it was then expected to obtain a different response. We did not perform the unidirectional test with a peak in compression, that is why there is no certainty on the results obtained in such case. However, all previous unidirectional studies presented in Chapter 2 emphasize the fact that EM tests (peak stress in extension) always induce lower cyclic strength than CM tests (peak stress in compression). The cyclic tests presented in Chapter 4 also indicate that such a test, placed on the compression side of q, would have yielded a higher strength than IUB1 (and IUB3).

The explanation for that unexpected behaviour is then related to the bidirectional loading. The Mohr circles of IUB3 (Fig. 6.17) show that, at some points, the stress state of the soil is closer to the origin of the Mohr plane, which could make it easier to cross the failure threshold. The interpretation of irregular tests in the p' - q plane is not simple. However, it is possible to see, in Fig. 6.18e, that the phase transformation line is first crossed by IUB3 during an extension peak, though this is not the maximum peak value. More precisely, the analysis of the time-history of u_r^q showed that the triggering event for cyclic liquefaction is a secondary peak in extension before the maximum peak in compression. This secondary peak is the apex locus on the extension side, in the total stress path of IUB3 (Fig. 6.18b).

The inclination of the total stress path of IUB3 and the location of the low apex at the left of the 1D stress path allow the effective stress path to cross the phase transformation line before the maximum loading peak. As shown from the comparison with IUB1, failure at such a level of $|CSR^{EQ}|$ would not

have been possible in a unidirectional loading having the same pattern of deviatoric stress.

We then demonstrated experimentally that the combination of irregular deviatoric stress and confining pressure of IUB3 significantly reduces the $|CSR^{EQ}|$ necessary to induce liquefaction, although the stress path, in the p - q plane, seems really similar to IUB1 at first sight (Fig. 6.18b).

Comparing IUB1 and IUB2, bidirectional effects in irregular conditions can also be small; yet the observed tendency, detailed below, shows a sensitivity to bidirectional conditions in good agreement with out-of-phase cyclic test results. The results are anyway taken with caution, because of the low number of irregular tests.

At medium strain, the bidirectional test exhibits a slightly amplified response: both peak and residual strains are higher than unidirectional loading for the two lower values of $|CSR^{EQ}|$. On the contrary, higher strains develop in unidirectional than bidirectional tests after cyclic liquefaction. The same tendency appears in cyclic OOP tests, in particular for positive phase angles: the medium strain response is amplified in bidirectional loading, but larger strains develop at cyclic liquefaction in unidirectional loading.

The pore pressure increase is slightly higher in unidirectional test at the smallest $|CSR^{EQ}|$, but lower at the medium strain level. At failure, at the third step, both responses are similar, although the threshold $u_r = 1$ is reached much earlier for the bidirectional u_r^q (t_1 = 26.6 s) than the unidirectional u_r (t_2 = 54.5 s). The rate of increase of u_r^q in 2D thus seems higher than the rate of increase of u_r in 1D, just previous to the triggering of cyclic liquefaction, as was obtained in OOP tests.

The state of the art provides reference of bidirectional irregular simple shear tests on undrained saturated sand, for example Nagase & Ishihara (1988) showed that there is no effect of 2D loading on settlements induced by liquefaction. However, the conclusions of these experiments do not really apply to our study, because (i) the equipment and loadings are different and (ii) our results are less focused on the quantitative comparison with cyclic loading, and more focused on the qualitative analyses and description of the nonlinear soil behaviour.

6.3.7 Conclusions

Three irregular tests, with seismic patterns and performed in unidirectional and bidirectional conditions, illustrate and emphasize the role of loading conditions on the nonlinear soil response. The 1D and 2D total stress paths, effective stress paths, stress-strain relations have the same shapes. They also present similarities with cyclic behaviour, although the strains are more limited, at cyclic liquefaction, in irregular loadings. It is for example interesting to see «S shape» stress-strain loops appearing in irregular tests, as they are characteristic of the cyclic alternation of increasing and

decreasing excess pore pressure in medium and dense undrained sand (cf. Chapter 4).

Looking at the response induced by the irregular loading, we observed that the deviatoric strains are mainly negative, i.e. on the extension side for most cases. Moreover, the peak values of ε_q are higher than residual strains. The relation between the peak deviatoric strain and the peak deviatoric stress is not trivial, i.e. it is nonlinear, even in unidirectional loading.

The pore pressures from bidirectional irregular tests are separated into two components, as was previously done in cyclic bidirectional loading. The unidirectional pore pressure u_r and the bidirectional pore pressure component u_r^q have similar shapes; their residual values are also close to each other in IUB1 and IUB2 tests. They reach the threshold value 1 at cyclic liquefaction, by a step increase which follows the maximum deviatoric stress. This sudden increase in one main step also arises for motions with lower $|CSR^{EQ}|$ which do not induce liquefaction.

Some bidirectional effects are observed, although they do not imply major differences in the soil response by considering only the two tests IUB1 and IUB2. These effects are similar to what was observed in out-of-phase cyclic tests: in bidirectional conditions, there are (i) stronger deviatoric strains at medium strain (ii) faster reach of cyclic liquefaction (iii) lower strains at large motions. The very unstable response of the test IUB3 is seen as a consequence of the bidirectional stress path; this shows that bidirectional loading can also have strong impact on soil behaviour in irregular conditions, and can significantly reduce the undrained strength.

6.4 Comments on bidirectional and irregular effects

6.4.1 Effect of complex loadings on nonlinear soil behaviour

The first scope of these experimental studies, cited in the introduction of the chapter, was to assess the effect of the superposition of two loadings on the nonlinear behaviour of granular soils. It is clear now that the superposition, in triaxial conditions, of a cyclic deviatoric stress and a cyclic confining pressure has an effect on the nonlinear stiffness degradation and failure of saturated Leman Sand. The response of the soil is not the simple superposition of a cyclic pore pressure, resulting from the variation of the total confining pressure, and the cyclic shearing of the sample, which also induces cyclic variation and gradual increase of the pore pressure. The consequences of bidirectional loading are complex, and the short summary below reflects the main points observed:

- In cyclic conditions, dynamic parameters are slightly influenced by the superposition of loadings. The secant shear modulus vs. deviatoric strain curve exhibits a peak at medium strains, but otherwise is very similar to the unidirectional curve. The damping ratio vs. deviatoric strain also exhibits a peak, arising from dilative effect and the formation of the «S shape» of the stress-strain relation (Chapter 4). That peak also happens in unidirectional loading, but it arises for smaller values of the deviatoric strain amplitude in bidirectional tests. That means that dilatancy occurs for lower strains in bidirectional loadings.

- Cyclic strength is either enhanced or reduced by bidirectional loading. The phenomenon is more obvious in cyclic loading, although the response of the test IUB3 in bidirectional irregular loading shows that rapid failure may arise as a consequence of a complex loading. The number of cycles to reach failure, N^f, which is the simpler tool to assess cyclic strength, is clearly influenced by bidirectional loadings. The difference, with identical CSR, can reach 30% for out-of-phase tests with opposite phase angles.

- Deviatoric strains were shown to exhibit nonlinear responses to unidirectional and bidirectional, cyclic and irregular stress-controlled tests. ε_q is stronger at medium motion amplitude (more generally before the triggering of cyclic liquefaction) for bidirectional irregular and cyclic conditions. After failure, bidirectional loading may slightly prevent the formation of large deviatoric strains, at least in certain conditions (e.g. positive phase angle).

- Pore pressures, in bidirectional loadings, are divided into two components to remove the cyclic effect of the purely isotropic part and visualize only the component related to the shearing part, u_r^q . In parallel to the deviatoric strain, pore pressures increase faster in bidirectional loading before cyclic liquefaction. After cyclic liquefaction, the level of u_r^q is limited to the threshold value 1, also no further evolution is expected. Negative spikes of excess pore pressure appear in all conditions.

6.4.2 Physical interpretation

The stress path only, and its distance to phase transformation and steady state lines, can not explain by itself the bidirectional effects observed in cyclic and irregular loadings. Indeed, even stress paths with the same shape but different direction of rotation, for example OOP2 and OOP3, exhibit completely different cyclic strength and nonlinear response.

We assume that any dynamic amplification can be withdrawn, because the pseudo-dynamic regime prevails in these studies, as for all tests previously presented.

The nonlinear superposition of two independent loading does not necessarily imply that the response will be the sum of the two loadings, like for the usual assumption of linear elastic behaviour. Indeed, we

showed that some kind of coupling appears as an effect of the combination of two cyclic or irregular loads. A possible explanation is that pore pressure itself influences the development of deviatoric strains, while the contractive behaviour of the soil matrix also induces increase of the pore pressure. This assumption is supported by the analyses, for OOP tests (section 6.2.9), of the effect of the phase angle with respect to time-history of the pore pressure ratio: negative spikes of u_r are enhanced for particular values of the phase angle, which also correspond to the tests with the lowest cyclic strength (i.e. lower N^f).

The bidirectional amplification of deviatoric strain amplitudes and of the rate of pore pressure increase, before cyclic liquefaction, could then result from the coupling between the pore fluid and the granular matrix. After the triggering of cyclic liquefaction, the pore pressure ratio stabilizes, also it seems reasonable to admit that there is no more amplification of the response, and that the strains may develop less strongly than in unidirectional conditions.

6.4.3 Consequences for modelling and design purposes

To fully take into account the bidirectional effects, in particular within the frame of geotechnical earthquake engineering, an accessible solution would be to evaluate the effect of 2D and irregular loading on the cyclic strength curves, CSR vs. number of cycles to reach failure. More tests would be needed to get significant curves for various initial states. That would also allow to define multiplying factors which take into account the superposition of stresses and irregular effect in triaxial conditions (cf. Nagase & Ishihara 1987).

Another question concerns the constitutive law and numerical modelling of the bidirectional effects. It is not really obvious now whether a constitutive law based on multi-mechanisms like the Hujeux model could account for the bidirectional effects described above, because the reason for these observed phenomenon are not fully understood yet. The following Chapter 7 addresses this question.

6.5 Conclusions

Significant examples of complex triaxial tests in bidirectional undrained conditions were described with a particular emphasis on the application to earthquake geotechnical engineering.

First, the cyclic tests demonstrated that the superposition of two stresses of different nature, one deviatoric and one isotropic, induced coupling effects in the nonlinear soil response. The bidirectional effects result in an amplification of motion before cyclic liquefaction, and a limitation of strains after

cyclic liquefaction. The phase angle between deviatoric and confining stress has a particularly strong influence on Leman Sand behaviour. Cyclic strength is significantly modified by complex loadings.

Three irregular seismic tests were also performed in unidirectional and bidirectional conditions to illustrate the effect of superposition of loadings in conditions closer to in situ seismic motions. Bidirectional irregular loadings can increase deviatoric strains and pore pressure build up compared to unidirectional motions. The conditions of amplification of the response are similar to cyclic tests: before cyclic liquefaction, the superposition of loading slightly accelerates stiffness degradation. In the case of seismic loading, soil behaviour after cyclic liquefaction is practically equivalent in unidirectional and bidirectional loading.

The parallel between cyclic and irregular loading was illustrated with (i) characteristic «S shape» stress-strain relations, which are a consequence of dilative behaviour, (ii) total and effective stress paths, (iii) the relation between pore pressure increase and deviatoric strains. In irregular tests, we also showed that the relation between the maximum strain amplitude and the maximum stress amplitude is not trivial, i.e. nonlinear, even in unidirectional loading.

In order to understand and compare the coupling between the two loadings, the pore pressure ratio of bidirectional tests is separated into two components. The unidirectional pore pressure ratio u_r and the bidirectional component u_r^q, which corresponds to the deviatoric part of the load, have similar shapes in both irregular and cyclic motions. They both reach the threshold value 1 at cyclic liquefaction.

The interpretation of bidirectional effects is based on the coupling between the pressure in the pore fluid and the deviatoric strains of the granular matrix. While the cyclic variation of the confining pressure are assumed to be reported only on the pore pressure, the coupling between pore pressure and deviatoric strains also amplifies the response to the variations of deviatoric stress. Stiffness reduction and the occurrence of cyclic liquefaction is then accelerated in bidirectional conditions.

CHAPTER 7

CONSTITUTIVE MODELLING OF CYCLIC SAND BEHAVIOUR

7.1 Introduction

Some of the dynamic tests performed with the triaxial press (presented in Chapters 4, 5 and 6) are now modelled to evaluate the capability of two quite different models to reproduce nonlinear sand behaviour. The identification of model parameters for Leman Sand is also described.

The two existing constitutive laws assessed in this chapter are: (i) the simple linear equivalent method and (ii) the complex Hujeux model for cyclic loading (both are described in section 2.7). The first simple model is widely used in practice for geotechnical earthquake engineering applications. It comprises 3 material parameters and two degradation curves (secant shear modulus decrease and damping ratio increase as a function of the shear strain amplitude). The second model, which is more research-oriented, is a multi-mechanism elastoplastic law designed to account for cyclic effects (Hujeux 1985); it is based on coupled hydro-mechanical equations, with a total of 18 parameters. Both models can be implemented in the commercial software CyberQuake, the elastoplastic law in a simplified version with 15 parameters (CyberQuake user's guide v.2.01). In the following study, the elastoplastic law is implemented in its complete form in an independent module (LAWYER routine, detailed later).

First, the linear equivalent method is used to model the beginning of a cyclic undrained test with symmetric stress reversal, which induced cyclic liquefaction (CYC2). The soil parameters for this model are directly calculated from the laboratory test results.

Then, the elastoplastic model is applied to several cyclic undrained tests and a monotonic test, in order to calibrate some of the model parameters for Leman Sand by curve fitting. The other parameters were obtained from different procedures, which are also described. The model is then applied to a cyclic dry test (DRY1).

The possibility to model rate effects and multidirectional effects with the two models is also discussed. The advantages and limitations of the two models are finally summarized in the discussions, with some possible extensions which could take into account the effects of complex loading observed in the laboratory tests.

7.2 Cyclic modelling of Leman Sand with a viscoelastic linear equivalent analysis

7.2.1 Introduction

The linear equivalent method is customary used in geotechnical earthquake engineering studies, in particular to model seismic wave propagation and site effect amplification. This chapter evaluates the local errors inherent to this simple method in the case of medium cyclic loading amplitudes, which induce acceleration up to 0.35*g*. We do not evaluate wave propagation phenomena, but rather the local response of the model at middle height of the soil layer. The strains induced for a given stress amplitude are compared with those measured in a cyclic stress-controlled undrained triaxial test on Leman Sand. The stress boundary conditions are the same at the numerical point of calculation and in the laboratory tests, with an isotropic consolidation at the confining pressure of 100 kPa.

After describing the procedure (the linear equivalent method was described in section 2.6.4), the two first steps of the test CYC2 are modelled. Then follows the description of the capability of the linear equivalent method to model the effects of loading frequency and multidirectional conditions.

7.2.2 Description of the procedure for linear equivalent simulations

7.2.2.1 Framework

The linear equivalent analyses are performed with CyberQuake, edited by the BRGM (France). For the linear equivalent model, the calculations of the soil layer response to an input acceleration are made in the total stress domain, with no pore pressure development. This condition is customary when the linear equivalent method is implemented. The programme assumes a homogeneous laterally infinite layer (Fig. 7.1), and computes the stress wave, which propagates vertically from the bedrock to the top, in the frequency domain. The strains induced in each soil layer are computed from the degradation curves within an iteration process (cf. section 2.6.4). The porous medium is divided into nine sub-layers, for a total uniform soil layer of 9.45 m depth.

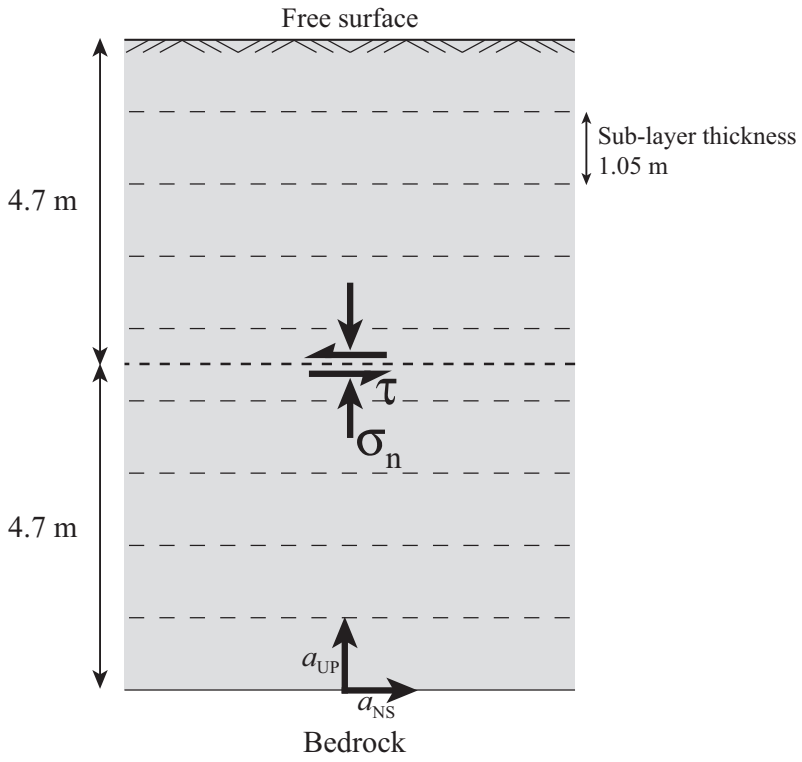

Fig. 7.1. Uniform soil layer for the linear equivalent model

7.2.2.2 Model parameters

The parameters of Leman Sand for the linear equivalent model are summarized in Tab. 7.1 and depicted in Fig. 7.1. The shear wave velocity and compressive wave velocity were calculated from the values of G_{max} determined in section 4.4.5. The parameters given below correspond to the actual confining pressure at the chosen depth (middle of the total soil layer), i.e. 100 kPa.

Tab. 7.1. Linear equivalent model parameters for Leman Sand

Parameter	Value	Unit
Time step	0.01	s
Cut-off frequency	10	Hz
ρ	2.17×10^3	kg/m^3
c_p	371	m/s
c_s	235	m/s
Numerical damping	5	%
Total layer thickness	9.45	m
Number of sub-layers	9	.
Bedrock	rigid	

The model calibration also requires the curves G_{sec} / G_{max} vs. γ and D vs. γ. The degradation curves used are those obtained for Leman Sand (Chapter 4). The degradation curve of the secant shear modulus (G_{sec} / G_{max} vs. γ) was plotted for small to large strain amplitude, at the confining pressure σ_3 = 100 kPa (cf. Fig. 4.20). The damping ratio curve is deduced from experimental data at medium to large strain amplitude (Fig. 7.2). Approximated curves were drawn, following the tests results, to implement these values in the linear equivalent model.

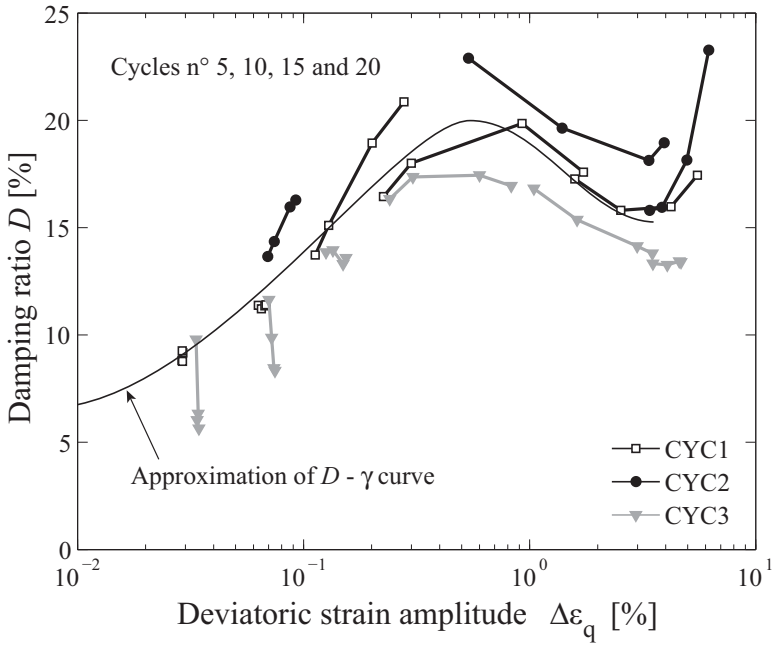

Fig. 7.2. *D* - γ curve of Leman Sand.

7.2.2.3 Input motion: acceleration and stress within the linear equivalent model

The input motion is a sinusoidal acceleration, imposed at the bottom of the soil layer, which can have, at maximum, two components in the horizontal plane and one component in the vertical direction. The shear and compressive waves are transmitted to the surface, thanks to a transfer function implemented in the frequency domain (cf. section 2.6.4).

The model response consists of total shear stress and shear strain, given at middle height of the soil layer. These values are compared to the cyclic triaxial test result. The principal stresses are calculated from τ and σ_n as described in Appendix 2 for the case of irregular loading. The amplitude of the input acceleration is calibrated so that the shear stress amplitude at middle height is equal to the value used in the experimental stress-controlled cyclic test.

The conditions met in the laboratory test CYC2 (Chapter 4), performed with Leman Sand, are modelled with the linear equivalent method. The load consists of 25 cycles at the amplitude $\Delta\tau$ = 20 kPa and 25 more cycles at $\Delta\tau$ = 35 kPa ($\Delta\tau = \Delta q / 2$). The input signal is a sinusoidal curve of frequency 1 Hz. In

unidirectional condition, only one component of the acceleration varies cyclically in the horizontal plane. At the depth 4.7 m, the medium is isotropically consolidated at the confining pressure σ_3 = 100 kPa, which corresponds to experimental conditions of the test CYC2. The relative density is not explicitly taken into account, but stiffness degradation curves correspond to the desired void ratio.

7.2.3 Results

Fig. 7.3a and Fig. 7.3b show the deviatoric stress variations corresponding to Δq = 40 kPa and 70 kPa, respectively obtained for cyclic acceleration amplitudes of 0.16g and 0.22g imposed to the bedrock.

Cyclic axial strains computed with the linear equivalent method are clearly lower than the experimental results, at both loading amplitudes (Fig. 7.4). At the 20th cycle for example, the strain amplitude is 1.5 times higher for experimental results at medium strain level (Fig. 7.4a), and 13 times higher for the larger strain level (Fig. 7.4b).

The large difference observed at large strain between the modelled values and the experimental results is reflected on the stress-strain relation (Fig. 7.5b). It is clear, from the loop shapes, that the modelled stiffness is too high and the damping ratio too low. The S shape, typical of the development of cyclic liquefaction, does not appear in the linear equivalent model because dilative behaviour cannot be modelled by this method. For medium strain level (Fig. 7.5a), the loop shape is well-reproduced; however, the evolution of the stress - strain relation does not appear in this model.

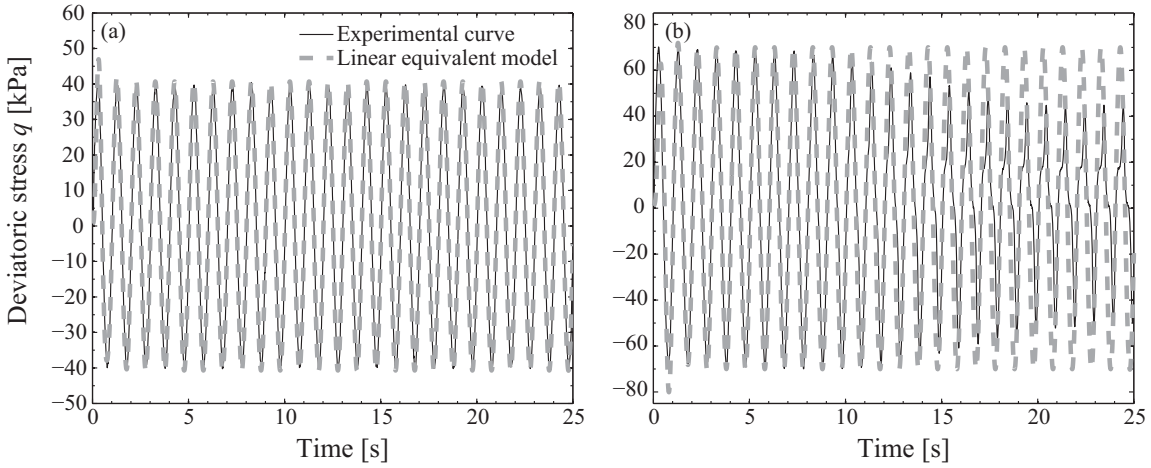

Fig. 7.3. Deviatoric stress of the linear equivalent model at mid-depth of the soil layer compared to the steps 1 (a) and 2 (b) of the cyclic triaxial test CYC2.

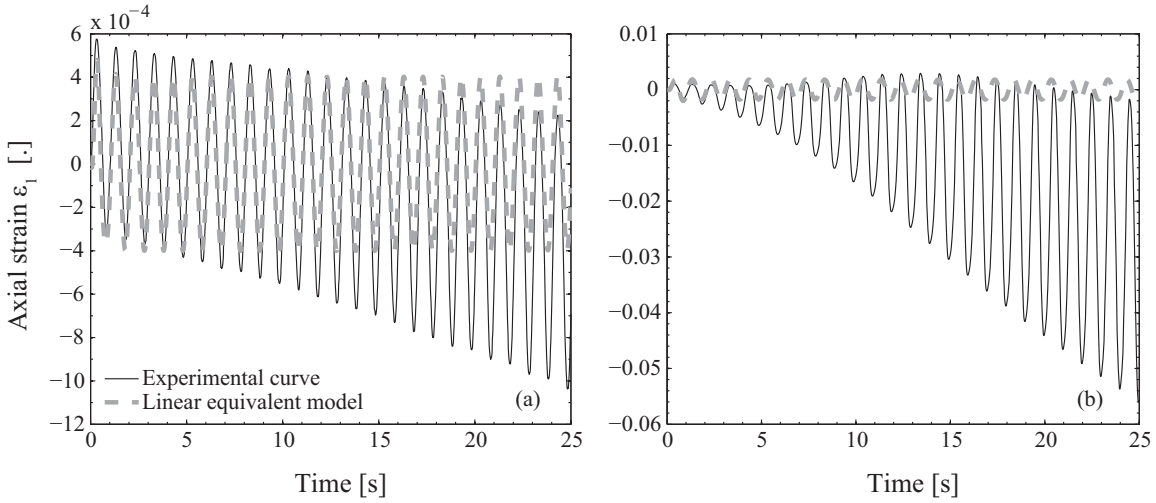

Fig. 7.4. Axial strains from the linear equivalent model and the cyclic test CYC2, for steps 1 (a) and 2 (b).

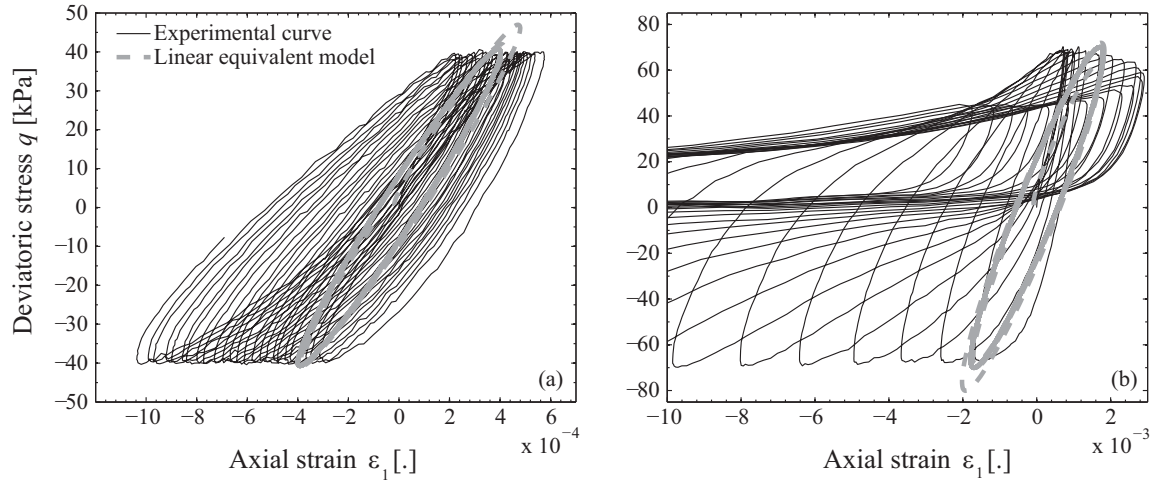

Fig. 7.5. Comparison of stress - strain relations from the linear equivalent model and the test CYC2, for steps 1 (a) and 2 (b).

The stress paths, depicted in Fig. 7.6, clearly show that the non negligible reduction of mean effective stress cannot be taken into account with the linear equivalent method. Indeed, the large increase of pore pressure ratio cannot be reproduced.

Stiffness degradation is not well represented by the model (dynamic parameters in Fig. 7.7). As inferred from the stress-strain curves, the secant shear modulus is overestimated and the damping ratio is underestimated in the linear equivalent method. These results are compatible with the fact that the strain amplitude is too low in both steps. Moreover, their evolution with the number of cycles is totally neglected. The $\Delta\varepsilon_q$ - G_{sec} / G_{max} curves follow the same line in the laboratory tests and the model (Fig. 7.8a), which means that the G - γ calibration curve was well chosen. The peak of the $\Delta\varepsilon_q$ - D experimental curve is not reproduced by the linear equivalent model (Fig. 7.8b).

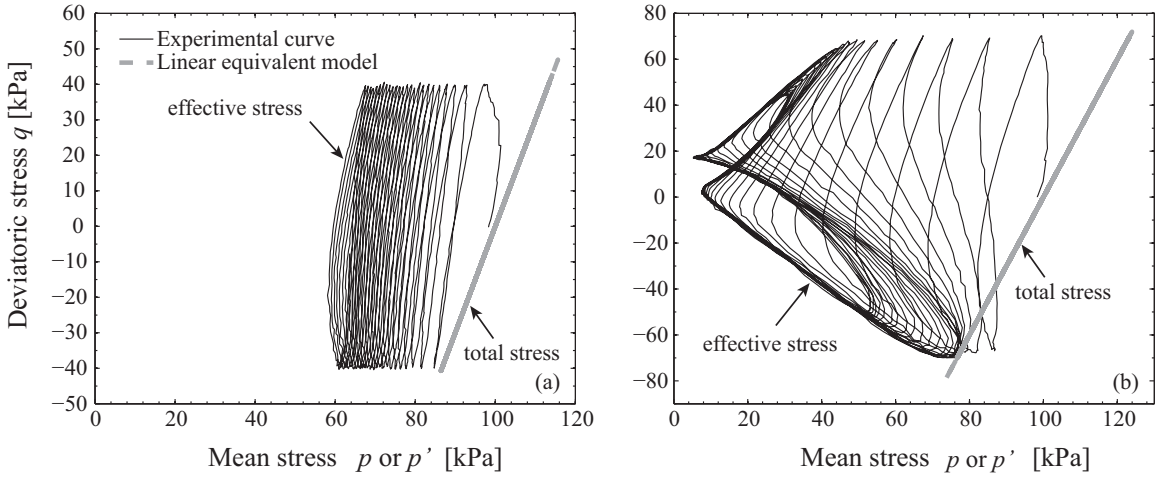

Fig. 7.6. Total stress paths obtained with the linear equivalent method and effective stress paths resulting from the increase of pore pressure during the test CYC2, for steps 1 (a) and 2 (b).

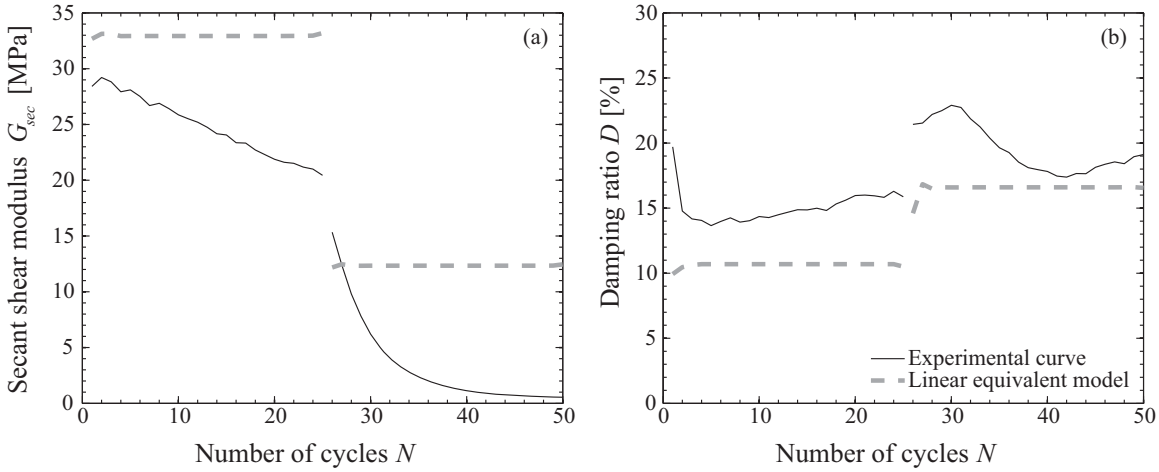

Fig. 7.7. Dynamic parameters vs. number of cycles of the CYC2 test.

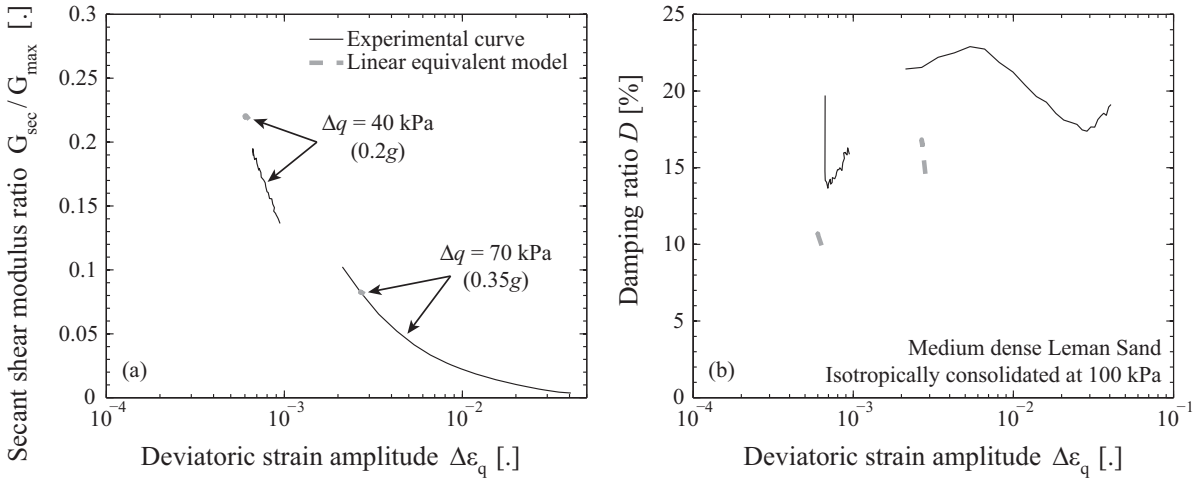

Fig. 7.8. Stiffness degradation curves of the CYC2 test.

7.2.4 Effect of frequency and complex loading in the linear equivalent model

To complete the comparison between modelled and experimental sand behaviour, we tried to reproduce the effects of frequency and multidirectional cyclic loading with the linear equivalent method.

The loading frequency slightly influences the model, in a way which is described now by comparing the previous results at 1 Hz with a similar harmonic model of input motion frequency 0.1 Hz. First, the wave propagation depends on the loading frequency, because the deviatoric stress amplitude evolves depending on input acceleration frequency. Adapting the input motion to get the same loading amplitude Δq at mid-depth, there is still a small difference between the two frequencies: D decreases, G_{sec} increases and $\Delta\varepsilon_q$ slightly decreases at low frequency (results commented in the discussion section 7.2.5). For example at large amplitude (second step), D decreases from 14.9 at 1 Hz to 13.5% at 0.1 Hz.

The multidirectional stress paths can be well reproduced at mid-depth of the soil layer. The cyclic evolution of the confining pressure is modelled thanks to a cyclic vertical acceleration, which induces a variation of the normal (vertical) stress σ_n. The cyclic q still results from the variations of one horizontal acceleration component. By comparing the simulation of laboratory tests OOP1 and OOP5 (e.g. stress - strain relation in Fig. 7.9) with or without the superposition of σ_n, it clearly appears that the linear equivalent model does not reproduce any effect of the superposition of two loadings. Indeed, there is an exact overlap of 1D and 2D loadings, including the dynamic parameters. The cyclic behaviour of the mid-depth element is independent from the variations of σ_n.

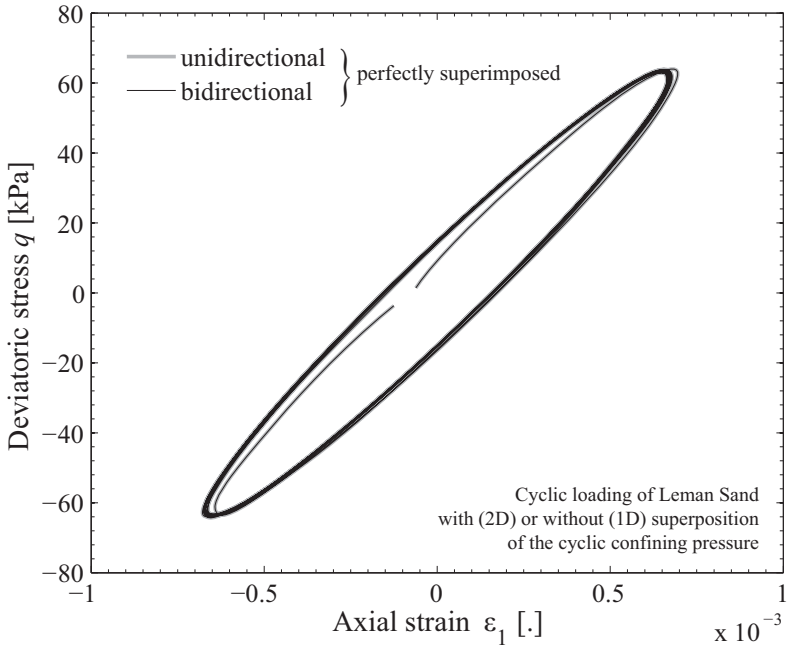

Fig. 7.9. Comparison of unidirectional and bidirectional Leman Sand simulations equivalent to OOP5 laboratory test conditions

7.2.5 Discussion

Nonlinear soil behaviour is supposed to happen for acceleration around 0.4*g*. In these simulations, accelerations involved are below that level, but significant stiffness degradation and pore pressure generation are observed in the laboratory. At the surface, the acceleration is 0.2*g* for step 1 and 0.35*g* for step 2.

The model underestimates axial strains, which are below the expected level, especially for the second step at the acceleration 0.35*g*. It reproduces well the degradation curve of the secant shear modulus, but the peak of the damping ratio does not appear, maybe because the modelled strains are too small. Stiffness degradation cannot be reproduced by the linear equivalent method, and the coupling with the pore pressure is neglected because this model is implemented as a total stress analysis. This model cannot discriminate between dry and saturated undrained conditions, although major differences were experimentally observed in Chapter 4.

Frequency effects are not well captured by the linear equivalent method. The increase of G_{sec} and decrease of $\Delta\varepsilon_q$ at low frequency are opposite to what was observed in our laboratory tests. However, the rate-dependency of damping is similar to the observed effect of frequency on undrained Leman Sand. Multidirectional effects are not at all taken into account, which was expected from this simple numerical tool.

7.2.6 Summary

Although it reproduces well the stiffness degradation curves, i.e. the relation between the dynamic parameters and shear strains, the linear equivalent model is not able to model the strain increase associated with undrained behaviour of dynamically loaded saturated sand at medium strain. The modelling of failure is even less possible. Strain amplitudes are underestimated, the accumulation of irrecoverable strain is not modelled, and neither is pore water pressure increase. The effects of frequency and multidirectional loading observed in triaxial tests cannot be modelled either. These observations apply to an acceleration at the top of the soil layer of maximum 0.35*g*, which is around the threshold usually considered for nonlinear soil behaviour. However, this model gives acceptable stress - strain relation at the lowest amplitude (which corresponds to an acceleration of 0.2*g* at the top of the soil layer), although strain amplitudes are underestimated.

7.3 Behaviour of Leman Sand with a multi-mechanism elastoplastic constitutive law

7.3.1 Introduction

A much more complex constitutive law is implemented in a local integration routine (on a soil element shown in Fig. 7.10) to simulate nonlinear sand response to cyclic loading. The higher number of parameters of this incremental constitutive law is supposed to allow taking into account both monotonic and cyclic loadings, including the hydro-mechanical coupling.

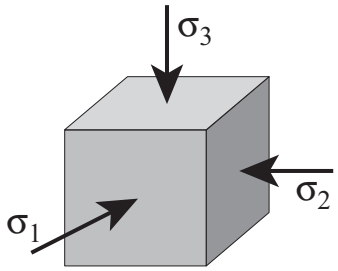

Fig. 7.10. Soil element of the local integration routine

In the following paragraphs, the calibration process is first described. Then, numerical results are compared to laboratory tests corresponding to the same initial state and boundary conditions. The laboratory cyclic tests CYC1 and CYC2 (CYC2 is presented in Appendix 3) and the monotonic test M4 were all used for calibrating model parameters. CYC1 and M4 numerical and experimental tests are compared below. The prediction of a dry test is also compared to the corresponding experimental result presented in Chapter 4 (DRY1 test). Finally the evaluation of these results is discussed and then compared to an example of cyclic liquefaction modelling with a different multi-surface plasticity model.

7.3.2 Model calibration

The simulation of soil behaviour with the Hujeux multi-mechanism elastoplastic law is performed in a Fortran routine, called LAWYER, provided by Ecole Centrale Paris (LAWYER manual 2007). It allows to simulate most loading paths used in our triaxial tests, and to identify the soil parameters involved. LAWYER is only meant to be used for modelling a homogeneous soil element, as it does not include any possibility to geometrically define a boundary conditions problem.

Some parameters were estimated from laboratory tests, while others were obtained by fitting cyclic and monotonic curves calculated from the triaxial tests on Leman Sand.

7.3.2.1 Elastic parameters

The determination of most elastic parameters of Leman Sand is presented in section 4.4.5. To summarize, (i) the Poisson's ratio is equal to $\nu = 0.3$, (ii) the coefficient n_e is estimated at 0.5 (similar to what is usually found in the literature), (iii) the reference secant shear modulus G_{ref} = 474 MPa. The reference bulk modulus K_{ref} = 546 MPa is deduced from G_{ref} and ν.

7.3.2.2 Plastic compressibility

A few virgin drained isotropic compression tests were recorded in the triaxial press for dry conditions. Recordings of radial strain by laser triangulation allow to continuously calculate the sample void ratio during consolidation. Three different virgin isotropic consolidations were selected, as shown on Fig. 7.11.

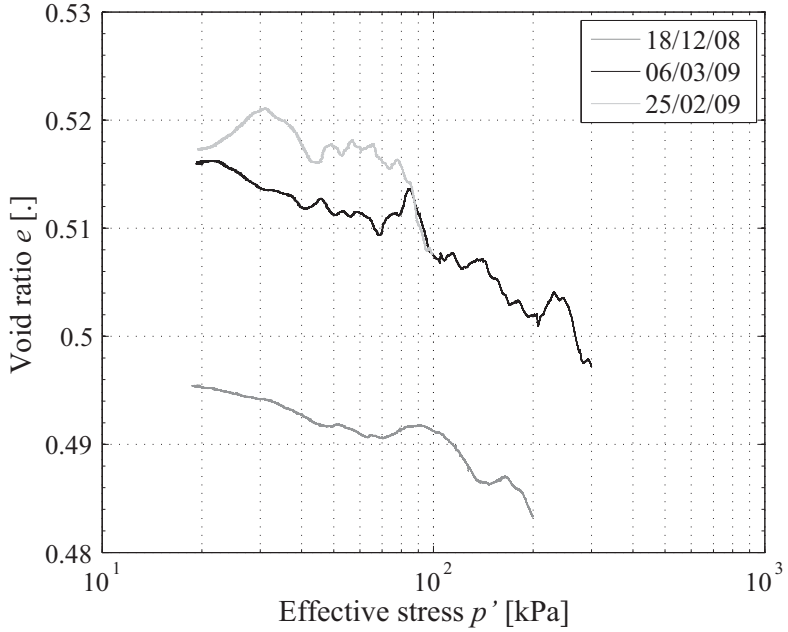

Fig. 7.11. Isotropic compression of dry Leman Sand.

The parameter λ_c, estimated by a linear regression of the slope of the virgin isotropic compression in the e - log(p') plan (Fig. 7.11), is λ_c = 0.0066. The plastic compressibility β = 200 is calculated by (Lopez-Caballero 2003):

$$\beta = \frac{1+e_0}{\lambda_c - \kappa} \simeq \frac{1+e_0}{\lambda_c} \tag{7.1}$$

7.3.2.3 Residual friction angle and dilatancy angle

These angles correspond to SS and PT lines calculated from undrained monotonic tests in compression.

The residual friction angle is estimated at 33°, and the dilatancy angle is equal to 39° (cf. Chapter 4). These parameters are lower in extension, but it is not possible to take that into account in the model.

7.3.2.4 Curve fitting

All other soil parameters are either fixed or manually fitted to the experimental curves mentioned in section 7.3.1. Some characteristic values for sand, provided by Lopez-Caballero (2003), were first used to start the calibration from an acceptable group of parameters. As model parameters are interrelated, the fitting process is a succession of trials and error steps, taking into account both monotonic and cyclic experimental data at the same time.

A few advices and rules were followed (Michalski & Rahma 1989), to help the calibration process:

- a_m, b, c_m and d are mainly determined with the monotonic tests
- a_{cyc}, c_{cyc}, m, r_{hys}, r_{mob} are determined with the cyclic undrained tests
- the initial preconsolidation pressure p_{c0} is estimated from initial test conditions (the denser the material, the higher p_{c0}). Moreover, a_m, b and p_{c0} are interrelated parameters.
- m influences the evolution of ε_v and u_r in cyclic loading; it is higher than 1
- b and α influence dilative behaviour
- b is around 0.1 to 0.2 for sand, and d is from 2 to 4; α is higher than 1 for dilative soils
- r_{hys} is a small multiple of r_{ela}
- a_{cyc} is approximately half the value of a_m, which is around 0.001 to 0.01; c_{cyc} should not be higher than c_m; c_m is around a_m, with $a_m \le c_m \le 3\,a_m$.

7.3.2.5 Summary

We kept in mind that the calibration of model parameters must involve the suitable representation of both monotonic and cyclic tests. The selected parameters are thus a compromise (values in Tab. 7.2); it is possible to model better (almost perfectly) one test alone, but instead we chose to allow an acceptable representation of the seven selected steps in three different situations (triaxial tests CYC1, CYC2, M2).

Tab. 7.2. Hujeux model parameters for Leman Sand

Parameter	Value	Unit
Elastic parameters		
K_{ref}	546	MPa
G_{ref}	474	MPa
n_e	0.5	.
Dilatancy rule		
φ	33	°
α	1.7	.
Deviatoric yield surface and hardening parameters		
ϕ	39	°
β	200	.
b	0.2	.
a_m	0.008	.
a_{cyc}	0.0015	.
Deviatoric domains		
r^{ela}	0.001	.
r^{hys}	0.004	.
r^{mob}	0.8	.
m	2.6	.
Isotropic yield surface and hardening parameters		
d	2.5	.
c_m	0.03	.
c_{cyc}	0.03	.
Initial state		
p_{c0} at $\sigma_3'^0$ = 100kPa	1.5	MPa
p_{c0} at $\sigma_3'^0$ = 200kPa	2.5	MPa

7.3.3 Results

7.3.3.1 Cyclic undrained test

The four first steps of CYC1 (initial confining pressure $\sigma_3'^0$ = 200kPa, Δq = 40, 70, 100 and 130 kPa in steps 1 to 4) were selected to be modelled with the elastoplastic law. The steps number 3 and 4 are depicted in details (stress-strain relation, stress paths, etc...) in Fig. 7.12 to Fig. 7.16 (step 3 in part (a) and step 4 in part (b)), followed by the evolution of the deviatoric strain amplitude (Fig. 7.17), maximum pore pressure ratio (Fig. 7.18) and dynamic parameters (Fig. 7.19 to Fig. 7.21) for all steps.

Both the experimental part and the model are stress-controlled, with a cyclic deviatoric stress of constant amplitude (Fig. 7.12). As a response, the axial strain below (Fig. 7.13) regularly increases. The slight anisotropy observed in the laboratory test response, with higher strain amplitudes on the side of extension, cannot be reproduced by the model, but stiffness degradation (i.e. strain amplitude increase) is finely reproduced, especially for step 3. In step 4, ε_1 eventually stabilises in the model (Fig. 7.13b), though it continuously increases in the experiment to reach the failure threshold. The reasons for that stabilization will be explained later in section 7.3.4.

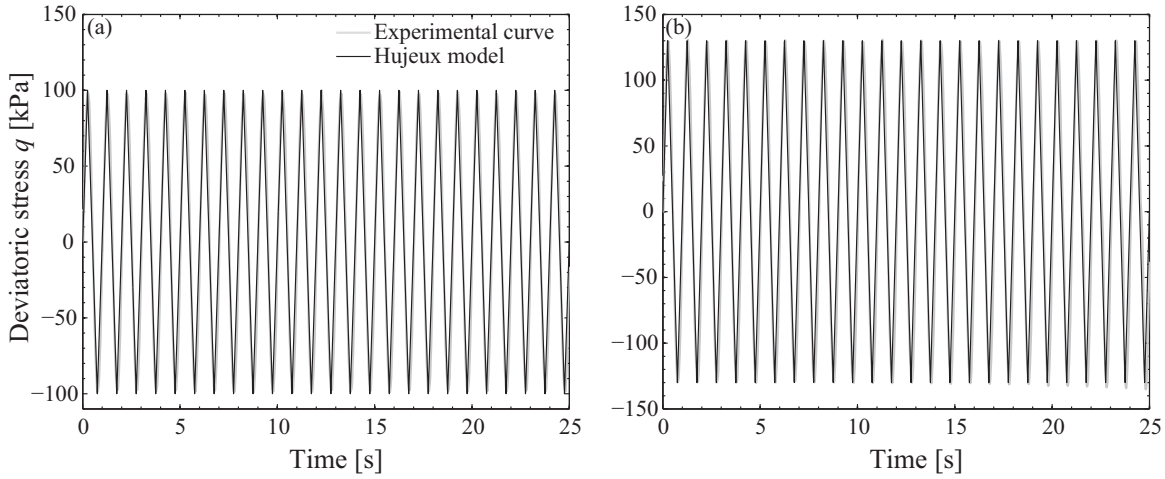

Fig. 7.12. Stress loading of CYC1 test with Leman Sand, step 3 (a) and step 4 (b).

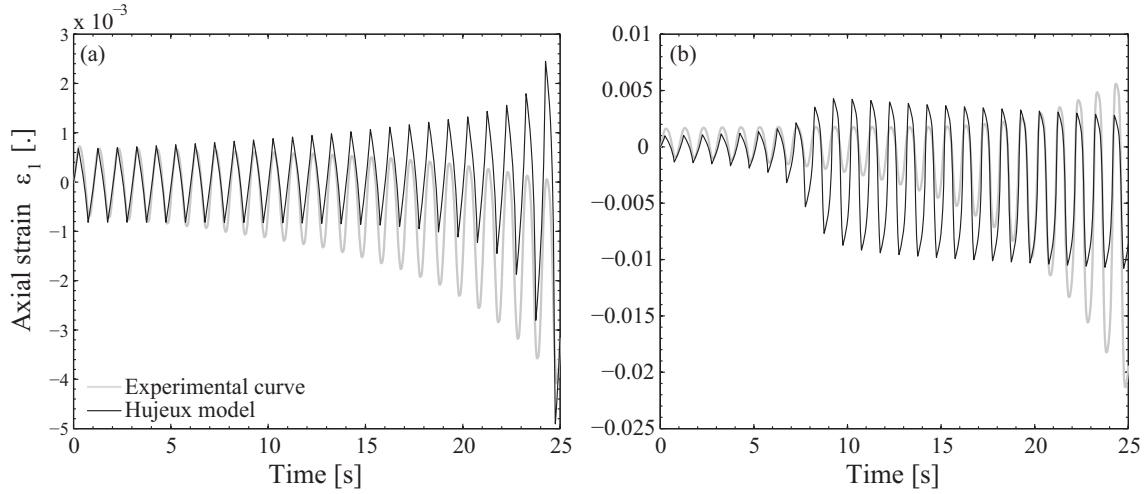

Fig. 7.13. Axial strain induced in CYC1 test.

The regular increase of pore pressure ratio with the number of cycles is well represented as well by the model (Fig. 7.14a). Both the amplitude of u_r and its rate of increase fairly match the experimental results. In the fourth step (Fig. 7.14b), a threshold is reached with $u_{r,m}$ = 0.82, instead of 1 in the laboratory tests. Some negative spikes of the pore pressure are present, although they do not appear

very clearly on the figure. This evolution is linked with the threshold observed in axial strains of the model, and will be discussed later as well.

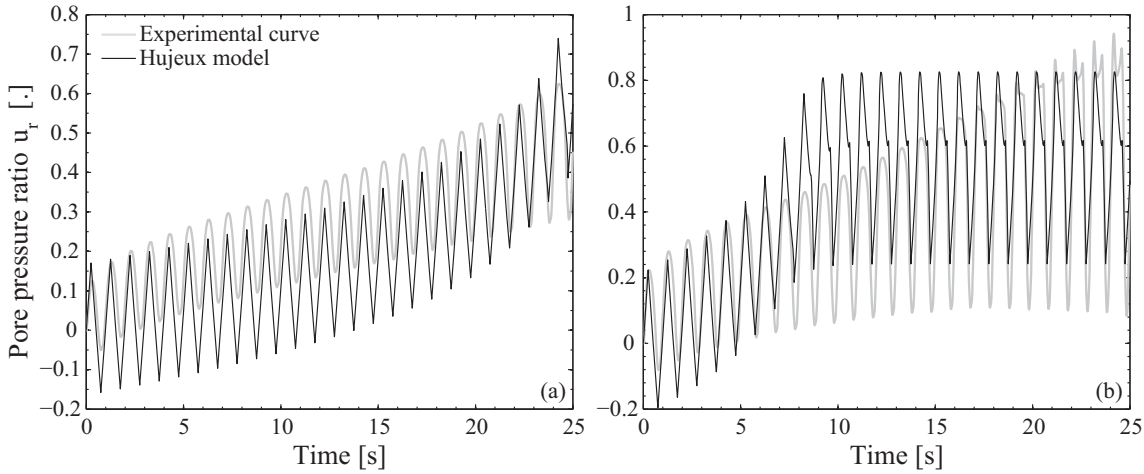

Fig. 7.14. Pore water pressure induced in CYC1 test.

Following these good trends, the stress-strain relation (Fig. 7.15) and the effective stress paths (Fig. 7.16) match well between laboratory tests and the elastoplastic model. Stiffness degradation and the decrease of the mean effective stress are clear in step 3, and the characteristic shapes, the S shape of the stress - strain relation and the wing shape of the effective stress path, are observed. The dilative behaviour of dense sand can be nicely reproduced, though the curves do not perfectly overlap as the amplitudes are not precisely equal in laboratory and modelling data.

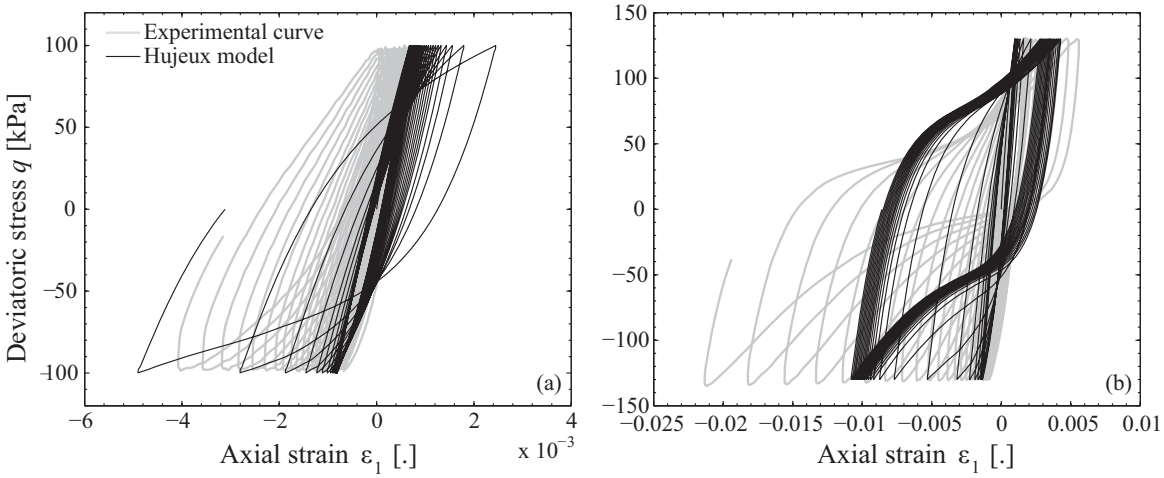

Fig. 7.15. Stress-strain relation of CYC1 test.

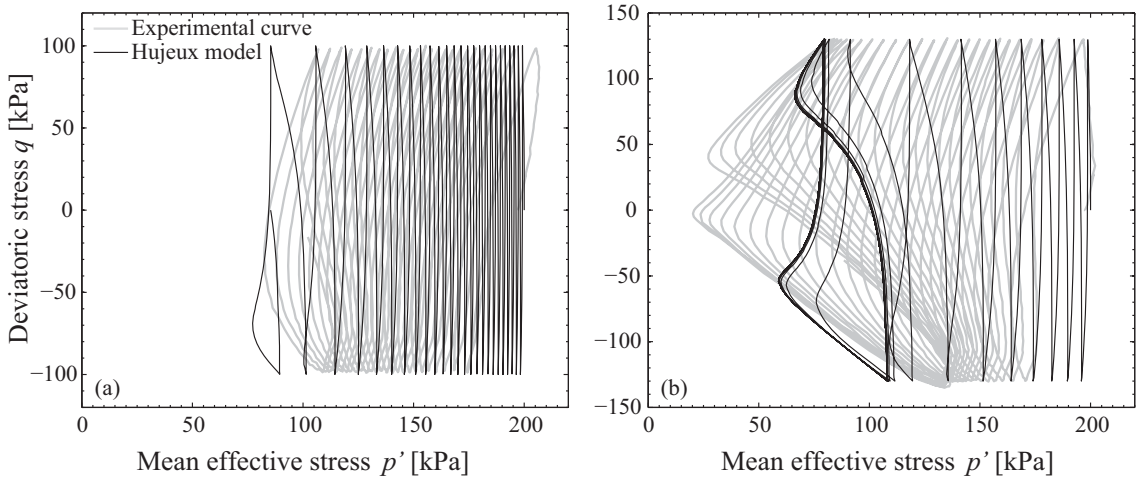

Fig. 7.16. Effective stress paths of CYC1 test.

In the following, complementary curves representing the deviatoric strain amplitude, secant shear modulus and damping ratio are commented for the four first steps. They show that the medium strain part is also fairly reproduced by the selected model parameters.

The deviatoric strain amplitude vs. number of cycles is presented with a log-scale so that all steps appear clearly (Fig. 7.17). $\Delta\varepsilon_q$ is slightly overestimated by the Hujeux model during the first two steps, but agrees anyway fairly well. The rate of stiffness degradation seems a bit strong during the development of large strains, and is then stopped at the threshold mentioned before.

The coupling between the pore pressure ratio and the deviatoric strain amplitude can also be reproduced by the elastoplastic model (Fig. 7.18). The rate of increase does not match perfectly for all four steps (i.e. there is not enough pore pressure increase at the 1st and 2nd step), but both the values and the overall shapes of the $u_{r,m}$ vs. $\Delta\varepsilon_q$ relations are in very good agreement between the Hujeux model and the laboratory test.

The dynamic parameters, calculated from the stress - strain loops at all cycles, are shown in Fig. 7.19 to Fig. 7.21. Following the strain amplitude, the evolution of the secant shear modulus with the number of cycles is in good agreement between the model and the experimental results. Stiffness degradation, in particular, is much better described than with the linear equivalent model.

On the other hand, the damping ratio is quite underestimated at medium strain and then overestimated, as the peak does not appear as expected around $\Delta\varepsilon_q = 7 \times 10^{-3}$. Instead, D stabilizes at its highest level when the accommodation process appears. However, it was noticed that another choice of parameters, which did not reproduce so well the monotonic behaviour, allowed to obtain that peak in the $\Delta\varepsilon_q$ - D curve. The model is thus able to reproduce that feature of dilative sand behaviour, even if the soil parameters selected here as a compromise do not show it.

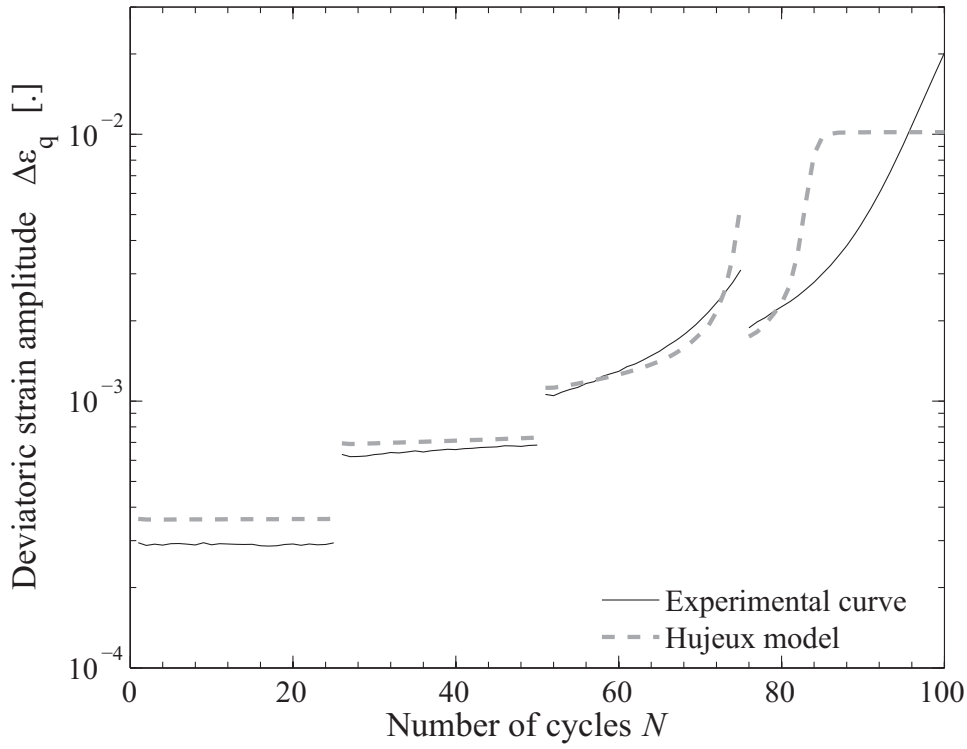

Fig. 7.17. Evolution of the deviatoric strain amplitude during CYC1 test, for Leman Sand (steps 1 to 4).

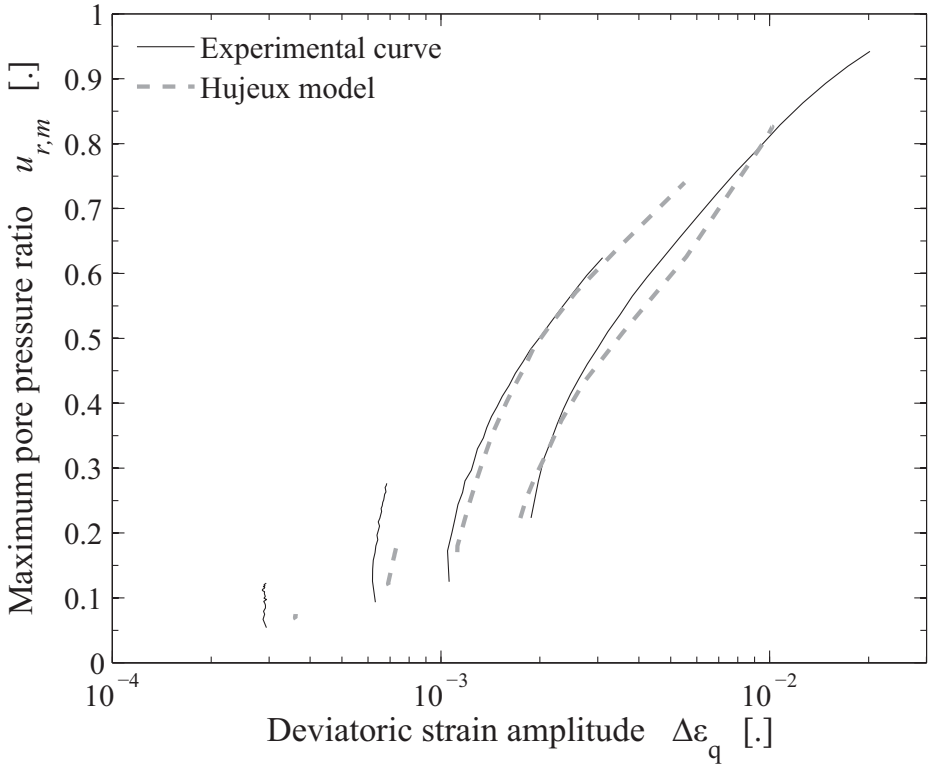

Fig. 7.18. Relation between the pore pressure and the deviatoric strain amplitude during CYC1 test.

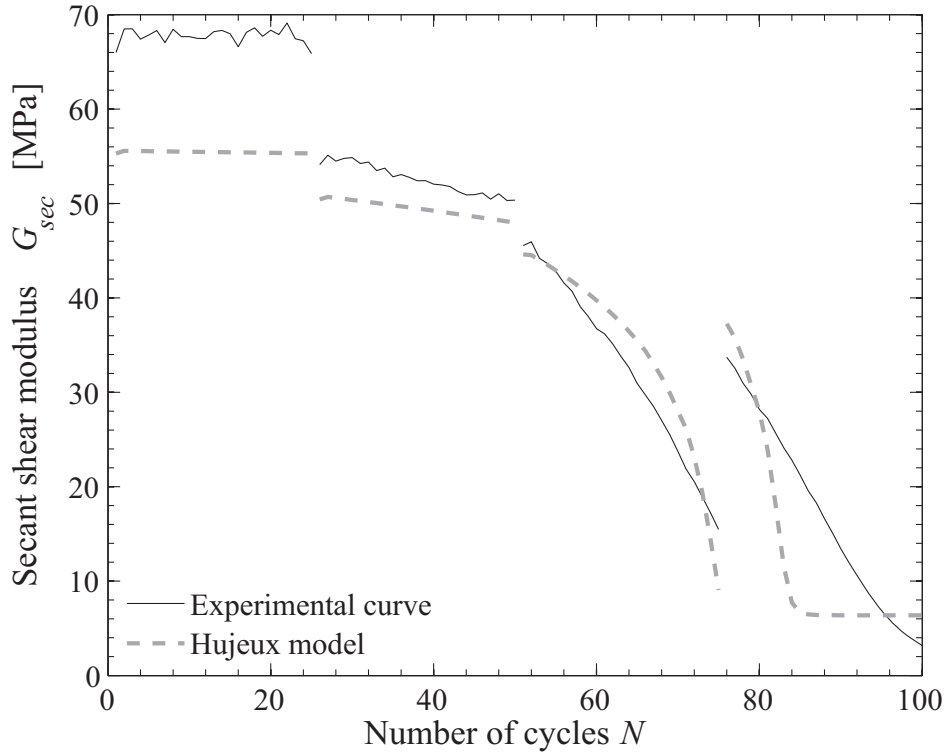

Fig. 7.19. Evolution of the secant shear modulus during CYC1 test.

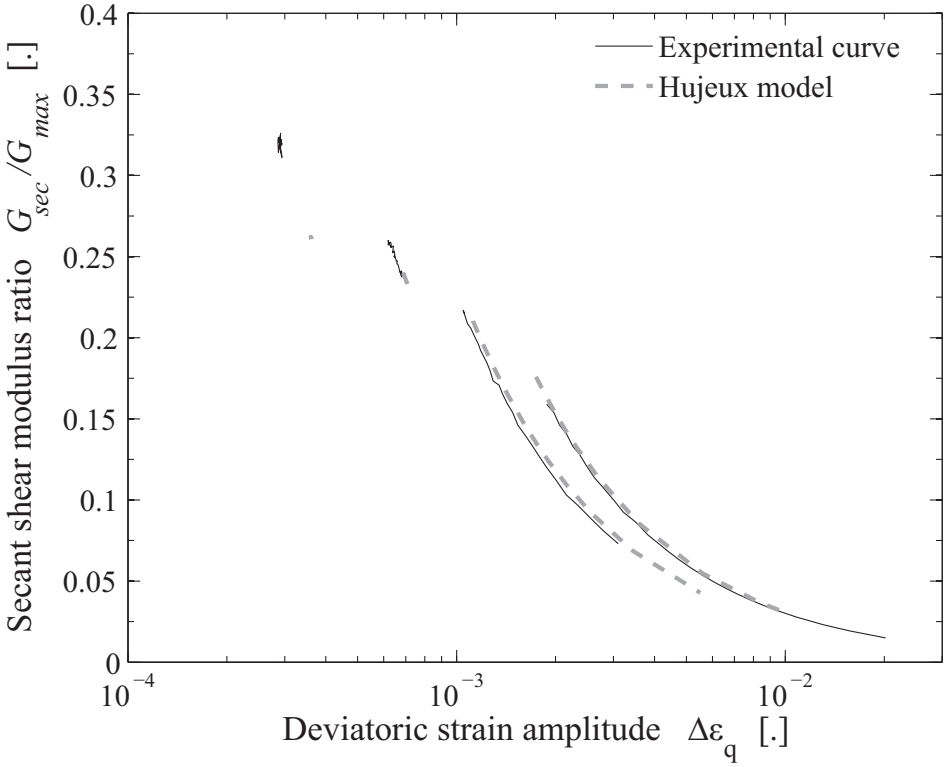

Fig. 7.20. Stiffness degradation curve of CYC1 test.

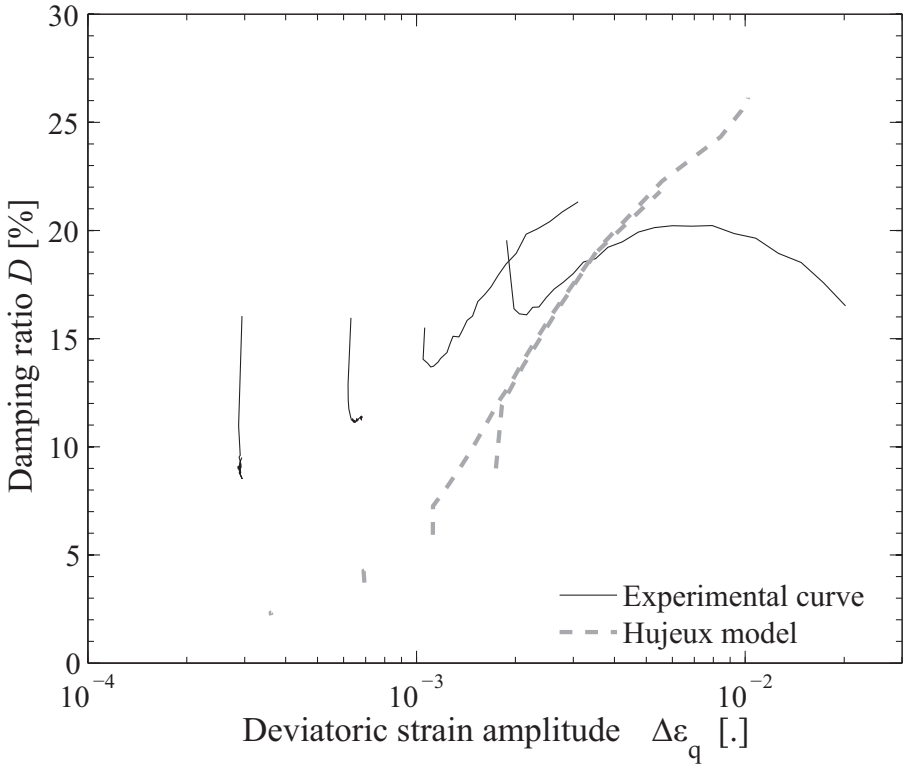

Fig. 7.21. Damping ratio vs. deviatoric strain amplitude for CYC1 test.

7.3.3.2 Monotonic test

The monotonic test M4 (initial confining pressure $\sigma_3'^0$ = 100kPa), which is also used for calibrating the model parameters, starts with a strain-controlled compression. The unloading part is modelled as well; it induces deviatoric stresses which reach extension ($q < 0$). The stress-strain relation and effective stress paths are displayed below (Fig. 7.22 and Fig. 7.23).

At large strain, the model underestimates the deviatoric stress, but the overall shapes of the numerical and experimental stress - strain relation matches very well (Fig. 7.22). Negative excess pore pressure as well is underestimated at unloading (Fig. 7.23). In particular, the part of unloading on the compression side arises at constant *p'* in the model, while major decrease arose in the laboratory test. Once again, another set of parameters allowed to get a better match with the monotonic curves, but it was not suitable for modelling cyclic tests. It is however possible to imagine that a better compromise exists, and could reproduce better the monotonic test at large strain. This matter is discussed later.

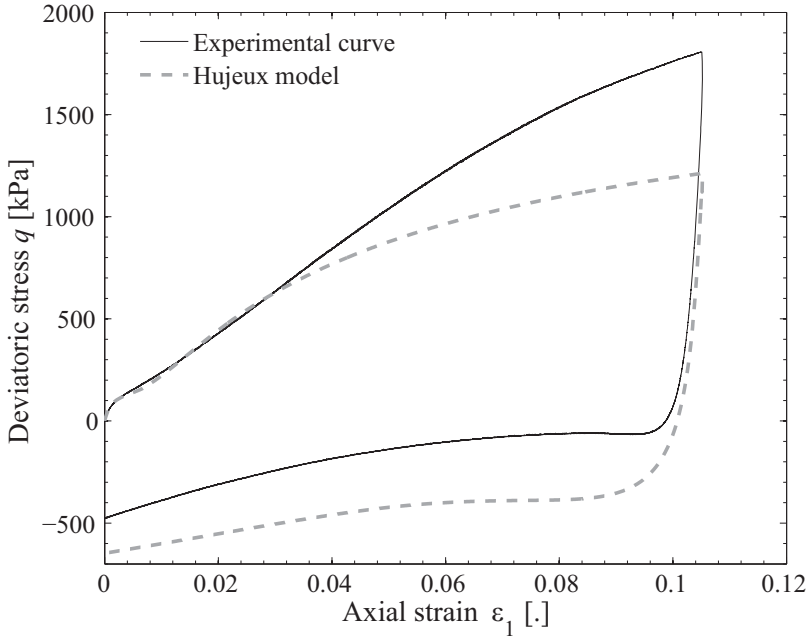

Fig. 7.22. Stress - strain relation in monotonic loading of Leman Sand (M4 test).

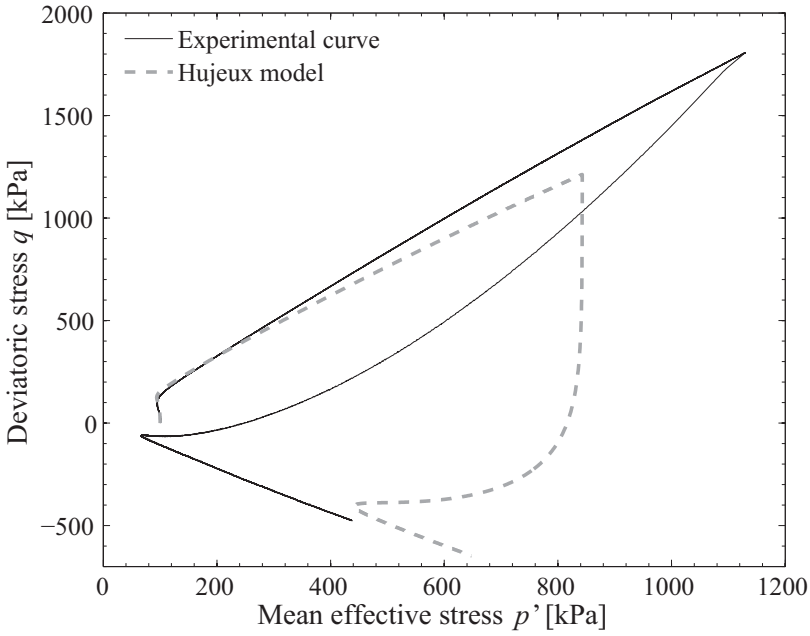

Fig. 7.23. Effective stress path in monotonic loading of Leman Sand (M4 test).

7.3.3.3 Application to a dry cyclic test

Using the soil parameters obtained with the triaxial tests CYC1, CYC2 and M4, the cyclic test DRY1 is modelled with the Hujeux elastoplastic law in dry soil conditions (initial confining pressure

$\sigma_3'^0$ = 200kPa). Steps number 1, 3 and 5 are shown below, at three different deviatoric stress amplitude, for comparing the dry experimental response to the elastoplastic model. Stress-strain relations and the volumetric behaviour ε_v vs. ε_1 are given to evaluate the model accuracy.

At small amplitude (Δq = 40 kPa, Fig. 7.24a), the first stress-strain loop, which induces a large irreversible axial strain in compression, is missing in the model; the stiffness of other cycles is similar in the model and experimental data. There is more difference for the volumetric behaviour (Fig. 7.24b). In overall, this step is not very well modelled, especially compared to the third step shown below (Fig. 7.25). At this stress amplitude (Δq = 100 kPa), the increase of volumetric strain and the secant shear modulus are slightly underestimated, but the overall trend matches well between the test and the model.

In the fifth step finally (Δq = 160 kPa, Fig. 7.26), the soil behaviour is also qualitatively well reproduced by the elastoplastic law. The overall shape of stress - strain loops is similar, and there is a shift towards the extension side in both case. Again, volumetric strains are underestimated by the model.

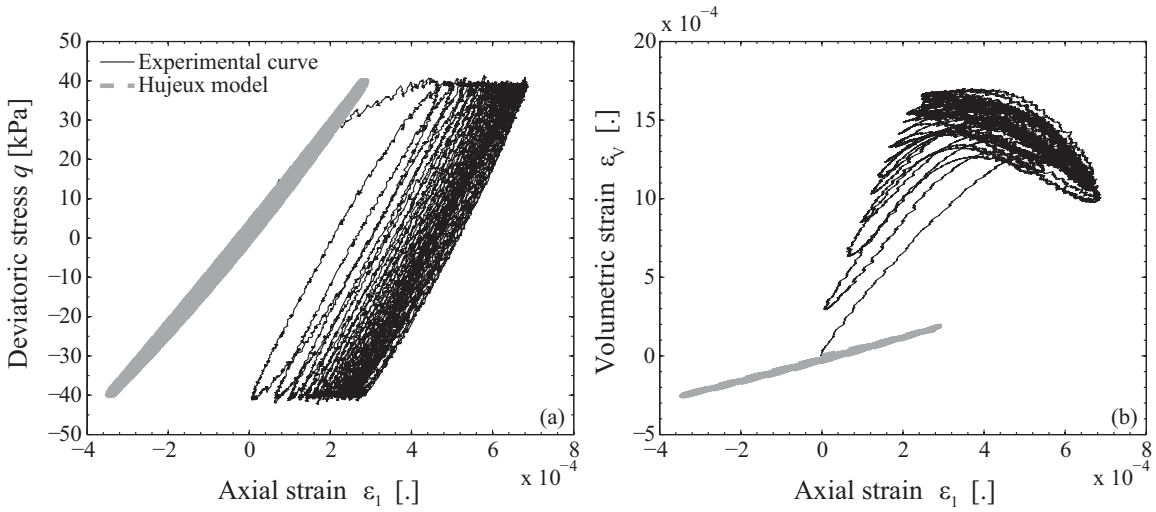

Fig. 7.24. Comparison of model and experimental test DRY1 - step 1: stress - strain relation (a) and volumetric behaviour (b).

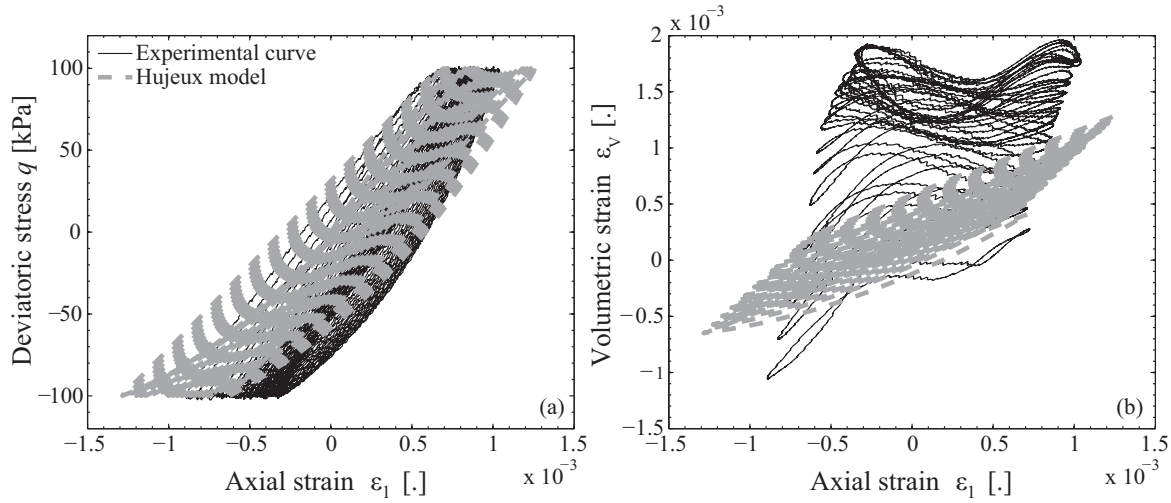

Fig. 7.25. Comparison of model and experimental test DRY1 - step 3: stress - strain relation (a) and volumetric behaviour (b).

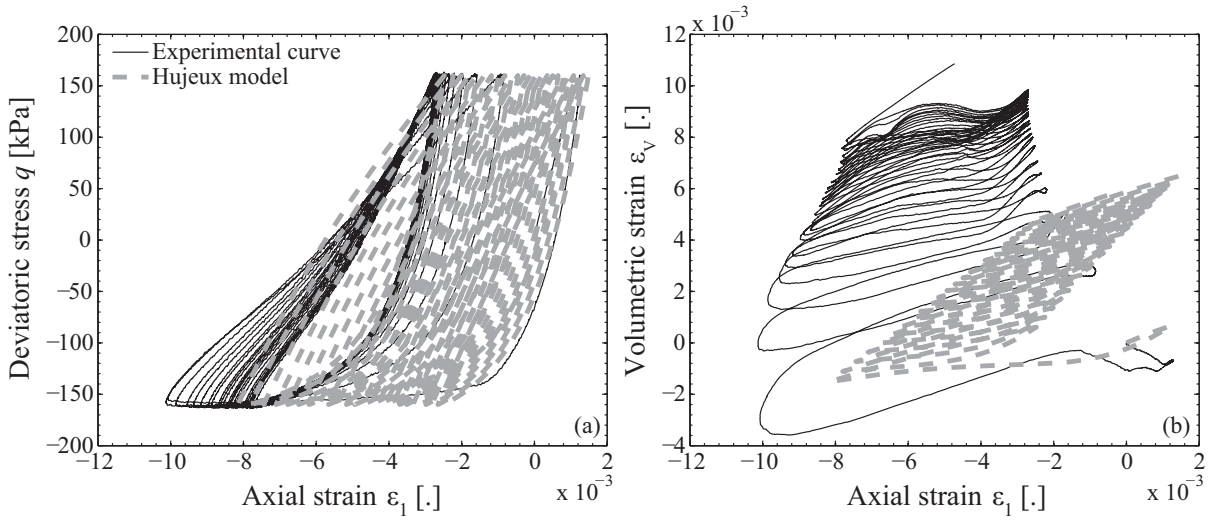

Fig. 7.26. Comparison of model and experimental test DRY1 - step 5: stress - strain relation (a) and volumetric behaviour (b).

7.3.3.4 Effect of frequency and multidirectional loading

The effect of frequency is not taken into account in that elastoplastic model. A viscoplastic model which takes into account cyclic effects could be a solution to evaluate and try to reproduce with numerical simulations the effect of frequency observed in our tests (Chapter 5).

The definition of loading in the LAWYER routine allows to take into account the superposition of loadings for in-phase multidirectional conditions only. The test CYC1 was modelled in a bidirectional configuration; compared to the unidirectional simulation, the strains and dynamic parameters are perfectly the same in 2D. Only the pore pressure amplitudes are influenced by the cyclic evolution of

the confining pressure: the increase of the cyclic amplitude of u_r exactly corresponds to the cyclic variation of the confining pressure. These observations show that there is no coupling effect resulting from the superposition of axial and lateral stresses, contrary to the experimental results presented in Chapter 6.

7.3.4 Discussion

The determination of the parameters of the Hujeux model results from a compromise, which aims at modelling the physical phenomenon observed in monotonic and cyclic loading in the best possible way. With a lot of available experimental data and interesting observed phenomenon, it was necessary to make a choice between the test results, in order to model accurately the features which are the most important to reproduce. An effort was made to reproduce most of the main features of cyclic behaviour of undrained saturated sand, rather than reaching very good quantitative results for a limited number of results. The features of undrained dense sand behaviour which could be well represented are summarized below:

- Regular pore pressure increase with the formation of negative spikes
- Regular stiffness degradation, with an increase of the deviatoric strain amplitude and a decrease of the secant shear modulus which matches very well experimental results
- Energy dissipation through damping, which increases with the deviatoric strain amplitude
- Accumulation of plastic strains
- Shapes of the stress - strain loops and effective stress paths corresponding to undrained sand behaviour at large strain

On the negative side, the elastoplastic Hujeux model does not solve all the problems of the linear equivalent method. In particular, the large strain behaviour is not quantitatively well simulated because $\Delta\varepsilon_1$ stabilizes instead of reaching the threshold for cyclic liquefaction. The set of parameters which fairly reproduces medium strain behaviour and stiffness degradation is not compatible with a good representation at large strain, around the failure threshold. This could be a limit of the model. However, it may also be possible to obtain a set of model parameters with better adequacy to the test results, by performing a systematic parametric study or implementing advanced algorithms, e.g. artificial neural networks (Obrzud 2009). The difficulty of calibration by curve fitting of such a high number of parameters is the major problem of the multi-mechanism elastoplastic law for cyclic loading.

The stabilization occurring at the end of all cyclic undrained simulations, when the maximum pore pressure ratio does not reach $u_{r,m}$ = 1.0, i.e. cyclic liquefaction does not fully develop, seems to correspond to accommodation. This kind of sand response at large strain is not really understood, but could be linked to the development of dilative behaviour. Different choices of model parameters can support the formation of much larger strains above a few percent, developing as cyclic liquefaction or flow liquefaction, also this is not an intrinsic limitation of the Hujeux model. Accommodation is rather a result of the compromise made to reproduce the overall sand behaviour.

The full complexity of the model is not necessary to simulate conventional triaxial tests. However, the multimechanisms are useful to try to capture the bidirectional effects observed in Chapter 6. Moreover, they are necessary in view of the applications of this research project: it is foreseen to apply the validated model parameters for multidirectional site effects analyses.

In the literature, a few advanced models based on incremental laws are able to reproduce, with good accuracy, stiffness degradation and cyclic liquefaction of saturated undrained sand (references in section 2.7.5). For example, the multi-surface plasticity model described by Elgamal et al. (2003) can also reproduce the features of cyclic undrained dense sand behaviour summarized above, like pore pressure increase and negative spikes of u_r or accumulation of irreversible strains. The few curves comparing experimental and numerical soil response give nice examples of very good match in terms of strains induced and pore pressure increase; the dynamic parameters are not calculated in the study, also there is no possible comparison for these test characteristics.

7.3.5 Summary

The Hujeux model is able to reproduce most of the physical phenomenon observed in cyclic loading of undrained sand, in conditions of unidirectional loading, at a given frequency, for symmetric CTC - RTE tests. Even if the calibration is a difficult process, some typical values exist for various soils and can facilitate the process. This study provides a new set of parameters for a natural poorly-graded sand. Although the irreversible strains could not be accurately reproduced, the most prominent features of cyclic soil behaviour at large strain, e.g. the S shape of the stress - strain loops and the increase of pore pressure with negative spikes, were satisfactorily modelled.

The difficulty of calibration is also increased by the fact that many laboratory tests are available, also the determination of the soil parameters is a compromise. Because of that, the robustness of the calibration is increased even if the application of the model on a case by case basis seems less accurate.

The multidirectional and frequency effects can not be taken into account directly by this elastoplastic constitutive law.

7.4 Comparison and evaluation of the models

An initial question raised in this work was to determine whether it is appropriate to use linear equivalent models for site effect analyses, as what is used in practise, if the seismic motion is strong and complex, and the soil response in the nonlinear regime. The answer is clearly negative; it can be further developed, with the following comments:

- The linear equivalent method is relatively easy to implement and calibrate, if laboratory tests (or in situ tests described in Appendix 1) provide P wave and S wave velocities as well as stiffness degradation parameters for all soil layers.
- The limit for nonlinear sand behaviour is usually defined for accelerations around 0.4*g*. The results of the experimental study and the comparison with the linear equivalent model show that, even below this limit (e.g. 0.2*g* for the first step of CYC2), this method does not reproduce correctly (i) stiffness degradation (ii) the strain amplitude (iii) the increase of irreversible strain (iv) the pore pressure increase. This fact can be compared to the seismic hazard map of Switzerland, which provides a PGA in Valais of 0.15*g* (section 2.3.2). The soil response to a strong event in this zone of medium seismicity could thus be underestimated by such model.
- The linear equivalent model can accurately reproduce the secant shear modulus and damping ratio from the degradation curves provided for calibration. With a known prescribed loading, it is thus possible to derive the dynamic parameters from laboratory tests or empirical equations, and then implement them in the linear equivalent model. However, the scopes of such applications seem limited. Moreover, the evolution of the dynamic parameters with the number of cycles is totally neglected.
- The multidirectional propagation of seismic waves of any kind and shape can be implemented without difficulty within the linear equivalent model until medium strain level (as mentioned before, the resulting strains are largely underestimated at medium strain level). However, the coupling effects resulting from the superposition of axial and lateral stresses, which can decrease cyclic strength (cf. Chapter 6), cannot be modelled.

On the other hand, the elastoplastic model used in this chapter provides much better results, though they

are not perfect either. It has the great advantage of being able to reproduce the complex phenomenon observed in undrained sand behaviour during cyclic loading, with alternate increase and decrease of the pore pressure. Cyclic liquefaction is adequately modelled, which is a great achievement. The problem, mentioned before, is that the calibration process is quite difficult, that is why obtaining the good set of parameters requires some practise. Because of that, obtaining accurate accumulated strains is difficult, even in the simple case of the modelling of a laboratory triaxial test. The extension to a real case of seismic wave propagation within relatively heterogeneous materials, which was not implemented within this research project, would be even more problematic.

Although both models allow to impose loading conditions similar to the complex loading presented in this research, neither of them can accurately take into account the frequency effect and the effect of superposition of loading observed in nonlinear cyclic sand behaviour. As described from the respective laboratory studies (Chapters 5 and 6), these two features of cyclic loading have non negligible impact on the triggering of failure in cyclic conditions, and also for irregular seismic loading (shown for bidirectional effect only).

Taking into account these two phenomena in the linear equivalent model may not be useful, as failure is anyway not adequately modelled. Refining such a tool, which provides broad approximations and is not suitable for nonlinear applications, would not make a lot of sense.

On the contrary, it would be interesting to implement in detail these experimental observations in a modified multi-mechanism elastoplastic model; this could allow to understand the physical mechanisms responsible for such behaviour. The possible modifications could be to:

- implement a viscoplastic model in a multi-mechanism framework, to try to take into account the effect of frequency
- re-evaluate the coupling of the isotropic and the deviatoric mechanisms, to give the possibility to model bidirectional effects
- introduce new functions, which could take into account the strain rate and a parameter for bidirectional effects, to enhance the volumetric response (pore pressure increase) and its coupling with strains.

These possibilities could all be implemented at the level of the constitutive law. The hydro-mechanical coupling is complex in such models, and also involves the balance equations. Even if we believe that dynamic wave propagation is not involved in the phenomena observed with the triaxial press, it could be interesting to evaluate the laboratory tests in a fully coupled finite element model.

7.5 Conclusions

Two models, able to reproduce cyclic soil behaviour, are presented in this chapter, including their calibration and the comparison with cyclic and monotonic triaxial tests.

We first showed that the linear equivalent model is not suitable for studying undrained sand behaviour for medium to high strains. The hydro-mechanical coupling, in particular, is an essential feature of our tests which is completely neglected in this model. Stiffness degradation is also underestimated. The peak ground acceleration of central Valais (Switzerland), defined by the Swiss Seismological Service, is very close to the acceleration needed to induce the nonlinear soil response characteristic of our tests. It is often considered that such a tool is adequate for regions of relatively medium seismicity, but this example demonstrates that the application of the linear equivalent model could imply non negligible underestimation of predicted strains.

On the contrary, the Hujeux elastoplastic law can model most features of nonlinear soil behaviour. In particular, the shape of stress - strain loops, observed in dense sand because of alternate increase and decrease of the excess pore pressure, is greatly reproduced. The hydro-mechanical coupling as well is finely obtained. By developing a systematic calibration procedure, it should be possible to facilitate the access to this efficient model and even improve the quality of the modelling. The model could also be developed to take into account the effect of frequency and the effect of multidirectional loading described in the previous chapters of this study.

CHAPTER 8

CONCLUSIONS AND PERSPECTIVES

8.1 Achievements

In order to evaluate the effect of complex loading (strong seismic motions) on the dynamic response of granular soils, cyclic sand behaviour was extensively analysed by means of various triaxial tests. The focus was put on several characteristics of seismic wave propagation:

- Loading amplitude, initial stress conditions, hydraulic conditions (Chapter 4)
- Effect of frequency, and evaluation of the parameters influencing the rate-dependency (Chapter 5)
- Effect of superposing axial and lateral stresses with cyclic loading (Chapter 6)
- Irregular seismic loading in unidirectional and bidirectional conditions (Chapter 6)

Besides the description of sand behaviour in strong and complex loading conditions, this study aims at evaluating the importance of particular loading features, which are usually neglected. It also provides good quality and innovative experimental results, helping to understand the physical processes involved in soil dynamics.

Such an experimental work was possible thanks to the developments of advanced laboratory equipments (described in Chapter 3). A short synthesis of the lessons learned from the technological developments, calibration and validation is first presented below.

These important laboratory test results are finally used to evaluate two very different but well accepted constitutive models (Chapter 7). In fact, reproducing cyclic soil behaviour at large strain comprises many difficulties. It is our now documented impression that the numerical methods currently used in practice may not be appropriate for modelling strong earthquake loading.

8.1.1 Developments of laboratory equipment

The dynamic triaxial press was designed to perform complex cyclic and seismic loadings, in conditions suitable for studying saturated and dry sand behaviour in the nonlinear regime (i.e. medium to large strains). We performed developments, calibrations and validation of this complex device.

An innovative non-contact technique, based on laser sensors, was conceived, built and calibrated to continuously measure local radial strains at middle height of the sample. The mounting frame also allows to perform vertical sample scanning. Besides the complete calibration process and validation with rubber and steel samples, we performed a validation of the laser sensors based on the assumption of zero volumetric strain during undrained loading of Leman Sand. This validation defines the limits of application of the laser sensors in terms of threshold strain amplitude; data analyses are improved thanks to smoothing and averaging procedures. Local radial strain amplitudes from 4×10^{-4} to 4×10^{-1}

can be monitored with loading frequency in the earthquake frequency range (0.1 to 10 Hz). An interesting application of this device is that it allows to verify that induced anisotropy is negligible for the cyclic triaxial tests performed on Leman Sand.

Other equipments were developed to ensure a good accuracy of the dynamic tests, mainly the sample mounting system and the aluminium triaxial cell. Together with all described equipment, they allow to perform reliable triaxial tests in drained and undrained conditions.

8.1.2 Cyclic dense sand behaviour

Several monotonic and cyclic triaxial tests on Leman Sand and Fonderie Sand were performed in the nonlinear regime. The different cyclic tests provide deep insight into stiffness degradation of both sands, up to failure. At large strain in undrained conditions, the occurrence of cyclic liquefaction or flow liquefaction is observed, depending on the soil tested. In dry conditions, sudden failure was observed in dense sand.

Cyclic soil behaviour is described for different initial and boundary stress conditions. The effects of the average deviatoric stress and the initial confining pressure on soil behaviour are the same in undrained saturated and dry loading of Leman Sand: the overall soil behaviour is stiffer for higher mean deviatoric stress (q_{av}) or higher initial confining pressure ($\sigma_3'^0$). Moreover, there are significant differences, observed in the stress - strain relations and the stress paths, for compression and extension monotonic and cyclic loading.

Undrained saturated tests exhibit stiffness degradation during continuous cyclic stress-controlled loading. Depending on the soil type, initial and boundary conditions, the rate of increase of strain amplitudes varies significantly. The conditions involving the highest rates of stiffness degradation are: (i) uniform sand (Fonderie Sand), (ii) higher void ratio, (iii) lower initial confining pressure, (iv) lower mean deviatoric stress. On the contrary, accommodation behaviour prevails in dry tests during steps of constant stress amplitude.

Excess pore pressures of undrained saturated Leman Sand and Fonderie Sand increase as a function of strain amplitudes. The curves $\Delta\varepsilon_q$ - u_r form a narrow band which mainly depends on the number of cycles. Slightly higher pore pressures are obtained in the uniform sand. The increase of volumetric strains with deviatoric strains in dry Leman Sand is represented by similar curves $\Delta\varepsilon_q$ - $\Delta\varepsilon_v$. They also seem to depend mainly on the number of cycles.

Dynamic material parameters, i.e. the secant shear modulus (G_{sec}) and damping ratio (D), are calculated for cyclic loading of Leman and Fonderie Sand. Stiffness degradation curves ($\Delta\varepsilon_q$ - G_{sec} / G_{max}) are obtained in the medium to large strain domain. They are similar in dry and

undrained saturated conditions. On the contrary, hydraulic conditions influence the evolution of the damping ratio. While *D* monotonically increases with the deviatoric strain amplitude in dry conditions, it exhibits a peak, at medium strains, in undrained saturated dense sand. This peculiar evolution is due to the evolution of excess pore pressure in negative spikes, during undrained cyclic loading, and it is linked with the «S shape» of the stress - strain loops.

Sample failure of dense undrained saturated Leman Sand arises by cyclic liquefaction. The material progressively softens, and its degradation index reaches very low values. The failure criterion can be based on a threshold deviatoric strain $\Delta\varepsilon_q$ = 2.5%. It matches the level of the degradation index well, which can thus be used as an alternative criterion for failure. Another candidate can be the pore water pressure ratio.

Three different behaviours are obtained with regard to failure in the rather uniform Fonderie Sand, depending on the relative density: accommodation, cyclic liquefaction and flow liquefaction. At the same relative density, the increase of deviatoric strain upon loading is very progressive and stable for the natural Leman Sand, while it is sudden, rapid and induces instability of the motion control system for Fonderie Sand. Fonderie Sand samples exhibit inhomogeneity above failure, especially concerning excess pore pressure which dramatically increases above 1 due to end-restraint and strain localization.

The different behaviours of Leman and Fonderie Sand is ascribed to their respective particle shape and grain size distribution, where round particles and uniform distribution induce higher liquefaction susceptibility in the case of Fonderie Sand. For both sands, the phase transformation line in extension is reached first, and most of deviatoric strains arise on the side of negative strains.

Shear strain localization was observed in particular loading conditions, and carefully analysed, thanks to the observation of direct records from the three laser sensors in dry tests. The clear discontinuity occurs above the threshold deviatoric strain failure criterion, around ε_q = 4 to 5%. Strain localization was found to (i) depend on confining pressure, (ii) depend on the hydraulic conditions, and (iii) be responsible for the large increase of damping ratio and excess pore pressure ratio.

8.1.3 Frequency-dependence of granular materials

Creep and relaxation tests reported in the literature provide examples of viscous behaviour of dry and saturated granular materials. However, rate effects are neither well-known nor understood, especially for conditions of strong seismic loading. This work provides laboratory tests showing the influence of loading frequencies on soil behaviour, applicable under such strain amplitude and frequency range conditions.

Monotonic triaxial undrained compression tests performed at different strain rates below 1 %/s show

that there is no observable monotonic strain rate effect in Leman Sand in this range of strain rate. On the contrary, the cyclic tests performed on dense Leman Sand show a frequency effect between 0.1 and 6.5 Hz in dry and undrained conditions.

Preliminary stress-controlled cyclic tests at four frequencies show that, compared to high frequencies, low frequencies induce higher strain amplitudes, lower stiffness and higher excess pore pressure at medium to large strain. The same consequences on stiffness degradation behaviour are inferred, in certain conditions, from undrained saturated tests at 15 different frequencies. Dry Leman Sand also exhibits frequency-dependent behaviour at medium strain level. As for undrained sand, deviatoric strain amplitudes increase at low frequency.

A strong frequency-dependence is found in an undrained saturated test: the deviatoric strain amplitude decreases by a factor of 3, the maximum pore pressure ratio decreases by a factor of 4.5 and the secant shear modulus increases by a factor of 3 when the frequency increases from 0.1 to 6.5 Hz. Interestingly, other test boundary conditions, inducing higher sample stiffness, lead to practically frequency-independent soil behaviour in approximately the same frequency range. This observation is also confirmed for a dry sample.

A dry cyclic test also exhibits frequency-dependent behaviour, therefore the coupled motion of the granular matrix and the pore water is not the sole phenomenon behind frequency effects in sand. As for creep described in the literature for dry and saturated sands, viscous behaviour of inter-particle contacts may then play a role in frequency effects.

8.1.4 Effect of cyclic bidirectional conditions on undrained sand behaviour

Cyclic bidirectional tests were performed on Leman Sand in saturated undrained conditions. They demonstrate that the superposition of axial and radial stresses induces coupling effects in the nonlinear soil response. Bidirectional loadings produce an amplification of motions before cyclic liquefaction, and a limitation of strains after cyclic liquefaction. The phase angle between axial and lateral stresses has a particularly strong influence on Leman Sand behaviour. Cyclic strength is significantly modified by complex loadings.

In order to understand and compare the coupling between the two loadings, the pore pressure ratio of bidirectional tests is separated into two components which account for the change in total applied stress. The unidirectional pore pressure ratio u_r and the bidirectional component u_r^q, which corresponds to the deviatoric part of the load, have similar shapes. Moreover, both reach the threshold value 1 at cyclic liquefaction. The component of pore pressure ratio which accounts for the cyclic isotropic load, u_r^{comp}, includes water compressibility by including the sample *B*-Skempton coefficient.

A possible explanation for bidirectional effects is that the pore pressure itself influences the development of deviatoric strains. At the same time, the contractive behaviour of the soil matrix induces pore water pressure build-up. This double-way coupling, which is emphasized in our bidirectional tests depending on the value of the phase angle, induces a reduction of stiffness, and the occurrence of cyclic liquefaction is then accelerated.

8.1.5 Seismic unidirectional and bidirectional loading

Three irregular seismic tests were also performed in unidirectional and bidirectional conditions to illustrate the effect of superposition of loading in conditions close to in situ seismic motions. For irregular amplitudes and frequency content, bidirectional loadings can also increase deviatoric strains and pore pressure build up compared to unidirectional motions. The conditions of amplification of the response are similar to cyclic tests: before cyclic liquefaction, the superposition of loading slightly accelerates stiffness degradation. In the case of seismic loading, soil behaviour after cyclic liquefaction is practically equivalent in unidirectional and bidirectional loading.

The parallel between cyclic and irregular loading is illustrated with (i) characteristic «S shape» stress-strain relations, as a consequence of the evolution of excess pore pressure, (ii) total and effective stress paths, (iii) the relation between pore pressure increase and deviatoric strains. In irregular tests, we also showed that the relation between the maximum strain amplitude and the maximum stress amplitude is nonlinear, even in unidirectional loading.

8.1.6 Modelling the cyclic behaviour of dense sand

Two different models were applied, the linear equivalent model and the multi-mechanism elastoplastic model of Hujeux. They both illustrate the difficulties of modelling the cyclic soil behaviour at medium to large strain. Model calibrations are presented for Leman Sand, and the comparison with cyclic and monotonic triaxial tests is analysed.

We first show that the linear equivalent model is not suitable for modelling undrained sand behaviour for medium to high strains, in terms of qualitative description of the physical mechanisms. The quantitative results as well are poorly adequate. The hydro-mechanical coupling, an essential feature of our tests, is completely neglected in this model. Stiffness degradation is also underestimated, as well as strain amplitude.

It is often considered that the linear equivalent model is adequate for regions of relatively medium seismicity; however, the comparison of peak ground acceleration defined for Valais (Switzerland) and the acceleration needed to induce the nonlinear soil response characteristic of our tests are very close.

This shows that the application of the linear equivalent model in such areas, for example in microzonation studies for evaluating site effects, could imply non negligible underestimation of predicted strains.

The Hujeux constitutive law, which was adapted to cyclic loading, belongs to the category of Cam-clay models in the sense that it is an elastoplastic model defined within the critical state framework. Strain amplitudes of Leman Sand are well reproduced by the elastoplastic law, except at cyclic liquefaction, for which they are underestimated. Moreover, most features of the nonlinear sand behaviour can be modelled. In particular, the elastoplastic model provides accurate «S shapes» of the stress - strain loops, which occur in dense sand because of alternate increase and decrease of the excess pore pressure. The hydro-mechanical coupling is thus finely obtained. This model thus seems adequate for applications to strong seismic motions.

8.2 Outlook

The results presented in this work should be taken into account when designing earthquake-resistant structures. In particular, they may affect performance-based design (PBD) in geomechanics, which relies on an accurate prediction of the behaviour of a soil deposit or structure subjected to various loadings, including nonlinear effects. Moreover, the consequences of our study could be important for the evaluation of site effects.

On laboratory test side, we demonstrate that some loading features which are usually neglected can have a strong impact on the soil response. How to take these loading features into account within design procedures and site effects analyses is an open question.

We propose relations of Leman Sand secant shear modulus and damping ratio as a function of the average strain rate. The parameters of these power laws seem to depend on soil stiffness, as well as the overall rate-dependent behaviour. In particular, pore pressure build-up was shown to increase at low frequency, with a higher rate-dependency at small soil stiffness. Complementary tests on Leman Sand at different confining pressures and void ratios could be useful to evaluate the range of variation of these parameters, and to more precisely evaluate the limit between rate-dependent and rate-independent sand behaviour. The effects of particle shape and hydraulic conditions on rate-sensitivity could be explored in depth, to help understanding the mechanisms responsible for frequency-dependent behaviour of granular materials.

We also showed that bidirectional conditions have an impact on stiffness degradation and the triggering of cyclic liquefaction. Bidirectional effects are strongly dependent on phase angle, i.e. coupling effects are not trivial. In order to obtain significant curves for design purpose, more tests at other phase angles and for different initial stress and void ratios would be needed in bidirectional conditions.

Moreover, it would be very interesting to introduce continuous rotations of principal stress directions within the laboratory triaxial tests, in order to obtain a more realistic simulation of complex seismic motions. Indeed, the dynamic triaxial press can also control cyclic and seismic axial rotations of the axisymmetric sample, which can be superimposed to the bidirectional loadings used in this research. This third independent component would allow to impose «tridirectional» stresses within the soil sample. Introducing the rotation of principal stresses represents more than just adding a new test parameter, it would allow to explore much more general stress states.

On the modelling side, we show that the linear equivalent model, usually used in practice for site effect analyses, is not suitable for conditions corresponding to strong earthquakes (at least for acceleration above $0.2g$). We recommend to use more complete models, which can reproduce soil behaviour more realistically, in particular for sensitive areas.

The Hujeux elastoplastic model is a possibility, but adequate training is necessary. By developing a systematic calibration procedure, it should be possible to facilitate the access to this efficient model and even improve the quality of the modelling.

It would be interesting to evaluate the effect of frequency observed in our tests within a viscoplastic framework suitable for cyclic loading. This could allow to verify if the observed frequency-dependent behaviour is linked with viscous phenomena. The Hujeux model could also be developed to take into account the effects of multidirectional loading on cyclic soil behaviour.

Finally, these results could also have applications to other dynamic loading of strong amplitude, especially the sand response to shock, explosion and blasting (mining applications, terrorism-related risks, dynamic compaction, etc...).

References

Abrantes, A.E., and Yamamuro, J.A. 2002. Experimental and data analysis techniques used for high strain rate tests on cohesionless soil. Geotechnical Testing Journal, **25**(2): 128-141.

Aggour, M.S., and Zhang, J.X. 2006. Degradation of sands due to combined sinusoidal loading. Journal of Geotechnical and Geoenvironmental Engineering, **132**(12): 1628-1632.

Altun, S., and Goktepe, A.B. 2006. Dependence of dynamic shear modulus of uniform sands on stress level and density. Civil Engineering and Environmental Systems, **23**(2): 101-116.

Amini, F., and Qi, G.Z. 2000. Liquefaction Testing of Stratified Silty Sands. Journal of Geotechnical and Geoenvironmental Engineering ASCE, **126**(3): 208-218.

AnhDan, L.Q., Koseki, J., and Sato, T. 2006. Evaluation of quasi-elastic properties of gravel using a large-scale true triaxial apparatus. Geotechnical Testing Journal, **29**(5): 374-384.

Assimaki, D., and Kausel, E. 2002. An equivalent linear algorithm with frequency and pressure-dependent moduli and damping for the seismic analysis of deep sites. Soil Dynamics and Earthquake Engineering, **22**(9-12): 959-965.

Assimaki, D., Kausel, E., and Whittle, A. 2000. Model for dynamic shear modulus and damping for granular soils. Journal of Geotechnical and Geoenvironmental Engineering, **126**(10): 859-869.

Augustesen, A., Liingaard, M., and Lade, P.V. 2004. Evaluation of time-dependent behavior of soils. International Journal of Geomechanics, **4**(3): 137-156.

Baldi, G., Hight, D.W., and Thomas, G.E. 1988. A reevaluation of Conventional Triaxial Test Methods. *In* Advanced triaxial testing of soil and rock. *Edited by* R.C.C. Robert t. Donaghe, Marshall L. Silver. Louisville, United States. ASTM, pp. 219-263.

Bard, P.-Y., and Riepl, J. 2000. Wave propagation in complex geological structures and their effects on strong ground motion. *In* Wave Motion in Earthquake Engineering. WIT Press, Southampton. pp. 37-95.

Benahmed, N. 2001. Comportement mécanique d'un sable sous cisaillement monotone et cyclique : application aux phénomènes de liquéfaction et de mobilité cyclique, Ecole Nationale des Ponts et Chaussées, Paris, PhD thesis.

Bernardie, S., Foerster, E., and Modaressi, H. 2006. Non-linear site response simulations in Chang-Hwa region during the 1999 Chi-Chi earthquake, Taiwan. Soil Dynamics and Earthquake Engineering, **26**(11): 1038-1048.

Biot, M.A. 1956. Theory of Propagation of Elastic Waves in a Fluid-Saturated Porous Solid. I. Low-Frequency Range. Journal of the Acoustical Society of America, **28**(2): 168-178.

Bolton, M.D., and Wilson, J.M.R. 1989. An experimental and theoretical comparison between static and dynamic torsional soil tests. Géotechnique, **39, No. 4**: 584-599.

Bolton, M.D., and Wilson, J.M.R. 1990. Soil stiffness and damping. *In* European conference on structural dynamics. *Edited by* K.e. al. Bochum, Germany. Balkema, Rotterdam, pp. 209-216.

Boukpeti, N., Mroz, Z., and Drescher, A. 2004. Modeling rate effects in undrained loading of sands. Canadian Geotechnical Journal, **41**(2): 342-350.

Boulanger, R.W., and Seed, R.B. 1995. Liquefaction of Sand under Bidirectional Monotonic and Cyclic Loading. Journal of Geotechnical Engineering, **121**(12): 870-878.

Bray, J.D., and Sancio, R.B. 2006. Assessment of the liquefaction susceptibility of fine-grained soils. Journal of Geotechnical and Geoenvironmental Engineering, **132**(9): 1165-1177.

Brennan, A.J., Thusyanthan, N.I., and Madabhushi, S.P.G. 2004. Evalution of Shear Modulus and Damping in Dynamic Centrifuge Tests. Technical report, Report CUED/D-SOILS/TR336, Cambridge University Engineering Department.

BRGM 2005. CyberQuake User's Guide Version 2.01. BRGM.

Bui, M.T., Clayton, C.R.I., and Priest, J.A. 2007. Effect of particle shape on small strain shear modulus of geomaterials. *In* 4th International Conference on Earthquake Geotechnical Engineering. *Edited by* K. Pitilakis. Thessaloniki, Greece, 8 pages.

Campanella, R.G., Robertson, P.K., and Gillespie, D. 1986. Seismic cone penetration test. *In* In Situ 1986, ASCE Specialty Conference on Use of In Situ Tests in Geotechnical Engineering. *Edited by* S.P. Clemence. Blacksburg, VA, pp. 116-130.

Carvajal, J.C., Taboada-Urtuzuastegui, V.M., and Romo, M.P. 2002. Influence of earthquake frequency content on soil dynamic properties at CAO site. Soil Dynamics and Earthquake Engineering, **22**(4): 297-308.

Cascante, G., and Santamarina, J.C. 1996. Interparticle contact behavior and wave propagation. Journal of Geotechnical Engineering-ASCE, **122**(10): 831-839.

Cekerevac, C. 2003. Thermal effects on the mechanical behaviour of saturated clays : an experimental and constitutive study. EPFL, Lausanne, PhD. Thesis.

Chaudhary, S.K., Kuwano, J., Hashimoto, S., Hayano, Y., and Nakamura, Y. 2002. Effects of initial fabric and shearing direction on cyclic deformation characteristics of sand. Soils and Foundations, **42**(1): 147-157.

Chazelas, J., Escoffier, S., Garnier, J., Thorel, L., and Rault, G. 2008. Original technologies for proven performances for the new LCPC earthquake simulator. Bulletin of Earthquake Engineering, **6**(4): 723-728.

Choi, C., and Arduino, P. 2004. Behavioral characteristics of gravelly soils under general cyclic loading conditions. *In* Cyclic Behaviour of Soils and Liquefaction Phenomena. *Edited by* T. Triantafyllidis. Bochum, Germany. Taylor and Francis Group, pp. 115-128.

Chu, J. 1995. An experimental examination of the critical state and other similar concepts for granular soils. Canadian Geotechnical Journal, **32**(6): 1065-1075.

Cid, J., Susagna, T., Goula, X., Chavarria, L., Figueras, S., Fleta, J., Casas, A., and Roca, A. 2001. Seismic zonation of Barcelona based on numerical simulation of site effects. Pure and Applied Geophysics, **158**(12): 2559-2577.

Cox, B.R., Stokoe, K.H., and Rathje, E.M. 2009. An In Situ Test Method for Evaluating the Coupled Pore Pressure Generation and Nonlinear Shear Modulus Behavior of Liquefiable Soils. Geotechnical Testing Journal, **32**(1): 11-21.

De Gennaro, V., Canou, J., Dupla, J.C., and Benahmed, N. 2004. Influence of loading path on the undrained behaviour of a medium loose sand. Canadian Geotechnical Journal, **41**(1): 166-180.

Delepine, N. 2007. Modélisation des effets de site sismiques dans les bassins sédimentaires et influence des non-linéarités de comportement des sols, Ecole nationale des ponts et chaussées, Marne-la-Vallée, PhD thesis.

Demircioglu, M.B., Sesetyan, K., Durukal, E., and Erdik, M. 2007. Assessment of earthquake hazard in Turkey. *In* 4th International Conference on Earthquake Geotechnical Engineering. *Edited by* K. Pitilakis. Thessaloniki.

Di Benedetto, H. 2006. Small strain behaviour and viscous effects on sands and sand-clay mixtures. *In* Soil Stress-Stain Behavior: Measurement, Modeling and Analysis. Geotechnical Symposium held to celebrate the 60th Birthday of Fumio Tatsuko. *Edited by* H. Ling, L. Callisto, D. Leshchinsky, and J. Koseki. Rome, Italy. MAR 16-17, 2006. Springer, pp. 159-190.

Di Benedetto, H., and Tatsuoka, F. 1997. Small strain behavior of geomaterials: modelling of strain rate effects. Soils and Foundations, **37**(2): 127-138.

Di Benedetto, H., Tatsuoka, F., and Ishihara, M. 2002. Time-dependent shear deformation characteristics of sand and their constitutive modelling. Soils and Foundations, **42**(2): 1-22.

Dobry, R.R., Ladd, S., Yokel, F.Y., Chung, R.M., and Powell, D. 1982. Prediction of pore water pressure buildup and liquefaction of sands during earthquakes by the cyclic strain method. National Bureau of Standards, Washington, DC.

Drosos, V., Gerolymos, N., and Gazetas, G. 2007. Calibration and verification of nonlinear wave propagation method. *In* 4th International Conference on Earthquake Geotechnical Engineering. *Edited by* K. Pitilakis. Thessaloniki.

Duttine, A., Tatsuoka, F., Kongkitkul, W., and Hirakawa, D. 2008. Viscous behaviour of unbound granular materials in direct shear. Soils and Foundations, **48**(3): 297-318.

Elgamal, A., Zeghal, M., Parra, E., Gunturi, R., Tang, H.T., and Stepp, J.C. 1996. Identification and modeling of earthquake ground response. 1. Site amplification. Soil Dynamics and Earthquake Engineering, **15**(8): 499-522.

Elgamal, A., Yang, Z.H., and Parra, E. 2002. Computational modeling of cyclic mobility and post-liquefaction site response. Soil Dynamics and Earthquake Engineering, **22**(4): 259-271.

Elgamal, A., Yang, Z., Parra, E., and Ragheb, A. 2003. Modeling of cyclic mobility in saturated cohesionless soils. International Journal of Plasticity, **19**(6): 883-905.

Elgamal, A., Yang, Z., Lai, T., Kutter, B.L., and Wilson, D.W. 2005. Dynamic response of saturated dense sand in laminated centrifuge container. Journal of Geotechnical and Geoenvironmental Engineering, **131**(5): 598-609.

Elgamal, A., Pitilakis, K., Dimitrios, R., Garnier, J., Madabhushi, S.P.G., Pinto, A., Steidl, J., Stewart,

H.E., Stokoe, K.H., Taucer, F., Tokimatsu, K., and Wallace, J.W. 2007. A review of large-scale testing facilities in geotechnical earthquake engineering. *In* 4th International Conference on Earthquake Geoechnical Engineering. *Edited by* K.D. Pitilakis. Thessaloniki, Greece. june 2007. Springer, pp. 93-127.

Endo, O., and Komanobe, K. 1995. Single- and multi-directional shaking table tests of sand liquefaction. *In* First International Conference on Earthquake Geotechnical Engineering. *Edited by* K. Ishihara. Tokyo. 14-16 November 1995. A.A. Balkema, Vol.2, pp. 675-680.

Enomoto, T., Tatsuoka, F., Shishime, M., Kawabe, S., and Di Benedetto, H. 2006. Viscous property of granular material in drained triaxial compression. *In* Soil Stress-Strain Behavior: Measurement, Modeling and Analysis. Geotechnical Symposium held to celebrate the 60th Birthday of Fumio Tatsuko. *Edited by* H.I. Ling, L. Callisto, D. Leshchinsky, and J. Koseki. Rome, ITALY. Mar 16-17. Springer, pp. 383-397.

Erten, D., and Maher, M.H. 1995. Cyclic undrained behavior of silty sand. Soil Dynamics and Earthquake Engineering, **14**(2): 115-123.

Finge, Z., Doanh, T., and Dubujet, P. 2006. Undrained anisotropy of Hostun RIF loose sand: new experimental investigations. Canadian Geotechnical Journal, **43**(11): 1195-1212.

Finn, W.D.L., Pickering, D.J., and Bransby, P.L. 1971. Sand liquefaction in triaxial and simple shear tests. Journal of the soil mechanics and foundations division, **97**(4): 20.

François, B. 2008. Thermo-plasticity of fine-grained soils at various saturation states: Application to nuclear waste disposal, EPFL, Lausanne, PhD thesis.

Fredlund, D.G., and Xing, A.Q. 1994. Equations for the Soil-Water Characteristic Curve (Vol 31, Pg 521, 1994). Canadian Geotechnical Journal, **31**(6): 1026-1026.

Gajo, A. 1995. Influence of Viscous Coupling in Propagation of Elastic Waves in Saturated Soil. Journal of Geotechnical Engineering, **121**(9): 636-644.

Gajo, A. 1996. The effects of inertial coupling in the interpretation of dynamic soil tests. Geotechnique, **46**(2): 245-257.

Gallage, P.C.K., Towhata, I., and Nishimura, S. 2005. Laboratory investigation on rate-dependent properties of sand undergoing low confining effective stress. Soils and Foundations, **45**(4): 43-60.

Georgiannou, V.N., and Tsomokos, A. 2008. Comparison of two fine sands under torsional loading. Canadian Geotechnical Journal, **45**(12): 1659-1672.

Georgiannou, V.N., Tsomokos, A., and Stavrou, K. 2008. Monotonic and cyclic behaviour of sand under torsional loading. Geotechnique, **58**(2): 113-124.

Gerolymos, N., and Gazetas, G. 2005. Constitutive model for 1-D cyclic soil behaviour applied to seismic analysis of layered deposits. Soils and Foundations, **45**(3): 147-159.

Ghionna, V.N., and Porcino, D. 2006. Liquefaction resistance of undisturbed and reconstituted samples of a natural coarse sand from undrained cyclic triaxial tests. Journal of Geotechnical and Geoenvironmental Engineering, **132**(2): 194-202.

Ghosh, B., and Madabhushi, S.P.G. 2003. A numerical investigation into effects of single and multiple frequency earthquake motions. Soil Dynamics and Earthquake Engineering, **23**(8): 691-704.

Giardini, D., Wiemer, S., Fah, D., and Deichmann, N. 2004. Seismic hazard assessment of Switzerland,

Swiss Seismological Service, Zurich.

Govindaraju, L., and Sitharam, T.G. 2007. Effect of loading frequency on cyclic behaviour of soils. *In* 4th International Conference on Earthquake Geotechnical Engineering. *Edited by* K. Pitilakis. Thessaloniki, Greece, p. p. 13.

Habib, P., and Luong, M.P. 1985. Comportement du milieu pulvérulent. *In* Génie Parasismique. Presses de l'Ecole Nationale des Ponts et Chausées, Paris. pp. 303-311.

Hardin, B.O., and Drnevich, V.P. 1972a. Shear modulus and damping in soils: measurement and parameters effects. Journal of the soil mechanics and foundations division, **98**(SM 6): 603-624.

Hardin, B.O., and Drnevich, V.P. 1972b. Shear modulus and damping in soils: design equations and curves. Journal of the soil mechanics and foundations division, **98**(SM 7): 667-692.

Hardin, B.O., and Kalinski, M.E. 2005. Estimating the shear modulus of gravelly soils. Journal of Geotechnical and Geoenvironmental Engineering, **131**(7): 867-875.

Hartzell, S., Bonilla, L.F., and Williams, R.A. 2004. Prediction of Nonlinear Soil Effects. Bulletin of the Seismological Society of America, **94**(5): 1609-1629.

Hatzor, Y.H., Gvirtzman, H., Wainshtein, I., and Orian, I. 2009. Induced liquefaction experiment in relatively dense, clay-rich sand deposits. Journal of Geophysical Research-Solid Earth, **114**: 22.

Head, K.H. 1984. Manual of soil laboratory testing. Volume 3: effective stress tests. Pentech Press, London.

Hecht, E. 1998. Physique. De Boek.

Hoque, E., and Tatsuoka, F. 2004. Triaxial testing system for measuring loading-rate effects during cyclic tests of sand. Geotechnical Testing Journal, **27**(5): 483-495.

Houlsby, G.T. 1998. Advanced interpretation of field tests. *In* 1st International Conference on Site Characterization (ISC 98). *Edited by* P.K. Robertson and P.W. Mayne. Atlanta, Ga. Apr 19-22. A.A. Balkema, pp. 99-112.

Hujeux, J.-C. 1985. Une loi de comportement pour le chargement cyclique des sols. *In* Génie Parasismique, Paris. pp. 287-302.

Huot, F. 1999. Caractéristiques élastiques des sols - Du comportement pseudo-statique à la propagation des ultrasons, Université de Lausanne, Lausanne, PhD thesis.

Huot, F., and Vulliet, L. 1998. Small strain elastic moduli of a saturated sand. *In* Biot Conference on Poromechanics. Louvain-La-Neuve, pp. 93-97.

Hyde, A.F.L., Higuchi, T., and Yasuhara, K. 2006. Liquefaction, cyclic mobility, and failure of silt. Journal of Geotechnical and Geoenvironmental Engineering, **132**(6): 716-735.

Hyodo, M., Hyde, A.F.L., and Aramaki, N. 1998. Liquefaction of crushable soils. Geotechnique, **48**(4): 527-543.

Hyodo, M., Hyde, A.F.L., Aramaki, N., and Nakata, Y. 2002. Undrained monotonic and cyclic shear behaviour of sand under low and high confining stresses. Soils and Foundations, **42**(3): 63-76.

Iai, S., and Tobita, T. 2006. Soil non-linearity and effects on seismic site response. *In* 3rd International Symposium on the effects of Surface Geology on Seismic Motion. *Edited by* P.-Y. Bard, E. Chaljub, C. Cornou, F. Cotton, and P. Gueguen. Grenoble. LCPC, Vol.1, pp. p 21-46.

Ibraim, E., Di Benedetto, H., and Doanh, T. 2009. Time-Dependent Behaviour and Static Liquefaction Phenomenon of Sand. Geotechnical and Geological Engineering, **27**(1): 181-191.

Ibsen, L.B. 1994. The Stable State in Cyclic Triaxial Testing on Sand. Soil Dynamics and Earthquake Engineering, **13**(1): 63-72.

Idriss, I.M., and Sun, J.I. 1992. User's manual for SHAKE91: a computer program for conducting equivalent linear seismic response analyses of horizontally layered soil deposits, Department of Civil & Environmental Engineering, University of California, Davis, California.

Idriss, I.M., and Boulanger, R.W. 2007. SPT- and CPT-based relationships for the residual shear strength of liquefied soils. *In* 4th International Conference on Earthquake Geotechnical Engineering. *Edited by* K.D. Pitilakis. Thessaloniki, GREECE. Jun, pp. 1-22.

Ishihara, K. 1996. Soil behaviour in earthquake geotechnics. Oxford University Press Inc., New York.

Ishihara, K., and Yasuda, N. 1972. Sand Liquefaction Due to Irregular Excitation. Soils and foundations, **12**(4): 65.

Ishihara, K., and Yasuda, S. 1975. Sand liquefaction in hollow cylinder torsion under irregular excitation. Soils and Foundations, **15**(1): 45-59.

Ishihara, K., and Yamazaki, F. 1980. Cyclic Simple Shear Tests on Saturated Sand in Multi-directional Loading. Soils and Foundations, **20**(1): 45-59.

Ishihara, K., and Nagase, H. 1988. Multi-directional irregular loading tests on sand. Soil Dynamics and Earthquakes Engineering, **7**(4): 201-212.

Ishihara, K., Tatsuoka, F., and Yasuda, S. 1975. Undrained deformation and liquefaction of sand under cyclic stresses. Soils and Foundations, **15**(1): 29-44.

Iverson, R.M., and LaHusen, R.G. 1989. Dynamic Pore-Pressure Fluctuations in Rapidly Shearing Granular Materials. Science, **246**(4931): 796-799.

Jaeger, H.M., and Nagel, S.R. 1992. Physics of the Granular State. Science, **255**(5051): 1523-1531.

Jahangir, E. 2008. Caractérisation du sable de Fonderie sous chargement sismique. EPFL, LMS. Master thesis.

Jeremic, B., Cheng, Z., Taiebat, M., and Dafalias, Y. 2008. Numerical simulation of fully saturated porous materials. International Journal for Numerical and Analytical Methods in Geomechanics, **32**(13): 1635-1660.

Ju, S.-H., and Ni, S.-H. 2007. Determining Rayleigh damping parameters of soils for finite element analysis, pp. 1239-1255.

Kalkan, E., and Gulkan, P. 2004. Site-Dependent Spectra Derived from Ground Motion Records in Turkey. Earthquake Spectra, **20**(4): 1111-1138.

Kammerer, A.M., Pestana, J.M., and Seed, R.B. 2003. Behavior of Monterey 0/30 sand under Multidirectional Loading Conditions. *In* Geomechanics: Testing, Modeling, and Simulation (GSP 143). *Edited by* J.K.-E. Jerry A. Yamamuro. Boston. 2005. ASCE, Vol.143, pp. 154-173.

Kammerer, A.M., Seed, R.B., Wu, J., Riemer, M.F., and Pestana, J.M. 2004. Pore Pressure Development in Liquefiable Soils Under Bi-Directional Loading Conditions. Report.

Karg, C., and Haegeman, W. 2009. Elasto-plastic long-term behavior of granular soils: Experimental

investigation. Soil Dynamics and Earthquake Engineering, **29**(1): 155-172.

Khalili, N., Habte, M.A., and Valliappan, S. 2005. A bounding surface plasticity model for cyclic loading of granular soils. International Journal for Numerical Methods in engineering, **63**: 1939-1960.

Khan, Z.H., Cascante, G., El Naggar, M.H., and Lai, C.G. 2008. Measurement of frequency-dependent dynamic properties of soils using the resonant-column device. Journal of Geotechnical and Geoenvironmental Engineering, **134**(9): 1319-1326.

Kim, S.I., Park, K.B., Park, S.Y., Hwang, S.J., Lee, J.H., and Choi, J.S. 2005. Effects of irregular dynamic loads on soil liquefaction. *In* 16th International Conference on Soil Mechanics and Geotechnical Engineering. Osaka, JAPAN. 2005. Millpress Science Publishers, pp. 2673-2676.

Kokusho, T. 1980. Cyclic triaxial test of dynamic soil properties for wide strain range. Soils and Foundations, **20**(2): 45-60.

Kokusho, T., Hara, T., and Hiraoka, R. 2004. Undrained shear strength of granular soils with different particle gradations. Journal of Geotechnical and Geoenvironmental Engineering, **130**(6): 621-629.

Koliji, A. 2008. Mechanical behaviour of unsaturated aggregated soils, EPFL, Lausanne, PhD thesis.

Kramer, S.L. 1996. Geotechnical Earthquake Engineering, Upper Saddle River, New Jersey.

Kuwano, R., and Jardine, R.J. 2002. On measuring creep behaviour in granular materials through triaxial testing. Canadian Geotechnical Journal, **39**(5): 1061-1074.

Lacave, C., Bard, P.Y., Kham, M., and Koller, M.G. 2008. 2D equivalent linear site effect simulation: example applications to two deep valleys. Bulletin of Earthquake Engineering, **6**(2): 197-211.

Laloui, L. 1992. Modélisation du comportement thermo-hydro-mécanique des milieux poreux anélastiques, Ecole Centrale Paris, Chatenay Malabry, PhD thesis.

Leroueil, S., and Marques, M.S. 1996. Importance of strain rate and temperature effects in geotechnical engineering. *In* Measuring and modelling time dependent soil behavior. *Edited by* T.C.S.a.V.N. Kaliakin. Washington, D.C. November, 10-14 1996 ASCE, pp. 1-60.

Li, X.S. 1990. Free field soil response under multidirectional earthquake loading, Univerity of California, Davis. PhD thesis.

Li, X.S. 1997. Rotational shear effects on ground earthquake response. Soil Dynamics and Earthquakes Engineering, **16**(1): 9-19.

Li, X.S., and Yang, W.L. 1998. Effects of vibration history on modulus and damping of dry sand. Journal of Geotechnical and Geoenvironmental Engineering, **124**(11): 1071-1081.

Li, X.S., Shen, C.K., and Wang, Z.L. 1998. Fully coupled inelastic site response analysis for 1986 Lotung earthquake. Journal of Geotechnical and Geoenvironmental Engineering, **124**(7): 560-573.

Li, X.S., Dafalias, Y., and Wang, Z.L. 1999. State-dependant dilatancy in critical-state constitutive modelling of sand. Canadian Geotechnical Journal, **36**(4): 599-611.

Lin, M.L., Huang, T.H., and You, J.C. 1996. The effects of frequency on damping properties of sand. Soil Dynamics and Earthquake Engineering, **15**(4): 269-278.

Lin, M.L., Wang, K.L., and Chen, T.C. 2009. Tsaoling landslide in Taiwan during the 1999 Chi-Chi earthquake. *In* Earthquake Geotechnical Case Histories for Performance-Based Design. Taylor & Francis Group - Balkema, London. pp. 273-287.

Ling, H.I., and Liu, H.B. 2003. Pressure-level dependency and densification behavior of sand through generalized plasticity model. Journal of Engineering Mechanics-ASCE, **129**(8): 851-860.

LMSSMAT, Ecole Centrale Paris. 2007. LAWYER: Logiciel de simulation d'essais homogènes de comportement des sols.

Lopez-Caballero, F. 2003. Influence du comportement non linéaire du sol sur les mouvements sismiques induits dans des géo-structures, Ecole Centrale Paris, Chatenay Malabry, PhD thesis.

Lopez-Querol, S., and Blazquez, R. 2006. Liquefaction and cyclic mobility model for saturated granular media. International Journal for Numerical and analytical methods in geomechanics, **30**: 413-439.

Lopez-Querol, S., and Blazquez, R. 2007. Validation of a new endochronic liquefaction model for granular soil by using centrifuge test data. Soil Dynamics and Earthquake Engineering, **27**(10): 920-937.

Lunne, T., Robertson, P.K., and Powell, J.J. 1997. Cone Penetration Testing in Geotechnical Practice. Blackie Academic & Professional, an imprint of Chapman & Hall, London.

Luong, M.P. 1980. Phénomènes cycliques dans les sols pulvérulents. Revue française de Géotechnique, **10**(1): 39-53.

Madabhushi, S.P.G. 2004. Modelling of earthquake damage using geotechnical centrifuges. Current Science, **87**(10): 1405-1416.

Matesic, L., and Vucetic, M. 2003. Strain-rate effect on soil secant shear modulus at small cyclic strains. Journal of Geotechnical and Geoenvironmental Engineering, **129**(6): 536-549.

Matsushita, M., Tatsuoka, F., Koseki, J., Cazacliu, B., Di Benedetto, H., and Yasin, S.J.M. 1999. Time effect on the pre-peak deformation properties of sands. *In* Second International Conférence on Pre-Failure Deformation Characteristics of Geomaterials. *Edited by* J.e. al. Torino. Balkema, Vol.1, pp. 681-689.

Mayoraz, F. 2002. Comportement mécanique des milieux granulaires sous sollicitations cycliques: Application aux fondations de chaussées, EPFL, Lausanne, PhD thesis.

Mellal, A. 1997. Analyse des effets du comportement non linéaire des sols sur le mouvement sismique, Ecole Centrale Paris, Châtenay Malabry, PhD thesis.

Meng, J. 2007. Earthquake ground motion simulation with frequency-dependent soil properties. Soil Dynamics and Earthquake Engineering, **27**(3): 234-241.

Messerklinger, S., and Springman, S.M. 2007. Local radial displacement measurements of soil specimens in a triaxial test apparatus using laser transducers. Geotechnical Testing Journal, **30**(6): 454-465.

Michalski, E., and Rahma, A. 1989. Modélisation du comportement des sols en élastoplasticité: définition des paramètres des modèles Hujeux-Cyclade et recherche des valeurs des paramètres pour différents sols, BRGM - Service géologique national.

Micro-Epsilon Instruction Manual optoNCDT1700, Ortenburg.

Mohajeri, M., and Towhata, I. 2003. Shake table tests on residual deformation of sandy slopes due to cyclic loading. Soils and Foundations, **43**(6): 91-106.

Mohkam, M. 1983. Contribution à l'étude expérimentale et théorique du comportement des sables sous chargements cycliques, Université Scientifique et médicale et Institut National Polytechnique de Grenoble, Grenoble, PhD thesis.

Mroz, Z., Norris, V.A., and Zienkiewicz, O.C. 1981. An Anisotropic, Critical State Model for Soils Subject to Cyclic Loading. Geotechnique, **31**(4): 451-469.

Muir Wood, D. 1990. Soil Behaviour and Critical State Soil Mechanics. Cambridge University Press

Muir Wood, D. 1998. Deformation properties of soils for dynamic analyses. *In* 6th SECED Conference on Seismic Design Practice into the Next Century. *Edited by* E. Booth. Oxford, England. Mar 26-27, pp. 15-24.

Muir Wood, D. 2001. Some observations of volumetric instabilities in soils. *In* Symposium on Material Instabilities and the Effect of Microstructure. Austin, Texas. May 07-11. Pergamon-Elsevier Science Ltd, pp. 3429-3449.

Muir Wood, D. 2004. Geotechnical Modelling. Spon Press, London.

Muir Wood, D. 2007. The magic of sands - The 20th Bjerrum Lecture presented in Oslo, 25 November 2005. Canadian Geotechnical Journal, **44**(11): 1329-1350.

Muir Wood, D., Sadek, T., Dihoru, L., and Lings, M. 2006. Deviatoric stress response envelopes from multiaxial tests on sand. *In* Soil Stress-Strain Behavior: Measurement, modeling and Analysis. Geotechnical Symposium held to celebrate the 60th Birthday of Fumio Tatsuko. *Edited by* H.I. Ling, C. L., L. D., and K. J. Rome, ITALY. Mar 16-17. Springer, pp. 253-262.

Muravskii, G.B. 2001. Application of experimental results on cyclic deforming of soils to seismic response analysis. Soil Dynamics and Earthquake Engineering, **21**(8): 661-669.

Nagase, H., and Ishihara, K. 1987. Effects of load irregularity on the cyclic behaviour of sand. Soil Dynamics and Earthquake Engineering, **6**(4): 239-249.

Nagase, H., and Ishihara, K. 1988. Liquefaction-induced compaction and settlement of sand during earthquakes. Soils and Foundations, **28**(1): 65-76.

Nawir, H., Tatsuoka, F., and Kuwano, R. 2003. Experimental evaluation of the viscous properties of sand in shear. Soils and Foundations, **43**(6): 13-31.

Nowacki, W.K. 1978. Stress waves in non-elastic solids, Oxford.

Nuth, M. 2009. Constitutive modelling of unsaturated soils with hydro-geomechanical couplings, EPFL, Lausanne, PhD thesis.

O'Reilly, M.P., and Brown, S.F. 1991. Cyclic Loading of Soils: from theory to design. Blackie and Son Ltd, Glasgow.

Obrzud, R.F. 2009. Numerical modeling and neural networks to identify constitutive parameters from in situ tests, EPFL, Lausanne, PhD thesis.

Okamoto, S. 1973. Introduction to earthquake engineering. University of Tokyo Press.

Okur, D.V., and Ansal, A. 2007. Stiffness degradation of natural fine grained soils during cyclic loading. Soil Dynamics and Earthquake Engineering, **27**(9): 843-854.

Osinov, V.A. 2003. Cyclic shearing and liquefaction of soil under irregular loading: an incremental model for the dynamic earthquake-induced deformation. Soil Dynamics and Earthquake Engineering, **23**(7): 535-548.

Pastor, M., Zienkiewicz, O.C., and Chan, A.H.C. 1990. Generalized Plasticity and the Modeling of Soil Behavior. International Journal for Numerical and Analytical Methods in Geomechanics, **14**(3): 151-190.

Pecker, A. 1984. Dynamique des sols. Presses de l'école nationale des ponts et chaussées, Paris.

Péron, H. 2008. Desiccation cracking of soils, EPFL, Lausanne, PhD thesis.

Pham Van Bang, D., Di Benedetto, H., Duttine, A., and Ezaoui, A. 2007. Viscous behaviour of dry sand. International Journal for Numerical and Analytical Methods in Geomechanics, **31**(15): 1631-1658.

Popescu, R., Prevost, J.H., Deodatis, G., and Chakrabortty, P. 2006. Dynamics of nonlinear porous media with applications to soil liquefaction. Soil Dynamics and Earthquake Engineering, **26**(6-7): 648-665.

Porcino, D., Caridi, G., and Ghionna, V.N. 2008. Undrained monotonic and cyclic simple shear behaviour of carbonate sand. Geotechnique, **58**(8): 635-644.

Poulos, S.J. 1981. The Steady-State of Deformation. Journal of the Geotechnical Engineering Division-ASCE, **107**(5): 553-562.

Puzrin, A.M., and Shiran, A. 2000. Effects of the constitutive relationship on seismic response of soils. Part I. Constitutive modeling of cyclic behavior of soils. Soil Dynamics and Earthquake Engineering, **19**(5): 305-318.

Pyke 1973. Settlement and Liquefaction of Sands Under Multidirectional Loading, University of California, Berkeley, PhD thesis.

Ray, R.P., and Woods, R.D. 1988. Modulus and Damping Due to Uniform and Variable Cyclic Loading. Journal of Geotechnical Engineering-ASCE, **114**(8): 861-876.

Richardson, A.M., and Whitman, R.V. 1963. Effect of strain-rate upon undrained shear resistance of a saturated remoulded fat clay. Geotechnique, **13**(4): 310-324.

Riemer, M.F., and Seed, R.B. 1997. Factors affecting apparent position of steady-state line. Journal of Geotechnical and Geoenvironmental Engineering, **123**(3): 281-288.

Robertson, P.K. 1994. Suggested terminology for liquefaction. *In* 47th Canadian Geotechnical Conference. Halifax, N.S., pp. 277-286.

Romero, E. 1999. Characterisation and thermo-mechanical behaviour of unsaturated Boon clay: An experimental study, UPC, Barcelona, PhD thesis.

Sadek, T., Lings, M., Dihoru, L., and Muir Wood, D. 2007. Wave transmission in Hostun sand: multiaxial experiments. Italian Geotechnical Journal, **41**(2): 69-84.

Salvati, L.A., and Anhdan, L.Q. 2008. Rate-dependent response of dense sand in cyclic triaxial tests. Soils and Foundations, **48**(3): 447-451.

Sanin, M.V., and Wijewickreme, D. 2006. Cyclic shear response of channel-fill Fraser River Delta silt. Soil Dynamics and Earthquake Engineering, **26**(9): 854-869.

Sassa, K., Wang, G.H., Fukuoka, H., and Vankov, D.A. 2005. Shear-displacement-amplitude dependent pore-pressure generation in undrained cyclic loading ring shear tests: An energy approach. Journal of Geotechnical and Geoenvironmental Engineering, **131**(6): 750-761.

Sawada, S., Tsukamoto, Y., and Ishihara, K. 2004. Residual deformation characteristics of partially saturated sandy soils subjected to seismic excitation. *In* 11th International Conference on Soil Dynamics and Earthquake Engineering/3rd International Conference on Earthquake Geotechnical Engineering. Berkeley, CA. Jan 07-09, pp. 175-182.

Schofield, A., and Wroth, P. 1968. Critical State Soil Mechanics. McGraw-Hill, London.

Schrott, L., and Sass, O. 2008. Application of field geophysics in geomorphology: Advances and limitations exemplified by case studies. Geomorphology, **93**(1-2): 55-73.

Seed, H.B. 1979. Soil liquefaction and cyclic mobility evaluation for level ground during earthquakes. Journal of the Geotechnical Engineering Division, **105**(2): 201-255.

Seed, H.B., and Idriss, I.M. 1971. Simplified Procedure for Evaluating Soil Liquefaction Potential. Journal of the Soil Mechanics and Foundations Division **97**(9): 1249-1273.

Seed, H.B., Tokimatsu, K., Harder, L.F., and Chung, R.M. 1985. Influence of SPT procedures in soil liquefaction resistance evaluations. Journal of Geotechnical Engineering, **111**(12): 1425-1445.

Seed, H.B., Wong, R.T., Idriss, I.M., and Tokimatsu, K. 1986. Moduli and damping factors for dynamic analyses of cohesionless soils. Journal of Geotechnical Engineering, **112**(7): 1016-1032.

Seed, R.B., Cetin, K.O., Moss, R.E.S., Kammerer, A., Wu, J., Pestana, J., and Riemer, M. 2001. Recent advances in soil liquefaction engineering and seismic site response evaluation. *In* 4th International Conference and Symposium on Recent Advances in Geotechnical Earthquake Engineering and Soil Dynamics. University of Missouri, Rolla.

Semblat, J.F. 1994. Sols sous sollicitations dynamiques et transitoire: Réponse dynamique aux barres de Hopkinson, propagation d'ondes en milieu centrifugé, Ecole Polytechnique, Palaiseau, PhD thesis.

Semblat, J.F. 1997. Rheological interpretation of Rayleigh damping. Journal of Sound and Vibration, **206**(5): 741-744.

Semblat, J.F., and Luong, M.P. 1998. Wave propagation through soils in centrifuge testing. Journal of Earthquake Engineering, **2**(1): 147-171.

Semblat, J.-F., Luong, M.P., and Gary, G. 1999. 3D-Hopkinson bar: new experiments for dynamic testing on soils. Soils and Foundations, **39**(1): 1-10.

Semblat, J.F., Kham, M., Bard, P.Y., Pitilakis, K., Makra, K., and Raptakis, D. 2005. Seismic wave amplification: Basin geometry vs soil layering. Soil Dynamics and Earthquake Engineering, **25**(7-10): 529-538.

Shahnazari, H., and Towhata, I. 2002. Torsion shear tests on cyclic stress-dilatancy relationship of sand. The Japanese Geotechnical Society, pp. 105-119.

Shibuya, S., Hight, D.W., and Jardine, R.J. 2003. Four-dimensional local boundary surfaces of an isotropically consolidated loose sand. Soils and Foundations, **43**(2): 89-103.

Sitharam, T.G., GovindaRaju, L., and Murthy, B.R.S. 2004. Evaluation of liquefaction potential and dynamic properties of silty sand using cyclic triaxial testing. Geotechnical Testing Journal, **27**(5): 423-429.

Sivathayalan, S., and Vaid, Y.P. 2002. Influence of generalized initial state and principal stress rotation on the undrained response of sands. Canadian Geotechnical Journal, **39**(1): 63-76.

Studer, J.A., Koller, M.G., Loew, S., and Lateltin, O. 2004. Classification of soil profiles with corresponding earthquake design spectra for specific conditions in switzerland. *In* 13th World Conference on Earthquake Engineering. Vancouver, B.C., Canada.

Swiss standard SNV 670 008a. 1997. VSS.

Tatsuoka, F. 2006. Inelastic deformation characteristics of geomaterial. *In* Soil Stress-Stain Behavior: Measurement, Modeling and Analysis. Geotechnical Symposium held to celebrate the 60th Birthday of Fumio Tatsuko. Ling, HI; Callisto, L; Leshchinsky, D; Koseki, J, Rome, ITALY, pp. 1-108.

Tatsuoka, F., Yasuda, S., Iwasaki, T., and Tokida, K. 1980. Normalized dynamic undrained strength of sands subjected to cyclic and random loading. Soils and Foundations, **20**(3): 1-16.

Tatsuoka, F., Ishihara, M., Di Benedetto, H., and Kuwano, R. 2002. Time-dependent shear deformation characteristics of geomaterials and their simulation. Soils and Foundations, **42**(2): 103-129.

Terzaghi, K. 1943. Theoretical Soil Mechanics. Chapman and Hall, London.

The MathWorks, I. 2009. Matlab Support http://www.mathworks.com/index.html?ref=logo&s_cid=docframe_homepage.

Towhata, I., and Ishihara, K. 1985. Undrained strength of sand undergoing cyclic rotation of principal stress axes. The Japanese Geotechnical Society, pp. 135-147.

Toyota, H., Nakamura, K., and Kazama, M. 2004. Shear and liquefaction characteristics of sandy soils in triaxial tests. Soils and Foundations, **44**(2): 117-126.

Tsukamoto, Y., Ishihara, K., and Sawada, S. 2004. Settlement of silty sand deposits following liquefaction during earthquakes. Soils and Foundations, **44**(5): 135-148.

Ueng, T.S., Wang, M.H., Chen, M.H., Chen, C.H., and Peng, L.H. 2006. A large biaxial shear box for shaking table test on saturated sand. Geotechnical Testing Journal, **29**(1): 1-8.

Uthayakumar, M., and Vaid, Y.P. 1998. Static liquefaction of sands under multiaxial loading. Canadian Geotechnical Journal, **35**(2): 273-283.

Vaid, Y.P., and Sivathayalan, S. 1996. Static and cyclic liquefaction potential of Fraser Delta sand in simple shear and triaxial tests. Canadian Geotechnical Journal, **33**(2): 281-289.

Vaid, Y.P., Chung, E.K.F., and Kuerbis, R.H. 1989. Preshearing and undrained response of sand. Soils and Foundations, **29**(4): 49-61.

Vaid, Y.P., Chung, E.K.F., and Kuerbis, R.H. 1990. Stress Path and Steady-State. Canadian Geotechnical Journal, **27**(1): 1-7.

Verdugo, R., and Ishihara, K. 1996. The steady state of sandy soils. Soils and Foundations, **36**(2): 81-91.

Verruijt, A., and Cordova, C.C. 2001. Moving loads on an elastic half-plane with hysteretic damping. Journal of Applied Mechanics-Transactions of the Asme, **68**(6): 915-922.

Vucetic, M. 1994. Cyclic threshold shear strains in soils. Journal of Geotechnical Engineering, **120**(12): 2208-2228.

Vucetic, M. 2004. Emerging Trends in Dynamic Simple Shear Testing. *In* International workshop on Uncertainties in Nonlinear Soil Properties and their Impact on Modeling Dynamic Soil Reponse. Peer Headquarters, UC Berkeley. March 18-19 2004, p. 15.

Vucetic, M., and Dobry, R. 1991. Effect of soil plasticity on cyclic response. Journal of Geotechnical Engineering, **117**(1): 89-107.

Vucetic, M., and Tabata, K. 2003. Influence of soil type on the effect of strain rate on small-strain cyclic shear modulus. Soils and Foundations, **43**(5): 161-173.

Vulliet, L., and Hutter, K. 1988. Viscous type sliding laws for landslides. Canadian Geotechnical Journal, **25**(3): 467-477.

Wang, G.X., and Kuwano, J. 1999. Modeling of strain dependency of shear modulus and damping of clayey sand. Soil Dynamics and Earthquake Engineering, **18**(6): 463-471.

Wang, Y.H., and Santamarina, J.C. 2007. Attenuation in sand: an exploratory study on the small-strain behavior and the influence of moisture condensation. Granular Matter, **9**(6): 365-376.

Wichtmann, T., and Triantafyllidis, T. 2004. Influence of a cyclic and dynamic loading history on dynamic properties of dry sand, part I: cyclic and dynamic torsional prestraining. Soil Dynamics and Earthquake Engineering, **24**(2): 127-147.

Wichtmann, T., Niemunis, A., and Triantafyllidis, T. 2005. Strain accumulation in sand due to cyclic loading: drained triaxial tests. Soil Dynamics and Earthquake Engineering, **25**: 967-979.

Wichtmann, T., Niemunis, A., and Triantafyllidis, T. 2007a. Strain accumulation in sand due to cyclic loading: Drained cyclic tests with triaxial extension. Soil Dynamics and Earthquake Engineering, **27**(1): 42-48.

Wichtmann, T., Niemunis, A., and Triantafyllidis, T. 2007b. On the influence of the polarization and the shape of the strain loop on strain accumulation in sand under high-cyclic loading. Soil Dynamics and Earthquake Engineering, **27**(1): 14-28.

Wolf, J.P. 1994. Foundation Viration Analysis Using Simple Physical Models. Prentice-Hall, Englewood Cliffs.

Yamada, S., Hyodo, M., Orense, R.P., Dinesh, S.V., and Hyodo, T. 2008. Strain-dependent dynamic properties of remolded sand-clay mixtures. Journal of Geotechnical and Geoenvironmental Engineering, **134**(7): 972-981.

Yamamuro, J.A., and Lade, P.V. 1993. Effects of strain rate on instability of granular soils. Geotechnical Testing Journal, **16**(3): 304-313.

Yasuda, N., Matsumoto, N., Yoshioka, R., and Takahashi, M. 1997. Undrained monotonic and cyclic strength of compacted rockfill material from triaxial and torsional simple shear tests. Canadian Geotechnical Journal, **34**(3): 357-367.

Yoshida, N., Kobayashi, S., Suetomi, I., and Miura, K. 2002. Equivalent linear method considering frequency dependent characteristics of stiffness and damping. Soil Dynamics and Earthquake Engineering, **22**(3): 205-222.

Zambelli, C., di Prisco, C., d'Onofrio, A., Visone, C., and de Magistris, F.S. 2006. Dependency of the mechanical behaviour of granular soils on loading frequency: Experimental results and constitutive modelling. *In* Soil Stress-Strain Behavior: Measurement, Modeling and Analysis. Geotechnical Symposium held to celebrate the 60th Birthday of Fumio Tatsuko. *Edited by* H.I.

Ling, C. L., L. D., and K. J. Rome, ITALY. Mar 16-17. Springer, pp. 567-582.

Zhang, H.M., and Garga, V.K. 1997. Quasi-steady state: a real behaviour? Canadian Geotechnical Journal, **34**(5): 749-761.

Zhang, J.M., Shamoto, Y., and Tokimatsu, K. 1997. Moving critical and phase-transformation stress state lines of saturated sand during undrained cyclic shear. Soils and Foundations, **37**(2): 51-59.

APPENDIX 1

IN SITU TESTING FOR THE EVALUATION OF DYNAMIC SOIL BEHAVIOUR

A1.1 Geophysical methods

Introduction

In situ investigations of the subsoil is a good method to obtain soil characteristics of a given site. Among common geophysical methods, the ones using seismic wave propagation are summarized here. These techniques use elastic wave propagation models. They aim at determining layering, elastic properties and inclusions. They are divided here between non-invasive and borehole methods.

Free surface measurement

Seismic waves are generated by a sledge hammer hitting a metal plate placed on the ground. The elastic wave signal is received by geophones strategically placed at known distance of the emission. The time delay between emission and reception of the elastic waves is precisely measured. These methods can provide celerity of the seismic waves, as well as the thickness of the soil layers and bedrock. It can also indicate water table depth. Small strain elastic moduli can be calculated.

Seismic refraction is the most popular seismic free surface measurement technique among geophysicists (Schrott & Sass 2008). It relies on the fact that soil layers become denser and wave velocities increase with depth. When the emitted wave hits a surface discontinuity at the critical refraction angle, the refracted wave follows the boundary (Fig. A1-1). Along its journey, the refracted wave emits head waves which travel back to the soil surface and are recorded by receivers. The P waves travel faster in deeper soil deposit, also the head waves are the first waves recorded by geophones.

To illustrate the results obtained by seismic refraction, a seismogram (Fig. A1-2) shows the sounding of a talus cone (Schrott & Sass 2008), with the distance between the source and geophones in abscissa. Each vertical signal is an average of several shots recorded on the geophones. There are three lines joining the first arrival of refracted waves. The slope of these lines is proportional to the velocity of the P wave in each soil layer, which is written on the figure.

Typical investigated profile have a depth of 10 to 30 m. Deeper soil profiles can be obtained with explosions, instead of sledge hammer. Problems related to seismic refraction are mainly (i) noise from human activities or natural sources, such as strong wind, rainfall, close torrents (ii) inaccurate detection of seismic wave onset (iii) hidden loose layers. Moreover P wave velocities are not uniquely related to one soil or rock type, also complementary drillings are necessary for a precise identification. The great advantage of seismic refraction is that it gives a continuous profile along the investigated zone, including the inclination of boundaries thanks to back analyses. Seismic refraction is best adapted to preliminary on site surveys. This method, as well as other geophysical methods, is a reliable source of

information as long as its conclusions are compared and confirmed by a complementary investigation method.

Two other seismic methods are seismic reflection and spectral analysis of surface waves (SASW). Both are suitable in different situations, when seismic refraction is not applicable. Seismic reflection method has higher costs, but it can be used even in case of velocity inversion (i.e. softer layer below harder layer). In SASW, Rayleigh waves are emitted instead of body waves.

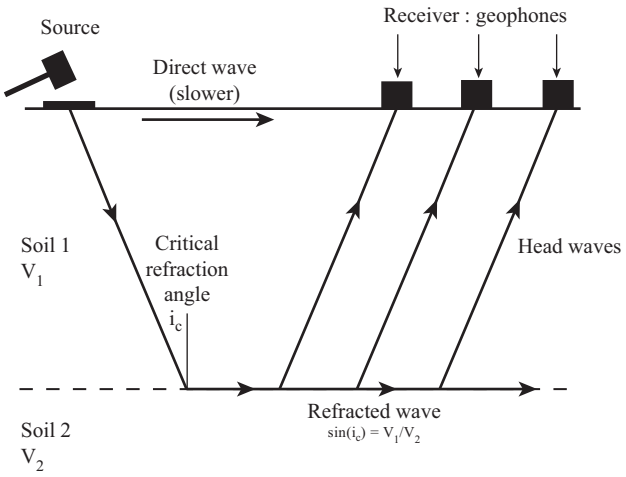

Fig. A1-1. Seismic refraction principle.

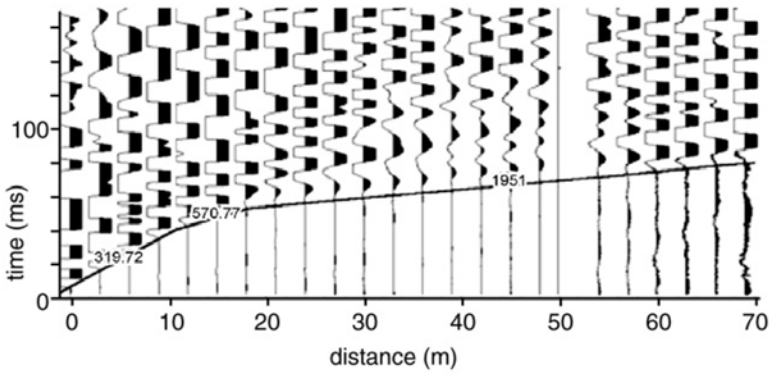

Fig. A1-2. Typical seismogram of seismic refraction (Schrott & Sass 2008).

Geophysical methods with drillings

Up-hole, down-hole, cross-hole tests and suspension method rely on the accurate measurement of the time length between the emission and the reception of seismic waves (Fig. A1-3). For up-hole techniques, the source is placed along the boundaries of the hole and the receiver records P waves and S waves. Down-hole techniques measure SH waves, and cross-hole technique SV waves. For cross-hole testing, slope inclinometers are placed inside the drilling for correcting the distance between the emitter and the receiver. The suspension sonde is a slightly more complicated method, described in details by

Ishihara (1996). The single drilling is filled with water, in which the sonde is immersed. A compression wave is emitted at the bottom, and induce, among others, a horizontally polarized shear wave travelling vertically in the soil deposit. The arrival time of this shear wave is recorded to calculate the velocity of wave propagation.

With these testing methods, the shear wave velocity can be measured also the maximum shear modulus G_{max} of soil layers is estimated.

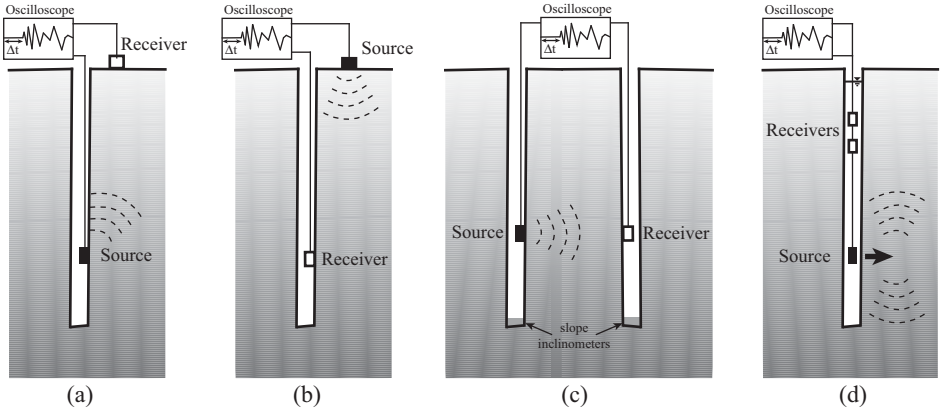

Fig. A1-3. (a) up-hole, (b) down-hole (c) cross-hole tests and (d) suspension sonde.

A1.2 Geotechnical in situ testing

Introduction

There are other possibilities for determining soil parameters in situ. Because so many techniques have been developed in the last forty years, it is not within the scope of this chapter to assemble all existing methods. Many empirical correlations can be found in the literature. Some of them, concerning soil dynamics and earthquake geotechnical engineering, are mentioned below. The emphasis is also put on methods which allow the direct evaluation of dynamic soil behaviour.

Measurement of G_{max}

Instead of using geophysical tests, Campanella et al. (1986) proposed a new method, the seismic cone penetration test, for determining the maximum shear modulus. Small geophones are incorporated to the cone, and measure the shear wave velocity resulting from an impact at the soil surface. This method is less expensive than down-hole tests (Lunne et al. 1997). Two penetrometers installed in parallel can also perform tests equivalent to the cross-hole method. Small strain damping ratio can also be calculated.

Stiffness degradation estimation

Pressuremeter tests can be used to obtain stiffness at different strain levels (Houlsby 1998), i.e. when the modulus non linearly decreases with increasing strains, which is called stiffness degradation phenomenon. Self-boring pressuremeter and full displacement pressuremeter (more adapted to clay or silt than sand), if equipped with displacement sensors, are suitable for evaluating G_{sec} at different strain amplitude. Another technique, described by Lunne et al. (1997), is the cone pressuremeter which allows as well to measure the shear modulus from unloading-reloading loops. In this test, the interpretation is more complicated with sand because of the difficulty to handle dilative frictional material (Houlsby 1998).

Liquefaction resistance

Correlations between cyclic strength and SPT penetration resistance is referred to since thirty years. The cyclic stress ratio which causes liquefaction is related to the number of SPT blowcount N_I. These correlations (Seed et al. 1985) are presented as curves limiting a sensitive area; for example the curve drawn in (Fig. A1-4) is the right boundary of points related to soils which had liquefied under real earthquakes, named field performance data. More recently, such correlations also were also produced for residual shear strength of liquefied soils (Idriss & Boulanger 2007).

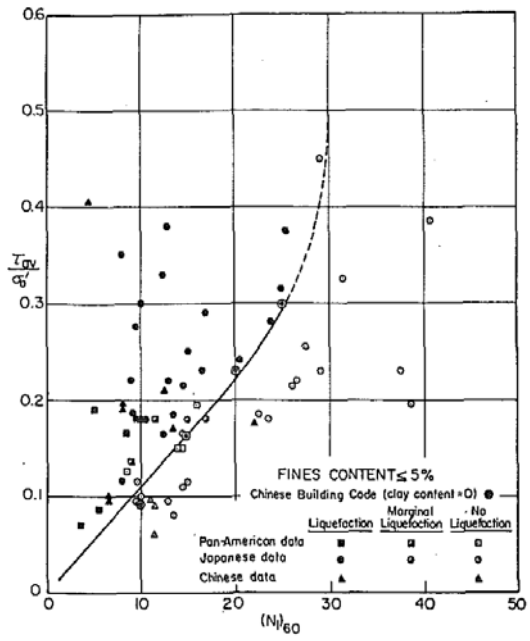

Fig. A1-4. Correlation between cyclic strength and N_I value of SPT for clean sands (Seed et al. 1985).

Liquefaction evaluation by CPT data is also possible (Lunne et al. 1997). The same kind of chart as (Fig. A1-4) gives the correlation between the normalized cone resistance and the shear stress ratio. The effect of fine content can be incorporated to the correlations.

An in situ test, which induces and measures liquefaction, has recently been developed for research purpose (Cox et al. 2009). A strong horizontal excitation is created at the soil surface by a specifically equipped vehicle. It generates shear waves travelling downward into the soil. The response of the soil layer is recorded by four «liquefaction sensors», which measure static and dynamic pore pressure, acceleration and tilt. As a result, the liquefaction process of a sand layer can be analysed in situ. Simpler methods, based on blasting performed in situ, can provide insight into liquefaction-induced settlement (Hatzor et al. 2009).

The in situ state of sandy soil can be identified along the soil profile by a range of in situ tests. Ground water conditions, density, grain size, fine content, shear wave velocity are parameters important for liquefaction potential assessment which can be measured in situ. If these tests reveal that the area is prone to liquefaction, and if the hazard level is high, sampling and laboratory tests on undisturbed soil is mandatory.

A1.3 Sumary and remarks

In situ methods for determining soil parameters for dynamic soil behaviour, and in particular for seismic applications, were briefly described. The investigation of a sensitive site for implementing earthquake resistant design usually requires to use a combination of these techniques, and also to perform complementary laboratory tests.

Geophysical methods gather various possibilities to investigate areas with different characteristics. Most of them allow to determine elastic moduli, which are then very usefull to calibrate geotechnical models. For example, the linear equivalent method, used in Chapter 7, requires both P wave and S wave velocities.

Among the many existing in situ tests, it is possible to find applications to various parts of geotechnical earthquake engineering. Besides the determination of elastic moduli, some methods focus on the determination of soil parameters in the nonlinear regime, and others on the assessment of liquefaction susceptibility. The dynamic laboratory tests presented in chapter 4 also provide this kind of identification of mechanical soil properties.

APPENDIX 2

DETERMINATION OF DEVIATORIC AND CONFINING STRESSES FROM SEISMIC ACCELERATION RECORDINGS

A2.1 Earthquake acceleration time histories

The chosen earthquake is the San Simeon earthquake, which occurred in California on December 22nd 2003. Acceleration recording data are provided by COSMOS Virtual Data Center (http://db.cosmos-eq.org/scripts/default.plx). It was obtained at Coalinga fire station (USGS station 1747) placed at 82.5 km from the epicentre. The station is placed on a rock geological site. The peak ground acceleration (PGA) of the North-South component (NS) is equal to 27.6 cm/s^2 and 15.9 cm/s^2 for the Up-Down or vertical component (UP). The depth of the earthquake is 7.6 km. Its moment magnitude is Mw = 6.5. The acceleration recordings used for obtaining stress evolution are given in Fig. A2-1.

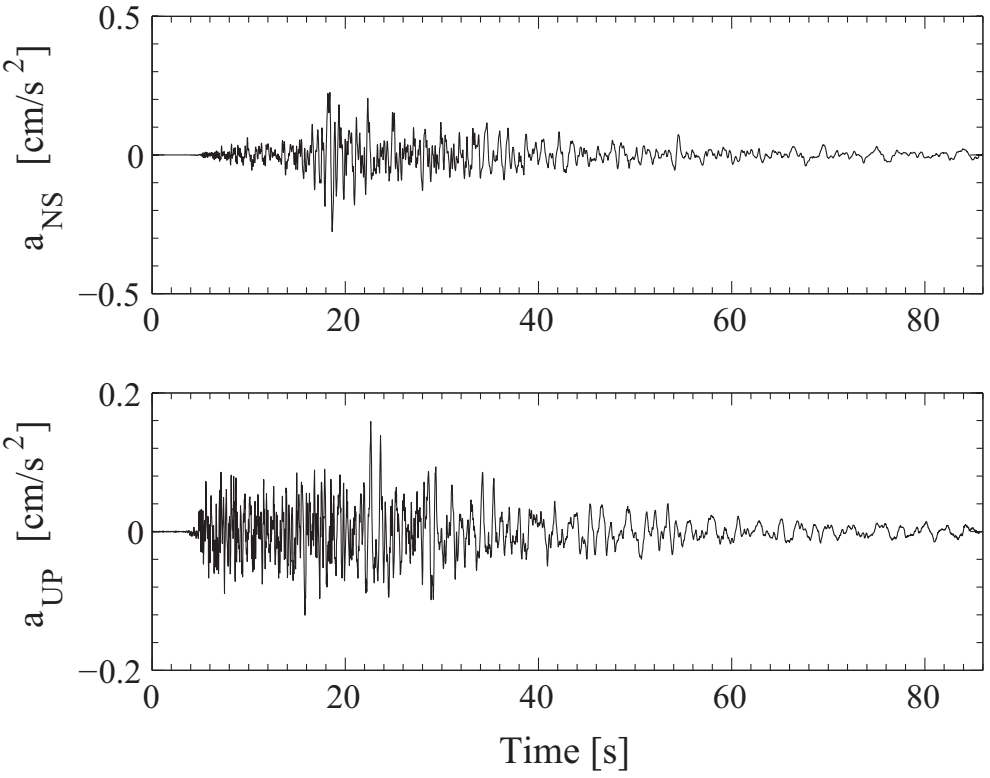

Fig. A2-1. Acceleration recordings of San Simeon earthquake: North-South and Up-Down components.

A2.2 Deconvolution method

To obtain the evolution of stresses at a certain depth, in triaxial conditions, the procedure proposed here is an advanced technique based on the modelling of a soil layer and a deconvolution method (explained for example by Kramer 1996). The CyberQuake software provides back analyses of the accelerogram recordings. Contrary to the usual method proposed by Seed & Idriss (1971) (cf. section 2.9), the deconvolution method can take into account the three acceleration recordings (two in perpendicular horizontal directions and one in the vertical direction). All components of the input motion are taken

into account simultaneously, i.e. there is no decomposition into SH-P / SV wave propagation (Bernardie et al. 2006). The calculation provides total stresses at mid height of the layer. Two perpendicular horizontal shear stresses, and the normal stress can be calculated at each time step. With the finite element computation, there is no coupling between the three axis motions. The component σ_0 is integrated from the vertical acceleration only, and the horizontal shear stresses from the North-South and East-West acceleration components. A true triaxial apparatus would be required to use these 3D data.

In the axisymmetric triaxial apparatus, only one shear plane can be controlled. That is why the calculation using CyberQuake is performed in bidirectional conditions, with one horizontal acceleration a_{NS} and the vertical acceleration a_{UP}. The input parameters of the model are summarized in Tab. A2-1. The geometry of the soil layer and the elastic parameters of sand were assumed to obtain relevant results.

The result of the deconvolution method is a horizontal shear stress component τ_{NS} and a vertical normal total stress σ_0, both evolving with time. These values are shown for the San Simeon earthquake, at 10 m depth, in Fig. A2-2. The weight of the soil column is not taken into account in the σ_0 value.

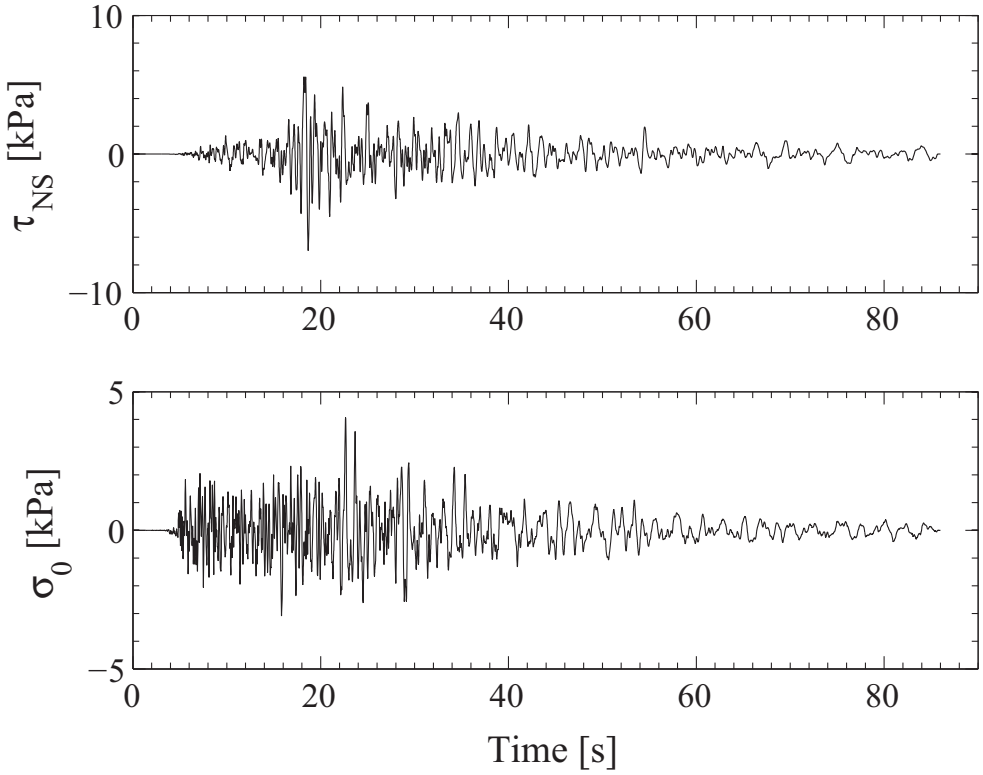

Fig. A2-2. Stresses obtained by the deconvolution method.

Tab. A2-1. Model parameter for CyberQuake deconvolution method

Parameter	Value	Unit
Time step	0.005	s
Cut-off frequency	10	Hz
ρ	2700	kg/m^3
c_p	358	m/s
c_s	192	m/s
Numerical damping	12	%
Layer thickness	20	m
Bedrock	rigid	

A2.3 Calculation of equivalent seismic deviatoric stress and confining pressure as function of time

The assumption of initial stress isotropy allows to calculate the principal stresses, σ_1 and σ_3. The Fig. A2-3 shows the Mohr plane, which geometrically explains the calculation of $q(t)$ and $\sigma_3(t)$. The principal stresses rotate at 90° when the shear stress becomes negative. The value σ_0 here takes into account the overburden stress: at a depth of 10 m, 207 kPa is added to the irregular normal stress.

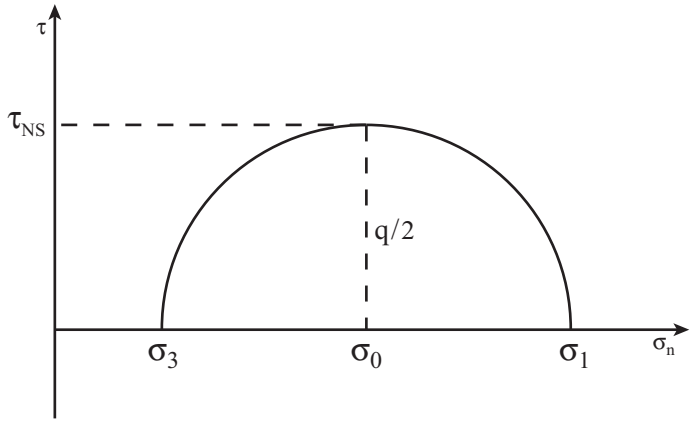

Fig. A2-3. Calculation of the total principal stress in the soil layer

As the PGAs of both acceleration time histories are low, the values of stress calculated by the deconvolution method are below the target stresses, not yet in the nonlinear regime. The choice of an amplification factor of 10 gives values of σ_1 and σ_3 closer to the tests that we had performed previously. The signals, for the San Simeon earthquake, are given in Fig. A2-4. The maximum deviatoric stress amplitude is 139.3 kPa, it arbitrarily arises in extension in this case. The maximum amplitude of σ_3 is 73.3 kPa, on the side of higher stresses.

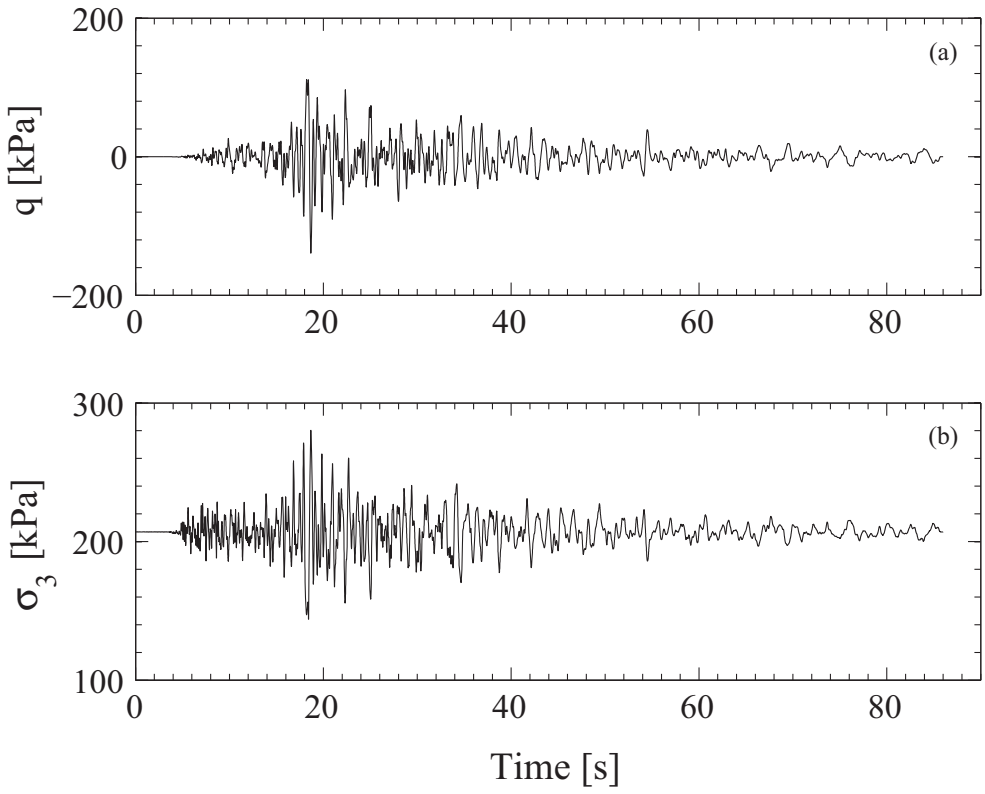

Fig. A2-4. Time histories of the deviatoric stress (a) and confining pressure (b) used for bidirectional irregular loading.

A2.4 Restrictions of the method for obtaining irregular loadings

The choice of amplifying the signal for convenience is not inconsequential. Earthquakes are not totally randomly distributed, in terms of frequency content and amplitude. Indeed a strong earthquake will have lower frequencies; the distance to the source is also important: the low frequency content decreases at higher distance from the source. As the aim is not to represent an engineering problem here, but to analyse a theoretical case based on plausible data, it is nonetheless assumed that this amplification of the signal is not a major issue.

Moreover the obtained stress time histories at mid-height of the soil layer do not correspond to any real site geology. The deconvolution method is applied assuming a linear sand of a given layer thickness.

It is thus reminded that the loading previously defined is only a theoretical case, and does not pretend to be related to any real field data.

APPENDIX 3

ADDITIONAL RESULTS:

MODELLING OF AN UNDRAINED CYCLIC TEST WITH THE ELASTOPLASTIC MODEL

The laboratory test CYC2 on Leman Sand (chapter 4) is used to calibrate the Hujeux elastoplastic model by curve fitting. Both the model and the experimental data are stress-controlled, with a constant amplitude Δq = 40 and 70 kPa for the first and second steps (Fig. A3-1a and b).

In overall, the first step (part (a) of Fig. A3-1 to Fig. A3-5), subjected to limited stiffness degradation, is well reproduced by the model. The amplitudes of ε_1 and u_r, the values of G_{sec} match very well. The mean value of ε_1 is not so accurate, because the shift to the side of extension is not reproduced in this step. The rate of increase of u_r is slightly underestimated, which is visible on the effective stress path.

The second step (part (b) of Fig. A3-1 to Fig. A3-5) is not accurate in terms of strain amplitude (which increased a lot during the triaxial test), but the increase of the pore pressure ratio is satisfactory. The spikes of u_r have an amplitude similar to the experimental curve. Cyclic liquefaction is thus partly well modelled.

On the other hand, the match between experimental and numerical values of $\Delta\varepsilon_q$ vs. N (Fig. A3-6), of u_r vs. $\Delta\varepsilon_q$ (Fig. A3-7), of the secant shear modulus (Fig. A3-8 and Fig. A3-9), is very good. Damping ratio (Fig. A3-10) is underestimated.

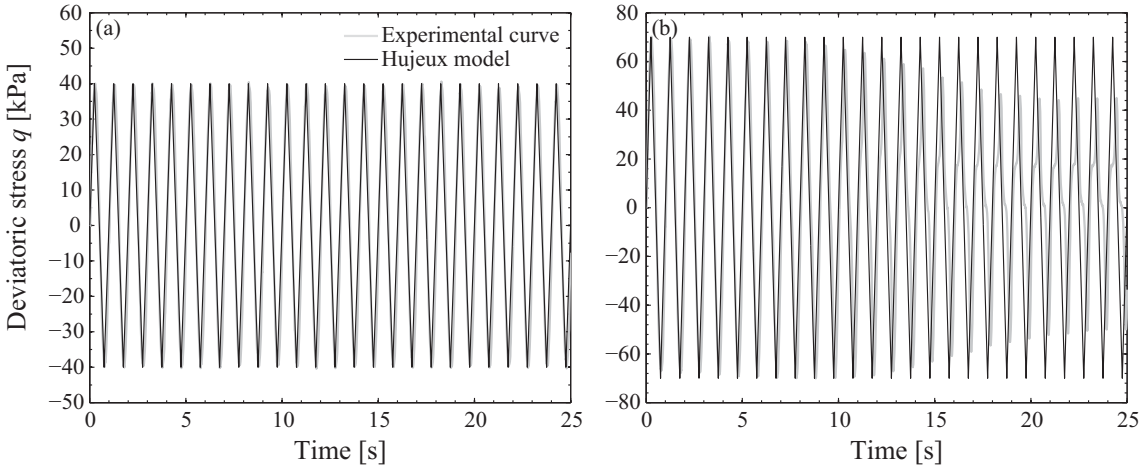

Fig. A3-1. Stress loading of CYC2, step 1 (a) and step 2 (b).

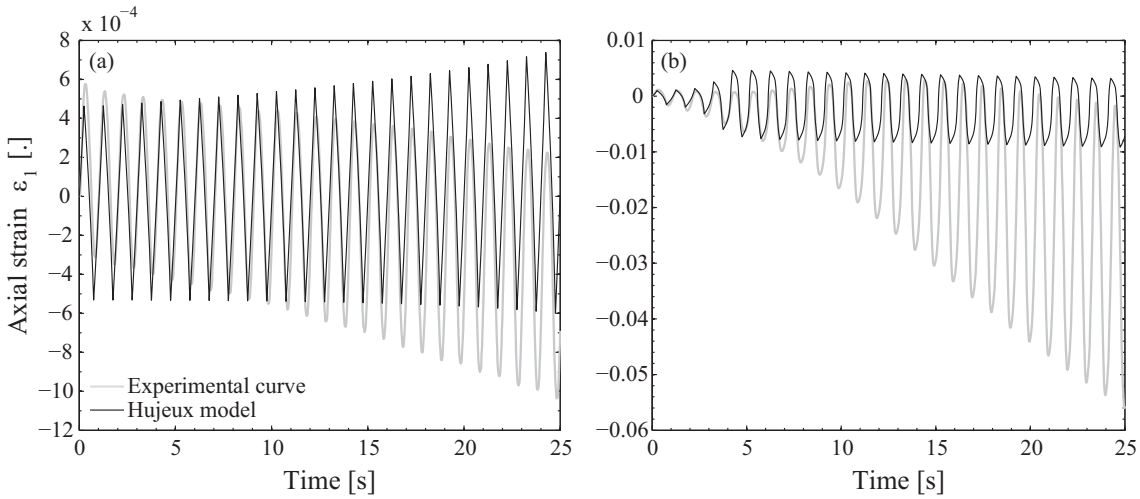

Fig. A3-2. Axial strain induced in CYC2.

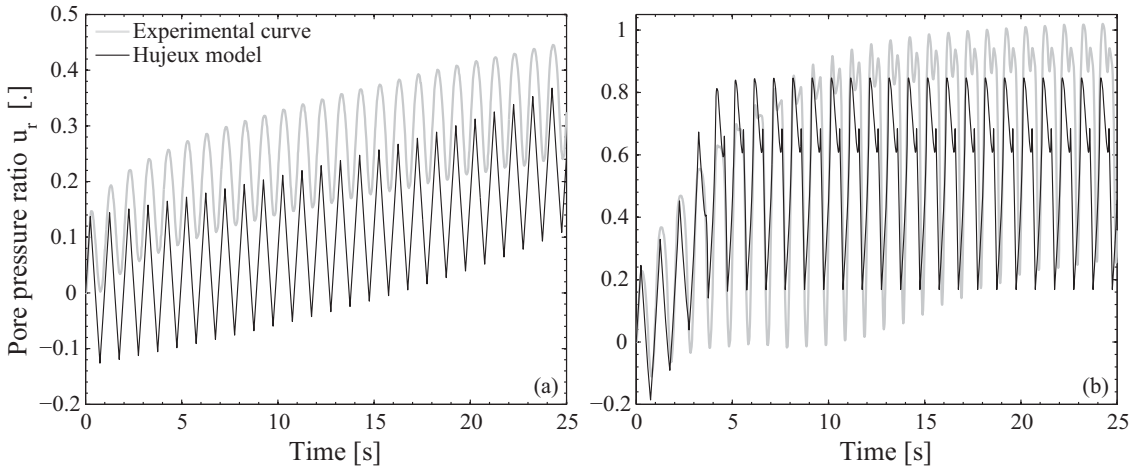

Fig. A3-3. Pore water pressure induced in CYC2.

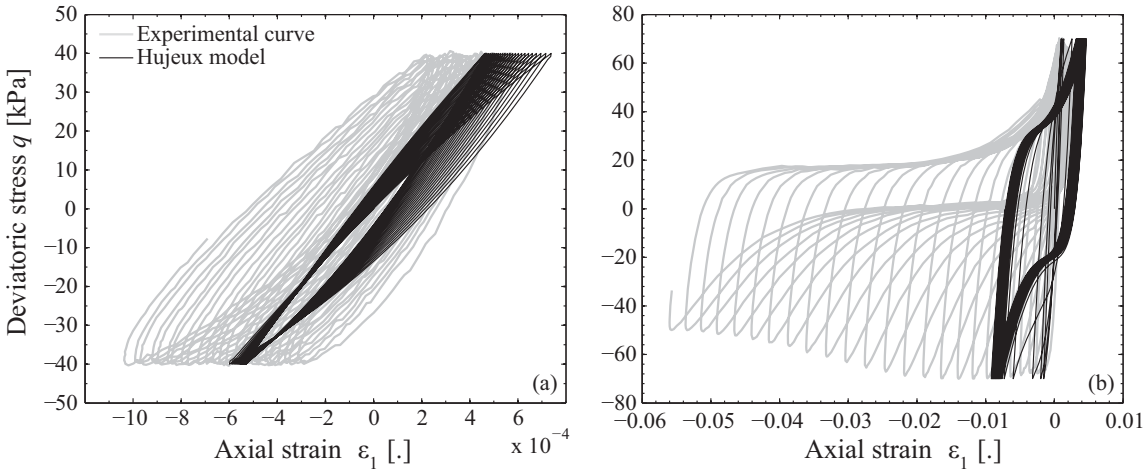

Fig. A3-4. Stress-strain relation in CYC2.

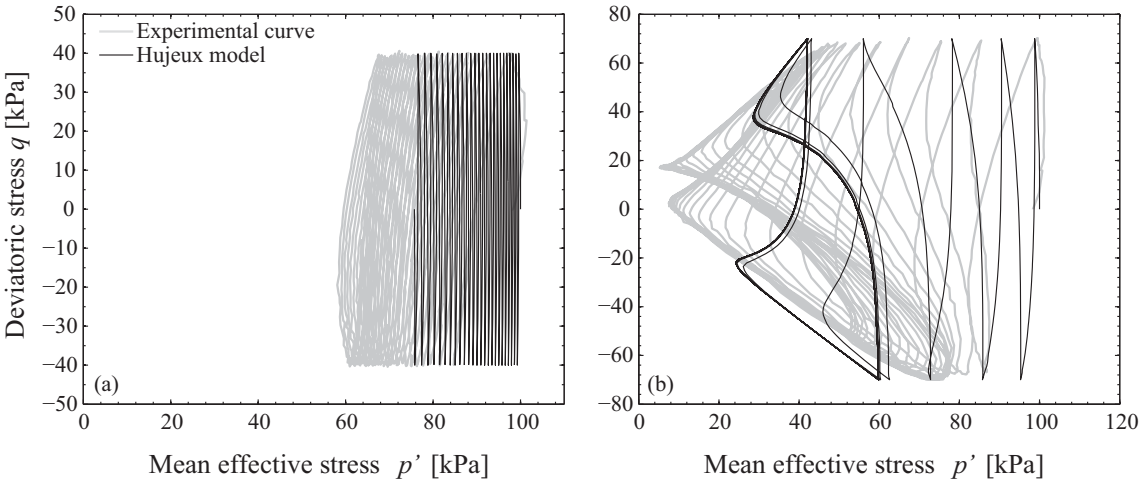

Fig. A3-5. Effective stress path of CYC2.

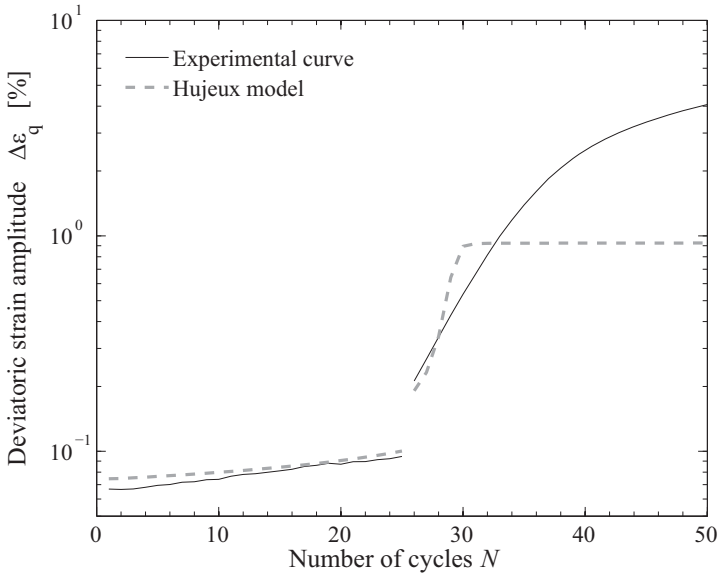

Fig. A3-6. Evolution of the deviatoric strain amplitude during CYC2.

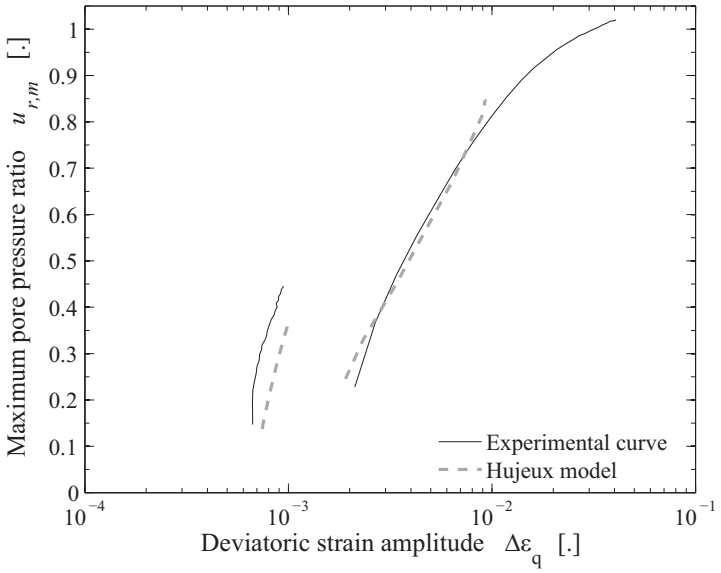

Fig. A3-7. Relation between the pore pressure and the deviatoric strain amplitude in CYC2.

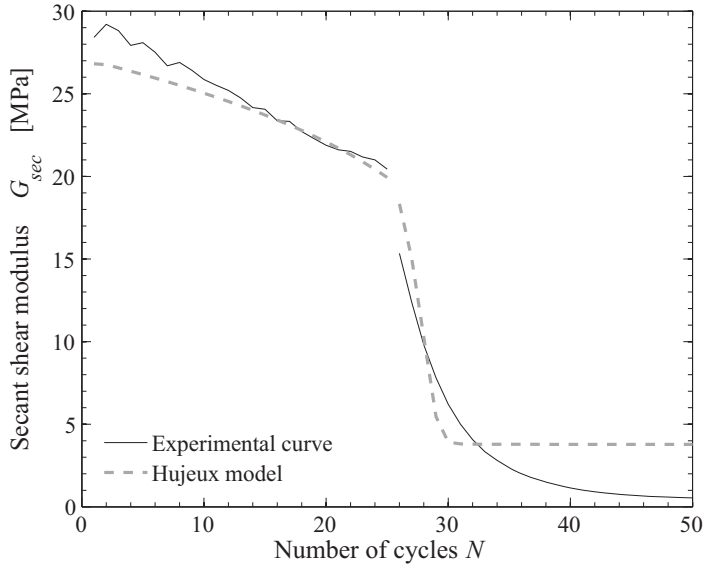

Fig. A3-8. Evolution of the secant shear modulus in CYC2.

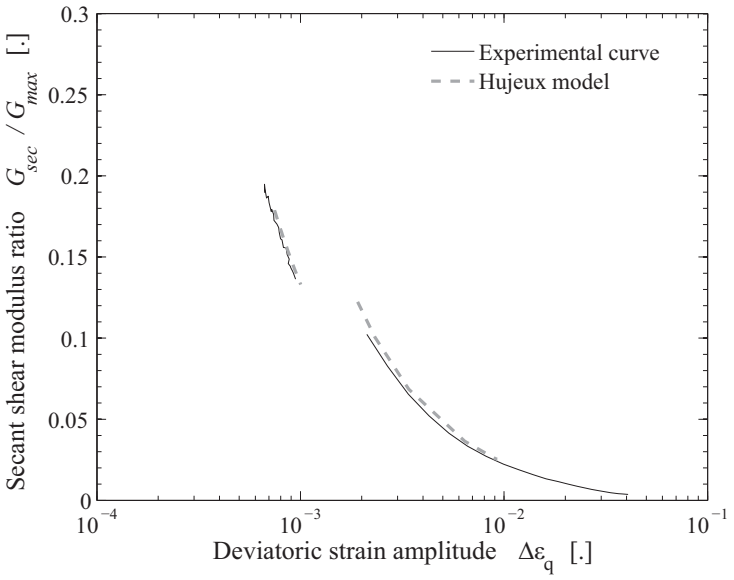

Fig. A3-9. Stiffness degradation curve in CYC2.

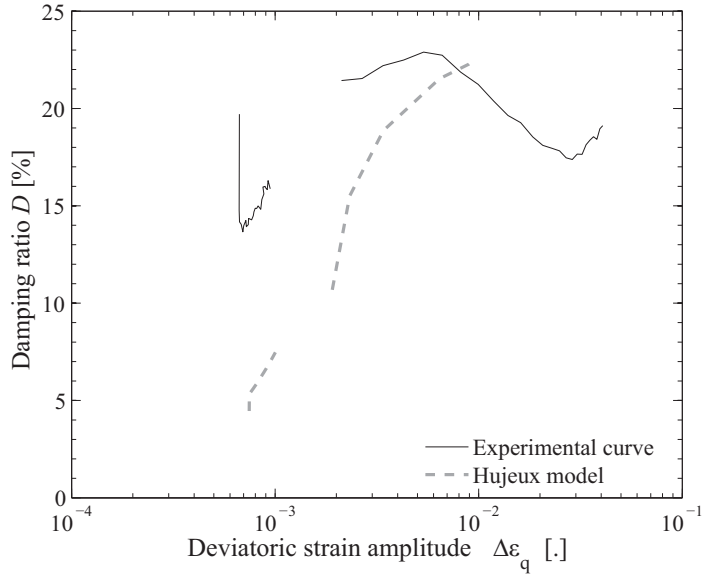

Fig. A3-10. Damping ratio vs. deviatoric strain amplitude in CYC2.

EMILIE RASCOL

AVENUE WARNERY 10, 1007 LAUSANNE, SUISSE
E-MAIL: EMILIERASCOL@HOTMAIL.COM
TELEPHONE: 078 637 80 47

NATIONALITE FRANCAISE
NEE LE 3 JUIN 1982
HTTP://PERSONNES.EPFL.CH/EMILIE.RASCOL

RESUMÉ DES QUALIFICATIONS:

- Doctorat EPFL en géotechnique.
- Ingénieure civil diplômée de l'Ecole Centrale Nantes.
- Mécanique et dynamique des sols, hydrologie, hydraulique : tests en laboratoire et modélisation numérique.
- Génie parasismique : propagation d'ondes sismiques, effets de sites, comportement dynamique des structures.

FORMATION

Doctorat - Ecole doctorale de Mécanique Laboratoire de Mécanique des Sols	2006 - 2009	**Ecole Polytechnique Fédérale de Lausanne** http://lms.epfl.ch/
Master Recherche Mécanique appliquée pour le Génie Civil - Classée 1ère	2004 - 2005	**Ecole Centrale Nantes (ECN), France** www.ec-nantes.fr
Ingénieure Génie Civil et Environnement Master Professionnel	2002 - 2005	**Ecole Centrale Nantes (ECN), France** www.ec-nantes.fr
Cours préparatoires pour le concours d'entrée aux grandes écoles françaises filière MP (Matières principales: Maths, Physiques, Chimie)	2000 - 2002	Lycée Saint-Louis, Paris, France
Baccalauréat scientifique option mathématiques Mention Bien	1997 - 2000	Lycée E. Branly, Nogent-sur-Marne, France

EXPERIENCE PROFESSIONELLE ET ACADEMIQUE

Laboratoire de Mécanique des Sols, EPFL, Lausanne **Avril 2006 – Décembre 2009**

Recherche de doctorat : **Cyclic Properties of Sand: Dynamic Behaviour for Seismic Applications**
Directeur de thèse : **Prof. Laurent Vulliet** - BG Ingénieurs Conseils - Laboratoire de Mécanique des Sols, EPFL.

- Définition et conduite de tests de laboratoire - tests triaxiaux dynamiques monotones, cycliques et chargements sismiques.
- Développement d'un appareil de mesure sans contact, basé sur de la triangulation par laser, pour mesurer les déformations radiales en continu pendant un chargement triaxial cyclique.
- Programmation d'un post-processeur Matlab pour traiter les résultats des tests, en incluant le module de cisaillement et le coefficient d'amortissement.
- Simulation des résultats expérimentaux avec un modèle linéaire équivalent et un modèle élastoplastique adapté aux chargements cycliques et sismiques.
- Encadrement d'un projet de Master.

Assistante responsable du cours de Mécanique des Sols, EPFL, Lausanne **Avril 2006 – Avril 2009**

Pour le Bachelor EPFL, section Génie Civil et le Master ELSTE (UNIL, section Géophysique). Définition et correction des exercices et des applications numériques, notation des examens écrits, logistique des documents du cours.

LCPC, Nantes (6 mois) et Karlsruhe Universität (1.5 mois) **Avril 2005 – Novembre 2005**

Travail de Master : Etude de l'infiltration de la nappe phréatique dans les réseaux d'assainissement

- Modélisation hydrologique d'un basin versant urbain à l'aide d'un système d'information géographique (MapInfo)-Application à Nantes
- Modélisation hydraulique de l'infiltration de la nappe dans les canalisations des réseaux d'assainissement

Bouygues, DV Construction, Bordeaux **Juin 2004 – Septembre 2004**

Stage d'ingénieur au département des Méthodes sur le chantier "Laser Mégajoule" pour le Commissariat à l'Energie Atomique

- Détermination et dessin des processus de construction de la zone centrale d'expérimentation

LANGUES

- Français : Langue maternelle
- Anglais : Courant
- Allemand : Niveau moyen
- Espagnol: Connaissances de base

COMPETENCES IT

- Outils scientifiques de modélisation numérique : Matlab, CESAR-LCPC, CyberQuake et Z-Soil (éléments finis), GEO-SLOPE (stabilité de pentes), Robot (structures), MapInfo (Systèmes d'Information Géographiques), Feflow (hydrogéologie), SolidWorks, AutoCAD.
- Maîtrise l'environnement Office, ainsi que les logiciels d'édition et de design: Adobe FrameMaker, Illustrator et Photoshop.

ACTIVITES EXTRA-PROFESSIONNELLES

- Aime les sports de montagne (escalade, snowboard, randonnée) et d'endurance (course à pied, natation).
- A participé, depuis l'enfance, à des compétitions dans de nombreux sports (par exemple judo et aviron).
- Apprécie la photographie, pratiquée surtout à l'occasion de voyages en Europe et en Asie (Japon, Inde, Indonésie).
- Intéressée par différents aspects des cultures européennes : cinéma, peinture, architecture, et littérature par-dessus tout.

COMMUNICATION SCIENTIFIQUE

Articles de journaux et de conférences

E. Rascol, L. Vulliet, 2009. **Frequency effects in natural sand under cyclic loading**. Canadian Geotechnical Journal, en révision.

E. Rascol, L. Vulliet, 2009: **Characterization of natural sand under complex dynamic loading**. *In*: Performance-Based Design in Earthquake Geotechnical Engineering, *p.* 1505-1513, CRC Press/Balkema, Taylor & Francis Group, London.

S. Vecchiato, E. Rascol, W.-J. Zwanenburg, 2009: **Earthquake protection for high-speed rail traffic: risky business?** *In*: Safety and Security Engineering III, *p.* 507-516, WIT Press, Southampton. doi: 10.2495/SAFE090471. En coopération avec le LITEP (Laboratoire d'Intermodalité des Transports et de Planification), EPFL.

Présentations à des conférences et séminaires

E. Rascol, L. Vulliet: **Characterization of natural sand under complex dynamic loading**. *In* IS Tokyo, International conference on Performance-Based Design in Geotechnical Earthquake Engineering, 15-18 Juin 2009, Tokyo, Japon.

E. Rascol: **Soil dynamics testing under seismic loading conditions**. Seminar on Geomechanics, Underground Construction and Environment, 8 - 10 Décembre 2008, EPFL, Lausanne.

E. Rascol: **Soil Dynamics**. Geomechanics research discussions, 21 Février 2008, EPFL, Lausanne.

E. Rascol, L. Vulliet: **Frequency effect for the Leman Sand under complex stress paths**. ALERT Geomaterials, 10 Octobre 2007, Aussois, France.

E. Rascol: **Comportement non linéaire des sols granulaires sous chargements cycliques complexes**. ROSOL meeting, 20 Novembre 2007, EPFL, Lausanne.

Posters

E. Rascol, L. Vulliet: **Dynamic non-contact measurement of radial strain during triaxial cyclic loading**. ALERT Geomaterials, 6-8 Octobre 2008, Aussois, France.

E. Rascol: **Comportement dynamique du sable sous chargement sismique**. Women of Sciences exhibition, 8 Avril 2008, EPFL, Lausanne.

E. Rascol, L. Vulliet: **Complex dynamic stress paths response of Leman Sand**. ALERT Geomaterials, 8-10 Octobre 2007, Aussois, France.

E. Rascol: **Dynamic behaviour of granular soils under strong and fast earthquake loading**. EPFL Research day, 16 Novembre 2006, Lausanne.